



**HAL**  
open science

# Réduction catalytique sélective des oxydes d'azotes par l'ammoniac : cinétique, mécanisme et modélisation du système cuivre Chabazite

Guillaume Pétaud

► **To cite this version:**

Guillaume Pétaud. Réduction catalytique sélective des oxydes d'azotes par l'ammoniac : cinétique, mécanisme et modélisation du système cuivre Chabazite. Catalyse. Université de Lyon, 2019. Français. NNT : 2019LYSE1230 . tel-03336141

**HAL Id: tel-03336141**

**<https://theses.hal.science/tel-03336141>**

Submitted on 7 Sep 2021

**HAL** is a multi-disciplinary open access archive for the deposit and dissemination of scientific research documents, whether they are published or not. The documents may come from teaching and research institutions in France or abroad, or from public or private research centers.

L'archive ouverte pluridisciplinaire **HAL**, est destinée au dépôt et à la diffusion de documents scientifiques de niveau recherche, publiés ou non, émanant des établissements d'enseignement et de recherche français ou étrangers, des laboratoires publics ou privés.

N°d'ordre NNT : xxx



## **THESE de DOCTORAT DE L'UNIVERSITE DE LYON**

opérée au sein de  
**l'Université Claude Bernard Lyon 1**

**Ecole Doctorale N° 206**  
**(Ecole Doctorale de Chimie de Lyon)**

**Spécialité de doctorat : Chimie**  
**Discipline : Catalyse**

Soutenue publiquement le 07/11/2019, par :  
**Pétaud Guillaume**

---

# **Réduction catalytique sélective des oxydes d'azotes par l'ammoniac : cinétique, mécanisme et modélisation du système cuivre Chabazite**

---

Devant le jury composé de :

Briançon Stéphanie	Professeur des Universités Université de Lyon 1	Examinatrice
Brilhac, Jean-François	Professeur des Universités UHA Haute-Alsace	Rapporteur
Delahay, Gérard	Directeur de Recherche ENSC Montpellier	Rapporteur
Iojoiu, Eduard Emil	Ingénieur Renault Trucks-Volvo	Examineur
Schweitzer, Jean-François	Ingénieur Institut Français du Pétrole et Energies Nouvelles	Examineur
Giroir-Fendler, Anne	Professeure des Universités Université Lyon 1	Directrice de thèse
Gil Villarino, Sonia	Maître de Conférence Université de Lyon 1	Co-Directrice de thèse
Tayakout Fayolles, Mélaz	Professeure des Universités Université de Lyon 1	Co-Directrice de thèse



# UNIVERSITE CLAUDE BERNARD - LYON 1

## Président de l'Université

**M. François-Noël GILLY**

Vice-président du Conseil d'Administration

M. le Professeur Hamda BEN HADID

Vice-président du Conseil des Etudes et de la Vie Universitaire

M. le Professeur Philippe LALLE

Vice-président du Conseil Scientifique

M. le Professeur Germain GILLET

Secrétaire Général

M. Alain HELLEU

## ***COMPOSANTES SANTE***

Faculté de Médecine Lyon Est – Claude Bernard

Directeur : M. le Professeur J. ETIENNE

Faculté de Médecine et de Maïeutique Lyon Sud – Charles Mérieux

Administrateur provisoire : M. le Professeur G. KIRKORIAN

UFR d'Odontologie

Directeur : M. le Professeur D. BOURGEOIS

Institut des Sciences Pharmaceutiques et Biologiques

Directeur : Mme la Professeure C. VINCIGUERRA.

Institut des Sciences et Techniques de la Réadaptation

Directeur : M. le Professeur Y. MATILLON

Département de formation et Centre de Recherche en Biologie Humaine

Directeur : M. le Professeur P. FARGE

## ***COMPOSANTES ET DEPARTEMENTS DE SCIENCES ET TECHNOLOGIE***

Faculté des Sciences et Technologies

Directeur : M. le Professeur F. De MARCHI

Département Biologie

Directeur : M. le Professeur F. FLEURY

Département Chimie Biochimie

Directeur : Mme le Professeur H. PARROT

Département GEP

Directeur : M. N. SIAUVE

Département Informatique

Directeur : M. le Professeur S. AKKOUCHE

Département Mathématiques

Directeur : M. le Professeur A. GOLDMAN

Département Mécanique

Directeur : M. le Professeur H. BEN HADID

Département Physique

Directeur : Mme S. FLECK

Département Sciences de la Terre

Directeur : Mme la Professeure I. DANIEL

UFR Sciences et Techniques des Activités Physiques et Sportives

Directeur : M. C. COLLIGNON

Observatoire de Lyon

Directeur : M. B. GUIDERDONI

Polytech Lyon

Directeur : M. P. FOURNIER

Ecole Supérieure de Chimie Physique Electronique

Directeur : M. G. PIGNAULT

Institut Universitaire de Technologie de Lyon 1

Directeur : M. C. VITON

Institut Universitaire de Formation des Maîtres

Directeur : M. R. BERNARD

Institut de Science Financière et d'Assurances

Directeur : Mme la Professeure V. MAUME-DESCHAMPS



# REMERCIEMENTS

Mes remerciements se dirigent tout d'abord vers Mme Catherine Pinel ainsi que Stéphanie Briançon pour m'avoir permis d'effectuer mes travaux de thèse au sein de leurs laboratoires respectifs : l'IRCELYon et le LAGEPP.

Je remercie profondément chacun des membres rapporteurs de cette thèse, Mr Gérard Delahay et Mr Jean François Brilhac, pour leur temps consacré à l'évaluation de ces travaux et l'intérêt porté au sujet. Je remercie également Mme Stéphanie Briançon, Mr Eduard Emil Iojoiu et Mr Jean-Marc Schweitzer d'avoir accepté de participer à ce jury et de participer à l'examen de cette étude avec sincérité.

Je remercie particulièrement Anne Giroir-Fendler, directrice de ces travaux, reconnaissant de m'avoir donné la possibilité d'exprimer ma curiosité et ma créativité au service d'un sujet de recherche me tenant à cœur, avec une grande liberté dans la conduite de mon sujet de thèse. Je profite aussi de l'occasion pour vous remercier de m'avoir accepté en stage IUT il y a de cela maintenant 7 ans, premier véritable stage scientifique m'ayant dès lors, mis la puce à l'oreille.

Un stage qui me donna une première occasion de découvrir le monde de la recherche, encadré par des personnes passionnées par leur métier, dont une en particulier : Mme Sonia Gil Villarino, post-doctorante alors, m'ayant accompagnée avec une grande sympathie tout au long de cette période de découverte. 7 années plus tard, ce sont la maîtresse de conférence et son thésard qui partagent toujours cette même sympathie, créant une atmosphère unique de travail propice à un plein épanouissement. Muchas gracias por todo Soni.

Cette thèse fut également dirigée par Mme Méla Tayakout-Fayolles à qui je dois énormément et aux côtés de qui j'ai beaucoup appris, m'ayant permis de concrétiser la liaison catalyse et génie des procédés au sein de mon projet de thèse. Une profonde gratitude pour m'avoir laissé largement profiter de votre rigueur ainsi que de votre patience mais aussi pour m'avoir partagé votre enthousiasme.

Je souhaite également remercier toutes les personnes avec qui j'ai pu échanger au cours de ces travaux, des responsables et personnels des services analyses de l'IRCELYon jusqu'aux équipes de recherches constituant l'institut dont notamment l'équipe CARE. Je souhaite à cette équipe, quel que soit son évolution dans le temps, de continuer à transmettre sa chaleureuse ambiance et ses valeurs auprès des jeunes chercheurs, ce qui est en très bonne voie au regard des nouveaux permanents en poste. Je tiens à remercier l'équipe DYCO du LAGEPP pour leur enrichissantes discussions aux grandes qualités scientifiques, merci Isabelle et Françoise de vos conseils avisés ainsi que de votre attention à mes travaux.

Un GRAND merci à tous mes voisins de bureaux, les post-doc motivés (*Calimera !*), les grands post-doc (*Hello Mrs Browning !*) et les post doc qui étaient dans d'autres bureaux bien entendu, Jesus, Diego, Marc, David, ... avec qui d'excellents moments furent passés et d'autres sont à venir encore. Merci aussi à mes camarades de thèse, Paolita, Thomas, Marième, Géraldine, Alvaro, Weidong, Maelenne... la fine fleur des labos à qui je souhaite une pleine réussite dans leur fraîche aventure en tant que docteur.

Je terminerai enfin par une pensée particulière pour ma famille m'ayant soutenue tout au long de mes études.

# CONTENTS

Nomenclature.....	ix
<b>General Introduction.....</b>	<b>1</b>
<b>Chapter 1</b>	
Bibliographic study .....	4
<b>I-1. La pollution atmosphérique change d'ordre de grandeur : du contexte historique déterminant jusqu'aux cibles de l'étude.....</b>	<b>4</b>
<b>I-2. Moteurs du progrès des technologies de post-traitement : les normes et contrôles.....</b>	<b>7</b>
<b>I-3. Tests en laboratoire versus mesures en conditions réelles. ....</b>	<b>11</b>
<b>I-4. La formation des polluants.....</b>	<b>15</b>
<b>I-5. Technologies de post traitements actuels.....</b>	<b>21</b>
<b>I-6. Les procédés de réduction catalytique sélective (SCR) : cahier des charges et innovations technologiques .....</b>	<b>26</b>
I-6.1. Le réducteur : L'ammoniac (NH <sub>3</sub> ) .....	26
I-6.2. Les catalyseurs développés en NH <sub>3</sub> -SCR .....	28
I-6.2.1. Catalyseur à base d'oxydes de Vanadium et Tungstène : .....	28
Fonctionnement et limites.....	28
I-6.2.2. Catalyseurs zéolitiques supportant un métal de transition (Cu et/ou Fe) des MFI aux CHA.....	30
I-6.2.3. Vieillessement du catalyseur .....	43
<b>I-7. Vers l'établissement d'un modèle cinétique .....</b>	<b>45</b>
I-7.1. Résumé des réactions impliquées et divergences de mécanisme réactionnels .....	45
I-7.2. Mécanismes et modèles du processus de NH <sub>3</sub> SCR proposés dans la littérature .....	50
I-7.2.1. "Global kinetic modeling of hydrothermal aging of NH <sub>3</sub> -SCR over Cu-zeolites" Supriyanto et al. (2015) : Modèle global [225] .....	52
I-7.2.2. "Development and validation of a two sites kinetic model for NH <sub>3</sub> -SCR over Cu-SSZ-13. Part 1 Detailed global kinetic development based on mechanistic considerations" Daya et al. (2018) : Modèle semi-détaillé [233] .....	54
I-7.2.3. "Unified mechanistic model for Standard SCR, Fast SCR, and NO <sub>2</sub> SCR over a copper chabazite catalyst" Bendrich et al. (2018) : Modèle détaillé [216] .....	55
<b>I-8. Conclusion and Thesis objective.....</b>	<b>57</b>
I-8.1. Conclusion .....	57
I-8.2. Thesis objective and outlines.....	58

## Chapter II

Materials & Methods.....	63
<b>II-1.</b> Introduction.....	63
<b>II-2.</b> Catalysts preparation.....	63
<b>II-3.</b> Physico-chemical and textural catalyst characterizations.....	65
II-3.1. Inductively Coupled Plasma Optical Emission Spectroscopy (ICP-OES).....	65
II-3.2. Dinitrogen adsorption and desorption .....	66
II-3.3. X-Ray Diffraction (XRD) .....	67
II-3.4. Thermogravimetry (TGA) .....	68
II-3.5. Transmission Electron Microscopy (TEM) .....	69
II-3.6. X-Ray Photoelectron Spectroscopy (XPS).....	69
II-3.7. Magic-angle spinning Nuclear Magnetic Resonance (MAS-NMR).....	70
II-3.8. H <sub>2</sub> Temperature Programmed Reduction (H <sub>2</sub> -TPR).....	71
II-3.9. Temperature Programmed Desorption (TPD).....	71
II-3.10. Spectroscopic analysis: Diffuse Reflectance Infrared Fourier Transform spectroscopy (DRIFT).....	73
II-3.10.1 Technical description.....	73
II-3.10.2 Ex-situ and in-situ measurements methods and conditions.....	75
II-3.11. Catalytic performance evaluations.....	78
II-3.11.1 Experimental bench.....	78
II-3.11.2 Operating conditions.....	79
II-3.11.3 Results analysis.....	80
<b>II-4.</b> Conclusion.....	82

## Chapter III

Towards a Catalyst reference for NH <sub>3</sub> -SCR.....	85
<b>III-1.</b> Introduction.....	85
<b>III-2.</b> Properties controlled CHA support and functionalization: .....	
Synthesis and Characterization.....	85
III-2.1. Chemical analysis: ICP measurements.....	86
III-2.2. Calcination step and Phases identifications: TGA and XRD measurements.....	87
III-2.3. Supports and catalysts textural properties: N <sub>2</sub> -adsorption/desorption.....	90
III-2.4. Building unit construction: MAS NMR measurements.....	92
III-2.5. Redox properties: H <sub>2</sub> -TPR measurements.....	95



III-2.6.	Surface sites investigation : Ex-situ DRIFT.....	96
III-3.	Catalytic performances of impregnated catalysts .....	98
III-4.	Conclusion.....	102

## Chapter IV

	Identification of reference catalyst: Active site configuration impacts on SCR performances.....	105
IV-1.	Introduction.....	105
IV-2.	Catalysts synthesis and experimental approaches .....	107
IV-3.	Physico-chemical and redox catalysts characterizations.....	108
IV-3.1.	Chemical and textural properties by ICP and .....	
	N <sub>2</sub> adsorption/desorption measurements .....	108
IV-3.2.	Structure and phase identification by XRD and HR-TEM.....	109
IV-3.2.1.	XRD .....	109
IV-3.2.2.	HR-TEM.....	110
IV-3.3.	Active sites environmental framework determination by MAS NMR and ex-situ DRIFTS experiments. ....	111
IV-3.4.	Investigations of catalysts redox properties: XPS and H <sub>2</sub> -TPR measurements.....	115
IV-3.4.1.	XPS.....	115
IV-3.4.2.	H <sub>2</sub> -TPR.....	116
IV-4.	Surface active sites characterization by NH <sub>3</sub> -TPD and in-situ DRIFTS spectroscopy using NH <sub>3</sub> , CO and NO probe molecules.....	117
IV-4.1.	NH <sub>3</sub> TPD.....	117
IV-4.2.	In-situ NH <sub>3</sub> DRIFT measurements.....	119
IV-4.3.	In-situ CO DRIFT measurements .....	123
IV-4.4.	In-situ NO DRIFT measurements.....	124
IV-5.	Catalytic performances: NH <sub>3</sub> -SCR, NO and NH <sub>3</sub> oxidation reactions. ....	127
IV-6.	Conclusion.....	131

## Chapter V

	NH <sub>3</sub> -SCR behavior investigation of reference catalyst: Kinetic approach and reaction network.....	137
V-1.	Introduction.....	137
V-2.	Kinetic studies on SCR reactions for selected reference catalyst .....	137
V-2.1.	External and internal mass transfer limitations.....	138
V-2.2.	STD SCR tests performance:.....	140

V-2.2.1.	Gas phase reaction.....	140
V-2.2.2.	Partial reaction orders and Activation energy.....	141
V-2.2.3.	Influence of water.....	145
V-2.2.4.	Influence of feed composition on catalytic activity and selectivity .....	147
V-2.2.5.	NH <sub>3</sub> inhibition effect .....	148
V-2.3.	Parallel oxidation: a) NH <sub>3</sub> oxidation reaction .....	150
V-2.4.	Parallel oxidation: b) NO oxidation reaction .....	153
V-2.5.	FAST SCR tests performance .....	156
V-2.6.	Catalyst Cu-SAPO-34-IE stability.....	156
<b>V-3.</b>	Sequenced In-Situ DRIFT STD NH <sub>3</sub> -SCR: Catalyst surface behaviour.....	158
<b>V-4.</b>	Conclusion.....	165

## Chapter VI

<b>PART 1:</b>	Multi-site kinetic model development.....	169
<b>VI-1.</b>	Introduction.....	169
<b>VI-2.</b>	Reactor model.....	170
VI-2.1.	Reactor hydrodynamic behaviour identification.....	170
VI-2.2.	Catalytic bench hydrodynamic: Residence time distribution (RTD).....	174
VI-2.3.	Linear Driving Force approximation.....	178
<b>VI-3.</b>	Kinetic Model .....	182
VI-3.1.	Model Input: NH <sub>3</sub> TPD experiments and Flow reactor measurements.....	182
VI-3.2.	Surface description : H-SAPO-34 & Cu-SAPO-34-IE.....	185
VI-3.3.	Reactions and rate expressions.....	187
<b>VI-4.</b>	Results and discussions.....	194
VI-4.1.	NH <sub>3</sub> and H <sub>2</sub> O adsorption-desorption: R1, R2 and R3.....	194
VI-4.2.	Cu-SAPO-34-IE NH <sub>3</sub> oxidation reactions: R5 and R6.....	198
VI-4.3.	NO oxidation reactions: R7, R9-11.....	201
VI-4.4.	Standard SCR behavior and parallel reactions: R4, R12.....	203
VI-4.5.	Model validation and prediction results.....	211
<b>VI-5.</b>	Characteristic times, parameters correlations and uncertainties intervals: Cu-SAPO-34-IE in STD SCR conditions.....	214
VI-5.1.	Characteristic time and limiting steps.....	214
VI-5.2.	Correlation between estimated parameters.....	219
VI-5.3.	Parameters uncertainties.....	221
<b>VI-6.</b>	Conclusion: Part 1: Multi-site kinetic model development.....	223

Part 2: Model Extension to different catalysts.....	226
<b>VI-7.</b> Introduction.....	225
<b>VI-8.</b> Kinetic model: Cu-SAPO-34-HT and –IMP Surface description .....	225
<b>VI-9.</b> Cu-SAPO-34-HT : One Pot Catalyst .....	227
VI-9.1. NH <sub>3</sub> and H <sub>2</sub> O adsorption-desorption .....	227
VI-9.2. Cu-SAPO-34-HT NH <sub>3</sub> oxidation reactions.....	232
VI-9.3. Standard SCR behavior and parallel reactions .....	234
<b>VI-10.</b> Cu-SAPO-34-IMP: Impregnated Catalyst .....	240
<b>VI-11.</b> Catalysts differences observed through the model.....	245
VI-11.1. Simulated sites densities comparison: Cu-SAPO-3-IE, -HT and - IMP .....	245
VI-11.2. Estimated kinetic parameters comparison: .....	
Ionically exchanged and One pot Catalysts .....	246
<b>VI-12.</b> Conclusion: Part 2: Model Extension to different catalysts .....	251
<b>Conclusions &amp; Perspectives</b> .....	252
References .....	257
<b>Annexes II</b> .....	284
<b>Annexes III</b> .....	285
<b>Annexes IV</b> .....	286
<b>Annexes V</b> .....	287
<b>Annexes VI</b> .....	290

# RESUME

Les oxydes d'azotes (NO<sub>x</sub>) sont un des groupes majeurs de polluants primaires émis dans l'atmosphère, principalement par les transports et l'industries, dont leur réduction constitue un enjeu sociétal crucial. Afin de répondre à l'évolution de normes environnementales plus exigeantes, la diminution des NO<sub>x</sub> est notablement explorée via la réaction clef de Réduction Catalytique Sélective par l'ammoniac (NH<sub>3</sub>-RCS) en employant des catalyseurs à base de cuivre et de fer. Le développement maîtrisé et perfectionné de cette solution requiert une profonde compréhension du système catalytique et ce à différentes échelles. Cette étude vise ainsi à développer un modèle cinétique multi-sites pour la représentation des performances NH<sub>3</sub>-RCS, par l'exploration des propriétés physico-chimiques, de surface et catalytiques d'une série de catalyseurs zéolitiques microporeux (Chabazite) supportant le cuivre. Cette série de catalyseurs imprégnés, échangés et « One-pot » permet la profonde caractérisation de différentes configurations de sites actifs dont les impacts sur les comportements catalytiques furent étudiés et identifiés selon différentes conditions opératoires. Ainsi, le modèle permet de prendre en considération, via la distinction selon leur nature, de 5 sites majeurs : la compétition d'adsorption, l'impact de l'eau, la formation et décomposition d'intermédiaires clefs et un schéma réactionnel précis, de représenter les activités des différents catalyseurs. De plus, l'étude In-situ de la surface de ces catalyseurs via spectrométrie infra-rouge à réflexion diffuse (DRIFT) fut complémentaire à la compréhension des dynamiques de surface et l'identification des mécanismes du procédé catalytique.

**Mots clefs** : Réduction catalytique sélective, dépollution atmosphérique, modélisation cinétique, In-situ DRIFT, sites actifs

# ABSTRACT

**Title:** Selective Catalytic Reduction of nitrogen oxides using ammonia: kinetic, mechanism and modelling of copper chabazite-based systems

The reduction of atmospheric pollution from stationary and mobile engines is a serious challenge associated with stringent environmental regulations. For nitrogen oxides (NO<sub>x</sub>) abatement in particular, the selective catalytic reduction using urea or ammonia (urea- or NH<sub>3</sub>-SCR) over copper- and iron-based catalysts is one of most effective and economic technologies. In this respect, revisiting after-treatment systems by a deep comprehension of the catalyst behavior at different scale may significantly improve their eco- and health-friendliness. **This study targets the development of a multi-site kinetic model using a series of copper chabazite-based catalysts**, as a selected model SCR catalyst. **To qualify these materials** as beyond-state-of-the-art catalysts and to **better understand the impact on different active site configurations, three catalysts were synthesized by different preparation methods** (impregnation, ionic exchange and one-pot), **finely characterized** by different techniques and **their ability to abate NO<sub>x</sub> via the ubiquitous NH<sub>3</sub>-SCR reaction was extensively assessed under several operating conditions**. Each catalyst behavior was quantified and associated to their respective main active sites (five different configurations described). The diffusion, water impact, adsorption competition between key reactants and storage sites were also ones of the main points spotlighted in this study. **In-situ characterization** of these catalysts was also performed, using Diffuse Reflectance Infrared Fourier-Transform Spectroscopy (DRIFTS) to understand the surface dynamical properties of the catalyst, and to unveil the mechanistic of the catalytic processes.

**Keywords:** Active sites, Selective Catalytic Reduction, Atmospheric pollution, Kinetic model, In-situ DRIFTS

# LABORATORIES

Institut de Recherche sur la Catalyse et l'Environnement de Lyon

IRCELyon

2 Avenue Albert Einstein, 69100 Villeurbanne, FRANCE

Laboratoire d'Automatique, de Génie des Procédés et de Génie Pharmaceutique

LAGEPP

3 Boulevard du 11 Novembre 1918, Bâtiment CPE 69622 Villeurbanne Cedex, FRANCE

# NOMENCLATURE

$a_{\text{geo}}$	Mean geometric specific surface area	$\text{m}^{-1}$
$C$	Concentrations	$\text{mol.m}^{-3}$
$C_{\text{ab}}$	Correlation coefficient between a and b variables	-
$C_{\text{p}_s}$	Heat capacity	$\text{J.g}^{-1}.\text{K}^{-1}$
$D_{\text{mj}}$	Gas molecular diffusion in binary system	$\text{m}^2.\text{s}^{-1}$
$D_{\text{p}}$	Particle diameter	$\text{m}$
$D_{\text{t}}$	Quartz tube diameter	$\text{m}$
$E$	First moment RTD	-
$E_{\text{a}}$	Activation energy	$\text{J.mol}^{-1}$
$F_{\text{i}}$	Molar flow	$\text{Mol.m}^3.\text{s}^{-1}$
$H$	FPB height	$\text{m}$
$\text{RES}$	Residual coefficient from <i>lsqnonlin</i>	$(\text{mol.m}^{-3})^2$
$J$	Jacobi matrix	-
$K$	Number of CSTR in series	-
$k$	Reaction rate constant	Depending on Pre-exponential factor expression
$k_0$	Pre-exponential factor	depending on reaction rate expression
$k_{\text{Boltz}}$	Boltzmann constant's ( $=1.38.10^{-23}$ )	$\text{J.K}^{-1}$
$k_{\text{s}}$	Thermal conductivity of gas	-
$k_{\text{tot}}$	Mass transfer coefficient	$\text{m.s}^{-1}$
$L$	Characteristic length	$\text{m}$
$N$	Flow density	$\text{mol.m}^{-2}.\text{s}^{-1}$
$P$	Pressure	bar
$\hat{p}$	Estimated parameter	Depend on the initial parameter dimensions
$\text{Pe}$	Péclet Number	-
$Q_{\text{tot}}$	Total volumetric flow	$\text{m}^3.\text{s}^{-1}$
$Q_{\text{wt}}$	Total mass flow	$\text{Kg.s}^{-1}$
$r$	Reaction rate	$\text{mol.s}^{-1}.\text{m}^{-3}$
$\text{Re}$	Reynolds	-
$R^{\text{g}}$	Gas constant	$\text{J.K}^{-1}.\text{mol}^{-1}$
$S_{N-K}$	Student variable	-
$\text{Sch}$	Schmidt	-
$T$	Temperature	$\text{K}$
$T_0$	Temperature at $0^{\circ}\text{C} = 273.16 \text{ K}$	$\text{K}$
$\text{TC}$	Characteristic time	$\text{s}$
$u_{\text{c}}$	average velocity of fluid	$\text{m.s}^{-1}$
$V$	Volume	$\text{m}^3$
$V_{\text{r}}$	Reactor volume	$\text{m}^3$
$x_{\text{mol},i}$	Molar fraction	-
$Y$	Least square sum	Depending on concerned expression
$\bar{y}$	Mean of experimental observations	depending on observation expression
$\hat{y}_i$	Estimated observation	depending on observation expression
$y_i$	Experiment observation	depending on observation expression

## Greek letters

$\mu$	Dynamic viscosity	Pa.s
$\alpha$	Presence ratio	-
$\beta_D$	Collision integral	-
$\theta$	Coverage	-
$\rho$	Density	kg.m <sup>-3</sup>
$\tau$	Mean residence time	s
$\Omega$	Sites densities	mol.m <sup>-3</sup>
$\varphi$	Thiele modulus	-

## Subscript

ads	Relative to adsorption process
ax	Relative to axial dimension
des	Relative to desorption process
ext	Relative to external position
film	Relative to interfacial film gas/solid
fluid	Relative to the fluid
g	Relative to the gas phase
g/s	Relative to the gas and solid interface
geo	Relative to the grain shape
i	Relative to i specie
in	Relative to inlet fluid
in	Relative to inlet fluid
int	Relative to internal position
interf	Relative to interface
intragranular	Relative to intragranular diffusion
j	Relative to j <sup>th</sup> adsorbed specie
k	k <sup>th</sup> sites (S1, 2, 3 or S4)
K	Relative to the total number of parameters
mol	Relative to molar quantity
N	Relative to the total number of observation
p	Relative to particle
s	Relative to active sites
s	Relative to active sites
surface	Relative to the catalyst surface
tot	Relative to the total value
transf	Relative to the global diffusional resistance

## Superscript

exp	Relative to experience
G	Relative to gas phase
mcat	Relative to catalyst mass
n	Relative to n <sup>th</sup> CSTR

S	Relative to surface phase
simu	Relative to simulation
tracer	Relative to tracer concentration

## Acronym

ASC	Ammonia Slip Catalyst
CAA	Clean Air Act
CHA	Chabazite
CR	Conversion rate
DOC	Diesel Oxide Catalyst
DPF	Diesel Particulate Filter
FPB	Fixed Packed Bed
GHSV	Gas Hourly Space Velocity
GWP	Global Warming Potential
ICCT	International council on Clean Transportation
LDF	Linear Driving Force
LNT	Lean NOx Trap
LPM	Libre Parcours Moyen
MFP	Mean Free Path
NOx	Nitrogen oxides (NO, NO <sub>2</sub> , N <sub>2</sub> O)
PFR	Plug Flow Reactor
QENS	Quasielectric Neutron Scattering
R	Reaction equation
RES	Residual
RTD	Residence Time Distribution
SCR	Selective Catalytic Reduction
SiC	Silicium Carbide
TPD	Temperature Programed Desorption





# GENERAL INTRODUCTION

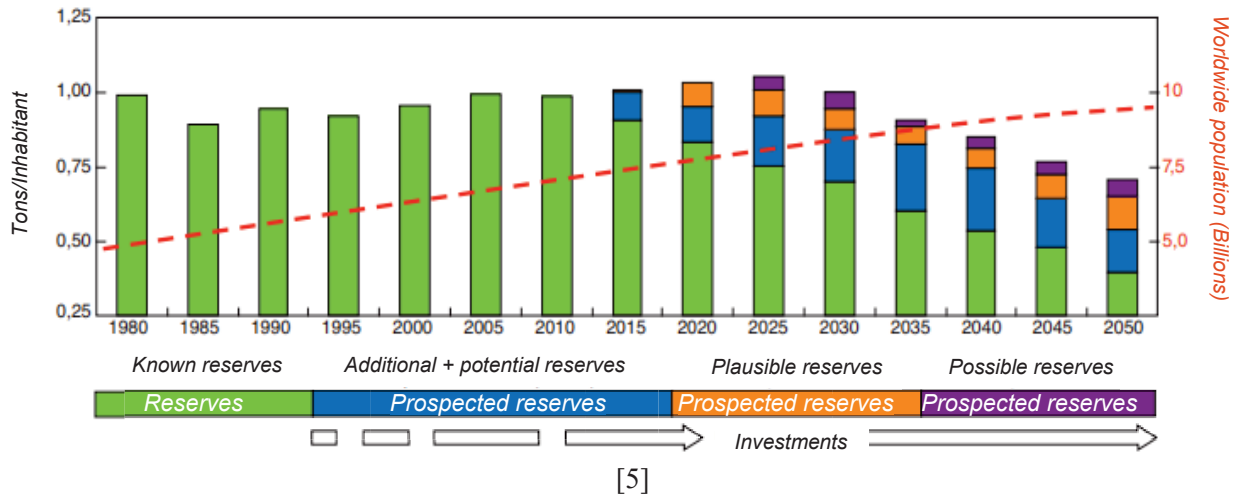
« *Nous n'héritons pas de la terre de nos parents, nous l'empruntons à nos enfants* »

**Antoine de Saint-Exupéry**

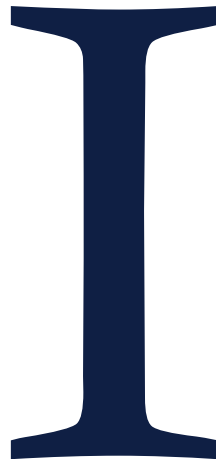
Development and environment are complementary, following Gro Harlem Bruntlund, the first person to firstly defined the expression “*sustainable development*” in 1987. This concept represents “The development that meets the needs of the present generation without preventing future generations from satisfying their own needs» [1]. The imbrication of these two terms required the establishment of long-term environmental objectives, to adopt a proactive attitude in all circumstances and to consider the plural bonds between the economy and the living through the societies. This, ideal, formula allows to conciliate the will of each individuals without compromising their interests. However, the concept of “*sustainable development*” so widely acclaimed, rely on a strongly biased mathematical equation. Indeed, to consider an increasing economic development (through the Gross Domestic Product (GDP) elevation of a country typically), it is equivalent to consider a constant flow of raw material to transform and a value production, at least constant, and above all for the developing countries. Yet, the totality of manufactured products today cannot be made of something else than the element present in the Mendeleev Periodic Table and only a certain quantity of these elements is available, which the reserves are more or less important today. Quantities which, from the beginning, did not increased, quite the opposite, as the consumption and prospected amount of rare earth elements through the years can displayed for instance [2]. Thus, this is all these non-renewable elements, which the reserves shrink inversely with the number of people consuming it (with more than 7.5 billion Humans), which could not even more feed in a similar rhythm a growth, already strongly solicited. A process marking the beginning of an unavoidable economic contraction, extremely dangerous if not anticipated. Under the current circumstances, the first warning signs of such a contraction are visible today through different indicators, including the availability of hydrocarbons per inhabitant as represented Figure I-1, which could only decrease with the time as the prospected reserves (unless the unconventionally ones as oil sands for instance which the open prospection can still lead to new reserves in some countries). This indicator is interesting due to the number one position occupied by the fossil energies in the world for feeding our respective machines, the most important share of the energetic mix, and thus, its availability represents a demonstrating vector of the different flux between people. This is for these diverse reasons that the economic issues still constitute the first driving force of financial and human investment for development and innovation. And by solution, it is important to reconsider the lever arms on which it is possible to act in order to get a general observation of the possibilities. Therefore, the question is not only to know how to motivate the energy sobriety, but also the depollution operation and this, at all the society levels. How to assimilate that economy and environment cannot be resilient if considered from an economical point of view without strict definition of the needs? How to resolve the inefficient application of the “polluter pays” principle dating from the seventies [3] and adopted by the Organization for Economic Co-operation and Development

(OECD)? It will be also at a same period, in 1972, that the “The Club Of Rome” became precursor of the energy sobriety thinking way through the presentation of their report “The Limits to growth” [4]. Despite the lack of consideration for their work, the reassessment of the machine exploitation from the man and its energetic race to feed it, will finally begin to profile in the minds the first limits of our planets with limited resources.

Figure I-1. Worldwide average availability in hydrocarbon resources per inhabitant from 1980 to 2050



[5]



This introduction, written in French, presents (1) the context in which had evolved the study and the environmental issues related to the atmospheric pollution problematic, (2-3) a panoramic view on the European standard regulations from its application to the reality, (4-6) a bibliographical review about the principal Selective Catalytic Reduction (SCR) technologies, and (7) the kinetic model description from the assumptions to the simulation construction for parameter estimation. The conclusion and Thesis outline will be written in English for the reader convenience

# CHAPTER I

## BIBLIOGRAPHIC STUDY

### I-1. La pollution atmosphérique change d'ordre de grandeur : du contexte historique déterminant jusqu'aux cibles de l'étude

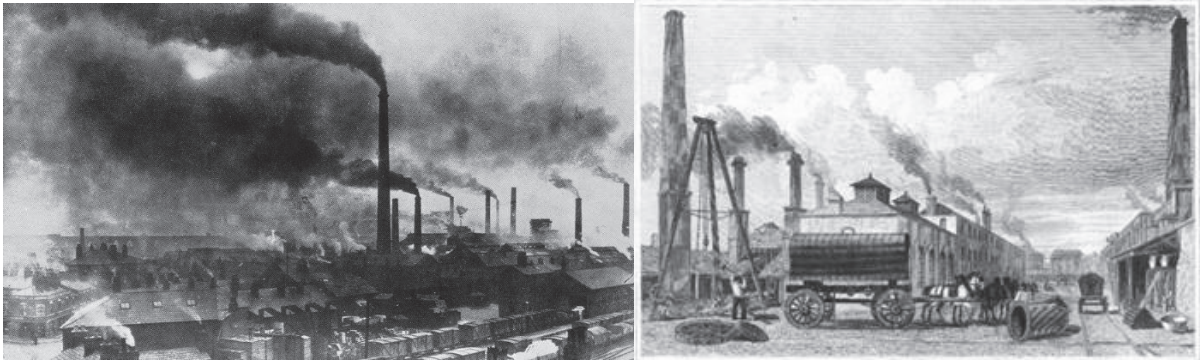
Dans le souci de traiter au mieux une problématique, il est important d'obtenir une représentation temporelle, une image des événements déterminants, qui sont en partie à l'origine de la situation actuelle. Ceci dans le but de constater d'une part, les différentes avancées scientifiques et technologiques clefs en la matière, et d'autre part de contempler toute l'ampleur du problème et observer d'un œil critique les faits passés. Tout d'abord, concernant la problématique de la pollution atmosphérique (restreinte aux actions de nature anthropomorphique ici), deux milieux sont à discriminer bien qu'ils soient unis : les pollutions émises dans les environnements clos comme les habitats, bureaux, habitacles de voitures etc... et la pollution atmosphérique extérieur. Chacun de ces milieux présentent leurs propres caractéristiques en termes de nature, concentrations de polluants, impacts humanitaires, types et nombre de sources d'émission.

Si la problématique des Composés Organiques Volatils (COV) occupe une place de plus en plus importante dans la thématique de la dépollution atmosphérique c'est parce que nous passons aujourd'hui en moyenne 80% de notre temps [6] dans des environnements clos (d'après l'Observatoire de la Qualité de l'Air Intérieur (OQAI)), dont les concentrations mesurées en polluants sont aussi importantes que variées. Et pour cause, ce même organisme missionné par les pouvoirs publics français entre 2003 et 2005 a mesuré que l'air intérieur des habitations présentait généralement de plus hautes concentrations de COV que l'air extérieur. En effet, 18 COV des 20 mesurés sont en plus fortes concentration en intérieur où près d'un quart des logements dépasseraient les valeurs guides européennes et dont le formaldéhyde et le toluène arriveraient en tête de la liste des fortes concentrations [7,8]. Si la problématique des COV se retrouve dans la ligne de mire de la dépollution de l'air depuis seulement les années 90 avec la mise en évidence de la relation asthme-COV [9,10], celle de la dépollution atmosphérique extérieure est bien plus antérieure à cela.

En effet, depuis la révolution industrielle du XIXe siècle, le développement technique et l'industrialisation massive des métropoles développées, provoque un changement radical de la composition de l'air ambiant, jamais observé auparavant. C'est à cette même période que les premiers liens entre les pluies acides et la pollution atmosphérique sont réalisés, que le physicien français Jean Baptiste Fourier donne une description du réchauffement climatique par effet de serre [11,12] et que l'ozone atmosphérique est découvert [13,14]. Ce sont les dessins et peintures réalisés à cette époque qui en témoignent le mieux, comme en Figure I-2, où les représentations des grandes villes d'Angleterre du XIXe comportent bien souvent des illustrations de fumées noires et épaisses caractéristiques d'une atmosphère pesante et chargée.

Cette révolution changea définitivement la relation entre l'Homme et son environnement, ce qui provoqua le changement d'ordre de grandeur des émissions de polluants dans l'eau, la terre et l'air et ce à différentes échelles. L'utilisation massive du charbon comme source d'énergie première remplaça les énergies naturelles comme le vent, l'eau ou le bois et permit l'essor de l'âge industriel certes, mais déclencha aussi rapidement la première prise de conscience de l'impact de la pollution sur la santé et l'environnement.

Figure I-2: A gauche: "Photographie de Widnes en Angleterre fin XIXe siècle, source : Hardie, D. W.



F., *A History of the Chemical Industry in Widnes*, Imperial Chemical Industries Limited, 1950. A droite : *Steam-Engine Manufactory, and Iron-Works, Bolton* par Watkins, d'après un dessin de Harwood.

Imprimé par Fisher, Son & Co., Londres, 1829.

A cette même période de l'autre côté de l'océan, de grandes villes comme New York font le constat elles aussi d'une problématique de plus en plus inquiétante au sujet de la dégradation de la qualité de l'air et de l'environnement. Comme en font part les auteurs Joel Tarr et Clay McShane dans leur article « The making of Urban America » [15], New York est l'une des premières villes à constater la pollution liée au transport. Ce sont en effet les entassements de déjections et de cadavres de chevaux alors en grands nombre à cette époque qui posent le plus de problème de pollution à la fois aérienne et sanitaire. De telles villes pouvaient compter jusqu'à des dizaines de milliers de montures et voitures hippomobiles. Cette prise de conscience contribuera par la suite au développement d'une « solution révolutionnaire », catalysée par l'ère de la révolution industrielle grondante aux quatre coins du monde et le besoin d'accélération des échanges entre les hommes : la voiture à essence. Vu à cette époque comme la solution à toutes ces problématiques de pollution liées au transport équestre, le nombre d'automobile par habitants explose après les années 1950 avec une population et une urbanisation toujours grandissante [16]. Seulement il n'aura fallu que quelques dizaines d'années pour que le problème de pollution atmosphérique lié aux voitures ne surpasse, et de loin, celui lié aux équidés. Les moteurs imposants à essence dépourvu de technologie de dépollution et peu efficaces génèrent des émissions gazeuses très importantes aux impacts sanitaires déplorables. Les premiers rapports et mesures de concentrations de polluants sont publiés. Aux vues de la situation, il se créa en 1963 aux Etats Unis les premières normes approuvées par le gouvernement : le « Clean Air Act (CAA) » ainsi que le « National Environmental Protection Act » (NEPA). Ils seront édités en 1970 sous la présidence de R. Nixon [17]. La Californie alors précurseur, montre la voie et de nombreux pays ne tarderont pas à lui emboîter le pas et développeront le pot catalytique afin de respecter

ces nouvelles réglementations. Alors qu'en Europe dans les années 1980, les petites cylindrées aux moteurs « pauvres » en carburant ne nécessitent pas de système de dépollution comme leurs homologues américains. En effet, leur moteur respectait par nature de conception les valeurs guides européenne de l'époque, valeurs émises en 1987 par l'Organisation Mondiale de la Santé (OMS) [18]. Ce sera 25 années après la Californie qu'à force de lobbying et pressions de la part de certains constructeurs automobiles sur le marché européen que des normes plus sévères se mettront en place petit à petit en Europe. Ceci forçant l'utilisation et le développement du pot catalytique malgré certaines réticences comme l'avait expliqué l'ex-président du directoire PSA (Peugeot Société Anonymes) Jacques Calvet le 25 juin 1985 ; « *Alors que nous avons déjà réduit la pollution de 70 à 80% [par l'utilisation des petits moteurs moins gourmands entre autres], une bande d'hystériques en Allemagne veut qu'on accélère et qu'on dépasse les rythmes industriels et techniques actuellement connus... L'Allemagne est en train de sacrifier l'ensemble de l'industrie automobile européenne, en pensant sans doute que la sienne sera épargnée, ce qui est faux* » [19]. La déclaration faisant référence à la technologie du pot catalytique alors présenté à l'époque par les autorités allemandes comme méthode d'abattement des polluants et considérée comme trop onéreuse par les constructeurs français. Cependant, catalysée par l'existence des normes américaines du CAA déjà en place ainsi que par la question inquiétante des pluies acides [20], cette nouvelle technologie sera rapidement adoptée par le gouvernement allemand. Puis, quelques temps plus tard, par la communauté européenne dans sa globalité afin de pouvoir faire respecter ces valeurs guides qui évolueront rapidement en normes. En effet, pendant la période transitoire de l'adoption du pot catalytique des années 1980 jusqu'aux années 1990 avec la première norme EURO 1, il se mettra en place de nombreux tournants décisifs pour la dépollution atmosphérique comme le montre la Figure I-3.

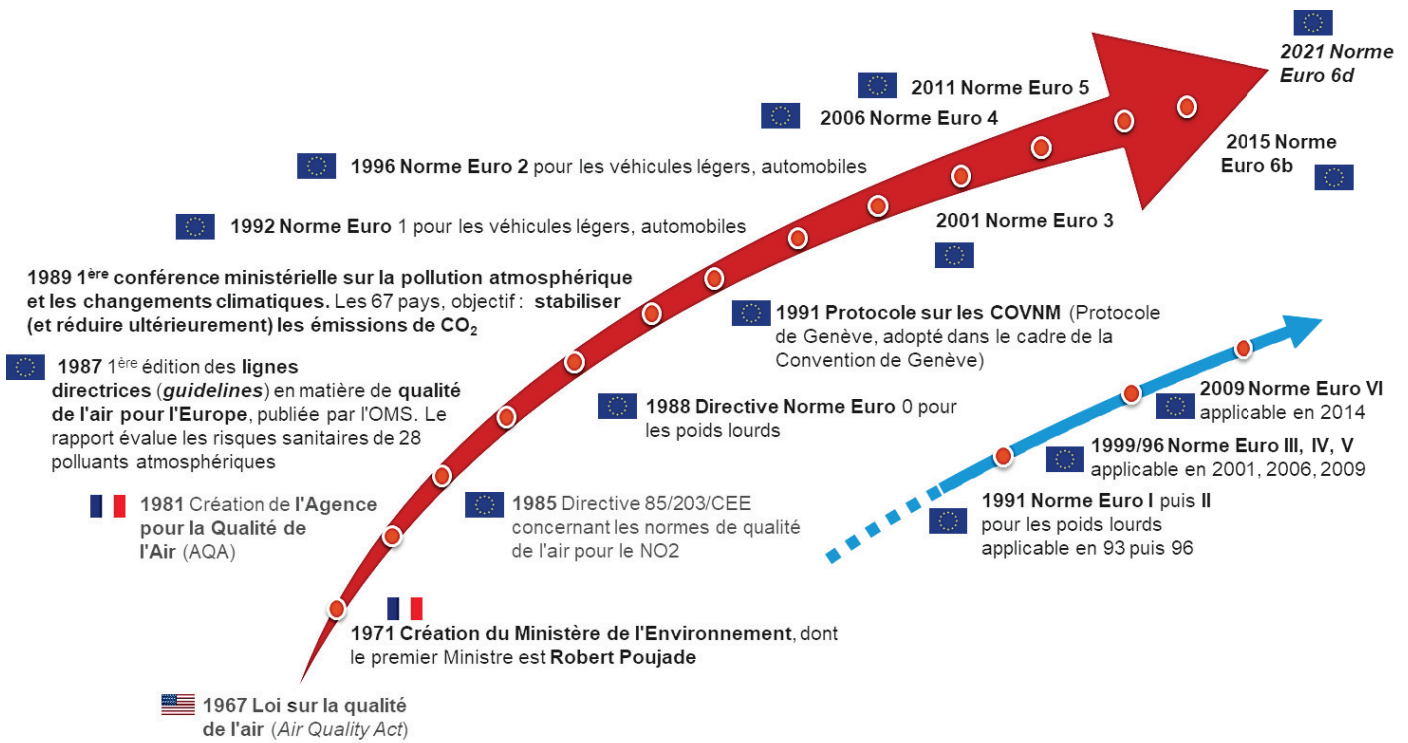


Figure I-3: Frise chronologique des événements et décisions déterminantes à la dépollution atmosphérique lié aux transports (en rouge, normes Euro de 1 à 6d relative plus particulièrement aux automobiles, en bleu plus particulièrement aux poids lourds) [21]

## I-2. Moteurs du progrès des technologies de post-traitement : les normes et contrôles

Les évolutions de ces normes, véritable moteur de la recherche industrielle en la matière, peuvent aussi s'observer selon l'évolution des seuils d'émission des polluants d'après la figure 4 ci-dessous. En effet, depuis les années 90 les normes se font de plus en plus drastiques et diminuent les seuils d'émissions autorisés ou tout du moins les maintiennent constants. Il est en effet important d'en observer leurs évolutions puisqu'elles dictent indirectement les futurs axes de recherches adoptés par les unités de recherches et développement ainsi que par les constructeurs automobiles.



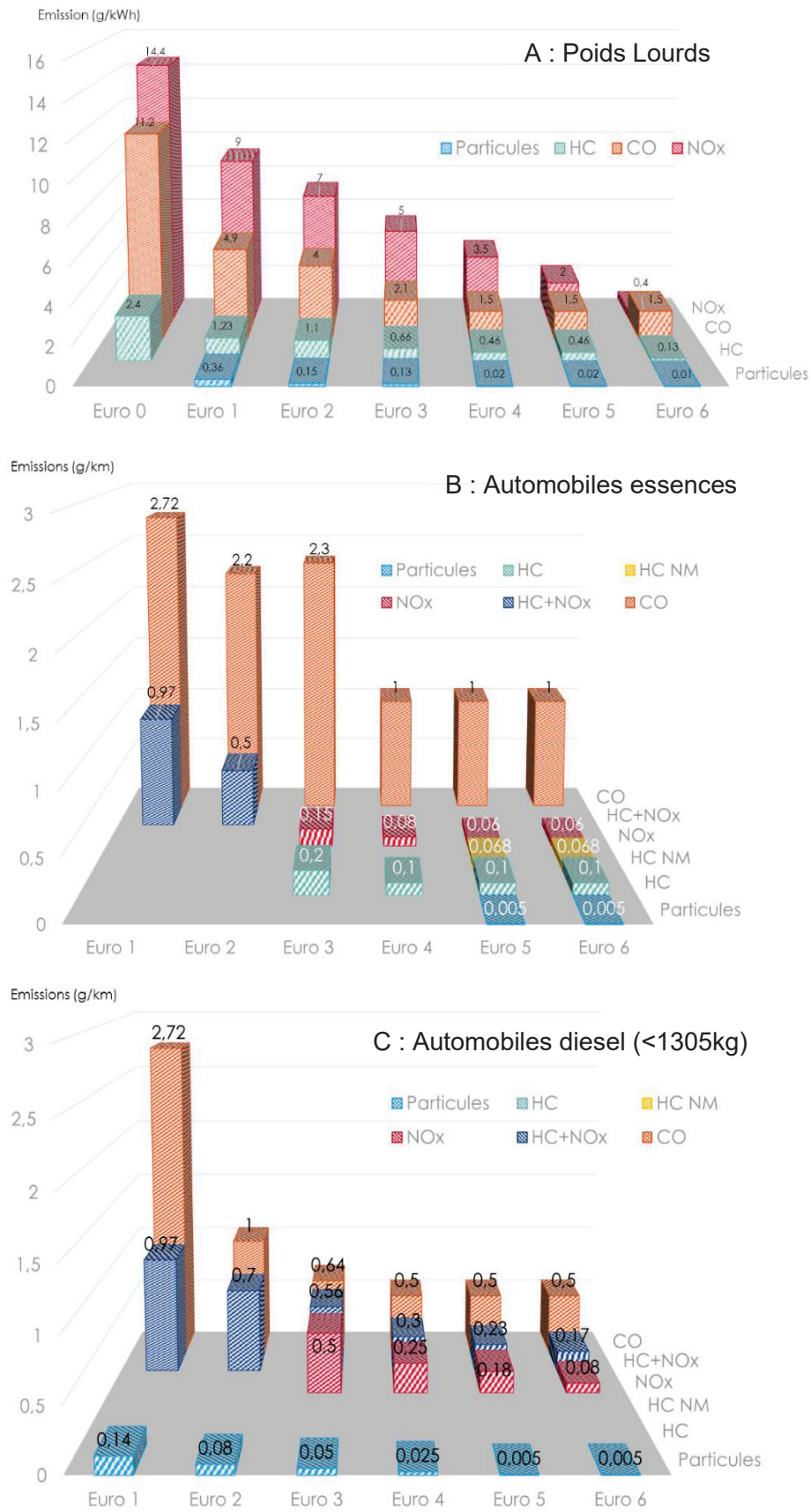


Figure I-4: A: Historique de la réglementation des émissions à l'échappement des poids lourds en régime constant, B: Historique de la réglementation des émissions à l'échappement des véhicules légers essence en régime constant, C : pour les véhicules légers Diesel en régime constant [22]

Cependant, les valeurs présentées ici sont à pondérer selon le nombre de kilomètres parcourus et la catégorie de norme respectée par le véhicule. En effet si l'on se réfère au graphique A de la figure ci-dessus, en 2017 en France, le parc poids lourds aux motorisations diesel était constitué à 56,7 % de véhicules lourds types Euro 6, 36,7 % de type Euro 5 et 4,6 % de type Euro 4. Le reste des véhicules étant plus anciens encore. Ici, propre aux poids lourds, l'unité d'émissions de référence est le g/kWh. Cette unité est difficilement comparable au g/km parcourus relatifs aux véhicules légers, représentés avec les deux graphiques B et C. Cette différence d'unité provient du fait que les tests de contrôle d'émissions sont différents selon que le véhicule soit considéré lourd ou léger. Pour les camions par exemple, les tests normalisés de la norme EURO VI (World Harmonized Stationary/Transient Cycle WHS/TC) [23] consistent en l'application d'un dynamomètre relié au moteur permettant de mesurer le couple développé selon la vitesse atteinte et le tout comparé simultanément aux masses de polluants émises. Ainsi les limites sont définies en termes de masse émise par unité de travail mécanique achevé (g/kWh). Par contre pour les véhicules légers, le dynamomètre se place sur le châssis, où les roues du véhicule reposent sur des rouleaux en liens avec des dynamomètres permettant de mesurer le couple et l'effort du véhicule. Ainsi selon la charge appliquée, la masse de polluant émise selon la distance parcourue (g/km) peut être mesurée. Si des différences de normes d'émissions persistent entre les pays (Etats Unis, Union Européenne, Asie...) la 6<sup>e</sup> génération de normes EURO a le mérite d'avoir unifié les cycles de tests d'émissions des véhicules lourds et légers pour 28 nations [24], dont les principes résumés par « The International Council On Clean Transportation » (ICCT) peuvent être consultés ailleurs [25]. Les tests de contrôle évoluant au fil des normes, ils deviennent plus adaptés et plus proches des conditions réelles d'utilisation du produit fini.

En effet depuis quelques années, des contrôles d'émission de polluants sont réalisés « on-road » avec le déploiement de système directement embarqué à l'arrière du véhicule appelé PEMS (Portable Emission Measurement System) dont un schéma est présenté Figure I-5. Le but étant pour les industriels et laboratoires impliqués de mesurer en conditions réelles, les véritables émissions des véhicules afin de pouvoir répondre toujours plus rapidement aux normes de régulation et de pouvoir corriger leur défaut d'abattement si nécessaire. Ici encore, l'état de Caroline du Nord aux Etats Unis est une force de proposition quant au développement de ces contrôles d'émissions atmosphérique. En effet ce procédé de mesure embarqué est relativement récent puisqu'il ne fut breveté il y a seulement une vingtaine d'année par Michal Vojtisek-Lom, conjointement avec le Clean Air Act Technologies International Inc. [26]. Il a été testé pour la toute première fois en 2003 par l'équipe de recherche de H. Christopher Frey de l'université de l'état de Caroline du nord aux Etats Unis [27]. Cependant, cet analyseur de gaz d'échappement embarqué démontre un certain nombre d'avantages par rapport à un banc de tests laboratoire tel que : faible poids, faible encombrement, utilisation aisée et résistance aux conditions de terrain. En effet, l'analyseur de gaz peut être un spectromètre à Infrarouge non dispersive (NDIR) comme utilisé par exemple par H. Christopher Frey [27], couplé à un ordinateur portable lui-même relié à l'ordinateur de bord du véhicule et le tout contenu dans une mallette. Cela constitue un système facilement manipulable, pratique et polyvalent par le fait de son application possible sur tout ou presque type

d'échappement (bateau, voiture, camion ...). En revanche, plusieurs désavantages viennent contrebalancer l'intérêt de son utilisation et montre alors tout l'enjeu du compromis entre banc de tests de laboratoire et systèmes embarqués. Le système sera limité par exemple en puissance de calcul ou d'énergie bien que branché sur la batterie du véhicule ou sur une batterie externe. De plus, la précision de mesure sera toujours moindre et les paramètres de mesures restreint comme le nombre de gaz analysés par exemple ou le temps de réponses de l'analyseur en ligne. A cela s'ajoute des possibilités de perte de communication entre l'ordinateur de bord et le PC portable ou bien même entre l'analyseur et son interface utilisateur. Enfin, si les systèmes de mesure embarqués se veulent plus pratique d'utilisation qu'un banc d'expériences, il n'est plus question lors de leur utilisation, de travailler à reproduire des émissions réelles de polluants et à modéliser le comportement de ces derniers, mais à mesurer des concentrations émises d'un système particulier. Les données recueillies par mesures PEMS en conditions de circulation réelle présentent, pour le moment, un important intervalle de confiance et montrent très peu de reproductivité, naturellement dû aux conditions climatiques et aux différentes densités de circulation (par exemple, le secteur géographique de réalisation du test) [28,29]. Même si la qualité du système embarqué évoluera rapidement, il est intéressant de relever que d'autres techniques de mesures voient le jour dans ce domaine et propose de nouvelles méthodes comme le dispositif « OHMS » utilisé par Bishop et al.[27]. Des appareils de mesures similaires au PEMS sont utilisés mais la différence est de demander au véhicule échantillon de passer au travers d'un couloir fermé permettant de recueillir le gaz d'échappement du véhicule. Cette méthode peut être située entre le test statique sur banc et le système embarqué. Avec le développement de ces méthodes de mesures, les banques de données s'agrandissent de jour en jour mais font preuve de grandes disparités. C'est pour cela que ces méthodes de mesures, l'une comme l'autre, doivent trouver leur place sans mutuellement essayer de se supplanter et les données extraites doivent être croisées pour optimiser les mesures.

Finalement, la qualification de leurs utilisations fut récemment amplifiée d'utile à nécessaire grâce notamment à l'affaire du « *scandale Volkswagen* » de septembre 2015[30,31]. Pour rappel, un programme informatique implémenté dans l'ordinateur de bord de la voiture était capable de détecter lorsque le véhicule passait en phase de test laboratoire réalisés sur banc moteur. Ainsi, cela permettait de contrôler les émissions en oxydes d'azote du véhicule, pendant un temps limité. Avec des systèmes « On-road », les concentrations mesurées auraient été réelles en condition normale d'utilisation et l'erreur sur ces seuils d'émissions aurait été détectée plus rapidement. Cette affaire eue des retombés et impacts politiques, comme économiques, importants que ce soit pour le constructeur lui-même, pour les autres constructeurs automobiles ou les fabricants de poids lourds. Ceci a certes catalysé la rigueur des contrôles et le développement des systèmes de dépollution mais souligne encore un peu plus la problématique du gap entre tests en laboratoire et mesures en conditions réelles et donc remet potentiellement en question de tels résultats.

**I-3.** Tests en laboratoire versus mesures en conditions réelles.

L'éclatement de ce scandale permet donc de soulever de nouvelles questions, fondamentales aux concepts de régulations et finalement propres aux enjeux de la dépollution atmosphérique. Et pour cause, les objectifs de dépollution atmosphérique fixés par l'Europe sont basés sur le respect progressif des normes d'émissions. Un écart massif à ces seuils multiplié par le nombre de véhicules en défaut peut avoir d'importantes répercussions sur les faisabilités d'atteindre de tels objectifs de dépollution, qui seraient alors surestimés. Avec le parc de véhicules diesel le plus important au monde (59% [32]) comptabilisant près de 9 millions de moteurs dont la majeure partie est faite de véhicules légers, l'Europe se doit de posséder une banque de données fiables et représentative des émissions de polluants produits par cette flotte de véhicule. La question est alors de savoir comment une telle fraude a pu être commise et de déterminer pourquoi de telles différences d'émissions de polluants se retrouvent aussi chez d'autres constructeurs automobiles. L'objectif étant de créer une base d'informations représentative de la réalité pour une utilisation intelligente. Cette remise en cause de crédibilité est justifiée car aujourd'hui pour les véhicules légers, les différences de concentrations en polluants annoncées par le constructeur et celles qui sont réellement émises, n'ont jamais été aussi importantes qu'auparavant [33].

Il est important d'aborder certains aspects de cette problématique. Tout d'abord, il sera noté que les normes et régulations appliquées sur les véhicules poids lourds devancent de quelques années celles appliquées sur les véhicules légers. Par exemple, si la norme EURO VI fut applicable dès 2014 sur les poids lourds, la norme EURO 6 pour les véhicules légers sortit un an plus tard n'est que très peu équivalente à EURO VI en termes de difficulté et de simulations des conditions réelles comme en témoigne le Tableau I-1 suivant [34]. Parmi ces différences, les plus notables concernent la disposition de tests en conditions réelles d'utilisation et la limite acceptable d'émission de NOx mesurée. En effet, si dès 2014 les systèmes PEMS évoqués plus haut sont employés de concert avec les tests en laboratoire pour la certification d'émission des véhicules lourds, aucune utilisation n'en est faite en 2015 pour les véhicules légers comme l'a confirmé le dit scandale. Quand bien même les systèmes PEMS commenceront à être déployés entre 2017 et 2020, le facteur de conformité d'émissions des NOx (le facteur multiplicatif à ne pas dépasser lors des mesures en conditions réelles) sera de 2.1 contre 1.5 pour les poids lourds [35]. Il sera donc toléré des émissions deux fois plus élevées que la limite demandée en laboratoire. Sachant que le facteur de conformité appliqué au poids lourds doit être respecté pour des véhicules déjà en circulation, alors que la limite appliquée aux véhicules légers sera quant à elle imposées sur des modèles neufs de pré-production. C'est pour ces raisons que les efforts en recherche et développement concernant la dépollution atmosphérique des véhicules lourds se doivent d'être précurseurs. Ces recherches contribuant notamment aux avancées technologiques dont bénéficient les véhicules légers. Et pour cause, les poids lourds démontrent qu'il est techniquement possible de respecter ces récents seuils d'émissions en conditions réelles, comme affiché sur la figure 6 ci-dessous.

Tableau I-1 : Comparaison des tests de contrôle réalisés sur les poids lourds et véhicules légers selon la réglementation EURO 6/VI [34]

	<b>EURO VI (2014)</b>		<b>EURO 6 (2015)</b>	<i>EURO 6 (futur)</i>	
<b>Type de tests</b>	Dynamomètre sur moteur	Conformité de mise en service avec système PEMS	Dynamomètre sur châssis	<i>Dynamomètre sur châssis</i>	<i>(sept. 2017) Real driving emission (RDE) avec PEMS</i>
<b>Protocole de cycles</b>	World Harmonized steady state/transient cycle (WHS/TC) prenant en compte les démarrages à froid et à chaud	Trajet urbain (0-50 km/h) pour 20 à 45% de la distance total/ Rural (50-75 km/h);25-30%/Autoroute (75 km/h et +);30-55%	Nouveau cycle européen de conduit (NEDC) prenant en compte que le démarrage à froid	<i>World Harmonized Light vehicles Tests Procedures (WLTP) prenant en compte que les démarrages à froid</i>	<i>Trajet urbain (0-60 km/h) pour 29 à 44% de la distance total/ Rural (60-90 km/h);23-43%/Autoroute (90 km/h et +);23-43%</i>
<b>Moteur au ralenti</b>	17% du temps total de WHTC		23.7% du temps total de NEDC	<i>12.6% du temps total de WLTP</i>	<i>6 à 30% du temps passé en milieu urbain</i>
<b>Charge utile</b>	25% en WHSC et 17% en WHTC	50-60%	N/A	<i>N/A</i>	<i>N/A</i>
<b>% de vitesse constante</b>	2 cycles séparés dont un à vitesse et charge constantes et l'autre en variant ces deux paramètres	/	40.3%	<i>3.7%</i>	<i>/</i>
<b>Durée du test avec PEMS</b>	/	5 fois les temps établis pour le WHTC	/	<i>/</i>	<i>90 à 120 min</i>
<b>Tests hors protocole (off-cycle tests)</b>	Points de contrôle en dehors des limites de WHTC lors des mesures sur bancs		Non réalisés	<i>Non réalisés</i>	<i>RDE considéré comme off-cycle</i>
<b>Type d'échantillon utilisé pour tests PEMS et fréquence de mesure</b>		3 moteurs en circulation en dessous de 700 000 km ou 7 ans d'utilisation par catégorie de véhicule testé au bout de 18 mois puis une fois tous les 2 ans			<i>1 test pour 1 Véhicule type d'avant production représentatif de sa catégorie</i>
<b>Facteur de conformité NOx</b>	1	1.5	/	<i>/</i>	<i>2.1 entre 2017 et 2020 puis 1.5 après 2020</i>

En effet de récentes mesures « On-road » des derniers modèles certifiés EURO VI menées dans différents pays de l'Union Européenne, les Etats Unis, la Chine et le Japon, démontrent le respect général de cette dernière par la majorité des véhicules [28]. Seulement une minorité dépasserai le seuil fixé avec un facteur de conformité de 1.5% au lieu du facteur 1 initialement requis. La Figure I-5, présente les taux moyens de dépassements des seuils selon les états, établit sur les différentes bases de données recueillies par des organismes indépendants très divers référencés par l'International Council of Clean Transportation (ICCT) dans son « Global Transportation Roadmap Model » [34].

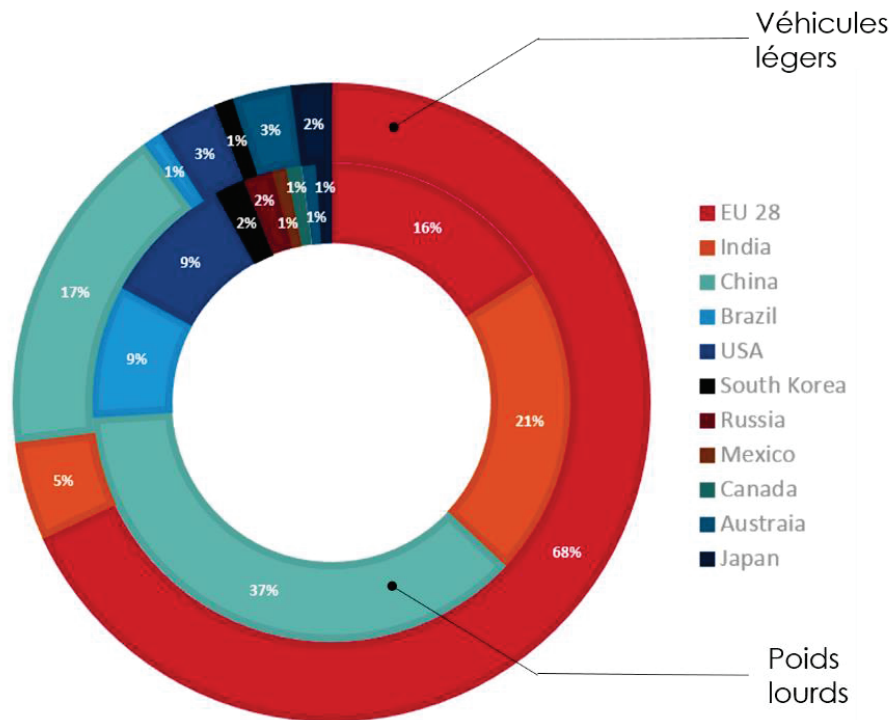


Figure I-7 : Taux moyens de dépassement des seuils d'émissions NOx en conditions réelles d'utilisation selon les normes des différents états (données de 2015) [28]

Tout d'abord concernant les poids lourds, la Chine présentait déjà les plus hauts dépassements de seuils autorisés avec 37%, suivi de près par l'Inde avec 21%. Malgré la gravité de ces abus, il est important de relever que les valeurs présentées ci-dessus pour des pays en développement comme la Chine ou l'Inde, ne sont pas uniquement le résultat d'un manque de rigueur de contrôle par le pays concerné mais peuvent aussi être en partie dû aux pays développés eux-mêmes. La raison en est simple, des pays en développement comme l'Inde sont en grandes demandes de moyens logistiques, et bénéficient généralement et à moindre coût des véhicules lourds en fin de vie aux dépens de technologies de dépollution obsolètes des pays les plus développés [36]. Cependant, des véhicules estampillés EURO V, IV ou bien III par exemple ne seront pas systématiquement adaptés à la qualité du carburant utilisé [37]. Des carburants à plus haute teneur de soufre et métaux inhiberont plus facilement le procédé catalytique, accéléreront leur vieillissement et diminueront rapidement la capacité de réduction des oxydes d'azotes [38-40]. Mise à part cette précision,

si les véhicules poids lourds de l'Union Européenne comme des USA font preuve d'une relative fidélité aux normes en vigueur, les émissions d'oxydes d'azote de la part des véhicules légers européens démontrent le fossé et donc l'abus qu'il existe aujourd'hui vis-à-vis de la non-conformité des émissions polluantes [41,42]. Ainsi les technologies de dépollution développées pour les poids lourds se distinguent par leurs efficacités, notamment via la mise en œuvre, suite à l'EURO VI, du procédé de réduction catalytique des oxydes d'azote par l'ammoniac. Un exemple pour le commerce des véhicules légers, qui entreprendra cette technologie peu de temps plus tard. Ces écarts entre émissions mesurées en conditions de laboratoire et celles mesurées en conditions réelles de la part des constructeurs automobiles européens n'est pas une problématique récente et daterait déjà des années 2000 [43]. Les causes de ces dérives sont diverses et sont majoritairement dues à l'exploitation des souplesses des conditions d'essai et à la mise en place de procédés d'évaluation propres aux tests en laboratoires. Mais aussi à l'exploitation de tous les avantages des intervalles de tolérances instrumentales possible. C'est en effet au constructeur de fournir un véhicule test pour réaliser les mesures sur banc d'essai. Les « *Golden Car* » étant vouées à disparaître avec l'établissement des futures normes réglementaires. La Figure I-8 extraite du rapport de « l'European Federation for Transport and Environment AISBL » présente les différents points techniques communément exploités lors des tests en laboratoire et notamment lors des mesures d'émission CO<sub>2</sub>.

Ceci étant, de futures normes seront rapidement mises en place et, force de constat et d'abus, des dispositions devront être prises en conséquence si les objectifs de dépollution fixés veulent être atteints. Par exemple, l'ICCT préconise la mise en place de points de tests « off-cycle », c'est-à-dire hors des limites du test. Des tests prenant en compte plus de démarrage des moteurs à froid et diverses mesures « on road » avec des systèmes de mesures embarqué (PEMS), dont les conditions aux limites seront clairement définies en indiquant ce qui est permis et ce qui ne l'est pas et comment traiter et lire les données obtenues. En plus des améliorations de normes, Transport & Environnement (T&E) propose aussi à la Commission Européenne de redéfinir les objectifs d'émissions de polluants en NO<sub>x</sub> et CO<sub>2</sub> selon les nouvelles données d'émissions « on-road ». Rendre les services d'accréditation indépendants et réaliser les mesures sur des véhicules en circulation afin de déterminer les émissions réelles comme avec les véhicules lourds. Enfin, il est proposé de mettre en place une autorité Européenne en charge du contrôle du respect des tests effectués, de leurs conformités et de la répétabilité des concentrations de polluants mesurés en conditions réelles [34,43].

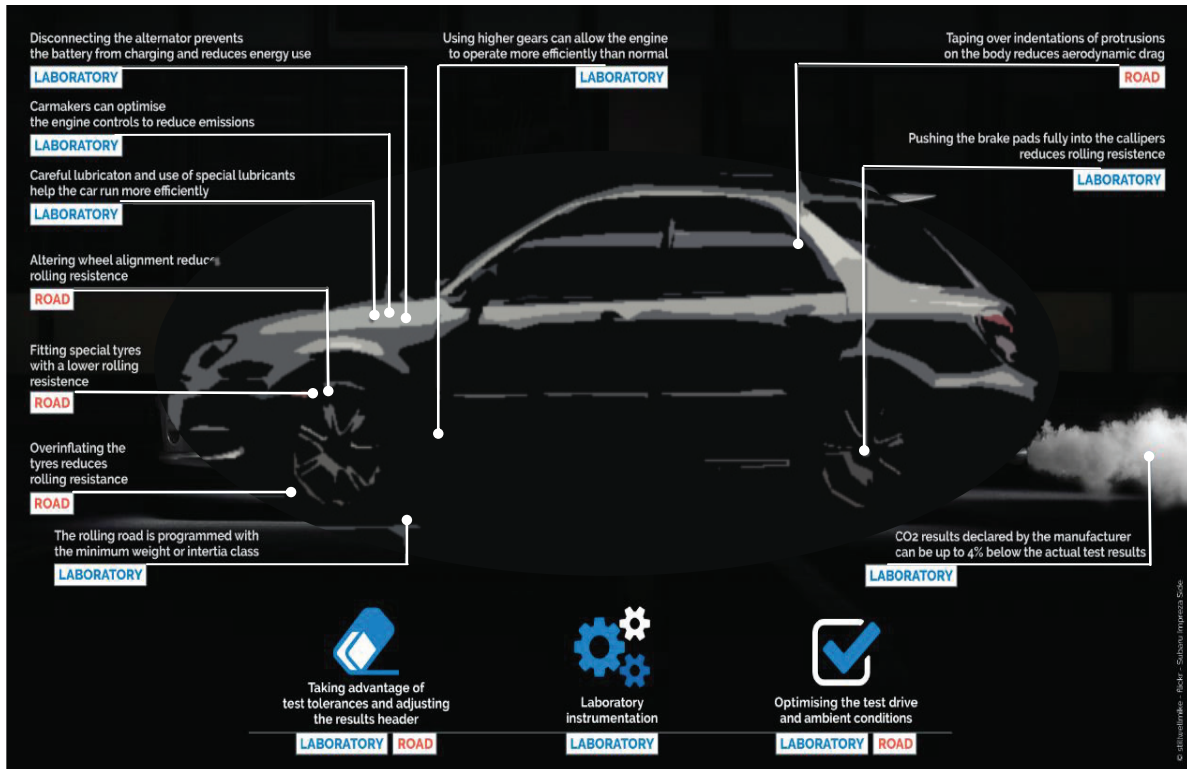


Figure I-8 : Biais potentiellement exploités lors des mesures d'émissions CO<sub>2</sub> pendant des tests sur banc moteurs [43]

#### I-4. La formation des polluants

Comme précédemment développé, les normes et réglementations à travers les pays incitent la recherche et le développement des systèmes de dépollution. Ainsi depuis le début des années 90, ces procédés ne cessent de se complexifier. Les moteurs deviennent plus efficaces et le carburant devient de meilleure qualité, ceci dans le but d'abattre un maximum de polluants [44]. La particularité du moteur diesel réside dans l'injection directe du carburant dans le cylindre où l'auto-inflammation se déroulera en excès d'air. Cette injection directe est donc plus propice aux combustions incomplètes et notamment à la formation de particules fines, de suies constituées d'agrégats de particules élémentaire de carbone amorphe, d'hydrocarbures lourds adsorbés de métaux d'usures, de cendres et de sulfates [45]. Typiquement, les émissions en polluants dépendront directement de la richesse du mélange de combustion, c'est-à-dire du rapport entre concentration en carburant et en air tel que :

$$Richesse = \frac{masse_{carburant}(injectée)}{masse_{carburant}(stoéchiométrie)} \times \frac{masse_{O_2}(stoéchiométrie)}{masse_{O_2}(injectée)}$$

Ainsi avec une richesse inférieure à 1 ( $R < 1$ ) le mélange est dit « pauvre ». La combustion se fait en excès d'air, typique de la combustion de diesel, et ce afin d'augmenter le rendement énergétique et de moins consommer de carburant. Cet oxygène en excès doit être finement dosé puisque les polluants émis par la suite en dépendent directement. Les oxydes d'azotes se formeront notamment plus facilement à hautes températures. A l'inverse une richesse supérieure à 1 ( $R > 1$ ) caractérisera les combustions de



carburant lors d'une accélération, par exemple, alors qu'une richesse balancée, dite stœchiométrique ( $R=1$ ) correspondra au fonctionnement normal d'un moteur à essence. C'est pour cela que les moteurs diesel émettent moins de monoxyde de carbone et d'hydrocarbures en général que les moteurs à essence. Il y a moins de carburant injecté donc moins de chaînes carbonées qui peuvent réagir en température et être découpées en CO ou CO<sub>2</sub>. Un exemple de composition de gasoil est présenté dans le Tableau 2 ci-dessous [44]. Afin de souligner que, malgré l'absence de composés azotés dans le carburant, les polluants NO<sub>x</sub> représentés par les produits azotés (oxyde d'azote (NO), dioxyde d'azote (NO<sub>2</sub>) et protoxyde d'azote (N<sub>2</sub>O)) créés par le phénomène de combustion sont un problème majeur des moteurs diesel.

Tableau I-2 : Exemple de composition de gasoil pour un carburant commun en Europe, % massique obtenu par spectrométrie de masse [44]

Famille Chimique	Type de motif structural	% Massique	Famille Chimique	Type de motif structural	% Massique
Paraffine	$C_nH_{2n+2}$	30,90	Acénaphène et diphényle		2,75
Naphtène non condensé		23,70	Fluorène et acénaphtylène		1,50
Naphtène condensé		15,10	Anthracène et phénanthrène		1,30
Alkylbenzène		9,20	Benzothiophène		1,60
Indane et tétraline		6,40	Dibenzothiophène		0,25
Indène		1,80	Naphtalène		5,50
				<b>Total</b>	<b>100</b>

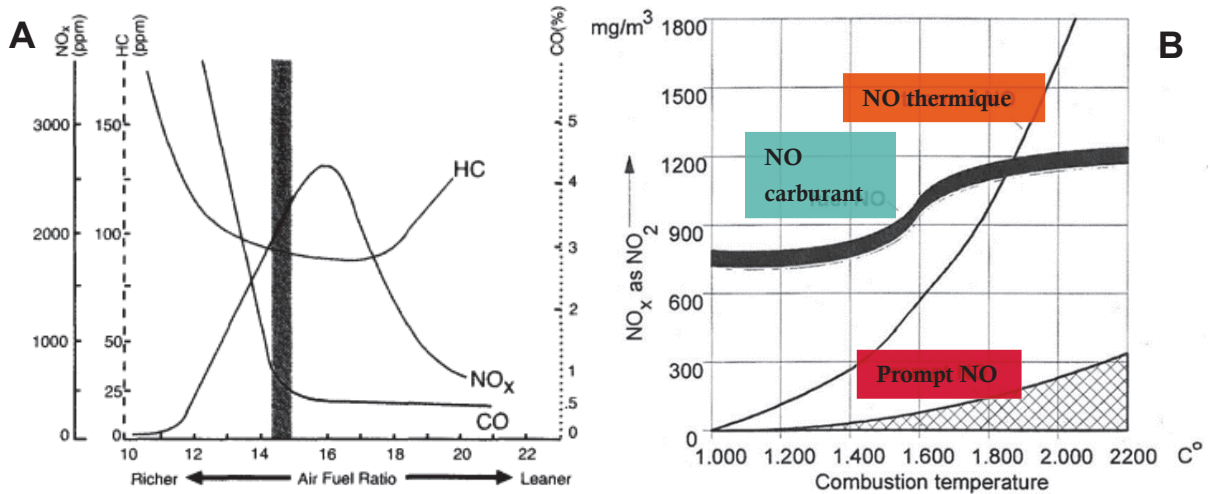


Figure I-9 : (A) Graphique résumant les concentrations émissibles des principaux polluants selon la richesse du mélange carburant/air et (B) Schématisation de la production de NO selon la température de combustion et le mécanisme de formation [46,47]

Cependant si le CO<sub>2</sub> est le polluant numéro 1 des motrices essences, ceux du diesel sont les oxydes d'azotes. En effet, en introduisant plus d'air, le diazote est plus susceptible de réagir avec l'oxygène et former de l'oxyde d'azote (NO). La production de NO<sub>x</sub> sera maximale en température pour un mélange légèrement pauvre comme montrée sur les Figures I-9 (a) et (b) [46,47]. Ainsi pour le Diesel, la combustion est beaucoup plus hétérogène car le mélange turbulent entre l'air et le combustible forme des concentrations d'espèces chimiques et des températures très variables au sein même de la chambre de combustion. C'est donc cette hétérogénéité qui est à l'origine de la formation des oxydes d'azotes dans les zones de très haute température et de la formation des fines particules de suies dans les zones localement déficitaires en oxygène. L'oxyde d'azote se produit alors selon trois mécanismes différents durant la combustion de carburant (cf. Figure I-9). Le premier est responsable du NO produit en front de flamme, appelé « **prompt NO** », dans les parties les plus froides de la flamme, où le N<sub>2</sub> réagit selon le mécanisme décrit par C.P. Fenimore [48] :

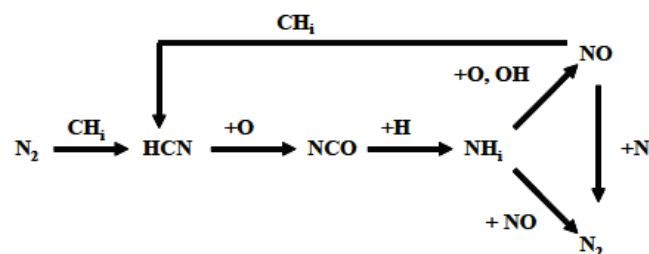


Figure I-10 : Chemin réactionnel du Prompt NO selon Fenimore

Le second mécanisme, majoritaire, forme le NO « **thermique** » entre l'azote et l'oxygène présent dans l'air à haute température (>1400°C) où  $\text{N}_2 + \text{O}_2 \rightarrow 2\text{NO}$ . Enfin le dernier mécanisme représente la plus petite partie de l'azote produit, le NO « **du combustible** », formé grâce à l'azote originaire du

carburant. Les deux autres NOx, le dioxyde d'azote et le protoxyde d'azote se formeront quant à eux plus tard dans le procédé de dépollution sur la ligne d'échappement. Ils seront principalement dûs aux opérations de dépollution elles-mêmes comme il sera détaillé dans la suite de l'exposé.

Ces polluants, et notamment le NO<sub>2</sub> et NO, se retrouvent donc acteurs dans la formation d'un oxydant naturel très puissant : l'ozone (O<sub>3</sub>), formé initialement selon le cycle de Chapman [49]. Comme schématisé sur la Figure I-11, l'ozone permet la transformation cyclique des oxydes d'azotes dans la troposphère contribuant ainsi à la formation de gaz à effet de serre [50].

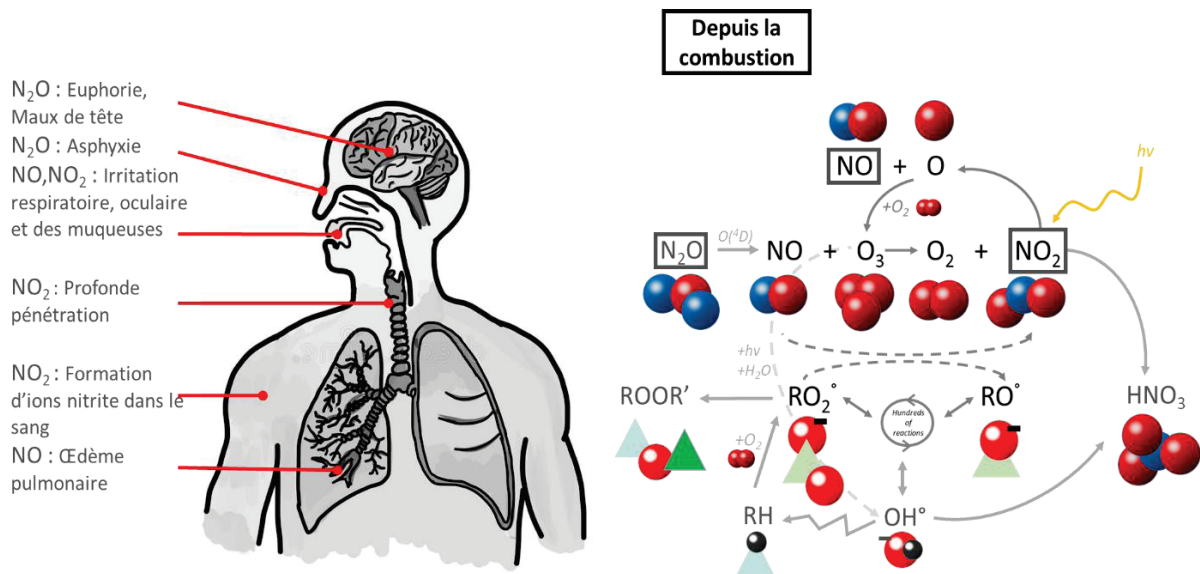


Figure I-11 : Chimie de l'ozone et cycle des oxydes d'azotes puis effet possible sur la santé de ces différents oxydes [51,52].

Il est important de considérer que le NO peut aussi réagir avec l'oxygène sans interaction aucune avec l'ozone pour former le NO<sub>2</sub> et réciproquement. De plus, le cycle des oxydes d'azotes interagit aussi avec celui des COV dont les radicaux oxydants permettent la formation de NO<sub>2</sub>. Ainsi, l'ozone formé n'est pas obligatoirement consommé et peut subsister selon divers chemins réactionnels [51]. C'est pourquoi un rapport élevé COV/NOx favorisera la formation de peroxydes comme H<sub>2</sub>O<sub>2</sub>, par exemple alors qu'une balance plus faible provoquera un bilan plus chargé en hydroxydes OH puisque moins sollicités pour réduire les NOx. Une plus grande concentration de radicaux -RO<sub>2</sub> sera donc susceptible de se former et de réagir pour former de l'ozone [53,54]. Pour terminer sur le résumé de ce cycle, nous remarquerons le lien direct de l'oxyde d'azote NO<sub>2</sub> avec le caractère acide des pluies par la formation d'acide nitrique HNO<sub>3</sub> lors de sa réaction avec les radicaux OH<sup>•</sup>.

Si aujourd'hui la sixième génération de norme demande la régulation du dioxyde d'azote et du monoxyde d'azote, la proportion du protoxyde d'azote dans ces 0.08g/km (cf. Figure I-4 (c)) autorisée n'est, elle, pas définie. Le problème étant que le protoxyde d'azote (N<sub>2</sub>O) possède un indice PRG (Pouvoir de Réchauffement Global) presque 300 fois supérieur à celui du dioxyde de carbone (CO<sub>2</sub>) [55]. Ce qui

fait de son contrôle, un enjeu imminent pour les prochaines réglementations européennes puisque la formation de ce dernier peut notamment être dû à un manque de sélectivité de la part du catalyseur et à un excès de  $\text{NO}_2$  [56–58]. Les technologies de dépollution ayant évoluées avec celles des normes, de nombreux procédés existent aujourd’hui, qu’ils soient propres aux constructeurs automobiles ou aux poids lourds, une architecture commune est souvent observée. Généralement, trois blocs plus ou moins distincts sont présents sur les lignes d’échappement de moteur diesel. Leurs positions dépendront fortement de leur fonction, c’est-à-dire des polluants cibles et donc des réactions chimiques mises en jeux et de leur température de fonctionnement. Mais de manière générale l’ordre est tel que présenté en Figure I-12: un Diesel Oxidation Catalyst (**DOC**) pour l’oxydation des hydrocarbures imbrulés et du  $\text{CO}$ , un Diesel Particulate Filter (**DPF**) pour filtrer mécaniquement les particules de suie et un organe de Selective Catalytic Reduction (**SCR**) pour réduire les oxydes d’azote en  $\text{N}_2$ . Le Tableau I-3 suivant fait un bref récapitulatif de ces quelques technologies. Mais il est tout à fait possible de retrouver des technologies combinatoires comme l’usage de filtre à particule fonctionnalisé pour l’élimination des  $\text{NO}_x$ , ou bien même des technologies de pièges à double fonctionnalités capturant les hydrocarbures et les oxydes d’azotes [59]. Il peut être aussi retrouvé sur la ligne d’échappement une vanne EGR (Exhaust Gaz Recirculation) permettant, à faible régime moteur, de refaire circuler les gaz vers l’injection pour réaliser une deuxième fois la combustion puis passer de nouveau dans la ligne d’échappement afin d’abattre une fraction de polluants plus importante.

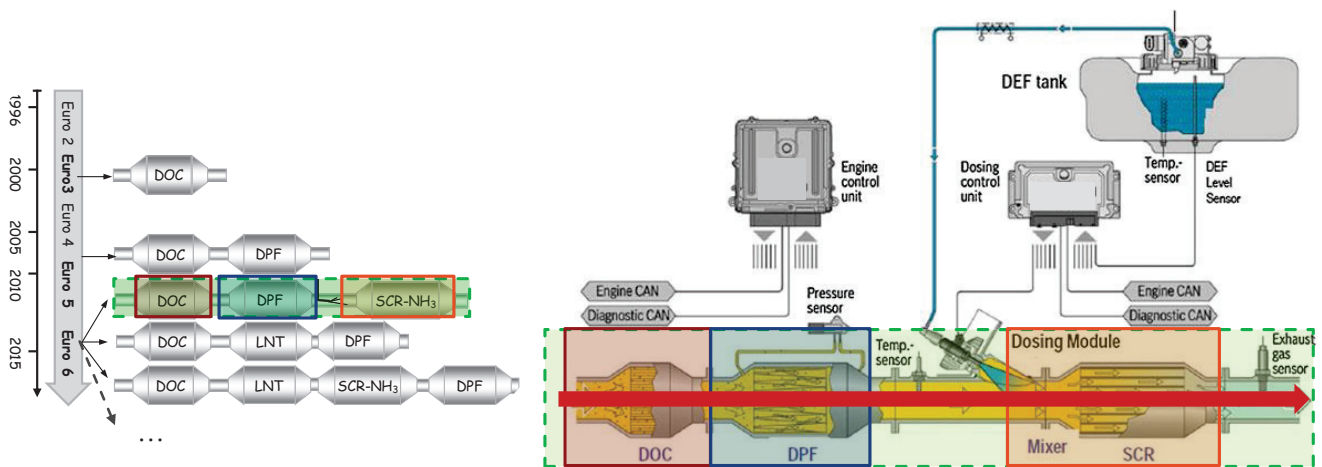


Figure I-12: Evolution des divers systèmes de post traitement dans le temps selon les normes (DOC Diesel Oxidation Catalyst, DPF : Diesel Particulate Filter, SCR : Selective Catalytic Reduction, LNT : Lean  $\text{NO}_x$  Trap) [59] avec schéma d’une configuration commune de post-traitement [61]

Tableau I-3 : Récapitulatif techniques de différents organes de dépollution pouvant être présents sur une ligne d'échappement

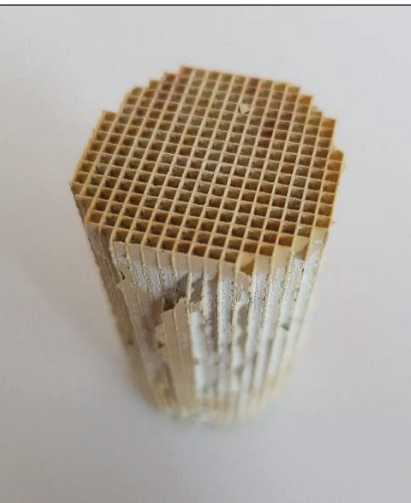
<b>Technologies</b>	<b>DOC</b>	<b>FAP</b>	<b>LNT</b>	<b>NH<sub>3</sub> SCR</b>
<b>Fonctions principales</b>	Oxydation du CO et HC	Stockage des suies Régénération active avec O <sub>2</sub> aux hautes températures (550°C-630°C)	Oxydation NO, stockage des NOx, puis réduction	Réduction des NOx par NH <sub>3</sub>
<b>Fonctions secondaires</b>	CRT : oxydation NO Régénération FAP Oxydation SOF	Régénération passive avec NO <sub>2</sub> aux faibles températures (340°C-450°C)	Oxydation CO et HC résiduel	Hydrolyse de l'urée (en amont de monolithe) Abatte excédent d'NH <sub>3</sub>
<b>Conditions opératoires</b>	150°C-600°C Phase riche	>450°C en phase de régénération	150°C-600°C Phase riche/pauvre	150°C-600°C
<b>Avantages</b>	Activité basse température Durabilité (>160 000km) Efficacité (>90%)	Amélioration de la filtration avec le piégeage jusqu'à point critique Peut-être fonctionnalisés	Stabilité thermique jusqu'à 850°C Activité basse température (150°C) pour démarrage à froid Pas d'injection supplémentaire (NH <sub>3</sub> )	Résistance hydrothermale avec zéolites Résistance au Phosphore Sélectivité N <sub>2</sub> Ratio NO <sub>2</sub> /NOx pouvant varier Pas de métaux précieux
<b>Inconvénients</b>	Faiblesses aux SOx Métaux précieux Stabilité thermique à 750°C	Demande à être régénéré Obstruction des pores menant à de forte perte de charge	Alternance de phase riche et pauvre (surconsommation) Piège aussi SO <sub>2</sub> et vieillit catalyseur Métaux précieux	Sublimation de métaux si Vanadium employés Résistance hydrothermale plus faible avec catalyseur base vanadium
<b>Contraintes</b>	Exposition aux plus fortes concentrations de poisons chimiques	Stabilité thermique jusqu'à 650°C	Passer en phase riche alors que la technologie diesel fonctionne en phase pauvre par nature	Transport de réservoir d'urée Assurer la conversion totale de NH <sub>3</sub> Travail à basse température difficile avec la formation de nitrate d'ammonium solide
<b>Éléments actifs</b>	Pt ; Pt/Pd	Aucun si non fonctionnalisés Sinon Pt ; Pd	Ba, Sr, (adsorption) Pd, Pt ; Rh (réduction)	V, Fe, Cu
<b>Nature des supports</b>	Al <sub>2</sub> O <sub>3</sub> ; SiO <sub>2</sub> ; CeO <sub>2</sub> ; CeO <sub>2</sub> -ZrO <sub>2</sub> TiO <sub>2</sub> ; zéolites	Cordiérite ; SiC	Al <sub>2</sub> O <sub>3</sub> ; SiO <sub>2</sub>	TiO <sub>2</sub> /WO <sub>3</sub> ; Zéolites

**I-5. Technologies de post traitements actuels**

Sur la ligne d'échappement il sera alors retrouvé un premier organe de dépollution, le monolithe d'oxydation (**DOC**). Physiquement, ce dernier se compose d'un monolithe et d'un revêtement catalytique dont les étapes de fabrication se composent comme suit et seront communes à la fabrication du 3<sup>e</sup> organe de dépollution (Selon la Figure I-12).

Le monolithe est tout d'abord produit via procédé d'extrusion par le fabricant A selon les dimensions données par le constructeur automobile B. Ainsi il peut choisir la porosité, l'ouverture de pore, la rugosité, le nombre de canaux, la forme, la tenue mécanique et la matière du monolithe. Le Tableau I-4 suivant donne quelques caractéristiques type d'un monolithe de cordiérite à titre d'exemple. Le fabricant C se charge quant à lui du revêtement de la « couche catalytique » sur le monolithe selon un procédé de revêtement (« coating ») où le monolithe est trempé dans une suspension comprenant la phase active et l'agent d'adhésion. Les paramètres de températures et de pH de la suspension seront finement contrôlés pour optimiser l'épaisseur de la couche et son adhésion aux parois [62]. L'agent d'adhésion varie selon le fabricant mais est souvent une silice colloïdale, et permet une bonne tenue mécanique après calcination de l'ensemble sans pour autant risquer de polluer les phases actives. L'opération de revêtement est délicate puisque le catalyseur ne doit pas être endommagé (par son stockage ou un environnement trop humide) ni recouvert sinon les sites actifs ne seront plus accessibles par les polluants. L'objectif est de tapisser de manière homogène les grains des parois du monolithe pour obtenir une couche uniforme de quelques micromètres seulement. Le fabricant C se procure ainsi la matière première chez un fournisseur D, développée selon les cahiers des charges du constructeur B. De manière générale, ce cheminement d'étapes sera employé pour la fabrication de chaque organe de dépollution du moment que ce dernier comporte une phase catalytique et un support monolithique.

Tableau I-5 : Caractéristique type d'un monolithe en céramique commercial et photographie d'une « Carotte » extraite de monolithe

<b>Composition</b>	Cordiérite (2 MgO, 2 Al <sub>2</sub> O <sub>3</sub> , 5 SiO <sub>2</sub> )	
<b>Porosité</b>	30%	
<b>Diamètre de pores (µm)</b>	2 – 10	
<b>Epaisseur parois (µm)</b>	100 – 200	
<b>Densité de cellule (cpsi)</b>	100 – 900	
<b>Surface géométrique (m<sup>2</sup>.L<sup>-1</sup>)</b>	2,6	
<b>Masse volumique (g/cm<sup>3</sup>)</b>	2,5	
<b>Conductivité thermique (W.m<sup>-1</sup>.K<sup>-1</sup>)</b>	0,8	
<b>Chaleur spécifique (kJ.kg<sup>-1</sup>.K<sup>-1</sup>)</b>	1,1	
<b>Expansion thermique (K<sup>-1</sup>)</b>	0,5 – 1 . 10 <sup>-6</sup>	
<b>Température limite d'utilisation (°C)</b>	1200	

Ainsi, le catalyseur DOC possède deux principales fonctions, l'une est d'oxyder les hydrocarbures imbrulés, le monoxyde de carbone et la fraction organique soluble des suies (SOF dont hydrocarbures polyaromatiques HAP) pour principalement former du dioxyde de carbone [63]. Et l'autre est d'oxyder le NO en NO<sub>2</sub> afin de permettre la régénération du FAP et la réalisation de la phase « FAST » de réduction catalytique sélective sur le monolithe SCR, phase détaillée dans la prochaine section. Le mécanisme réactionnel consiste donc en (I) l'adsorption d'O<sub>2</sub> sur le site actif, (II) la diffusion et adsorption des polluants CO et autres hydrocarbures pour que (III), les produits se désorbent de la surface tel que le CO<sub>2</sub> et la vapeur d'eau. Ainsi les réactions chimiques en jeux sur ce catalyseur se présentent communément selon les réactions 1 et 2 suivantes :

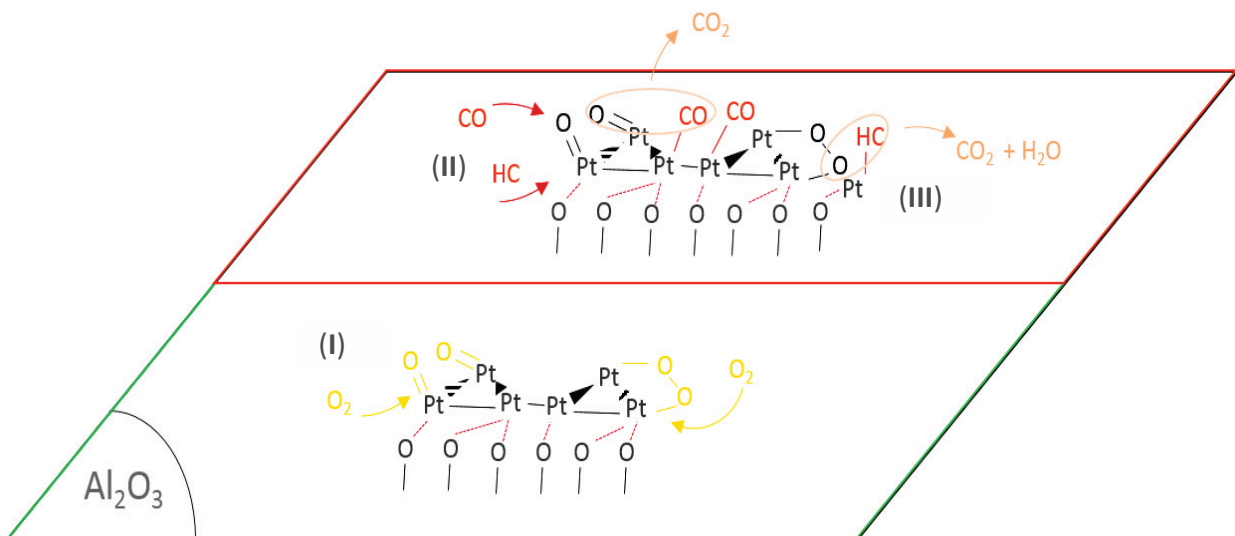


Figure I-13 : Mécanisme simplifié de la réaction de CO et HC à la surface d'un catalyseur type Pt/Al<sub>2</sub>O<sub>3</sub> [64,65] (les liaisons O support/Pt représente le phénomène de Strong Metal Support Interaction (SMSI))[66,67]

L'organe DOC étant généralement le premier sur la ligne d'échappement, il est le plus exposé aux espèces sulfurées et autres métaux alcalins (Na, K, ...) présents dans le carburant et les lubrifiants. Leurs concentrations auront un impact direct sur la désactivation et le vieillissement des différents catalyseurs[68,69]. Les réactions 4 et 5 montrent la formation de ces oxydes de soufre pouvant pénaliser le catalyseur. De plus, lors de passage de point froid, l'acide sulfurique H<sub>2</sub>SO<sub>4</sub> gazeux aura tendance à se

piéger dans la fraction de vapeur d'eau présente afin de former des particules sulfurées supplémentaires à celle des suies carbonées.

Les technologies DOC retrouvées aujourd'hui sur la plupart des véhicules consistent en un monolithe en céramique, en cordiérite ou carbure de silicium (SiC), revêtu d'une couche d'un matériau peu poreux en alumine ( $Al_2O_3$ ), ou silice ( $SiO_2$ ) ou alors très poreux avec l'emploi de zéolites. Ils servent tous de supports aux métaux nobles utiles à l'oxydation des polluants et dont leurs propriétés physico-chimiques respectives justifient leurs emplois. Les paramètres importants inhérents au support sont sa résistance thermique, sa surface spécifique, son volume de pores et sa réactivité de surface [70]. Par exemple, la faible surface spécifique de l'alumine avec une grande ouverture de pores permet la diffusion de plus grosses molécules comme les xylènes et donc de meilleurs taux de conversion [71], alors que les tamis moléculaires comme les zéolites permettent l'adsorption des HC à basse température pour les oxyder à plus haute température [72]. Une propriété qui est exploitée pour les démarrages à froid [73,74]. En ce qui concerne les métaux employés, les sites actifs pour la catalyse, ce sont le platine et le palladium qui arrivent en tête de liste. Leurs fonctionnements sont bien étudiés et ce depuis plusieurs décennies déjà [75,76]. Mais leur problème est double : le prix de ces précurseurs d'une part et leur stabilité thermique à haute température d'autre part. Effectivement le prix déjà conséquent de ces matières premières est amené à augmenter dans un futur proche dû à leur surexploitation. Aujourd'hui, une partie des recherches liées aux catalyseurs DOC visent à améliorer les performances de ces catalyseurs bimétalliques Pt/Pd pour augmenter leurs tenues en température et les rendre plus stables en présence de polluants induits par l'utilisation de biocarburant [69]. Par exemple, sont largement étudiés les supports d'alumine stabilisés par un oxyde mixte de cérium et de zircon (CeO<sub>2</sub> ZrO<sub>2</sub>). Utilisé alors comme phase complémentaire, la cérium permet une diffusion plus aisée de l'oxygène lors du procédé d'oxydation ainsi que son stockage, ce qui est utile lors des phases moins riches en oxygène [77]. D'autres catalyseurs à base de pérovskite sont aussi étudiés afin d'améliorer l'oxydation de NO et résoudre la problématique de formation des suies et montrent des résultats déjà très encourageant [78–80].

En entrée du second organe de dépollution sont alors retrouvés le CO<sub>2</sub>, H<sub>2</sub>O, SO<sub>2</sub>, N<sub>2</sub>, O<sub>2</sub>, NO, NO<sub>2</sub> et les suies. Ces dernières sont constituées de particules solides enrobés d'huile d'hydrocarbures, de sulfates et autre poison et doivent être filtrées puis éliminées. Le procédé le plus utilisé est celui du Diesel Particulate Filter **DPF** (ou FAP en français) permettant d'atteindre des performances de filtration supérieure à 90 % en masse. Il se doit d'avoir un haut pouvoir filtrant, de donner de faible perte de charge sur la ligne et de supporter de hautes températures lors des périodes de régénération. Pour cela, des céramiques poreuses comme le carbure de silicium (SiC) et la cordiérite sont principalement employées [81]. Il peut être aussi utilisé d'autres alliages comme des nitrures de silicium (Si<sub>3</sub>N<sub>4</sub>), le titanate d'aluminium (Al<sub>2</sub>TiO<sub>5</sub>) ou de la mullite (3Al<sub>2</sub>O<sub>3</sub>, 2SiO<sub>2</sub>) pour leurs caractères hautement réfractaires. Les différences avec le monolithe d'un DOC ou SCR résident en la différence de circulation des gaz dans le cylindre. Si les canaux du monolithe sont tous ouverts et permettent au gaz de directement le traverser de part en part, le DPF lui,



force le gaz à traverser ses parois en obstruant la sortie d'un canal sur deux. C'est l'exemple de la Figure I-14. Il possède aussi une plus faible densité de cellule (100 à 200 cpsi) que le monolithe standard (300 à 400 cpsi) et des parois plus épaisses (300 à 500 μm contre 300 pour un monolithe de cordiérite courant).

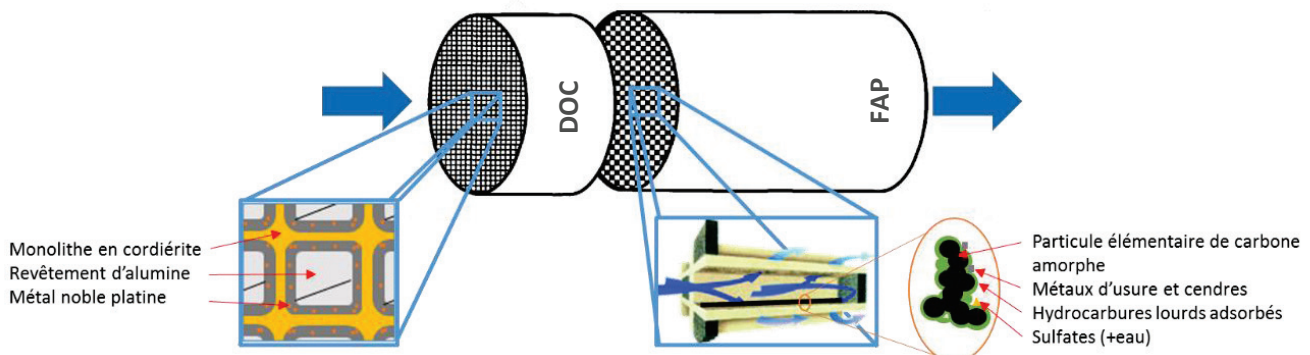


Figure I-14 : Comparaison et exemple de monolithe et de filtre à particules (avec principe « wall-flow ») présents dans la ligne d'échappement.

Le filtre à particule se charge donc en suite au fil du temps puisque les particules d'abord retenues dans les porosités des parois finissent par former, couche après couche, une barrière (appelé un « gâteau ») de moins en moins perméable au passage de ces dernières. C'est pourquoi avant d'arriver à saturation et de provoquer de trop forte perte de charge, il doit dégager ses porosités, être régénéré. Pour ce faire, des températures supérieures à 550°C doivent être atteintes dans le filtre afin de brûler les suies soit en injectant du carburant directement dans la ligne d'échappement avant le DOC, soit en l'injectant lors de la phase de détente du cycle moteur [82]. De telles températures influencent directement les conditions opératoires des catalyseurs DOC et SCR qui se doivent alors d'être stable à ces températures. Le DPF peut aussi être fonctionnalisé avec un revêtement catalytique similaire au DOC afin de faire réagir plus rapidement les suies avec l'oxygène et de régénérer le dioxyde d'azote (oxydant plus fort) consommé. Il s'agit alors de la technologie communément appelée « Continuously Regenerating Trap » (CRT) [83,84], tel que :



Cela peut provoquer la variation du ratio  $NO_2/NO_x$  du flux gazeux arrivant sur le monolithe suivant. Il peut aussi être fonctionnalisé pour la réduction des oxydes d'azote en intégrant la fonction SCR en revêtant le catalyseur adéquat, type cuivre – zéolite par exemple <sup>[A39]</sup>, illustré sur la figure 15 suivante. Cependant, Colombo et al. [85] ont aussi démontré un impact non négligeable de la charge en suie du filtre sur les performances de dénoxyfication, où l'activité de réduction de NO par  $NH_3$  est pénalisée par la diffusion plus difficile de NO à travers la couche de suie. Enfin, une dernière façon d'activer cette combustion consiste à directement injecter quelques ppm de catalyseur dans le carburant. La technologie « Fuel-borne catalyst » développée par le groupe PSA [86] permet le contact intime des suies et du catalyseur, généralement un précurseur de cérium ou de fer, lors de la combustion du carburant. Ceci permet donc une élimination des suies à plus basse température. Chaque technologie concentre plus ou moins

l'effluent gazeux en espèces chimiques. Elles doivent être prises en compte lors du choix des catalyseurs qui doivent être employés à la suite sur la ligne d'échappement.

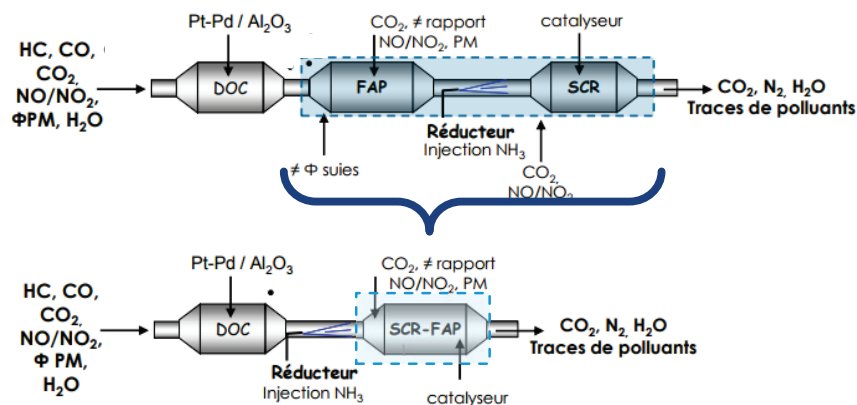


Figure I-15 : Exemple d'intégration de fonction de réduction catalytique sélective des NOx au FAP [59]

La plupart des polluants ont déjà été abattus depuis leur entrée dans la ligne d'échappement, il est donc retrouvé en sortie de DPF: CO<sub>2</sub>, N<sub>2</sub>, H<sub>2</sub>O, NO, NO<sub>2</sub>, O<sub>2</sub> et quelques poisons n'ayant pas déjà été retenues par les différents monolithes précédents. Ainsi pour traiter la dernière famille de polluants, deux procédés peuvent être employés : le piégeage ou la réduction des NOx. La première technologie communément dénommée Lean NOx-Trap (LNT) ou NOx Storage Reduction (NSR) est un catalyseur, appliqué sur monolithe lui aussi, reposant sur les propriétés acido-basiques et d'oxydant/réducteur des matériaux qui le compose. Il est important de noter que cette technologie de réduction des oxydes d'azotes se place généralement en amont du filtre à particule du fait de la nécessité des réducteurs pouvant se piéger dans le DPF. Sa principale fonction est d'abattre les NOx en deux phases distinctes, présenté en Figure I-16.



La première, se caractérise par un mélange gazeux pauvre ( $R < 1$ ), permettant l'adsorption de NO et de O<sub>2</sub> sur le platine (I) puis son oxydation formant NO<sub>2</sub>. Ceci permettant de désorber le NO<sub>2</sub> sur le baryum par voie nitrite, représenté par la réaction (9), formant Ba(NO<sub>3</sub>)<sub>2</sub> (II). Ensuite lors de la deuxième phase, par injection de phase riche dans l'effluent gazeux (de carburant directement), les NOx stockés désorbent (III) puis sont réduits par les hydrocarbures injectés en N<sub>2</sub> et O<sub>2</sub> via adsorption sur les clusters de rhodium (IV).

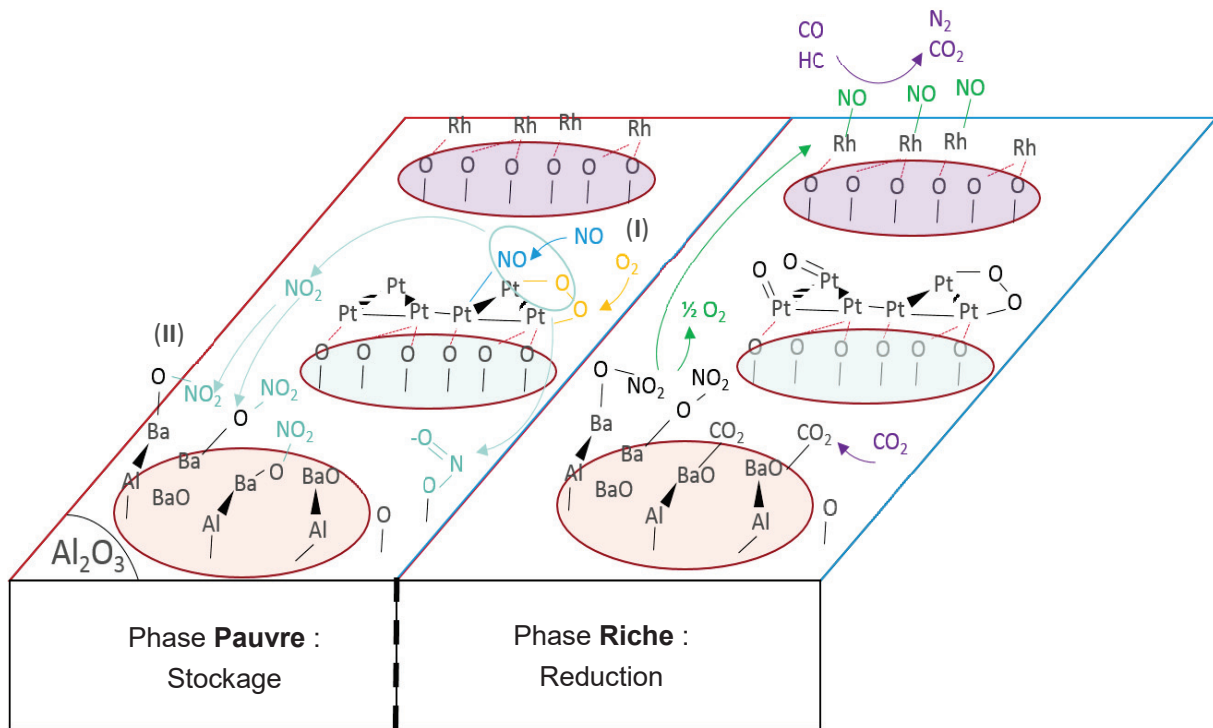


Figure I-16 : Mécanisme simplifié du LNT avec Platine, Rhodium, Barium en phases actives [87,88]

Les sites actifs permettant le stockage des NO<sub>x</sub> peuvent être de nature diverses comme des métaux alcalins (K, Na) ou alcalino terreux (Ba, Sr) ou encore des terres rares [89,90]. Le site réducteur des NO<sub>x</sub> pourra être quant à lui l'élément rhodium par exemple [91]. Comme pour le DOC, les composés soufrés auront un grand pouvoir de désactivation sur le catalyseur, d'autant plus qu'à haute température il pourra former avec le baryum des espèces stables comme le BaSO<sub>4</sub>, ce qui diminuera fortement les performances du catalyseur puisque incapable de stocker les NO<sub>x</sub> [92,93]. Les opérations de désulfatation du catalyseur lors des séquences répétées riche/pauvre produiront de l'H<sub>2</sub>S dans l'effluent gazeux qui est un polluant supplémentaire [94,95]. Cette opération aura donc l'inconvénient de demander un autre procédé pour les éliminer. Comme reporté en Tableau I-3, le LNT possède des avantages certains mais aussi de nombreux inconvénients. Notamment les phases répétées de régénération en phase riche, qui permettent de libérer les sites de stockage des NO<sub>x</sub> plus souvent, mais consomme fatalement plus de carburant [96]. C'est pourquoi la recherche de catalyseur moins chargée en métaux précieux, plus efficace à haute température et plus résistante aux sulfures, est primordiale sur cette technologie, afin de rester compétitif face à la Réduction Catalytique Sélective à l'ammoniac (NH<sub>3</sub> SCR).

## I-6. Les procédés de réduction catalytique sélective (SCR) : cahier des charges et innovations technologiques

### I-6.1. Le réducteur : L'ammoniac (NH<sub>3</sub>)

Il existe depuis les années 1970 déjà, un procédé de réduction d'oxydes d'azote très performant abattant plus de 90% de ces polluants et utilisant relativement peu de métaux nobles. En effet, le catalyseur trois voies (Three Way Catalyst) utilise les hydrocarbures imbrulés et le monoxyde de carbone (CO)

présent dans l'effluent gazeux riche comme réducteur des oxydes d'azotes. Il emploie, par exemple, des sites actifs de rhodium pour catalyser ces réactions [97]. Cependant, les motorisations Diesel fonctionnent en excès d'O<sub>2</sub>, cette technologie TWC ne peut donc malheureusement pas fonctionner. Afin de réaliser cette tâche, un procédé plus récent commercialisé en 2003 [98] et breveté par EngelHard Corporation (BASF de nos jours) en 1957, permet de réduire la fraction de polluants en composés inoffensifs : la Réduction Catalytique Sélective à l'ammoniac (NH<sub>3</sub> SCR). Le réducteur NH<sub>3</sub> est stocké sous forme d'urée (CH<sub>4</sub>N<sub>2</sub>O) en solution, plus connu sous le nom d'*Ad blue*® en Europe, marque déposée par l'association Allemande de l'industrie automobile : Verband Der Automobilindustrie e.V. (VDA) qui équipe les premiers poids lourds en 2005. Le « Diesel Exhaust fluid » (DEF) ou aqueous urea solution (AUS) concentré à 32.5% en urée, se doit d'être non toxique, d'avoir une température de gel basse (-11°C généralement) et de libérer l'ammoniac par hydrolyse à de faibles températures (133°C), lors de son entrée dans la ligne d'échappement [A41]. Cette décomposition se déroule en deux étapes comme suit en Figure I-17:

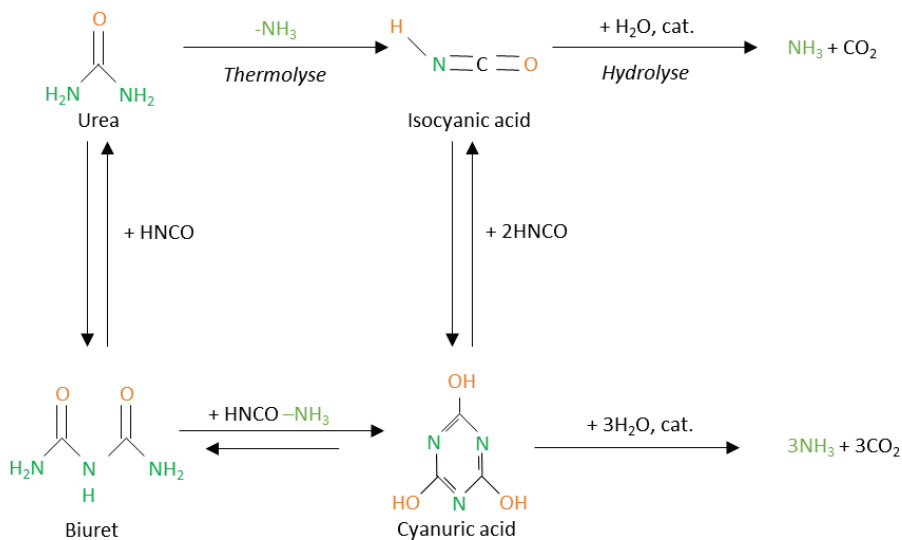


Figure I-17 : Schéma réactionnel de la décomposition de l'urée et de la formation des sous-produits [99,100].

Pour ce faire l'urée liquide est injectée via une buse dans les gaz d'échappement suffisamment en amont de monolithe SCR pour obtenir l'ammoniac en phase gaz. Pour mélanger le réducteur au flux, il est souvent employé un « mélangeur » en métal, dont le but est de créer suffisamment de turbulence afin de disperser et distribuer l'ammoniac de manière la plus homogène possible dans le flux passant. Dans le cas contraire, si certains canaux du monolithe se retrouvent pauvres en NH<sub>3</sub> la réduction sera moins performante, alors que des canaux plus riches que nécessaire ne consommeront pas la totalité de l'ammoniac et seront retrouvés dans l'effluent rejeté à l'atmosphère. C'est en partie pour cela qu'un dernier monolithe (l'Ammonia Slip Catalyst : ASC) dont l'objectif est la transformation de NH<sub>3</sub> en N<sub>2</sub>, peut se retrouver derrière le bloc SCR. L'injection de l'urée dans le gaz d'échappement est une problématique à part entière au procédé de SCR qui est l'objet de nombreuses études aujourd'hui. Elles demandent une transversalité de compétences entre mécanique des fluides, simulations de comportement

de fluides et mécanismes réactionnels [101,102]. Mais malgré ses avantages, l'Adblue pose certains problèmes qui demandent eux aussi à être étudiés, par exemple, la décomposition de l'urée peut avoir tendance à former un précipité d'urée condensé et ainsi détériorer les performances d'injection du réducteur [98]. De plus comme montré en Figure I-17, si l'acide isocyanique est stable et demande un catalyseur pour s'hydrolyser rapidement, différents sous-produits faits de chaînes de polymères peuvent se former entre temps comme le biuret et l'acide cyanurique mais aussi le triuret ((H<sub>2</sub>NC(O)NH)<sub>2</sub>CO) la melamine (C<sub>3</sub>H<sub>6</sub>N<sub>6</sub>), ammeline (C<sub>3</sub>H<sub>5</sub>N<sub>5</sub>O) et l'ammelide (C<sub>3</sub>H<sub>4</sub>N<sub>4</sub>O<sub>2</sub>) [100]. Autant de composés pouvant être parasites au bon déroulement du procédé de SCR. Cette problématique ne sera pas soulevée dans cette étude, puisque l'ammoniac en phase gaz sera considéré comme étant le seul produit de décomposition et directement injecté au mélange réactionnel.

## I-6.2. Les catalyseurs développés en NH<sub>3</sub>-SCR

### I-6.2.1 Catalyseur à base d'oxydes de Vanadium et Tungstène : Fonctionnement et limites Les catalyseurs développés en NH<sub>3</sub>-SCR

Différentes phases actives et supports ont été employés et justifiés au gré des innovations et des normes de régulations. La Figure I-18 retrace les principaux catalyseurs utilisés en NH<sub>3</sub> SCR dans le temps. Un catalyseur en supprime un autre lorsque ce dernier affiche une meilleure efficacité, stabilité et un faible coût de production.

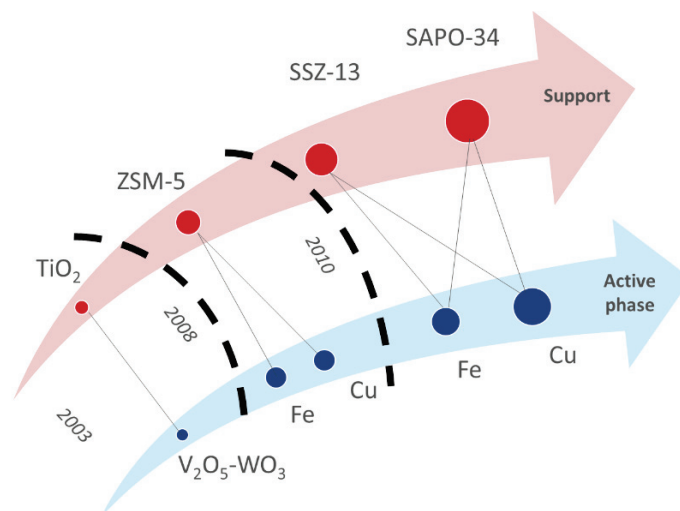


Figure I-18 : Chronologie de l'emploi des catalyseurs pour la NH<sub>3</sub> SCR [98,103]

Parmi les différents catalyseurs développés pour les opérations de réduction catalytique sélective, une formulation d'oxyde mixte s'est particulièrement imposée pour les applications mobiles et stationnaires ces dernières décennies. En effet, depuis les années 1970 déjà, le Japon employait sur ces installations industrielles d'extraction de charbon et de gaz, des catalyseurs à base de vanadium et de titane [104]. Aux vues des diminutions d'émissions de polluants des industries japonaises, l'Europe ne tarda pas à prendre exemple et équipa ces installations du précieux catalyseur dans les années quatre-vingt. Motivée par la mise en place des premières normes EURO visant la régulation des émissions des sources mobiles,

l'idée d'employer cette technologie sur les sources mobiles, et notamment les poids lourds, ne tarda pas à éclore dans les années 1990 [105]. C'est après la démonstration de performance sur poids lourds et avec la parution des normes automobiles EURO 4 et 5 que le procédé de  $\text{NH}_3$  SCR employant de l'urée fut majoritairement mis en place à grande échelle dès 2003. Typiquement, le catalyseur se constitue d'un composé actif : l'oxyde de vanadium ( $\text{V}_2\text{O}_5$ ), d'un support : oxyde de titane ( $\text{TiO}_2$ ) et d'un promoteur : l'oxyde de tungstène ou de molybdène ( $\text{WO}_3$  ou  $\text{MoO}_3$ ). Sur la Figure I-18, est schématisé le mécanisme simplifié de l'opération de  $\text{NH}_3$  SCR à la surface du support de  $\text{TiO}_2$  sur les complexes activés de vanadium. Sont aussi indiqués les représentations de Lewis des espèces polymériques et monomérique du vanadium ainsi que son promoteur de tungstène. Le rôle du promoteur ( $\text{WO}_3$  ou  $\text{Sb}_2\text{O}_3$ ) consiste quant à lui à augmenter le nombre de sites acides et de diminuer l'activité catalytique de la réaction d'oxydation du dioxyde de soufre en anhydride sulfurique [106,107].

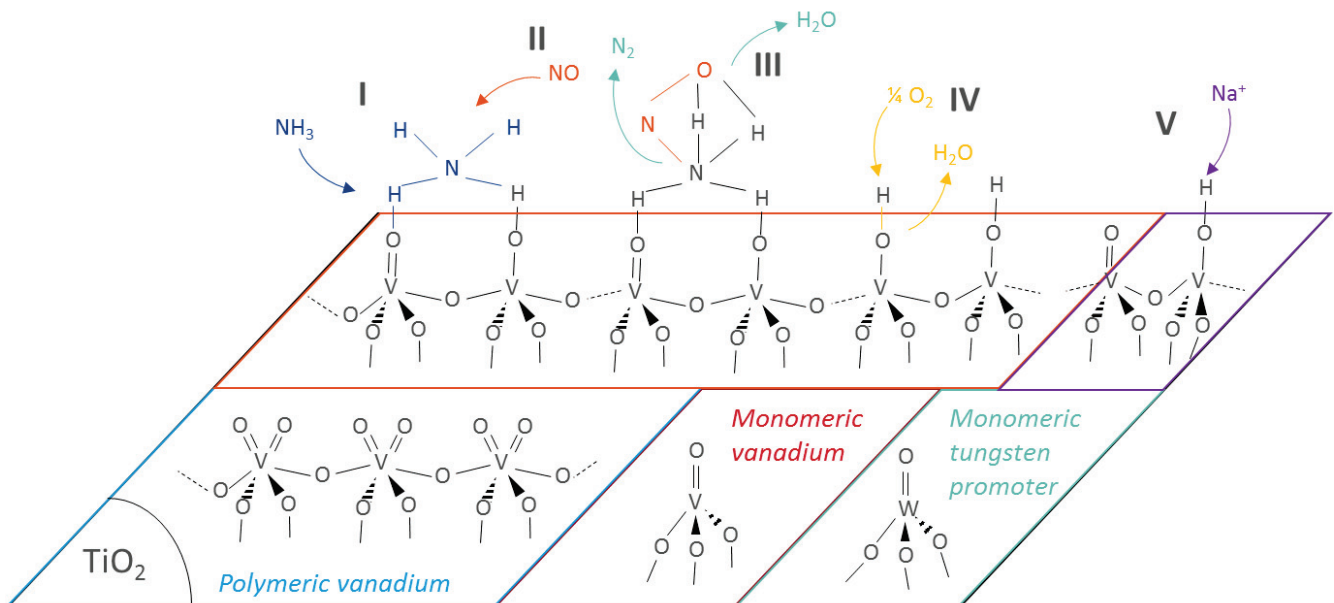


Figure I-19: Mécanisme simplifié de la réaction de  $\text{NO}/\text{NH}_3$  à la surface d'un catalyseur type  $\text{V}_2\text{O}_5$ - $\text{WO}_3/\text{TiO}_2$  selon Inomata et al. [108] ainsi que Miyamoto et al. [109] avec les différentes espèces de surface.

Le mécanisme commence alors par l'adsorption du réducteur  $\text{NH}_3$  sur le site acide double pour former  $\text{NH}_4^+$  (I), puis le  $\text{NO}$  gazeux réagit selon un mécanisme Eley-Rideal avec le  $\text{NH}_4^+$  afin de former un complexe activé (II). S'ensuit la désorption de  $\text{N}_2$  et de  $\text{H}_2\text{O}$  du complexe (III) laissant deux sites acides dont l'un sera régénéré en double liaison oxygène  $\text{V}^{5+} = \text{O}$  via une oxydation avec  $\frac{1}{4} \text{O}_2$ , libérant par la même occasion de l'eau (IV). Enfin si ce type de catalyseur est plutôt robuste aux agressions de soufre [110], les métaux alcalins sont de forts poisons selon l'ordre  $\text{Li} < \text{Na} < \text{K} < \text{Rb} < \text{Cs}$  pouvant faire perdre totalement l'activité catalytique avec seulement moins d'un pourcent molaire [111]. Comme le montre la dernière étape de la Figure I-19 (V), le métal réagit avec le site acide  $\text{V}-\text{OH}$  empêchant ainsi l'adsorption de l'ammoniaque. Une autre faiblesse du catalyseur a remis directement en compte son utilisation depuis

quelques années, son comportement au vieillissement hydrothermal. Effectivement, le point faible du catalyseur  $V_2O_5-WO_3/TiO_2$  est sa résistance aux conditions hydrothermales montrant une diminution de l'activité catalytique très importante à partir de  $600^\circ C$  après seulement quelques heures d'exposition [112,113]. Il a été attesté qu'il s'agit d'une part de la diminution de la surface spécifique du support  $TiO_2$  lors de sa phase de frittage et de son changement de phase en rutile. D'autre part, proche des  $500^\circ C$ , le  $V_2O_5$  commence par amorcer sa sublimation faisant alors passer dans le mélange d'échappement du vanadium et du tungstène métal, ce qui diminue grandement les performances catalytiques sur le long terme et relargue des espèces supplémentaires très nocives dans l'atmosphère [114].

#### I-6.2.2 Catalyseurs zéolitiques supportant un métal de transition (Cu et/ou Fe) des MFI aux CHA

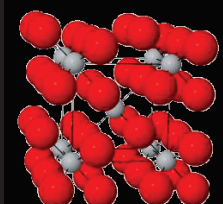


##### (1) *Le support*

Si les catalyseurs  $V_2O_5-WO_3/TiO_2$  ont été déployés en masse sur les installations stationnaires et les poids lourds, leur manque de stabilité une fois dans la ligne d'échappement a favorisée l'utilisation d'une autre nature de catalyseurs : les zéolites supportant des métaux de transition. En effet, ces céramiques appelées aussi « tamis moléculaires », se caractérisent par une structure cristalline constituée d'une succession tridimensionnelle d'enchaînement de tétraèdre ( $TO_4$  avec T le Si, Al, P ...) pouvant former des cages de diverses dimensions aux ouvertures de centaines de nm jusqu'aux centaines de pm [115]. L'atome T du tétraèdre peut varier mais généralement ce sont des Si et Al qui constitue l'entièreté de la maille cristalline. Chaque atome d'oxygène étant lui-même partagé avec deux éléments T, la formule générale peut être représentée telle que :  $(M_{x/n}^{m+}[Al_x Si_y O_2(x+y)]^{x-} z H_2O)$ . De plus, les extensions reliant ces tétraèdres, de séquence type [T-O-T], se définissent comme des unités de construction secondaires (Secondary building unit construction).

La définition de zéolite ne peut être accordée que si les canaux ainsi formés et les cavités sont suffisants pour laisser traverser de la matière de part en part du matériau et si des cations de charge compensatoires peuvent s'y loger (eau, sels...) [116]. Il est recensé et approuvé par la communauté scientifique 235 codes de zéolites de structures différentes sachant que chaque code peut lui-même représenter des zéolites de compositions chimiques différentes, comme le référence la base donnée de l'International Zeolite Association (IZA). Autant de variétés pouvant présenter des propriétés plus ou moins exploitables en  $NH_3$  SCR. Effectivement, les propriétés physiques d'un support catalytique se caractériseront par sa surface spécifique, son volume poreux, son agencement (forme), sa distribution en taille de pores et sa granulométrie. Alors que ses propriétés chimiques regrouperont entre autres : l'acidobasicité de la surface, la composition chimique de la structure ou bien l'état d'oxydation des espèces actives. Propriétés pouvant être modulées selon la voie de synthèse sol-gel entreprise en contrôlant la température, le type de solvant, le pH, l'agent structurant, les précurseurs et le temps de vieillissement du gel. Ainsi il est possible de former des supports zéolitiques à caractéristiques contrôlées [117].

C'est pourquoi des catalyseurs aux supports zéolitiques comme la ZSM-5 (MFI), à ouverture de pore moyenne (0,5 nm) ont commencés à remplacer les catalyseurs au vanadium. Leur propriété leur permettant d'être plus actifs, plus stables en température et n'employant pas de métaux rares comme le souligne le Tableau I-6 [118,119]. Mais la demande de catalyseurs plus stable en conditions hydrothermales se faisant, les limites de résistances des supports catalytiques ont dû être repoussées à d'autres extrêmes. Ainsi le support zéolitique de structure Chabazite, à faible ouverture de pore (35Å), se voit être aujourd'hui le sujet de nombreuses recherches afin de pouvoir proposer un système catalytique plus résistant et plus efficace encore. Il fut démontré que l'emploi de support à petite ouverture de pore telle que les Chabazites permet d'obtenir une plus grande activité à basse température et une résistance hydrothermale accrue en comparaison avec d'autres zéolites à ouverture de pore plus grande [98,118]. Concernant leurs performances, il a été proposé dans la littérature que la formation de complexes activés de  $[\text{NH}_4^+_x][\text{NO}]$  ( $x=1,2$ ), intermédiaires pivots de la SCR ici, pourraient être facilités avec de petits pores [120,121]. Une seconde hypothèse pouvant justifier cette hausse de performance concernerait la concentration élevée d'intermédiaires  $3\text{H-NH}_4^+$  [122] à l'intérieur des petites cages de la zéolite qui favoriserait la formation de  $[\text{NH}_4^+_x][\text{NO}]$ . Leur résistance hydrothermale quant à elle, pourrait se justifier par leur caractère réfractaire en tant que matériaux céramique et une diminution du phénomène d'hydrolyse des liaisons  $-\text{Si-O(H)-Al}-$  entre la structure et les molécules d'eau, diminuant ainsi les probabilités de déalumination [123,124]. Processus d'autant plus limité que les faibles ouvertures de pores permettraient de contenir les espèces  $\text{Al(OH)}_3$  se décrochant de la structure à l'intérieur des cages [125].

Tableau I-6 : Informations physicochimiques de supports types utilisés en  $\text{NH}_3$  SCR [126]

Nom (code structure)	Oxyde de Titane	Zeolite Socony Mobil-5 : ZSM-5 (MFI)	SSZ-13 (CHA)	SAPO-34 (CHA)
<b>Composition élémentaire</b>	$\text{TiO}_2$ Phase active : $\text{V}_2\text{O}_5$ $\text{W}_2\text{O}_3$	$[\text{Na}_n\text{Al}_n\text{Si}_{96}\text{O}_{192} \cdot 16\text{H}_2\text{O}]$ ( $0 < n < 27$ ). Phase active : Fe / Cu	$\text{R}_x[\text{Na}_y\text{Al}_{2.4}\text{Si}_{133.6}\text{O}_{72} \cdot z\text{H}_2\text{O}]$ ( $1.4 < x < 27$ ) ( $0.7 < y < 4.3$ ) ( $1 < z < 7$ ) avec Q étant N,N,N-1-triméthyladamantammonium Phase active : Fe / Cu	mR $[\text{H}_3\text{Si}_3\text{Al}_{18}\text{P}_{15}\text{O}_{72}]$ avec R étant Tetraéthylammonium hydroxide Phase active : Fe / Cu
<b>Schéma maille cristalline</b>	 (rutile : Tetragonal)	 (orthorhombic)	 (rhombohedral)	
<b>Taille de pore (nm)</b>	18 (P25) pas de cages	0.55	0.38	
<b>Surface spécifique (<math>\text{m}^2/\text{g}</math>)</b>	35-65 ( $\text{TiO}_2$ rutile, P25) 200 ( $\text{TiO}_2$ anatase)	300-400	500-700	
<b>Cages</b>	/	10 6 5 4	8 6 4	
<b>Acidité</b>	Acido-basique	Acide (Si/Al = 10-100)	Acide moyen (Si/Al = 1-50)	Acide moyen (Si/Al = 0.05-2)
<b>Régime de diffusion intra</b>	/	Knudsen	Configurationnel	



Dans la famille des Chabazites, zéolites à petits pores, deux principales structures sont employées : la SSZ-13 et la SAPO-34. La majeure différence entre les deux supports réside dans la manière d'introduire le Si dans la maille cristalline et du rapport Si/Al en résultant. Un contraste qui aura, *in fine*, un fort impact sur les performances catalytiques et la résistance du catalyseur. Lors de la synthèse sol-gel pour SSZ-13, le silicium et l'aluminium forme la structure aluminosilicate de concert lors de l'interaction de leurs précurseurs respectifs. Ainsi, plus le ratio Si/Al sera élevé, plus les tétraèdres de SiO<sub>2</sub> seront en minorité face aux tétraèdres de AlO<sub>2</sub><sup>-</sup>, chargés négativement. C'est par leur biais que les ions compensatoires H<sup>+</sup>, apporté par l'agent structurant, pourront alors se positionner pour stabiliser la liaison Si-OH-Al et donc former les acides de Brønsted fort. Ces sites formés par les espèces hydroxyles (OH) à l'interface entre le silicium et l'aluminium se caractérisent par leur capacité à échanger leur proton de balance (H) avec d'autres espèces afin de les rendre adsorbées à la surface. Ainsi le NH<sub>3</sub> s'adsorbant sur un site de Brønsted passe par un état protoné : NH<sub>4</sub><sup>+</sup>.

Avec la zéolite SAPO-34 en revanche, une première structure aluminophosphate (AlPO<sub>4</sub>) se forme entre l'Al et le P. Cette structure neutre cantonnée à la formation d'enchaînement de tétraèdres AlO<sub>2</sub><sup>-</sup> et PO<sub>2</sub><sup>+</sup> ne possède pas de cations ou anions compensatoires et ne possède donc pas intrinsèquement de sites acides de Brønsted. Ainsi lors de la synthèse hydrothermale, le silicium présent dans le mélange réactionnel parvient à se substituer au phosphore de la structure selon trois mécanismes [127,128] :

- SM1 : Un atome d'aluminium est remplacé par un atome de silicium. Mécanisme peu courant puisque deux charges positives seraient apportées, la liaison Si-O-P est par ailleurs démontrée instable [129,130].
- SM2 : Un atome de phosphore (V) est remplacé par un atome de silicium (IV) passant de P-O-Al à Si-OH-Al. L'hydroxyle OH compensant la charge monovalente créée par le Si.
- SM3 : Deux atomes de silicium substituent à la fois un Al et un P de la structure.

Selon SM2 ou 3, un site acide de Brønsted pourra être mis en place pour chaque P substitués (SM2) ou alors des agrégats de Si seront formés (Si-island) par l'expression des deux mécanismes simultanément (SM2 et 3) [131,132]. La Figure I-20 ci-dessous permet de schématiser ces différents mécanismes. Ces regroupements de Si diminueront le nombre de sites acides du support, en revanche des sites plus forts pourront se mettre en place en bordure de ces Si-islands. Dans le cas où ces îlots sont suffisamment larges, un élément Al pourra s'y loger, isolé et former un site acide plus fort [133,134]. Ces regroupements de Si-island peuvent être vu comme une sous structure zéolitique locale, à part entière au sein de la SAPO-34 et s'étendant sur quelques nanomètres. La formation de Si-island favorisera le vieillissement par procédé de désilication alors qu'une désalumination pourra altérer la SSZ-13[124]. Par ailleurs il sera noté qu'un caractère moins acide de la part du support donne plus de stabilité au catalyseur en condition hydrothermale et en fait l'une des propriétés propres au support SAPO-34 par rapport à la SSZ-13 [135,136]. Cette dernière caractéristique semblant justifier en partie, l'engouement des études plutôt réalisées sur SAPO-34

que sur support SSZ-13 malgré sa structure plus complexe (3 éléments au lieu de 2 et possibilité de Si-island).

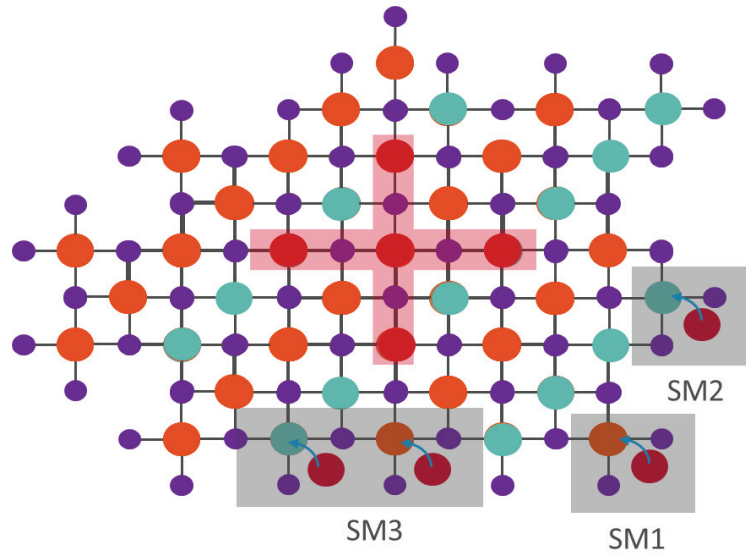


Figure I-20 : Schéma plan des mécanismes de substitution de Si (SM1,2,3) dans la structure AIPO et formation de Si-islands type  $\text{Si}(\text{OAl})_4$  (Orange : Phosphore, Bleu : Aluminium, Rouge : Silicium et Violet : Oxygène) [128,131]

Ainsi, la manière dont se coordonne le Si dans la structure après interaction avec l'agent structurant et la concentration de charge apportée, va directement influencer le caractère acide du support. Acidité qui conditionnera les possibilités d'incorporation des cations compensatoires au sein de la structure [137] lors de la synthèse du catalyseur. Enfin, ce sont les sites acides de Brønsted qui permettent l'adsorption et la désorption de  $\text{NH}_3$  en température. Parmi les types d'acides de Brønsted potentiels il sera donc retrouvé :

- Les groupes silanols terminant la structure Si-OH, Al-OH et P-OH [138,139]
- Les hydroxyles aux défauts structurels [140]
- Les groupes OH pontant Si-O(H)-Al de structure

Leur propriété confère au support un rôle de réservoir à  $\text{NH}_3$ , caractéristique directement dépendante de l'acidité du support. Cette propriété d'adsorption et de désorption sera des plus importantes en conditions SCR puisque responsable d'une partie des échanges avec la phase active. Autant de considérations qui soulignent toute l'importance du contrôle de la synthèse du support.

La topologie idéale de la structure cristalline CHAbazite, obtenue en fin de synthèse, se caractérise comme étant un enchaînement de cages dans les 3 directions de l'espace, constituées d'anneaux de 4, 6 et 8 côtés, dont chaque côté se termine par l'un des éléments Si, Al ou P [141,142]. Comme montré Figure I-21, chaque cage est de ce fait liée à 36 T-atomes dont chaque élément est partagé avec 3 cages. L'architecture ainsi imposée, la structure idéale sera une présence exclusive d'atomes isolés tels que  $\text{Si}(\text{OAl})_4$  et  $\text{P}(\text{OAl})_4$ .

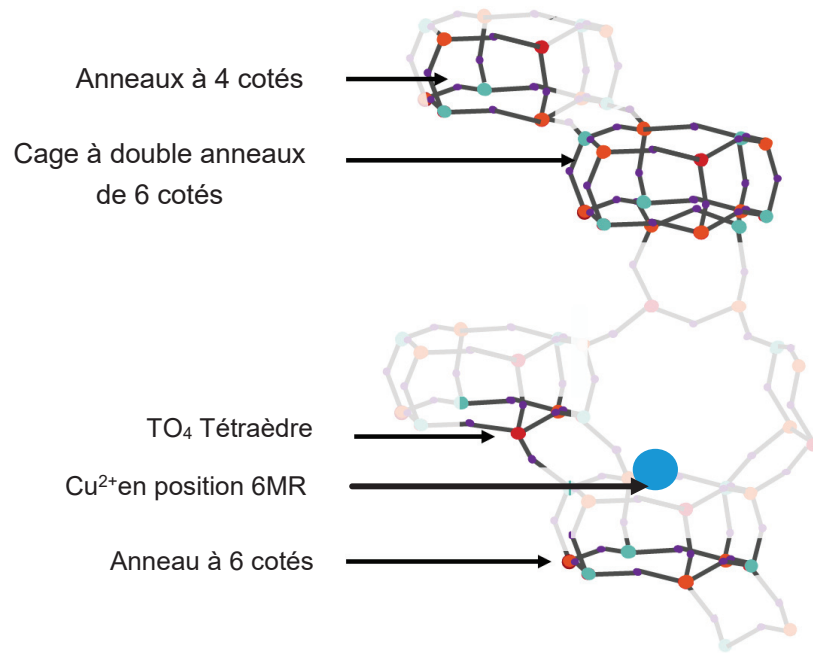


Figure I-21 : Les différentes configurations structurales des éléments de la SAPO-34 cristalline

Puisque le catalyseur possède un support zéolitique (CHA) de faible ouverture de pore, il est important de noter que, pour des considérations de chemin réactionnel et afin de mieux apprécier le phénomène de catalyse hétérogène, dont les principales étapes de transports sont rappelées en Figure I-22, la diffusion des espèces réactives intra cristallin sera spécifique au système microporeux. La Chabazite possédant des dimensions de pores de 0.48 nm, les molécules traversant le réseau de diamètre cinétique très proche de l'ouverture de pore, comme montré en Tableau I-8, seront assujetties aux interfaces avec les parois des canaux où les effets d'encombrement stérique seront plus importants que pour un matériau mésoporeux. Leur libre parcours moyen (lpm) se résumera alors aux trajets réalisés ailleurs qu'aux parois. De plus, les molécules auront plus de difficultés à se dépasser par chevauchement au sein des micropores si le diamètre du pore est inférieur à deux fois le diamètre des molécules se chevauchant. Ainsi comme présenté en Figure I-23 et développé en Tableau I-7, le régime de diffusion pourra être caractérisé par des phénomènes de transport selon des sauts successifs de sites actifs, en anglais « Configurational » ou encore par des phénomène d'encombrement stérique : « Single file diffusion » [143].

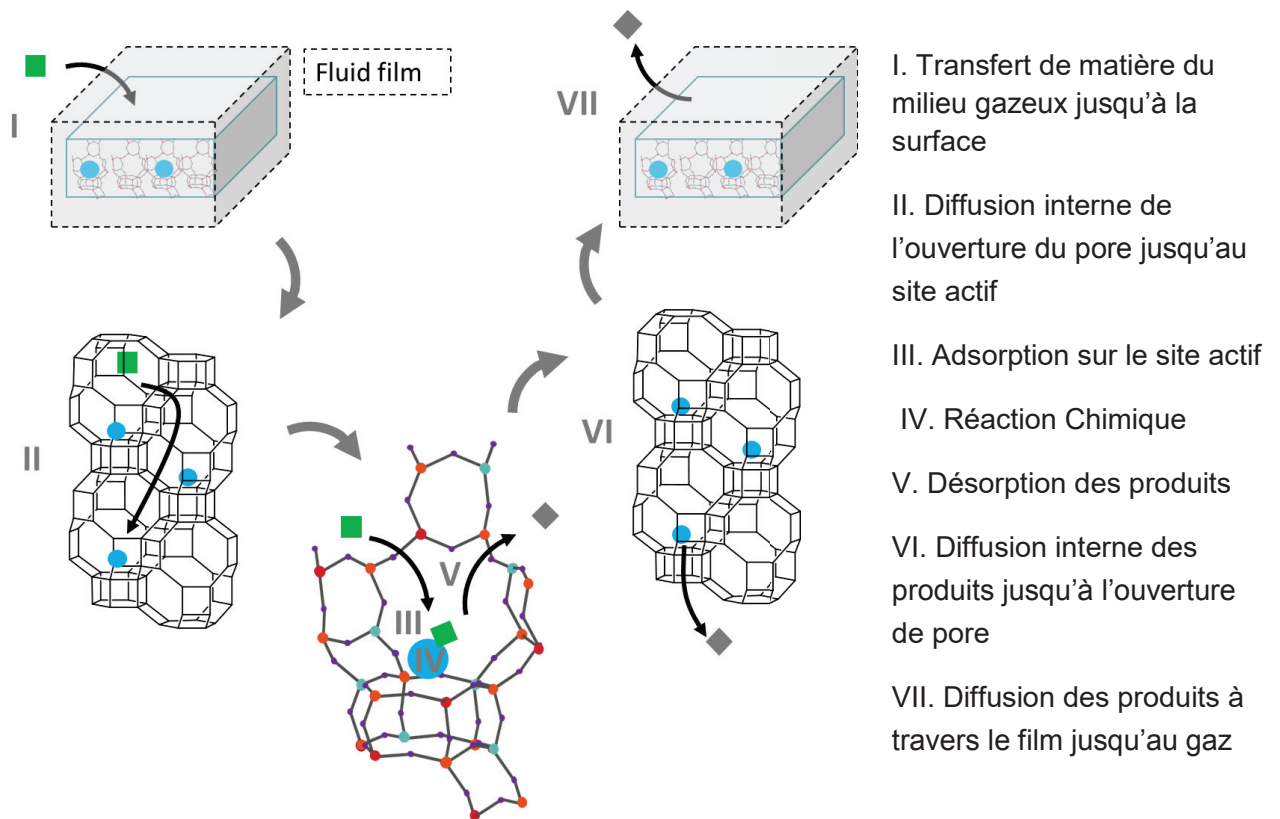


Figure I-22. Résumé schématique des étapes principales constituant le procédé de catalyse hétérogène (solide/gaz)

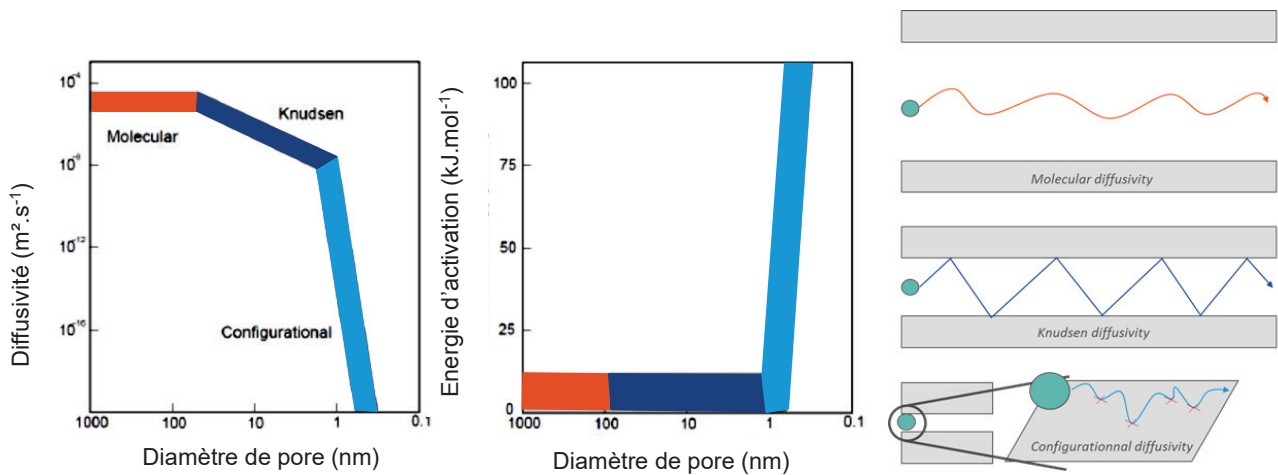


Figure I-23 : Représentation schématique des principaux régimes de diffusion des matériaux macro (50 nm), méso (2-50 nm) et microporeux (2 nm) [144,145]

Table I-7. Mécanisme et application des régimes de diffusion présentés dans l'étude [145]

Mécanismes	Application
<i>Diffusion moléculaire</i> : Les collisions intermoléculaires sont prépondérantes.	<ul style="list-style-type: none"> <li>▪ Le diamètre des pores est très supérieur aux diamètres cinétique des molécules.</li> <li>▪ La pression appliquée est élevée.</li> <li>▪ Le <math>l_{pm}</math> est faible devant le diamètre des pores</li> </ul>
<i>Diffusion de Knudsen</i> : Les collisions entre molécules et parois sont plus fréquentes que celles entre molécules uniquement.	<ul style="list-style-type: none"> <li>▪ Le diamètre des pores est du même ordre de grandeur que la tailles des molécules diffusant.</li> <li>▪ Le <math>l_{pm}</math> est supérieur au diamètre moyen des pores.</li> <li>▪ La pression du s'exerçant sur le milieu poreux est faible.</li> </ul>
<i>Diffusion de surface</i> : les molécules activées se déplacent par saut successifs de sites d'adsorption de faible énergie à un site voisin.	<ul style="list-style-type: none"> <li>▪ Le diamètre des pores est équivalent au diamètre des molécules les traversant.</li> <li>▪ Le <math>l_{pm}</math> représente les distances parcourues ailleurs qu'à la surface des parois.</li> </ul>

Table I-8: Diamètres cinétique des molécules présentes dans le mélange réactionnel [146,147] [148,149].

Molécules	H <sub>2</sub> O	N <sub>2</sub>	O <sub>2</sub>	NO <sub>2</sub>	NH <sub>3</sub>	NO	N <sub>2</sub> O	He	Diamètre moyen des cages des CHA (6MR, 8MR)
Diamètre cinétique (nm)	0,265	0,364	0,346	0,240	0,260	0,317	0,330	0,260	<b>0,460</b>

## (2) La phase active

Le support SAPO-34 est alors fonctionnalisé par l'incorporation d'une phase active, généralement un métal de transition tel que le Cu et le Fe comme il en était déjà le cas avec le support ZSM-5. L'élément métallique va alors prendre la place d'un cation H<sup>+</sup>, compensateur et se retrouvera en position échangée dans la maille. Les catalyseurs zéolitiques au fer se montrent plus actifs que ceux au cuivre à hautes températures, au-dessus de 350°C. Alors qu'à plus basses températures entre 200°C et 300°C, régime de fonctionnement plus commun aux lignes d'échappement Diesel, c'est la phase active au cuivre qui est la plus intéressante [150,151]. De plus, les catalyseurs au Cu sont moins sensibles aux variations de NO<sub>2</sub>/NO<sub>x</sub> à faible température, ce qui en améliore la stabilité de leurs performances [152]. Cependant le catalyseur au Cu présente le désavantage d'être un peu moins sélectif envers NH<sub>3</sub> pour la déNO<sub>x</sub> à haute température, puisque favorisant l'oxydation de l'ammoniac [57]. Quand bien même des catalyseurs bimétalliques Cu/Fe sont sujets de recherches aujourd'hui, c'est la phase active au cuivre qui est la plus étudiée et employée

actuellement [153–155]. La Figure I-24 ci-dessous représentant les principaux domaines de performances des catalyseurs  $V_2O_5-WO_3/TiO_2$ , Cu-CHA et Fe-CHA.

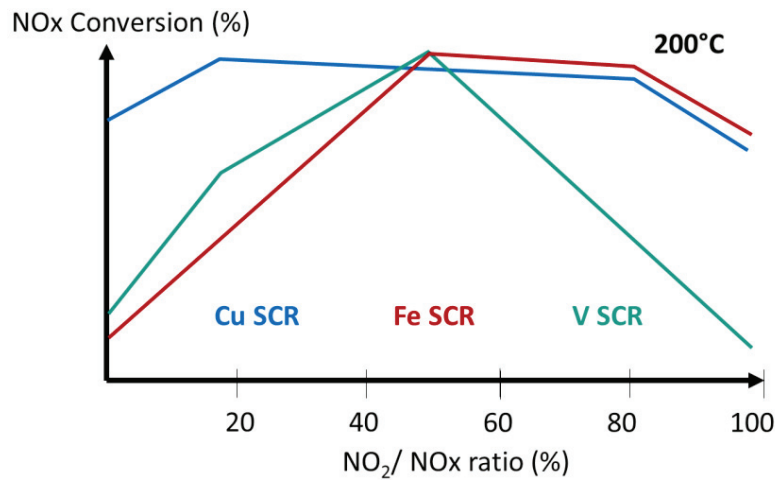


Figure I-24 : Sensibilité des principaux catalyseurs SCR présentés selon le ratio  $NO_2/NO_x$  à  $200^\circ C$  [98]

Ainsi, l'incorporation du métal peut être conduite selon différentes méthodes, répertoriées dans le Tableau I-9. Cette étape d'introduction de la phase active est aussi importante si ce n'est plus, que celle de la formation du support en lui-même. Car c'est notamment par les échanges entre les sites acides de Brønsted (apportés par le support) et les sites acides de Lewis (amenés par la phase active du cuivre), que le processus de SCR sera le plus efficace [156]. A titre de rappel, les sites acides de Lewis décrivent une espèce électropositive insaturée (comme  $Cu^{2+}$  ou un Al extrastructurel) pouvant interagir avec une base de Lewis (typiquement  $NH_3$ ) afin de former une liaison covalente. La réaction acide-base en découlant représente donc une réaction de complexation.

Effectivement lors de l'incorporation du métal dans le support et de plus généralement en fonction des conditions opératoires, différentes espèces de Cu sont susceptibles de se former telles que des cations de  $Cu^{2+}$  et  $Cu^+$  isolés en position échangés proches des mailles 6MR ou 8MR, ou complexés tel  $[Cu-OH]^+$ , des oligomères de  $[Cu-O-Cu]^{2+}$  et des cluster de surface comme CuO,  $Cu_2O$  et  $CuO_x$ . A titre d'exemple, Paolucci et al. [157] calculèrent par modèle mathématique suivant les théories de la fonctionnelle de la densité (Density Functional Theory DFT) diverses configurations possibles du cuivre en position au sein d'une maille de SSZ-13 selon la température, la pression en oxygène relative et la présence d'un ou plusieurs éléments d'aluminium apportant les charges. Ainsi la Figure I-25 (Figure 3 extraite de leurs travaux) présente les diagrammes de phase de spéciation du cuivre selon différents environnements, démontrant des différentes possibilités de spéciation du cuivre.

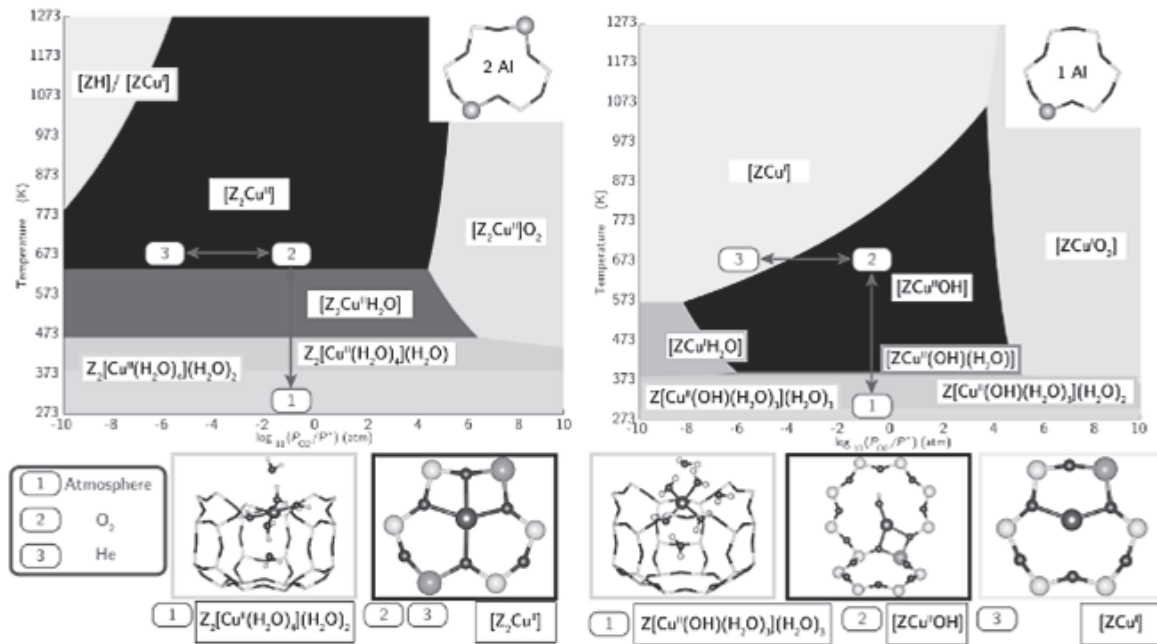


Figure I-25 : Diagramme de phase de la spéciation de Cu. Les régions en nuances de gris indiquent les compositions de sites minimisant l'énergie libre à T, P et % H<sub>2</sub>O donnés [157].

Mais il est communément démontré que l'espèce la plus active pour l'opération de réduction des NO<sub>x</sub> est le cation isolé Cu<sup>2+</sup> (sans espèce adsorbée ni complexes formés) en position échangée proche de la cage 6MR (indiqué en Figure I-21). En effet, l'équipe de recherche de Gao. et al. [158] a démontré par mesures de performances catalytiques et la caractérisation de plusieurs catalyseurs aux teneurs en cuivre différentes, la corrélation linéaire entre le taux de réaction et le pourcentage de Cu à hautes températures. Ainsi, par la linéarité des Turn Over Freqencie (TOF) obtenus selon des catalyseurs de rapport Si/Al, de concentration de Cu différentes et en faisant, entre autres, l'hypothèse d'une réaction SCR de premier ordre, il est possible d'en conclure que l'espèce isolé de cuivre pourrait être l'espèce la plus active. Ce Cu monomère serait positionné à hautes températures dans sa forme déshydratée en position la plus stable de la maille, en 6MR tel que présenté en Figure I-25 [157].

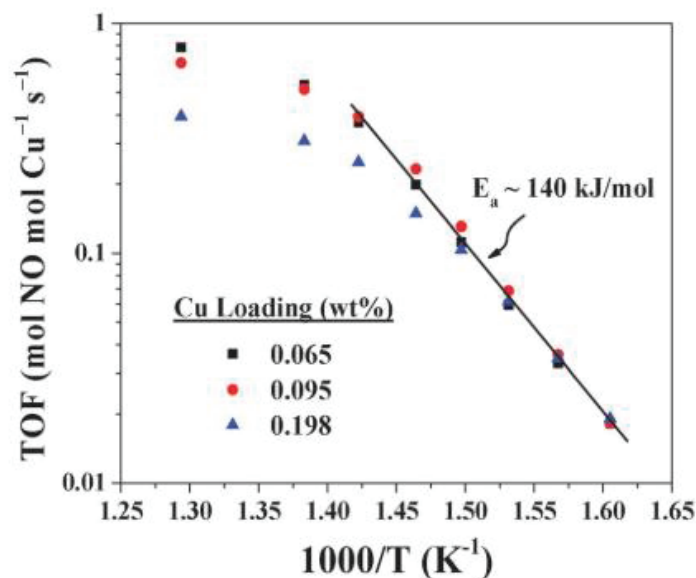


Figure I-26: TOF vs. Charge en cuivre à haute température. Mélange réactionnel composé de 350 ppm NO, 350 ppm NH<sub>3</sub>, 14% O<sub>2</sub>, 2.5% H<sub>2</sub>O, avec N<sub>2</sub> en inerte pour balance (GHSV = 1 200 000 h<sup>-1</sup>) [158].

Cependant à basses températures, les espèces les plus actives ne semblent pas encore clairement identifiées, ceci dépendant grandement de la proportion de cuivre introduite [159–161]. Il se peut aussi que les sites de cuivre soient suffisamment solvatés et mobiles aux basses températures pour se transformer en espèces hydratées ou dimérisées dans la maille zéolitique et participer aux performances SCR [157]. Différentes études [162–164] tendent aussi à démontrer que l'adsorption de NH<sub>3</sub> sur ces espèces actives de cuivre échangés passent par un état de complexe, pouvant lier plusieurs molécules de NH<sub>3</sub> (jusque 4) sur le site redox, formant des espèces tels que : [Cu<sup>II</sup>(NH<sub>3</sub>)<sub>4</sub>]<sup>2+</sup>, [Cu<sup>I</sup>(NH<sub>3</sub>)<sub>2</sub>]<sup>+</sup> et [Cu(OH)(NH<sub>3</sub>)<sub>x</sub>]<sup>+</sup>.

Les probabilités d'obtenir une plus forte proportion de ces sites actifs Cu<sup>2+</sup> isolés dépend en majorité de la méthode d'incorporation du cuivre au sein de la structure. Dans cette optique, quand bien même la mise en place d'espèces de cuivre de surface est difficilement évitable, c'est l'incorporation par échange ionique en solution aqueuse qui reste la plus efficace pour obtenir de tels sites [160,165]. Lors de la migration des cations de Cu dans la maille zéolitique, le remplissage des différentes cages suit théoriquement un ordre préférentiel où les emplacements proches des 6MR sont les premiers investis puisque permettant une position des cations plus stable en énergie. C'est une fois la majorité de ces emplacements remplis que les positions en 8MR se voient attribuer des cations de cuivre [166,167]. Il est généralement observé qu'au-dessus de 2% massique de cuivre incorporé, la structure est « sur-échangée », impliquant la présence quasi systématique de clusters de surface et d'espèces dans les cages les plus grandes. Sites jugés moins actifs puisque, pour un même support, les performances DéNO<sub>x</sub> de ces catalyseurs sur-échangés ont été mesurées plus faibles que celles des catalyseurs « sous-échangés », [57,161]. Un meilleur contrôle de la configuration de tels sites ainsi que la compréhension de leurs impacts respectifs et de leur mécanisme de fonctionnement pourrait alors apporter de nouvelles lumières sur le développement de catalyseur optimisés.



Table I-9 : Méthodes d'incorporation du cuivre pour un support CHA généralement rencontrées, échelle de 1 (min) à 5 (max) représentant de manière globale selon un échantillon de la littérature la proportion atteinte de cations échangés et le cout de synthèse [159,168–172].

Méthodes	Avantages	Inconvénient	Cations en position échangés	Coût	Ref
Imprégnation	-Rapide -Peu de contrôle	-Peu reproductible -Important clusters de surface	2	3	[168]
Echange ionique en voie aqueuse	-Plus efficace -Nano cluster de Cu en surface -Large plage de température	-Multi étapes -Contrôle fin -Déchets	5	4	[169]
Synthèse directe (One pot)	-La plus rapide des synthèses -Peu de déchets	-Difficile -Besoin de co-template onéreux	3	2	[170]
Echange ionique en voie solide	- Méthode + simple -Limite les pertes de matières	-Hautes températures requises -Demande une zéolite sèche	2	1	[171]
Déposition par voie vapeur (CVD)	-Technique déjà exploitée dans l'industrie	-Contrôle difficile	1	5	[159,172]

Concernant les autres espèces de cuivre potentiellement présentes, il est communément acquis que les espèces oxydées de cuivre en surface sont responsable d'une diminution de sélectivité de  $N_2$  à haute température puisque favorisant l'oxydation de  $NH_3$  [173,174]. Ceci étant, d'autres auteurs stipulent le contraire, où la répartition homogène d'oxydes de cuivre en surface, combinés aux sites redox échangés, permet d'atteindre de fortes performances catalytiques [175]. La problématique d'identification des sites actifs en température est double puisque ce sont des interactions de ces sites redox avec les sites acides de Brønsted que les performances SCR découlent principalement.

C'est pour l'ensemble de ces différentes raisons qu'une attention toute particulière doit être portée sur la synthèse du catalyseur, du choix des précurseurs et de l'agent structurant (=Template), jusqu'à l'étape de maturation et de calcination finale lors de l'évacuation du template. Ce sont lors de ces étapes que les différents sites actifs du support et du métal adopteront une configuration particulière, définissant en grande partie, par leur synergie avec leur environnement, l'activité catalytique finale du solide. Les précautions et études liées à l'impact des méthodes de synthèses des catalyseurs auront d'autant plus d'importance si les voies de synthèses en question ont pour perspectives d'être adaptées à échelle industrielle pour commercialisation. Plusieurs travaux de recherche se sont penchés sur cette problématique de synthèse de catalyseur afin de définir quels étaient les impacts de l'emploi de différents templates par exemple, de temps de maturation différents ou bien encore d'observer l'effet sur les propriétés de surface redox [176–178].

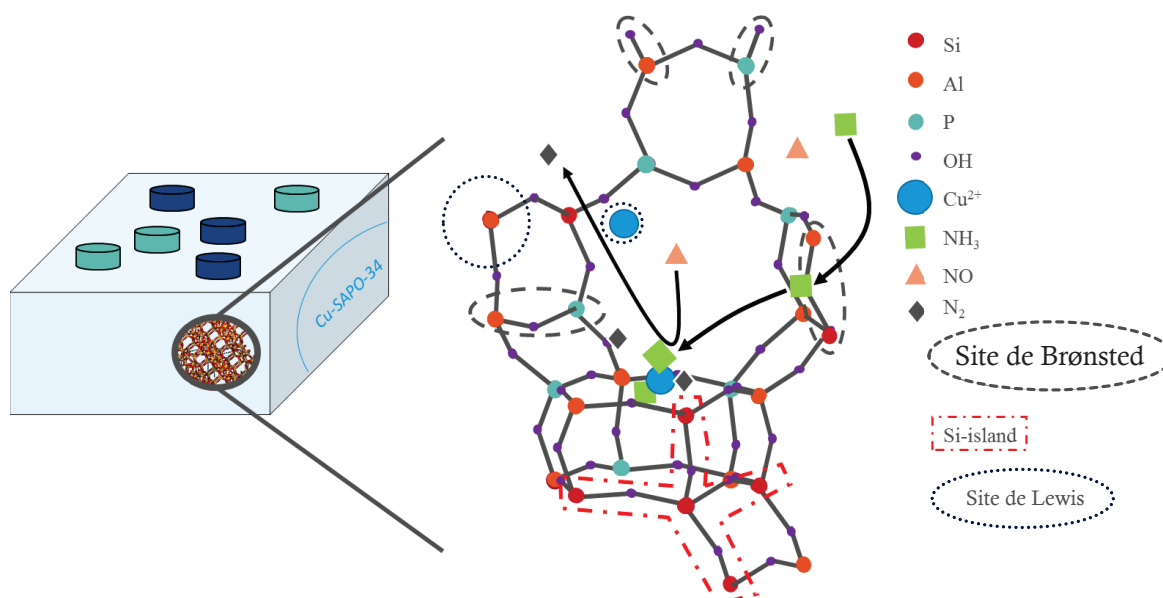


Figure I-27 : Récapitulatif de la composition d'un catalyseur Cu-SAPO-34, avec des sites de Cu sous forme de cluster de surface et des cations en position échangée 6MR et 8MR.

### (3) Propriétés avantageuses du catalyseur Cu-SAPO-34

Ainsi par son support et sa phase active, le catalyseur Cu-SAPO-34 démontre plusieurs qualités distinctives en plus de celles présentées ci-dessus, lui offrant un avantage certain lors de son utilisation en condition réelles.

Premièrement, il est tout d'abord répertorié que son excellente tenue en condition hydrothermale n'est pas seulement due à sa structure microporeuse mais aussi à la capacité des atomes en position extra-réseau, tel le phosphore, de pouvoir migrer jusqu'à la lacune de silicium produite suite à une désilication de la structure [179–181]. En d'autres termes, cette capacité d'auto-régénération (self healing) permet de

maintenir une cohérence de structure suite au départ des éléments de silicium lors des prémices de processus de desilication.

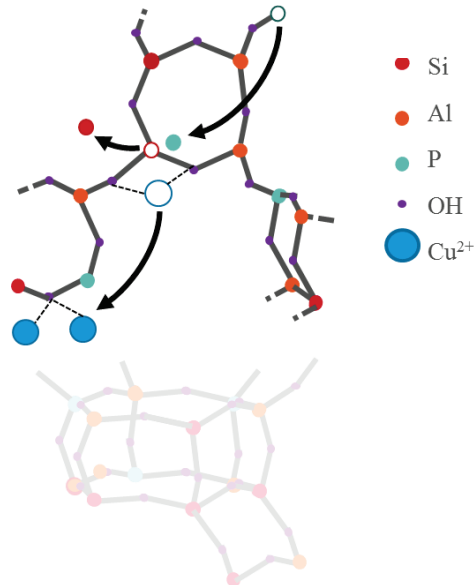


Figure I-28 : Schéma de la capacité d'auto-régénération de la structure SAPO-34 lors du départ de Si

Deuxièmement, le cuivre en position d'échange au sein de la structure zéolitique, permet préférentiellement d'adsorber les molécules d'eau et évite ainsi leur adsorption directe sur les sites de Brønsted voisins, plus sujet au vieillissement hydrothermal par hydrolyse. Cet « umbrella effect » ajoute un degré supplémentaire de résistance hydrothermale au catalyseur [182].

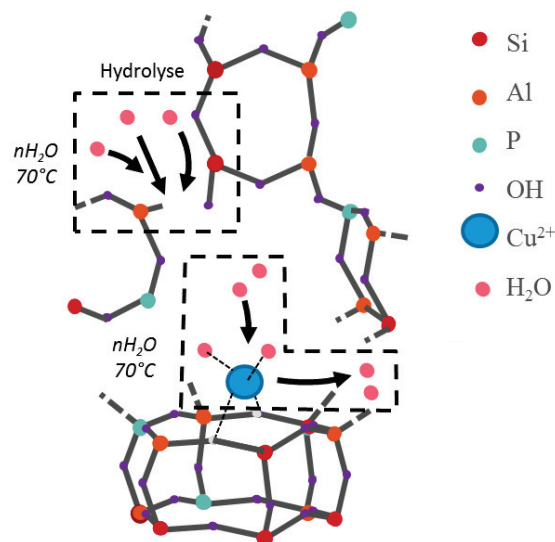


Figure I-29 : Schéma de la capacité de protection des sites Brønsted voisin des cations de cuivre échangés

Enfin, une autre propriété intéressante de la phase active, concerne la capacité des éléments cuivre à migrer de leur position de surface jusqu'en position échangées libres, dans la structure de la zéolite. Ceci permettant de mettre en place de nouveaux sites actifs et donc d'améliorer de manière générale les performances SCR. Cette migration intervient lors de conditions hydrothermales modérées, et limite de vieillissement du catalyseur [183,184].

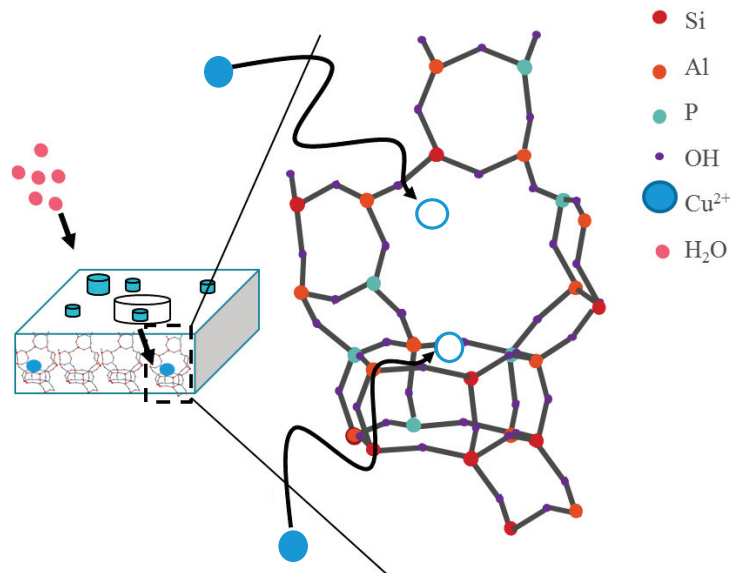


Figure I-30 : Schéma de la capacité migration des espèces cuivre de surface jusque dans la structure

### I-6.2.3 Vieillessement du catalyseur

Les conditions d'utilisation des catalyseurs de  $\text{NH}_3$ -SCR sont sévères à en observer leur plage de températures de fonctionnement allant de  $50^\circ\text{C}$  jusqu'à  $600^\circ\text{C}$  en phase de régénération du FAP, la présence importante de vapeur d'eau, l'atmosphère oxydante via la particularité du régime diesel, le débit important de flux gazeux traversant ainsi que la présence abondante du réducteur d'abord à l'état liquide puis gazeux. Ainsi lors de son utilisation, le catalyseur perd progressivement ses performances, il vieillit et se désactive. Cette durée de vie est d'un enjeu primordial puisque de celle-ci dépendra directement la valeur finale du produit, le système se doit d'être efficace et robuste dans le temps. Ces désactivations peuvent être d'ordres différents selon l'emploi et la position de la brique de dépollution SCR dans la ligne d'échappement. Par exemple, si le monolithe DeNOx est placé en dernière position tel qu'en Figure I-12, alors les processus de désactivation physique pourraient être [185]:

- L'obstruction des porosités par dépôt de suies et diverses solides se décrochant ou traversant l'amont de la ligne pouvant entraîner la perte de surface spécifique.
- L'érosion de la surface du catalyseur par le passage à grande vitesse de particules solides diminuant le nombre de sites actifs en surface.

Les méthodes chimiques quant à elles peuvent se présenter sous diverses formes :

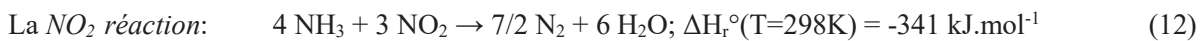
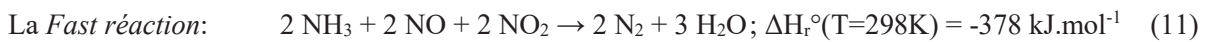
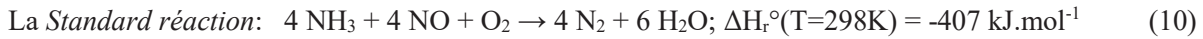
- En présence d'eau (3-9%vol. en conditions réelles) et de températures élevées (200-500°C) le vieillissement hydrothermal peut entraîner la desilication du support SAPO-34 (alors que pour des structures Si-Al type SSZ-13, c'est un phénomène de déalumination qui prend place dans de mêmes conditions), c'est-à-dire l'hydrolyse des liens T-O-T pontant de la structure. Pour la SAPO-34 lors de condition hydrothermale suffisante, le Si tend préférentiellement à adopter une charge nulle, alors que l'Al tend vers une charge -1, le proton prendra part quant à lui à une position plus stable dans une liaison entre l'H<sub>2</sub>O et l'Al plutôt que de se lier à un atome d'oxygène [124]. Le procédé de desilication se déroule ainsi en plusieurs étapes successives, dont les îlots de Si formés peuvent refléter le passé du catalyseur. Ainsi l'observation de ces regroupements de Si permet via leurs caractérisations, d'obtenir de premières informations quant au vieillissement enduré par le catalyseur ou bien même encore, des informations sur la qualité de synthèse de la structure.
- Souvent, la cause de l'empoisonnement chimique du catalyseur SCR, bien que placé en aval de la ligne et moins exposé que le DOC ou le FAP, sont les teneurs en soufre, en métaux alcalins (tel que Na ou K par exemple) et en Ca, Zn et P des différentes huiles et lubrifiants moteurs utilisés, qui, sous forme de résidus et transportés par l'effluent gazeux, se déposent et interfèrent avec les sites actifs du catalyseur. Cette présence d'impuretés est d'autant plus importante à prendre en compte au vue de l'emploi grandissant des Bio-carburants aujourd'hui. En effet, sa synthèse demande la transformation de matières premières comme l'huile végétale, graisse animale ou huile alimentaire usagée pouvant elles-mêmes contenir de telles impuretés à l'origine [69]. Cette synthèse est généralement réalisée via l'utilisation de catalyseurs. Par exemple, en voie homogène, ce sont des hydroxydes de potassium et sodium (KOH et NaOH) qui sont employés [186,187]. Aujourd'hui, la norme européenne comme américaine et canadienne réglemente la présence de ces impuretés à hauteur de 5 ppm pour la somme des concentrations maximales de Na + K, idem pour Ca + Mg et une concentration maximale de 4 ppm pour le P (voir Norme française en vigueur : NF EN 14214+A2 (février 2019)). Les métaux alcalins auront donc comme particularités, même à faible concentrations, d'interagir avec les cations en positions échangés jusqu'à diminuer les performances SCR [188,189]. Le soufre aura plutôt tendance à former des sulfates d'ammonium diminuant l'activité catalytique aux basses températures [93]. Il pourra aussi s'adsorber en site de cuivre, diminuer la réductibilité des sites redox et limiter par conséquent le processus de SCR [93,190]. Le potassium pourra agir de la même manière sur les sites de cuivre, cependant, à hautes températures, l'activité peut parfois être augmentée jusqu'à une certaine concentration limite d'impureté [191]. Enfin, le phosphore quant à lui, semblerait avoir des propriétés encore controversées [192,193]. En effet, d'une part le phosphore fut identifié comme bloquant les sites actifs par dépôt de polyphosphate, puis déstructuration de la structure zéolitique par substitutions d'élément P (phénomène plus violent pour des structures ne comprenant pas de P) et enfin perte d'activité par formation de clusters de CuO [194]. D'autre part, le phosphore semble n'avoir qu'un

impact mineur sur les performances catalytiques, voir même en améliorant certains aspects comme participer à l'inhibition de la réaction parasite de l'oxydation de NH<sub>3</sub> [195].

## I-7. Vers l'établissement d'un modèle cinétique

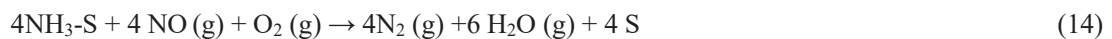
### I-7.1. Résumé des réactions impliquées et divergences de mécanisme réactionnels

Concernant le procédé de réduction des oxydes d'azotes en lui-même, trois réactions de réductions sont généralement présentées comme piliers, depuis les années 1970, à savoir [98 p.313] :



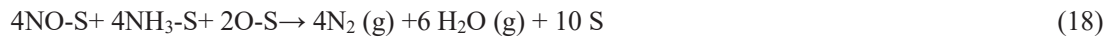
La réaction (10) est à la stœchiométrie entre le réducteur NH<sub>3</sub> et le NO et est dite standard puisque le monoxyde d'azote compose pratiquement 90% des NO<sub>x</sub> du flux réactionnel en condition opérationnelle type de la ligne d'échappement. Les 10% restant correspondent généralement au NO<sub>2</sub> et permettent de réaliser la réaction (11), dont la cinétique s'avère être plus rapide à basse température, la formation d'intermédiaire clefs nitrite et nitrate et leur rapide décomposition en N<sub>2</sub> pouvant être à l'origine de ce comportement [196,197]. De plus, par rapport à la réaction STD (10), le caractère FAST de la réaction dépend aussi de la capacité du mécanisme réactionnel à faciliter le cycle de réoxydation du site actif [198]. Cependant concernant les Cu-CHA plus particulièrement, il fut observé que les nitrates seraient plus stables en température (≈ 200°C) et bloquerait une fraction des sites disponibles, le phénomène étant plutôt connu sous « NH<sub>4</sub>NO<sub>3</sub> blocking effect » [199,200]. Pour ce type de catalyseur, le caractère Fast de la réaction est moins évident aux vues des divergences de mécanismes présents dans la littérature et les énergies d'activation apparente relevées (Gao et al. E<sub>a</sub>FAST = 160 kJ.mol<sup>-1</sup> [199], E<sub>a</sub>STD = 60-90 kJ.mol<sup>-1</sup> [158]).

D'autres différences apparaissent aussi quant aux types de mécanisme réactionnel, où les réactions de NH<sub>3</sub>-SCR sont peuvent être considérées comme suivant un mécanisme réactionnel de type Eley-Rideal ou Langmuir-Hinshelwood. Dans le premier cas, NH<sub>3</sub> est adsorbé en site actif, comme sur les cations Cu<sup>2+</sup> échangés par exemple et réagit avec le NO en phase gaz (avec S pour site actif) [201,202]:



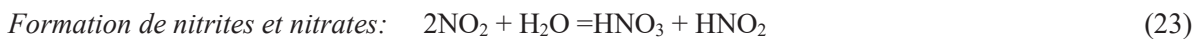
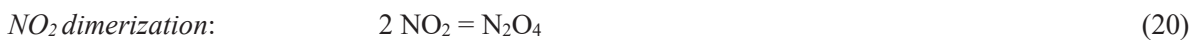
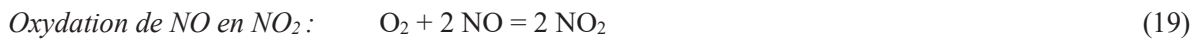
Il est possible de rencontrer des mécanismes SCR suivant un type Langmuir-Hinshelwood, mais ces derniers sont plus rares [203,204]. Ils représentent typiquement la chimisorption des réactifs NH<sub>3</sub> et NO, puis leurs diffusions respectives en surface du catalyseur afin de procéder aux réactions leurs réactions :



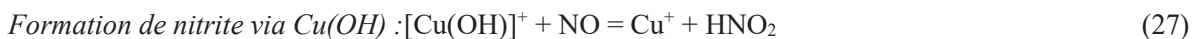


Ces différents mécanismes régiront directement l'écriture des jeux de réactions des modèles cinétiques puisqu'ils définissent les espèces qui seront adsorbées et celles qui ne le seront pas. La Figure I-31 ci-dessous donne un support visuel de ces deux mécanismes communément retrouvés en catalyse hétérogène.

Lors du processus SCR impliquant  $\text{NO}_2$ , il est aussi communément admis dans la littérature que le chemin réactionnel passe préférentiellement par la formation d'espèces intermédiaires nitrates et nitrites [205–207]. Leurs formations dépendent directement du ratio de concentration  $\text{NO}_2/\text{NO}_x$  présent dans le mélange réactionnel, dont la formation de nitrite pourrait être avantagée à faibles concentrations de  $\text{NO}_2$  alors que les espèces nitrates se formeraient à de plus fortes concentrations. Si leurs identification et implication furent observées via mesures spectroscopiques in-situ, leurs mécanismes de formation reste encore un sujet de débat central puisqu'ils ne sont pas encore clairement reconnus [156,208]. Cependant, leur formation peut être représentée comme suivant les étapes (21-27) suivantes [209–211] :



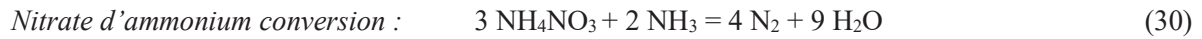
Un autre mécanisme de formation pourrait avoir lieu via l'oxydation de NO en prenant en compte l'impact de  $\text{H}_2\text{O}$  sans passer par l'implication de  $\text{NO}_2$  tel que :



Après quoi la formation d'ammonium peut se réaliser via l'interaction avec l'ammoniac tel que :



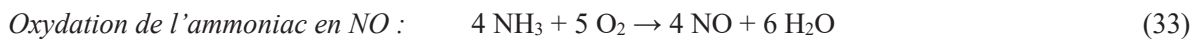
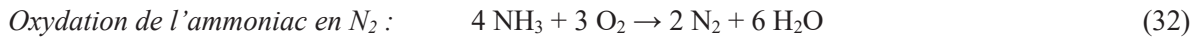
Puis réagir avec NH<sub>3</sub> pour former du diazote :



Ou se décomposer en N<sub>2</sub>O et H<sub>2</sub>O :



En plus de ces trois principales réactions (Standard, Fast, NO<sub>2</sub>), deux autres réactions importantes sont à considérer l'oxydation de NH<sub>3</sub> en NO et/ou H<sub>2</sub>O tel que :



L'oxydation de l'ammoniaque peut être considérée comme une réaction parasite, puisque cette réaction favorise la consommation du réducteur pour produire du diazote plutôt que de le consommer via SCR.

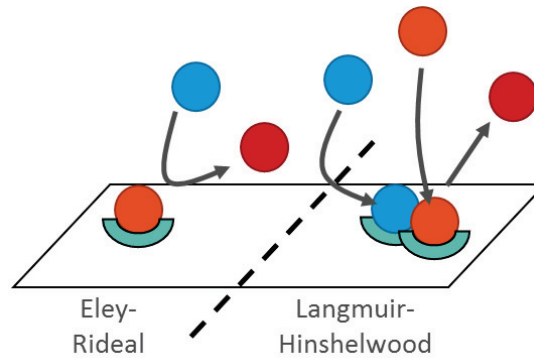


Figure I-31 : Hypothèses d'interaction entre espèces réactionnels les plus rencontrés en NH<sub>3</sub>-SCR

Ces 6 réactions générales (10,11,12,19,32) sont communes aux différents catalyseurs SCR et sont étudiées en profondeur depuis plusieurs décennies déjà, mais la complexité du jeu d'équation est en réalité bien plus grande selon les différents mécanismes réactionnels envisagés. Un aperçu de jeu de réaction est donné en Tableau I-10, soulignant ainsi le nombre des différentes possibilités réactionnelles. Chaque chemin pouvant contenir autant d'équation qu'il n'y a de types de sites actifs différents, ce qui est responsable d'ailleurs de la diversité des mécanismes réactionnels présents dans la littérature.



Tableau I-10 : Récapitulatif des réactions d'adsorption, désorption, réduction et oxydation des différentes molécules lors de NH<sub>3</sub> SCR.

Hypothèse :	
<ul style="list-style-type: none"> <li>- Présence d'eau et température comprise entre 200-500°C</li> <li>- Catalyseur pouvant adsorber en un type de site actif (S) : NH<sub>3</sub>, H<sub>2</sub>O</li> <li>- Mécanisme Eley-Rideal pour la réduction des NO<sub>x</sub></li> </ul>	
Dénomination	Réaction chimique
<b>Compétition d'adsorption et de désorption</b>	
Adsorption/désorption NH <sub>3</sub> sur S	NH <sub>3</sub> + S ↔ NH <sub>3</sub> -S
Adsorption/désorption H <sub>2</sub> O sur S	H <sub>2</sub> O + S ↔ H <sub>2</sub> O-S
<b>Réaction Globales</b>	
Standard réaction	4 NH <sub>3</sub> -S + 4 NO + O <sub>2</sub> → 4N <sub>2</sub> + 6 H <sub>2</sub> O + 4S
FAST réaction	4 NH <sub>3</sub> -S + 2 NO + 2 NO <sub>2</sub> → 4N <sub>2</sub> + 6 H <sub>2</sub> O + 4S
NO <sub>2</sub> réaction	4 NH <sub>3</sub> -S + 3 NO <sub>2</sub> → 3.5 N <sub>2</sub> + 6 H <sub>2</sub> O + 4S
<b>Oxydation de NH<sub>3</sub></b>	
Oxydation de NH <sub>3</sub> en N <sub>2</sub>	2NH <sub>3</sub> -S + 3/2O <sub>2</sub> → N <sub>2</sub> + 3H <sub>2</sub> O + 2S
NH <sub>3</sub> oxydation formant NO	4 NH <sub>3</sub> -S + 5 O <sub>2</sub> → 4NO + 6 H <sub>2</sub> O + 4S
NH <sub>3</sub> oxydation formant NO <sub>2</sub>	4 NH <sub>3</sub> -S + 7 O <sub>2</sub> → 4NO <sub>2</sub> + 6 H <sub>2</sub> O + 4S
NH <sub>3</sub> oxydation formant N <sub>2</sub> O	4 NH <sub>3</sub> -S + 4O <sub>2</sub> → 2N <sub>2</sub> O + 6 H <sub>2</sub> O + 4S
<b>Oxydation de NO</b>	
Oxydation de NO en NO <sub>2</sub>	NO + ½ O <sub>2</sub> ↔ NO <sub>2</sub>
<b>N<sub>2</sub>O formation</b>	
N <sub>2</sub> O formation via NH <sub>3</sub> et NO <sub>2</sub> :	4 NH <sub>3</sub> -S + 4 NO <sub>2</sub> + O <sub>2</sub> → 4N <sub>2</sub> O + 6 H <sub>2</sub> O + 4S
N <sub>2</sub> O formation via NH <sub>3</sub> :	4 NH <sub>3</sub> -S + 4 NO <sub>2</sub> + O <sub>2</sub> → 4N <sub>2</sub> O + 6 H <sub>2</sub> O + 4S
N <sub>2</sub> O formation via NH <sub>3</sub> et NO	4 NH <sub>3</sub> -S + 4 NO + 3 O <sub>2</sub> → 4N <sub>2</sub> O + 6 H <sub>2</sub> O + 4S
<b>N<sub>2</sub>O décomposition</b>	
N <sub>2</sub> O décomposition en N <sub>2</sub>	2N <sub>2</sub> O → 2 N <sub>2</sub> + O <sub>2</sub>

Le mécanisme de la SCR par NH<sub>3</sub> ainsi que la nature des espèces intermédiaires intervenant dans le processus de réduction des oxydes d'azote sur ces catalyseurs zéolitiques sont encore largement débattus dans la littérature. Les mécanismes liés aux catalyseurs Cu ou Fe SAPO-34 ou SSZ-13 sont pour la plupart hérités des mécanismes ayant été déterminés pour des catalyseurs plus anciens comme avec le catalyseur Cu ZSM-5. Et cela à juste titre puisque dans ce cas-ci les catalyseurs présentent d'importants points communs comme le métal de transition ou un support zéolitique. Le catalyseur de V<sub>2</sub>O<sub>5</sub>-WO<sub>3</sub>/TiO<sub>2</sub> jouit de nombreux travaux de recherche approfondies au vue de son ancienneté et de l'intérêt qu'il lui a été porté, que ce soit sur certains de ses mécanismes réactionnels opérant lors de la SCR ou des chemins de

désactivation et vieillissements chimiques. C'est effectivement cette technologie qui est à l'origine de l'établissement des mécanismes réactionnels sur catalyseur SCR et c'est pour cela que de nombreux points communs sont retrouvés avec des catalyseurs plus récents, que ce soit d'un point de vue de la physique des interactions ou de la chimie de surface. Cependant, la problématique reste la même quand il s'agit d'établir un chemin réactionnel complet et fidèle de ce qu'il se passe en opérando et ce, quel que soit le catalyseur étudié. Souvent un compromis entre fidélité et simplicité de modèle est fait, selon une approche étape par étape du procédé SCR. Un mécanisme réactionnel simplifié montrant les principales considérations citées ci-dessus pourrait être formulés tel que présentés Figure. I-32 pour plus de clarté.

Avec la modernisation des appareillages de mesures ainsi que des techniques, comme avec les études par spectroscopie infrarouge *operando* ou par spectrométrie d'adsorption de rayons X (X-ray absorption fine structure (XAFS)) *in-situ*, les différents mécanismes ont évolués et tendent communément vers de mêmes considérations. Cependant, certains points sont encore largement débattus dans la littérature et ne permettent pas d'aboutir sur un consensus général au vue de la complexité du système, ce qui motivent encore de nombreuses investigations. Certains de ces points sont exposés ci-dessous, dont les références citées donnent un aperçu seulement des différents points de vues :

- Quel mécanisme prévaut pour l'opération de NH<sub>3</sub>-SCR : Langmuir Hinshelwood [203,204] ou Eley-Rideal [201,202] ?
- L'espèce réactive pour la réaction SCR avec NO est considérée être NH<sub>3</sub> coordonné à Cu<sup>2+</sup> [163] ou alors NH<sub>4</sub><sup>+</sup> en site de Brønsted OH [212] ?
- Les espèces les plus actives du procédé sont-elles soit des monomères soit des dimères voire même certains oligomères de cuivre [213,214] ?
- Dans quels états (oxydés, hydratés, etc...) doivent être considérés de tels sites actifs [157]?
- Comment prendre en compte la mobilité des espèces actives selon les conditions opératoires [215]?
- En condition STD SCR, la formation de NO<sub>2</sub> peut-elle être encore considérée comme limitante [216,217] ?
- Le cycle de réduction et d'oxydation des espèces actives de cuivre se déroule selon quelles réactions et quelles est l'implication de Cu<sup>+</sup> [218,219]?
- Est-ce que NO passe par une étape activée et quel serait son rôle dans le mécanisme réactionnel [220]?
- Quels mécanismes régit la formation des espèces intermédiaires clefs [207,221]?
- Quel est l'impact de l'eau sur le cycle redox [222,223]?

Autant d'hypothèses qui justifient alors jusqu'à aujourd'hui, la diversité des modèles cinétiques développés par les équipes de recherche et défendus dans la littérature, représentant tout l'enjeu du développement de modèle se devant à la fois d'être juste et fidèle.

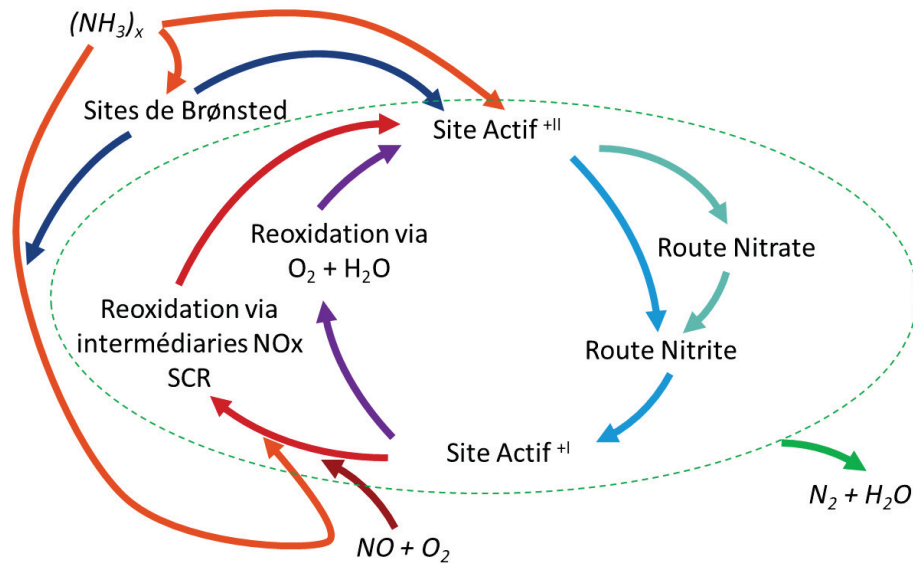


Figure I-32 : Schéma proposant un cycle réactionnel de  $NH_3$  SCR global et simplifié

#### I-7.2. Mécanismes et modèles du processus de $NH_3$ SCR proposés dans la littérature

Les modèles cinétiques sont des outils permettant d'apporter des informations qualitatives et quantitatives précieuses à la commande de procédés, l'optimisation de rendement, au design de réacteur ou encore à la compréhension des phénomènes physico-chimiques ayant lieu dans le système d'étude. Cependant, ils dépendent de différents paramètres (facteur pré exponentiels ( $k_0$ ), énergie d'activation ( $E_a$ ), chaleur d'adsorption et de désorption ( $H_{ads/des}$ ), nombre de sites actifs ( $\Omega$ )...) qui ne peuvent être directement déduits de considérations théoriques. Pour cela, des jeux de mesures expérimentales doivent d'abord être obtenus sur des bancs d'expériences pilotes afin d'estimer ces paramètres et de pouvoir fidèlement simuler la réponse du système et d'en prédire les comportements. En catalyse hétérogène des polluants gazeux par exemple, les modèles prédictifs, sont très utiles pour l'optimisation des rendements d'efficacités. En simulant les conséquences de diverses conditions opératoires, un modèle cinétique peut permettre de cibler les conditions optimales de fonctionnement du catalyseur. Sa durée de stabilité peut aussi être appréhendée via l'emploi de modèle. La durée de vie du catalyseur peut alors être améliorée via l'étude de sa dégradation simulée dans le temps, sans avoir à recourir à de longues expériences. D'une manière générale, l'application de modèles cinétiques permet d'accélérer le développement de nouveaux catalyseurs à coûts réduits, diminuant le nombre des expériences coûteuses des campagnes de mesures.

L'étude du modèle en lui-même permet aussi de dégager certains mécanismes réactionnels, via notamment la prise en compte de diverses intermédiaires clefs, la composition du mélange gazeux à l'entrée et à la sortie du réacteur et de la nature des sites actifs par exemple. La justesse de la réponse simulée pourra donc être appréciée selon les variations en température, pression, composition et catalyseur appliqués aux systèmes.

Au vu des considérations précédemment présentées, différents modèles cinétiques sont proposés dans la littérature, des modèles dits globaux [224–226], d'autres dit détaillés ou de microcinétiques [227,228] et enfin d'autres encore à l'intersection des deux appelés modèles semi-globaux ou semi-détaillés [216,229,230] comme schématisé sur la Figure I-33 suivante.

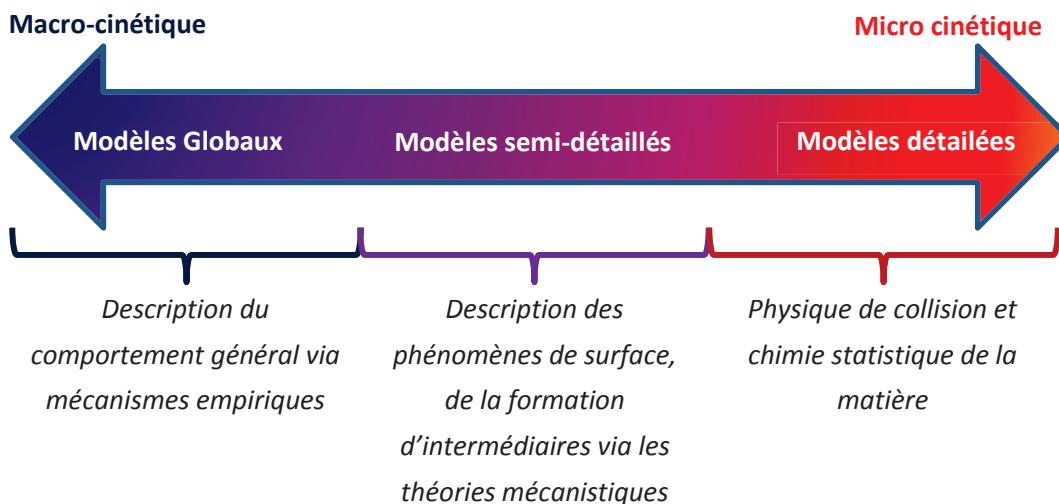


Figure I-33. Schéma résumant les types de modèles rencontrés dans la littérature sur la thématique SCR.

Les modèles microcinétiques décrivent les réactions selon des successions d'étapes élémentaires, ce qui a l'avantage de permettre d'estimer directement les paramètres cinétiques théoriques des différentes étapes. Les modèles globaux en revanche formulent l'hypothèse d'avoir des étapes élémentaires représentatives des réactions générales, soit à l'état d'équilibre soit indirectement influentes sur les vitesses de réactions. Cela permet d'établir des expressions de vitesses de réaction représentant l'ensemble du jeu d'étapes élémentaires avec un nombre significativement réduit de paramètres par rapport aux modèles détaillés. Les expressions de vitesse de réaction employées dans les modèles globaux sont souvent exprimées en fonction des concentrations des espèces en phase gaz, aussi bien pour des vitesses de réaction représentant des effets d'inhibition, d'adsorption que de désorption. Cependant, puisque le mécanisme liant les différentes réactions intermédiaires n'est pas encore clairement identifié, il est rare de rencontrer des vitesses de réactions globales strictement définies selon les étapes intermédiaires. Il est plus souvent retrouvé des facteurs correcteurs ou des expressions semi-empiriques pour ajuster l'écart entre les mesures expérimentales et les courbes simulées. Au prix de ces simplifications et modifications des vitesses de réaction, le modèle deviendra moins représentatif des comportements physiques généraux et plus spécifique aux cas expérimentaux sur lequel il est appliqué [231]. Néanmoins, le nombre de paramètres à estimer étant bien plus faible, les modèles globaux sont plus souvent utilisés pour les simulations des phénomènes de post traitement et des algorithmes de contrôle. A la rencontre de ces deux catégories, les modèles semi-détaillés permettront de prendre en compte une ou plusieurs espèces intermédiaires clefs, de rendre compte des interactions aux interfaces et de représenter plus fidèlement les expériences menées en régime transitoire via un nombre de paramètres cinétiques à estimer optimisé.

Certains de ces modèles simulant le procédé de NH<sub>3</sub>-SCR furent répertoriés dans le Tableau I-11 selon plusieurs critères (nature de sites actifs, nombre de sites, nombre de réactions...) afin d'en apprécier leurs différences. Trois d'entre eux furent sélectionnés pour leurs représentativités et décrits ci-après.

Tableau I-11. Différences entre certains modèles cinétiques représentant le procédé NH<sub>3</sub> SCR disponible dans la littérature

Ref.	Auteurs	Catalyseur	Réactions considérée	Définition des sites actifs	Régime expérimental
[232]	Jian G. et al.	Cu-CHA	STD SCR NO, NH <sub>3</sub> oxidation	S1: NH <sub>3</sub> faiblement adsorbés and NH <sub>3</sub> physisorbés S2 : NH <sub>3</sub> fortement adsorbés	Constant
[229]	Svövall et al.	Cu-ZSM-5	STD SCR NO, NH <sub>3</sub> oxidation	S1a,b: Sites Cu pour interaction avec (NH <sub>3</sub> ,H <sub>2</sub> O,O,OH,NO <sub>2</sub> ,NO <sub>3</sub> ,HNO <sub>3</sub> ) ligands S2: Bronsted acid sites S3: NH <sub>3</sub> physisorbés	Transitoire
[224]	De-La-torre et al.	Cu-SSZ-13	STD, FAST, NO <sub>2</sub> SCR N <sub>2</sub> O formation/decomposition NO, NH <sub>3</sub> oxidation	S1 : Tous confondus	Constant
[233]	Daya et al.	Cu-SSZ-13	STD, FAST, NO <sub>2</sub> SCR N <sub>2</sub> O formation NH <sub>4</sub> NO <sub>3</sub> decomposition NO, NH <sub>3</sub> oxidation	S1: Sites Cu hydratés et Bronsted acid sites S2: Cu cation isolés (6MR) et sites physisorbés	Constant
[234]	Olsson et al.	Cu-SSZ-13	NH <sub>3</sub> oxidation STD SCR N <sub>2</sub> O formation/decomposition NH <sub>3</sub> -NO formation/decomposition	S1: Cu cation isolés (6MR) et Bronsted acid sites S2: Bronsted acid sites et Cu proche larges cages S3: NH <sub>3</sub> physisorbés	Transitoire
[154]	P.S. Metkar et al.	Cu-CHA	NO, NH <sub>3</sub> oxidation STD, FAST, NO <sub>2</sub> SCR NH <sub>4</sub> NO <sub>3</sub> formation/decomposition N <sub>2</sub> O formation/decomposition N <sub>2</sub> O reduction	S1 : Tous confondus	Constant
[216]	Bendrich et al.	Cu-CHA	STD, FAST, NO <sub>2</sub> SCR NO, NH <sub>3</sub> oxidation NO <sub>2</sub> adsorption/decomposition NH <sub>4</sub> NO <sub>3</sub> formation/decomposition Nitrite ONO formation/decomposition	S1: Sites Brønsted et Redox pour le stockage de NH <sub>3</sub> S2: Cu cations isolés	Transitoire
[225]	Supriyanto et al.	Cu-BEA	STD, FAST, NO <sub>2</sub> SCR NO, NH <sub>3</sub> oxidation N <sub>2</sub> O formation NO <sub>2</sub> dissociation	S1 : Tous confondus	Transitoire

#### I-7.2.1 “Global kinetic modeling of hydrothermal aging of NH<sub>3</sub>-SCR over Cu-zeolites” de Supriyanto et al. (2015) : Modèle global [225]

Un modèle cinétique peut se caractériser selon différents points tel que le jeu d'hypothèses adopté, la définition des sites actifs considérés, la série de réactions du mécanisme (conséquence des points précédents) et l'objectif principal. Ainsi Supriyanto et al., poursuivant la volonté de modéliser le phénomène de vieillissement hydrothermal de catalyseurs au cuivre, choisirent de définir un unique site

actif pour tout le catalyseur, sans différenciation entre site de cuivre et ceux de la structure zéolitique. En lien avec leur objectif, cette forte simplification réduit certes considérablement les possibilités d'interprétation, mais cela permet aussi de simplifier le modèle et d'explorer d'autres phénomènes comme ici l'effet du vieillissement. De cette manière un modèle global est développé, suivant 16 réactions différentes, depuis l'adsorption et désorption de NH<sub>3</sub> sur un unique site jusqu'aux réactions de STD, FAST et NO<sub>2</sub> SCR impliquant les NH<sub>3</sub> de surface, en passant par les réactions parallèles d'oxydation sans pour autant définir d'intermédiaires réactionnels. L'expression de la vitesse globale de STD SCR se définit comme suit :

$$r_{STD\ SCR} = \Omega_S \cdot k_{STD\ SCR} \cdot C_{NO} \cdot C_{O_2}^{0.5} \cdot \theta_{NH_3}^S \quad (35)$$

Avec  $\Omega_S$  la densité de sites de stockage du site S (kmol/m<sup>2</sup>),  $k_{STD\ SCR}$  la constante de vitesse (m<sup>-1</sup>.s<sup>-1</sup>),  $C_i$  la concentration de l'espèce i où les auteurs prennent ici l'hypothèse de l'ordre 1 pour le NO et 0.5 pour O<sub>2</sub>, et  $\theta_{NH_3}^S$  le taux de recouvrement de NH<sub>3</sub> en site S (-) défini comme étant le nombre d'espèces adsorbées sur le nombre de sites d'adsorption total.

Ici la constante de vitesse est définie suivant l'expression de la loi d'Arrhenius :

$$k_i = k_{0,i} \cdot \exp\left(-\frac{Ea_i}{RT_S}\right) \quad (36)$$

Avec  $k_{0,i}$  le facteur pré-exponentiel de la réaction i (m<sup>-1</sup>.s<sup>-1</sup>),  $Ea_i$  l'énergie d'activation de la réaction i (J . mol<sup>-1</sup>), R la constante des gaz parfaits (J . mol<sup>-1</sup>.K<sup>-1</sup>) et  $T_S$  la température de la surface du catalyseur (K).

De plus, la chaleur d'adsorption de NH<sub>3</sub> est supposée dépendante du taux de recouvrement, suivant l'isotherme de Temkin tel que [235] :

$$Ea_{desorption,NH_3} = E^{\circ}_{desorption,NH_3} (1 - \alpha \cdot \theta_{NH_3-S}) \quad (37)$$

Avec  $E^{\circ}_{desorption,NH_3}$  l'énergie d'activation pour un recouvrement nul (J/mol) et  $\alpha$  le degré de dépendance de l'espèce NH<sub>3</sub> pour la réaction de désorption. Cette hypothèse de l'isotherme de Temkin pour l'évolution de la chaleur d'adsorption du réactif NH<sub>3</sub> est communément rencontrée dans la construction de modèles globaux, puisqu'il fut démontré par mesures microcalorimétriques, la linéarité de la dépendance de la chaleur d'adsorption avec le taux de recouvrement [235].

Cette équation (35) montre la proportionnalité directe de la vitesse avec le taux de recouvrement de NH<sub>3</sub>, où une diminution du nombre d'espèces adsorbées entraînera la diminution de l'activité catalytique. Par conséquent, l'impact du taux de recouvrement devient clef pour la vitesse de réaction NH<sub>3</sub>-SCR. De la même manière, le nombre de sites d'adsorption, proportionnel à la vitesse de réaction, sera déterminant pour l'expression de la vitesse, où une diminution de la disponibilité de ces derniers par vieillissement ou empoisonnement par exemple, entrainera l'affaiblissement des performances du

catalyseur. La définition ainsi que la disponibilité de ces sites actifs en température est alors un second paramètre essentiel pour l'interprétation de la vitesse de réaction.

Ce modèle cinétique pourrait presque déjà être considéré comme semi-détaillé dans la mesure où plusieurs espèces, NO et NO<sub>2</sub> en l'occurrence, s'adsorbent en cet unique site et participent au mécanisme réactionnel en phase adsorbée. La mise en place d'une succession de réactions d'adsorption pour permettre la formation d'une espèce particulière est aussi une caractéristique retrouvée pour des modèles plus détaillés. A titre d'exemple, la formation de N<sub>2</sub>O est représentée par les réactions successives (38) et (39):



En revanche, un exemple de modèle plus global prendra en compte moins de sous-réaction dans son mécanisme et exprimera certaines vitesses de réaction en fonction des concentrations uniquement en phase gaz. Un exemple de cette catégorie de modèle peut être retrouvé dans certains travaux de Auvray et al. [236], dont la mise en place d'un modèle global plus simple, permet de rendre compte d'une caractéristique complexe, dans ce cas-ci, l'impact de la distribution axial des espèces au sein de monolithe.

I-7.2.2 “Development and validation of a two sites kinetic model for NH<sub>3</sub>-SCR over Cu-SSZ-13. Part 1 Detailed global kinetic development based on mechanistic considerations”  
de Daya et al. (2018) : Modèle semi-détaillé [233]

Ici le modèle se caractérise par la prise en compte de 20 réactions différentes dont 5 mettant en jeux un intermédiaire réactionnel, le nitrate d'ammonium (NH<sub>4</sub>NO<sub>3</sub>). La construction du mécanisme réactionnel possède comme point de départ la définition de deux hypothétiques sites actifs. Ensuite son évolution dépendra directement des interprétations réalisées suite aux mesures expérimentales (NH<sub>3</sub> -TPD (Temperature Programmed Desorption), tests d'oxydation de NH<sub>3</sub> et de NO, mesures de performances catalytique SCR...). Cette construction du modèle cinétique selon la définition de deux catégories de sites actifs, représente la majorité des modèles cinétiques de la littérature relatifs aux catalyseurs aux cuivres (cf. Tableau I-11). En effet, cette hypothèse permet un compromis entre complexité de modèle et fidélité, où les conclusions peuvent être plus discriminantes qu'avec un modèle global.

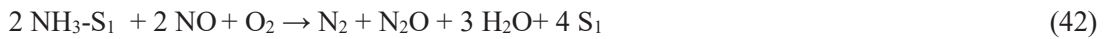
Par exemple, Daya et al. définissent un site S1 comme représentant à la fois les sites cuivre oxydés tel que ZCuOH au sein des cages CHA, mais aussi les sites acides de Brønsted. Le site S2 quant à lui représente les espèces Z<sub>2</sub>Cu dans une configuration spécifique 6MR ainsi que les sites pour NH<sub>3</sub> physisorbés. L'hypothèse de la chaleur d'adsorption des espèces suivant l'isotherme de Temkin n'est ici appliquée que sur S2, S1 suivant l'approche thermodynamique selon Langmuir. Ceci étant par ailleurs justifié selon les auteurs par la densité plus importante de sites dans S2, augmentant ainsi la probabilité d'avoir des sites actifs d'énergies d'activations différentes. Les définitions de ces sites actifs font directement suite aux observations des mesures de NH<sub>3</sub> TPD, elles définiront par la suite les différentes réactions du mécanisme. Par exemple, la formation directe (sans intermédiaire) de N<sub>2</sub>O se réalisera sur S2

uniquement alors que sur S1, un mécanisme en deux temps est défini. Ici seul NH<sub>3</sub> et le nitrate d'ammonium sont considérés comme s'adsorbant sur les sites actifs, l'adsorption de l'eau n'est par exemple par prise en compte :

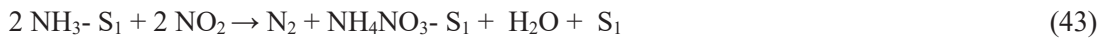
$$1 = \theta_{\text{NH}_3}^{S1} + \theta_{\text{NH}_4\text{NO}_3}^{S1} + \theta_{\text{vacant}} \quad (40)$$

Les réactions établies dans le mécanisme réactionnel suivent principalement le modèle Eley-Rideal mis à part pour l'oxydation de NO en NO<sub>2</sub> en phase gaz.

Daya et al. choisirent dans leur mécanisme réactionnel, d'établir 4 réactions pouvant mener à la STD SCR, où sur chaque site S1 et S2 la STD SCR s'établit directement, mais aussi permet de former N<sub>2</sub>O lors d'une même réaction, tel que sur S<sub>1</sub> (idem sur sur S<sub>2</sub>):



Au sein de ce mécanisme, la formation de l'intermédiaire NH<sub>4</sub>NO<sub>3</sub> passe par la réaction de NH<sub>3</sub> adsorbé avec NO<sub>2</sub> (g) et sert principalement à représenter la formation de N<sub>2</sub>O sur chacun des deux sites, tel que sur S1 par exemple :



Ces choix et ces hypothèses sont la conséquence directe des observations faites lors des tests de performances cinétiques et de TPD. Les étapes de construction du modèle se reflètent alors par la stratégie expérimentale suivie par les expérimentateurs et montrent ainsi toute l'étendue des possibilités de chemins réactionnels.

### I-7.2.3 "Unified mechanistic model for Standard SCR, Fast SCR, and NO<sub>2</sub> SCR over a copper chabazite catalyst" de Bendrich et al. (2018) : Modèle détaillé [216]

Dans cette étude, Bendrich et al. prennent en compte 18 réactions chimiques en définissant la présence de deux types de sites actifs, à l'instar du modèle précédemment présenté. Le premier site représente l'adsorption en site acide de Brønsted et en site de cuivre alors que le second se veut représenter particulièrement les espèces ZCu<sup>2+</sup>-OH sur lesquels les espèces nitrates et nitrites peuvent se former. L'objectif principal de ce travail fut de développer un mécanisme réactionnel suffisamment détaillé pour traiter des réactions de STD, FAST et NO<sub>2</sub> SCR prenant en compte différentes espèces intermédiaires retrouvées dans la littérature comme HNO<sub>3</sub> (g), NH<sub>4</sub>NO<sub>3</sub>, OH, ONO, NO<sub>3</sub> et NO<sub>3</sub>NH<sub>3</sub>. Le choix des espèces intermédiaires, décrit clairement l'objectif entrepris par cette étude, voulant satisfaire les différentes possibilités de formation d'espèces intermédiaires retrouvées dans la littérature. D'autre part, la volonté de vouloir représenter la mécanistique des réactions globales est aussi très recherchée ici, où chaque réaction



principale sont formulées comme la combinaison linéaire de sous réactions suivant de précédents résultats et conclusions de la littérature. Ainsi par la corrélation de données simulées et de données expérimentales principalement obtenues en régime stationnaire, Bendrich et al. proposent un mécanisme très détaillé de la  $\text{NH}_3$  SCR sur catalyseurs Cu-CHA commerciaux, au prix d'un nombre conséquent de paramètres cinétiques et d'hypothèses réalisées au sujet de nombreuses espèces chimique non observées directement.

Ainsi, les trois modèles cinétiques présentés ci-dessus démontrent plusieurs points communs qui, une fois regroupés, représentent les éléments déterminant à l'établissement de modèle :

- Plusieurs sites actifs sont nécessaires à la représentation des phénomènes d'adsorption et de désorption mais aussi de la chimie en elle-même, où une réaction redox ne peut être réalisée sur un site de Brønsted par exemple.
- L'écriture du mécanisme réactionnel dépendra grandement de la définition des sites actifs considérés ainsi que des hypothèses liées.
- Le nombre d'espèces intermédiaires, dans l'objectif d'une simulation à coût réduit, devrait se limiter au nombre des espèces pivots des réactions simulées.
- La vitesse de réaction de réduction des  $\text{NO}_x$  est proportionnelle au recouvrement des espèces réactives.

Ainsi, depuis la définition de la problématique de la pollution atmosphérique datant du 19<sup>e</sup> siècle jusqu'aux sites actifs des futurs catalyseurs de SCR du 21<sup>e</sup>, le développement de nouvelles solutions représente encore aujourd'hui un challenge considérable.

## **I-8.** Conclusion and Thesis objective

### I-8.1. Conclusion

Ambient air depollution represents one of our main challenges to tackle down this 21<sup>st</sup> century as it is a general threat to health and climate. The main anthropic outdoor pollution sources include building heating systems, agriculture and waste incineration and industry, power generation and vehicles. Accordingly with the World Health Organization (WHO), the virtuous loop is maintained through 3 billion people worldwide relying on polluting technologies and fuels (including biomass, coal and kerosene) for household heating, lightning, transport mobility and commercial interaction. Despite the alarming situation on the air pollution around the world and its impact on climate change, the future short- and medium-term trend in energetic mix will probably be still represented by the predominant fossil energies share, including petroleum, coal and natural gas. Meanwhile large-scale deployment of solutions and restrictions, the development of more efficient technologies for the pollution abatement is crucial to stem atmospheric pollution and so health hazard: a win-win strategy. Therefore, as light and heavy-duty vehicles will still running on fossil energies next decades, until the final regulation publication, it is compulsory to develop innovative and competitive solutions for the abatement of generated pollutant. The next generation of industrially developed catalyst for NO<sub>x</sub> emissions control of lean burn engines could greatly be represented by microporous zeolites supporting transition metal as copper, regarding the research intensification in literature these last decades and their attracting properties. Until now, these catalytic systems are heavily studied in literature, they were characterized to present excellent NO<sub>x</sub> reduction activity, superior N<sub>2</sub> selectivity and important hydrothermal stability. Fundamental investigations allowed the determination of the most active sites for SCR process, which the development of in situ and operando spectroscopic techniques as Diffuse Reflectance Infrared Fourier Spectroscopy (DRIFT), X-ray absorption spectroscopy (XAS) and X-ray absorption near edge structure (XANES), greatly enhanced the investigations of varieties of adsorption and redox sites though temperature. However, with the aim to manufacture the catalyst at a commercial scale and expend its implication in future after-treatment technologies, different points still under debates in literature must be treated and resolved. Typically, different catalyst synthesis strategies are available but not all of them are interesting for a scale up process, for instance, ionic exchange provide a great control of the active sites implementation but required several steps and large amount of solvent. On the other hand, one pot synthesis is interesting for a rapid catalyst synthesis but are less controlled. As the active site configurations will depend on the preparation method, it is a priority to master its control and to specifically incorporate the sites of interest. The active sites speciation and segregation are thus important for apprehending their effect on catalyst performances. With different active sites, different mechanistic paths are suspected, which justify the wide variety of proposed SCR mechanistic paths in literature. Consequently, the precise full catalytic cycle over the whole temperature range is still under investigations yet, interrogations which the development of numerical simulation can greatly enhanced.

I-8.2. Thesis objective and outlines

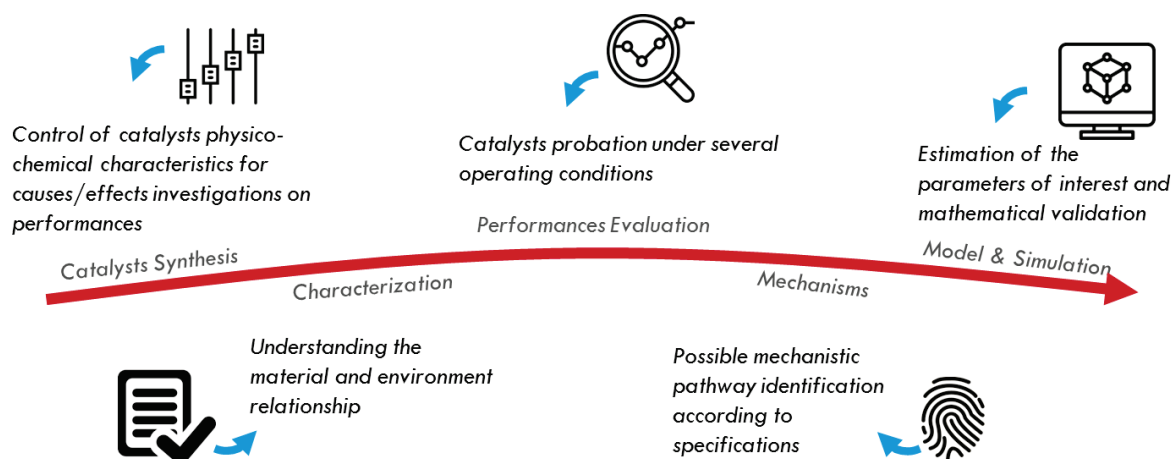


Figure I-34 : Thesis red wire from the catalysts synthesis under requirements specification to kinetic model construction

According to the working content and chapter segmentation, the project of this thesis consists of four main parts:

1. The first one focuses on the zeolite SAPO-34 synthesis method, where a commercial support was employed for comparison purposes, in order to verify the fulfillment of the different pre-made support characteristic requirements prior to its functionalization. Consequently, the supports were functionalized through a conventional impregnation method, employed for first catalytic behavior investigation. The catalysts performances were characterized and put into perspective with the developed impregnation protocol and the pro and cons of the method for STD SCR process characterization purposes were enlighten. The conducted tests performances on impregnated catalysts will also constitute experimental data points for model assessments. In that respect, following the stated requirements, different protocol strategies were adopted for incorporating active phase in specific configurations and finally developed a reference catalyst.
2. The second part is centered on the synthesis of different Cu-SAPO-34 catalysts with specified redox active sites for describing their respective impacts in SCR processes. This sites speciation was performed comparing a one-pot catalyst, initially deprived of highly active redox sites and an ionically exchanged support, which on the opposite, was comports SCR active copper cations. As different active sites configurations are implemented through the synthesis at a laboratory scale, this study has also the will to bring further insight concerning hardly avoidable surface clusters role within SCR reactions. Following this development, a reactional mechanism was proposed for the one pot catalyst, accordingly with its characterized DeNO<sub>x</sub> performances. Consequently, to this investigation, information was acquired on the active site presence relative to each catalyst and were employed for the model construction, defining different Bronsted and redox active sites. Through the study of different site configurations, the model adaptability can be enlarged to

different Cu-SAPO-34 catalysts, obtain with different synthesis method and thus displaying different active sites.

3. The third part consists in the catalytic behavior investigation of the ionically exchanged catalyst under several operating conditions, leading to the proposition of an optimized reactional network. In this chapter, the key performance tests constitute the experimental set of data required for the reference catalyst simulation. Thus, different input variations were studied as the temperature, concentrations and reaction time for constituting a dynamic representation of the catalyst capacities. The proposition of relevant mechanistic path is mandatory to the model construction, as can be the active sites definition, and the experimentally obtained kinetic parameters was employed as initial values during the model estimation process.
4. The last part concerns the model construction, performed by the combination of conducted active sites configuration investigation and mechanistic path information. Firstly, the experimental reactor and catalytic bench hydrodynamic was investigated for accurately describing the kinetic parameters inherent to the reactions. The assumptions were consequently carried out prior to the reactor model construction, thus defining the limits and possibilities of the model representation. Next, the proposed kinetic model was described according to the required reactions rates expression, based on literature and performed kinetic study in precedent Chapter. The model was therefore firstly implemented for the reference catalyst in a primary section, considering the parent support impact on storage sites, where the parameters ascribed to the raw support were primarily obtained and used as locked reference values for the parameter estimation of the catalyst. After model validation and rate limiting investigation for the reference catalyst in STD SCR conditions, the model was extended to other catalysts which their active sites were characterized: one pot and impregnated catalysts.

In that respect, the second section consists in the model application on two different catalysts, displaying different active sites configuration as previously characterised. By the conservation of the reactor and kinetic model, the catalyst surface definition was modified for corresponding to the one pot catalyst specifically. Finally, by the representation of the ionically exchanged and one pot catalysts dynamic behaviour, the third catalyst, obtained by impregnation and susceptible to present the whole defined active sites as developed in first part, was used for simulation purposes in order to observe if the direct gathering of kinetics parameters from other catalysts could represent its behaviour in similar conditions. After the model deviation investigation about the last catalyst and its correction, the different estimated kinetic parameters were compared between catalysts and related to their active sites configurations differences, validating the model representativeness,



II



# CHAPTER II

## MATERIALS & METHODS

### II-1. Introduction

The principal objective of this work lies on the different catalyst behaviors under NH<sub>3</sub> SCR conditions, and so, on the active center interaction with the different molecules. In order to observe different phenomena, several catalysts were firstly synthesized, then physically and chemically characterized. After what, the catalytic performances were evaluated, for finally proceed to a mathematical description of their catalytic behaviors by model construction. In that respect, the first work consisted to finely control the laboratory synthesis of the solid catalysts, from the support itself to the different redox active center implementation.

In this study, synthesized catalysts were constituted of a CHAbazite support further functionalized with copper transition metal following different synthesis routes as impregnation, ionic exchange and one pot method respectively denoted through the document as -IMP, -IE and -HT. Among them, the ionic exchange method was chosen for preparing the reference catalyst, based on laboratory synthesis knowledge [237] and literature [168,178,238]. This method was chosen, as it will be demonstrated through the next chapters, for its efficiency in copper cations integration within the structure, knowing that such sites represent the main active centers for NH<sub>3</sub> SCR as developed during the introduction chapter. The impregnation protocol was selected as conventional method and its capacity to place copper both at the surface and within the catalyst cavities [183]. Finally regarding the one pot method, based on literature [239], the protocol was set up in order to preferentially incorporate copper at the SAPO-34 top surface and further studied for its interesting potential in low waste water production and rapid process compared to previously mentioned synthesis routes.

### II-2. Catalysts preparation

Therefore, for the support preparation, the templating agent is primarily mixed with aluminium isopropoxide (Al[OCH(CH<sub>3</sub>)<sub>2</sub>]<sub>3</sub> CAS 555-31-7) for 90 min, after that the proper amount of silica precursor (SiO<sub>2</sub> CAS 112945-52-5) is stirred with the initial suspension during 30 min until homogeneity. Next, phosphoric acid (85wt% H<sub>3</sub>PO<sub>4</sub> CAS 7664-38-2) is poured with water in the mixture under stirring for 30 min. Finally, the generated mixture is sealed in an autoclave with Teflon chamber and placed in a furnace at 200°C for 96 hours. Once the hydrothermal treatment is over, the autoclave is temperature quenched and the white as-synthesized sample is wash-centrifuged with distilled water until pH 7 and finally dried at 100°C for 6 hours. The CHAbazite structure H-SAPO-34 is obtained after calcination of the dried powder in dynamic flow of synthetic air (Q = 4.5 L.h<sup>-1</sup>) firstly with a 1°C/min ramp and a 2 hours step at 200°C, followed with a 0.5°C ramp and a second step for 6 hours at 550°C, which the temperatures were defined following the ATG experiments presented in next Chapter (See Figure III-1) [240].



For the impregnation route, once the H-SAPO-34 support was calcined, the white solid was mixed with an aqueous solution made of the diluted copper salt in proper amount in order to reach the required Cu content. After 30min of impregnation under agitation, a sequence of 20 min in ultrasonic bath and 20 min under stirring was repeated twice. The solvent was evacuated in a rotavapor before being calcined in a dynamic flow of synthetic air ( $Q=4.5\text{L/h}$ ) following a  $1^\circ\text{C}/\text{min}$  ramp and a 2 hours step at  $200^\circ\text{C}$ , next with a  $0.5^\circ\text{C}$  ramp and a second step for 6 hours at  $550^\circ\text{C}$ . The pre-made catalyst is assigned as Cu-SAPO-34-IMP. Comparatively, a commercially available catalyst SAPO-34 support provided by ACS material (USA) was purchased and impregnated with the same protocol as above. The formulated catalyst is designated as Cu-SAPO-34-COM.

Concerning the two steps ionic exchange method, the copper species are incorporated in the  $\text{NH}_4$ -SAPO-34 material by liquid ion exchange (LIE) method [241–243]. Firstly, the zeolite is stirred in a 0,1 M ammonium nitrate solution ( $\text{NH}_4\text{NO}_3$  CAS 6484-52-2) at  $80^\circ\text{C}$  for 3h and the formed  $\text{NH}_4$ -SAPO-34 material is then filtered, washed to pH 7 and centrifuged before drying at  $100^\circ\text{C}$  for one night. The second step consists in preparing a 0,01M copper (II) acetate solution and adding the  $\text{NH}_4$ -SAPO-34 zeolite once the aqueous solution is heated at  $80^\circ\text{C}$ . After 30 min, several filtration cycles were performed. The final Cu-SAPO-34-IE catalyst was then washed, dried and calcined at  $1^\circ\text{C}/\text{min}$  ramp and a 2 hours step at  $200^\circ\text{C}$ , with after a  $0.5^\circ\text{C}$  ramp and a second step for 6 hours at  $550^\circ\text{C}$  in air for 6h.

Compared with a silicoaluminate (Si,Al) support for instance, the exchange cation rate within a Si,Al,P structure is more difficult to estimate. Indeed, the exchange rate can be easily approximated with a SSZ-13 support typically, assuming that two copper cations will compensate the charge deficit of one Al element. Thus, the ratio  $(2 \text{ Cu (mol.g}^{-1}) / \text{Al (mol.g}^{-1})) \times 100\%$  can directly provide an approximated maximum exchange rate. However for SAPO-34 like support, following the previously described substitution mechanism Chapter I, the exchange level can be approached by making the assumption that  $\text{Si(OAl)}_4$  building units are the exclusive unit in presence with  $\text{Al(OP)}_4$  as [244] :

$$\text{Level}\% = \frac{\%mol\text{ Cu}}{\%mol\text{ Si}} \cdot 100\% \quad (1)$$

Finally, the one pot catalyst Cu-SAPO-34-HT was synthesized by a single step, where the same different zeolite precursors was added after the first formation of a modified template constituted of the templating agent mixed with the copper precursor (acetate copper salt -  $\text{Cu}(\text{CO}_2\text{CH}_3)_2$  CAS 142-71-2). After what, the next steps are identical to the ionic exchange method.

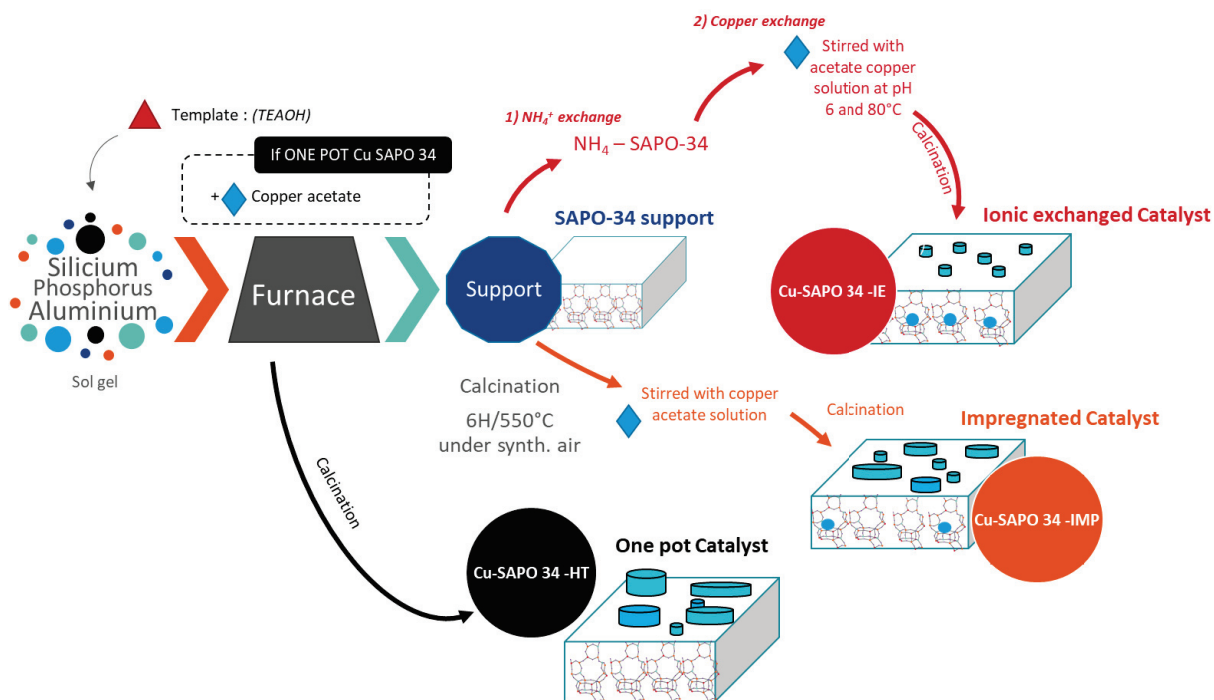


Figure II-1. Schematic representation of support protocol synthesis and copper incorporation methods

### II-3. Physico-chemical and textural catalyst characterizations

#### II-3.1. Inductively Coupled Plasma Optical Emission Spectroscopy (ICP-OES)

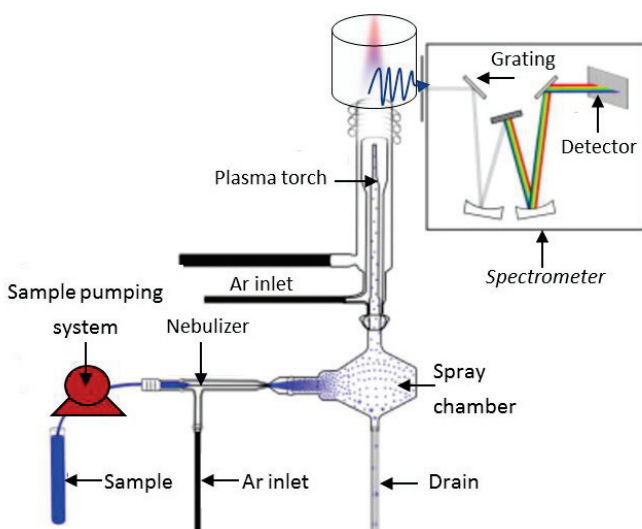


Figure II-2 ICP OES technique synoptic [12]

The chemical composition of the different catalysts was quantitatively determined by the Inductively Coupled Plasma Optical Emission Spectroscopy (ICP OES) technique as the synoptic Figure II-2. below displays. It commonly uses inductively coupled plasma to produce excited atoms and ions that emit electromagnetic radiation at wavelengths characteristic of a particular element. The intensities of the obtained emissions are indicative of the concentration of the element within the sample. More precisely, the measurements were made with an Activa

instrument from Horiba Jobin Yvon. Powders were completely dissolved with a mixture of lithium tetraborate and 20% HCl at 1100°C in Pt-Au crucible for Si percentage determination. For Cu, P and Al determination, samples were attacked with a mixture of sulfuric acid (H<sub>2</sub>SO<sub>4</sub>), nitric acid (HNO<sub>3</sub>) and hydrofluoric acid (HF) at 250-300°C [245].

## II-3.2. Dinitrogen adsorption and desorption

Specific surface area (SSA) of a catalyst plays a primordial role on its performance where a high surface interaction with the reactive phase is generally sought for a maximum of activity. The use of boiling nitrogen (77 K) as the adsorbed specie represent the common method for specific surface area determination and porous texture characterization [246]. After sample degassing during 4h at 300°C, the powder is firstly cooled using liquid dinitrogen, then exposed to gaseous N<sub>2</sub> molecules at increasing relative pressures in order to obtain a series of p/p<sub>0</sub> (with p the equilibrium pressure and p<sub>0</sub> the saturation pressure) in isothermal condition. In this study, measurements were pursued on Micrometrics ASAP 2020 instrument. The molecules close to the solid surface area are attracted by Van der Waals forces arising from inter-molecular attraction. If during the adsorption on mesoporous material and more precisely during the condensation phase of the probe molecule, usually no difference is made between gas and liquid phase densities, this assumption cannot be followed with microporous material [246]. Concerning the microporous CHAbazite materials, the pores size limits the number of N<sub>2</sub> adsorbed layers, and typically follow a Langmuir isotherm (Type I as displayed on Figure II-3) during desorption operation. The molecules arrangement will be more sensitive to the micropores shape and width. Due to this configuration, SSA representing the microporosity cannot be directly obtained through the Brunauer-Emmett-Teller (BET) method commonly applied for meso and non-porous material, the BET mathematical model actually required the verification of several hypothesis as : the lack of steric limitation to the multi-layer thickness, the second and further layers start to build up before the completion of the first one, the arrangement of these molecules is assumed to be hexagonal close packing and the molecular cross sectional area can be derived from the density of the adsorptive in the bulk liquid state [246]. Such hypothesis which are not verified for microporous materials. Regarding these considerations, the microporosity SSA ( $S_{micro}$ ) is usually obtained after t-plot operation, firstly introduced by de Boer [247], consisting to represent the adsorbed volume vs the statistic film thickness (t) of adsorbed molecules in a certain isotherm region, e.g. at a particular pressure range. Where at low (t) values, the large pores are filled and also the smaller pores. At higher (t) values, only the wide pores are represented except the micropores which are presumed filled for higher (t). Therefore, from the slopes representing the linear dependence of the adsorption in this area, the total surface area and the microporous volume can be calculated following Eq. 2 below:

$$a_{(p/p_{sat})} = a_{micro} + k S_{ext} t_{layer}^{(p/p_{sat})} \quad (2)$$

With,  $a_{(p/p_{sat})}$  the adsorbed volume at relative pressure (cm<sup>3</sup>),  $a_{micro}$  the adsorbed volume in saturated micropores (cm<sup>3</sup>),  $S_{ext}$  the external surface area corresponding to pores larger than the micropores (m<sup>2</sup>),  $t_{layer}^{(p/p_{sat})}$  (Å) represents the statistical thickness of adsorbed layer here defined as following Harkin-Jura model represented by Eq. 3 [248,249]. Finally, k corresponds to a coefficient equal to:

$$k = \frac{1}{4.3532 \cdot t_{mono}} \quad (3)$$

With  $t_{mono}$  corresponding here to a monolayer thickness of spherical nitrogen atomic diameter of 0.354 nm and “4.3532” a coefficient representing the changing state from occupied area to adsorbed N<sub>2</sub> at 78K.

$$t_{layer} = \sqrt{\frac{13.99}{-\log(p/p_0) + 0,034}} \quad (4)$$

Thus, for high values of (t), the intercept of the regression line informs about the microporous volume ( $V_{micro}$ ) and the slope represents the external sample SSA. Then at lower (t) values, the surface area of the wider pores can be obtained from the slope of Eq. 2, corresponding to the total sample specific surface area ( $SSA_{tot}$ ). In that respect,  $SSA_{micro}$  can be obtained by the difference between  $SSA_{tot}$  and  $SSA_{ext}$ .

Moreover, the Horvath-Kawazoe (HK) method was employed for the microporous size distribution determination, in order to characterize the N<sub>2</sub> isotherm obtained from our molecular sieve. The method was initially used with slit shaped porosity for estimating the pore size distribution but it was further extended to cylindrical and spherical pores following Saito-Foley assumptions [250]. By taking into account the adsorbate-adsorbate interaction, HK model were successfully employed for zeolite and activated carbon porous size distribution estimation [251–253].

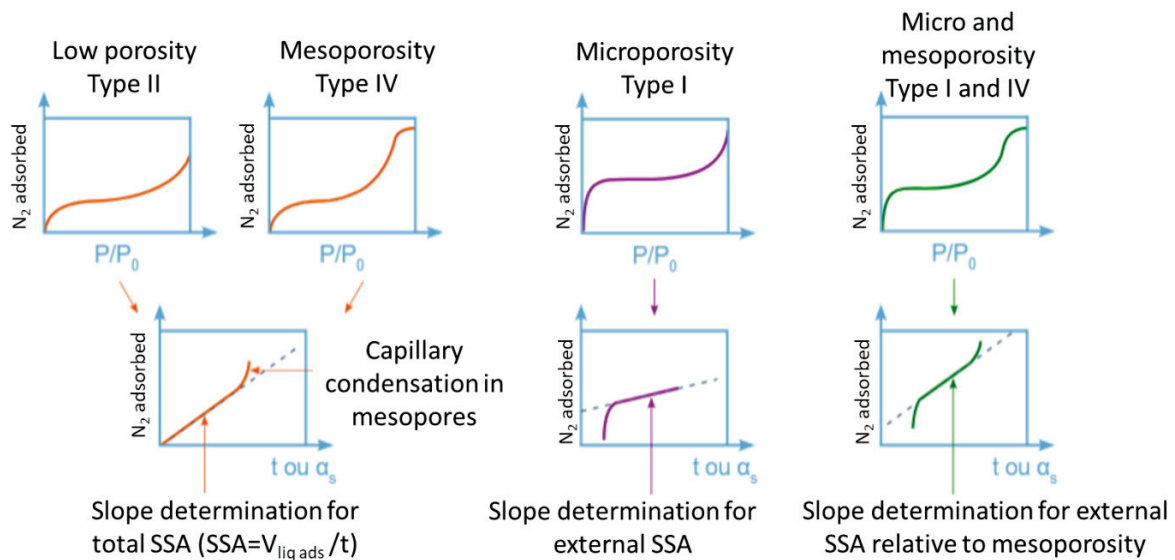


Figure II-3. Representative types of adsorption isotherm usually found by nitrogen adsorption and its exploitation through t-plot method [254]

### II-3.3. X-Ray Diffraction (XRD)

The catalysts crystalline phase was characterized by XRD, as the synoptic scheme remind below Figure II-4, based on the diffracted ray produced by the interaction of monochromatic X-rays generated by a cathode ray tube, and the crystalline sample. The law of Bragg (Eq. 5) relates the wavelength of electromagnetic radiation to the diffraction angle and the lattice spacing in the crystalline solid as follows:

$$2d_{hkl} \cdot \sin \theta = n \cdot \lambda \quad (5)$$

With  $d_{hkl}$  representing the lattice spacing,  $\theta$  the incidence angle (rad),  $n$  the integer and  $\lambda$  the wavelength of incident X-ray beam (Å).

In order to identify the material phases, the diffraction peaks obtained through a range of  $2\theta$  angles are converted to d-spacing and compared with standard reference patterns. X-ray Diffraction measurements of all samples were pursued at ambient atmosphere employing a Bruker D8 diffractometer (CuK $\alpha$  radiation at 0,154184 nm) equipped with a Ni filter and 1-D fast multistrip detector (LynxEye, 192 channels on  $2.95^\circ$ ).  $2\theta$  steps of  $0.02^\circ$  from  $4^\circ$  to  $40^\circ$  for a total acquisition time of 32 min were used for the diffractograms collect. Phase identification was performed using the ICDD-PDF4+ database and using the Diffrac.Eva software (Bruker).

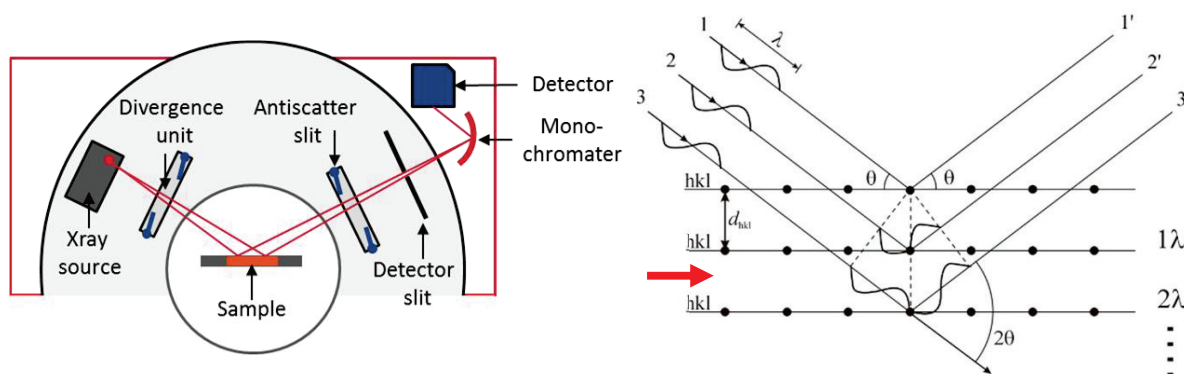
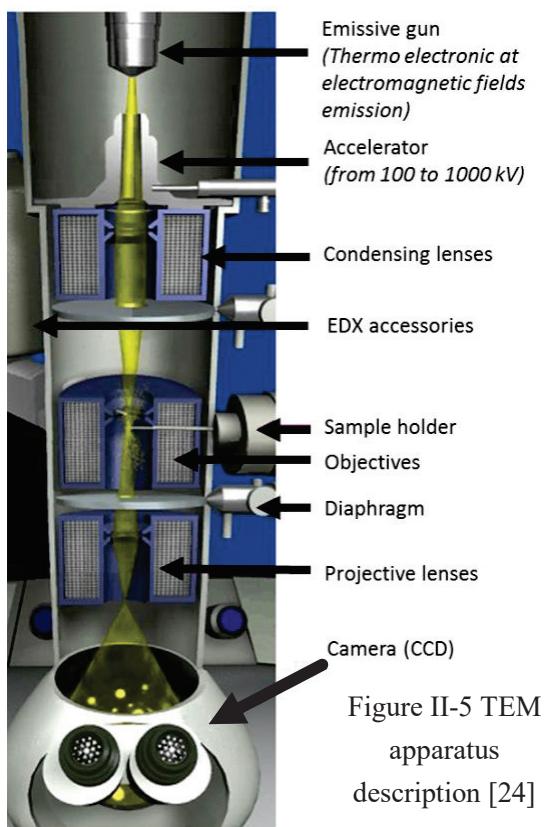


Figure II-4. XRD technique synoptic scheme with the scattered X-ray construction from crystalline lattice [255]

#### II-3.4. Thermogravimetry (TGA)

Thermogravimetric analysis allows, by monitoring the sample mass loss during thermal treatment in specific conditions, to quantitatively follow the mass variation of a given sample and correlate it with the nature of the lost species. Typically, 5 to 15 mg of sample is placed inside an alumina or platinum crucible and placed within the thermobalance apparatus (TA TGA Q500). The crucible can be heated following different heating programs under different atmospheres (inert, oxidative or reductive). Here, 14 mg were weighted and monitored under synthetic air at  $20 \text{ ml}\cdot\text{min}^{-1}$  from  $35^\circ\text{C}$  to  $800^\circ\text{C}$  with a heating ramp of  $5^\circ\text{C}\cdot\text{min}^{-1}$ . For zeolites investigations, knowing their high absorbance capacity, this technique can give several information about the adsorbed species and their desorption temperature (Water,  $\text{NH}_3$ , pollutant...). Information about the templating agent (SDA) decomposition temperature can be obtained too and the corresponding SDA molecules number required for zeolite cages formation can also be determined [256].

## II-3.5. Transmission Electron Microscopy (TEM)



This characterization technique allows the indirect observation of the morphologies, size and local distribution of the surface solid phases by forming image from the interaction of the electrons with the sample as the beam is transmitted through the sample. Following the instrumental description depicted Figure II-5 [257] typically, an electron gun illuminates the sample by passing through an illuminating system of condenser lenses. The electron gun can be either a tungsten filament heated at 2500 °C or a LaB6 cathode heat at 1600 °C as in this study. The system of condenser lenses gives a demagnified image of the source on the sample. The radiation interacts with the surface and is scattered. The scattered radiation is then focused by objective lens, which gives a 2D magnified image of the surface. Then, a system of projection lenses magnifies the

intermediate image on a fluorescent screen [258]. TEM study are of primary interest for supported catalyst, where the surface species configuration will be evaluated in size, shape and nature through the d-space observation and identification. These analyses were achieved with a JEOL 2010 microscope, its acceleration voltage was 200 kV with a resolution point about 0.19 nm and a LaB6 emission current. Before measurements, a dispersion of catalyst crushed in ethanol was deposited on standard holey carbon-covered copper TEM grids.

Complementary to TEM measurements, the chemical analysis system of the energy-dispersive X-ray spectroscopy (EDX) can be employed to locally quantify the chemical composition of the surface. EDX relies on the counting of X-rays emitted from the beam-illuminated specimen region as a function of the photon energy [259].

## II-3.6. X-Ray Photoelectron Spectroscopy (XPS)

XPS is a method allowing quantitative determination of surface composition and differentiation of elements oxidation states. The technique, Figure II-6, consists to measure the kinetic energy and electrons emission obtained by the collision of X-ray beam on the sample through 10 nm depth. As the emitted electrons are readily absorbed by any material, the technique requires operation in a high vacuum ( $10^{-6}$  –  $10^{-9}$  Pa) [258]. Here,  $K\alpha$  emissions was produced by aluminium ( $h\nu = 1486.6$  eV) cathodes as X-ray sources. The induced energy conversion principle is:

$$h\nu = E_k + E_b + \phi_{sp} \quad (6)$$

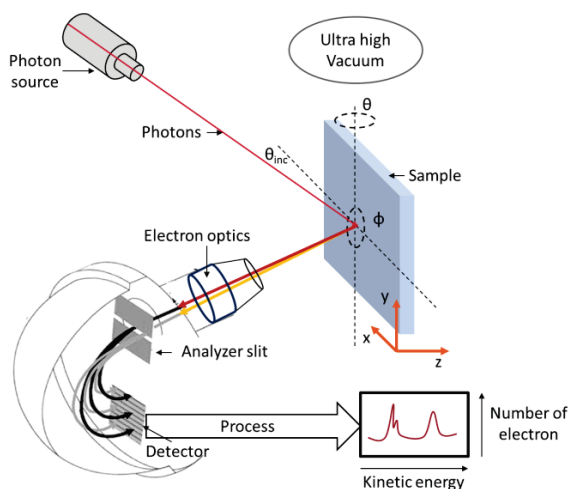


Figure II-6 XPS technique synoptic

Where  $h\nu$  is the incident photon energy (eV)  $E_k$  the kinetic energy of the electrons emitted analyzed with an appropriate detector (eV),  $E_b$  the binding energy of the electrons in their orbital level (eV) and  $\phi_{sp}$  the work function characteristic of the spectrometer. The depth of the electron levels excited, core and valence band electrons, depends upon the energy of the incident beam photons. The obtained XPS spectrum corresponds to the plot of the variations in the numbers of emitted electrons vs. their kinetic energy values.

In this study the x-ray photoelectron spectroscopy measurements (XPS) were performed with an Axis Ultra DLD spectrometer from Kratos Analytical using a monochromatic Al-K X-ray source with a pass energy of 20 eV. Tests were performed in ultra-high vacuum ( $>10$  mbar) on the as-synthesized samples. Spectra of Si 2p, P 2p, Al 2p, Cu 2p, O 1s, C 1s and N 1s levels were measured at  $90^\circ$ . The binding energy of the C1s intense peak corresponding to double carbon (C-C) bonds was taken as reference for energy calibration and fixed at 283,9 eV. The signal intensities were measured using integrated areas under the detected peak of the spectrum, where the  $\text{Cu}^{2+}$  and  $\text{Cu}^{d+}$  signal peaks were associated to a binding energy close to 934 eV and 931 eV, respectively. The experimental precision of the XPS semi-quantitative measurements was close to 20%.

### II-3.7. Magic-angle spinning Nuclear Magnetic Resonance (MAS-NMR)

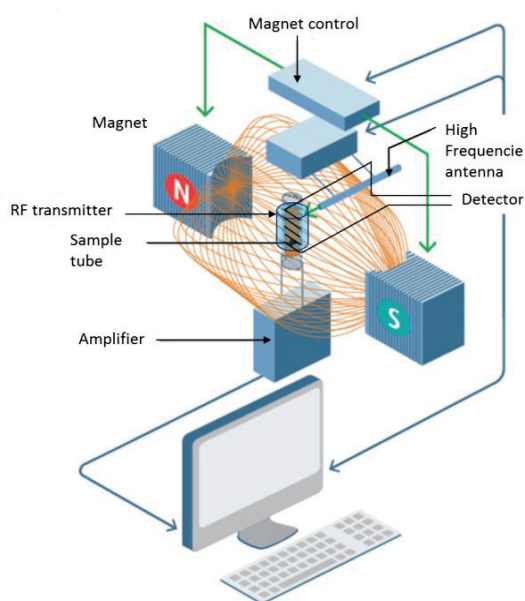


Figure II-7. MAS NMR technique synoptic [29]

Solid state NMR spectroscopy is a characterization technique allowing structural and conformational material investigation and chemical function identification. It represents a powerful technique for the study of the building unit's arrangement constituting the zeolite bulk. The principle behind this spectroscopic technique is that many nuclei have spin and all of them are electrically charged. By applying an external magnetic field, an energy transfer can occur passing from the base energy to a higher energy level. This transfer takes place at a particular wavelength (that corresponds to radio

frequencies) and when the spin returns to its base level, the emitted energy is at the same frequency. The energy difference between spin states will be modified following the element chemical environment and their respective electronic state. The signal that matches this transfer is measured in many ways and processed in order to form an NMR spectrum for the concerned nucleus ( $^{27}\text{Al}$ ,  $^{31}\text{P}$ ,  $^{29}\text{Si}$ ...) [260]. Magic angle spinning spectrometry stands for the choice during measurements to use a particular angle ( $\theta \approx 54,7^\circ$ ) which allows to remove or reduce the influence of anisotropic interactions and increase spectral resolution [261,262].

The  $^{27}\text{Al}$ ,  $^{29}\text{Si}$  and  $^{31}\text{P}$  MAS NMR measurements were performed on Bruker AVANCE III 500 WB spectrometer at resonance frequencies of 130, 99 and 202 MHz, respectively with a sample spinning rate of 10 kHz in a commercial 2.5 mm MAS probe at room temperature. The samples were hydrated prior to measurements by atmospheric exposition for 5 days. All NMR spectra were fitted with Gaussian functions for semi-quantitative deconvolution of overlapping peaks.

#### II-3.8. $\text{H}_2$ Temperature Programmed Reduction ( $\text{H}_2$ -TPR)

The reducibility of copper species was estimated by  $\text{H}_2$ -TPR experiments, this thermal method is related to catalyst transformation rather than an adsorption process on its surface. This technique is based on the reductive molecule (generally  $\text{H}_2$ ) consumption following a temperature ramp comparatively to a reference  $\text{H}_2$  concentration. This difference can provide quantitative information about the oxidation state of the reduced elements. The samples were firstly pre-treated under 40% vol. oxygen balanced in  $\text{N}_2$  during 30 min at  $500^\circ\text{C}$ . Thus, the sample surface is cleaned of adsorbed species and the copper sites are more likely to be present as  $\text{Cu}^{2+}$  form than  $\text{Cu}^+$  on each catalysts [263]. Then, the sample was flushed under argon at room temperature until residual  $\text{O}_2$  presence. Argon or nitrogen are usually employed as carrier gas regarding their thermal conductivity (respectively  $45.4 \cdot 10^6 \text{ cal} \cdot \text{cm}^{-1} \cdot \text{s}^{-1} \cdot \text{K}^{-1}$  and  $65.7 \cdot 10^6 \text{ cal} \cdot \text{cm}^{-1} \cdot \text{s}^{-1} \cdot \text{K}^{-1}$ ) different to the one of hydrogen ( $471 \cdot 10^6 \text{ cal} \cdot \text{cm}^{-1} \cdot \text{s}^{-1} \cdot \text{K}^{-1}$ ). This wide difference will not perturb the TCD detector, measuring the thermal difference between the reference flow of carrier gas and the experimental effluent. The profiles were recorded under a flow of 2% vol.  $\text{H}_2$  in Ar ( $40 \text{ ml} \cdot \text{min}^{-1}$ ) from 20 to  $500^\circ\text{C}$  at a rate of  $10^\circ\text{C} \cdot \text{min}^{-1}$ .  $\text{H}_2$  consumption was quantitatively calculated by time integration of  $\text{H}_2$ -TPR profiles. Simultaneous  $\text{H}_2\text{O}$  evolution was also recorded.

#### II-3.9. Temperature Programmed Desorption (TPD)

The catalyst acidity and its storage capacity were investigated through  $\text{NH}_3$ -TPD, where the different active sites strengths were segregated in temperature. After ammonia adsorption at constant temperature and sites saturation assumption, the sample was firstly flushed in He prior to temperature increasing. The resultant temperature at which species desorbed from the active sites indicate the strength of the latter. It is important to note that no difference can be made between Brønsted and Lewis acid sites by simple TPD measurements. The convoluted profile can thus represent different type of sites but of similar strength.  $\text{NH}_3$ -TPD profiles were obtained by loading samples into a U-shaped quartz tube and



further pre-treated under oxidative atmosphere for 30 min at 500°C with a heating ramp of 10°C.min<sup>-1</sup>. After 30 min flush of He at the required temperature of adsorption, a total flow of 40 ml.min<sup>-1</sup> of 1000 ppm NH<sub>3</sub>, 80000 ppm (8%) O<sub>2</sub> and 40000 ppm (4%) H<sub>2</sub>O was injected at 200 °C until saturation. The catalysts were then exposed to He for 30 min to remove all the physically adsorbed species before starting the desorption temperature program, which consisted of a ramp of 2 °C · min<sup>-1</sup> until 500°C. Desorbed ammonia was analysed by Fourier Transform Infrared (FTIR) spectrometer (NICOLET) equipped with a heated 2m gas cell and a DTGS detector. All profiles comprising overlapping peaks were fitted with Gaussian during semi-quantitative deconvolution analysis.

Concerning NH<sub>3</sub> TPD experiments, a precision must be pointed out concerning the experimental quantities of adsorbed and desorbed probe molecules. Indeed, three phases characterize the measurements: 1) the adsorption step, 2) the cut-off in probe molecule supply and 3) the desorption process during heating ramp. Following the example Figure II-X, three main areas can therefore be observed, where the first one (red), assuming a constant volumetric flow, can be integrated for obtaining the total quantity of adsorbed NH<sub>3</sub>. The third one (green) is also integrated for obtaining the NH<sub>3</sub> quantity desorbed through the investigated temperature window. However, the second area (blue) can represent the desorption of physisorbed NH<sub>3</sub> from weakest sites during the He flush operation after the cut off, but also, the decreasing profile represents the hydrodynamic behaviour of the manual three way valve switching off and the corresponding NH<sub>3</sub> concentration inlet decrease ( $Q_{transit}$ ). Therefore, the total quantity of desorbed NH<sub>3</sub>, obtain through the integration signal from the cut off to the end of ramping temperature is superior to the integrated area of adsorption peak and no difference can be made between desorption of physisorbed species and the impact of hydrodynamic profile. Therefore, assuming that all NH<sub>3</sub> molecules adsorbed is desorbed during the experiment without retention, the real quantity completely desorb from the catalyst can be obtained through:  $Q_{des\ real} = Q_{ads} = Q_{physisorbed} + Q_{des}$ . Table II-1 displays these differences for all experiments employed in this study and the considered NH<sub>3</sub> quantities measured between catalysts.

Table II-1. Differences between adsorbed and desorbed quantities of NH<sub>3</sub> measured during TPD experiments: 1000 ppm NH<sub>3</sub> adsorbed at 150°C with 80000 ppm (8%) O<sub>2</sub> and 40000 ppm (4%) H<sub>2</sub>O in the inlet

Catalyst	Dry or Wet experiment	Q <sub>ads</sub> (mol)	Q <sub>des</sub> (mol)	Q <sub>physisorbed</sub> (mol) calculated	Figure
H-SAPO-34	wet	2.84.10 <sup>-5</sup>	1.87.10 <sup>-5</sup>	9.80.10 <sup>-6</sup>	IV-4
Cu-SAPO-34-IE	dry	3.66.10 <sup>-5</sup>	2.37.10 <sup>-5</sup>	1.29.10 <sup>-5</sup>	VI-9 (B)
	wet	3.77.10 <sup>-5</sup>	2.09.10 <sup>-5</sup>	1.68.10 <sup>-5</sup>	IV-4
Cu-SAPO-34-HT	dry	2.94.10 <sup>-5</sup>	2.41.10 <sup>-5</sup>	5.30.10 <sup>-6</sup>	VI-31 (A)
	wet	2.67.10 <sup>-5</sup>	1.40.10 <sup>-5</sup>	1.27.10 <sup>-5</sup>	IV-4
Cu-SAPO-34-IMP	wet	2.98.10 <sup>-5</sup>	1.56.10 <sup>-5</sup>	1.42.10 <sup>-5</sup>	VI-40

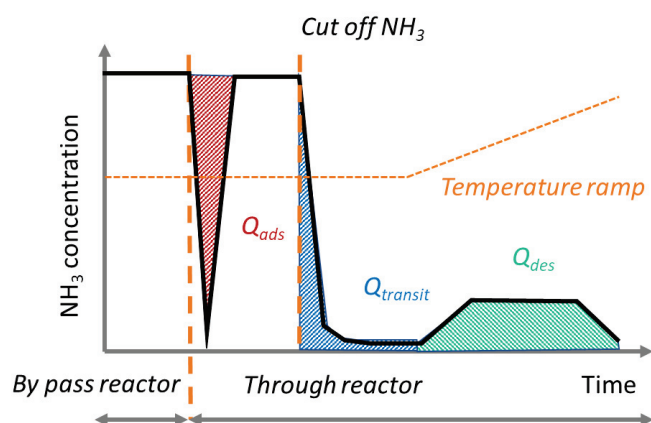


Figure II-8.  $\text{NH}_3$  TPD experiment scheme for depicting the different integrated areas and their meaning.

### II-3.10. Spectroscopic analysis: Diffuse Reflectance Infrared Fourier Transform spectroscopy (DRIFT)

Diffuse Reflectance Infrared Fourier Transformed Spectroscopy (DRIFT) experiment is a powerful technique for the nature surface sites characterisation without (ex-situ) or with (in-situ) probe molecules during transient conditions. The technic allows to record IR spectra directly on solids and in powder form (which is not the case with FTIR analysis requiring the sample pelleting prior to measurements, which can be a tiresome task). Molecules interaction mechanism with the surface and particular species formation can be investigated and monitored in temperature during in-situ experiments. The main goal during this study was to discriminate the different catalysts active sites through Brønsted or Lewis acid and observing their interaction in temperature with different probe molecules as  $\text{NH}_3$ , NO and CO, where each molecule provided specific information. To gain further insight into the possible mechanism reactions path and investigate the different catalysts behaviour during SCR conditions, in-situ experiments were exclusively done on a semi-qualitative order. Due to experimental configuration (unmodified DRIFT cell, bed temperature shift, resolution analysis and data time acquisition) quantitative analysis was not possible [264–266]. Semi-qualitative experiments were performed, comparing the different signal intensities for time resolved information acquisition.

#### II-3.10.1 Technical description

Localized infrared irradiation of a non IR transparent solid surface can create, among others, directly reflected (specular reflection) and diffused beams, as displayed in Figure X, after it penetration through the first sample layers (nm) depending on the sample absorptivity and refractive index. Note that transmission and diffuse reflection spectra are similar due the type of collected beam, mainly constituted of diffused IR radiation. In that way, the specular reflection is generally suppressed in order to avoid further

spectra distortion effect. Particular attention is required regarding certain solid properties which can alter the DRIFT spectra, known as [264,267]:

- A low refractive index and high IR absorption coefficient. *Solution:* with really absorbent solid, it is usually advised to dilute the solid particle with IR transparent material as KBr.
- Particle dimensions and packing density. *Solution:* in order to decrease the external reflection from the largest particle, it is recommended to decrease the grain size below 10  $\mu\text{m}$ .
- Surface homogeneity

Thus, the IR beams passing through the dome above the solid surface are collected by a series of mirrors, leading them to the mercury cadmium telluride (MCT) based detector and then computed as interferograms. If most mid-infrared (mid-IR) analyses are performed with the standard deuterated L-alanine doped tryglycerine sulfate (DLATGS) detector as during NO<sub>x</sub> and NH<sub>3</sub> gas concentration monitoring during catalytic tests (see section II-3.11 below), DRIFT experiments due to the higher speed acquisition requirement and low IR input (Xx times less IR beams due to the loss in the solid, mirror, target...), highly sensitive MCT detector are typically employed. These detectors require to be filled with liquid N<sub>2</sub> for avoiding spectra noises and rapid saturation.

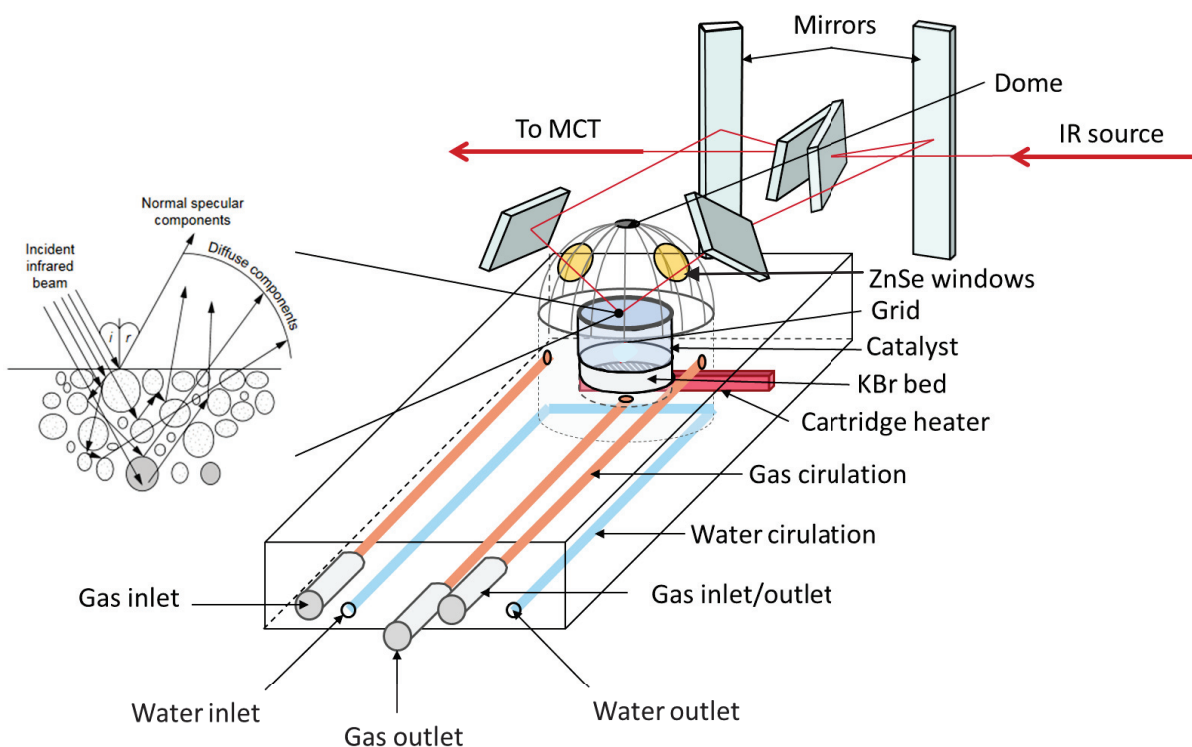


Figure II-9 : DRIFT cell composition with representation according to commercial ThermoFisher © high temperature cell with in insert [268], representation of scattered IR beam on a solid surface generating the IR spectrum.

## II-3.10.2 Ex-situ and in-situ measurements methods and conditions

More precisely, DRIFT experiments were performed, using a NICOLET FTIR analyser equipped with a praying mantis accessory from Harris Scientific © (provide mirrors and alignment with the cell) and a high temperature cell as schematized on Figure II-9. The surrounding atmosphere of the IR beam throughout its path was purged with CO<sub>2</sub>-free dry and synthetic air provided by an online air purifier system (Parker Balston, FTIR purge gas generator). Typically, less than 20 mg of sample are required, the catalyst is deposited above a KBr bed within the micro reactor (total volume of  $\approx 10 \text{ cm}^3$ ). The surface is flattened as for XRD measurement, avoiding preferential grain orientation and surface distortion for maximizing the IR beam collection. Due to reductive (NH<sub>3</sub>, CO) or oxidative gas (NO) phase and possible presence of water, the dome windows were made of ZnSe (Transmission range 20 000 - 454 cm<sup>-1</sup>, Refractive index of 2.4, insoluble in water). Typically during experiments, spectra were collected at a resolution of 1 cm<sup>-1</sup>, one spectrum was the compilation of 32 scans and the used blank consists in pure and dry KBr spectrum. Spectra were collected from 4000 cm<sup>-1</sup> to 650 cm<sup>-1</sup> wavenumbers. The total flow rate was fixed at 40 ml·min<sup>-1</sup>, consisting of the probe molecule diluted in Helium.

Each sample were pre-treated at 500°C under pure O<sub>2</sub> for 30 min in order to remove absorbed water and other surface pollutants. The temperature profiles were followed thanks to a temperature controlled (ATC) Harrick Scientific, connected to the high temperature cartridge heater and a water-cooling system circulation (temperature maintained at 25°C). The deviation between the bed temperature and temperature set point are visible in Annexes Figure II-1. Then, ex-situ measurements under pure He at room temperature were performed. After ex-situ measurements, the catalysts were exposed to the adsorption process, with a gas composition of 1000 ppm of the probe molecule (NH<sub>3</sub>, CO, NO) diluted in He during 30 min, controlled by BROOKS mass flow controllers. A bypass system right before the cell allows rapid composition modification of the atmosphere). The desorption steps during thermal desorption spectroscopy measurements were made as follow: a first measure was done at 35 °C after the flush of weakly physisorbed ammonia. Next the sample was heated at 10 °C·min<sup>-1</sup> under He until it reached 100°C with a 30 min plateau for stabilization. After this step, the chamber was cooled down to room temperature at 10 °C·min<sup>-1</sup> for 30 min to quench the desorption process. It allowed us to perform measurements with a minimum of perturbations due to active sites stretching vibrations at elevated temperature and allow better interpretations. Next, a temperature ramp of 10 °C·min<sup>-1</sup> was applied to reach 100 °C with a followed 30 min step for signal stabilization before to cool down again. This procedure was applied for each temperature desorption steps from 100 °C to 500 °C. The different spectres are realised in a 4000 – 800 cm<sup>-1</sup> range and are the result of subtraction between the measured spectra at room temperature after desorption at 100, 200, 300, 400 or 500 °C and the reference one at room temperature before any adsorption (corresponding to the ex-situ spectra). The detailed temperature program is described below Figure II-10 for more convenience. The software used during DRIFT experiments and for the different data manipulation was the Nicolet OMNIC™ series. The temperature program used during the in-situ

sequenced STD SCR analysis is displayed Figure II-11 with the corresponding gaseous inlet through the time. Only the first step done at 200°C is displayed, the following one at 300°C, 400°C and 500°C were made in a same manner. For the sake of clarity, all the displayed DRIFT spectra are represented in Absorbance units better than Kubelka-Munk (KM), due to the cited experimental conditions. It is worth reminding that KM units can effectively be used if specific criteria are fulfilled, as the necessity to work in diluted IR transparent matrix material and in fine and uniform particles granulometry (2-5 µm diameter) finally forming a bed thickness of at least 3 mm [264,267].

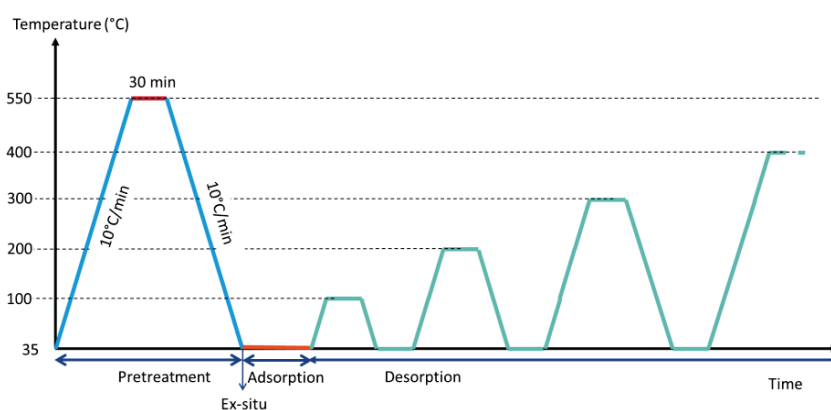


Figure II-10 : Profile temperature used during DRIFT analysis

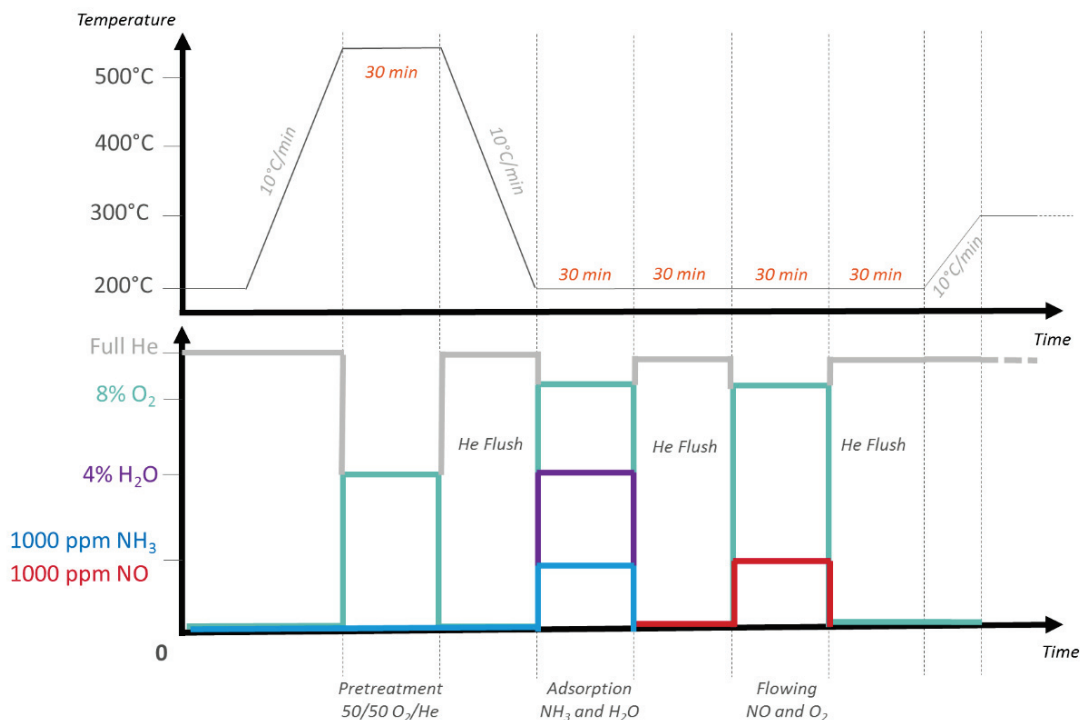


Figure II-11 : Profile temperature used during in-situ sequenced DRIFT analysis of STD SCR reaction

Finally, Table II-2 below summarize different of the employed characterizations techniques during this study and provide a quick overview on these methods.

Table II-2. Characterization techniques used during this study and their potential for active phases identification.

<b>Technique</b>	<b>Utilization</b>	<b>Limitations</b>	<b>In situ possibilities?</b>
<b>ICP</b>	Chemical composition determination Impurities detection	Destructive method Blind to certain element (H...) No information on oxidation state	no
<b>N<sub>2</sub> sorption</b>	Pores sizes and volumes determination Microporosity characterization Structural pores identification through isotherm shape	Assumption on mathematical model and pore geometries for pore size distribution (BJH, HK...)	no
<b>XRD</b>	Long-range crystalline phase identification Rough particles size determination Surface cluster phase information if large enough	No information for small surface cluster Average technique	✓
<b>TEM</b>	Structures visualization at atomic level Coupled with EDX for further identification	Local interpretation Strong incident beam can disturb the sample stability	✓
<b>XPS</b>	Quantitative atomic concentrations, oxidation state at surface Possible observation through Auger spectra for state differentiation	UHV required High interval confidence for atomic concentration Difficult peaks deconvolution and assignments at small %	✓
<b>NMR</b>	Concentration, building unit environment investigation Visible aging effect on material	Only nuclei with non-zero spin possible, and possible sensitivity trouble.	✓
<b>H<sub>2</sub> TPR</b>	Determination of activation temperature for redox process Differentiation of phases during reduction step	Assignment of the overlapped peaks, assumption of initial oxidation state for quantitative interpretations	no
<b>TPD</b>	Sites strength observation in temperature	No segregation between nature sites	no
<b>DRIFT</b>	Surface active sites identifications by nature (Brønsted, redox...) Different probe molecules for different information, structural information Ease of sample preparation	Difficult quantitative interpretation Signal saturation at low wavenumber	✓

## II-3.11. Catalytic performance evaluations

## II-3.11.1 Experimental bench

Figure II-12 displays the three different parts composing the catalytic set-up which are the feeding, reaction and analyses system.

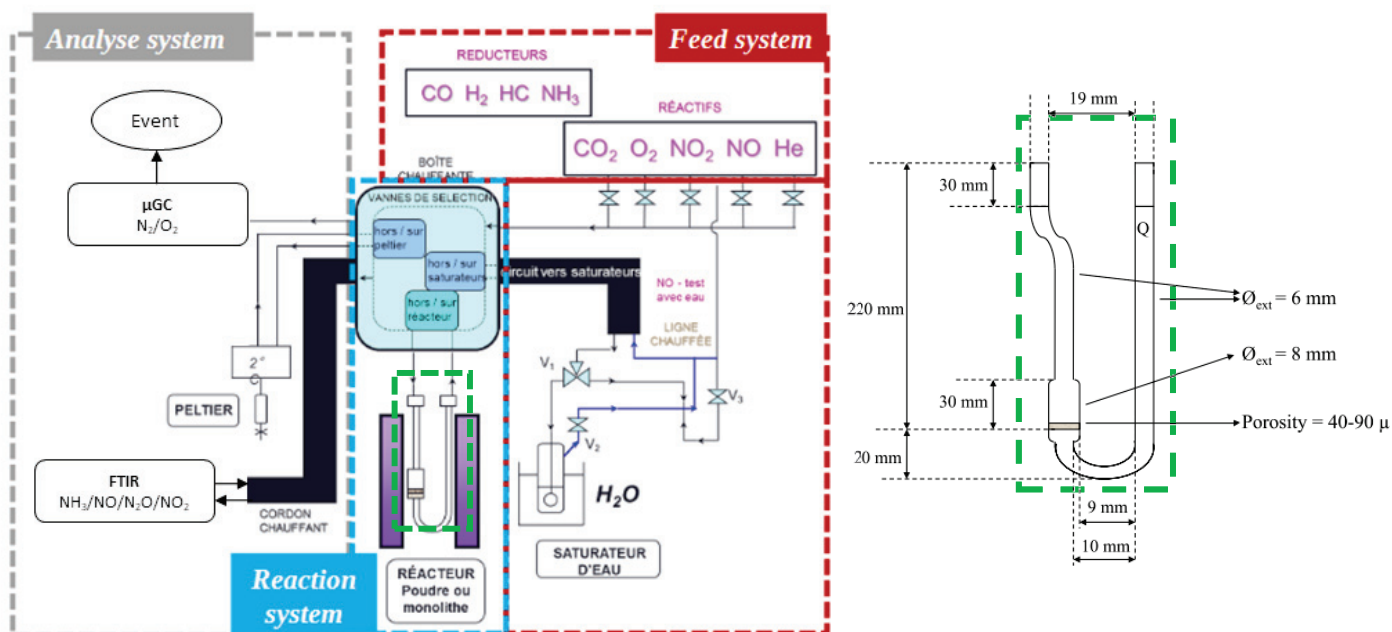


Figure II-12. Experimental set-up synoptic with the used quartz reactor dimensions

- Feed system:** Following the  $\text{NH}_3$  SCR reaction system, several gases were accessible as reactants as  $\text{NO}$ ,  $\text{NH}_3$ ,  $\text{NO}_2$  and  $\text{O}_2$  and controlled through Brooks © flowmeters. In order to work in presence of water as presumed during real working conditions, the vapor fraction was introduced thanks to a heated and regulated water bath by controlling the vapor pressure of  $\text{H}_2\text{O}$ . All lines placed downstream from the saturator were heated at  $200^\circ\text{C}$  in order to prevent condensation but also to prevent the precipitation of ammonium nitrate once  $\text{NH}_3$ ,  $\text{NO}$  and  $\text{H}_2\text{O}$  are mixed together [269]. Figure II-13 displays pictures of an inlet mix (1000 ppm  $\text{NH}_3$ , 500 ppm  $\text{NO}/\text{NO}_2$  80000 ppm (8%)  $\text{O}_2$  and 40000 ppm (4%)  $\text{H}_2\text{O}$  in  $\text{He}$   $166 \text{ ml}\cdot\text{min}^{-1}$ ) impact on reactor tube without heating lines. The white crystals in the inner tube are clearly visible here. The carrier gas in our condition was  $\text{He}$ .
- Reaction system:** With pneumatic three ways valves network it was possible to switch on or bypass the reactor, saturator and Peltier system. Prior to the tests, the solid catalyst powder was introduced into a u-shaped quartz reactor (3 mm internal diameter) containing 35 mg of crushed catalyst deposited on the quartz frit. A K-type thermocouple was inserted near to the catalytic bed to monitor the temperature and the reactor was placed inside a temperature-controlled furnace.

- *Analyses system:* The effluent  $\text{NH}_3$ ,  $\text{NO}$ ,  $\text{NO}_2$  and  $\text{N}_2\text{O}$  gas concentrations were monitored by a Fourier Transform Infrared (FTIR) spectrometer (NICOLET) equipped with a heated 2 m gas cell and a DTGS detector. Outlet nitrogen and oxygen concentrations were followed with an in-line micro gas phase chromatography (SRA % GC-R3000). The  $\mu\text{GC}$  column for  $\text{N}_2$  and  $\text{O}_2$  analysis was a molecular sieve of 0.5 nm aperture.



Figure II-13. Pictures of  $\text{NH}_4\text{NO}_3$  ammonium nitrate solidified on inner tube walls during Fast SCR conditions.

#### II-3.11.2 Operating conditions

Before testing, fresh catalyst surface was cleaned at 200 °C for 30min in flowing He. Catalytic tests were pursued at an estimated total Gas Hourly Space Velocity (GHSV) of 142 000  $\text{h}^{-1}$ , at a total volumetric flow of 160  $\text{ml}\cdot\text{min}^{-1}$ . In most of the cases, the % vol. of water was about 40000 ppm (4%) and selected for representing an averaged water fraction commonly measured in real exhaust condition and typically used in literature as reported in Table II-3. A blank was made before every experiment with the required effluent condition in by-pass mode. The reacting temperature did not reach lower temperature than 150°C in SCR conditions regarding the solid precipitation possibilities. A standard temperature cycle was composed of a step at 200°C for 30 min, a heating ramp of 2°C.min<sup>-1</sup>, a stabilization step at 500°C for 30 min and a cooling ramp of 2°C.min<sup>-1</sup>. This process was repeated three times prior to catalyst stability observations.

The investigated operating conditions were determined following: a) typical concentrations retrieve in real exhaust condition of lean-burn aftertreatment system, and b) usual condition used in literature for similar experiments, as the Table II-4 below figure out :



Table II-3. Experimental operating conditions retrieve in several studies for comparison

Ref	GHSV (h <sup>-1</sup> )	Catalyst mass (g)	System	Max. %vol. O <sub>2</sub>	Max. %vol. H <sub>2</sub> O	Concentration range NH <sub>3</sub> -NO (ppm)	Temperature range (°C)	Pretreatment
[270]	194000	0.06	Bed through	8	10	0-500	150-550	5°C/min 600°C 5h 10% H <sub>2</sub> O
[57]	30300	-	Coated Monolith	8	5	0-400	150-600	600°C 20 min 8% O <sub>2</sub>
[271]	100000	0.2	Plug flow	5	0	0-1000	150-500	550 N <sub>2</sub> 8H and 550 air 8H
[170]	400000	0.06	Bed through	5	0	0-500	15-550	air 500-800°C 5H
[243]	300000	-	Bed through	8	10	0-200	150-550	550°C 4h
[229]	18400	-	Coated Monolith	8	5	0-500	100-500	550°C 3h
[221]	300000	0.1	Bed through	5	3	0-500	150-600	550°C 4h
[272]	800000	0.015	Coated Monolith	14	2.5	0-350	150-500	550°C 8H
[224]	90000	0.5	Bed through	6	0	0-800	150-500	580°C 4H
[195]	22100	-	Coated Monolith	8	5	0-400	250-500	550°C 4h air
[273]	100000	-	Bed through	5.3	10	0-500	100-550	550°C 6h air

### II-3.11.3 Results analysis

All gases concentrations were measured and expressed in ppm regarding the FTIR and  $\mu$ GC calibration. By assuming a reactor free of diffusion limitations, the NH<sub>3</sub>-SCR reaction rates and NO<sub>x</sub> production rates can be calculated following:

$$r_{STD\ SCR}^{NH_3} = \frac{[NH_3]^{in} - [NH_3]^{out}}{m_{cata} \times \%wt.Cu \times V_m \times 10^6} \times \frac{Q_{flow}}{1000} [\text{mol}_{NH_3} \cdot \text{min}^{-1} \cdot \text{g}_{Cu}^{-1}] \quad (6)$$

$$r_{STD\ SCR}^{NO} = \frac{[NO]^{in} - [NO]^{out}}{m_{cata} \times \%wt.Cu \times V_m \times 10^6} \times \frac{Q_{flow}}{1000} [\text{mol}_{NO} \cdot \text{min}^{-1} \cdot \text{g}_{Cu}^{-1}] \quad (7)$$

With  $r_{STD\ SCR}^A$  = reaction rates (mol<sub>A</sub> .min<sup>-1</sup> .g of Cu<sup>-1</sup>), [A]<sup>in</sup> and [A]<sup>out</sup> the concentrations of reactant A (ppm) in the inlet and outlet respectively, V<sub>m</sub> = molar flow = 24.5 (m<sup>3</sup>.mol<sup>-1</sup>) at 20°C under 1 atm, m<sub>cata</sub> = sample mass (g), %wt.Cu = Weight copper percentage from ICP OES results.

NH<sub>3</sub>, NO conversion rates and N<sub>2</sub> selectivity were defined as follows:

$$CR_{NH_3} = \frac{[NH_3]^{in} - [NH_3]^{out}}{[NH_3]^{in}} \times 100 \quad (8)$$

$$CR_{NO} = \frac{[NO]^{in} - [NO_3]^{out}}{[NO_3]^{in}} \times 100 \quad (9)$$

Where,  $CR_A$  is the conversions rate of specie A,  $[A]^{in}$  and  $[A]^{out}$  the concentrations of specie A (ppm) in the inlet and outlet respectively.

$$selectivity_{N_2} = \left(1 - \frac{[NO_2]^{out} + 2 \times [N_2O]^{out}}{[NO_x]^{in} + [NH_3]^{in} - [NO_x]^{out} - [NH_3]^{out}}\right) \times 100 \quad (10)$$

Finally concerning the accuracy measurements of experimental concentrations detected in the outlet, 3 main bias were spotted: 1) the first one concerned the inlet concentrations, which comes from the mass flow controllers calibration and the obtained regression straight line between the percentage of Brook aperture and the volumetric gas flow as:

$$\% \text{ Brooks aperture} = a \cdot (\text{Volumetric flow in outlet}) + b \quad (11)$$

With a and b the obtained parameters from regression line

In that respect, a confidence interval band was calculated for inlet concentrations calibration, where typically for 1000 ppm  $NH_3$  the confidence interval was of +/- 36 ppm, for 1000 ppm NO: +/- 50 ppm and for 1000 ppm  $NO_2$  injected a confidence of +/- 12 ppm.

At this first bias is added the one from the calibration curve of detected gaseous concentrations from FTIR apparatus. The calibration was performed through TQ Analyst software © where the regression curve between collected spectra (corresponding absorbance peak area) depending on model adjustment method (least square method) and injected concentrations of each constituents is automatically constructed and the confidence interval is consequently given with data for each observation. Typically, for 1000 ppm  $NH_3$  measured correspond a +/- 3 ppm interval, 1000 ppm NO a +/- 11 ppm confidence, 500 ppm  $NO_2$  +/- 5ppm and 15 ppm  $N_2O$  +/- 0.5 ppm. Accordingly for lower concentrations, near the confidence limit, 50ppm  $NH_3$  is in a confidence interval of +/- 1.8 ppm, 50 ppm NO +/- 7 ppm, 50 ppm  $NO_2$  +/- 17 ppm and 5 ppm  $N_2O$  +/- 4 ppm. 3).

Finally, the largest error was made on NO concentration measurements and specifically in presence of water. Indeed, regarding the exploited IR wavelength window between 4000 and 700  $cm^{-1}$ , NO spectra typically appears from 1950 to 1800  $cm^{-1}$ , directly included within the IR signal of water (2000 – 1300  $cm^{-1}$ ). The NO concentration is consequently obtained by suppressing the water profile alone to the final spectra, in order to reach a processed profile as close as possible with the NO signal without water. In that respect, the NO concentration calibration curve was performed in presence of water for minimizing the impact of the water spectra noises.

#### **II-4. Conclusion**

These different techniques enabled the deep structural, physical and chemical characterization of the different zeolite supports and catalysts. The different synthesis impact on the catalysts were reported thanks to these techniques, the detailed description from the bulk to the surface were obtained and allowed an accurate comparison between catalysts. Indeed, the catalyst surface and bulk description are of primary interest for the study of the different active site configurations and their impact on the catalysts behavior following different operating conditions representing SCR processes. The gas chamber accessory employed with the FTIR apparatus was of great importance for the kinetic study of the reference catalyst and the acquisition of the main kinetic parameters, participating to the initialization step of the parameter estimation process of the model. In that way, the overall set of data obtained through the different bench tests were directly used as inputs for the model construction and the parameters estimation. The hydrodynamic relative to the experimental bench was also taken into account for accuracy purposes in the model, in order to not impair the parameters validity by hydrodynamic features. Thus, these different characterization tools were employed for the catalyst's behavior observation, and consequently, for the proposition of a mechanistic path. Key intermediaries and concentration impacts were investigated thanks to the several applied conditions in the experiment tests bench.

III



# CHAPTER III TOWARDS A CATALYST REFERENCE FOR NH<sub>3</sub>-SCR

## III-1. Introduction

The aim of this chapter is to investigate the suitability of classical impregnation method to develop an active, selective and hydrothermally stable catalyst for NH<sub>3</sub> SCR reaction, compared with state-of-the-art catalysts [274–276]. For this purpose, a pre-made SAPO-34 support was synthesized and compared with a commercially available SAPO-34 support, in order to verify that the preparation method allows to obtain the required physico-chemical, structural and surface properties for the above-mentioned reaction. This study provides an entry point to better understand the role of support properties and redox phase within the catalytic process, where the support and active sites share intimately linked properties. In that respect, several techniques were employed for investigating the supports textural and physicochemical characteristics. Once the support accordingly synthesized, the commercial and pre-made CHA-support were functionalized by classical impregnation protocol. Their respective active sites configurations were characterized and put in perspective regarding their NH<sub>3</sub>-SCR performances, following different operating conditions as STD SCR, NH<sub>3</sub> and NO oxidations.

## III-2. Properties controlled CHA support and functionalization: Synthesis and Characterization

As mentioned in the first chapter, chabazite zeolites, whose small pore were loaded with Cu, shows excellent activity for the NH<sub>3</sub>-SCR of NO<sub>x</sub>, and most importantly a higher hydrothermal stability than Cu-exchanged zeolites with medium and large pores [277,278]. However, its synthesis and its functionalization remain a great challenge. For example, 100g of SAPO-34 zeolite can be purchased to “ACS Material” supplier, for a price of 240\$ in 2019 [279] and only few manufacturers can provide this service [279–281]. The mentioned commercial support was employed and characterized to optimize the pre-made CHA-based support. The pre-made CHA support was synthesized by exploring in more details the complementarity between our optimized one-pot hydrothermal crystallization method [237] and literature specifications, in order to reached the following defined properties:

1. The support has to present high crystallinity, without residual AlPO phase nor amorphous phase after the synthesis process [282,283].
2. The support acidity, defined following the Si/Al molar ratio, need to be carefully tuned, obtaining an acids support without the presence of Si-island defects [284,285].
3. A zeolite support with a high specific surface area and microporous volume and a monomodal microporosity representative of the CHA molecular sieve need to be synthesized [172,286,287].

4. The support building unit configuration has to principally display a structure composed by tetrahedral Si(OAl)<sub>4</sub> and P(OAl)<sub>4</sub>, which is the building unit configuration characteristic of CHA SAPO-34 material [130].

Different characterization techniques were performed to validate the preparation method and to finely optimize the physico-chemical and structural properties of synthesized support (N<sub>2</sub> sorption, MAS NMR, XRD, ICP analyses). The copper active sites were then incorporated by impregnation route and the NH<sub>3</sub> standard SCR catalytic performances of both commercial and pre-made Cu-CHA catalysts were evaluated. The pre-made support and corresponding catalyst are denoted ‘‘H-SAPO-34’’ and ‘‘Cu-SAPO-34-IMP’’, respectively and were compared to the commercial ones, which are denoted as ‘H-SAPO-34-COM’’ and ‘Cu-SAPO-34-COM’’.

### III-2.1. Chemical analysis: ICP measurements

The chemical composition of both supports and corresponding catalysts was firstly measured by ICP analysis and is presented in Table. III-1. The commercial support contains traces and non-negligible amount of Mg, Na, Ni and Fe species, which are not presented in the case of pre-made support. These metals could typically come from the preparation process where for instance, the mechanical grinding step in order to latter obtain a particular granulometry could add non negligible amount of iron [288]. These metals can act divisively as active sites together with copper sites due to redox ability (Fe, Ni) [289,290], promoters (Mg) [291] or perturbators (Na) on SCR reactions [68,292], which could easily interfere with our active site configuration investigations.

Table III-1. Chemical composition of commercial and pre-made impregnated catalysts.

SAMPLE	Cu (wt%) <sup>a</sup>	Si (%wt) <sup>a</sup>	Al (%wt) <sup>a</sup>	P (%wt) <sup>a</sup>	Fe (%wt) <sup>b</sup>	Mg (%wt) <sup>b</sup>	Na (%wt) <sup>b</sup>	Ni (%wt) <sup>b</sup>	Si/Al <sup>c</sup>	(Si+P)/Al <sup>c</sup>
Cu-SAPO 34-IMP	1.1	2.5	16.7	15.6	0	0	0	0	0.14	0.96
H-SAPO 34	0	2.5	16.8	15.9	0	0	0	0	0.14	0.97
Cu-SAPO 34-COM	1.1	3.4	15.4	14.9	0.41	<300 ppm	<900 ppm	<90 ppm	0.21	1.05
H-SAPO 34-COM	<300 ppm	3.5	15.7	14.9	0.41	<300 ppm	<900 ppm	<90 ppm	0.21	1.03

<sup>a</sup> Amount determined by ICP measurements,

<sup>b</sup> Elemental traces obtained by scan analysis

<sup>c</sup> molar ratio

These results also showed that the H-SAPO-34-COM presented a higher Si amount and, as a consequence, a higher Si/Al molar ratio compared with the pre-made H-SAPO-34 support, which could be rise to a wider concentration of Brønsted acid sites [132,276]. Moreover, the (Si + P)/Al ratio superior to 1 in the case of commercial support, could indicates about the presence of undesirable Si-islands [293]. Indeed, such ratio typically represents the over implementation of Si elements in the structure regarding the Al proportion, where the adjacent substitution of P and Al by two Si more likely occurs through SM-3 substitution mechanism. It will be by the adjacent position of 4 Si element that the islands are finally

formed in the structure (Si(OSi)<sub>4</sub>). On the other hand, with a ratio below one, the P substitution better proceeds through SM-1 and SM-2, decreasing the probability to promptly form Si islands during the synthesis [131,294]. This higher amount of Si and the potential presence of Si-island in commercial support could consequently weakens the support stability during hydrothermal conditions [295] and gives difficulties to incorporate copper cations in exchanged positions, which are the main active sites for this NH<sub>3</sub> SCR reaction [296]. Indeed, both features are related to the Si concentration, taking account that the Si destabilize the overall electronic structure of the starting neutral AlPO arrangement during the hydrothermal synthesis, more Si substitutes P, more the chances to create charges deficit can occur (Si(OAl)<sub>4</sub>). A concentration of charge deficit which will impact the capacity to integrate counterbalancing cations within the structure [297,298]. However, the progressive side formation of Si islands (Si(nOAl)<sub>n=0-3</sub>) could be also improved during the synthesis in this case. Si island formation cannot generates acidic sites (-Si-O-Si-), decreasing the potential charges concentration in the structure comparing to the charged tetrahedral Si(OAl)<sub>4</sub> building units [127,131]. Thus, knowing that the copper counter ions are stabilized in the structure by these charges [125,214,299], a generated deficit will consequently decrease the copper incorporation possibilities in exchanged position [176,276]. Nevertheless, the Si/Al and (Si + P)/Al ratio of pre-made H-SAPO-34 support seem to be high enough to avoid the (Si(OSi)<sub>4</sub>) formation, providing the adequate acidity for displaying hydrothermal resistance and allowing cations incorporations.

Finally, 1.1 %wt. of copper was impregnated on each support through the same method. As expected, the incorporation of transition metal on both H-SAPO-34 supports through aqueous solution do not modify the chemical composition of the support: the Si/Al ratio is conserved and no desilication process can be suspected regarding the (Si+P)/Al ratio.

### III-2.2. Calcination step and Phases identifications: TGA and XRD measurements

The weight loss and template removal were verified by thermogravimetric analysis (TGA/DTG measurements), Figure III-1, in order to determine the calcination protocol. TGA analyses were performed on supports before calcination. Temperature at which derivative maximum is reached indicates the adequate calcination temperature. Indeed, the maximum derivative corresponds to the weight loss of template decomposition. More precisely, two weight loss regions are observed in Figure III-1. The first one in the range of 100-227°C is related to the desorption of chemically and physically adsorbed water molecules from the molecular sieve with a weight loss of 3% and the second one in the 346-525 °C temperature range, which represent the oxidative decomposition/calcination of the TEAOH template [300]. Therefore, the calcination temperature is selected at 550 °C to be sure that all organic compounds and template are entirely removed.



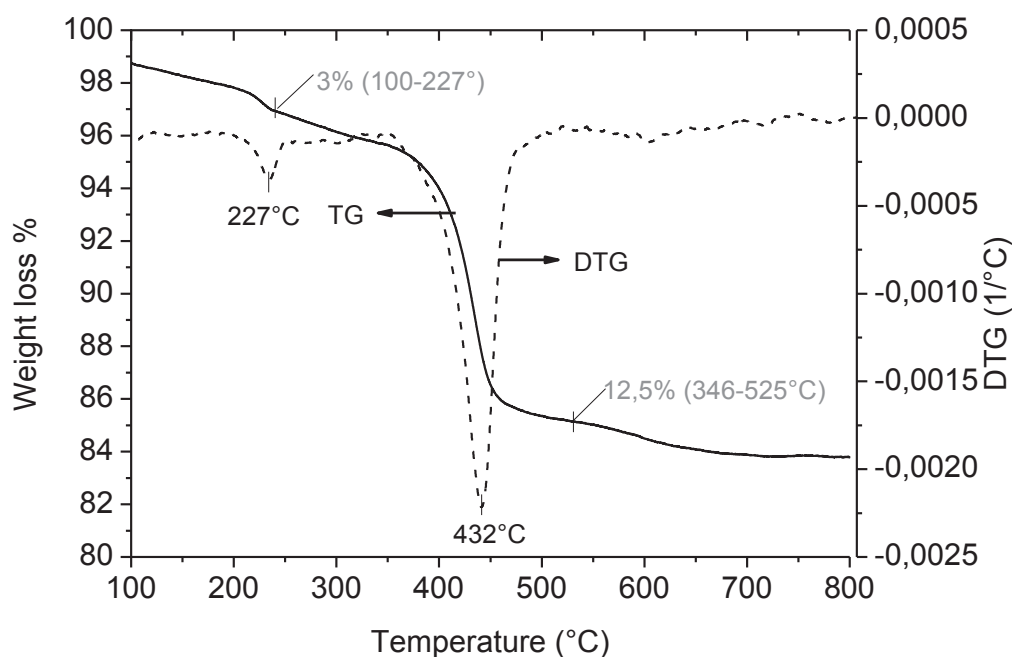


Figure III-1. TGA/DTG profiles of SAPO-34 (4.5L.h<sup>-1</sup> Total mass flow of synthetic air, 5°C/min ramp from 30°C to 800°C under 20 ml.min<sup>-1</sup>)

The crystal phase of pre-made support was identified and compared with that of the commercial SAPO-34 support in order to appreciate their relative crystalline structure and verify the efficiency of support preparation route. Figure III-2. displays the XRD patterns of the commercial and pre-made SAPO-34 support. Accordingly with the JCPDS phase identification data [301], both supports exhibited XRD characteristic peaks of the conventional SAPO-34 CHA-based zeolite reported in literature[274,283,302]. Moreover, no crystalline nor amorphous parasitic phases were detected. The corresponding XRD profiles associated to Cu-SAPO-34 catalysts are also reported in this Figure III-2. In both cases, the characteristic peaks at  $2\theta = 35, 29^\circ, 38$  and  $49^\circ$  related to copper cluster heterogeneously distributed at the catalyst surface are presented [256]. This observation corroborates that the impregnation method favours the formation of large surface cluster oxides and thus informs about the quality of copper incorporation in the zeolite support.

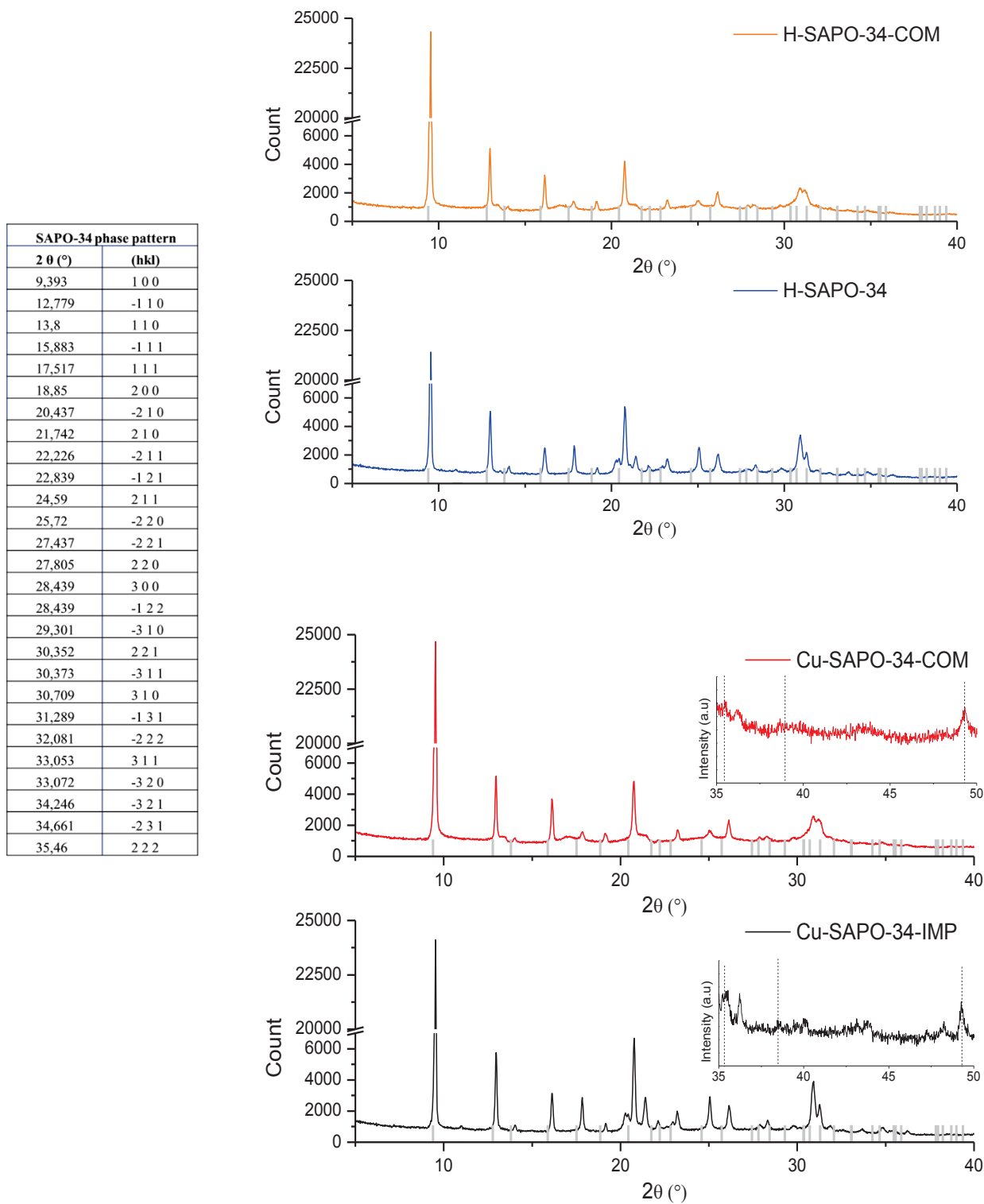


Figure III-2. XRD patterns of commercial (H-SAPO-34-COM) and pre-made (H-SAPO-34) CHA support and the corresponding impregnated catalysts (Cu-SAPO-34-COM and Cu-SAPO-34-IMP). CuO phase centered at  $2\theta = 35, 29^\circ, 38^\circ$  and  $49^\circ$  [JCPDS: PDF-04-007-0518]. The joint table displays the hkl  $2\theta$  positions of SAPO-34 pattern [JCPDS: PDF-00-047-0429] in light grey.

III-2.3. Supports and catalysts textural properties: N<sub>2</sub>-adsorption/desorption.

Moreover, the textural properties of microporous zeolite support were investigated prior and after the copper impregnation in order to observe any evolution of the microporous volume, specific surface area (SSA) and pores dimensions. These results are displayed Table III-2. The corresponding catalysts Cu-SAPO-34-COM and -IMP N<sub>2</sub> –adsorption/desorption isotherms are display in Figure III-3 and the one relative to raw support available in supplementary material Annexes Figure III-1.

Table III-2. N<sub>2</sub> adsorption and desorption analysis for pre-made H-SAPO-34, -COM support, Cu-SAPO-34-IMP and -Cu-SAPO-34-COM catalysts

	H-SAPO 34	Cu-SAPO 34-IMP	H-SAPO 34-COM	Cu-SAPO 34-COM
Specific Surface area (m <sup>2</sup> .g <sup>-1</sup> )	573	554	≥550 <sup>b</sup>	679
Micro (t-plot) Specific Surface area (m <sup>2</sup> .g <sup>-1</sup> )	535	501	-	647
Microporous volume (cm <sup>3</sup> .g <sup>-1</sup> )	0.20	0.20	≥0.27 <sup>b</sup>	0.26
Average pores size (nm) <sup>a</sup>	0.46	0.9	0.9	0.95

<sup>a</sup>Following the Horvath-Kawazoe model with cylinder pore geometry corrections of Saito-Foley [303]

<sup>b</sup> Manufacturer information

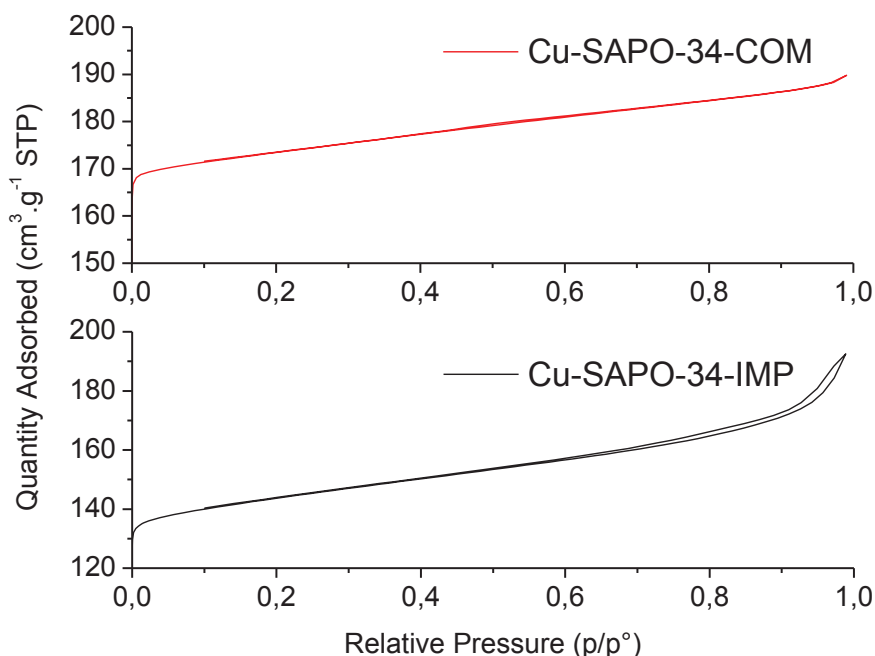


Figure III-3. N<sub>2</sub>-adsorption/desorption isotherms of Cu-SAPO-34-COM and -IMP catalysts.

As expected for micro-porous structure, the isotherms are recognized as type I following the Brunauer-Deming-Deming-Teller (BDDT) classification, characteristic of microporous material [304,305]. It is particularly observed with Cu-SAPO-34-IMP, a mixed hysteresis of types 3 and 4, which

could inform about the potential aggregates formation or capillary condensation of N<sub>2</sub> during the measurements [238,306,307]. Moreover, according to the measured SSA and microporous volume depicted Table III-2, all values are typical from CHA support, with SSAs ranging between 500 and 700 cm<sup>2</sup>.g<sup>-1</sup> [176,286,308], which a main part is attributed to the micropores (for H-SAPO-34 for instance : 535/573=93%).

Moreover, for both catalysts, the SSA was conserved after copper incorporation as displayed in Table III-2. No structure damage or pores blockage are observed after the functionalization method, which is of primary interest for the final active site availability and so catalyst performances. These results show that the preparation route seems to not promote the formation of large copper cluster within the porosity apertures. Furthermore, the pores sizes distributions of both catalysts are presented in Figure III-4 A and B. The pore diameters distribution of catalysts, which were obtained using the Horvath-Kawazoe (H-K) method, clearly shows the presence of a micropores structure. The pore sizes were centered at 0.46 nm for the pre-made support, which is close to the theoretical value of the CHA 6MR cages apertures (0.38 nm) [309], further shifted to 0.9 nm after impregnation protocol for Cu-SAPO-34-IMP. On the other hand, the commercial support presented a pore size distribution readily centered at 0.9 as after the impregnation process. This enlargement, in accordance with the slight loss of microporous SSA (30 m<sup>2</sup>.g<sup>-1</sup>), could be due to the surface deposition of copper clusters (of lower SSA), limiting the zeolite micropores access, but also to the blockage of smaller CHA membered cages. Note that the pores size distributions of both supports are available in Annexes Figure III-2.

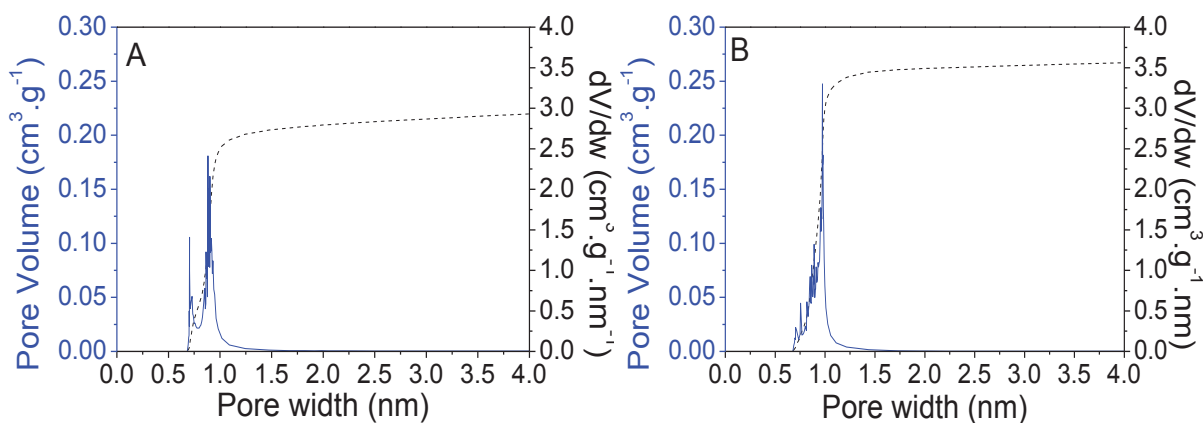


Figure III-4. Pore size distribution according with H-K model of Cu-SAPO-34-IMP (A) and Cu-SAPO-34-COM (B)

## III-2.4. Building unit construction: MAS NMR measurements

The bulk composition of zeolite materials and the building unit sequences were analyzed by MAS NMR measurements. Theoretically, the CHA material are constituted by a succession of tetrahedral Si(OAl)<sub>x</sub>, Al(OP)<sub>x</sub> (x=4) and linking building unit with x=3 [130,131]. Therefore, each deviation presents a valuable information about the structure modification or structural defaults. Figure III-5 (A) displays the <sup>28</sup>Si chemical shifts of pre-made and commercial support and corresponding catalysts, containing information about the Si substitution mechanism, which can take place during the synthesis, the Si migration after hydrothermal treatment and the possible Si-island formation. Note that the Si(OAl)<sub>x</sub> building unit with x=4, 3, 2, 1, 0 respectively provoke a chemical displacement at -89, -95, -99.6 and -110 ppm, respectively [128,221,310,311]. The different atomic displacements are listed Table III-3. Regarding the profiles corresponding to the commercial support and catalyst, a main peak corresponding to the Si(OAl)<sub>3</sub> groups can be observed. The signal intensity consequently decreases after copper impregnation due to the formation of Si(OAl)<sub>x</sub> (x=2,1) and Si-island Si(OSi)<sub>4</sub>. At lower displacement, Si-Si coordination were also found for both of them. These results agree with the previous assumption related to the initial presence of Si-islands in commercial support. This fact could be attributed to a non-optimized synthesis (high Si precursor loading during the synthesis or a long slurry aging) [282,284,312], and even to the possible hydrothermal treatment after synthesis process. Note that the present material is a commercial support whose synthesis protocol was not specified. The presence of Si-island, after the impregnation protocol on the commercial support, are also in accordance with previous assumptions, indicating the occurring of Si migration. The copper impregnation impact was also appreciable on Cu-SAPO-34-IMP, regarding the strong diminution of the sharp Si(OAl)<sub>x</sub> (x=4,3) peaks, which were associated to the well-structured CHA zeolite support. A diminution which can be also associated to the migration of Si atoms in different positions (Si(OAl)<sub>x</sub> (x=2,1,0)). Therefore, the <sup>28</sup>Si NMR analysis unfortunately confirmed that the Cu-SAPO-34-IMP catalyst also presents such structural defaults as Si-islands. As expected, the impregnation method seems to be not suitable for NH<sub>3</sub>-SCR catalyst synthesis. The impregnation preparation procedure seems not suitable for the conservation of hydrothermal resistance capacity of the catalyst, neither for the improvement of NH<sub>3</sub> storage capacity knowing that Si(OSi)<sub>4</sub> building units affect the support acidity by depriving the framework of isolated Si which constitutes a part of the SAPO-34 Brønsted acid sites [295].

Regarding the <sup>27</sup>Al MAS NMR spectra Figure III-5 (B), two main peaks are observed at 37 ppm and -15 ppm, which the preponderant, one centred at 37 ppm, is attributed to the main proportion of isolated Al as Al(O P or Si)<sub>4</sub>. A shoulder can be spotted at 12 ppm, indicating about the presence of pentacoordinated Al as (Al(OP)<sub>4</sub>(OH)<sub>2</sub>) in the bulk structure. The second main signal represents octahedrally coordinated Al with H<sub>2</sub>O, a structure hydration which could be associated to the hydrothermal synthesis of the pre-made support and the aqueous protocol for copper impregnation of commercial and pre-made supports. The phenomenon is reversible, where the complete dehydration of Al occurs around

1100°C, a calcination probably carried out on commercial support as regarding the lack of signal at -15 ppm.

Finally, concerning <sup>31</sup>P spectres, Figure III-5 (C), the spectres confirmed that the P atoms were mainly in coordinated position with Al through a P(OAl)<sub>4</sub> building unit (peak centred at -30 ppm for all materials), which is in agreement to the previous main Al(OP)<sub>4</sub> configuration observed in Figure III-5 (B). In the same way that for Al atoms, the catalyst hydration was observed through the spectra. A shoulder peak centred at -17 ppm, which could be associated to the P in coordination position with water molecules as a P(OAl)<sub>4</sub>(H<sub>2</sub>O) [313,314], was notably presented in the case of pre-made support and corresponding catalyst.

Table III-3: MAS NMR chemical displacement observed for SAPO-34 building units by <sup>28</sup>Si, <sup>27</sup>Al and <sup>31</sup>P elements investigation [128,221,310,311].

Element	Chemical shift (ppm)	Building unit represented
<sup>29</sup> Si	-110	Si(OSi) <sub>4</sub> (Si-island)
	-104,3	(Si (O Al) <sub>1</sub> )
	-99,6	Si(OSi) <sub>2</sub> (OAl) <sub>2</sub>
	-95	(Si (O Al) <sub>3</sub> )
	-89	(Si (O Al) <sub>4</sub> )
<sup>27</sup> Al	-15	Octahedrally coordinated Al with 3 H <sub>2</sub> O
	12	Pentacoordinated Al in bulk
	37	Al(O P orSi) <sub>4</sub>
<sup>31</sup> P	-30	P(OAl) <sub>4</sub>
	-26	P(OAl) <sub>4</sub>
	-17	P(OAl) <sub>4</sub> (H <sub>2</sub> O)

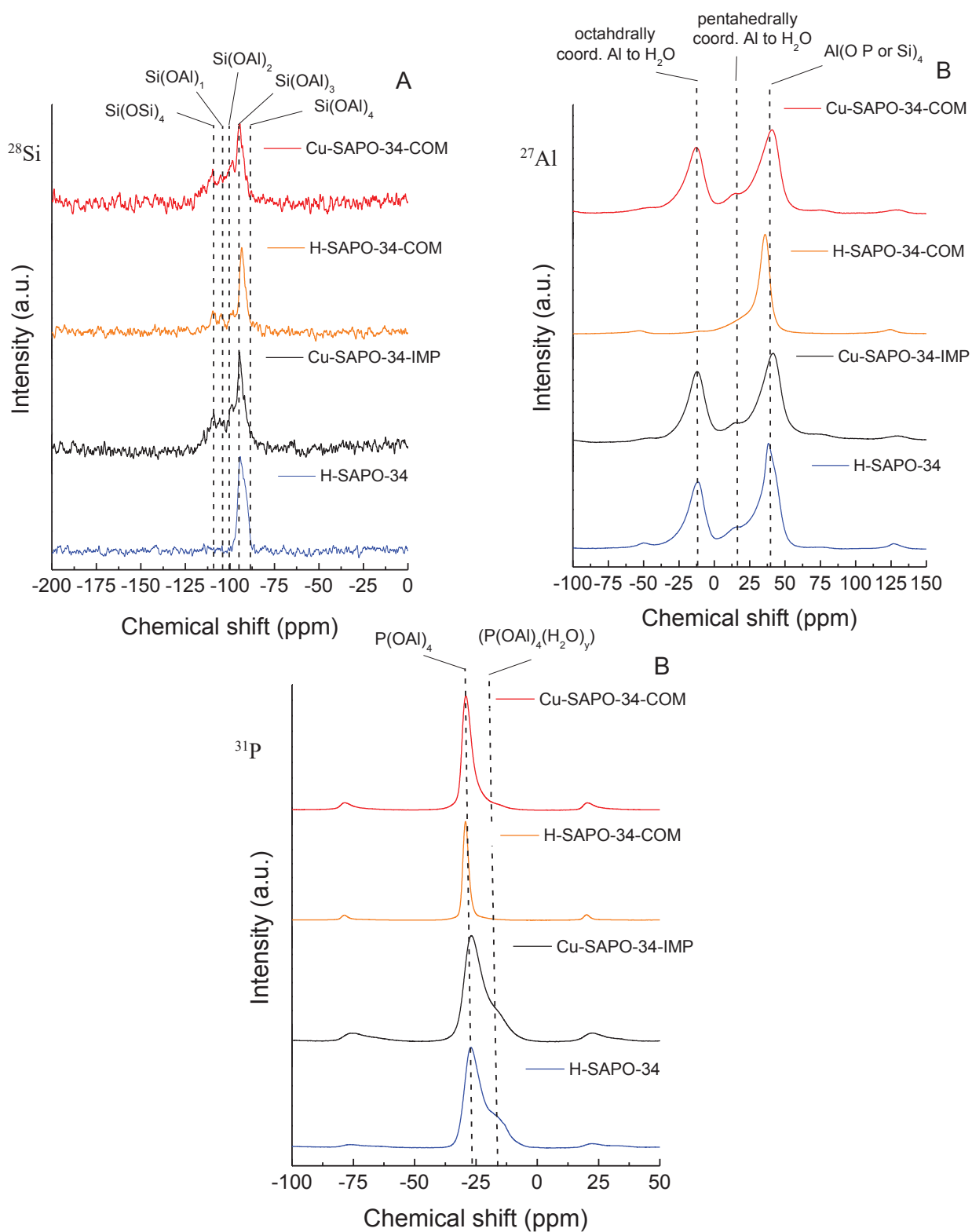


Figure III-5: Solid state MAS NMR spectra of (A) <sup>28</sup>Si, (B) <sup>27</sup>Al and (C) <sup>31</sup>P of pre-made H-SAPO-34 and commercial-COM supports and the corresponding Cu-SAPO-34-IMP, -COM catalysts.

III-2.5. Redox properties: H<sub>2</sub>-TPR measurements

H<sub>2</sub>-TPR measurements were carried out to obtain further information concerning the distribution and reducibility of copper species. As displayed Figure III-6, the broad peak ranging from 150°C to 500°C indicates the coexistence of multiple Cu species within each catalyst. From a qualitative point of view, the H<sub>2</sub>-TPR spectra was decomposed in three main reduction zones according to the literature [241,243,315]. The first one at low temperature between 160°C and 250°C corresponds to the reduction of the isolated Cu<sup>2+</sup> as  $Cu^{2+} + \frac{1}{2} H_2 \rightarrow Cu^+ + H^+$  [241,243,315], the second one between 250°C and 340°C represents the reduction of surface oxidized copper species as  $CuO + H_2 \rightarrow Cu^0 + H_2O$  [316]. Finally, at higher temperature, the most stable copper cations are reduced following the last step:  $Cu^+ + \frac{1}{2} H_2 \rightarrow Cu^0 + H^+$  [316–318]. Note that the profiles were deconvoluted for better representing the concerned area throughout the investigation.

Comparing the H<sub>2</sub>-TPR profiles for both catalysts, Cu-SAPO-34-IMP redox sites start to be reduced at lower temperature than that of the commercial one, between 150°C and 250°C. This observation could indicate about the proportion difference of isolated Cu<sup>2+</sup> cations present in both catalysts. A feature in accordance with the low copper loading employed during the functionalization processed here, condition which promotes the migration of Cu ions until cationic sites near the 6MR [319,320], but where less cations reached exchanged position in the case of the commercial catalyst, knowing that the support displayed strong proportion of neutral Si-islands.

A pronounced peak centered at 300°C can also be identified for both catalysts, as corresponding to the following reduction mechanism  $CuO + H_2 \rightarrow Cu^0 + H_2O$  and thus representing the main proportion of surface cluster sites. The total H<sub>2</sub> consumption is also in accordance with these observations, where concerning Cu-SAPO-34-COM, the catalyst consumes a close quantity of H<sub>2</sub> (170 μmol, determined by H<sub>2</sub> TPR) as its copper proportion (115 μmol, according to ICP measurements and the sample mass employed for H<sub>2</sub> TPR measurement). On the other hand, one gram of Cu-SAPO-34-IMP (containing 170 μmol of copper according with ICP) consume twice the quantity of H<sub>2</sub> (370 μmol). In that respect, the reduction steps accounting for the reduction of 2 H<sub>2</sub> could be depicted by both the consecutive reduction of Cu<sup>2+</sup> to Cu<sup>+</sup> (1/2 H<sub>2</sub>) and to Cu<sup>0</sup> (1/2 H<sub>2</sub>), and the reduction of surface CuO species in metallic copper (1 H<sub>2</sub>). These different mass balance were made assuming that the proportion of iron oxidized species will be reduced as higher temperature than 400°C for not impacting the copper reduction profiles between 150°C and 400°C, which is typically the case with Fe-CHA catalysts or mixed Cu/Fe zeolite catalysts [321–323].

However, the presence of cationic isolated species in Cu-SAPO-34-COM cannot be completely ruled out due to the observed high temperature peak which could be associated to the reduction of more stable Cu<sup>+</sup> species [316–318]. Indeed, both profiles showed a shoulder centred at 425°C, which could represent the reduction of these Cu<sup>+</sup> cations. In that respect, both catalysts display similar reducibility



capacity, where the proportion of isolated cations seems more important for Cu-SAPO-34-IMP catalyst than that of commercial Cu-SAPO-34-COM catalyst. Indeed, although some isolated species seem to be present in pre-made Cu-SAPO-34-IMP catalyst, the main reduction peak centred at 300°C remains the more representative of this catalyst, in agreement to large surface copper cluster identified by XRD measurements. Supplementary measurements are still required to confirm the presence of these highly active exchanged cations sites, which was pursued by DRIFT experiences.

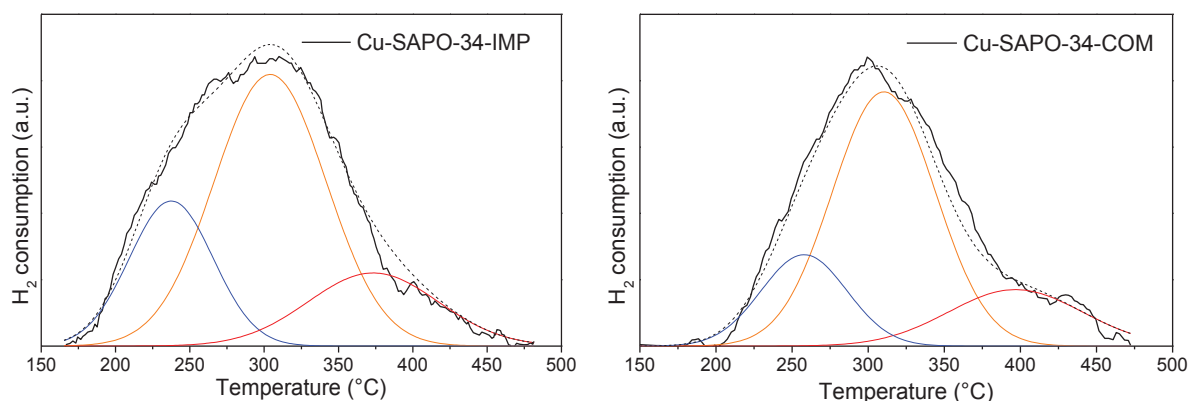


Figure III-6: H<sub>2</sub>-TPR profiles of Cu-SAPO-34-IMP and –COM catalysts with respective deconvoluted profiles. (Reduction feed: 2 vol.% H<sub>2</sub> in Ar, total flow of 40 ml.min<sup>-1</sup>, heating ramp from 30 °C to 500 °C with a heating rate of 10 °C/min)

### III-2.6. Surface sites investigation : Ex-situ DRIFT

Ex-situ DRIFT measurements of both catalysts were finally carried out in order to evaluate the different active sites and verify the previous assumptions. These ex-situ DRIFT measurements will allow to precise the copper positions inside the zeolite lattice [221,324]. As shown in Figure III-7, both catalysts display copper sites in, in some extent, inside the zeolite lattice, according to the slight vibrations detected at 891 and 844 cm<sup>-1</sup>. These vibrations could be associated to the copper cations interfering with T-O-T structure (as Si-O-Si or Si-OH-Al for type 1) in the former and type 2 perturbation in the latter [168,243]. Thus, the impregnation protocol seems to allow the introduction of some copper cations inside the zeolite support in exchange positions. No particular differences were spotted at lower wavelength, in the Brønsted acid sites area vibration (4000-3000 cm<sup>-1</sup>) [156]. Both catalysts showed quite similar absorbance profiles where external Si-OH species, P-OH and lattice Al-OH-Si are located at 3730 cm<sup>-1</sup>, 3671 cm<sup>-1</sup> and 3625 and 3600 cm<sup>-1</sup>, respectively [206,306,325,326]. Thus, the impregnation protocol described earlier seems to allow the introduction of some copper cations inside the zeolite support in exchange positions. In that respect, both catalysts display copper sites in at least two different configurations over the surface and, in some extent, inside the zeolite lattice. These findings would demonstrate the capacity of both synthesis routes to prepare comparable Cu-CHA catalyst with close active sites configuration, with a slightly less

promoted incorporation of cations in exchanged positions of the commercial support, which the Si configuration limit the process.

Therefore, the above characterization results show that the impregnation procedure allows the incorporation of copper cations on exchanged positions within the structure, but in some extent only, where the main copper sites remain surface copper clusters on both catalysts. Moreover, CHA building units were modified by the formation of so-called Si-island after the preparation protocol, implementing unnecessary defects, weakening the structure and the hydrothermal catalysts resistance. Nevertheless, the impregnation simplicity and ease of preparation, are strong arguments for considering its competitive interest from an industrial point of view, compared with ionically or solid-state exchange processes [162,238]. Thus, the catalytic performances of these catalysts were also evaluated in the following section, which could allow to better understand the role of different active sites implemented by impregnation.

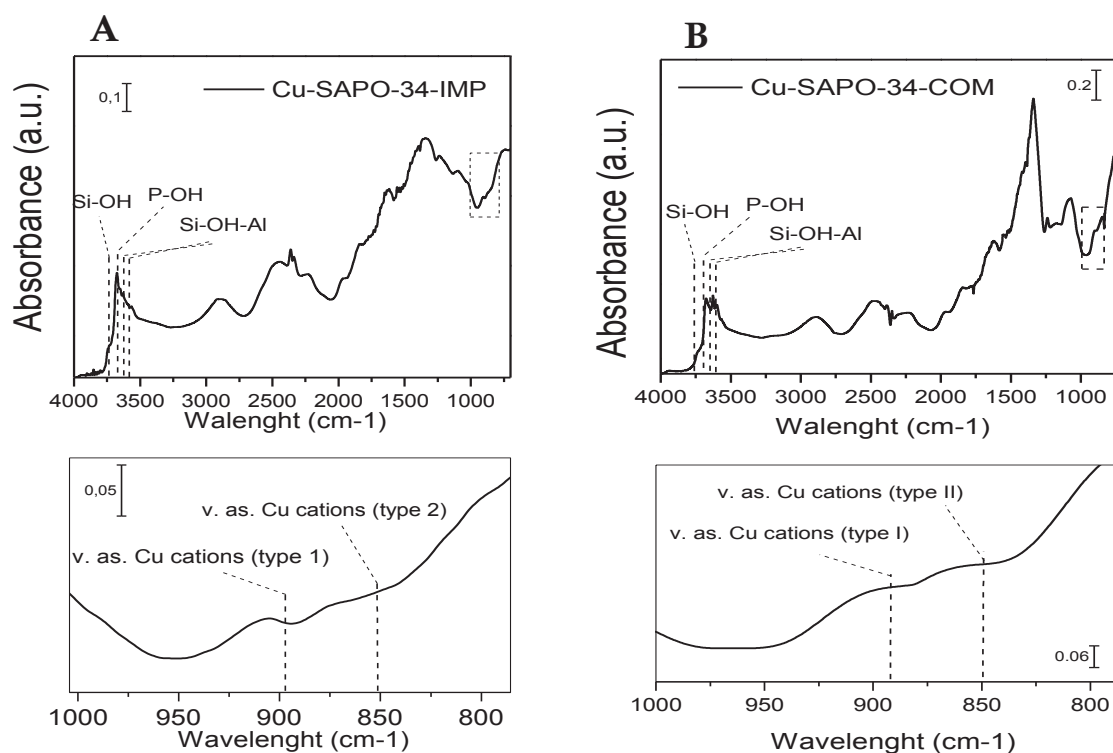


Figure III-7: Ex-Situ DRIFT profiles under He at room temperature for Cu-SAPO-34, -IMP (A) and Cu-SAPO-34-COM (B) catalysts after oxidative pretreatment:  $10 \text{ L.h}^{-1}$  during 30 min of 50/50  $\text{O}_2$  in He at  $500^\circ\text{C}$ . With an insert corresponding to the zoomed area profile between  $1000$  and  $800\text{cm}^{-1}$ .

### III-3. Catalytic performances of impregnated catalysts

Firstly, the possible catalytic activity for NH<sub>3</sub>-SCR reaction of the commercial support was evaluated, taking account the trace of Cu, Fe, Mg, Na and Ni presented in this support. The catalytic activity was evaluated in standard conditions of NH<sub>3</sub>-SCR reaction and the results are displayed Figure III-8 for both supports.

These catalytic results show, as expected, that these metal traces are active for NH<sub>3</sub>-SCR reaction. Thus, the commercial support promotes different reactions as the NO oxidation in NO<sub>2</sub> ( $\text{NO} + \frac{1}{2} \text{O}_2 \rightarrow \text{NO}_2$ ) until 300°C and the NH<sub>3</sub> oxidation in N<sub>2</sub> ( $2 \text{NH}_3 + 1.5 \text{O}_2 \rightarrow \text{N}_2 + 3 \text{H}_2\text{O}$ ) in a large extent, reaching 100% NH<sub>3</sub> conversion readily at 400°C. Regarding the low consumption of NO and the lack of SCR process on the whole temperature window, these results allow to conclude that the exchanged Cu<sup>2+</sup> or Fe<sup>3+</sup> were not the active sites of this support [327–329]. Nevertheless, the observed NH<sub>3</sub> oxidation starting at 250°C could mean that the commercial H-SAPO-34-COM support is constituted by oligomers Fe active species and/or Fe<sub>2</sub>O<sub>3</sub> clusters, which are responsible of this undesirable oxidation reaction, according to the literature [327]. In addition, a low concentration of extra lattice dimeric Fe sites could be also suspected regarding the NO oxidation activity into NO<sub>2</sub>.

On the contrary, any conversion was observed with pre-made H-SAPO-34 support. Moreover, the desorption of stored NH<sub>3</sub> on pre-made support Brønsted acid sites was observed at high temperature, according to the observed negative NH<sub>3</sub> concentration, Figure III-8 (A). The NH<sub>3</sub> oxidation into N<sub>2</sub> was additionally observed at high temperature, coming from the gas phase reactions [330].

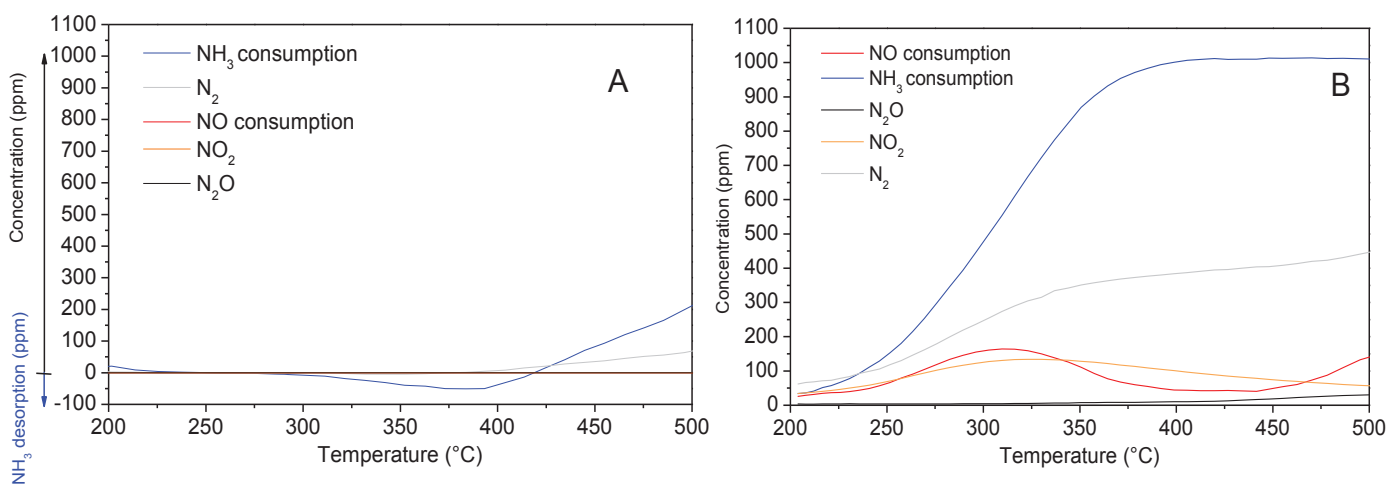


Figure III-8: NH<sub>3</sub>, NO, N<sub>2</sub>, NO<sub>2</sub> and N<sub>2</sub>O concentration evolutions during NH<sub>3</sub>-SCR reaction of H-SAPO-34 (A) and –COM (B) supports. Catalyst weight: 35mg; inlet gas composition: 1000 ppm NH<sub>3</sub>; 1000 ppm NO<sub>x</sub>, 80000 ppm (80000 ppm (8%) O<sub>2</sub>; 40000 ppm (4%) H<sub>2</sub>O, balanced He; total flow= 10 L/h; GHSV=142.000h<sup>-1</sup>

Finally, the catalytic performances of Cu-SAPO-34-IMP and commercial Cu-SAPO-34-COM catalysts were evaluated in standard NH<sub>3</sub>-SCR conditions, Figure III-9 (A and B). Both catalysts presented almost identical SCR performances profiles in term of conversion and selectivity, which corroborate the close active phase configuration implemented on both catalysts, in which the role of copper species seems to be more pronounced than that of the iron sites presented on commercial catalyst regarding the differences between Figure III-8 and 9. This close active sites configuration can be even more appreciated regarding the similar reaction regime occurring between 200°C-250°C and 300°C-450°C. Indeed, if the exchanged cations activity will be particularly observable at low temperature proceeding NH<sub>3</sub>-SCR ( $4 \text{ NH}_3 + 4 \text{ NO} \rightarrow 4 \text{ N}_2 + 6 \text{ H}_2\text{O}$ ) [158,331], species responsible for NH<sub>3</sub> oxidation reaction (such as  $2 \text{ NH}_3 + 1.5 \text{ O}_2 \rightarrow \text{N}_2 + 3 \text{ H}_2\text{O}$ ) are also clearly noticed since the NH<sub>3</sub> over consumption is visible on the whole temperature window Figure III-9 (A and B). These similar profiles give an idea about the redox properties of the different cations observed by H<sub>2</sub>-TPR measurements, which don't have a significant influence on NH<sub>3</sub>-SCR catalytic performances. These observations also indicate about the relevant reproducibility of the impregnation method for incorporating similar active sites nature.

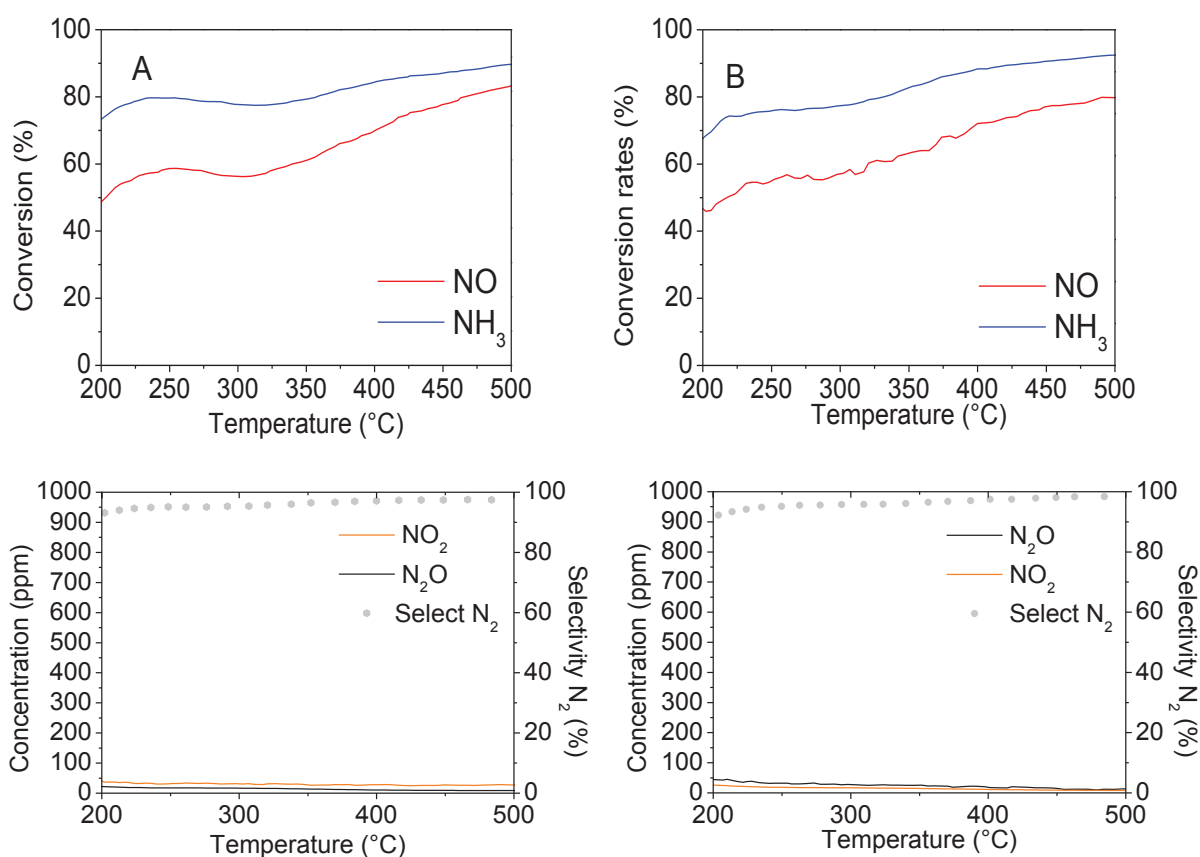
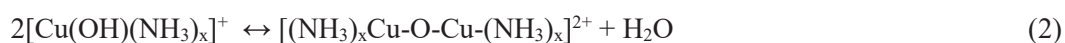
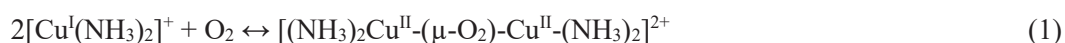


Figure III-9: NO and NH<sub>3</sub> conversion rates in SCR conditions with their respective N<sub>2</sub> selectivity for Cu-SAPO-34-IMP (A,C) and -COM (B,D) catalysts. Catalyst weight: 35mg; inlet gas composition: 1000 ppm NH<sub>3</sub>; 1000 ppm NO<sub>x</sub>, 80000 ppm (8%) O<sub>2</sub>; 40000 (4%) H<sub>2</sub>O, balanced He; total flow= 10 L/h; GHSV=142.000h<sup>-1</sup>

The constated strong oxidation behavior of both catalysts was further investigated, Figure III-10 (A and B), with a reactional flowing mixture composed of 1000 ppm NH<sub>3</sub>, 80000 ppm O<sub>2</sub>, and 40000 ppm of water and He as a gas balance. As expected, both profiles are again almost identical for both catalysts, emphasizing the identical active site configuration on both IMP and COM catalysts allowing the complete NH<sub>3</sub> oxidation in N<sub>2</sub> on identical temperature ranges. As displayed through the NH<sub>3</sub> consumption profiles, two different activation regimes can be spotted. The first one occurs between 200°C and 400°C, allowing a low NH<sub>3</sub> conversion (20%) in N<sub>2</sub> according to following oxidation reaction:  $2 \text{NH}_3 + 1.5 \text{O}_2 \rightarrow \text{N}_2 + 3 \text{H}_2\text{O}$ . A behavior also characterized during NH<sub>3</sub>-SCR experiments Figure III-9, where the low temperature NH<sub>3</sub> oxidation was observed on a similar temperature window. Above 400°C, the second reaction regime takes place, where the NH<sub>3</sub> conversion increases, reaching 80% at 500°C. A modification which could indicate the participation of different copper active sites and additional reactions as Cu cation monomers [332,333] and NH<sub>3</sub> oxidation in gas phase (See Figure V-2). Indeed, these observations are in accordance with the active sites proposition formation made by Beale et al. [333] during its development on Gao et al. results [158], where at low temperature the main active species for NH<sub>3</sub> oxidation are copper dimers formed through monomer coupling steps (1) and dehydration as (2):



An active site formation enlighten by the invariant NH<sub>3</sub> oxidation step between 200°C and 400°C, where the presence of excess of water allow an improved cation mobility within the lattice of the suspected heterogeneously distributed copper species in exchanged position, as the impregnation method did not allow such control. The dimerization will be easier for close packed exchanged cations than for homogeneously distributed species, where higher mobility will be required. A speculated cation configuration within the impregnated catalysts which could be in accordance with this mechanism and explain such important NH<sub>3</sub> oxidation behaviour at low temperature [332]. Still, the direct observation of such reactive species is difficult, and no spectroscopic method are sufficiently sensitive to provide further information on this mechanism today. The reactant evolutions remain the more accurate investigation possible for such active site modification.

At elevated temperature, the dimers become unstable and may split in Cu monomer through the reversible reactions (1) and (2), representing a different active site for the NH<sub>3</sub> oxidation, consequently displaying the reaction regime rupture at 400°C. Moreover, the surface clusters oxidation activity can also be assumed, regarding its important proportion compared to exchanged species [57]. Indeed, these actives sites typically oxide NH<sub>3</sub> in NO [174,286] according to:  $4 \text{NH}_3 + 5 \text{O}_2 \rightarrow 4 \text{NO} + 6 \text{H}_2\text{O}$ . However, only a slight proportion of NO was detected, depicting the active site selectivity toward N<sub>2</sub>. Indeed, as investigated by Yu et al. [174], it could indicate that the produced NO is readily consumed by SCR reaction in this temperature interval, a twostep reaction for N<sub>2</sub> formation in accordance with the characterized surface site

and the presence of active exchanged cations in both catalysts for proceeding to the SCR reaction at elevated temperature. A NO formation which will be clearly experienced later in the study with catalyst initially displaying as unique active redox site, surface copper clusters.

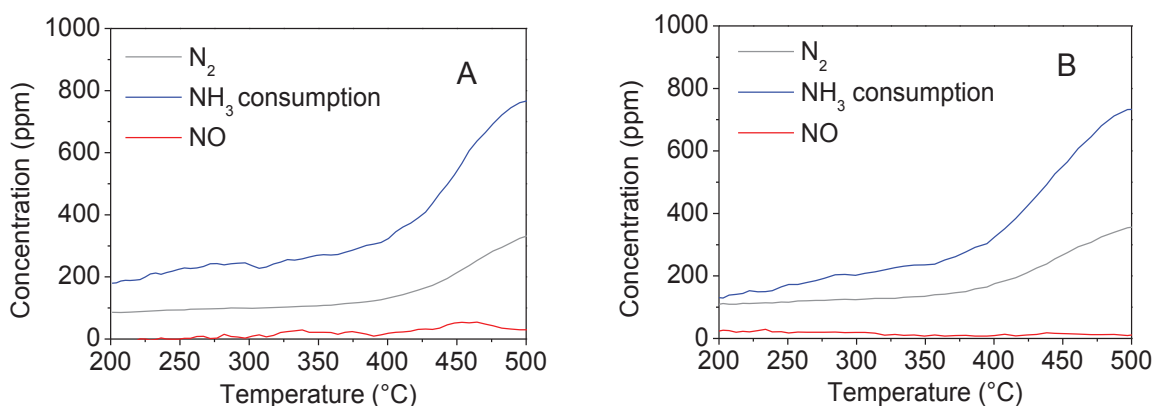


Figure III-10: NH<sub>3</sub> consumption and N<sub>2</sub>, NO concentration in NH<sub>3</sub> oxidation for Cu-SAPO-34-IMP (A) and -COM (B) catalysts. Catalyst weight: 35mg; inlet gas composition: 1000 ppm NH<sub>3</sub>; 80000 ppm (8%) O<sub>2</sub>; 40000 ppm (4%) H<sub>2</sub>O, balanced He; total flow= 10 L/h; GHSV=142.000h<sup>-1</sup>

An additional catalytic test was finally performed in NO oxidation condition, with 1000 ppm NO, 80000 ppm O<sub>2</sub>, and 40000 ppm of water in He, Figure III-11 (A and B). As expected, these catalytic results show that any of both catalysts are not active for NO oxidation. Indeed, as such active sites were characterized in literature to be represented by oligomeric form of mobile exchanged cations activating neighbor oxygen for the NO<sub>2</sub> production [334], species which seems to be absent on both catalysts and different from the dimers active centers evidenced during NH<sub>3</sub> oxidation measurements.

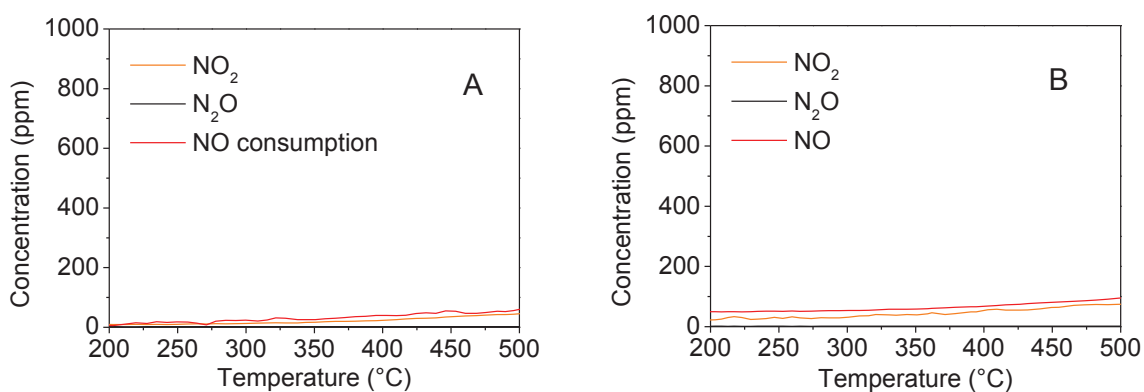


Figure III-11: NO consumption and NO<sub>2</sub>, N<sub>2</sub>O concentration in NO oxidation conditions Cu-SAPO-34-IMP (A) and -COM (B) catalysts. Catalyst weight: 35mg; inlet gas composition: 1000 ppm NO; 80000 ppm (8%) O<sub>2</sub>; 3% H<sub>2</sub>O, balanced He; total flow= 10 L/h; GHSV=142.000h<sup>-1</sup>

#### III-4. Conclusion

In the aim to develop a state of the art of Cu-SAPO-34 catalyst, two CHA-zeolite support were firstly studied, a commercial support and a pre-made one synthesized by hydrothermal preparation method. First, the different physico-chemical and textural characterizations performed on both raw supports H-SAPO-34 allow to verify the laboratory protocol suitability for the CHA zeolite synthesis according with the defined requirements previously enounced. After this verification, these supports were subsequently impregnated with copper by classical impregnation preparation method. Both supports and catalysts were finely characterized by different techniques and tested in standard NH<sub>3</sub>-SCR reaction in order to better understand the relationship between physico-chemical, structural and catalytic properties. Although the commercial and pre-made supports presented some chemical, physico-chemical differences (such as chemical composition, porosity, building unit configurations, ...), the attention was notably focalized on copper active sites configuration, which was expected the most important parameter for NH<sub>3</sub>-SCR catalytic activity. In that respect, both impregnated catalysts, commercial and pre-made Cu-SAPO-34, showed several copper active site configurations with low density of exchanged cations and more pronounced density of surface sites. Prior to their test performances, the NH<sub>3</sub> SCR activity of raw commercial support was investigated for observing the impact of the impurities during STD SCR operating condition. Consequently, a strong NH<sub>3</sub>oxidation activity was observed and attributed to the metal traces (notably iron species) contained in this support. The standard NH<sub>3</sub>-SCR catalytic tests performed on both Cu-SAPO-34 catalysts also showed the participation of above-mentioned exchanged species, with about 50% of SCR conversion at low temperature for both. However, several active sites were implemented through impregnation protocol. It resulted in an insufficient activity at low temperature for SCR catalysts with an important NH<sub>3</sub>oxidation process. A low temperature DeNO<sub>x</sub> activity, which is the key feature for these kind of post-treatment catalytic systems (notably under cold-start conditions) was observed. Therefore, the improvement of NO<sub>x</sub> efficiency, notably at low temperature, the improvement of hydrothermal stability (expected decreased by the presence of Si-island) of Cu-loaded CHA zeolite and the search for a reference catalyst for the development of a kinetic model remains a great challenge. For this purpose, in the next chapter, the active site configuration differences of two Cu-loaded CHA-zeolite catalysts synthesized by one-pot hydrothermal and ionic exchange preparation methods were investigated and put in perspective with their respective NH<sub>3</sub> SCR performances.

IV





# CHAPTER IV

## IDENTIFICATION OF REFERENCE CATALYST: ACTIVE SITE CONFIGURATION IMPACTS ON SCR PERFORMANCES

### IV-1. Introduction

Among the different active sites present on Cu-SAPO-34 catalysts, the Lewis acid sites formed by incorporated copper species are considered as the most efficient when they are located within the lattice framework in ionic exchanged positions near 6MR openings [214,335]. Usually, the most conventional method for the incorporation of cations inside CHA structure zeolites is the aqueous ionic exchange method, compared to other processes as impregnation or solid-state ionic exchange (SSIE). Still, most of Cu-SAPO-34 catalysts contain a combination of all the suggested species as isolated  $\text{Cu}^{2+}$  and  $\text{Cu}^+$  cations, but also  $[\text{Cu-O-Cu}]^{2+}$  dimers,  $[\text{Cu-OH}]^+$  species and other  $\text{CuO}_x$  clusters [298,336,337] the different proportions of which will greatly depend on the selected preparation method. Moreover, the wide literature reporting the nature of these copper active sites during  $\text{NH}_3$  SCR and the different occurring mechanisms on them is still under debates [163,219,227,333,338,339]. For more convenience, the following Table IV-1 listed the different active sites mentioned during this study which can be part of support and Cu-SAPO-34 catalysts.

Despite all, the usual metal incorporation techniques as impregnation, one pot synthesis or ionic exchange protocol, usually place copper species in both positions, on the surface in oxide cluster configuration and/or inside the zeolite lattice. Thus, surface copper species can easily represent a non-negligible fraction of the total metal amount. Despite this, their roles played in SCR reactions are less understood than the  $\text{Cu}^{2+}$  exchanged sites and remain controversial [208,340]. It is generally accepted that CuO surface clusters combined with exchanged cations are more active for catalysing nonselective  $\text{NH}_3$  oxidation than for SCR reactions, which negatively affect the  $\text{N}_2$  selectivity during  $\text{NO}_x$  reduction and this without particular site configuration distinction [173,174]. In order to optimize the SCR performance and stability of Cu-SAPO-34 catalysts for  $\text{NH}_3$  SCR, it is of great interest to control the oxidation state and structure of those widespread active sites. By controlling the synthesis method, two distinct catalysts presenting distinct redox site configurations were confronted for active sites investigations, where catalytic performances obtained thanks to the one pot catalyst were compared with an ionically exchanged catalyst.

Table IV-1. Active sites denomination possibly encountered within Cu-SAPO-34 catalysts with corresponding scheme. [128,137,298,336,337]

Denomination	Species example	Relative position	
Weak <sup>a</sup> Brønsted acid sites	T-OH (T = Si, Al or P)	External (support) (S1)	
Strong <sup>a</sup> Brønsted acid sites	T-OH-T (ex : Si-OH-Al)	Internal (support) (S2 and S2a for the strongest)	
Weak <sup>a</sup> Lewis acid sites	Nonframework Al / Copper species	External (S7) / (S8)	
Strong Lewis acid sites: Exchanged copper cations	ZCu <sup>2+</sup> , ZCu <sup>+</sup>	Internal (6MR / 8MR) (S3/S4)	
Nano/Micro copper oxide surface cluster	ZCuO <sub>x</sub> (x≤1)	External (support surface) (S5/S6)	

<sup>1</sup> from the point of view of NH<sub>3</sub> adsorption strength through investigated temperature [341–344]

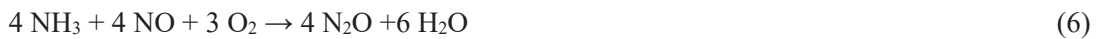
In the present study, the catalytic role and behaviour of different copper cluster configurations during NH<sub>3</sub> SCR, NO and NH<sub>3</sub> oxidation reactions will be studied in detail. For this purpose, two preparation methods (one-pot hydrothermal and ionic exchange) were performed for the incorporation of two specific groups of redox sites. The physico-chemical and surface properties were characterized by different techniques, such as XRD, ICP, N<sub>2</sub> ads/des, HR-TEM, XPS, NMR, ex-situ/in-situ DRIFT (NH<sub>3</sub>, CO), NH<sub>3</sub> TPD and H<sub>2</sub> TPR, in order to evaluate the impact of copper incorporation method on redox active sites, and, as a consequence, to better understand the mechanism responsible of the obtained NH<sub>3</sub> SCR performances. In that respect, and regarding the difficulties to selectively incorporate only exchanged active phases, the study seeks to further improve the role of surface species in DeNO<sub>x</sub> process and their control.

#### IV-2. Catalysts synthesis and experimental approaches

Two different Cu-SAPO-34 catalysts were prepared with a similar copper amount following distinct synthesis routes: by one-pot hydrothermal method, which will be denoted “Cu-SAPO-34-HT” and a second one by conventional ionic exchange, denoted “Cu-SAPO-34-IE” according to our method described in Chapter II. Both zeolite supports were formed with a targeted theoretical molar gel composition of 1SiO<sub>2</sub>: 6.7 Al<sub>2</sub>O<sub>3</sub>: 6.2 P<sub>2</sub>O<sub>5</sub>: 161.3 H<sub>2</sub>O and 7.7 of TEAOH (35 wt% (C<sub>2</sub>H<sub>5</sub>)<sub>4</sub>N(OH); CAS 77-98-5).

In order to fully understand the impact of the different preparation methods on the active site configurations and explain the different catalytic behaviours, four approaches were followed. The first one consists in characterizing both support and catalysts physico-chemical properties and surface morphology of copper sites through XRD, ICP, N<sub>2</sub> ads/des, HR-TEM, XPS and H<sub>2</sub> TPR measurements. Then, the Brønsted acid sites environment of catalysts were studied to further considerations of the Brønsted and Lewis sites interactions by MAS NMR and ex-situ DRIFT analysis. The third approach consisted in analysing different probe molecules (NO, NH<sub>3</sub> and CO) interactions with the catalyst’s active sites, followed by TPD and in situ DRIFT experiments, in order to characterize the active sites behaviours as a function of the temperature. Finally, specific investigations on redox active sites following different catalytic performance tests were conducted in order to validate the observations and hypothesis made on both catalysts and further understand their particularity.

Corresponding to studied Cu-SAPO-34 catalysts and above conditions, the possible and considered global reactions were respectively the STD SCR, NH<sub>3</sub> and NO oxidation, N<sub>2</sub>O formation and Fast SCR which the stoichiometries are shown below:



NH<sub>3</sub>, NO conversion and N<sub>2</sub> selectivity were defined as follows:

$$C_{\text{NH}_3} = \frac{[\text{NH}_3]^{in} - [\text{NH}_3]^{out}}{[\text{NH}_3]^{in}} \times 100 \quad (7)$$

$$C_{\text{NO}} = \frac{[\text{NO}]^{in} - [\text{NO}_3]^{out}}{[\text{NO}_3]^{in}} \times 100 \quad (8)$$

Where,  $C_A$  is the conversions of specie A,  $[A]^{in}$  and  $[A]^{out}$  the concentrations of specie A (ppm) in the inlet and outlet respectively.

$$selectivity_{N_2} = \left(1 - \frac{[NO_2]^{out} + 2 \times [N_2O]^{out}}{[NO_x]^{in} + [NH_3]^{in} - [NO_x]^{out} - [NH_3]^{out}} \times 100\right) \quad (9)$$

### IV-3. Physico-chemical and redox catalysts characterizations.

#### IV-3.1. Chemical and textural properties by ICP and $N_2$ adsorption/desorption measurements

Table IV-2 shows the chemical compositions of synthesized catalysts, which evidenced the close elemental composition between the SAPO-34 supports (HT and IE catalysts) with similar copper content (around 1.5%wt.) and close (Si+P)/Al molar ratio (~0.95). Moreover, the final Si/Al molar ratio Table IV-2 is also in good accordance with the theoretical one where a ratio of 0.15 was targeted. These results also suggest, regarding the close support chemical composition between the H-SAPO-34 support and the IE catalyst, that the incorporation method by ionic exchange had no important impact on the elemental composition of final catalyst and keep the initial composition of the support. This observation could be corroborated with the theoretical and experimental (measured by OES-ICP) compositions. Indeed, by considering a dehydrated SAPO-34 unit cell formed with TEAOH as templating agent, three charges would be created by hexagonal unit cell [137,345], which will give rise to a theoretical unit cell of  $H_3Si_3Al_{18}P_{15}O_{72}$  (36T, 72O) [256]. This theoretical composition was very close to the estimated compositions obtained through OES ICP results Table IV-2 with  $H_3Si_{2,6}Al_{18,3}P_{15,1}O_{72}$ ,  $H_3Si_{2,3}Al_{18,2}P_{15,5}O_{72}$  and  $H_3Si_{2,7}Al_{18,5}P_{14,8}O_{72}$  corresponding to raw H-SAPO-34 support, IE and HT catalysts, respectively. Moreover, if the catalysts and support SSA assigned in Table IV-2 are typical values encountered for chabazite zeolites [174,286], similar microporous volume was also observed between raw support and catalysts, which could mean that the microporous framework is not modified after copper incorporation for both methods. Isotherms and pore size distribution of Cu-SAPO-34-IE and -HT are available in supplementary material Annexes IV-1 and 2.

Table IV-2. Elemental composition by OES ICP of the Cu-SAPO-34 –IE, HT catalysts and H-SAPO-34 with adsorption/desorption nitrogen analysis.

	Cu <sup>a</sup> (wt%)	Si <sup>a</sup> (%wt)	Al <sup>a</sup> (%wt)	P <sup>a</sup> (%wt)	Si/Al (molar ratio)	(Si+P)/Al (molar ratio)	SSA <sup>b</sup> (m <sup>2</sup> .g <sup>-1</sup> )	Microporous volume <sup>b</sup> (cm <sup>3</sup> .g <sup>-1</sup> )
<b>H-SAPO-34</b>	0	2.5	17	16	0.14	0.96	573	0.20
<b>Cu-SAPO 34-IE</b>	1.5	2.7	21	20	0.13	0.96	577	0.20
<b>Cu-SAPO 34-HT</b>	1.2	3.0	20	18	0.15	0.94	590	0.17

<sup>a</sup> Amount determined by ICP measurements,

<sup>b</sup> Specific surface area (SSA) and total microporous volume determined by nitrogen adsorption/desorption experiments

## IV-3.2. Structure and phase identification by XRD and HR-TEM.

## IV-3.2.1. XRD

Figure IV-1. depicts the XRD patterns of H-SAPO-34 zeolite, Cu-SAPO-34 -IE and Cu-SAPO-34-HT catalysts. All support and catalysts presented exhibited XRD characteristic peaks at  $2\theta = 9.5, 12.9, 16.3, 17.7, 21.4, 24.9, 25.9, 30.6$  and  $31^\circ$  in good agreement with the patterns of SAPO-34 CHA-based zeolite reported in literature (PDF-00-047-0429) [346,347]. These results show that the chabazite zeolite structure was maintained after the copper introduction for both preparation methods. XRD diffractograms can also provide information about the presence of copper clusters at the surface, if they are large enough to be detected by XRD, regarding the characteristic peaks of CuO phase centred at  $2\theta = 35,29^\circ$  and  $38,49^\circ$  (PDF-04-007-0518) [256]. As expected, these signature peaks associated to CuO phase were observed with the Cu-SAPO-34-HT catalyst, which indicates the presence of relatively large surface clusters and homogeneously distributed regarding the corresponding low peak intensities. By comparison, no signal from the CuO phase have been detected for the ionically exchanged catalyst, informing on the absence or at least the presence of small sized and well dispersed surface copper clusters [241].

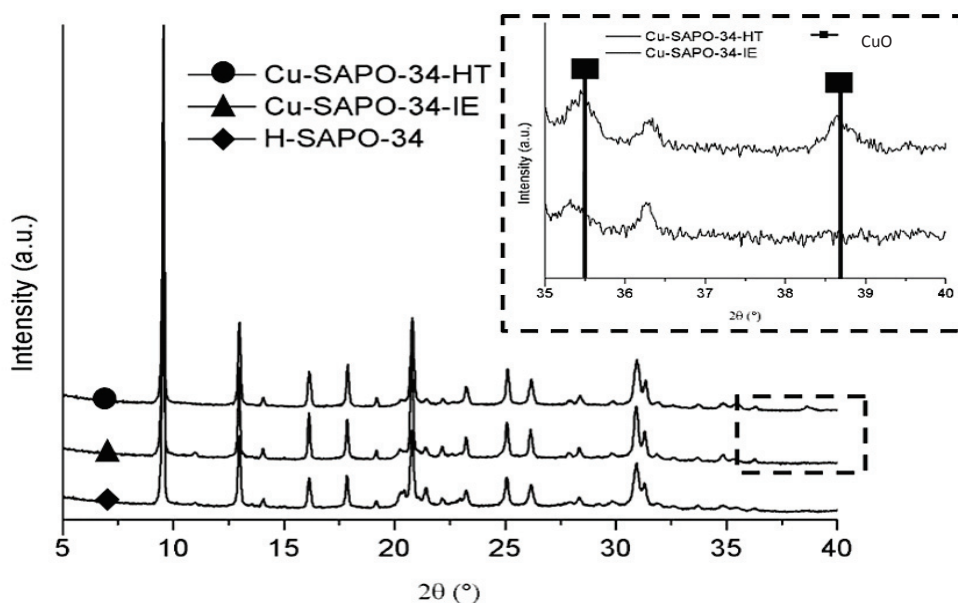


Figure IV-1. XRD patterns of H-SAPO-34, Cu-SAPO 34-IE and -HT catalysts with the corresponding zoom at  $2\theta = 35^\circ$  and  $40^\circ$  (CuO phase identification area).

## IV-3.2.2. HR-TEM

Additionally, the high resolution TEM images provide information about the surface composition, metal dispersion and particle size distribution of copper clusters Figure IV-2. Here, the impact of the metal incorporation method was clearly visible.

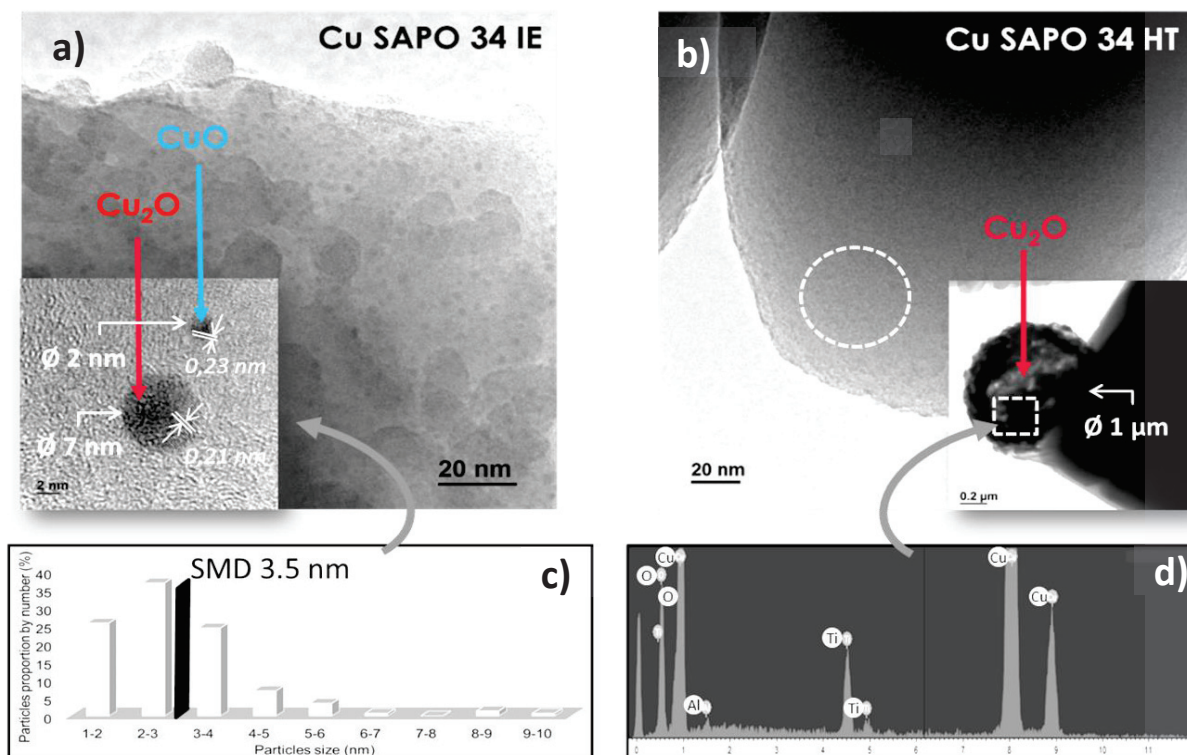


Figure IV-2. HR-TEM micrographs of (a) Cu-SAPO-34-IE and (b) –HT catalysts with corresponding particles size distribution of the observed (c) Cu-SAPO-34-IE clusters and (d) EDX scan of the Cu-SAPO-34-HT micro cluster.

According to micrograph displayed Figure IV-2, the catalyst synthesized by one-pot hydrothermal method, Cu-SAPO-34-HT, presented large copper oxide clusters ( $\text{Cu}_2\text{O}$ ) as shown by the EDX point-scanning measurements (within white dotted square in Cu-SAPO-34-HT Figure IV-2 (d)), with an average particles size about  $\approx 1\ \mu\text{m}$ . Moreover, the support surface of Cu-SAPO-34-HT did not display particular presence of copper through EDX scans (not shown here) observation (inside white dotted circle in Cu-SAPO-34-HT Figure IV-2 (b)), supporting the main copper configuration in large cluster form. On the contrary, well dispersed nano-sized copper clusters were observed for the catalyst synthesized by ionic exchange method, as visible in Figure IV-2 (a). Considering this figure, some copper clusters, with a lattice fringe of 0.23 and 0.21 nm, were identified in Cu-SAPO-34-IE catalyst Figure IV-2 (a) by their characteristics lattice interplanar d-space values, corresponding to the (200) crystal plane of CuO and (111) crystal plane of cuprite  $\text{Cu}_2\text{O}$ , respectively [301,348,349]. This catalyst presented a Sauter mean diameter (SMD) of 3.5 nm, which was estimated by counting around 300 particles on the TEM images. The corresponding particles size distribution of surface copper cluster for Cu-SAPO-34-IE catalyst is represented in Figure IV-2 (c).

### IV-3.3. Active sites environmental framework determination by MAS NMR and ex-situ DRIFTS experiments.

#### IV-3.3.1. MAS NMR

MAS NMR semi-quantitative technique was employed to spotlight and explain the chemical bulk architecture of Cu-SAPO-34-IE, -HT catalysts and H-SAPO-34 support. Figure IV-3 (a) presents the  $^{29}\text{Si}$  MAS NMR spectra for both support and catalysts. No peak in -110 ppm chemical shift region was detected, which indicates that all three bulk structures are free of Si-island  $\text{Si}(\text{OSi})_4$  [130,350]. Defects which typically affect the acidity of the support by depriving the framework of isolated Si which constitutes a part of the SAPO-34 Brønsted acid sites [295]. These results are in accordance with our ICP OES results Table IV-2, where the calculated (Si+P)/Al ratio was inferior to 1, informing about a preferential isolated position for Si elements (Si(OAl)) within the framework [276]. Thus, the different synthesis methods did not favour the creation of Si islands. Regarding the principal peak centred at a chemical shift of -89 ppm, which could mean that the main building unit on parent support and catalysts are the isolated Si atoms ( $\text{Si}(\text{OAl})_4$ ) [350]. Slight differences were observed for H-SAPO-34 support, which presented a greater proportion of  $\text{Si}(\text{OAl})_3$  than  $\text{Si}(\text{OAl})_4$  building units, according to the shifted peak better centred at -95 ppm than -89 ppm [221,311]. This observation could indicate that the ionic exchange process possibly continue the Si reorganization inside the catalyst framework, passing from a proportion majority of Si in  $\text{Si}(\text{OAl})_3$  building unit configuration before copper exchange, to a main tetrahedral configuration in  $\text{Si}(\text{OAl})_4$  at the end of the incorporation process [128].

Moreover, Figure IV-3 (b) and (c) show that the parent H-SAPO-34 support used for copper ionic exchange and the resultant Cu-SAPO-34-IE catalyst presented similar  $^{27}\text{Al}$  and  $^{31}\text{P}$  profile spectres. Indeed, the main peaks at a chemical shift of 37 ppm and -26 ppm correspond to  $\text{Al}(\text{O P or Si})_4$  and  $\text{P}(\text{O Al})_4$ , respectively [137,294,314]. However, their building unit environment seems to present some irregularities (Figure. 3 (b) and (c)), comparing to the theoretical CHA structural zeolite configuration where most of the elements would be in tetrahedral configurations [284]. This hypothesis is based on the presence of the peaks centred at -15 and 12 ppm, corresponding to structural octahedrally and pentahedrally coordinated Al species with  $\text{H}_2\text{O}$  [137,351], and the peak centred at -17 ppm, which was attributed to disordered P formed by SAPO-34 reversible hydrolysis ( $\text{P}(\text{OAl})_4(\text{H}_2\text{O})_y$ ) [310,314]. These peaks were not observed for the HT-catalyst (Figure IV-3 (a) ,(b) and (c)), in which the main peaks were sharp and centred at 89 ppm , 37 ppm and 26 ppm, corresponding to the tetrahedrally coordinated  $\text{Si}(\text{OAl})_4$ ,  $\text{Al}(\text{O P or Si})_4$  and  $\text{P}(\text{O Al})_4$  chemical shift. These results mean that the Cu-SAPO-34-HT catalyst give rise to a building unit environment in more appreciably closer CHA configuration (exclusively constituted of isolated elements) than Cu-SAPO-34-IE catalyst does [131,284,350]. Note that for similar catalysts, building units mainly composed of isolated elements and specifically of Si as  $\text{Si}(\text{OAl})_4$  are characterised to be strongly stable structure with high resistance capacity during hydrothermal condition[293,352].



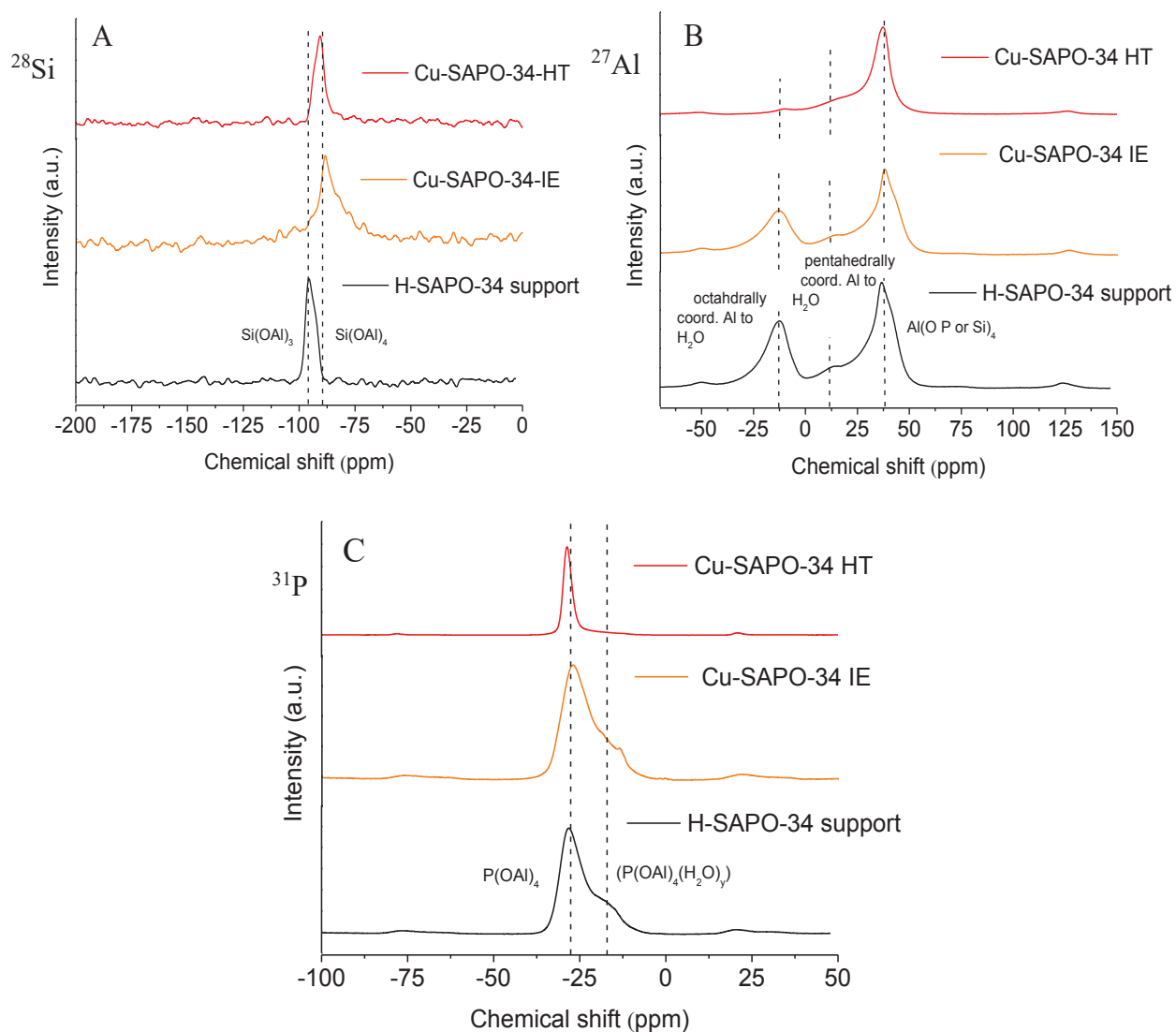


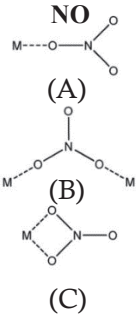
Figure IV-3. Solid state MAS NMR spectra of  $^{28}\text{Si}$  (A),  $^{27}\text{Al}$  (B) and  $^{31}\text{P}$  (C) of Cu-SAPO-34-IE, HT catalysts and H-SAPO-34 zeolite support.

#### IV-3.3.2. Ex-situ DRIFTS

Surface site characterisations performed by ex-situ DRIFTS are presented in Figure IV-4. This technique is complementary to  $^{28}\text{Si}$ ,  $^{27}\text{Al}$  and  $^{31}\text{P}$  MAS NMR analysis, where the fine configuration of the Cu-SAPO-34-HT catalyst building units was compared with those of the support and Cu-SAPO-34-IE. Ex-situ DRIFTS measurements were carried out to investigate the presence of copper cations in exchanged position but also to compare the surface Brønsted acid sites presented on both catalysts. Surface extra framework Si-OH, P-OH and intracrystalline bridged Al-OH-Si were observed at 3730, 3671 and 3625-3600  $\text{cm}^{-1}$ , respectively [326]. Similar profiles were obtained for both support and catalysts in the region of 4000-3000  $\text{cm}^{-1}$ , which corresponds to the Brønsted vibration sites region [353], suggesting similar surface site configurations between the different samples. All the different stretching vibrations are referenced in Table 3 for more convenience. Moreover, the vibrations at 891 and 844  $\text{cm}^{-1}$  assigned to

copper cations interfering with T–O–T structure (as Si–O–Si or Si–Al–Si) for type 1 in the former and type 2 perturbation in the latter [168,173,325] were exclusively observed for Cu-SAPO-34-IE catalyst Figure IV-4 (b). As expected, H-SAPO-34 support Figure. 3a. and Cu-SAPO-34-HT catalyst Figure. 3c. did not exhibit these vibrations. These results suggest that only in the case of Cu-SAPO-34-IE catalyst synthesized by ionic exchange method, the copper cations are clearly localised in exchanged positions [156,222,354].

Table IV-3 Referenced stretching vibrations of exploited probe molecules (NH<sub>3</sub> and CO)

Molecule	Vibrations (cm <sup>-1</sup> )	Compound	[Ref]
NH <sub>3</sub>	3730	External Si-OH	[44,45]
	3671	External P-OH	
	3625,3600	Bridged Si-(OH)-Al	
	3333	NH <sub>3</sub> molecules	[44,45,76]
	3283	NH <sub>4</sub> <sup>+</sup> adsorbed species	
	3182	Cu <sup>+</sup> -NH <sub>3</sub>	[77]
	1620	NH <sub>3</sub> on Lewis acid sites	[62]
	1460	v <sub>as.</sub> NH <sub>4</sub> <sup>+</sup> on Brønsted acid sites	[44,77]
	891, 844	v <sub>as.</sub> framework vibration (type1 and type 2) perturbed by copper cations	[20,46,47,78]
CO	2154	Mono carbonyl complex [Cu(CO)] <sup>+</sup> near 8MR	[81,82,83,84]
	2136	Mono carbonyl complex [Cu(CO)] <sup>+</sup> near 6MR	
	2150	Multi carbonyl complex [Cu(CO) <sub>2</sub> ] <sup>+</sup>	
	1904	NO- isolated Cu <sup>2+</sup>	[168,355]
	1875	NO- bidimensional CuO	[356,357]
	1625/1610/1578	(C) Chelating nitrates	[358]
	1495	(A) Monodentate nitrate	[359]
	1436	(A) Monodentate nitrites O-N-O-M	[360]
	1375-1314 1203-1176	(C) v <sub>sym</sub> / v <sub>as</sub> Chelating nitrites	[361]

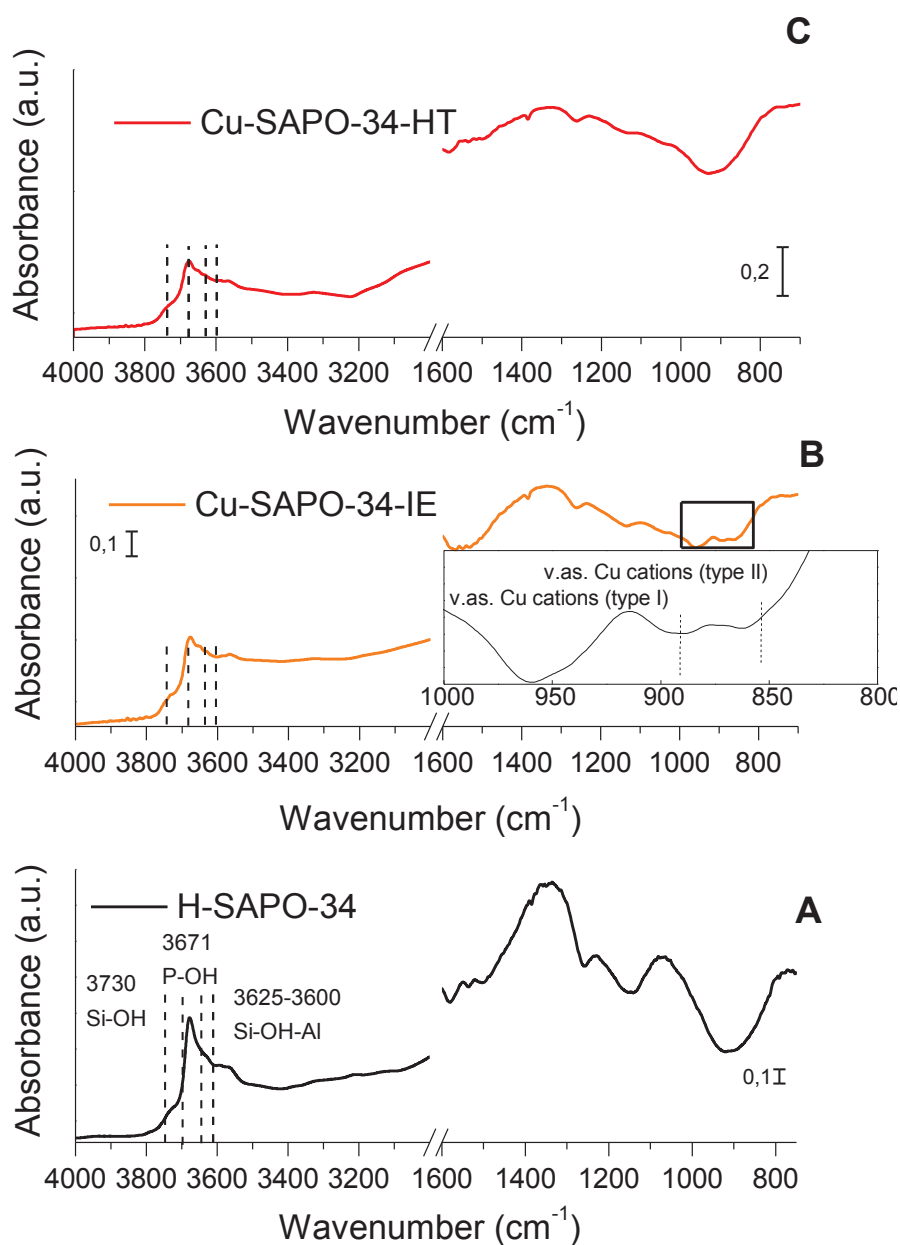


Figure IV-4. Ex-Situ DRIFT profiles under He at room temperature for (A) H-SAPO 34 support, (B) Cu-SAPO-34-IE and (C) -HT catalysts after oxidative pretreatment. *With an insert corresponding to the zoomed area of Cu-SAPO-34-IE profile between 1000 and 800cm<sup>-1</sup>.*

IV-3.4. Investigations of catalysts redox properties: XPS and H<sub>2</sub>-TPR measurements.

IV-3.4.1. XPS

XPS measurements of Cu-SAPO 34-IE and -HT catalysts were carried out in order to evaluate the chemical state of copper species on both catalysts and corresponding spectra are presented in Figure IV-5. The binding energy of the Cu 2p transition peak will provide information about the oxidation state of Cu species at the catalyst surface. For both catalysts, the Cu 2p<sub>3/2</sub> spectra in Figure IV-5 displays two peaks around binding energies of 934 eV and 932 eV and shake-up satellites signal at 942 eV and 962 eV [213]. The binding energies at 934.8 eV and 934.6 eV for Cu-SAPO-34-IE and Cu-SAPO-34-HT catalysts, respectively, were attributed to the Cu<sup>2+</sup> species [362]. This assumption was confirmed by the corresponding shake-up satellites peaks, which are clearly associated to Cu<sup>2+</sup> species in the literature [363]. In addition, the binding energies at 932.8 eV and 931.7 eV for Cu-SAPO-34-IE and Cu-SAPO-34-HT catalysts, respectively, could be attributed to the Cu<sup>+</sup> and Cu<sup>0</sup>. However, for catalysts containing low amounts of copper, this assumption is still controversial in the literature, where the differentiation between Cu<sup>+</sup> and Cu<sup>0</sup> is limited by the collection of Auger electron peaks at lower binding energy (916 eV) [184,364]. Indeed, some authors tried to identify the CuO species through the satellite peaks in the region of 940-948 eV without taking into consideration the Cu 2p<sub>3/2</sub> asymmetric profile information and so, the possible presence of different oxidation state [170,340,365]. On the contrary, others authors [366,367] consider the deconvolution of Cu 2p<sub>3/2</sub> spectra in three main contributions centered at 935.8, 934.6 and 932.6 eV, which are assigned to Cu<sup>2+</sup> species coordinated to framework oxygen atoms, CuO species and Cu(I) species as isolated Cu<sup>+</sup> ions and Cu<sub>2</sub>O, respectively [368]. For this reason, the peaks centred at 932.8 eV or 931.7 eV were here denoted as Cu<sup>δ+</sup> species, corresponding to copper species surrounded by surface oxides without net distinction between Cu<sup>0</sup> and Cu<sup>+</sup> species. Thus, by Cu 2p<sub>3/2</sub> spectra deconvolution, the estimated proportions of Cu<sup>2+</sup> species presented on Cu-SAPO-34-IE catalyst (~30%) was slightly higher than on Cu-SAPO-34-HT catalyst (~20%). This difference is directly observable notifying the Cu<sup>2+</sup> peak shape difference, where only a small shoulder appears at 934.8 eV on the profile Figure IV-5, while a distinct profile is observable for Cu-SAPO-34-IE. However, the Cu<sup>δ+</sup> species share (~80%) on both Cu-SAPO-34 catalysts remains higher than the (II) copper oxidation state. Therefore, these XPS results confirmed that the Cu<sup>2+</sup> and Cu<sup>+</sup> species were present on both catalysts, which is in agreement with the previous XRD and TEM results.

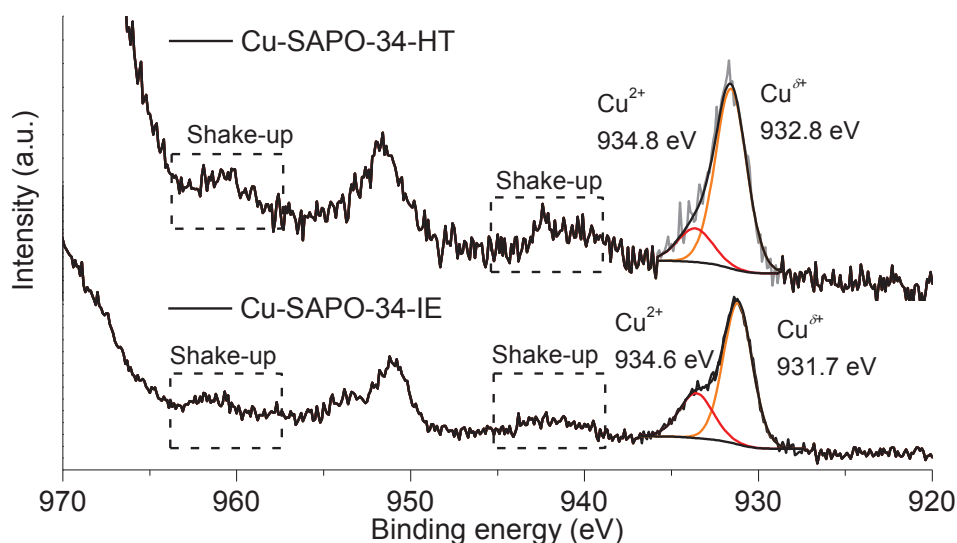


Figure IV-5. XPS spectra  $\text{Cu}2p_{3/2}$  of Cu-SAPO-34-IE and -HT catalysts.

#### IV-3.4.2. $\text{H}_2$ -TPR

$\text{H}_2$ -TPR measurements shown in Figure IV-6 (from room temperature to  $500^\circ\text{C}$ ) were performed to characterize the reducibility of catalysts, which will allow to compare the impact of preparation method in redox properties. The peaks attribution remains under debates because of the different copper species coexistence, which make peaks deconvolution really delicate [165,175,315]. For this reasons, TPR profiles were interpreted on a qualitative basis. While the Cu-SAPO-34-HT catalyst showed a single reduction state with a quite symmetrical peak between  $250^\circ\text{C}$  and  $340^\circ\text{C}$  well synchronized with a  $\text{H}_2\text{O}$  desorption peak, the Cu-SAPO-34-IE catalyst presented a broad peak from  $200^\circ\text{C}$  to  $500^\circ\text{C}$ , demonstrating the presence of different copper site configurations [165,243]. For Cu-SAPO-34-IE catalyst, the broad shoulder peak defined between  $160^\circ\text{C}$  and  $250^\circ\text{C}$  is delimited in one first consumption zone, which could be attributed to reduction of the isolated  $\text{Cu}^{2+}$  as  $\text{Cu}^{2+} + \frac{1}{2} \text{H}_2 \rightarrow \text{Cu}^+ + \text{H}^+$  [241,315]. Otherwise, the following reduction zone between  $250^\circ\text{C}$  and  $340^\circ\text{C}$ , which represents an important  $\text{H}_2$  consumption centred at  $315^\circ\text{C}$ , could be related to the single step reduction of the Cu-SAPO-34-IE dispersed nanosized copper oxides ( $\text{CuO} + \text{H}_2 \rightarrow \text{Cu}^0 + \text{H}_2\text{O}$ ) presented the catalyst surface [316]. Finally, at higher temperature, one last reduction step associated to the reduction of native  $\text{Cu}^+$  and the previously reduced  $\text{Cu}^{2+}$  to  $\text{Cu}^0$  could be considered ( $< 500^\circ\text{C}$ , not shown) as  $\text{Cu}^+ + \frac{1}{2} \text{H}_2 \rightarrow \text{Cu}^0 + \text{H}^+$  [316–318]. By comparison, Cu-SAPO-34-HT catalyst showed a sharp centred peak around  $280^\circ\text{C}$ , demonstrating the presence of one main copper configuration, which could be attributed to the single step reduction in  $\text{Cu}^0$  of the large surface  $\text{CuO}_x$  clusters previously observed by HR-TEM [165,256]. This sharp peak located near the reduction region of the nano-sized copper cluster  $\text{CuO}$  but shifted towards lower temperature, further confirms the presence of  $\text{CuO}$  clusters on both catalysts but in different configurations.

These results lead to conclude that the preparation methods had an important influence on redox properties of catalysts. Indeed, species in Cu (II) valence state, in Cu-SAPO-34-IE catalyst, presented easily reducible nano-sized copper cluster at its surface, and on the contrary, only micro CuO<sub>x</sub> species were presented on Cu-SAPO-34-HT catalyst surface, without any main detection of isolated Cu<sup>2+</sup> cations. Knowing that, the reduction capability on the whole temperature range (200°C to 500°C) for Cu-SAPO-34-IE, and more specifically the temperature reduction centred at 280°C of Cu-SAPO-34-HT redox sites, will consequently impact the catalytic activity of both catalysts, which will be demonstrated with the following tests performance.

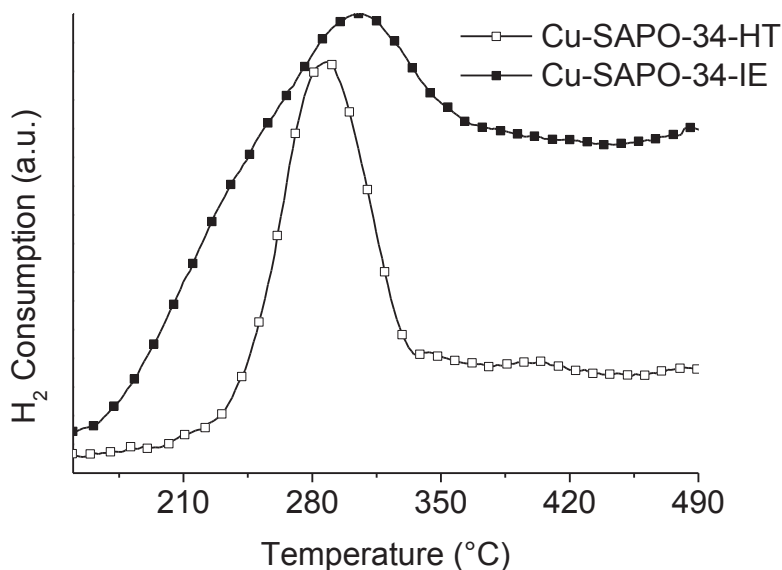


Figure IV-6. H<sub>2</sub>-TPR results of Cu-SAPO-34-IE and -HT catalysts. Reduction feed: 2 vol.% H<sub>2</sub> in Ar, total flow of 40 ml.min<sup>-1</sup>, heating ramp from 30 °C to 500 °C with a heating up rate of 10 °C/min.

**IV-4.** Surface active sites characterization by NH<sub>3</sub>-TPD and in-situ DRIFTS spectroscopy using NH<sub>3</sub>, CO and NO probe molecules.

#### IV-4.1. NH<sub>3</sub> TPD

Temperature-programmed desorption of ammonia was performed to determine the NH<sub>3</sub> affinity with H-SAPO-34 support, Cu-SAPO-34-IE and -HT active sites. During adsorption steps at 150°C, the gas feed was composed of 1000 ppm NH<sub>3</sub>/He, 8% O<sub>2</sub> and 4% H<sub>2</sub>O in order to better represent the NH<sub>3</sub> and H<sub>2</sub>O competitive adsorption on the catalyst surface and the corresponding hydration copper sites [222,369]. The corresponding NH<sub>3</sub> desorption profiles from H-SAPO-34 support, Cu-SAPO-34-HT and -IE catalysts are represented below, Figure IV-7. All the support and catalysts presented similar NH<sub>3</sub> desorption profiles with two main desorption regions before 400°C (denoted as low temperature (LT) and medium temperature (MT)). A third region at higher temperature above 400°C was also detected for the ionically exchanged catalyst, spotted as high temperature peak (HT). The corresponding acid sites assignments in temperature are assigned in Table 4 below with S1, S7 assigned to weak Brønsted acid site surface hydroxyl on SAPO-34 as T-OH (with T = Si, Al and P) and weak copper Lewis acid sites, for the LT signal [222,256]. S2, S8

representing bridged Brønsted sites and moderately strong copper sites, for the MT peak [241] and S2a, S3, S4 corresponding to the strongest Brønsted acid sites and the strongest exchanged copper cations (HT) [176,353]. This description is further assigned Table IV-1 for more convenience.

Table IV-4 Desorbed NH<sub>3</sub> quantities according to NH<sub>3</sub>-TPD measurements of H-SAPO-34 support, Cu-SAPO-34-HT and Cu-SAPO-34-IE catalysts with related median peak temperature<sup>a</sup>

Peak category <sup>a</sup>	H-SAPO-34			Cu-SAPO-34-HT			Cu-SAPO-34-IE		
	LT	MT	HT	LT	MT	HT	LT	MT	HT
Desorbed NH <sub>3</sub> (mmol g <sup>-1</sup> catalyst)	0.162	0.398	-	0.113	0.317	-	0.210	0.276	0.09
Total desorbed NH <sub>3</sub> (mmol g <sup>-1</sup> catalyst)	0.560			0.430			0.576		
Temperature (°C)	263	349		267	349		255	323	421

<sup>a</sup> The LT, MT and HT peaks respectively correspond to the weak, medium and strong acid sites, and are estimated from the corresponding area of the deconvoluted peaks.

These peaks were observed and quantified by deconvolution with Gaussian from the different profiles reported Figure IV-7 Regarding the insert Figure IV-7, the profile differences can be enlightened, where the support H-SAPO-34 and the hydrothermal catalyst display close desorption curve shapes. Regarding the main sites difference between both samples, where large copper oxide clusters are specifically present on Cu-SAPO-34-HT, it could be firstly assumed that these large clusters had substituted a non-negligible part of MT sites from the support. In other words, the presence of large copper oxides clusters on Cu-SAPO-34-HT catalyst could inhibit a small fraction of the support Brønsted acid sites by substitution of Lewis sites of similar strength. However, even with this obstruction, the desorption ability of Cu-SAPO-34-HT catalyst remains close to the support capacity, according to the total amount of desorbed NH<sub>3</sub> displayed Table IV-4, a similar desorption trend in temperature, with a maximum desorption intensity centred at 349°C. This important MT peak, consequence of the bridged Brønsted acid sites and moderately strong Lewis acid sites desorption, represents the principal proportion of ammonia storage capacity of Cu-SAPO-34-HT catalyst and support. Compared to H-SAPO-34 support, these TPD results showed that the exchanged catalyst presented a higher capacity to desorb NH<sub>3</sub> at low temperature, with a shifted LT and MT peak at lower temperature. The overall stronger desorption at low temperature of Cu-SAPO-34-IE catalyst seems to be due to the weak copper and Si, Al or P Lewis acid sites, which are a consequence of the copper incorporation method and the subsequent formation of weak Brønsted sites (as P-OH) [285,370]. On the other hand at elevated temperature, Cu-SAPO-34-IE catalyst particularly presented a HT peak, not observed in the support desorption profile. Indeed, for the exchanged catalyst around 420°C, ammonia desorbed from the strongest acid sites of the catalyst, which could be attributed to the presence of strong Brønsted acid sites as T-OH-T but also and mainly to the Cu<sup>2+</sup> within the support [241,369]. These remarkable differences in profile shape and desorption regions between both Cu-SAPO-

34-HT and Cu-SAPO-34-IE directly demonstrated that the preparation method had an important impact on the acid sites nature and their relative proportion for ammonia storage capacity. Particularly, ammonia desorbed from Cu-SAPO-34-HT strong sites around 350°C could desorb from bulk to the reducible surface copper species (H<sub>2</sub>-TPR results), and consequently improve the redox capability. For Cu-SAPO-34-IE, the desorption profile is more complex to correlate with the performances knowing that the stored NH<sub>3</sub> in the support will more easily interact with the exchanged redox centres due to their proximity within the zeolite structure. But it can be specified that for the exchanged catalyst, the important LT storage capacity will strongly impact the performances at this temperature [242,371].

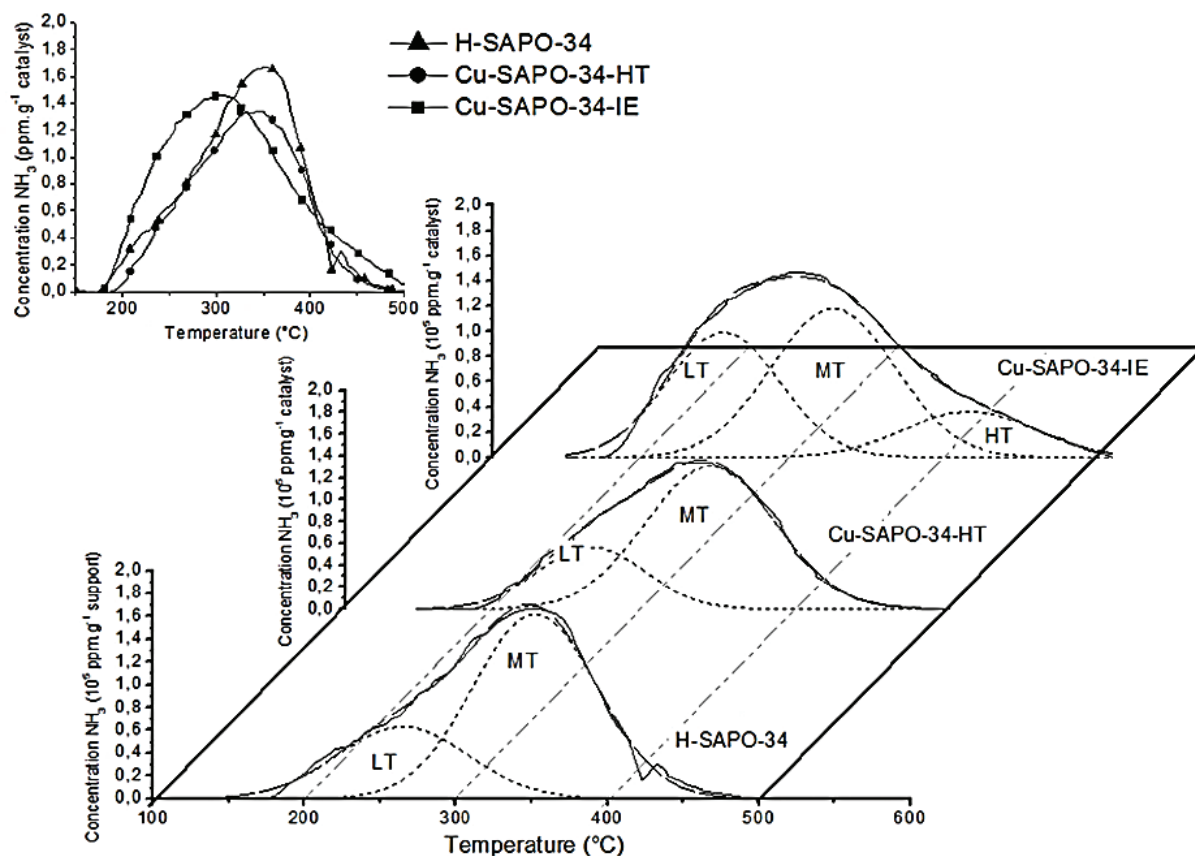


Figure IV-7. NH<sub>3</sub>-TPD profiles with the corresponding deconvoluted peaks of H-SAPO-34 support, Cu-SAPO-34-HT and -IE catalysts with an insert at upper left corner representing the 3 corresponding TPD profiles stacked. Inlet gas composition: adsorption of 1000 ppm NH<sub>3</sub>; 8% O<sub>2</sub>; 4% H<sub>2</sub>O and He as a balance at 150°C with a total Flow of 40 mL/min.

#### IV-4.2. In-situ NH<sub>3</sub> DRIFT measurements

In addition, the NH<sub>3</sub>-DRIFTS measurements were carried out to identify the acidic surface sites on both catalysts and characterize their affinity with NH<sub>3</sub> in temperature. Thus, the ammonia was firstly adsorbed on catalyst surface and the DRIFTS spectra were collected during 30 min of NH<sub>3</sub> exposure, Fig. 7. (A and G). Then, the NH<sub>3</sub> desorption profiles were collected from 35 °C to 500 °C, Figure IV-8 (B-F and H-L). Note that the catalyst surface was purged in He at room temperature in order to remove the weakest physisorbed molecules.



First, two regions can be distinguished, in the range of 3700 and 3500  $\text{cm}^{-1}$  and between 3400 to 3000  $\text{cm}^{-1}$ , which are assigned to the O-H and the N-H stretching mode vibrations, respectively [156] where the latter represent the occupation of Brønsted acid sites by  $\text{NH}_3$  [372]. In the region of O-H stretching vibrations, the bands at 3730  $\text{cm}^{-1}$ , 3671  $\text{cm}^{-1}$  and 3625-3600  $\text{cm}^{-1}$  are assigned to the  $\text{NH}_3$  adsorption onto extraframework Si-OH, P-OH and bridged Al-OH-Si respectively, as previously observed during Ex-situ experiments (Figure IV-4).

In addition, in the region of N-H stretching vibrations, the bands at 3333  $\text{cm}^{-1}$  and 3283  $\text{cm}^{-1}$  are accordingly associated to the  $\text{NH}_3$  molecules and  $\text{NH}_4^+$  groups, the coordinated ammonia species on Brønsted acid sites [326,353,372]. A band at 3182  $\text{cm}^{-1}$  in this region could also be observed, attributed to the adsorption of  $\text{NH}_3$  on  $\text{Cu}^+$  sites [206]. Moreover, a secondary region between 1700-700  $\text{cm}^{-1}$  with four main bands at 1620, 1460, 891 and 844  $\text{cm}^{-1}$  was also observed, which can be respectively assigned to  $\text{NH}_3$  adsorbed on Lewis acid sites, such as exchanged copper cations and external Al [243], to  $\text{NH}_4^+$  ammonium species resulting from ammonia adsorbed on Brønsted acid sites such as Si-OH, P-OH and Al-OH-Si [206,353]. Finally, the last pair of stretching vibrations could be attributed to the Lewis acid sites, and more particularly, to the T-O-T internal framework vibrations perturbed by copper ions with adsorbed  $\text{NH}_3$  [373].

Regarding Cu-SAPO-34-HT, the evolution of the external Si-OH, P-OH and bulk Al-OH-Si Brønsted acid sites bands showed a fast ammonia adsorption within the first minutes, reaching a maximum of absorbance value after 5 min, according to the bands intensity at 30 min saturation. A similar evolution profile on the same period was found for the bands assigned to  $\text{NH}_4^+$  and  $\text{NH}_3$  groups. Moreover, in the 1700-700  $\text{cm}^{-1}$  region, the 1460  $\text{cm}^{-1}$  band assigned to  $\text{NH}_4^+$  ammonium species bounded to Brønsted acid sites such as Si-OH, P-OH and Al-OH-Si also showed a fast  $\text{NH}_3$  adsorption on these sites. Moreover, these results demonstrated that Cu-SAPO-34-HT exhibited only few ammonia interactions with the Lewis acid sites corresponding to the transition metal during the adsorption process. Indeed, the  $\text{NH}_3$  adsorption seems quite low on these sites, according to the slight detected band at 1620  $\text{cm}^{-1}$  assigned to  $\text{NH}_3$  adsorbed on Lewis acid sites. This last conclusion is also in accordance with the lack of signal at 891  $\text{cm}^{-1}$  and 844  $\text{cm}^{-1}$ , where no manifestation of stretching vibration from possible interaction between  $\text{Cu}^{2+}$  active sites, interfering in exchanged position, and adsorbed  $\text{NH}_3$  were detected. These results agree with the previous Ex-situ DRIFTS measurements, Figure IV-4, in which the absence of  $\text{Cu}^{2+}$  ions in exchanged position was probed.

According to Cu-SAPO-34-IE, the  $\text{NH}_3$  adsorption behavior was quite similar to the hydrothermal catalyst profiles Figure IV-8 (G), however, the adsorption on Brønsted acid sites was slower within the first minutes from 5 to 10 min, according to the bands evolution in the 4000 – 3000  $\text{cm}^{-1}$  region. In the other hand, copper site interactions with  $\text{NH}_3$  were more visible, where the bands at 3182  $\text{cm}^{-1}$  and 1620  $\text{cm}^{-1}$  attributed to  $\text{NH}_3$  adsorbed on  $\text{Cu}^+$  sites and on Lewis acid sites, respectively were also observed. In that way, the  $\text{NH}_3$  adsorption on exchanged copper cations interfering with the T-O-T structure was faster

and the saturation was reached within the first minutes, according to the bands at  $891\text{ cm}^{-1}$  and  $844\text{ cm}^{-1}$  [354]. After  $\text{NH}_3$  adsorption at  $35^\circ\text{C}$ , a temperature-programmed desorption was performed in order to evaluate the  $\text{NH}_3$  adsorption strength and acidic surface sites presented on both catalysts. The DRIFTS spectra collected at different desorption temperatures, from  $35^\circ\text{C}$  to  $500^\circ\text{C}$ , are presented in Figure IV-8(B-F) and (H-L) for Cu-SAPO-34-HT and Cu-SAPO-34-IE, respectively. All the N-H and the O-H stretching mode vibrations remain appreciable for both catalysts at  $100^\circ\text{C}$ .

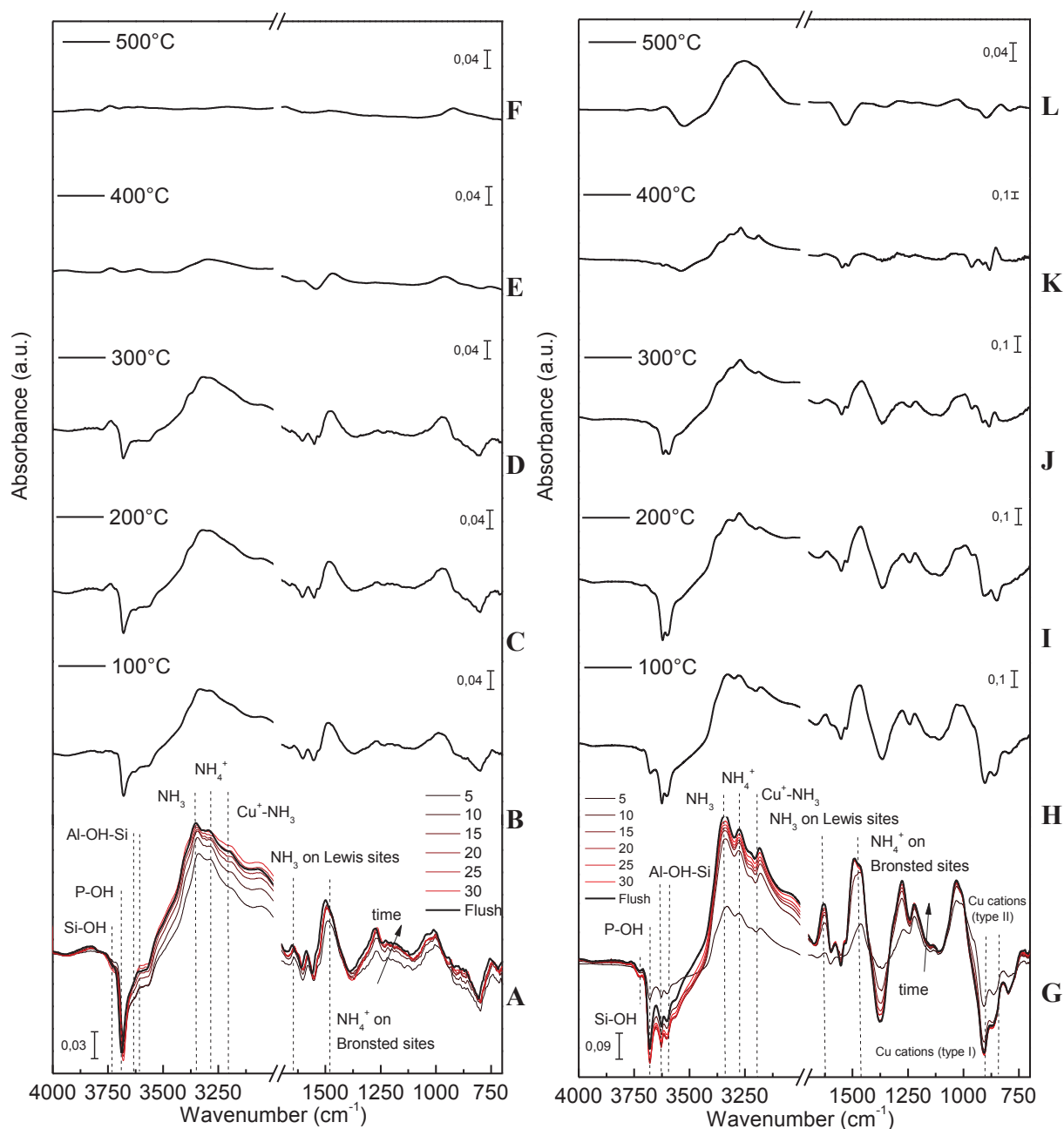


Figure IV-8. (A) Cu-SAPO-34-HT and (G) Cu-SAPO-34-IE DRIFTS spectra recovered during  $\text{NH}_3$  adsorption for 30 min to 1000 ppm  $\text{NH}_3/\text{He}$ , after 30 min He flush, followed by (B-F) desorption from room temperature to  $500^\circ\text{C}$  and (H-L) under He. Total Flow=  $40\text{ mL}\cdot\text{min}^{-1}$ .

According to the DRIFTS spectra associated to Cu-SAPO-34-HT, Figure IV-8 (B-F), the overall intensities of N-H and O-H stretching vibration from  $4000\text{ cm}^{-1}$  to  $3000\text{ cm}^{-1}$  decreased with the temperature increase from  $35^\circ\text{C}$  to  $300^\circ\text{C}$ . Note that the first Brønsted acid sites to desorb were the external Si-OH, following the vibration band at  $3730\text{ cm}^{-1}$ , which disappeared at  $100^\circ\text{C}$ . This could indicate that only a small proportion of the total stored  $\text{NH}_3$  was desorbed from weak Brønsted acid sites at this temperature. Nevertheless, the strongest desorption was observed between  $300^\circ\text{C}$  and  $400^\circ\text{C}$  and from the Brønsted groups, with an overall decreasing of the bands corresponding to the O-H and N-H vibration bands within  $4000 - 3000\text{ cm}^{-1}$ . At higher temperature, only a small amount of  $\text{NH}_3$  seems to desorb from the Brønsted acid sites, Figure IV-8 (E and F). This same desorption behaviour from  $100^\circ\text{C}$  to  $500^\circ\text{C}$  for Cu-SAPO-34-HT catalyst was also observed during  $\text{NH}_3$ -TPD measurements Figure IV-7, where a first desorption ascribed to the weak Brønsted adsorption sites was found between  $150^\circ\text{C}$  and  $300^\circ\text{C}$  with a centred peak at  $267^\circ\text{C}$ . Moreover, the second and main desorption peak was observed at higher temperature centred at  $350^\circ\text{C}$ , which is in agreement to the In-situ  $\text{NH}_3$ -DRIFT measurements at  $300^\circ\text{C}$  and  $400^\circ\text{C}$ , Figure IV-8 (D-E). For the referenced stretching vibrations, the profile remains generally flat after  $400^\circ\text{C}$  from  $4000\text{ cm}^{-1}$  to  $700\text{ cm}^{-1}$ .

Concerning Cu-SAPO-34-IE catalyst, the desorption from external Brønsted acid sites did not occur in the same manner as Cu-SAPO-34-HT. The band relative to external Si-OH at  $3730\text{ cm}^{-1}$  was the first to vanish at  $100^\circ\text{C}$ , but at the same time, the external P-OH band identified at  $3671\text{ cm}^{-1}$  strongly decreased, and was completely removed at  $200^\circ\text{C}$ . Moreover, the band intensity relative to Al-OH-Si Brønsted acid sites was strongly decreased between  $200^\circ\text{C}$  and  $300^\circ\text{C}$ , and completely disappeared at  $400^\circ\text{C}$ . This desorption trend corresponding to O-H sites was also observed through the intensities of the band ascribed to  $\text{NH}_3$  and  $\text{NH}_4^+$  sites at  $3333\text{ cm}^{-1}$  and  $3283\text{ cm}^{-1}$ , where only a slight intensity decrease was observed, which was associated to the desorption of molecularly adsorbed  $\text{NH}_3$  and  $\text{NH}_4^+$  between  $100^\circ\text{C}$  and  $200^\circ\text{C}$ . As observed through the DRIFT profiles Figure IV-8 (J-K), the most important Brønsted acid sites desorption occurs between  $300^\circ\text{C}$  and  $400^\circ\text{C}$ , according to the strong intensity decrease of the bands relative to N-H vibration. The band at  $1460\text{ cm}^{-1}$  relative to  $\text{NH}_4^+$  adsorbed on Brønsted acid sites globally reflects this Brønsted desorption dynamic from  $35^\circ\text{C}$  to  $400^\circ\text{C}$ . Moreover, the  $\text{NH}_3$  desorption trend from the copper sites, such as  $\text{Cu}^+$  observed at  $3182\text{ cm}^{-1}$ , and the exchanged  $\text{Cu}^{2+}$  assigned to  $891\text{ cm}^{-1}$  and  $844\text{ cm}^{-1}$ , exhibited different desorption behaviors. The surface  $\text{NH}_3 - \text{Cu}^+$  species followed the same trend comparing to that of O-H Brønsted acid sites bands between  $35^\circ\text{C}$  to  $300^\circ\text{C}$  with a strong desorption between  $300^\circ\text{C}$  and  $400^\circ\text{C}$ . At low temperature, the  $\text{NH}_3$  desorption from Lewis sites was strong and almost complete at  $300^\circ\text{C}$ , according to the band centered at  $1630\text{ cm}^{-1}$ . The same evolution was observed at  $891\text{ cm}^{-1}$  and  $844\text{ cm}^{-1}$ , where the ammonia adsorbed on exchanged cations strongly desorbs between  $35^\circ\text{C}$  and  $300^\circ\text{C}$ . Finally, at higher temperature between  $400^\circ\text{C}$  and  $500^\circ\text{C}$ , the desorption was not completed on some Brønsted acid sites and exchanged  $\text{Cu}^{2+}$ , according to the relative N-H stretching bands and the vibrations due to perturbed T-O-T structure, Figure IV-8 (K-L). A similar desorption profile was observed during  $\text{NH}_3$ -TPD, Figure IV-7. Indeed, the first peak centered around  $255^\circ\text{C}$  was observed at lower

temperature than HT catalyst (267°C), which could be associated to the better participation of copper sites, such as surface  $\text{Cu}^+$  and exchanged  $\text{Cu}^{2+}$ , and to the desorption from weak external P-OH Brønsted sites [183]. Moreover at higher temperature, the results presented in Figure IV-8 (J-K) profiles associated to Al-OH-Si relative bands, show an intense desorption between 300°C and 400°C, coming from a large desorption of ammonia on Brønsted acid sites. Finally, the last desorption peak at high temperature around 420°C could be associated to the desorption from the strongest exchanged cations but also some remaining strong Brønsted acid site, Figure IV-8 (L) [183]. This could indicate that the number of strong acid sites was higher on this catalyst than on the Cu-SAPO-34-HT catalyst, in agreement to the  $\text{NH}_3$ -TPD results at high temperature.

#### IV-4.3. In-situ CO DRIFT measurements

In addition, CO adsorption and desorption DRIFTS measurements were carried out in order to discriminate the  $\text{Cu}^+$  active species as a function of temperature for both catalysts. Indeed,  $\text{Cu}^{2+}$  ions are not able to form stable carbonyls during CO adsorption due to their electrostatic interaction [374]. Nevertheless,  $\text{Cu}^+$  species strongly interact with CO to form mono or multi carbonyl complexes such as  $[\text{Cu}(\text{CO})]^+$  and  $[\text{Cu}(\text{CO})_2]^+$ , which are respectively assigned at  $2136\text{ cm}^{-1}$  (site near 6MR cages),  $2154\text{ cm}^{-1}$  (site near 8MR cages) for the former and  $2150\text{ cm}^{-1}$  for the latter [160,375,376].

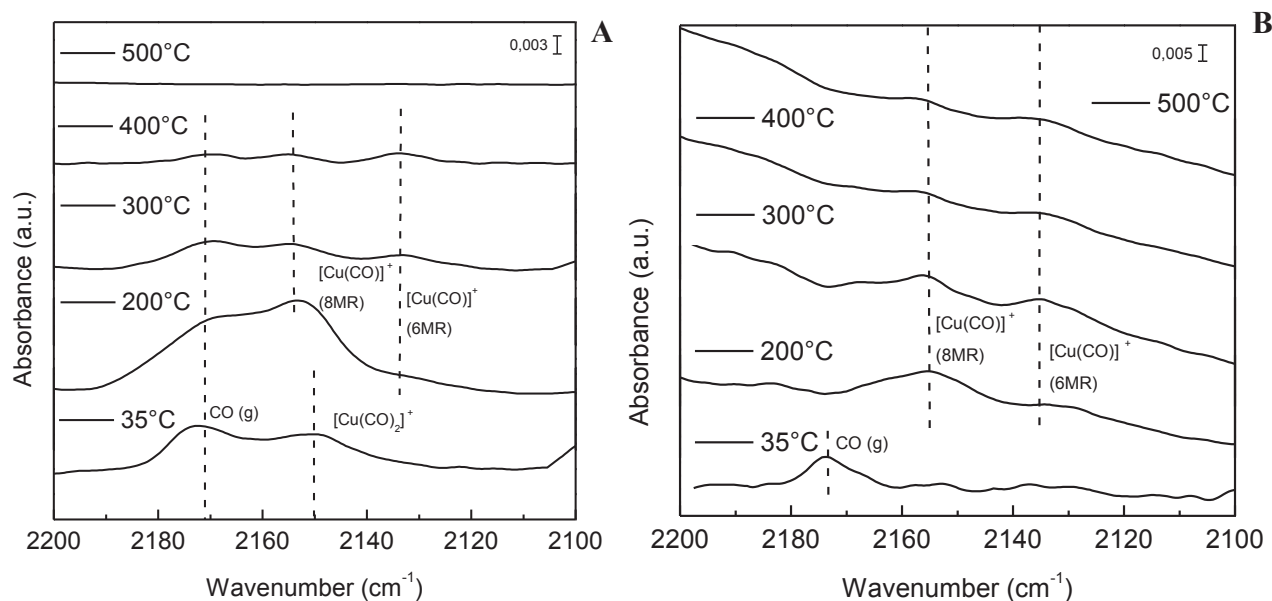


Figure IV-9. DRIFTS spectra recovering the evolution of desorbed species after previous CO-adsorption (1000 ppm CO/He) and He flush as a function of temperature from 35°C to 500°C for (A) Cu-SAPO-34-IE and (B) Cu-SAPO-34-HT catalysts; Total Flow= 40 mL·min<sup>-1</sup> He.

The CO-DRIFT spectra, Figure IV-9, displayed the desorption profile from 35 °C to 500 °C for (A) Cu-SAPO-34-IE and (B) Cu-SAPO-34-HT from 2200 to 2100  $\text{cm}^{-1}$  in the Cu-CO stretching vibration range. This desorption process was monitored right after the CO-adsorption and He purge step. Concerning Cu-SAPO-34-IE catalyst, two major bands at  $2150\text{ cm}^{-1}$  and  $2175\text{ cm}^{-1}$  are spotted following the CO-

adsorption at 35 °C, Fig. 8 (A). The first one could be attributed to the CO adsorption on Cu<sup>+</sup> ions in a coordinated position with the O atoms on the SAPO-34 framework (Cu<sup>+</sup>-(CO)<sub>2</sub>) and the second one, to the stretching vibrations associated to the gaseous CO [160] (Note that for both catalysts, the purging step under 40ml/min He seems to not be sufficient to completely vanish the gaseous CO as visible at 2175 cm<sup>-1</sup> at 35°C and some residual CO (g) are still detected for both catalyst). The intensity of these two 2150 cm<sup>-1</sup> and 2175 cm<sup>-1</sup> bands decreased during the desorption process, which suggest the gradual decrease of CO coverage and the removal of gaseous CO. Next, two new bands at 2136 and 2154 cm<sup>-1</sup> appeared at 200 °C, which are associated to the formation of the above mentioned carbonyl complex, and more specifically, to the Cu<sup>+</sup>-CO species coordinate to the O atoms on two different sites of the zeolite framework. These two bands are associated to the Cu<sup>+</sup> species near of 6MR positions and Cu<sup>+</sup> cations near of 8MR, respectively [168,263]. Indeed, a chemical vibration shift between 35°C and 200°C was firstly observed, indicating the conversion of Cu<sup>+</sup>-(CO)<sub>2</sub> to Cu<sup>+</sup>-CO species, which is associated to the Cu<sup>+</sup> adsorbates interaction modification within the catalyst cavities. Moreover, during the desorption process, the band at 2154 cm<sup>-1</sup> decreased while the band at 2136 cm<sup>-1</sup> increased in temperature, which could indicates the migration of some copper species in a more confined position, such as isolated Cu<sup>+</sup> into 6MR positions [160,168,263]. Therefore, Cu-SAPO-34-IE catalyst seems to beneficiate the migration of Cu<sup>+</sup> species into the 8MR exchanged positions and, then into 6MR positions at high temperature (between 200°C and 400°C). However, the reduction possibilities of Cu<sup>2+</sup> cations within the lattice cannot be completely ruled out under these conditions and required careful precautions during interpretations.

Correspondingly, regarding the Cu-SAPO-34-HT catalyst, Figure IV-9 (B), the isolated Cu<sup>+</sup> species were identified only after increasing the temperature to 200 °C, further confirming the absence of initially present isolated Cu<sup>+</sup> cations at the catalyst top surface. Next, the same two bands at 2136 cm<sup>-1</sup> and 2154 cm<sup>-1</sup> were found during the heating process. These results confirm the similar capacity regarding Cu-SAPO-4-IE, to display a Cu<sup>+</sup> species migration to the support cavities (8MR and 6MR positions) from 200 °C to 400°C [160]. However, the low intensities of these stretching vibration signals for -HT catalyst seems to indicate a less pronounced Cu<sup>+</sup> species migration capacity comparing to the IE-catalyst. On the other hand, since the exchanged Cu<sup>2+</sup> cations presence was ruled out for Cu-SAPO-34-HT, this observation adequately correspond to a specie migration process. Such exchanged copper species are, indeed, NH<sub>3</sub>-SCR active for NO<sub>x</sub> abatement and play a role in the SCR reaction mechanism [219,338].

#### IV-4.4. In-situ NO DRIFT measurements

Finally, NO-adsorption DRIFT experiments were performed to acquire further information about the nature of copper cationic sites and the different NO<sub>x</sub> adsorbed species on both catalyst regarding their relative stretching vibrations within the 2000 and 1400 cm<sup>-1</sup> region. Figure IV-10 displays the NO adsorption profile of (A) Cu-SAPO-34-IE and (B) Cu-SAPO-34-HT catalysts as a function of time, from 0 to 30 min until surface saturation. The adsorption is fast for both catalyst within the first minutes, but concerning IE catalyst specifically, a large peak emerges after 10 min adsorption around 1900 cm<sup>-1</sup>,

reaching the sites saturation shortly after indicating, the strong interaction between concerned active sites and NO molecules. Indeed, this profile is composed of a strong signal at  $1904\text{ cm}^{-1}$  which could be related to NO on isolated copper cations (*NO-Cu<sup>2+</sup> exch.*) [93,168] which strongly participate to the peak shape due to the particular presence of exchanged cations in IE-catalyst. A second and third stretching vibration at  $1890\text{ cm}^{-1}$  and  $1875\text{ cm}^{-1}$  were also observed whose the assignment of the former is more complicated. However, the third stretching vibration which participate to this large peak, can be related to adsorbed NO on bidimensionnal CuO like phase, notably observable due to the presence of the previously characterized surface copper clusters (*NO-CuO*) [356,357]. Concerning the  $1890\text{ cm}^{-1}$  signal, in Cu exchanged ZSM-5 for instance [377], it was reported that Cu<sup>2+</sup> sites in square planar coordination within the zeolite provoke a signal around  $1898\text{-}1894\text{ cm}^{-1}$  by NO adsorption on easily reduced copper sites. It was reported also, that NO molecule adsorbed on isolated extraframework cations Cu (II) could display a vibration band at  $1889\text{ cm}^{-1}$  [378]. Nevertheless, [Cu-OH]<sup>+</sup> species in a position relatively close to the widest cages opening of the zeolite support were also speculated in another study [379] to be responsible of an IR band close to  $1890\text{ cm}^{-1}$ . Thus, this band located at  $1890\text{ cm}^{-1}$  was assigned here to surface and non-exchanged Cu<sup>2+</sup> species bound to hydroxyl group such as [Cu-OH]<sup>+</sup> species. This hypothesis is also supported by the Cu (II) electronic valence state observed for IE-catalyst by XPS measurements, Figure IV-5.

Moreover, these three bands are appeared after 10 min of NO adsorption and are quite stable during the 30 min of NO exposition, which could indicate a strong NO interaction between the exchanged Cu<sup>2+</sup> sites on IE catalyst, but also with its copper (II) surface species presented in this catalyst. Contrary, in the case of Cu-SAPO-34-HT catalyst, Figure IV-10 (B), only two bands seems to be clearly observed in the  $2000\text{-}1700\text{ cm}^{-1}$  region. The first band at  $1890\text{ cm}^{-1}$  corresponding to [Cu-OH]<sup>+</sup> surface species overtake the second one at  $1875\text{ cm}^{-1}$ , which could be related to adsorbed NO on bidimensionnal CuO like phase [356,357]. These results could indicate a weak interaction of NO with this CuO phase, where NO preferentially adsorbed on the presented [Cu-OH]<sup>+</sup> species at the surface of HT-catalyst.

Additionally, in the  $1700\text{-}1400\text{ cm}^{-1}$  region, both catalysts presented a band at  $1628\text{ cm}^{-1}$ , whose intensity increases gradually from 0 to 30 min and which could be associated to the chelating nitrates [358]. Another two band around  $1606\text{ cm}^{-1}$  and  $1436\text{ cm}^{-1}$ , Figure IV-10 (B), were particularly observed for Cu-SAPO-34-HT catalyst, which are assigned to NO<sub>2</sub> a second chelating nitrate type according to Negri et al. operando studies [227], and bidentate nitrites as O-N-O-M [360], respectively. The first of these two bands contribute to the peak shape and increases in the same way that the above mentioned band corresponding to chelating nitrates at  $1628\text{ cm}^{-1}$ . Parallely, the increasing signal centered around  $1436\text{ cm}^{-1}$  was observed. In addition, both catalyst showed the presence of another band at  $1495\text{ cm}^{-1}$ , informing on the presence of monodendate nitrate on copper cations in both catalysts [359]. These results indicate that the nitrate and nitrite species are easily formed on the Cu-SAPO-34-HT surface, which underline the multiple NO interaction with the surface copper clusters sites. Indeed, this different interaction could be partially attributed to the large copper clusters presented on the HT-catalyst, according to the above physico-

chemical characterization results, which demonstrate the main concentration of copper species at the top surface catalyst in large cluster. Nitrites and Nitrates species which are proposed and well characterized as key intermediaries to the  $\text{NH}_3$ -SCR process [207,221].

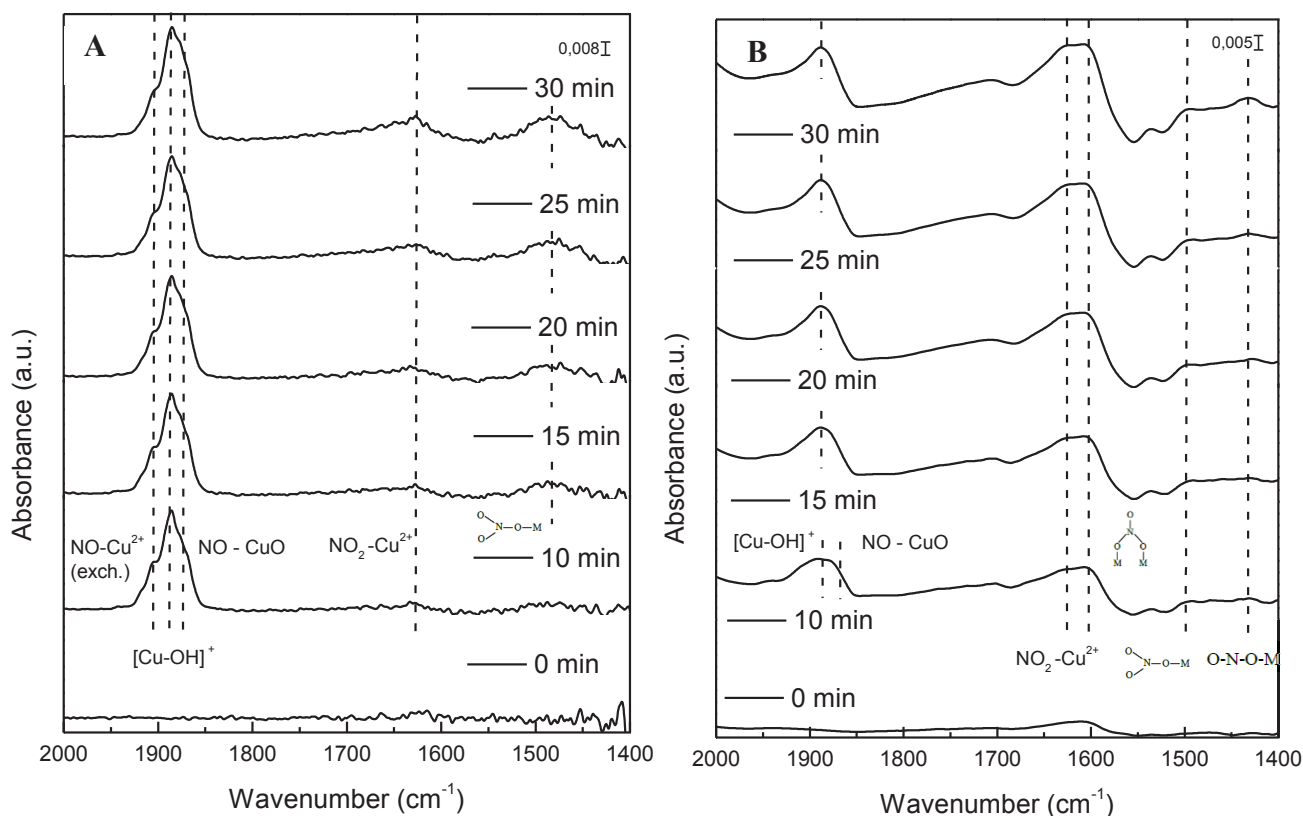


Figure IV-10 DRIFTS spectra recovered during the adsorption of NO at room temperature of (A) Cu-SAPO-34-IE and (B) Cu-SA PO-34-HT catalysts, with an exposure of 1000 ppm NO/He; Total Flow=  $40 \text{ mL} \cdot \text{min}^{-1}$ .

This multiple interaction of NO with Cu-SAPO-34 surface and more precisely, the particular affinity of NO with the large copper cluster species, is also visible through the NO desorption process Figure IV-11. The low stability in temperature of nitrate and nitrite intermediates molecules [207,380] is readily evidenced from  $100^\circ\text{C}$ , where no more NO based molecule was detected at the Cu-SAPO-34-IE surface. However, nitrate species seem to be in more stable position on Cu-SAPO-34-HT copper active sites at  $100^\circ\text{C}$  than Cu-SAPO-34-IE, where the temperature elevation compared to signal at  $35^\circ\text{C}$  (Figure IV-10), seem to promote the nitrate formation within the  $1550\text{-}1500 \text{ cm}^{-1}$  wave number range. Nitrates species which practically vanish from both surface at elevated temperature but which the better stability on surface sites of Cu-SAPO-34-HT could improve the performance of the catalyst in temperature.

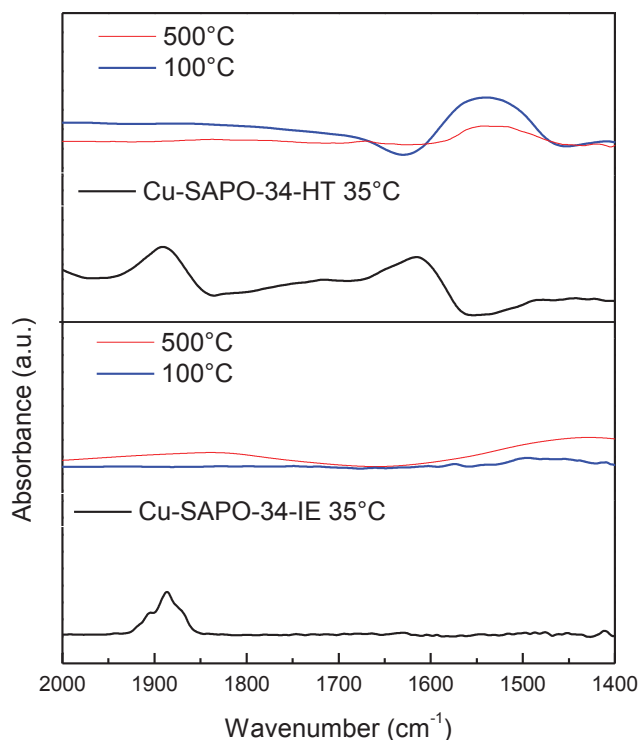


Figure IV-11 DRIFTS spectra recovered during the NO desorption at 100°C and 500°C of Cu-SAPO-34-IE (A) and Cu-SA PO-34-HT (B) catalysts under He; Total Flow= 40 mL·min<sup>-1</sup>.

#### IV-5. Catalytic performances: NH<sub>3</sub>-SCR, NO and NH<sub>3</sub> oxidation reactions.

In Figure IV-12 are displayed the NH<sub>3</sub>-SCR performances in standard condition (1) of Cu-SAPO-34-IE and Cu-SAPO-34-HT catalysts, with in insert, the corresponding production of by-products. Regarding Cu-SAPO-34-IE, the catalyst presented a stable DeNO<sub>x</sub> activity over the whole temperature range, according to the previously characterized redox active sites properties and the strong NH<sub>3</sub> affinity in temperature between Brønsted acid sites and copper species (Figure IV-8 (A-F)). These performances are in accordance with previous studies based on similar exchanged catalysts [176,243,366]. On the other hand, Cu-SAPO-34-HT catalyst behaviour showed three main zones. First of all, almost no activity is detected at 200°C, according to the lack of active sites at this temperature, as exchanged Cu<sup>2+</sup>, where the catalytic reduction of NO<sub>x</sub> via NH<sub>3</sub> start only at higher temperatures. Next, the NO conversion rate increases quite exponentially with the temperature, from 200°C to 425°C. Here during this temperature increase, the important desorption around 350°C, mainly from Brønsted acid sites characterized by TPD (Figure IV-7), is consistent with the modification of the reaction regime within the same temperature window, Figure IV-12. The strong desorption from the bulk support to the active surface cluster (Figure IV-7) could explain the better SCR performances reached for this catalyst in this temperature range. Simultaneously, the formation of additional active sites, by the migration of some copper cations from the surface to exchanged position following the similar temperature window (Figure IV-9), is in agreement with the observed overall enhancement of the redox Cu-SAPO-34-HT performance displayed between 200°C and 400°C Figure IV-12 (B). Following these characteristics, at 425°C, Cu-SAPO-34-HT catalyst



displays a NO conversion even higher than the one of Cu-SAPO-34-IE, demonstrating a higher SCR activity behavior and the complementary effect of the different properties assigned earlier. However, at higher temperatures ( $> 425^{\circ}\text{C}$ ), Cu-SAPO-34-HT displayed a sharp decrease in activity for NO abatement comparing to Cu-SAPO-34-IE catalyst. It is worth noting that the low generation of by-product  $\text{NO}_2$  and  $\text{N}_2\text{O}$ , following reaction (4,5) during the whole temperature range (insert Figure IV-12), demonstrates a good  $\text{N}_2$  selectivity from both catalysts.

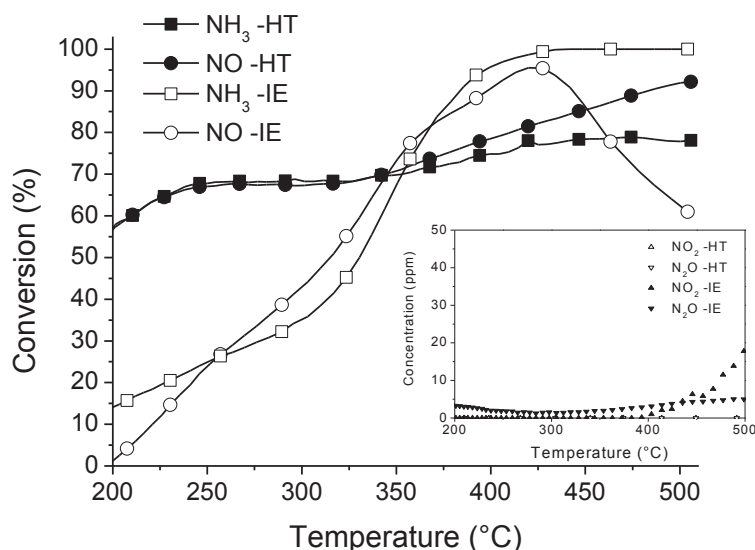


Figure IV-12.  $\text{NH}_3$  and NO conversion vs. temperature for standard  $\text{NH}_3$ -SCR reaction. Cu-SAPO-34-IE catalyst (full symbol), Cu-SAPO-34-HT catalyst (empty symbol) with in insert the corresponding  $\text{NO}_2$  and  $\text{N}_2\text{O}$  concentrations.

As it has been described in the literature, the catalytic conversion of NO and  $\text{NH}_3$  in the  $250 - 425^{\circ}\text{C}$  range is not only due to the simultaneous consumption of  $\text{NH}_3$  and NO via standard  $\text{NH}_3$ -SCR but also by NO and  $\text{NH}_3$  oxidation. Regarding to the specifically performed  $\text{NH}_3$  and NO oxidation reactions (2,3,4) in the temperature range of  $200$  and  $425^{\circ}\text{C}$  displayed in Figure IV-13 (A,C) and (B,D), respectively, the  $\text{NH}_3$  and NO conversion of Cu-SAPO-34-HT do not exceed the conversion of Cu-SAPO-34-IE catalyst for both oxidation reactions. This observation can indicate that these side oxidation reactions had a low impact in the NO conversion during the standard SCR reaction of Cu-SAPO-34-HT catalyst and could have a stronger impact on Cu-SAPO-34-IE catalytic performances, especially between  $300^{\circ}\text{C}$  and  $400^{\circ}\text{C}$ . In contrast,  $\text{NH}_3$  oxidation (Figure IV-13 (A,C)) becomes prevalent at higher temperature than  $425^{\circ}\text{C}$  for Cu-SAPO-34-HT, with simultaneous production of  $\text{N}_2$  and NO, which could explain the clear NO conversion decreases during SCR as shown in Figure IV-12. Such behaviour seems to be exclusive to Cu-SAPO-34-HT catalyst. However, the NO production for Cu-SAPO-34-IE catalyst started at lower temperature (at  $350^{\circ}\text{C}$ ) compared with Cu-SAPO-34-HT ( $400^{\circ}\text{C}$ ). This NO production decreases after

425°C, where the catalyst showed an increased N<sub>2</sub> selectivity (Figure IV-13 (A)), which could be related to the higher selectivity of NH<sub>3</sub> oxidation to N<sub>2</sub>.

This catalytic behaviour can also be associated to the different redox copper species. Regarding the respective NO and NO<sub>2</sub> conversion of both catalysts during NO oxidation (Figure IV-13 (B,D)), the NO<sub>2</sub> production was higher for the catalyst synthesized by ionic exchange than for Cu-SAPO-34-HT in the whole temperature range. Typically, Cu-SAPO-34-IE seems to be more susceptible to form Cu-moieties (such as [Cu-O-Cu]<sup>2+</sup> species), which combined with extra lattice oxygen (ELO), could be active for NO reaction [381]. Therefore, the presence of copper species initially in exchange positions, which were close enough to the zeolite framework to employ such oxygen atoms, allows a high activity. However, the large copper clusters on the surface of Cu-SAPO-34-HT catalyst seems to be less active for this oxidation reaction, regarding their extra lattice position [381–384]. Thus, the higher NO oxidation behaviour of Cu-SAPO-34-IE could be associated to the higher proportion of Cu cations active centres close to support ELO. An observation also in accordance with the NH<sub>3</sub> oxidation behaviour at low temperature of formed copper dimer through monomers assembly [158]. On the other hand, these observations during NO oxidation reaction also suggested that copper active centres of Cu-SAPO-34-HT catalyst were almost not active for this reaction until 400°C. Actually, regarding the two different NO and NH<sub>3</sub> oxidation behaviours between 200°C and 425°C, Figure IV-13 (B, D), the characterized micro-sized clusters, which are the main redox active centres presented on Cu-SAPO-34-HT, do not seem to be implicated in both oxidation reactions as much as the redox centres of Cu-SAPO-34-IE catalyst. Moreover, corresponding to Cu-SAPO-34-HT, the parasitic oxidation of ammonia increase of reaction regime at higher temperature than Cu-SAPO-34-IE catalyst, Figure IV-13 (A,C). Which is in agreement with the difficulty to form ammonia oxidant copper dimers for this catalyst initially deprive of exchanged species, compared with Cu-SAPO-34-IE. At higher temperature, the NH<sub>3</sub> oxidation will mainly be performed by surface copper clusters, which the production of NO can be related [174,286], and copper monomers [158]. Regarding Cu-SAPO-34-HT NH<sub>3</sub> conversion and NO concentration profiles compared with the exchanged catalyst, the oxidation process on micro sized copper cluster is activated at higher temperature than on nano-sized copper clusters and monomers. This phenomenon will give benefit to the NO reduction due to the direct application of NH<sub>3</sub> in the reduction operation (1) better than in parasitic oxidation (2-3). Therefore, the behaviour of both catalysts could be explained regarding their respective copper redox sites and their interaction with ammonia in temperature. These results finally demonstrated the important influence of preparation method and the active site configurations on catalytic performances.

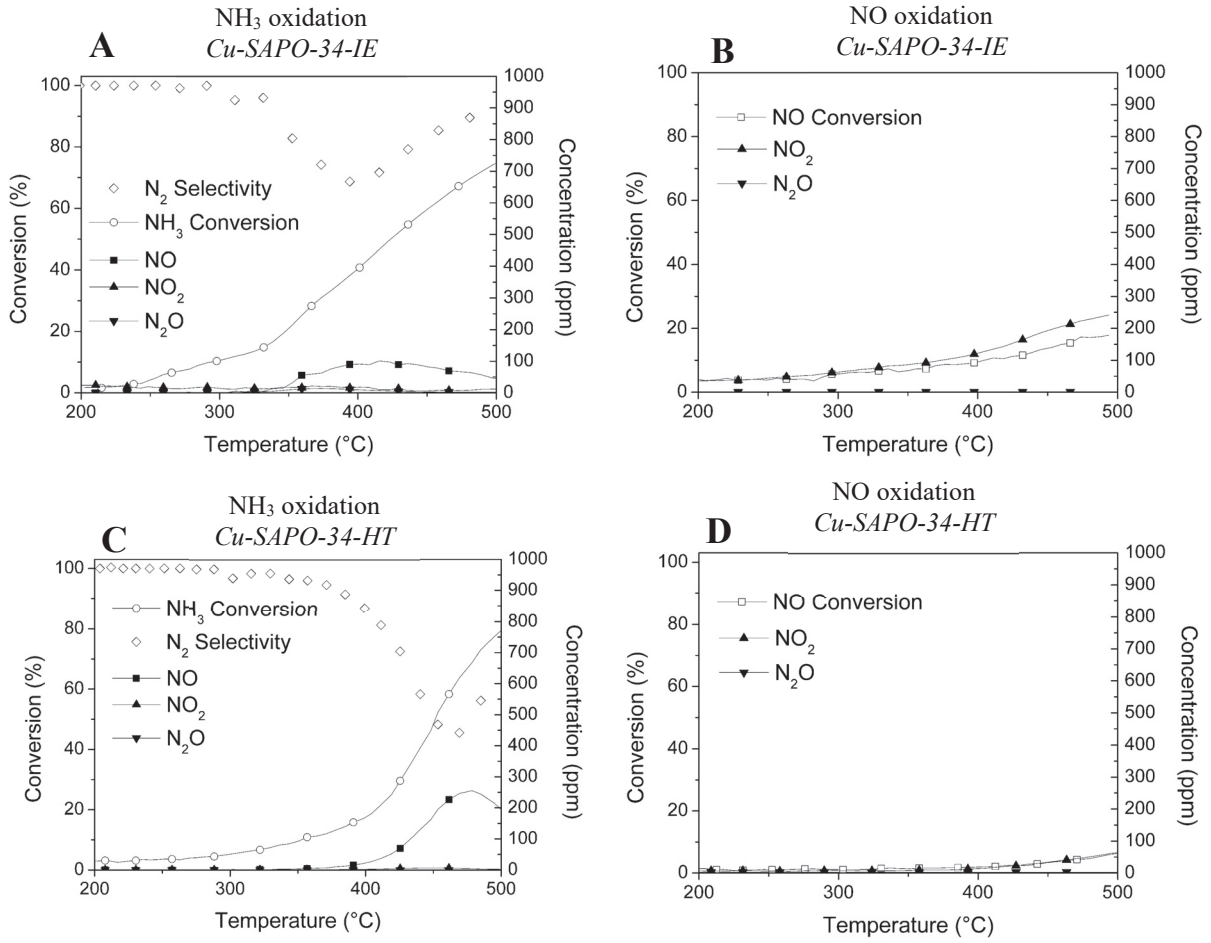


Figure IV-13. NH<sub>3</sub> conversion, N<sub>2</sub> selectivity, N<sub>2</sub>O and NO<sub>2</sub> concentrations vs. temperature for (A) Cu-SAPO-34-IE and (C) Cu-SAPO-34-HT catalysts during NH<sub>3</sub> oxidation reactions. And NO conversion, N<sub>2</sub>O and NO<sub>2</sub> concentrations vs. temperature for (B) Cu-SAPO-34-IE and (D) - Cu-SAPO-34-HT catalysts during NO oxidation reactions.

#### IV-6. Conclusion

Knowing the increasing interest in more simple, fast and effective catalyst synthesis, the different active sites configuration implementation through different preparation procedure as the one-pot method, required better understanding about the different redox active species activities. By different catalyst preparation routes, the role of several copper species and more precisely of surface copper cluster were pointed out and further investigated comparing two distinct catalysts with close chemical support composition SAPO-34. By local observations through HR-TEM instruments and phase identification with XRD, the presence of different configuration of copper sites was revealed, displaying micrometric surface cluster on Cu-SAPO-4-HT and nano sized CuO and Cu<sub>2</sub>O clusters on the top surface of Cu-SAPO-34-IE catalyst. The incorporation of copper cations was shown through Ex-situ Drift analysis in a first time, where, through the different synthesis, the surface Brønsted acid sites remain similar between catalysts at room temperature. In addition, the Cu<sup>2+</sup> exchanged cations were not observed within the Cu-SAPO-34-HT catalyst structure, indicating the particular copper configuration in surface cluster form. This specificity was further confirmed with H<sub>2</sub>-TPR results also where only one sharp signal was observed, corresponding to the reduction of CuO species to Cu<sup>0</sup>. In comparison, Cu-SAPO-34-IE catalyst displayed a large signal through the whole temperature range indicating about the reduction of different copper species. Finally, probe molecules as NH<sub>3</sub> and CO were employed for further active site investigations, where NH<sub>3</sub>-TPD profiles were used for the acid sites strength appreciation. Indeed, TPD measurements informed about the similar storage capacity of both catalyst and support, and about the strong desorption capacity of the Cu-SAPO-34-HT at medium temperature, displaying a similar profile shape with the support H-SAPO-34. These results were extensively corroborated with in-situ DRIFT measurements, where CO probe molecule allowed the demonstration of a copper active sites migration into exchanged position for both catalysts. The combinations of these phenomena enhance the SCR performances, as observed, of the one pot catalyst, particularly between 200°C and 400°C. These different conclusions were correlated with the SCR measured performances for both catalysts, and further investigated by NH<sub>3</sub> and NO oxidation reactions. The reaction regime modification displayed by Cu-SAPO-34-HT corresponded with the active site characterizations, where the delayed NH<sub>3</sub> oxidation seemed to benefit the NO reduction process while the surface nano cluster of Cu-SAPO-34-IE enhanced this parasitic reaction at medium temperature. The mechanism proposed for this activity enhancement is schematized on Figure IV-14 corresponding to Cu-SAPO-34-HT characterization study.

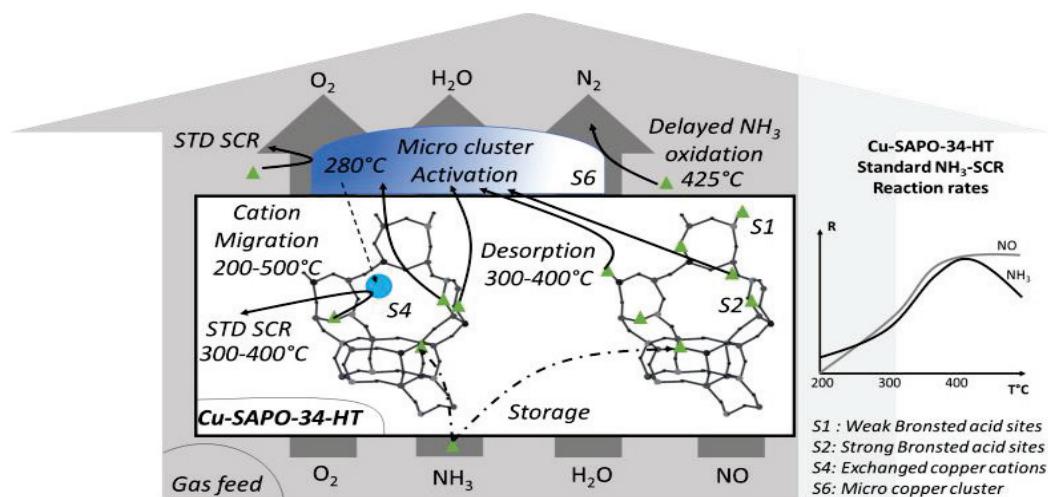


Figure IV-14. Proposed mechanism for Cu-SAPO-34-HT catalyst

In order to summarize the different active site configurations of the investigated Cu-SAPO-34-IMP, -HT and -IE catalysts and their impact on the three-principal investigated operating conditions, the global reactions were depicted as following:

- STD SCR: It was clearly demonstrated that the exchanged cations sites as  $ZCu^{2+}$  species near 6 and 8 MR positions were the most active sites for DeNO<sub>x</sub> abatement at low temperature. Copper cations with lower oxidation state as  $ZCu^+$  were also spotted as active site during STD SCR process. Moreover, it was also observed the participation of surface sites, less selective, but which the micro sized form can be activated increasing the temperature, giving rise a high temperature NH<sub>3</sub> SCR activity. A promoted activity by the stability in temperature of surface nitrates and nitrites, key intermediaries during the DeNO<sub>x</sub> abatement reactional mechanism. At high temperature, the exchanged cations were the main active sites for NH<sub>3</sub> SCR process whereas the surface sites mainly promoted NH<sub>3</sub> oxidation reactions, through NO and N<sub>2</sub> formation mechanism. Concerning Brønsted acid sites, it was observed that their desorption capacity on the whole temperatures window impacted the catalyst performance, where NH<sub>3</sub> can migrate from storage sites to redox ones.
- NH<sub>3</sub> oxidation: Two different regimes were typically observed, informing about two distinct behaviour and active sites activities. At low temperature and in presence of water, the mobility of exchanged species was increased and the formation of active sites copper dimers through their combination was eased. This phenomenon seems to be even more favoured with heterogeneously distributed exchanged sites, where the proximity of packed cations requires a lower mobility to form active complexes. On the contrary, homogeneously distributed exchanged sites requires a higher mobility, so the formation of copper dimers become more difficult due to the spacing between monomers. Consequently, the absence of exchanged sites at low temperature was less favourable for NH<sub>3</sub> oxidation behaviour. Accordingly, impregnated catalysts particularly displayed of an important NH<sub>3</sub> oxidation readily at 200°C until high temperature, where the heterogeneous implementation of exchanged sites promoted the formation of active dimers. By comparison, NH<sub>3</sub> oxidation increased gradually and in a lower extent with the ionically exchanged catalyst, where the process was limited by the difficulties to form

these active species. In accordance, the oxidation on one pot catalyst was much lower thanks to the low possibility to form copper dimer from exchanged sites. The slight activity could correspond to the dimerization of migrated cations and activity of surface sites. At higher temperature, the dimers could split in isolated Cu cations regarding their low stability [158], forming active site for NH<sub>3</sub> oxidation. An active site modification was clearly observed through the different transition in reaction regimes around 325°C for Cu-SAPO-34-IE catalyst and at 425°C for -HT and -IMP catalysts, which the latter is in accordance with the potential proportion of exchanged active sites. Regarding the ammonia oxidation process displayed by catalysts with lower proportion of exchanged sites as Cu-SAPO-34-HT and -IMP, the micro surface clusters and the smaller nano-sized sites also clearly contribute to NH<sub>3</sub> oxidation, which the production of NO rely on.

- NO oxidation: the NO oxidation was accordingly enhanced by exchanged species which a better employ of the oxygen lattice from the SAPO-34 support. In that respect, Cu-SAPO-34-IE favoured the conversion of NO into NO<sub>2</sub> through the temperature window than -HT or -IMP catalysts, in which the proportion of exchanged copper is not enough to perform such oxidation either its configuration.

Finally, the different active site configurations regarding the studied catalysts could be represented with five main configurations, as displayed Figure IV-15. With S1 and S2, which represent both weak and strong Brønsted acid site, regarding NH<sub>3</sub> adsorption capacities; S4 and S5, which were associated to nano-sized and micro surface copper clusters, respectively; and S3 sites corresponding to the exchanged copper cations within the oxygen lattice. Each of them are presented in different proportion as a function of the preparation method. Since the reference catalyst is now assigned as Cu-SAPO-34-IE for its elevated NH<sub>3</sub>-SCR performances representative of state-of-the-art SCR catalyst, the catalyst behavior in different operating condition can be investigated.

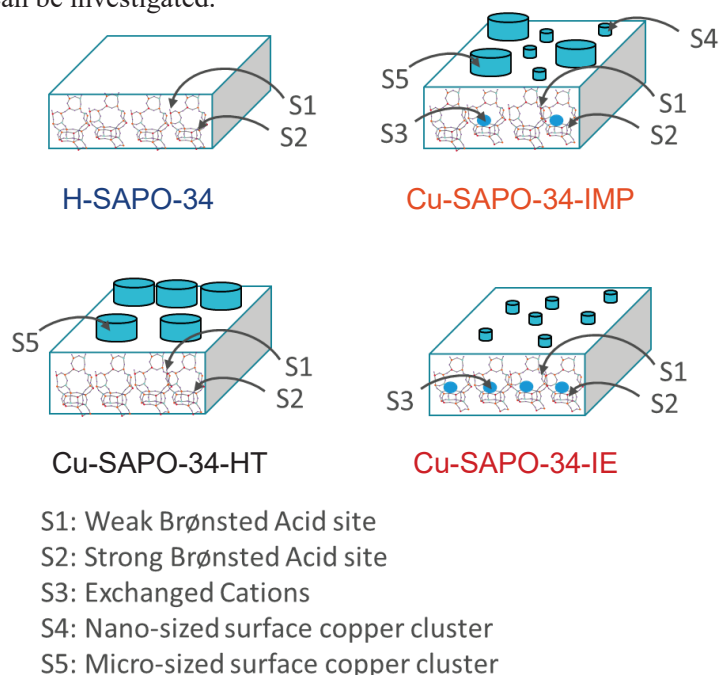


Figure IV-15. Schematization of principal active sites configuration on support H-SAPO-34 and Cu-SAPO-34-IE - HT and -IMP catalysts.



V





# CHAPTER V

## NH<sub>3</sub>-SCR BEHAVIOR INVESTIGATION OF REFERENCE CATALYST: KINETIC APPROACH AND REACTION NETWORK

### V-1. Introduction

After the development of H-SAPO-34 support, displaying the several queries, and the investigation of the different active sites as a function of the preparation method used, the Cu-SAPO-34-IE catalyst synthesized by ionic exchanged protocol was selected as a reference catalyst for the current kinetic study. As described in the last Chapter, the ionic preparation route allows the incorporation of copper cations in exchanged position within the zeolite framework and surface nano copper clusters, sites which their activities will be further investigated here. In that respect, a kinetic study, implemented under several transient and steady state conditions, will be performed for soliciting the catalyst under different dynamic conditions. The obtained experimental kinetic parameters such as the activation energies will be used as initial kinetic parameters during estimation purposes. A mechanism path will be finally proposed according to the catalyst behaviour observations, literature surveys and time resolved catalyst surface observations obtained by in-situ DRIFT analysis. The proposed reactional network will be therefore implemented in the kinetic model, in which the two main requirements are to: 1) represent the standard NH<sub>3</sub>-SCR process, taking into account the presence of water and the different nature of active sites and 2) an optimized number of reactions for not burden the computations.

### V-2. Kinetic studies on SCR reactions for selected reference catalyst

The general Cu-SAPO-34-IE catalyst behaviour was investigated under several conditions in the present chapter (standard NH<sub>3</sub>-SCR, oxidation reactions, Fast NH<sub>3</sub>-SCR...), using the presented experiments design, Figure V-I. This scheme displays the NH<sub>3</sub>, NO and H<sub>2</sub>O concentrations and gas phase parameters variations. Similar experiments were also carried out under different temperature ramps in order to observe the variation of this additional parameter on catalyst response.

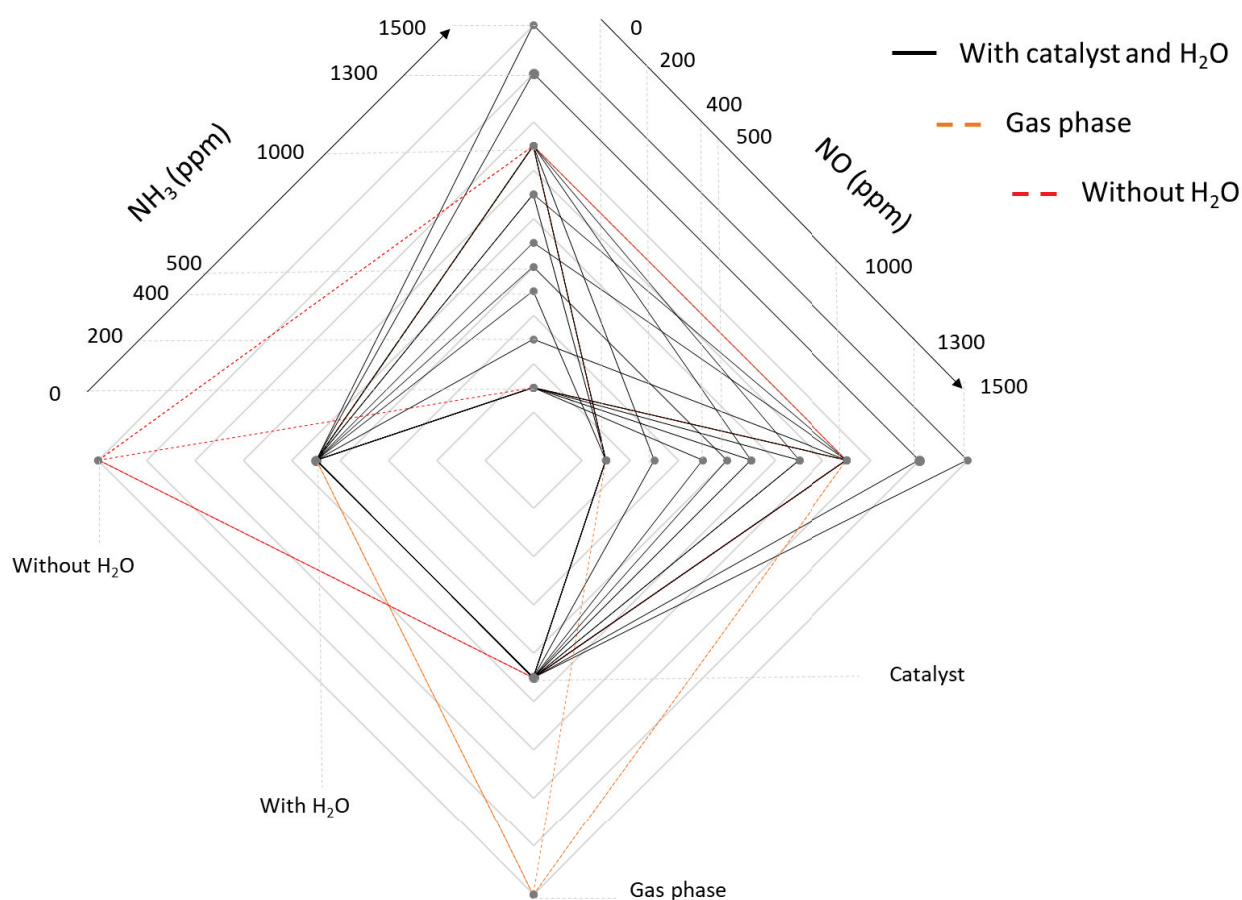


Figure V-1. Experiments Design used for Cu-SAPO-34-IE behavior investigations following NO, NH<sub>3</sub> and H<sub>2</sub>O concentrations with gas phase reactions

#### V-2.1. External and internal mass transfer limitations

The absence of external transfer limitations can be investigated by working at a constant gaseous hourly spatial velocity (GHSV) with different loadings of catalysts (catalytic bed volume) [385,386]. Thus, if the conversion remains constant through the temperature, the apparent reaction rates are not limited by external mass transfer [387]. In that respect, a GHSV was settled at  $142\ 000\ \text{h}^{-1}$ , similar to that currently employed in literature (see Table II-3). Different loadings (0.05 (17.5 mg), 0.1 (35 mg), 0.15 ml (53.5mg)) of Cu-SAPO-34-IE catalyst were used and consequently, the volumetric flow was adjusted in order to conserve the same GHSV. The catalytic feed, containing 1000 ppm of NO, 1000 ppm of NH<sub>3</sub>, 80000 ppm (8%) of O<sub>2</sub> and 40000 ppm (4%) of H<sub>2</sub>O, was maintained constant for all experiments. The obtained conversions are displayed in Table V-1. These results display that NO and NH<sub>3</sub> conversions remained constant around 90% conversion from low to high temperature, meaning that the external diffusion limitations were assumed to not impact the DeNO<sub>x</sub> performances of the catalyst.

Table V-1. NO and NH<sub>3</sub> conversion obtained for standard NH<sub>3</sub>-SCR reaction: External limitation investigation, inlet gas composition: 1000 ppm NO; 80000 ppm (8%) O<sub>2</sub>; 0-4% H<sub>2</sub>O and He as balance; GHSV=142.000h<sup>-1</sup>

GHSV=142 000 h <sup>-1</sup>			
Temperature (°C)	Volume of catalyst bed (ml)	NO conversion rate (%)	NH <sub>3</sub> conversion rate (%)
200	0.15	0.8	0.89
	0.1	0.86	0.86
	0.05	0.96	0.9
250	0.15	0.86	0.92
	0.1	0.92	0.93
	0.05	0.97	0.92
300	0.15	0.87	0.93
	0.1	0.92	0.94
	0.05	0.97	0.95
350	0.15	0.89	0.94
	0.1	0.91	0.98
	0.05	0.98	0.99
400	0.15	0.89	0.96
	0.1	0.92	1
	0.05	0.91	0.99
450	0.15	0.92	0.97
	0.1	0.91	1
	0.05	0.76	0.99
500	0.15	0.91	0.98
	0.1	0.89	1
	0.05	0.63	0.99

On the other hand, the internal mass transfer limitations can be evaluated by measuring the performance stability of catalyst with different granulation in identical operating conditions [385–387]. As the reactive molecule travelled path is function of its diffusion capacity, smaller particles are less concerned by intra crystalline diffusion than the bigger one. As the synthesis of catalyst particle of controlled dimensions requires several protocol adjustments and the identification of synthesis parameters, the catalyst is often pelletized and sieved for obtaining larger catalyst grains. However, the pelletization of such catalyst grains, sometimes employed for intra-diffusion limitation investigation, would clearly lead to a dual porous system with micro pores from the bulk SAPO-34 and macro pores from the interstitial void formed by grain compression [388]. This bimodal pore network could not represent the proper intra crystalline diffusion limitation of the catalyst but the one of the interstices, thus making the pellets kinetic study irrelevant for this specific case. That is why the catalyst particle size itself has to be modified through synthesis in order to observe the impact of such intra crystalline limitations. A similar work was conducted by Hu. et al. with Cu-SAPO-34 catalyst grains of different dimensions varying from 1 to 10 μm [389]. This work was conducted trying to conserve similar active sites types and concentrations through the

different catalysts and demonstrated that the synthesized catalyst are free from pore diffusion control during NH<sub>3</sub> SCR measurements (25mg of catalyst bed, Cu=2%wt., 1500 ml.min<sup>-1</sup> flow rate, 500 ppm of NO and NH<sub>3</sub> with 5% of O<sub>2</sub>) relatively to activation energy at low temperature.

A second technique consists to synthesize similar catalysts with different copper loadings for observing the Turn Over Frequency (TOF) evolution in identical operating conditions [320]. By verifying that external limitations are ruled out, the observation of a decreasing TOF for increasing Cu loadings (i.e. ineffective copper active sites) could represent either different sites activities or, if the latter is ruled out, a reaction controlled by intra particle diffusion limitations. However, the TOF calculation is based on single definition of active sites and because of Cu dimers, oligomers, monomeric and surface clusters can be easily implemented, the conclusion rely on strong assumptions namely: 1) the catalyst is made of only one site, 2) all the sites are identically active and 3) the effective diffusivity decreases linearly with increasing the Cu loading. Aware of these hard considerations, the reaction rates were assumed in this study as free of severe intra diffusional limitations and the measured activation energies (E<sub>a</sub>) will be considered as apparent (E<sub>a,app</sub>) for better convenience.

On the other hand, such limitations, if encountered, would approximately divide the true E<sub>a</sub> value by two [390]. Indeed, as it was demonstrated by R. Aris (1957) [391] for strong internal limitations, E<sub>a,app</sub> would be equal to (E<sub>a,Diffusion</sub> + E<sub>a,chemical</sub>)/2. Considering as first assumption (E<sub>a,Diffusion</sub> ≈ 0-5 kcal with zeolites [392–394]): E<sub>a,Diffusion</sub> << E<sub>a,chemical</sub>, the apparent activation energy would represent in this case only the half of the true energy, falsifying as E<sub>a,app</sub> = E<sub>a,chemical</sub>/2. Further information concerning the detailed demonstration can be also retrieved in following references [390,395]. Consequently, such important gap was not observed during the current study, as the measured activation energies Table V-2 on Cu-SAPO-34-IE concerning STD SCR, NH<sub>3</sub> and NO oxidation are similar to the one displayed in literature on similar catalysts.

#### V-2.2. STD SCR tests performance:

##### V-2.2.1. Gas phase reaction

Before to start with the evaluation of catalytic performance of the denoted reference catalyst under different operating conditions, the possible gas phase reactions, taking place within the gaseous atmosphere in function of the temperature, were evaluated in absence of catalyst. In addition to the gaseous oxidation of NO in NO<sub>2</sub> widely considered in SCR mechanisms [216,232,233,396], under STD SCR conditions, the NH<sub>3</sub> (g) conversion into NO (g) was clearly identified as the main reaction, Figure V-2. Indeed, the ammonia oxidation into NO starts about 350°C, displaying the participation of NH<sub>3</sub> oxidation into NO from the gas phase. These results better comfort in the ammonia incomplete oxidation process, where NO is primarily formed through NH<sub>3</sub> oxidation and reduced by STD SCR reactions. The mechanism was also demonstrated by Piubello et al. [355] over Cu-SAPO-34 catalyst and presents the advantage to consider the NO production from ammonia oxidation which is not systematically the case in literature [153,203,221]

neither in kinetic model [224,232,233], in which the complete NH<sub>3</sub> oxidation in N<sub>2</sub> is preferentially considered.

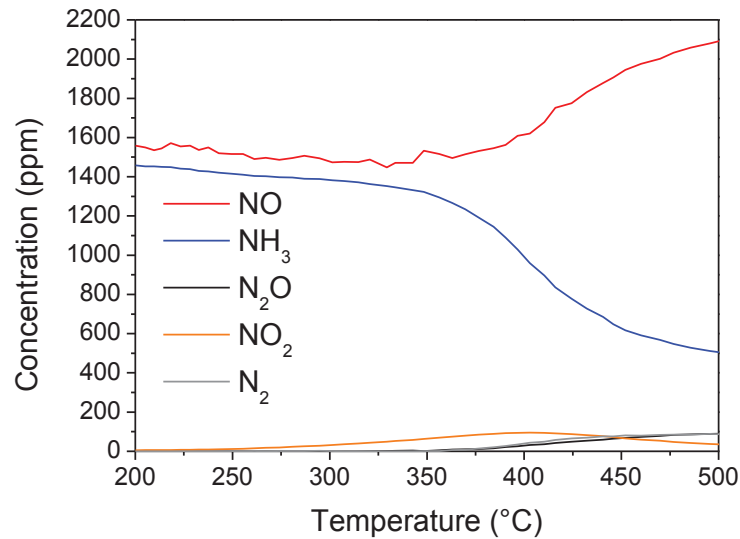


Figure V-2: STD NH<sub>3</sub>-SCR reaction without catalyst. Inlet gas composition: 1500 ppm NH<sub>3</sub> and NO; 80000 ppm (8%) O<sub>2</sub>; 40000 ppm (4%) H<sub>2</sub>O, with He as gas balanced; total flow= 10 L/h;

#### V-2.2.2. Partial reaction orders and Activation energy

Once the external mass transfer limitation ruled out, the definition of an accurate mass balance expression has to be made prior to the catalyst kinetic study for reaction rate calculations. In that respect, the kinetic parameters acquisition will rely on the employed experimental reactor and operating conditions. Typically, two expressions can characterize the observed mass balance, the Plug Flow Reactor (PFR) and the Continuously Stirred Tank Reactor (CSTR) model.

Under the constraints of following assumptions: 1) A constant reactor section, 2) The fluid is well mixed in radial and angular directions, 3) Fluid velocity depends only of the axial position within the tube, 4) Lack of inter and intra diffusion resistance, 5) Constant density of the fluid and a 6) Constant flow; A large packed bed modeled by a PFR at steady state, will be represented with a mass balance defined as following:

$$\sum_j \nu_j R_j dV_s = dF'_i(x) \text{ where with } dF'_i(x) = F_{i,0} dX_i \text{ for a unique reaction gives:}$$

$$R_j = F_{i,0} \frac{dX_i}{dV_s} \quad (1)$$

With the molar flow rate  $F'_i$  of  $i^{\text{th}}$  specie (mol. s<sup>-1</sup>), a volume element of solid  $dV_s$  (m<sup>3</sup>),  $X_i$  the conversion ratio and  $R_j$  the reaction rates of  $j$  reaction (mol.m<sup>-3</sup>.s<sup>-1</sup>).

As depicted by Eq. 1, differential conditions will be thus required for the reaction rates determination. In the case of low conversion conditions, ( $X_i < 10\%$ ), the relation between the inlet and outlet variations are assumed linear. In that case, the mass balance can be thus approximated by:

$$R_j = F_{i,0} \frac{\Delta X_i}{\Delta V_s} \quad (2)$$

On the other hand, the mass balance Eq 2. can be rewritten with the assumption of homogenous concentrations in a constant reactor volume and with constant density ( $Q_{in} = Q_{out}$ ) as:

$$R_j = F_{i,0} X_i \quad (3)$$

In that respect, Eq. 3 represents the mass balance expression for a CSTR model, an assumption particularly interesting where wide  $X_i$  can be observed for the reaction rate determination.

However, the assumption of a CSTR model for a packed bed reactor can be made following two cases: the first one for low conversion experiment in the case of large packed bed as seen previously (Eq. 2) or for a thin packed bed whatever the conversion rate. The latter will be demonstrated in a dedicated section Chapter VI, where the experimental bench behavior was investigated prior to model establishment and was assumed as behaving like a CSTR. The reader is invited to consult the section VI-2.2 of the manuscript for a detailed description of the experimental reactor. Thus, assuming the CSTR behavior, the reaction rates can be obtained in more accessible conditions, through wider conversion rates, necessary to the partial order and activation energy estimations regarding the elevated activity from the reference catalyst readily at low temperature.

Thus, the different reaction orders of the principal SCR process were verified, according to the standard reaction rate expression defined as:

$$r_{STD\ SCR} = k C_{NO}^\alpha C_{NH_3}^\beta C_{O_2}^\gamma \quad (4)$$

With  $\alpha$ ,  $\beta$  and  $\gamma$  the respective reaction order of NO, NH<sub>3</sub> and O<sub>2</sub>.

For the partial order determination, the different reactants concentrations were set constants one after the others. In that respect,  $\alpha$  was estimated with  $C_{NH_3}^{in}$  constant and  $\beta$  with  $C_{NO}^{in}$  constant, in order to measure an apparent rate ( $k_{app}$ ) as  $r_{STD\ SCR} = -d C_{NO} / dt$ , assuming that the concentration variation of the constantly injected reactant are negligible regarding the concentration variation of the second one, allowing a constant  $k_{app}$ . The pressure was kept constant ( $P_{tot} = 1\ atm$ ) and the respective partial orders were verified at 200°C, 250°C, 300°C and 350°C in isothermal mode. Above 350°C, additional reactions as parallel oxidations can occur and modify the assumed apparent first order of STD SCR. In that respect following the same procedure as Brandenberger et al. during their kinetics investigation of SCR reactions [397], by reporting the STD SCR reaction rates vs. initial reactant concentrations in natural logarithm scale, the

apparent reactional order relative to NO was determined through the slope of Eq 5 and the one of NH<sub>3</sub> by Eq. 6:

$$\ln(r_{\text{STD SCR}}) = \ln(k_{\text{app}})_{\beta} + \alpha \ln(C_{\text{NO}}) \quad (5)$$

$$\ln(r_{\text{STD SCR}}) = \ln(k_{\text{app}})_{\alpha} + \beta \ln(C_{\text{NH}_3}) \quad (6)$$

Where the first term  $\ln(k_{\text{app}})$  englobes the reaction constant, constant concentration of fixed reactant and corresponding partial order.

Accordingly with the reaction order displayed through Figure V-3 (A and B), the NO conversion increases with rising NO (A) which is also the case with NH<sub>3</sub> (B). Here, the different straight lines overlap due to the important NH<sub>3</sub> and NO conversion rates displayed by the catalyst, where at 200°C already, NO and NH<sub>3</sub> are both consumed up to 80%. As the temperature can be hardly investigated below 200°C due to nitrate precipitation risks, it will be crucial for the determination of activation energy to respect the differential regime during the kinetic measurements. Finally, according to the estimated partial order Figure V-3 (A and B), the reactional rate expression of STD SCR was depicted as:

$$r_{\text{STD SCR}} = k_{\text{app}} C_{\text{NO}} C_{\text{NH}_3} \quad (7)$$

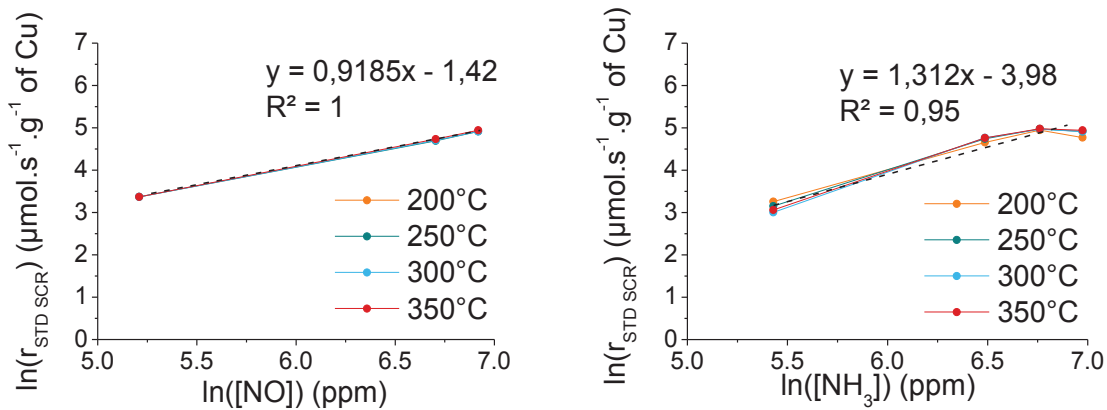


Figure V-3. Partial reaction order determination of NO (A) and NH<sub>3</sub> (B) according with differential method.

Concerning O<sub>2</sub>,  $\gamma$  partial order was considered as equal to 0 according with the order degeneration method, also known as Ostwald isolation principle [398]. Indeed, the large excess of oxygen imply slight variation of its concentration only, thus the corresponding rate dependences is neglected and  $\gamma=0$ . Moreover, knowing that NH<sub>3</sub> typically reacts from an adsorbed state, it is usually assumed in literature [397,399,400] that the reaction rate (Eq. 7) can be better rewritten as:

$$r_{\text{STD SCR}} = k_{\text{app}} C_{\text{NO}} \theta_{\text{NH}_3} \quad (8)$$



With  $\theta_{\text{NH}_3}$  the ammonia coverage defined, in equilibrium conditions, as following the Langmuir isotherm:

$$\theta_i = \frac{K_j C_j}{1 + \sum_{j=1}^n K_{j'} C_{j'}} \quad (9)$$

And  $K_j$ ,  $K_{j'}$  the adsorption constant (-) and  $C$  the concentrations of component  $j$  and  $j'$  respectively ( $\text{mol.m}^{-3}$ ).

In the literature, the STD SCR reaction order is assumed equal to one as “ $r_{\text{STD SCR}} = k_{\text{app}} C_{\text{NO}}$ ”, which typically comes from the consideration that at low temperature and low conversion, the catalyst surface is considered as completely covered ( $\theta_{\text{NH}_3}=1$ ) and the reaction rate appears almost independent of the NH<sub>3</sub> concentration [98,397]. In that respect, knowing the concentration dependency of the reaction rate thanks to the applied simplification, the reaction constant can be examined through the variation of the reaction rate  $r_{\text{STD SCR}}$  in temperature by the Arrhenius relation for the estimation of apparent activation energy [398,401]:

$$k_{\text{app}} = k_0 e^{\frac{-E_{\text{aapp}}}{RT}} \quad (10)$$

With  $k_0$  the pre-exponential coefficient (dimensions depending on reaction rate expression),  $E_{\text{aapp}}$  the apparent activation energy ( $\text{J.mol}^{-1}$ )  $R$  the ideal gas constant ( $\text{J.mol}^{-1}.\text{K}^{-1}$ ) and  $T$  the temperature (K).

$E_{\text{aapp}}$  was therefore determined within low conversion rate conditions ( $X_i < 40\%$ ) Figure V-4, assuming that  $[\text{NO}]_{\text{bed}} = [\text{NO}]_0$  is homogeneously distributed within the whole catalyst bed volume. A condition further verified as the reactor is considered to behave like a CSTR. The different assumptions made for the consideration of this regime are: 1) a low conversion rate, 2) no concentration gradient, 3) negligible reactional heat released, 4) no gas bypass in catalyst bed and 5) no catalyst deactivation. Verifications which were made for the different estimation of apparent activation energies.

Thus, the estimated STD SCR activation energy of  $E_{\text{aapp}} = 56 \text{ kJ.mol}^{-1}$  in Figure V-4 is in accordance with other kinetic analysis on similar catalysts as determined by Gao. et al. ( $E_a = 57.5 - 90 \text{ kJ.mol}^{-1}$ ), assuming as main active sites isolated cations  $\text{ZCu}^{2+}$ . Other literatures presented close estimation results on copper zeolites as Wang. et al. ( $E_a = 35.8 - 39.8 \text{ kJ.mol}^{-1}$ ) or Kwak. et al. ( $E_a = 41.2 \text{ kJ.mol}^{-1}$ ) for instance [161,173,256]. The estimated  $E_{\text{aapp}}$  are reported in Table V-2 and compared with literature for more convenience.

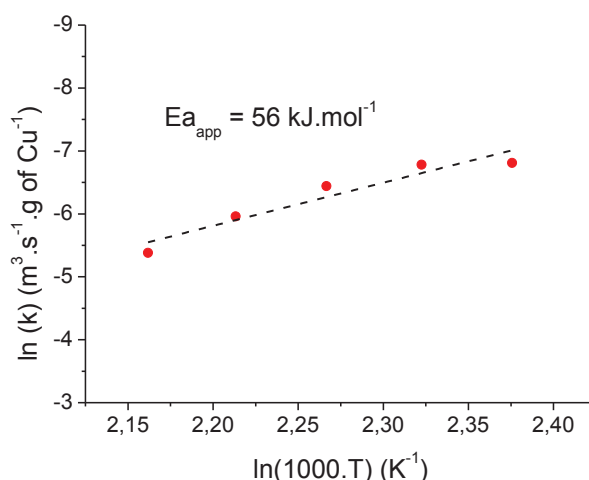


Figure V-4. Arrhenius plot of the apparent NO reaction rate constants from 160°C to 200°C

### V-2.2.3. Influence of water

In Figure V-5 is displayed the catalytic performances under standard NH<sub>3</sub>-SCR conditions for Cu-SAPO-34-IE reference catalyst, with an inlet mixture containing 1000 ppm of NO and 1000 ppm of NH<sub>3</sub>, 80000 ppm (8%) of O<sub>2</sub>, 40000 ppm (4%) of H<sub>2</sub>O and He as a gas balance. All gas concentrations are represented in this Figure V-5, including the N<sub>2</sub>O and NO<sub>2</sub> concentrations. Indeed, the low N<sub>2</sub>O production is one of the interesting characteristics of Cu-SAPO-34 catalyst, compared with Cu-BEA or Cu-SSZ-13 catalysts in similar conditions, where not negligible amount of N<sub>2</sub>O is observed [402]. On the other hand, the low NO<sub>2</sub> concentration slightly detected can either be due to the backward thermodynamic NO oxidation in gas phase [403,404] or its implication in NO consumption by Fast reaction ( $4 \text{ NH}_3 + 2 \text{ NO} + 2 \text{ NO}_2 \rightarrow 4 \text{ N}_2 + 6 \text{ H}_2\text{O}$ ). Indeed, the second hypothesis, which will be studied in a dedicated section below, could represent the catalytic activity under Fast SCR reaction or, following the mechanism, nitrite formation and reduction on the catalyst surface [120,405,406]. Moreover, comparing the catalyst performance at low temperature between 200°C and 350°C with Figure V-5 (A) and without water Figure V-5 (B), it is clear that H<sub>2</sub>O influences the overall NO<sub>x</sub> consumption. In presence of water, the NO<sub>x</sub> concentration is stable until 350°C, consuming NH<sub>3</sub> and NO in equimolar proportion and producing N<sub>2</sub> as a main product. However in the absence of water, the catalytic activity was decreased by 20%, as depicted by the conversion Figure V-6, demonstrating that H<sub>2</sub>O had an interaction with the catalyst active sites and an important implication in the SCR process. This phenomena was observed in several studies for SCR reactions [222,407–409]. Indeed, the H<sub>2</sub>O adsorption and desorption dynamic within the catalyst could greatly determine its performances at low temperature knowing that hydrated copper could represent the key active site as previously described [223,407]. H<sub>2</sub>O molecules could directly interact with copper cations favoring the intermediates formation. But the complete implication of water is still unclear in literature [223,298,320,333,410,411]. Some of the hypothesis mentioned in literature are the following: H<sub>2</sub>O molecules could adsorb on redox active sites due to its capacity to oxidize the metal sites [223,298], the cations could endure hydrolysis effect [412], strong adsorption competition with NH<sub>3</sub> [410,411] or

even allowing cations mobility promotion [320]. Indeed, H<sub>2</sub>O is also described as an inhibitive molecules in other kinetics studies such as NO oxidation reaction [58,413], displaying a negligible or lower impact in STD SCR reaction [226]. Regarding the water promoting effect Figure V-5, the enhanced performance at low temperature could be related to the formation of hydroxyl on active redox centers as it can be proposed by Gao et al. [158] and further investigated through IR spectroscopy [157,414] for the formation of reactive nitrites and nitrates ad-species. Both intermediates are largely considered as key intermediates during NO<sub>x</sub> abatement, which the proportion greatly depend on the inlet composition [190,208,216].

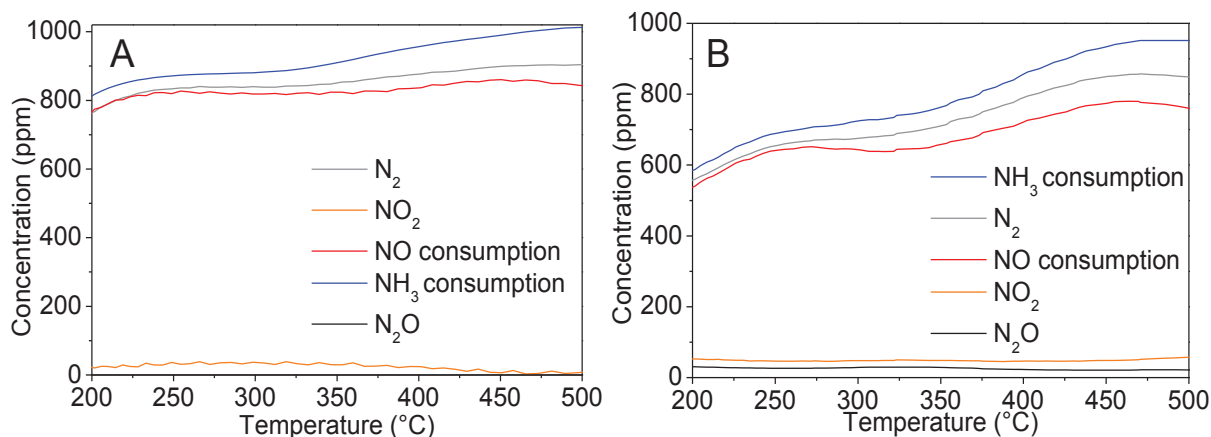


Figure V-5: STD SCR performance from 200°C to 500°C for Cu-SAPO-34-IE reference catalyst (A) with water and (B) without water. Catalyst weight: 35mg; Inlet gas composition: 1000 ppm NO; 80000 ppm (8%) O<sub>2</sub>; 0-4% H<sub>2</sub>O and He as balance; total flow= 10 L/h; GHSV=142.000h<sup>-1</sup>

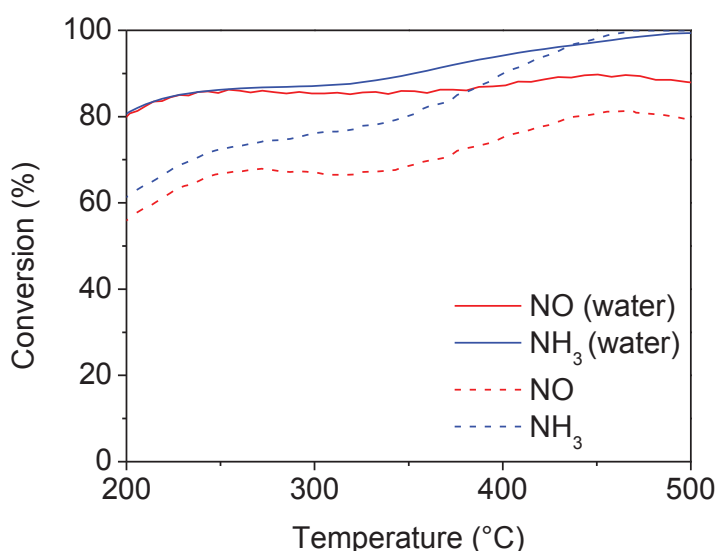


Figure V-6: NH<sub>3</sub> and NO conversion with and without water according to Figure V-5 A and B.

Moreover, in presence of water, NH<sub>3</sub> conversion increases starting at 350°C, while NO conversion remains stable until 500°C, which is a direct consequence of the parasitic oxidation of NH<sub>3</sub> at high temperature. Without water, the oxidation of NH<sub>3</sub> is even more pronounced and starts at relatively lower temperature (around 300°C), Figure V-5 (B). Without the promotion effect of water, the NH<sub>3</sub> oxidation can better competes with the STD SCR reaction. If at higher temperature copper sites are not expected to be hydrated, the comparison of Figure V-5 (A and B) indicates that wet conditions could impact the catalyst surface even at high temperature.

#### V-2.2.4. Influence of feed composition on catalytic activity and selectivity

In order to evaluate the influence of feed composition over the catalytic performances, the reference catalyst was tested under different concentrations (500/500, 1300/1300 and 1500/1500 ppm) of NH<sub>3</sub> and NO in standard SCR conditions. The catalytic tests were performed in stepwise heating (each 100°C) by a heating ramp of 10°C.min<sup>-1</sup>, from 200°C to 500 °C with isothermal period of 30 min. As shown on Figure V-7, the NO reaction rates increase with the inlet NO and NH<sub>3</sub> concentrations. No limitations were observed increasing the inlet concentrations, which is in accordance with the postulated early assumptions concerning the absence of hard intra-crystalline diffusion resistance. Moreover, the N<sub>2</sub> selectivity remains constant around 90% from 200°C to 500°C, which corroborate the greater efficiency of this reference Cu-SAPO-34-IE catalyst for DeNOx abatement

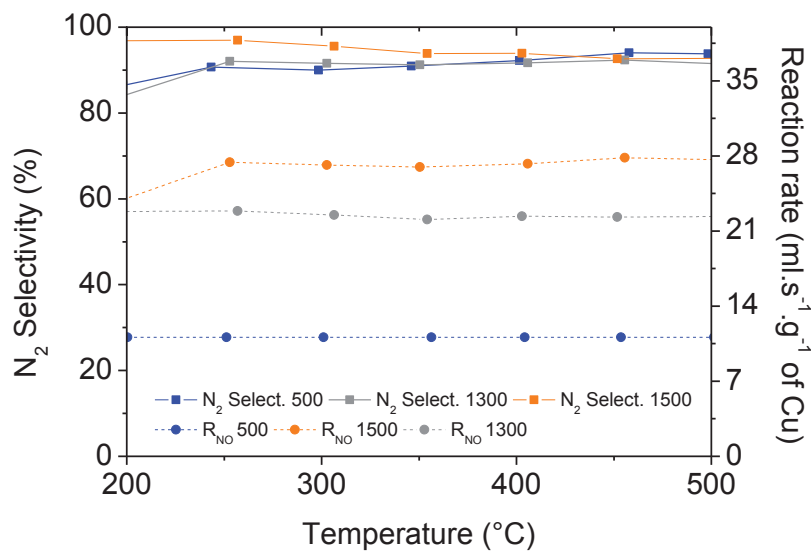


Figure V-7: Influence of different initial concentration of NO and NH<sub>3</sub> in STD NH<sub>3</sub>-SCR catalytic performances: N<sub>2</sub> selectivity and corresponding reaction rate as a function of the reaction temperature.

Catalyst weight: 35mg; inlet gas composition: 500/500, 1300/1300 and 1500/1500 ppm of NO/NH<sub>3</sub> ; 80000 ppm (8%) O<sub>2</sub>; 40000 ppm (4%) H<sub>2</sub>O and He as a balance; total flow= 10 L/h; GHSV=142.000h<sup>-1</sup>

V-2.2.5. NH<sub>3</sub> inhibition effect

By varying the temperature input in a different manner, another important phenomenon can be studied during the STD SCR process. Thus, Figure V-8 (A) displays the catalyst behaviour under stepwise heating (each 50°C) from 200°C to 500°C with a heating ramp of 10°C.min<sup>-1</sup> and with an isothermal period of 60 min. At low temperature during each temperature ramp, prior to NH<sub>3</sub> oxidation impact at 350°C, the NH<sub>3</sub> concentration sharply increases and the formation of N<sub>2</sub> consequently arises. This phenomena is a direct consequence of the NH<sub>3</sub> inhibition impact on SCR performances, where the desorbed NH<sub>3</sub> from redox sites allows a better NO reduction through SCR and formation of N<sub>2</sub> [415,416]. Indeed, when ammonia desorbs, an extended number of redox active sites are readily available for the formation and adsorption of key intermediaries such as nitrites species, which their reduction increases the N<sub>2</sub> production. However, these sharp NH<sub>3</sub> concentration uptakes are not only due to NH<sub>3</sub> desorbing from redox sites, but also to the NH<sub>3</sub> desorption from weak Brønsted acid sites and physisorbed state [234]. Actually, the NH<sub>3</sub> proportion desorbing from redox sites is directly related to the N<sub>2</sub> concentration uptake as the NO conversion is enhanced by the higher proportion of free redox sites. And regarding the slight N<sub>2</sub> concentration increases (N<sub>2</sub> concentration peaks on Figure V-8), even with the assumption of one redox site freed by one desorbed NH<sub>3</sub> (knowing that until 4 NH<sub>4</sub> can bound with one copper site [157,417]) allowing the production of one N<sub>2</sub>, the proportion of released copper sites is much lower than the one of weak Bronsted acid sites. In that respect, only a small proportion of desorbed NH<sub>3</sub> observed through the peaks Figure V-8 are responsible of the inhibition the STD SCR process, the main proportion coming from the storage sites. The improved NO consumption is more evidenced in Figure V-9, within the first minutes after the NH<sub>3</sub> cut-in, where the NO consumption is clearly improved until redox site saturation. Regarding the inhibiting effect of NH<sub>3</sub>, a lower proportion of adsorbed species could enhance the STD SCR process thus evidencing a hypothetical ideal ratio between NH<sub>3</sub> and NO concentrations. Note that Figure V-8 (B) displays the steady state conversion of NH<sub>3</sub> and NO for each investigated temperature in Figure V-8 (A). The overall catalytic behavior was similar with Figure I-5 during light-off tests, further demonstrating the feasibility of both methods, stepwise heating and light-off tests.

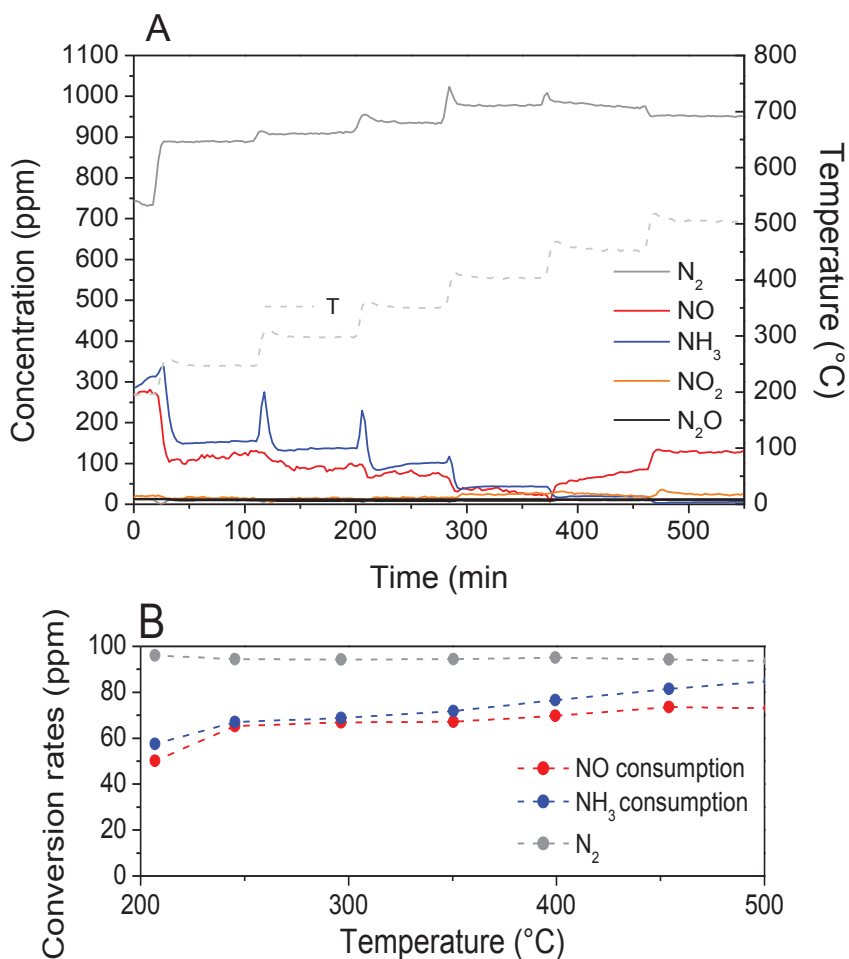


Figure V-8: STD SCR performance from 200°C to 500°C for reference Cu-SAPO-34-IE catalyst in (A) stepwise heating and (B) the corresponding conversion. Catalyst weight: 35mg; inlet gas composition: 1000 ppm NO and 1000 ppmNH<sub>3</sub>; 80000 ppm (8%) O<sub>2</sub>; 40000 ppm (4%) H<sub>2</sub>O and He as a balance; total flow= 10 L/h; GHSV=142.000h<sup>-1</sup>

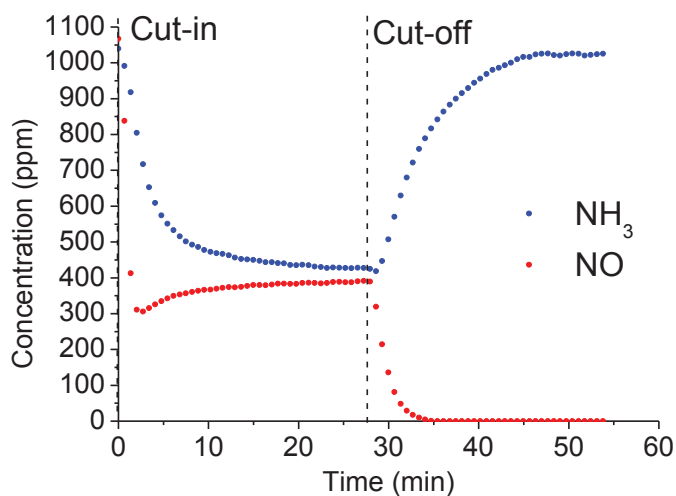


Figure V-9: NH<sub>3</sub> cut in/off at 200°C for NH<sub>3</sub> inhibition verification. Catalyst weight: 35mg; inlet gas composition: 1000 ppm NH<sub>3</sub> and 1000 ppm NO; 80000 ppm (8%) O<sub>2</sub>; 40000 ppm (4%) H<sub>2</sub>O and He as a balance; total flow= 10 L/h; GHSV=142.000h<sup>-1</sup>

V-2.3. Parallel oxidation: a) NH<sub>3</sub> oxidation reaction

After having described the general behavior of the reference Cu-SAPO-34-IE catalyst, the specific case of the parasitic ammonia oxidation was investigated. First, the presence of potential ammonia oxidation in gas phase was observed Figure V-10, in a wet feed of NH<sub>3</sub> in presence of oxygen (1400 ppm NH<sub>3</sub>, 80000 ppm (8%) O<sub>2</sub> and 40000 ppm (4%) H<sub>2</sub>O in He). As depicted, NO selectivity was higher than the one of N<sub>2</sub>, indicating an uncomplete NH<sub>3</sub> oxidation according to the following reactions:



Compared with the presence of catalyst Figure V-12 (A), these gas phase results indicate that only the catalyst redox sites can provide a sufficient decrease of the energy barrier for a complete formation of N<sub>2</sub>. Furthermore, this observation is in accordance with the gas phase STD SCR reaction, Figure V-2, where the NH<sub>3</sub> was oxidized into NO at a similar temperature (about 350°C).

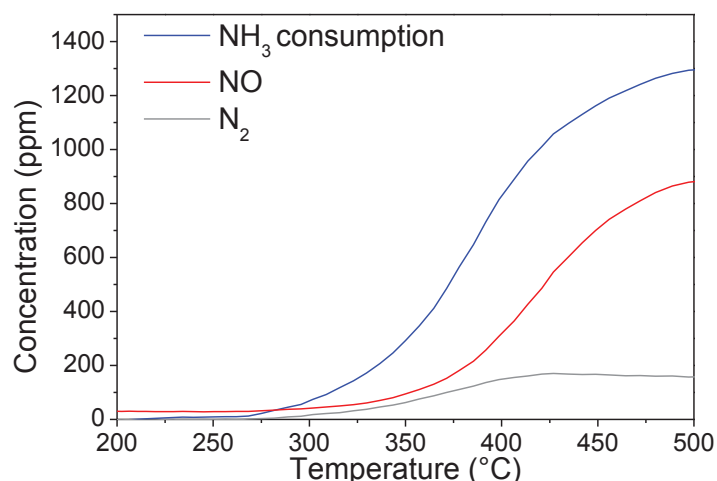
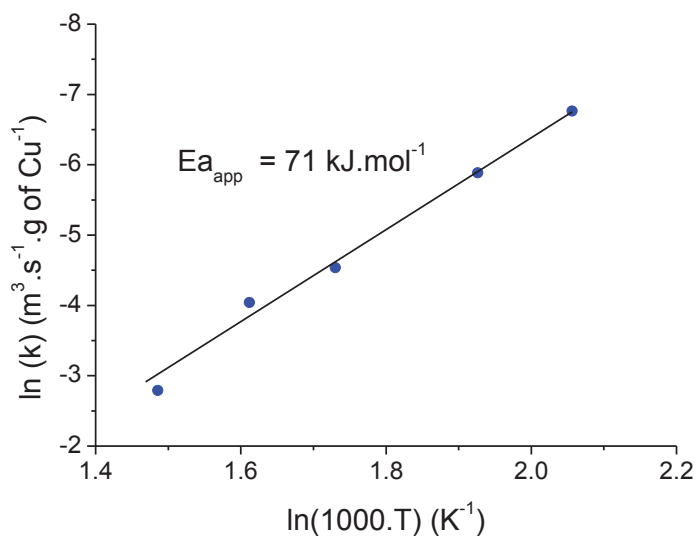


Figure V-10: Gas phase NH<sub>3</sub> oxidation. Inlet gas composition: 1400 ppm NH<sub>3</sub>; 80000 ppm (8%) O<sub>2</sub>; 40000 ppm (4%) H<sub>2</sub>O and He as a balance; total flow= 10 L/h; Note that no N<sub>2</sub>O nor NO<sub>2</sub> were detected

After gas phase investigation, by assuming a similar method as above used for the estimation of  $E_{a,app}^{STD\ SCR}$ , the first order reaction was studied at low conversion between 250°C and 380°C considering the global oxidation reaction between NH<sub>3</sub> and O<sub>2</sub> (11) to be the main one (See Figure V-12 (A)). The linear plot Figure V-11 shows an apparent activation energy of 71 kJ.mol<sup>-1</sup>, similar to that obtained in literature as reported Table V-2. The close values between  $E_{a,app}^{STD\ SCR}$  and  $E_{a,app}^{NH_3\ oxy}$  demonstrate the competition between both reactions, which can take place in catalyst surface as well as the important unselective impact of this oxidation on the catalyst performances.

Table V-2. Cu-SAPO-34-IE E<sub>a,app</sub> measured for STD SCR, NH<sub>3</sub> and NO oxidation reactions compared to literature.

	Experimentally estimated		Literature				
	Activation Energy (E <sub>a</sub> ) (kJ.mol <sup>-1</sup> )	Temperature (°C)	Activation Energy (E <sub>a</sub> ) (kJ.mol <sup>-1</sup> )	Temperature (°C)	Presence of water	References	Reactor
<b>STD SCR</b>	56	160-200	40-80	100-200	2.5%	[158]	PFR
			66	120-180	10%	[418]	-
			41	150-250	10%	[161]	Fixed bed
			45-90	110-180	2.5%	[256]	Fixed bed
			38	150-225	0%	[176]	Fixed bed
			41	140-200	10%	[173]	Fixed bed
<b>NH<sub>3</sub> oxidation</b>	71	250-380	80	140-220	0%	[176]	Fixed bed
			88	300-400	0%	[419]	Fixed bed
			110-140	175-250	2.5%	[158]	PFR
			62	400-470	2.5%	[420]	PFR
<b>NO oxidation</b>	42	200-350	31	180-350	0%	[421]	-
			56	290	2%	[226]	PFR
			58	300-400	10%	[161]	Fixed bed

Figure V-11. Arrhenius plot of the apparent NH<sub>3</sub> reaction rate constants from 200°C to 350°C (X<15%) in NH<sub>3</sub> oxidation reaction

Moreover, the NH<sub>3</sub> oxidation was studied in both dry and wet conditions in order to evaluate its influence on product selectivity, Figure V-12 A and B. Note that any amount of N<sub>2</sub>O nor NO<sub>2</sub> were produced during these catalytic tests. As during the STD SCR test performances Figure V-5 A and B, ammonia oxidation is detected at 350°C in presence of water, and at relatively lower temperature in dry



condition. Indeed, in specific oxidation condition and in presence of water NH<sub>3</sub> oxidation produces N<sub>2</sub> and NO in parallel, according to (11) and (12) reactions.

However, at higher temperature, the NH<sub>3</sub> oxidation into NO (12) decreases, where the complete oxidation of ammonia into N<sub>2</sub> (11) becomes the main reaction. The observation of NO production with the increasing temperature is in accordance with the obtained activation energies, where  $E_{a_{app}}^{NH_3\ oxy}$  is more important than  $E_{a_{app}}^{STD\ SCR}$ . On the other hand, in dry condition, the NO concentration detected in the outlet was lower, which could indicate that the produced NO from surface sites is faster consumed through SCR operation, or, the N<sub>2</sub> selectivity toward NO is decreased and the NO formation mechanism in presence of water is favored. This assumption cannot be directly discerned and requires further investigation at the redox sites scale, where models with Density Functionnal Theory (DFT) for instance, could bring further insight by the production of reliable energy-minimized structural representation of copper sites interacting with NH<sub>3</sub>, O<sub>2</sub> and H<sub>2</sub>O molecules.

Comparing both Figure V-12 A and B, two different regimes take place starting around 350°C, where the complete conversion of NH<sub>3</sub> in N<sub>2</sub> (11) is favored at high temperature without water, a characteristic also observed during dry STD SCR test performances described above. These results seem to be in accordance with the speculated mechanism of dimer formation proposed by Beale et al. [412]. Indeed Figure V-12 (A), the distribution of exchanged cations seems sufficiently homogeneously dispersed through the zeolite lattice to not promptly form copper dimers at low temperature, even with an enhanced mobility favored in presence of water. At higher temperature, the dimers dissociate in monomer, species activated in temperature regarding the reaction regimes difference. However, compared with the high temperature reaction regime observed without water Figure V-12 (B), where the active monomers are free from any interaction with water molecules, the increased conversion (better visible Figure V-13) could inform about an inhibition effect of water with monomer active sites at elevated temperature.

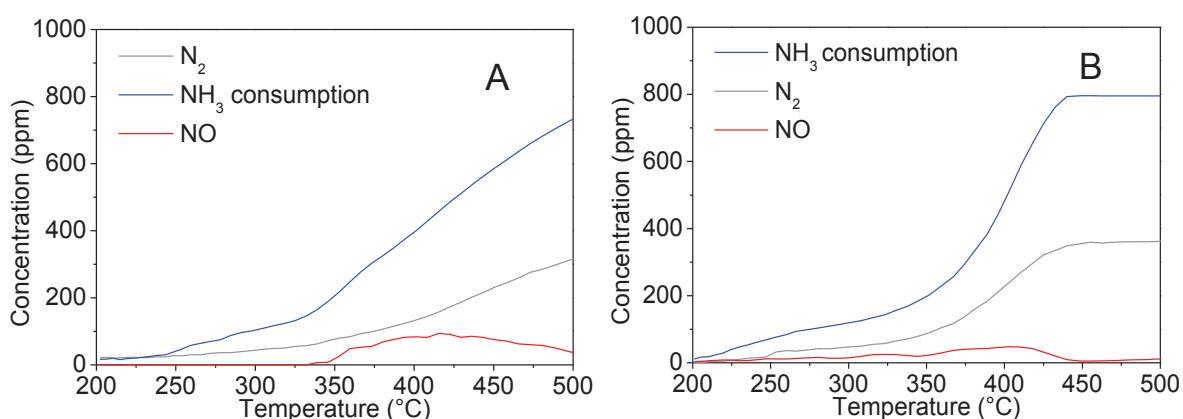


Figure V-12: NH<sub>3</sub> oxidation reaction. Inlet gas composition: 1000 ppm NH<sub>3</sub>; 80000 ppm (8%) O<sub>2</sub>; 0-40000 ppm (4%) H<sub>2</sub>O and He as a balanc; total flow= 10 L/h; GHSV=142.000h<sup>-1</sup>

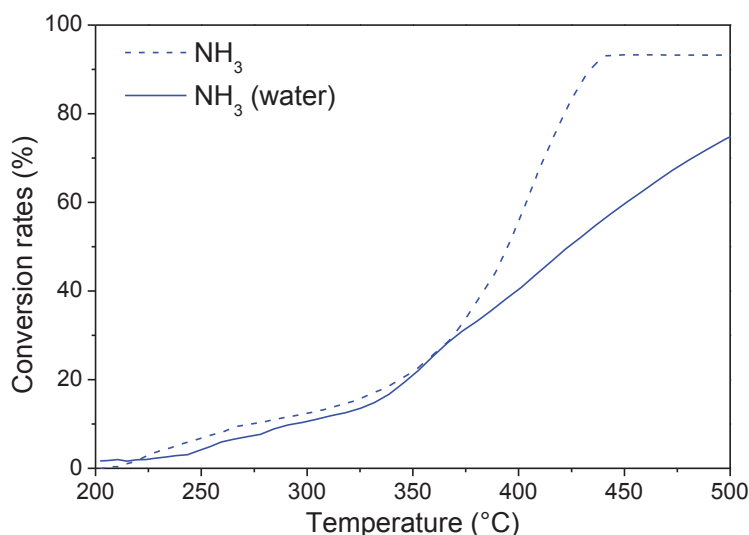


Figure V-13: NH<sub>3</sub> conversion rates with and without water according to Figure V-12.

#### V-2.4. Parallel oxidation: b) NO oxidation reaction

NO oxidation reaction was also separately studied regarding its importance in NO<sub>2</sub> production at elevated temperature accordingly with thermodynamic equilibrium, and its consequent impact via FAST SCR reaction and interaction with catalyst surface. An important implication to take into consideration regarding the high temperature phenomena as the parasitic NH<sub>3</sub> oxidation and the NH<sub>3</sub> desorption from the surface.

Indeed, according with adsorption and desorption dynamic of NH<sub>3</sub> molecules over Cu-CHA surface, the coverage ( $\theta_{\text{NH}_3}$ ) as defined in Eq. 9 is much lower than at low temperature. This observation can easily be conclude through the NH<sub>3</sub> adsorption isotherms evolution in temperature [373] or through the decreasing tendency of NH<sub>3</sub> TPD profiles at elevated temperature (See Figure IV-7) [171,389,422]. Thus, according to the low activation energy required for STD SCR reaction, the NO<sub>x</sub> abatement at high temperature via adsorbed NH<sub>3</sub> on redox sites cannot be only represented by STD SCR process neither the activity from zeolite acid sites (See Figure III-8 (A)) [333]. Therefore, with the formation of NO<sub>2</sub>, the overall NO abatement could be effectively enhanced through the participation of Fast SCR reaction for instanec and more particularly through the implication of NO<sub>2</sub> in the mechanism. A participation that could give rise to the formation of reactive key intermediaries nitrates and/or nitrites species at low temperature [207,211,423] or their direct reaction at elevated temperature [198,424].

In that respect, the first order NO oxidation reaction was firstly verified and the corresponding estimation of  $E_{\text{app}}^{\text{NO oxy}}$  was calculated, Figure V-14, according to the above described method. A conversion < 15% was maintained between 200°C and 350°C.

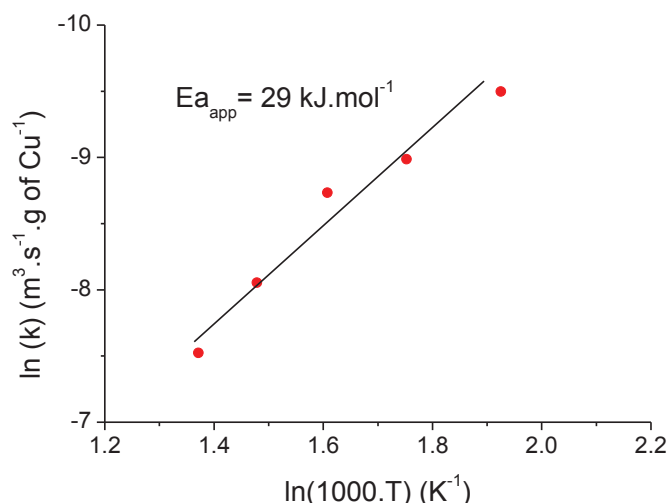


Figure V-14. Arrhenius plot of the apparent NO conversion rate constants from 200°C to 450°C ( $X < 15\%$ ) in NO oxidation reaction.

Therefore, NO oxidation  $E_{a,app}^{NO\ oxy} = 29 \text{ kJ.mol}^{-1}$  was obtained, which was lower than that obtained in literature [161,226]. One possible reason is the deviation of the reaction rate first order expression in a more accurate one, as depicted by Metkar et al. [226] with:  $r_{NO\ oxy} = k ([NO]^{\alpha} [O_2]^{\beta} / [NO_2]^{\gamma})$ , where  $\gamma = 1$ , thus taking into account the NO<sub>2</sub> concentration in the rate law expression. In that case,  $E_{a,app}^{NO\ oxy}$  is adjusted to  $43 \text{ kJ.mol}^{-1}$  and more similar with literature studies Table V-2.

Finally, the NO oxidation was studied with Cu-SAPO-34-IE through 200°C to 500°C in presence of water. As shown in Figure V-15 (A), a full selectivity to NO<sub>2</sub> was observed, where the NO start its conversion around 300°C. Therefore, the reaction seems to be kinetically controlled prior to any thermodynamic limitations. On the other hand, starting at 400°C and without water feed, as depicted in Figure V-15 (B), the reaction seems to be thermodynamically controlled. Without water, a maximum is reached around 400°C, demonstrating the water inhibiting effect on NO oxidation. This phenomenon is in accordance with the previously cited study conducted by Metkar et al. [226], where water inhibition impact was demonstrated on Cu-CHA catalyst. In any way, the presence of water in the feed allows to consider that the NO oxidation is kinetically controlled on the whole investigated temperature range. Studies carried out on Fe-CHA (Fe-SSZ-13) catalyst under NO oxidation atmosphere indicated that dimeric transition metal complexes were the most favorable active sites for NO oxidation, as investigated by Mossbauer techniques [425]. The activity of Cu moieties with Extra Lattice Oxygen (ELO) was comforted by Verma et al. [334] and Gao et al. [426] through In situ XANES measurements (Cu<sub>x</sub>O<sub>y</sub> oligomers pointed out) and Ex-situ EPR (Cu<sup>2+</sup> monomer), respectively. According to the varying configuration of active center through the temperature, in other words the sites mobility, the dimer formation was speculated as following, for copper sites and reversible reactions:





In that respect, either already present dimers can employ ELO for NO conversion (14) either the isolated active sites  $\text{ZCu}^{2+}$  are able to oligomerize themselves for the reaction (13). Therefore, a catalyst with copper redox sites and displaying non negligible NO conversion at high temperature could also inform about the presence of isolated active copper moieties, an observation which was further demonstrated in precedent the Chapter (See Figure IV-13).

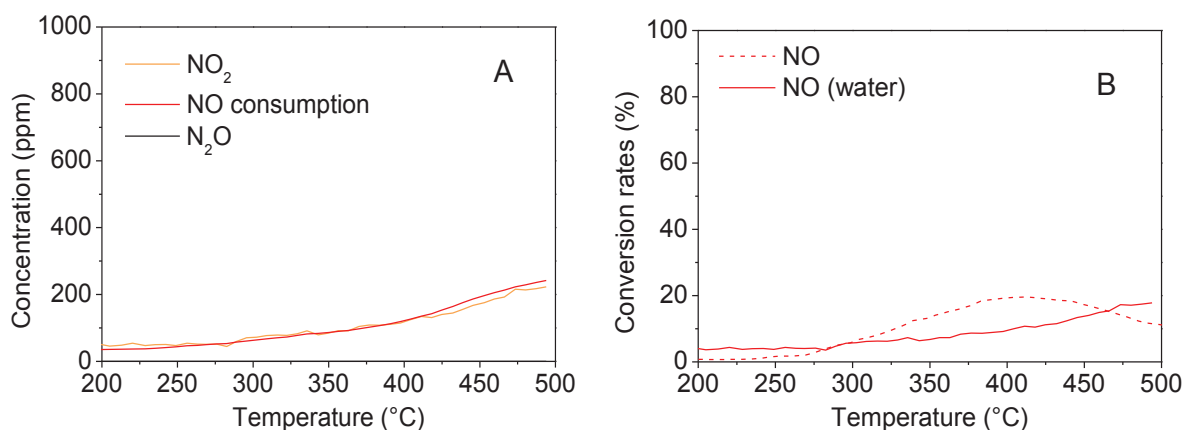


Figure V-15: NO oxidation reaction with catalyst in (A) presence of water and (B) in dry conditions. Inlet gas composition: 1000 ppm NO; 80000 ppm (8%) O<sub>2</sub>; 40000 ppm (0 or 4%) H<sub>2</sub>O with He as gas balance; total flow= 10 L/h; GHSV=142.000h<sup>-1</sup>

Finally, the gas phase NO oxidation was also investigated, in similar conditions Figure V-16 (A). The influence of the catalyst is readily observable in Figure V-16 (B), where 20% conversion is reached at high temperature against 10% in gas phase. Therefore, it will be important to consider both reaction for representing the global NO<sub>2</sub> production.

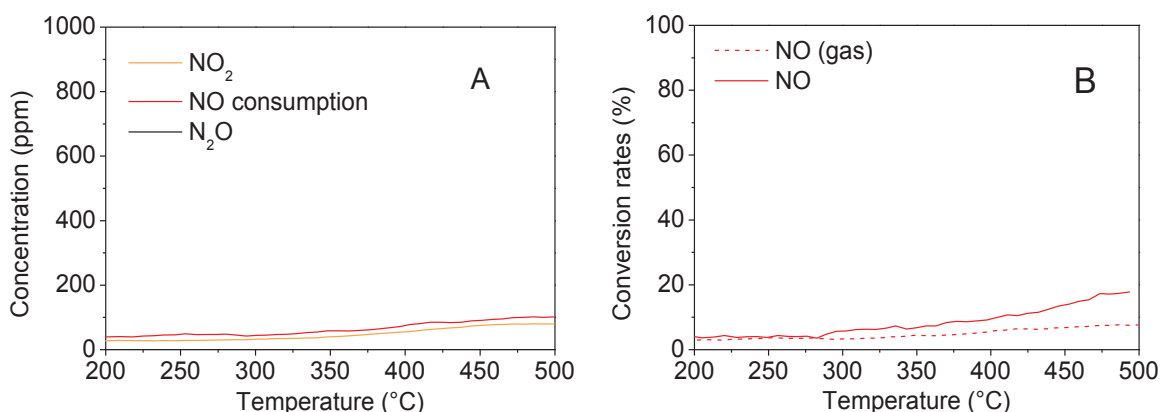


Figure V-16: NO oxidation reaction without catalyst (A) in presence of water (gas phase) and (B) comparison of NO conversion with and without catalyst. Inlet gas composition: 1000 ppm NO; 80000 ppm (8%) O<sub>2</sub>; 40000 ppm (4%) H<sub>2</sub>O and He as a balance; total flow= 10 L/h

## V-2.5. FAST SCR tests performance

Accordingly with the NO<sub>2</sub> production, the reference catalyst was also tested under FAST SCR conditions in order to evaluate the catalytic behavior from 200°C to 500°C. Note that in presence of NO<sub>2</sub>, nitrates are more easily formed than nitrites, which is one of common mechanistic pathway reported in literature [196,197]. As displayed in Figure V-17, the NO<sub>x</sub> abatement is maintained through all investigated temperature window, displaying comparable performance with the above presented performances during STD SCR catalytic tests. Nevertheless, the NH<sub>3</sub> oxidation is observed at higher temperature than for STD condition (around 400°C). According to these profiles, the NO<sub>2</sub> consumption from low to high temperature allows an important N<sub>2</sub> selectivity and no N<sub>2</sub>O was detected.

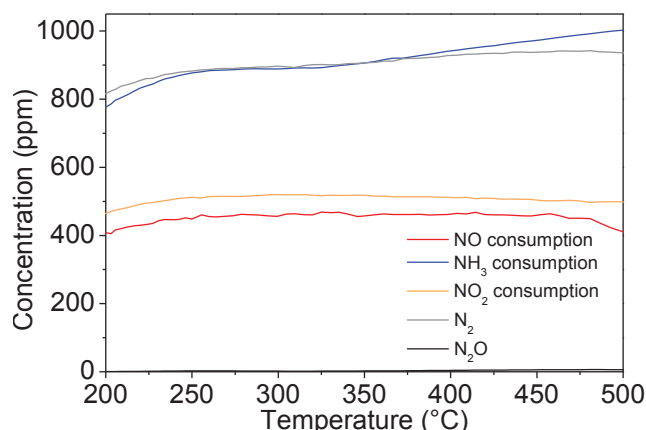


Figure V-17: FAST SCR reaction. Inlet gas composition: 1000 ppm NH<sub>3</sub>; 500 ppm NO/NO<sub>2</sub> 80000 ppm (8%) O<sub>2</sub>; 40000 ppm (4%) H<sub>2</sub>O and He as a balance; total flow= 10 L/h; GHSV=142.000h<sup>-1</sup>

## V-2.6. Catalyst Cu-SAPO-34-IE stability

Finally, the catalyst stability was studied under STD NH<sub>3</sub>-SCR condition during 72h, starting from fresh catalyst Cu-SAPO-34-IE. Several cycles were applied from 200°C to 500°C with 30 min step between each temperature ramp (10°C.min<sup>-1</sup>), which made 36 ramps in total. In that respect, Figure V-18 displays the outlet concentrations during the first temperature ramp from first cycle (straight lines) and the concentrations measured during the last temperature ramp (36<sup>th</sup>) (dotted lines). As depicted, the concentration of NH<sub>3</sub> and NO remain constant presenting a 90% of conversion in the entire temperature window. Moreover, N<sub>2</sub>O was no more detected and NO<sub>2</sub> formation is identical to that obtaining during the first catalytic run. This catalytic test can be considered as a slight aging hydrothermal treatment performed on fresh Cu-SAPO-34-IE because of the presence of water and the long time exposition of reactants for 72 hours, according to the literature [340,427,428]. Regarding the constant selectivity here, the reference catalyst displays high hydrothermal resistance, which the main exchanged active sites seem to be not irreversibly modified under these conditions. To verify this hypothesis and the storage sites capacity improvement, the used catalyst was further characterized (available in Annexes Figure V-1 to 3). The main conclusions were: 1) the exchanged cations sites of used catalyst was conserved, according to the peaks

relative to copper cations in exchanged positions detected before and after SCR process; 2) The NH<sub>3</sub> TPD experiments showed a better NH<sub>3</sub> storage capacity with the used Cu-SAPO-34-IE than with the fresh catalyst (576  $\mu\text{mol}\cdot\text{g}^{-1}$  for fresh versus 731  $\mu\text{mol}\cdot\text{g}^{-1}$  for used catalyst). By peak deconvolution comparison, it reveals that the used catalyst improved the relative proportion of strongest sites by 10% compared with the fresh catalyst, which is in accordance with the cation migrations capacity of the surface active sites reported in literature for Cu-SAPO-34 catalysts [184]. 3) Complementary to Ex-Situ DRIFTS measurements performed on the used catalyst, the <sup>27</sup>Al and <sup>31</sup>P MAS NMR experiments were conducted in order to observe the potential building unit modification within the bulk catalyst after the 72h of STD SCR conditions. Note that <sup>28</sup>Si measurements were not obtained due to the low quantity of sample available after the running test (less than 35mg) and the low sensitivity of the <sup>28</sup>Si characterization. In any way, a chemical shift observed for Si would provoke shifts at least for Al species due to the intricate chemical environment of Si-OH-Al units. In that respect, both <sup>27</sup>Al and <sup>31</sup>P profiles do not present main differences, which means that the building unit arrangements are preserved after long stability test. Moreover, relative peak intensities corresponding to hydrated form of Al and P were lower for the used catalyst than for the fresh catalyst, where the tetrahedral unit corresponding peak was sharper indicating a better structure coherence. This observation is also in accordance with above characterizations where the used catalyst structure seems slightly better configured. A rearrangement made possible through the soft hydrothermal conditions applied during the STD SCR process.

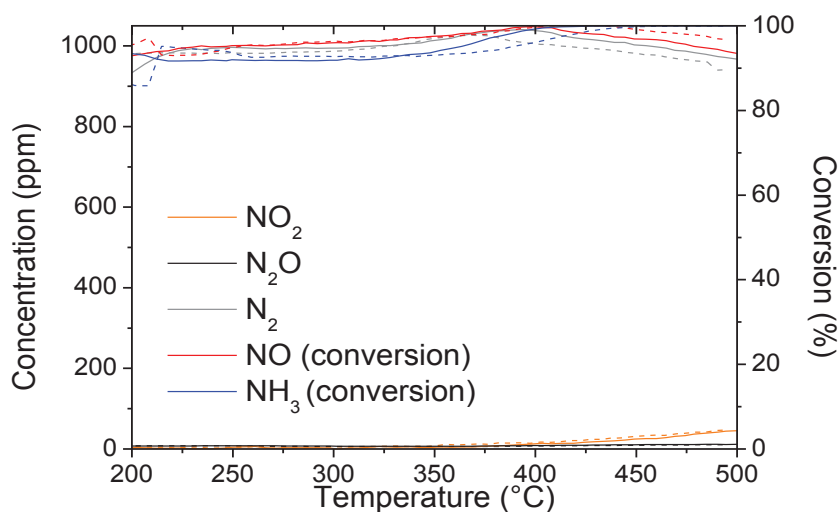


Figure V-18. Cu-SAPO-34-IE stability in STD SCR reaction with first (straight) and last (dotted) temperature ramp. Inlet gas composition: 1000 ppm NH<sub>3</sub>; 500 ppm NO/NO<sub>2</sub> 80000 ppm (8%) O<sub>2</sub>; 40000 ppm (4%) H<sub>2</sub>O and He as a balance; total flow= 10 L/h; GHSV=142.000h<sup>-1</sup>, test of 72h.

### V-3. Sequenced In-Situ DRIFT STD NH<sub>3</sub>-SCR: Catalyst surface behaviour

After kinetic investigations of Cu-SAPO-34-IE catalyst performances under several operating conditions, in-situ DRIFTS analysis in sequenced STD SCR conditions was carried out in order to acquire further information about the relationship between reactive species, potential intermediates and available storage and redox active sites. This study is inherent to the reference catalyst and complementary to the one presented Chapter IV. According to the protocol described in Figure II-11 the different steps of NH<sub>3</sub>, H<sub>2</sub>O adsorption on Brønsted and Lewis acid sites and the corresponding NO reductions were followed under isothermal steps at 200°C, 300°C, 400°C and 500°C. Only the spectrums corresponding to the 200°C and 500°C isothermal steps are presented in this chapter. The 300°C and 400°C isothermal results are reported in Annexes from Figure V-4 to -7 for complementary information.

At each isotherm step, a gas feed containing 1000 ppm NH<sub>3</sub>, 40000 ppm of H<sub>2</sub>O and 80000 ppm of O<sub>2</sub> were firstly adsorbed during 30 min on catalyst surface. After a flushing period with pure He for 20 min in order to remove the weakest adsorbed NH<sub>3</sub> species, 1000 ppm of NO and 80000 ppm of O<sub>2</sub> were then adsorbed for 30 min on catalyst surface. After that, the catalyst surface was flushed in He prior to temperature ramping (10°C·min<sup>-1</sup>) for reaching next step. In that respect, the dynamic adsorption of NH<sub>3</sub> related species were monitored and their consumption by SCR reaction thanks to NO injection also. NH<sub>3</sub> was chosen as the adsorbed species regarding the low NO adsorption affinities with the Cu-CHA catalyst, experimentally observed during NO TPD experiments (not shown). From Figure V-19 to 23, more the color tends to the dark blue, more the measured absorbance is low and inversely, more the color become red and more the absorbance is elevated. In that respect from the lowest to the highest measured absorbance, the color ranges from dark blue, light blue, green, yellow, orange to red. The different intensities are better comparable regarding the 3D Figures. Table V-3 reminds the different wavelength exploited during the study with corresponding literature references.

The overall spectra were separately presented, the first one corresponding to Brønsted acid sites (4000 cm<sup>-1</sup> – 2800 cm<sup>-1</sup>) and the second one for Lewis acid sites (2100 cm<sup>-1</sup> – 700 cm<sup>-1</sup>), Figure V-19,22 and Figure V-20, 21, 23, respectively. Regarding the adsorption process first, and more particularly on Brønsted acid sites, displayed Figure V-19, the NH<sub>3</sub> adsorption is fast within the first minutes as NH<sub>3</sub> is injected, according to the emergence of the blue and red area. More precisely, the adsorption on external Si-OH, P-OH and bridged Al-OH-Si respectively assigned at 3730, 3671 and 3625, 3600 cm<sup>-1</sup>, take place in less than 1 minute according to the monitored absorbance variations. Note that the deep blue area corresponds to the bridged support's sites and enlighten the adsorption on these sites compared with external sites. Indeed, in the 2D graph Figure V-19, P-OH and Si-OH vibrations are less pronounced, and they were pointed out in 3D graph. On a same manner, NH<sub>4</sub><sup>+</sup> and NH<sub>3</sub> are readily detected within first minute on Brønsted sites positions at 3283 cm<sup>-1</sup> and 3333 cm<sup>-1</sup> respectively representing the fast adsorption process on each nature site at 200°C. A weaker peak is also observed at 3182 cm<sup>-1</sup>, which is assigned to adsorb NH<sub>3</sub> on Cu<sup>+</sup> sites. Consequently to NH<sub>3</sub> adsorption on the surface, the adsorption corresponding to

the asymmetrical vibration of NH<sub>4</sub><sup>+</sup> was also observed at 1460 cm<sup>-1</sup>, as presented in Figure V-20. Moreover, within the 2100-700 cm<sup>-1</sup> wavelength range, the vibration observed at 1620 cm<sup>-1</sup> can be assigned to the NH<sub>3</sub> molecules adsorbed on Lewis acid sites such as extra framework Al or copper sites. Finally, concerning the adsorption of NH<sub>3</sub>, two clear blue bands are displayed at low wavelength: 891 and 844 cm<sup>-1</sup>, assigned to two mode of support framework vibrations perturbed by exchanged copper cations [163,241,348,371].

After a flush with pure He, NO and O<sub>2</sub> were injected for 30 min on the saturated catalyst surface, starting at 55 min according to Figure V-19 and 20. Concerning the redox sites first, Figure V-20, the band at 891 and 844 cm<sup>-1</sup> fade in 10 minutes simultaneously with the band at 1620 cm<sup>-1</sup>, which could be associated to the NH<sub>3</sub> consumption on the exchanged redox sites, displaying their reactivity. Simultaneously, the intensity of the dark blue bands associated to the strong Brønsted acid sites Si-OH-Al (from NH<sub>3</sub> adsorption/desorption point of view [176]), Figure V-19, decrease and disappear before 20 min of NO exposure. On the other hand, the external Si-OH and P-OH bands fade within 15 min, either indicating the rapid NH<sub>3</sub> depletion on these sites and/or their lower proportion. The decreasing intensity of Si-OH band can be better observed in 3D graph Figure V-19. Accordingly, orange band corresponding to NH<sub>4</sub><sup>+</sup> adsorbed species on Brønsted acid sites at 3283 cm<sup>-1</sup> simultaneously decreases and finally disappears after 15 min, representing the global NH<sub>4</sub><sup>+</sup> consumption. Compared with this observation, the delay of Al-OH-Si total depletion indicates that the bridged Al-OH-Si Brønsted sites supply the reductive molecule over a longer period than the external Si-OH and P-OH. These results indicating that the NH<sub>3</sub> storage capacity and supply mainly comes from the bridged hydroxyl Si-OH-Al. The observed NH<sub>3</sub> and NH<sub>4</sub><sup>+</sup> depletion is the direct demonstration of the reductive molecule migration towards redox copper sites, a dynamic exchange in accordance with the study of Wang et al. [205], which could be associate to the nitrates and nitrites potential mechanism.



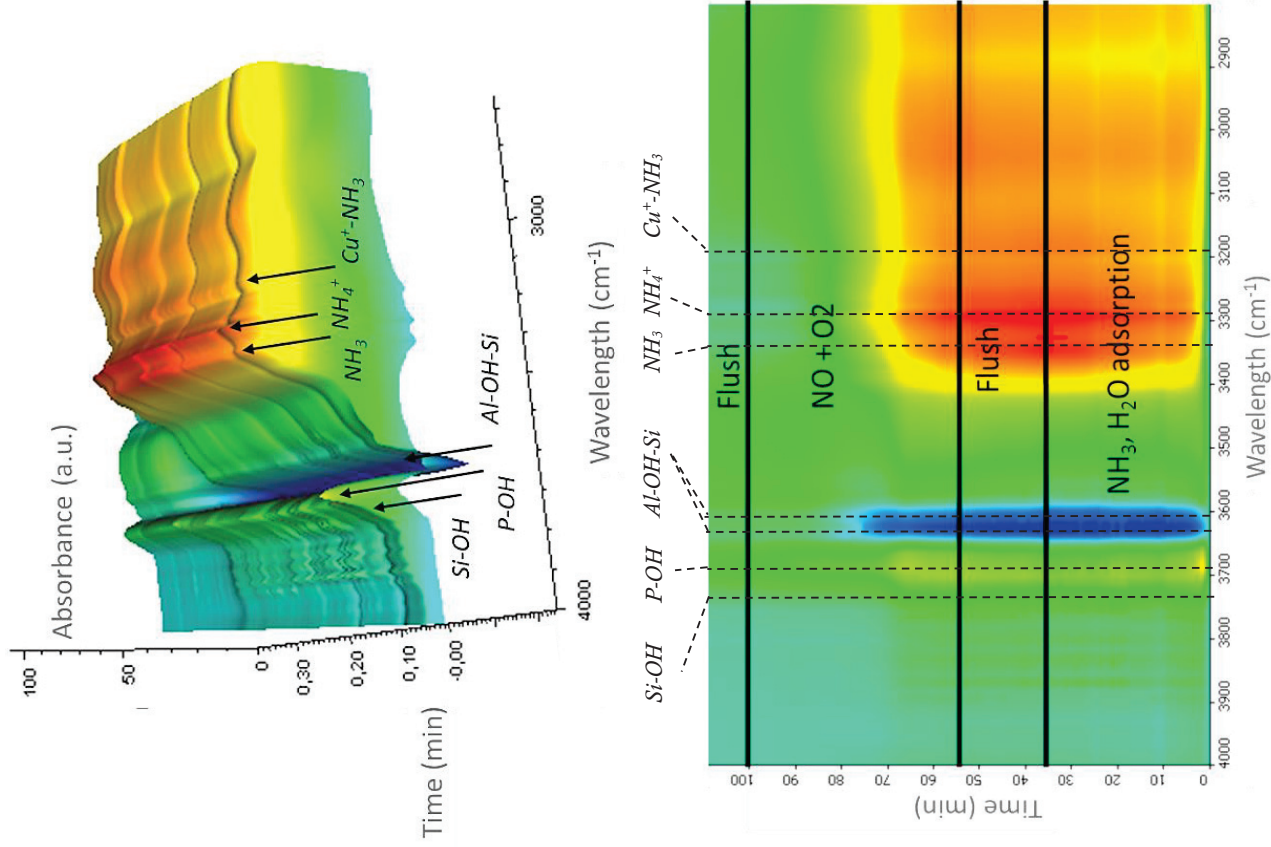


Figure V-19. Time resolved In-situ DRIFTS analysis at 200°C in Brønsted acid sites range

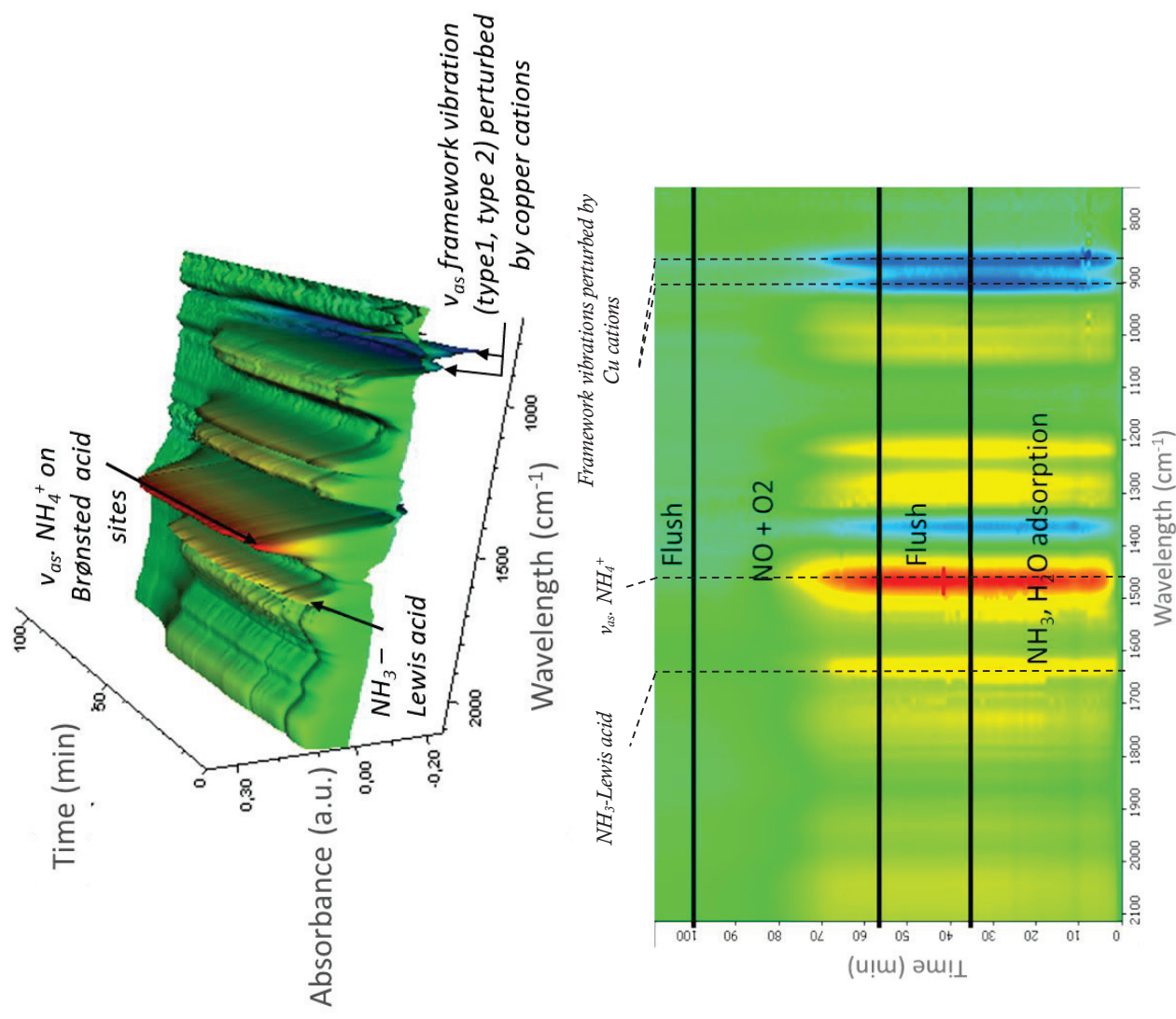


Figure V-20. Time resolved In-situ DRIFTS analysis at 200°C in Lewis acid sites range

The key intermediaries taking place in the mechanism are hardly observable within the direct process because of the time resolution of spectroscopic apparatus which is still limited, barely reaching the couple of second with optimized settings (minimum number of compiled scans per observation). However, it is possible to monitor the formation of these intermediaries after the total consumption of NH<sub>3</sub>. Indeed, as displayed Figure V-21, which is the Figure V-20 under a different angle and different contrast, the nitrates and nitrites species were monitored during the injection of NO + O<sub>2</sub>. Both chelating nitrates and nitrites are spotted on catalyst surface, at 1610 - 1578 cm<sup>-1</sup> and 1314 - 1203 cm<sup>-1</sup>, respectively. Note that in this experience only NO and O<sub>2</sub> are supplied. Although the NO activation route is still under debates concerning the type of required sites (monomeric or dimeric sites) and the mechanism of activated species formation [220,406], one plausible mechanism for the formation of reactive nitrites could be the interaction between NO and redox sites, Eq. 15 Nevertheless, the nitrates could be also produced by the reaction between formed NO<sub>2</sub> and surface nitrites, Eq. 16 a situation better plausible in NO oxidation conditions.

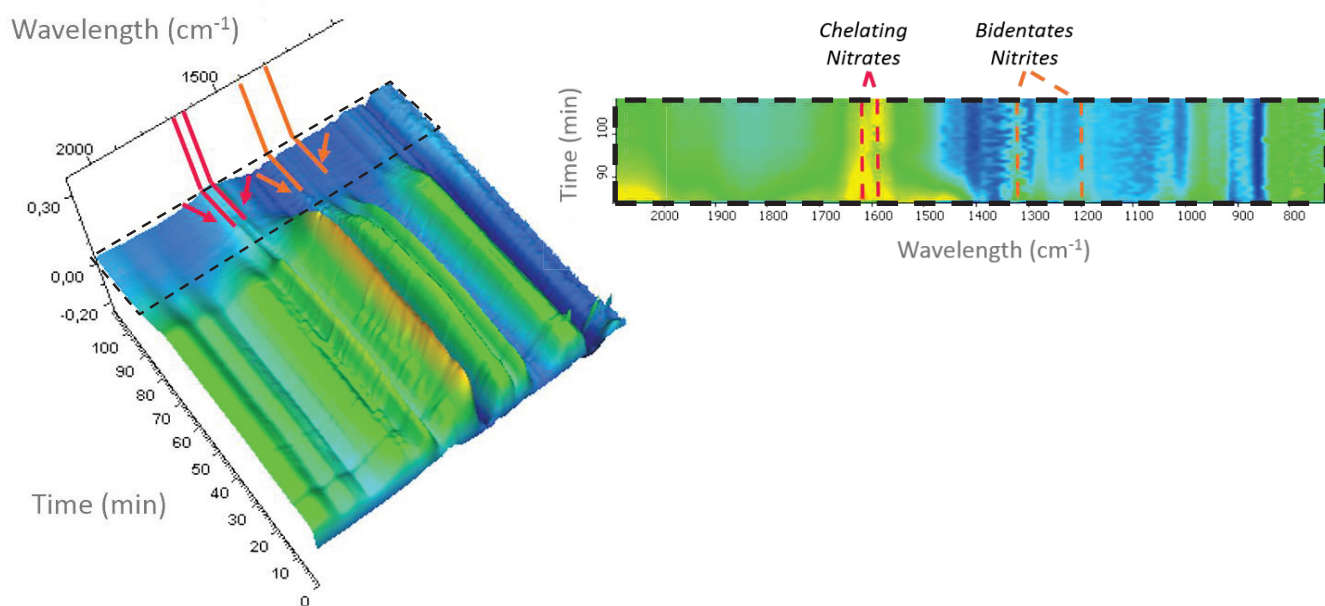


Figure V-21. Time resolved In-situ DRIFTS analysis at 200°C in Lewis acid sites range

Finally, the sequenced STD SCR measurements was carried out at 500°C, a temperature where only the strongest sites store the NH<sub>3</sub> for reduction process. Both Figure V-22 and 23 display the steps in which the catalyst is flushed with He prior to NH<sub>3</sub> adsorption for better appreciation of the dynamic process (3D graphs). As expected, the absorbance spectra within the 3400-3100 cm<sup>-1</sup> range corresponding to adsorbed NH<sub>3</sub> on Brønsted acid sites are less pronounced compared against that one displayed at 200°C, demonstrating the support capacity to store reductive molecule until elevated temperature. Moreover, the strength difference between the different type of Brønsted sites can be observed. Indeed, while the Si-OH and P-OH signals are barely detected, the NH<sub>3</sub> is still adsorbed on bridged Al-OH-Si, according to the corresponding blue bands at 3625 and 3600 cm<sup>-1</sup>, Figure V-22. In that respect, the bands in the region between 3400 – 3250 cm<sup>-1</sup> representing adsorbed NH<sub>3</sub> and NH<sub>4</sub><sup>+</sup> could be principally associated to the adsorbed species on Al-OH-Si. Note that NH<sub>3</sub> adsorbed on Cu<sup>+</sup> is still detected at 3182 cm<sup>-1</sup>. Within the Lewis acid site range, Figure V-23, the adsorption on exchanged copper sites (891 cm<sup>-1</sup>) remains important regarding the blue band, which appears as soon as NH<sub>3</sub> is injected. A band particularly observed on type I perturbation (891 cm<sup>-1</sup>), comparing the profiles made at 300°C and 400°C displayed in Supplementary Materials Annexes V-5 and 7, where the type II perturbation (850 cm<sup>-1</sup>) is no more detected once reached 400°C. On the opposite, the band at 891 cm<sup>-1</sup> is clearly spotted. An observation which could inform about different types of framework perturbations and thus of potential active sites definitions differences.

All along the NO+O<sub>2</sub> injection, the temperature activated SCR reactions of NH<sub>3</sub> with NO molecules are visible through the Al-OH-Si band fading Figure V-22, informing about the migration on the redox sites. It is important to notice that after the NO introduction, some reductive molecule remain on the surface on Brønsted acid sites, which is evidenced by the yellow band at 3283 cm<sup>-1</sup> until 68 min, informing that not all stored reductive molecules were consumed. A different behavior than at 200°C potentially indicating the species stability on these sites and the consequent difficulty of strongly adsorbed NH<sub>3</sub> to desorb and migrate until redox site. Similar observations are made with exchanged cations, which the signal at 891 cm<sup>-1</sup> is more pronounced than 844 cm<sup>-1</sup>, where the former vibration becomes more intense as NO is introduced (spotted by dotted black circle in Figure V-23). These observations could indicate that the Cu cations in exchanged position are strong adsorbents for NH<sub>3</sub> reductive molecule until elevated temperature, continuing to perform the reduction process with the migrated NH<sub>3</sub> from the strongest Brønsted acid sites. Moreover, as the 891 cm<sup>-1</sup> band gains in intensity with the introduction of NO, the greater perturbation of the framework could indicate the interaction of supplementary molecules than NH<sub>3</sub> with exchanged cations, as NO<sub>2</sub> for instance [402].

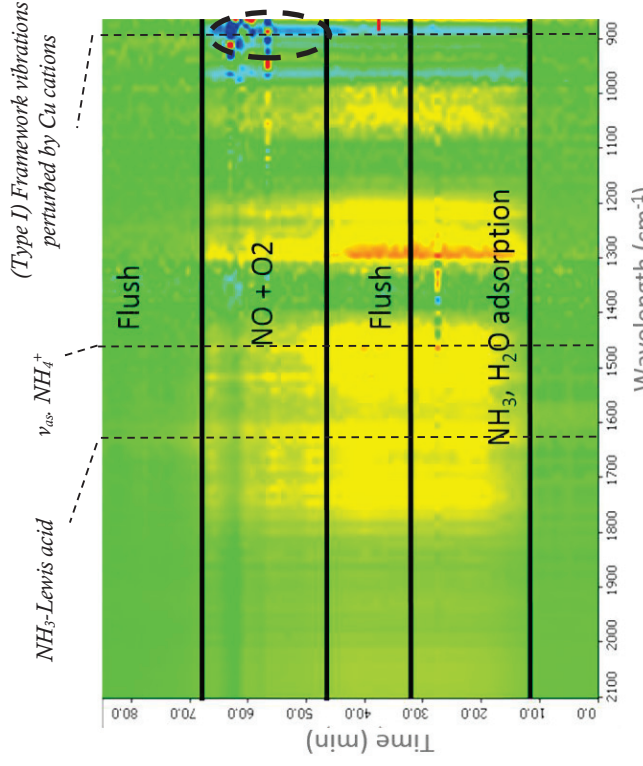
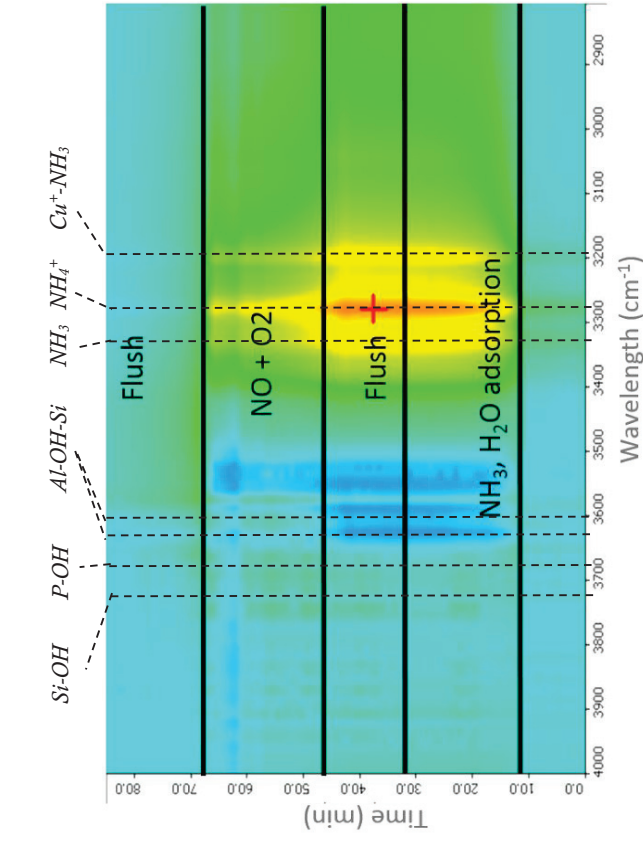
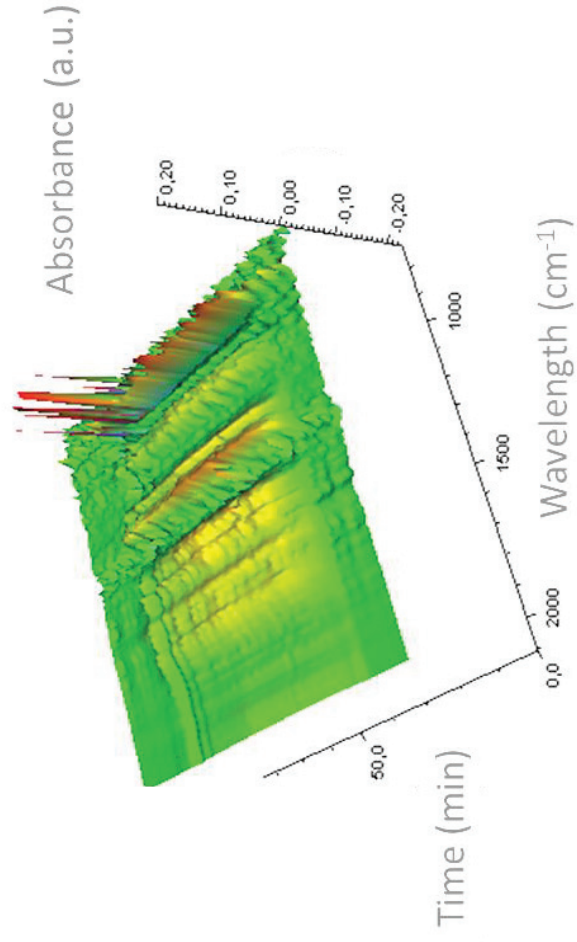
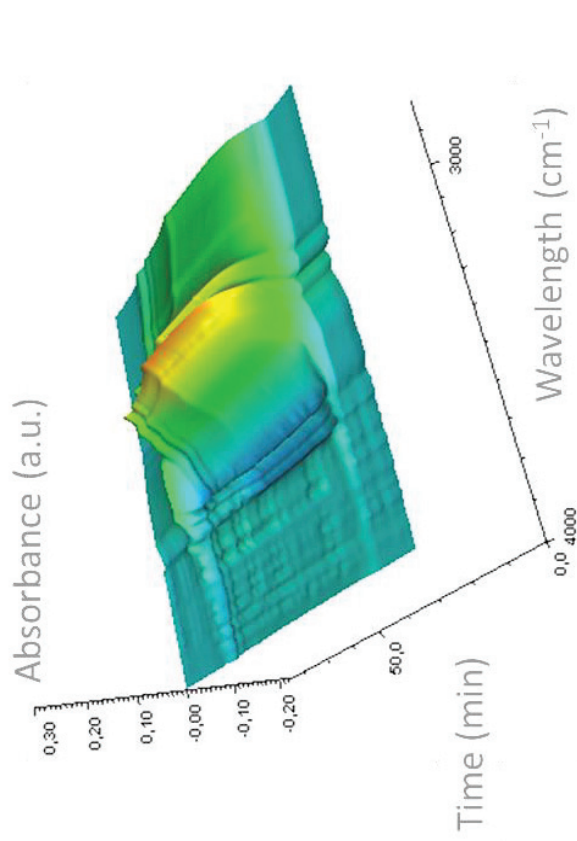


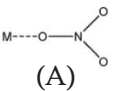
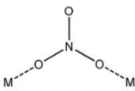
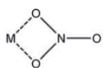
Figure V-22. Time resolved In-situ DRIFT analysis at

500°C in Brønsted acid sites range

Figure V-23. Time resolved In-situ DRIFT analysis at

500°C in Lewis acid sites range

Table V-3 NH<sub>3</sub> and NO stretching vibrations according to literature for in situ DRIFT measurements

Probe Molecule	Vibrations (cm <sup>-1</sup> )	Compound	[Reference]
-	<b>3730</b>	External Si-OH	[346,347]
	<b>3671</b>	External P-OH	
	<b>3625,3600</b>	Bridged Si-(OH)-Al	
NH <sub>3</sub>	<b>3333</b>	NH <sub>3</sub> molecules	[285,346,347]
	<b>3283</b>	NH <sub>4</sub> <sup>+</sup> adsorbed species	
	<b>3182</b>	Cu <sup>+</sup> -NH <sub>3</sub>	[242]
	<b>1620</b>	NH <sub>3</sub> on Lewis acid sites	[365]
	<b>1460</b>	v <sub>as</sub> . NH <sub>4</sub> <sup>+</sup> on Brønsted acid sites	[242,346]
	<b>891, 844</b>	v <sub>as</sub> . framework vibration (type1 and type 2) perturbed by copper cations	[163,241,348,371]
NO  (A)  (B)  (C)	<b>1904</b>	NO- isolated Cu <sup>2+</sup>	[168,355]
	<b>1875</b>	NO- bidimensional CuO	[356,357]
	<b>1625/1610/1578</b>	(C) Chelating nitrates	[358]
	<b>1495</b>	(A) Monodentate nitrate	[359]
	<b>1436</b>	(A) Monodentate nitrites O-N-O-M	[360]
	<b>1375-1314</b> <b>1203-1176</b>	(C) v <sub>sym</sub> / v <sub>as</sub> Chelating nitrites	[361]

#### V-4. Conclusion

In this chapter, the catalytic performances of the reference Cu-SAPO-34-IE with highly active exchanged copper sites and surface nano-sized clusters were evaluated under several operating conditions. From the STD to Fast NH<sub>3</sub> SCR reactions, the catalyst performance was investigated through the whole temperature window (200°C-500°C). Particular behavior were also pointed out during the kinetic study, as the inhibitive effect of NH<sub>3</sub>, the water promoting effect at low temperature and its implication within the NO<sub>x</sub> abatement process or the NH<sub>3</sub> high temperature oxidation in NO and N<sub>2</sub>. The catalyst stability was also demonstrated in aging hydrothermal conditions, under long exposure STD NH<sub>3</sub>-SCR operating conditions.

At low temperature, it was clearly observed that the overall catalyst behavior mainly depends on the adsorption competition between reactive species as NH<sub>3</sub> and H<sub>2</sub>O and the resulting formation of key intermediaries. Therefore, sequenced in-situ STD NH<sub>3</sub>-SCR experiments were carried out to further detail the active sites relationship toward the reductive molecule and their consequent responses under NH<sub>3</sub>-SCR conditions. Thus, the adsorption on the different Brønsted and Lewis acid sites presented on catalyst surface was depicted through the simultaneous evolution of relevant bands. After a fast adsorption, the NH<sub>3</sub> consumption was probed until the complete depletion by NO at 200°C (regarding the low ammonia oxidation impact). It was also observed the consequent migration of reductive molecule to redox sites, in accordance with literature investigations [205,215]. The potential key nitrites intermediaries and nitrates, were detected under flowing NO and O<sub>2</sub> during the time resolved experiment at 200°C regarding their low stability. Exchanged cations sites were also monitored until 500°C, displaying a pronounced framework perturbation during the NO injection, which spotlight the important activity of these redox sites until elevated temperature.

Thus, regarding the acquired data and the detailed catalyst behavior, a reactional network can be proposed. Note that the mechanism need to be as simple as possible in order to not burden the catalyst description during the model construction. In that respect, a reactional network for STD NH<sub>3</sub>-SCR reaction description was proposed in Figure V-24, taking into consideration:

- The adsorption of NH<sub>3</sub> and H<sub>2</sub>O on active species as Brønsted and Redox sites
- The key intermediary formation of nitrites
- The water interaction with redox sites allowing the copper hydrated form as reactional site
- The consideration of the NO<sub>2</sub> formation through the gas phase and the oxidation on catalyst surface
- The reaction through Fast NH<sub>3</sub> SCR of NO<sub>2</sub>, NO and NH<sub>3</sub>
- The oxidation of NH<sub>3</sub> through a two-step mechanism considering the NO formation
- The NO formation in gas phase with the presence of STD SCR mixture inlet

According with the active sites configurations characterizations from precedent Chapters and the representative reactional network Figure V-24, all the required kinetic and catalyst information will be employed for the construction of a multi-site kinetic model.

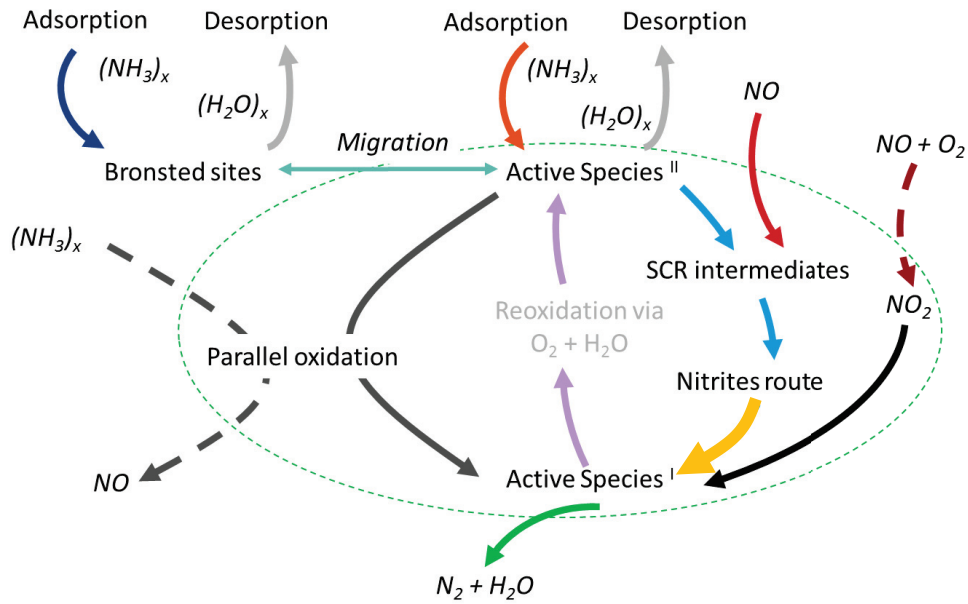


Figure V-24. Proposed reactional network for STD  $\text{NH}_3$ -SCR process

VI





# CHAPTER VI

## PART 1: MULTI-SITE KINETIC MODEL DEVELOPMENT

### VI-1. Introduction

In previous chapters, the catalytic behaviour investigation of the reference catalyst led to the proposition of a STD SCR reactions network, which the reactional steps were defined on the catalyst kinetic study. Combined with the investigations of active site configuration impacts on the different catalyst activities, the performance simulation of an optimized reactional pathway occurring with different active site configurations on Cu-CHA type catalyst can therefore be initiated.

With the purpose to estimate catalyst's physicochemical intrinsic parameters, it is crucial to take into consideration different chemical engineering problematics, as the experimental reactor hydrodynamic behaviour and the residence time distribution taking place through the whole experimental test bench. Knowing that the evolution of measured concentrations through the time are shaped both by chemical and physical aspects but also by gases hydrodynamic behaviour, their clear definitions within the model prevent to mislead kinetic parameters with hydrodynamic effects. Moreover, regarding the heterogeneous reactions taking place between gas and solid phase, from the adsorption/desorption steps to the NO<sub>x</sub> reduction, interface mass transfer phenomena were also implemented in the model and finally put in perspective with chemical reactions characteristic times once the model settled.

Thus, the will of the following model construction is to propose a mechanistic STD SCR path, constituted of an optimized number of reactions in respect with the different catalytic behaviour, taking into account previously characterized active sites configurations present on studied catalysts: Cu-SAPO-34-IE, Cu-SAPO-34-HT and Cu-SAPO-34-IMP. These several configurations consequently induced different SCR behaviour which will be described with adequate corresponding modelled sites. By the combination of flow reactor experiments in different transient conditions through a broad temperature window and corresponding ammonia TPD measurements, the proposed mechanistic path incorporated in the model has the vocation to take into account NH<sub>3</sub> and water adsorption/desorption dynamics, standard SCR reactions, and finally NH<sub>3</sub> and NO oxidation steps. These reactions will be also defined as following key intermediaries formation and decomposition dynamics.

This last Chapter is divided in two parts, which the first one concerns the model construction and its application with the reference catalyst Cu-SAPO-34-IE for kinetic parameter estimation and performance simulation studies. After the model acquisition, the different limiting steps were investigated through the determination of different characteristic times and further verifying the developed assumptions. Moreover, the parameters accuracies were calculated and the correlation between parameters investigated for model accuracy verifications.

On the other hand, the second part represents the extension of the developed model for supplementary catalysts with different active sites configurations, namely Cu-SAPO-34-HT and Cu-SAPO-34-IMP. This study was performed in order to compare the kinetic simulation between several catalysts, and thus, their corresponding estimated parameters. Moreover, the model extension allowed us to observe the model limits and its potential enhancement relatively to previous characterisation.

## VI-2. Reactor model

### VI-2.1. Hydrodynamic behaviour identification: Experimental reactor

In order to adequately represent the observed catalytic performances, the model reactor has to be firstly defined, regarding the experimental specifications and consequent assumptions. In this study, U-shape quartz reactor was used for the kinetic investigation of powdered catalyst. All the catalytic tests were performed using 0.035 g of catalyst which, following the quartz reactor description in Chapter II, involves a total reactor volume  $V_{\text{tot}} = 8.6 \cdot 10^{-8} \text{ m}^3$  with a section  $S_{\text{bed}} = 2.82 \cdot 10^{-5} \text{ m}^2$  on 0.003 m height. The Gas Hourly Space Velocity (GHSV) was equal to  $142\,000 \text{ h}^{-1}$ , except for TPD experiments, where a GHSV of  $30\,000 \text{ h}^{-1}$  was employed. These conditions were referred here as normal conditions and employed for the model construction. The model input, characteristic to the reactor, are displayed Table VI-1 for more convenience. Different approximations were assumed for the required hydrodynamic investigation and reactor representation under the cited operating conditions, as:

1. The solid catalyst density ( $\rho_{\text{app}}$ ) was roughly estimated by water volume displacement.
2. Extra granular FPB porosity is assumed based on literature values on similar solid catalysts [429–431].
3. Gases are at constant atmospheric pressure and cause negligible pressure drop in FPB. Further measured with manometers at the reactor inlet and outlet (e.g. at inlet FTIR gas chamber position) at 800 mmHg.
4. Volumetric flow was verified as constant from inlet to outlet of reactor.
5. At the Gas-solid interface and within the porous particle, mass transfer resistance was represented by the linear driving force model.
6. The temperature employed for simulations was the one measured within the catalyst bed. Regarding the low reaction heats associated with SCR reactions, the energy balance was not considered. This approach has been followed in many models according with the literature for similar catalysts [58,225,432,433]. Moreover, the experimental reactor was considered as isothermal.
7. No material accumulation in the external film at solid-gas interface.
8. No radial concentration gradient.
9. The investigated catalytic system is in non-equilibrium thermodynamic at the solid interface.
10.  $\text{NH}_3$  and  $\text{H}_2\text{O}$  are assumed as the only species to process adsorption and desorption steps.

Table VI-1: Reactor characteristics related to experimental bench specifications and assumptions made during standard tests performances.

Characteristic	Nomenclature	Value	Unity
Volumetric flow (25°C)	$Q_{vol.}$	$2.66.10^{-6}$	$m^3.s^{-1}$
Reactor section	$S_{bed}$	$2.82.10^{-5}$	$m^2$
FPB height	H	0.003	m
Mean particle diameter <sup>a</sup>	$D_p$	$10.10^{-6}$	m
Catalyst density	$\rho_{app}$	410	$kg.m^{-3}$
FPB porosity <sup>b</sup>	$\epsilon$	0.4	-
Quartz reactor diameter	$D_t$	0.006	m
Total pressure	$P_{tot}$	101325	Pa
Solid Calorific capacity	$C_{p_s}$	700	$J.kg^{-1}.K^{-1}$

<sup>a</sup>estimated by MEB and TEM microphotography observations, sampling several particles dimensions and further approximated as spherical particles (See Figure IV-2).

<sup>b</sup>observed from different literature data dealing with similar material [434]

As it will be demonstrated after, the gas chamber volume of FTIR analyser is far superior to the experimental reactor. A hydrodynamic study by residence time observation of a tracer would not be sensitive enough for the acquisition of relevant information about the experimental reactor. In that respect, a first estimation was carried out by calculating the dimensionless Péclet number in order to apprehend its hydrodynamic representation. Then the hydrodynamic model was further developed by the investigation of residence time distribution of probe species within the experimental bench, including FTIR gas cell, in representative tests conditions. Therefore, the model will be defined following the overall apparent hydrodynamic behaviour made by both characteristic volumes.

In order to represent their mixing characteristics, two main types of model reactors and their combination can typically be used. For instance, ideal plug flow reactor (PFR) is characterized by a lack of molecules dispersion in the volume since all molecules display a similar residential time within the reactor. At the opposite, ideal Continuous Stirred Tank Reactor (CSTR) represents a complete molecular mix in the volume, at any time, as the feed is injected in the reactor. For real system, where molecules display different time residences, the overall hydrodynamic can be represented by the combination of different CSTR in series, where an infinity of them mathematically corresponds to one ideal PFR and some to a PFR with dispersive behaviour [435]. Thus, the experimental reactor hydrodynamic behaviour can be apprehended regarding the abacus correlation between Péclet number and ideal reactor model configuration [435], where Péclet and axial Péclet number ( $Pe_{ax}$ ) were calculated as Eq. 1 and 2:

$$Pe = Pe_{ax} \frac{H}{D_p} \quad (1)$$

With H and  $D_p$  the FPB height (m) and particle diameter (m) respectively.

The axial Péclet number can be estimated according to Edwards and Richardson correlation for flowing gas through FPB ( $D_t / D_p > 0.15$ ) in laminar flow ( $0.008 < Re < 400$  and  $0.28 < Sc < 2.2$ ), respected conditions as it will further be demonstrated Figure VI-1 [436]:

$$\frac{1}{Pe_{ax}} = \frac{0.3}{Re Sc} + \frac{0.5}{1 + \frac{3.8}{Re Sc}} \quad (2)$$

Where Sc and Re respectively correspond to Schmidt and Reynolds numbers. Following the applied volumetric flow and FPB characteristics, the fluid flow regime occurring within the quartz pipe and around the catalyst particles was firstly estimated by the Reynold and the Reynold particulate number:

$$Re = \frac{\rho_{fluid} u L_c}{\mu} \quad (3)$$

$$Re_p = \frac{Q_{wt} D_p}{\mu} \quad (4)$$

With  $\rho_{fluid}$  ( $\text{kg}\cdot\text{m}^{-3}$ ) the fluid density at a given temperature,  $u$  ( $\text{m}\cdot\text{s}^{-1}$ ) the fluid velocity,  $L_c$  (m) the characteristic length,  $\mu$  ( $\text{Pa}\cdot\text{s}$ ) the fluid dynamic viscosity at temperature  $T$  (K),  $Q_{wt}$  ( $\text{kg}\cdot\text{s}^{-1}$ ) the mass flow and  $D_p$  (m) the characteristic particle diameter.

The fluid density was approximated to be the one of Helium (He) regarding the dilution condition ( $x_{\text{mol}}^{\text{He}} = 0.86$  vs.  $x_{\text{mol}}^{\text{NO}} = 0.001$  for  $1 \text{ m}^3$  of flowing inlet gas) depending on the temperature from  $200^\circ\text{C}$  to  $500^\circ\text{C}$ . The He mass density in function of temperature was obtained through the following correlation from “*The properties of helium*” (Eq. 3-19 [437]):

$$\rho_{He} = 0.17623 \frac{P}{\left(\frac{T}{T_0}\right)} \cdot \left[1 + 0.53 \cdot 10^{-3} \frac{P}{\left(\frac{T}{T_0}\right)^{1.2}}\right]^{-1} \quad (5)$$

With  $P$  the pressure (atm),  $T$  the temperature (K) and  $T_0$  the one at  $0^\circ\text{C} = 273.16 \text{ K}$ .

According to the density evolution displayed Figure VI-1 (A), the viscosity was consequently estimated as (Eq. 6-1[437]):

$$\mu_{He} = 1.865 \cdot 10^{-5} \left(\frac{T}{T_0}\right)^{0.7} \quad (6)$$

Therefore, the Re was estimated as shown Figure VI-1 (C) and informs about the clear laminar regime ( $Re < 2000$ ) of the flowing fluid in the quartz reactor and around the particle also, with  $Re_p = 0.011$  at  $200^\circ\text{C}$  and through the whole temperature range too.

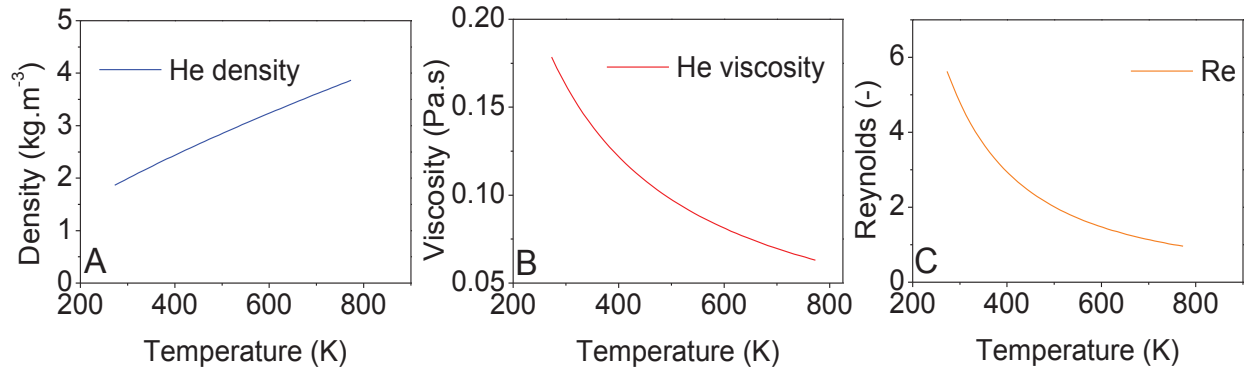


Figure VI-1 : Estimated He density (A) and viscosity (B) and corresponding flowing Re in tubular reactor (C) in function of temperature

Next, the estimation of dimensionless Schmidt number, representing the ratio of kinematic viscosity and molecular diffusivity was carried out at a typical STD SCR and constant operating condition, which means for an inlet gaseous mixture of 1000 ppm NH<sub>3</sub> and NO with 80000 ppm (8%) O<sub>2</sub> and 40000 ppm (4%) H<sub>2</sub>O diluted in He, at 200°C and 1atm. Correspondingly, the Schmidt number was defined as following:

$$Sc = \frac{\mu}{\rho_{fluid} D_{mj}} \quad (7)$$

Eq 7. requires the estimation of the mass diffusivity  $D_{mj}$  ( $m^2.s^{-1}$ ) of each component in the fluid within the tubular reactor. In order to represent the mean Schmidt number of the gaseous mixture applied in Eq 7., each diffusion coefficient of A in B ( $D_{AB}$  with A and B = NH<sub>3</sub>, NO, H<sub>2</sub>O, O<sub>2</sub> or He, without A=B) was estimated and further averaged together, obtaining a summed up coefficient diffusion for each gas molecules. These estimations were carried out according to Chapman and Enskog equation [438] which the application concerns the binary gas system of close molar mass, at low pressure and considering hard sphere collisions processes:

$$D_{molec} = \frac{3}{16} \frac{(4\pi k \frac{T}{M_{AB}})^{1/2}}{n \pi \sigma_{AB}^2 \beta_D} \quad (8)$$

With  $M_A$  and  $M_B$  the molecular weights ( $kg.mol^{-1}$ ),  $M_{AB} = 2[(1/M_A)+(1/M_B)]^{-1}$ ,  $n$  the number density of molecules in fluid,  $k$  the Boltzmann's constant ( $J.K^{-1}$ ) and  $T$  absolute temperature (K). The corresponding collision integral for diffusion  $\beta_D$  was estimated regarding the correlation of Neufield (Eq. 11-3.6 [438]).

Thus  $Sc = 1.15$  was injected for the Péclet estimation, resulting in a  $Pe$  equal to 12.8. As  $Pe = 0$  corresponds to an ideal Continuously Stirred Tank Reactor (CSTR) and  $Pe = \infty$  to a Plug Flow reactor (PF), then the experimental reactor model will follow a transitory system between both of idealistic models. Accordingly to abacus data [435], a  $Pe=13$  indicates a total of 8 CSTR of same volume ( $K=8$ ) disposed in

series number. The schematic representation of the modelled hydrodynamic corresponding to the employed experimental reactor is displayed Figure VI-2 for  $K=8$ .

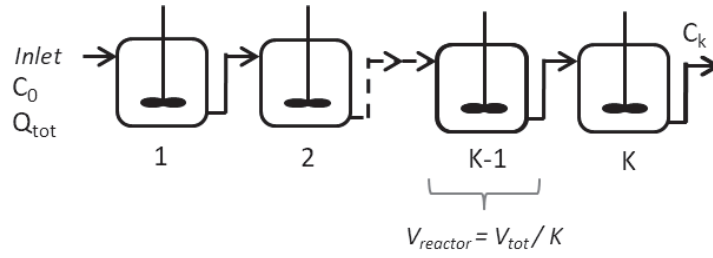


Figure VI-2: Hydrodynamic model reactor schematization

#### VI-2.2. Residence time distribution (RTD): Catalytic test bench

Once the hydrodynamic behaviour of the experimental reactor determined, the rest of the bench (without experimental reactor) must be investigated regarding the important volume involved. Indeed, the FTIR analyser gas cell represent a 200 ml tank volume (displayed by Thermo-fisher © specification sheet) and the connection inox tubes a total volume estimated to 90 ml from the experimental reactor outlet to FTIR gas chamber. The hydrodynamic study has the purpose to precise these volumes and their corresponding reactor model representations. In that respect, NO was used as a tracer for measuring the residential time distributions (RTD) of flowing fluid and the corresponding mean residence time ( $\tau$ ) through the bench. Thus, a pulse of NO was realized by opening and closing in short times a three-way valve at the rector up-stream, at atmospheric pressure flowing gas. The different tests were carried out with a similar sample bed volume (of inert SiC grains in order to avoid any NO adsorption phenomenon) at 40 ml.min<sup>-1</sup> and 160 ml.min<sup>-1</sup> at different temperatures for similar performances tests conditions. Accordingly, RTD experiments can be represented as the evolution of function  $E(t)$  through the time defined as [439]:

$$E(t_s)dt_s = \frac{Qv C_{tracer}(t)dt}{N_0} \quad (9)$$

Where  $E(t_s)$  is the RTD function under pulse injection following  $t_s$  the time when the tracer was measured in the outlet and  $C_{tracer}$  the tracer concentration (mol.m<sup>-3</sup>),  $Qv$  the volumetric flow (m<sup>3</sup>.s<sup>-1</sup>) and  $N_0$  the total molecular amount of tracer injected where  $C_{tracer,0} = N_0/V_{reacteur}$ . Regarding the constant volumetric flow and the lack of possible leaks, the function can be rewritten as:

$$E(t) = \frac{c(t)}{\int_0^\infty c(t)dt} \quad (10)$$

In that respect, the consequent determination of RTD first moment gives the mean residence time ( $\tau$ ) of the fluid in the reactor:

$$\tau = \frac{\int_0^\infty t E(t) dt}{\int_0^\infty E(t) dt} = \int_0^\infty t E(t) dt \quad (11)$$

Typically, each ideal reactor: CSTR and PFR, display a specific  $E(t)$  profile in time. Their respective combination modifies the macro representation of the time spent for a molecule within the

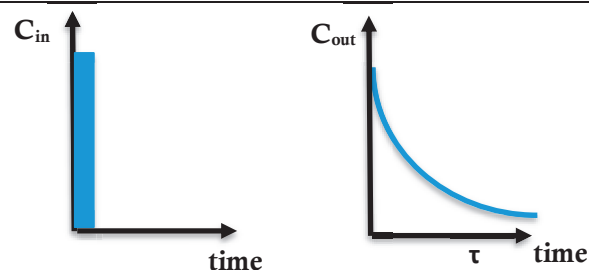
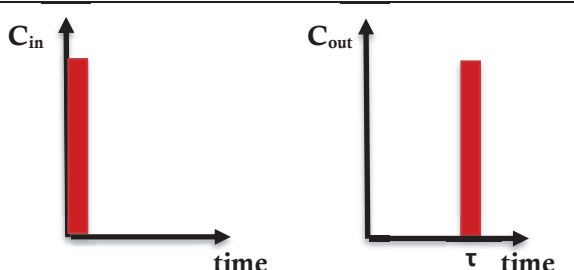
system as represented through Figure VI-3. Thus, by fitting the hydrodynamic model representation with the experimental  $E(t)$  profiles, the optimized number of each ideal reactor in series can be obtained.

Thus, the number of CSTR required to represent the FTIR gas cell and the delay induced by tubing connection were estimated by the resolution of the different mass balance equations presented Table VI-2 taking into consideration the experimental reactor model Figure VI-2. In that respect, the least square method was employed for the difference minimization between the measured  $E(t)$  profile (input) with the simulated one according to Eq. 12. The numerical resolution of differential equations system was done through *ode23s* subroutine (employed for stiff differential equation consequently to the sharp concentration input of tracer) and the parameter estimation with *lsqnonlin* which the objective function (RES) was:

$$RES = \sum_1^N (E(t)_{exp} - E(t)_{sim})^2 \quad (12)$$

With RES the residual (-) and N the number of observations on each run.

Table VI-2. Mass balance equations representing ideal reactors with corresponding  $E(t)$  responses in time for a Dirac input injection.

$i^{th}$ CSTR	PFR
$n_{CSTR} = \frac{V_{cell}}{V_i}$	$t_{delay} = \sum \tau_{PFR,i}$
$\tau_i = \frac{V_i}{Q_{tot}}$	$\tau_{PFR} = \frac{V_{PFR}}{Q_{tot}}$
$\frac{dC_i}{dt} = \frac{1}{\tau_i} (C_{i-1} - C_i)$	$\frac{\partial C}{\partial t} + \frac{1}{\tau_{PFR}} \frac{\partial C}{\partial \delta} = 0^a$
	
Assumptions: - Perfect mixing, the concentrations are uniform in reactor	Assumptions: - No radial concentration gradient - No diffusive transport in flow direction

<sup>a</sup>with  $\delta$  the dimensionless axial coordinate



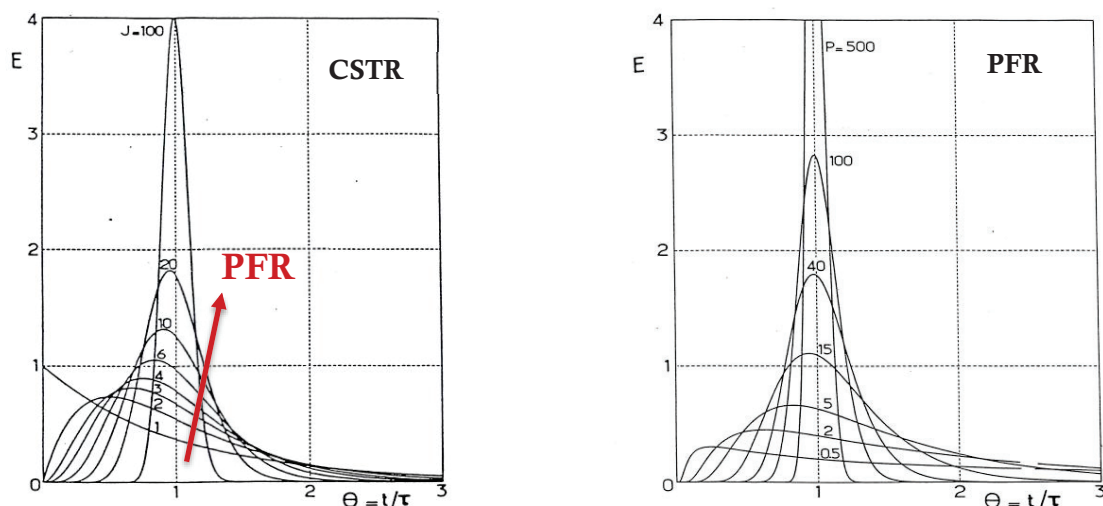


Figure VI-3. Idealistic representation of  $E(t)$  function for series of CSTR (left panel) and PFR (right panel) with  $J$ =number of CSTR in series and  $P$ =number of PFR in series [435].

The estimated mean residence times according to the tracer evolution through the experimental bench are represented Table VI-3. The hydrodynamic system was characterised at  $160 \text{ ml}\cdot\text{min}^{-1}$  and  $40 \text{ ml}\cdot\text{min}^{-1}$  according to operating conditions and at  $200^\circ\text{C}$  and  $500^\circ\text{C}$  respectively for representing the potential temperature impact on concentration measurements. Following the estimated ( $\tau$ ) Table VI-3 and the applied volumetric flow, the FTIR gas chamber volume was estimated at  $260 \text{ ml}$  ( $2.6 \cdot 10^{-4} \text{ m}^3$ ) and employed in the model construction. The optimal number of CSTR in series for depicting the gas cell was estimated to 1 reactor, which represent a typical dispersive behaviour. Only a slight delay was observed at the experience beginning, inferior at 15 sec, less than the 1.3 min required to obtain 32 scans during the different experimental tests. This pure delay was therefore neglected here. Note that the number of scans (e.g. the time required for one observation acquisition) was decreased during the hydrodynamic study in order to obtain a better time resolution.

Following these results, the overall hydrodynamic behaviour, from the experimental reactor to the FTIR gas chamber, was assumed to be mainly directed by the FTIR chamber volume, with an experimental reactor volume of  $8.58 \cdot 10^{-8} \text{ m}^3$  represented by 8 CSTR in series and a dispersive gas chamber of  $2.6 \cdot 10^{-4} \text{ m}^3$  represented by 1 CSTR. This behaviour is transcript through the scheme Figure VI-5 for more convenience, representing the overall experimental bench hydrodynamic in our conditions.

Table VI-3: Estimated mean residence time versus space velocities for different flow rates and temperature with corresponding volume ( $V_{cell}$ ) estimation.

Temperature Experimental reactor ( $^{\circ}\text{C}$ )	Experimental reactor Flow rate ( $\text{m}^3 \cdot \text{s}^{-1}$ )	Temperature FTIR cell ( $^{\circ}\text{C}$ )	FTIR Cell Flow rate ( $\text{m}^3 \cdot \text{s}^{-1}$ )	$\tau$ (sec)	$V_{cell}$ (ml)	Optimal $n_{CSTR}$
200	$4.85 \cdot 10^{-6}$	150	$4.85 \cdot 10^{-6}$	60	260	1
500	$7.93 \cdot 10^{-6}$			60		1
150	$1.04 \cdot 10^{-6}$		$1.04 \cdot 10^{-6}$	250		1

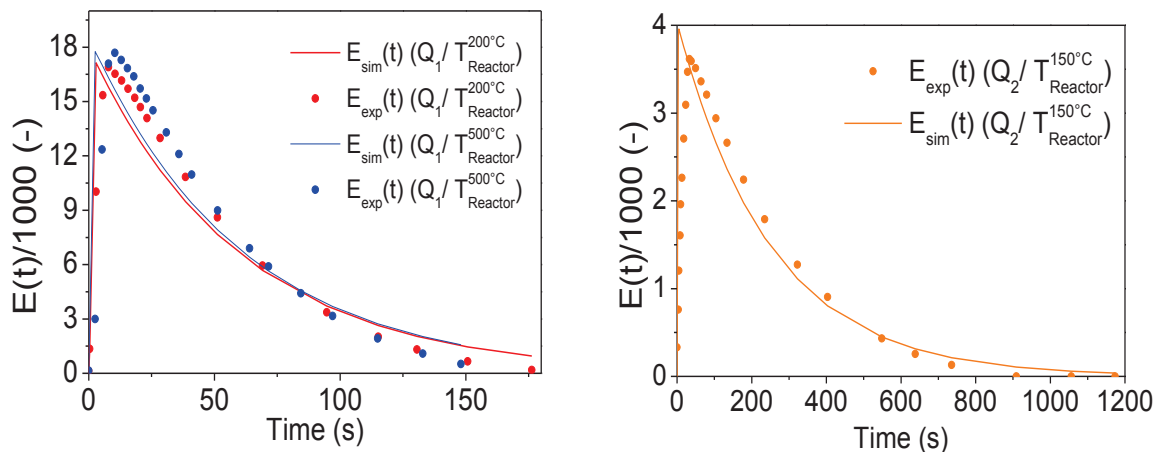


Figure VI-4: Experimental  $E(t)$  function compared with simulated one at different temperature and flow rates:  $160 \text{ ml} \cdot \text{min}^{-1}$  (A) and  $40 \text{ ml} \cdot \text{min}^{-1}$  (B).

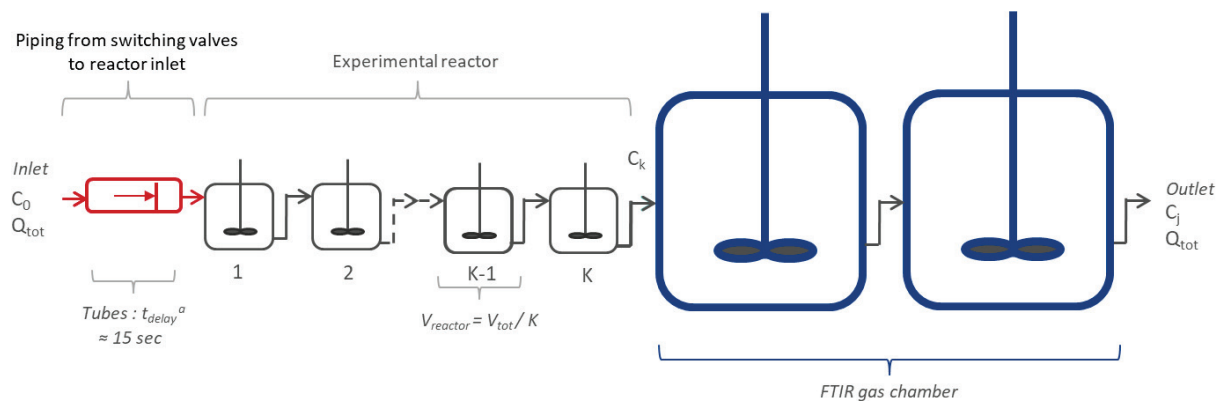


Figure VI-5: Schematization of the overall experimental bench hydrodynamic composition

## VI-2.3. Linear Driving Force approximation

Typically for heterogeneous reactions, reactant has to migrate through the different phases until the active sites prior to its reaction. In this study, with gaseous mixture flowing through a porous solid catalyst, the reactive molecules have to be transferred from the bulk gas to the different active sites. From a general point of view, different mechanisms take place during this migration, depending on the molecule environment, which 3 types are generally assumed for solid composed of macro, meso and micropores (See Figure I-23). Accordingly, from a respective decreasing  $lpm/D_{pore}$  ratio point of view, the mechanisms are characterized as 1) molecular diffusion when  $lpm/D_{pore} \ll 1$ , 2) Knudsen diffusion for  $lpm/D_{pore} > 1$ , and 3) surface diffusion if  $lpm/D_{pore} \gg 1$  (and  $D_{pore} \approx D_{molecule}$ ) [440,441]. In the case of microporous material as CHA zeolites, the resistance can be expressed by the consecutive resistances from molecular and surface diffusion processes respectively, as represented with the equivalent electric model Figure VI-6 regarding the resistance in series law [442].



Figure VI-6. Equivalent electrical model for mass transfer representation in porous media.

Typically, the most rigorous formulation to model the depicted flow densities considering the detailed mass transfer resistance is the Maxwell-Stefan law, describing the mass balance between the diffusion driving force, defined by chemical potential gradient with the molecules-molecules (molecular diffusion) and molecules-solid (surface diffusion) interactions [441,443]. Compared with Fickian representation, the Maxwell-Stefan approach allow the crucial consideration of multicomponent system and the intermolecular interaction. This model is widely employed for zeolite diffusion representation but the complex system discretization, do not directly allow the determination of analytical solutions and required further numerical computation method [444–446]. In that respect, the overall mass transfer resistance can be linearized by one and only ordinary differential equation, an approximation firstly developed by Glueckauf et al. (1947) [447]: The Linear Driving Force (LDF). The LDF account for the mass transfer between the fluid and intra-particle phases with constant diffusion coefficients depicting the resistance occurring through the system. It was characterized to well described the adsorption kinetics on heterogeneous solids and for evaluating adsorbent column dynamics prior to its simple expression [448,449], where the flow density is considered proportional to the differences between the bulk gas and the external concentrations [450]:

$$N_i = k_{TOT} (C_{i,g} - C_{i,interf\ g/s}) \quad (13)$$

With  $N_i$  the transferred molar flux ( $\text{mol.m}^{-2}.\text{s}^{-1}$ ),  $k_{TOT}$  the mass transfer coefficient ( $\text{m.s}^{-1}$ ) and the driving force  $C_{i,g} - C_{i,interf\ g/s}$  concentrations difference of specie  $i$  in bulk gas and at the interface with active sites respectively ( $\text{mol.m}^{-3}$ ).

Thus, the film model was applied in the current proposed model for its simple, analytical and physically consistencies which therefore not further burden the model computation of the heterogeneous catalytic system. The mass transfer resistance is concentrated within a fine film adjacent to the solid surface, where mass accumulation is assumed not possible within the film thickness. This approximation is typically used in literature on similar topic for the same reasons evoked here [190,225,451]. Considering a microporous system only, as it was previously demonstrated with CHA material, with monodispersed and spherical particles, the overall mass transfer resistance related to the depicted flow densities can be linearized and ascribed as the following sum of resistances [440]:

$$\frac{1}{a_{geo} \cdot k_{TOT}} = \frac{R_p}{3k_{fluid}} + \frac{R_p^2}{15 D_c} \quad (14)$$

With  $a_{geo}$  the mean geometric surface area ( $m^{-1}$ ),  $k_{TOT}$  the global mass transfer resistance ( $m \cdot s^{-1}$ ),  $R_p$  the particle radius (m),  $k_{fluid}$  the mass transfer resistance from the external fluid film ( $m \cdot s^{-1}$ ) and  $D_c$  the related crystal diffusion coefficient ( $m^2 \cdot s^{-1}$ ).

Regarding Eq. 14, the particle dimensions' role is clearly visible, which the second term relative to the surface diffusion will greatly depend. It is evident that external mass transfer resistance will become lower as the particle radius  $R_p$  is sufficiently small, a conclusion directly probed in Chapter V during the evaluation of potential external mass transfer resistance (See Table V-1). The mass transfer resistance at the grain boundary  $k_{fluid}$  can be approximated in a first attempt, for comparison purpose with the second term of Eq. 14, through the Sherwood number reflecting the convective and diffusion mass transfer ratio as:

$$Sh = \frac{k_{fluid} L_c}{D_{molec}} \quad (15)$$

With  $D_{molec}$  the molecular diffusion coefficient ( $m^2 \cdot s^{-1}$ ) (Eq. 8).

According to the experimental reactor configuration, the Sh number was therefore estimated with a correlation developed by Kunii & Levenspiel (1969) for FPB reactor [452,453], demonstrated between Re and Sc numbers. Knowing that Re and Sc were estimated in previous section (VI-2.1) for typical STD SCR operating condition, representative of the low temperature mass transfer, Sh were estimated to 2.2 according to Eq 16:

$$Sh = 2 + 1.8 Re_p^{0.5} Sc^{1/3} \quad (16)$$

Which further provide according to Eq. 15 above, with  $L_c$  the particle diameter and  $D_{molec}$  the previously determined molecular diffusion coefficient, a mass transfer coefficient  $k_{fluid}$  estimated at  $240 m \cdot s^{-1}$ . An elevated external transfer which represents in the first term in Eq. 14 a characteristic time ( $\tau_{film}$ ) of  $10^{-9}$  sec order of magnitude. A resistance therefore neglected during test performances, as compared with longer time taken by chemical processes [226,454,455] as  $NH_3$  adsorption steps for instance [456,457].

Comparatively, the characteristic time representing the second term Eq. 14, relative to surface diffusion, can be approximated taking into consideration an estimated diffusion coefficient  $D_c$  for Cu-CHA solid. For instance, O'Malley et al. studied through QENS and corresponding Molecular Dynamics (MD) simulations, the  $NH_3$  diffusivity in commercial Cu-CHA catalyst and estimated a self-diffusion coefficient for  $NH_3$  of  $10^{-11} \text{ m}^2.\text{s}^{-1}$  magnitude order [215]. Similarly, Krishna reported in his review on diffusion in crystalline materials a  $10^{-10}$  to  $10^{-11} \text{ m}^2.\text{s}^{-1}$  diffusion coefficient in CHA [458]. In that respect, the characteristic time  $\tau_{\text{surface}}$  can be firstly approached with similar magnitude order diffusion coefficient for comparison purposes with the external resistance. In that respect, a corresponding  $\tau_{\text{surface}}$  is estimated to  $10^{-1}$  sec order of magnitude, much higher than  $\tau_{\text{film}}$ , directly displaying the resistance proportion induced by diffusion within CHA material. Once the kinetic model done, these characteristic times will be calculated on the estimated parameters basis and compared with the one relative to the different reactional characteristic times during simulated STD SCR conditions, for potential rate limiting process investigation.

#### VI-2.4. Model structure and parameter estimation with Matlab © software

In this study, the non-linear system of equations is firstly composed of mass conservation balances between bulk gas species, using the different gas concentrations, described through Eq. (17, 18, 21 and 22) as ordinary differential equation (ODE):

For first tank (n=1):

$$\frac{dC_{i,g}^{n=1}}{dt} = -\frac{1}{\tau}(C_{i,in} - C_{i,g}^{n=1}) - \frac{1}{\tau_{\text{transf}}}(C_{i,g}^{n=1} - C_{i,interf}^{n=1}) \quad (17)$$

For n<sup>th</sup> tank:

$$\frac{dC_{i,g}^n}{dt} = -\frac{1}{\tau}(C_{i,g}^{n-1} - C_{i,g}^n) - \frac{1}{\tau_{\text{transf}}}(C_{i,g}^n - C_{i,interf}^n) \quad (18)$$

$$\text{With } \tau = \frac{\varepsilon.V_{\text{Bed},i}}{Q_{\text{tot}}} \quad \text{And } \tau_{\text{transf}} = \frac{1}{k_{\text{tot}}.a} \quad (19-20)$$

Where  $C_{i,in}$  ( $\text{mol}.\text{m}^{-3}$ ) the inlet gas concentration of the i<sup>th</sup> bulk gas,  $C_{i,g}$  ( $\text{mol}.\text{m}^{-3}$ ) the bulk gas concentration and  $C_{i,interf}$  ( $\text{mol}.\text{m}^{-3}$ ) the interfacial concentration.  $\varepsilon$  is related to the solid void fraction,  $V_{\text{Bed},i}$  ( $\text{m}^3$ ) to the n<sup>th</sup> CSTR volume and  $Q_{\text{tot}}$  ( $\text{m}^3.\text{s}^{-1}$ ) the volumetric flow. Finally,  $k_{\text{tot}}$  represents the global mass transfer coefficient ( $\text{m}.\text{s}^{-1}$ ) and  $a = (3/R).(1-\varepsilon)/\varepsilon$  assuming spherical particles of R (m) radius in the fixed packed bed reactor of  $\varepsilon$  porosity (-).

Moreover, the so-called film model is employed to describe mass transfer between bulk gases and the catalyst surface as for the n<sup>th</sup> reactor:

$$0 = \sum_j^{NR}(\nu_{i,j}R_j) + \frac{1}{\tau_{\text{transf}}}(C_{i,g}^n - C_{i,interf}^n) \quad (21)$$

With  $\nu_{i,j}$  the stoichiometric coefficient relative to  $i^{\text{th}}$  specie in  $j^{\text{th}}$  reaction and  $R_j$  the corresponding reaction rate ( $\text{mol.m}^{-3}.\text{s}^{-1}$ ), where  $\text{NR} = \text{reactions relative to adsorption/desorption processes (NR}_{\text{ads/des}}) + \text{reaction relative to the chemical transformation (NR}_{\text{chemistry}})$ .

The adsorbed species onto catalyst active sites are represented as following the Langmuir isotherm. Langmuir isotherm seems better suitable for the definition of sites discretized by their nature, according with the site definition described next section. Temkin isotherm were successfully employed in other studies [190,233,459], where the gathering of different active sites nature in a lumped site, explicit the need to represent the adsorbate-adsorbate interactions with the use of an additional parameter [235]. The coverage evolution in time is represented through:

$$\Omega_k \frac{d\theta_i}{dt} = \sum_j N_i (\mu_{i,j} R_j) \quad (22)$$

Where  $\theta_i$  (-) described the  $i^{\text{th}}$  specie coverage, respecting for each sites  $1 = (\sum_i^{N_{\text{ads/des}}} \theta_i) + \theta_{\text{free}}$ ,  $\Omega_k$  the storage capacity of  $n^{\text{th}}$  sites and  $R_j$ , the reaction rates concerning adsorbed species ( $\text{mol.m}^{-3}.\text{s}^{-1}$ ), and  $N_i = N_{i,\text{chemistry}}$  the surface reactions implying specie  $i$ .

The global mass transfer ( $k_{\text{tot}}$ ) coefficient between gas and catalyst surface is determined through the numerical computation and represents the global diffusion resistance encountered within the solid material through the film model as developed earlier.

Figure VI-7. displays the global structure of the proposed model, representing the parameter estimation procedure. The software employed was MATLAB R2013b © and two principal subroutines were employed, namely: “*ode15i*” and “*lsqnonlin*”. More precisions can be found on the subroutines description and their limits elsewhere [460,461]. The model was developed to simulate the catalyts performances from 200°C to 500°C or in other words, from the tests beginning  $t_0$  to the end of temperature program. Providing as initial conditions the experimentally measured concentrations and temperature at  $t_0$ , the differential and algebraic set of equations representing the mass balances were solved by *ode15i* subroutine, for each time intervals, accordingly with the non-linear behavior of the system. The model outputs are the simulated gas concentrations in  $\text{mol.m}^{-3}$  ( $C^{\text{simu}}_{i,g}$ ) evolutions through the time. The sum of their squared differences with experimental observations ( $C^{\text{exp}}_{i,g}$ ) in  $\text{mol.m}^{-3}$  was minimized thanks to *lsqnonlin* subroutines, by iterative parameter adjustments. The following Eq. 23 gives the performed least-square sum:

$$Y = \sum_1^N (C^{\text{exp}}_{i,g} - C^{\text{simu}}_{i,g})^2 \quad (23)$$

The estimated parameters were the pre-exponential factors ( $k_{o,j}$ ) and activation energies ( $E_{a_j}$ ) of each  $j^{\text{th}}$  implied reaction within the mechanistic path, reaction constant ( $k_{j,\text{ads}}$  and  $k_{j,\text{des}}$ ) of non-activated adsorption processes of  $\text{NH}_3$  and  $\text{H}_2\text{O}$ , the active sites densities ( $\Omega_i$ ) and the global mass transfer coefficient

( $k_{tot}$ ). On the other hand, the model inputs were the experimental time, temperature, catalyst mass and inlet concentration compositions.

As shown on Figure VI-7, the coherence of the estimated kinetic parameters was controlled prior to the acquisition of the final parameters. It was conducted through the analysis of the different active site performances behaviour provided by the model and compared with the dedicated investigations performed in previous Chapter III,IV and V. In that respect, the characteristic role of the different site configurations were verified for each simulations. For instance, according both with literature studies and presented investigations through the current work, this step was the opportunity to verify the main role of strong exchanged cations during STD SCR reaction or the strong  $\text{NH}_3$  oxidation displayed by surface nano-copper clusters.

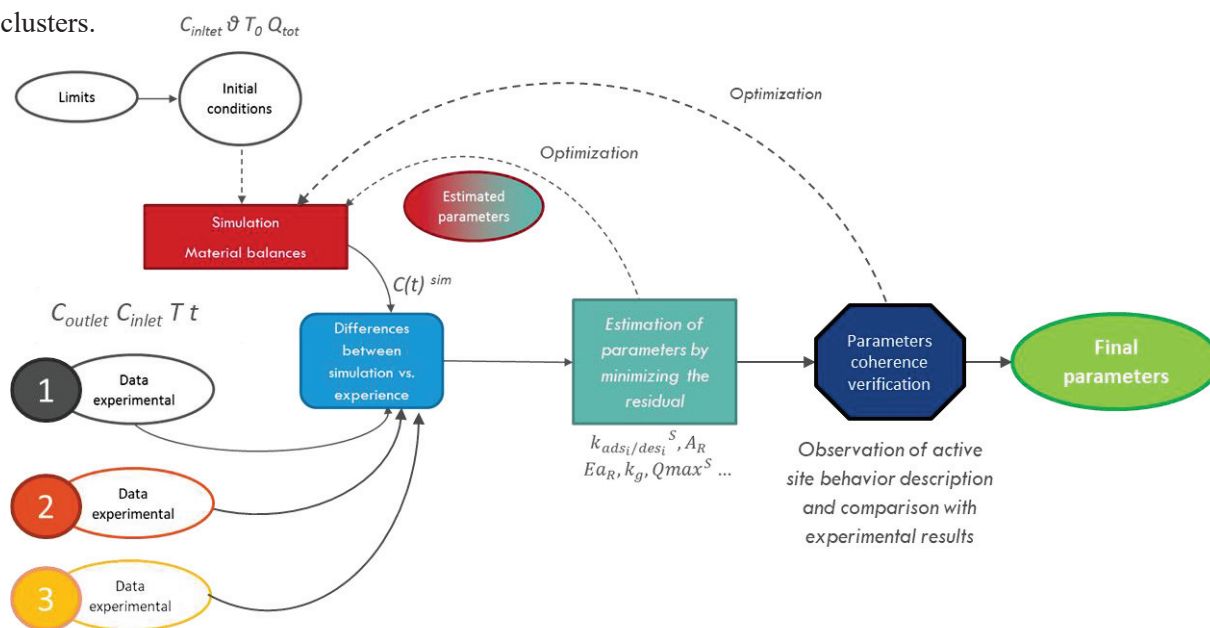


Figure VI-7. Model structure and parameter estimation procedure for 3 data set of experiments in parallel.

### VI-3. Kinetic Model

#### VI-3.1. Model Input: $\text{NH}_3$ TPD experiments and Flow reactor measurements

TPD experiments were obtained by using ammonia as a probe molecule ( $\text{NH}_3$ -TPD). 0.035g of crushed samples were deposited on ceramic frit into a U-shaped quartz tube. To monitor the sample temperature, a thermocouple was inserted near to the catalytic bed and the reactor was placed inside a temperature-controlled furnace. The sample was pre-treated under oxidative atmosphere at  $500^\circ\text{C}$  for 30 min with a heating ramp of  $10^\circ\text{C}\cdot\text{min}^{-1}$ . After a 30 min He flush at  $35^\circ\text{C}$ , a flow of  $40\text{ ml}\cdot\text{min}^{-1}$  made of 1000 ppm  $\text{NH}_3$ , 80000 ppm (8%)  $\text{O}_2$  and 0-40000 ppm (4%)  $\text{H}_2\text{O}$  was injected at  $150^\circ\text{C}$  until signal stabilization. The catalysts were then exposed to He after the gases was cut off, until signal stabilization before starting the desorption temperature program. The desorption temperature program consists of a  $2^\circ\text{C}\cdot\text{min}^{-1}$  ramp until  $500^\circ\text{C}$ . Desorbed ammonia molecules were analysed and quantified with a Fourier

Transform Infrared (FTIR) spectrometer (NICOLET) equipped with a DTGS detector and a heated 2m gas cell. In this study, regarding the catalytic test temperature window (200°C-500°C), the adsorption step during the NH<sub>3</sub>-TPD experiments were conducted at 150°C for obtaining further information about the accessible site densities at relevant temperatures. This temperature was chosen to remain relatively close to the starting SCR test temperature, without risking any beginning of NH<sub>3</sub> parasitic oxidation, thus preventing of possible impact of low temperature chemical reactions on adsorption and desorption parameters evaluation.

Moreover concerning NH<sub>3</sub>-TPD, it is important to note that the obtained characterization profiles have to be exploited with great care [462]. Indeed, in the case of parallel readsorption processes, mass transfer limitations, ammonia solvation or modified experimental conditions (different temperature heating ramp or temperature adsorption difference for instance) the maximum temperature peaks of desorption can be shifted or overestimated, and so, alter the corresponding interpretations [344,353]. In that respect, the coherence of simulated surface coverage evolutions in temperature during NH<sub>3</sub> TPD were monitored, and the absence of consequent NH<sub>3</sub> solvation verified, as displayed through low temperature NH<sub>3</sub> DRIFT experiments (Figure IV-8 A,B) [353,463].

Concerning the transient SCR test performances, the fresh (0.035 g in U-shaped quartz reactor) catalyst surface was firstly cleaned at 200 °C in flowing He. The whole experimental test bench is represented on the Process Flow Diagram (PFD) Figure VI-8. In order to avoid water condensation and risks of ammonium nitrate precipitation, the system temperature limit was fixed at a minimum of 200 °C and all the gas lines were heated (thick lines on the PFD). The introduction of reactants gases was made by flow controllers and the water vapour fraction was separately supplied by a thermostated saturator, reaching a total Gas Hourly Space Velocity (GHSV) of 142 000 h<sup>-1</sup>. The NH<sub>3</sub>, NO, NO<sub>2</sub> and N<sub>2</sub>O effluent gas concentrations, at atmospheric pressure, were monitored by FTIR spectrometer (NICOLET) thanks to a gas cell chamber of 200 ml. Outlet dinitrogen was followed with an in-line micro gas phase chromatography (μGC SRA % GC-R3000). Transient SCR tests were conducted with an inlet gas range composition of 0-1000 ppm NH<sub>3</sub>, 0-1000 ppm NO, 80000 ppm (8%) O<sub>2</sub> with 0-40000 ppm (4%) H<sub>2</sub>O and He as gas balance for a total volumetric flow of 10 L/h. Both slow and rapid temperature input modifications were investigated in order to observe the different model simulated responses in time. The aim is to solicit the model under several operating conditions for better investigating the model capacity to simulate dynamic behavior. Additional performances tests were carried out in isothermal conditions (200°C) with constant feed of 1000 ppm NO, 80000 ppm (8%) O<sub>2</sub> and 40000 ppm (4%) H<sub>2</sub>O in He with stepwise increase of NH<sub>3</sub> concentration of 100 ppm as input modification. At such low temperature, the NH<sub>3</sub> interaction with the surface is strong and different catalyst behavior are expected. All operating conditions are further described in the Table VI-4.

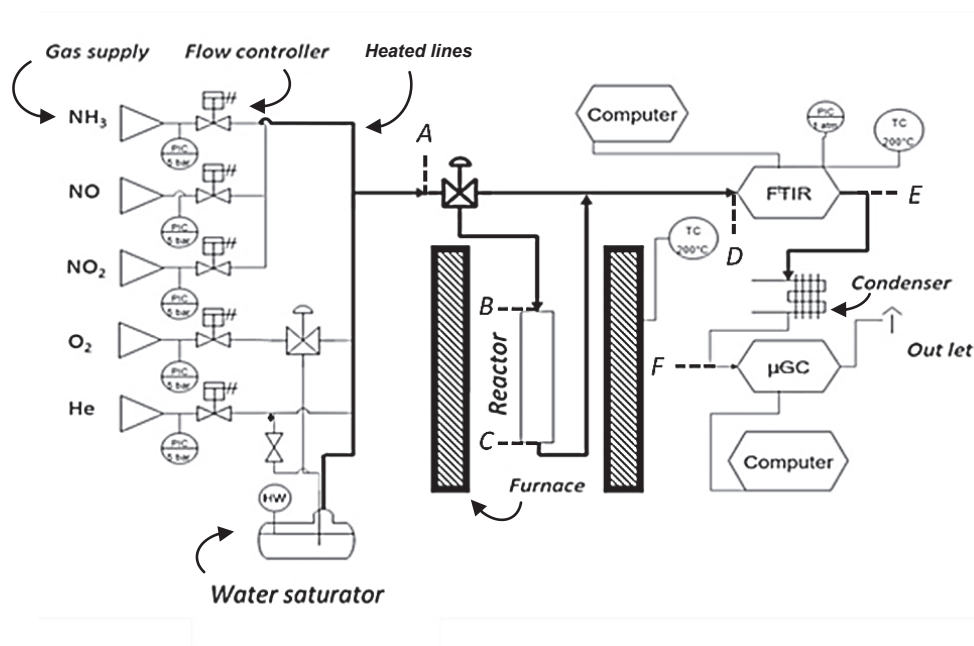
Finally, note that a specific attention was given to the first experimental point obtain during micro reactor test performances and the corresponding input values at  $t_0$ , for adequately representing the



experimental concentration profile evolutions during the first seconds. Indeed, the initial time ( $t_0$ ) corresponds to the experience beginning, the moment when the reactional gaseous flow is switch on the loaded reactor by pneumatic valve, which the catalyst site coverages are assumed equal to 0. However, the FTIR analyzer synchronized with  $\mu$ -GC equipment display a time resolution above the minute, which do not allow to accurately capture the first experimental point. In the case where the first experimental observation was not exploitable, the model was initialized on the following one ( $t_{0+1}$ ), implying therefore a different surface state with different coverage values. In that respect, the species coverage on storage sites at  $t_{0+1}$  were adequately tuned for taking into consideration the experimental difference.

Table VI-4. Summary of experiments conducted on reference catalyst Cu-SAPO-34-IE for model establishment

Figure	Experiments	Inlet gas composition	Operating conditions
9 (A)	H-SAPO-34 NH <sub>3</sub> TPD	1000 ppm NH <sub>3</sub> , (8%) O <sub>2</sub> , (4%) H <sub>2</sub> O, Q <sub>tot</sub> = 2.4 L.h <sup>-1</sup>	Adsorption: 150°C (steady state) Desorption: 2°C.min <sup>-1</sup> ramp until 500°C
9 (B)	Cu-SAPO-34 NH <sub>3</sub> TPD	1000 ppm NH <sub>3</sub> , (8%) O <sub>2</sub> , Q <sub>tot</sub> = 2.4 L.h <sup>-1</sup>	
9 (C)	Cu-SAPO-34 NH <sub>3</sub> TPD	1000 ppm NH <sub>3</sub> , (8%) O <sub>2</sub> , (4%) H <sub>2</sub> O, Q <sub>tot</sub> = 2.4 L.h <sup>-1</sup>	
10	NH <sub>3</sub> oxidation	1000 ppm NH <sub>3</sub> , (8%) O <sub>2</sub> , (4%) H <sub>2</sub> O, Q <sub>tot</sub> = 10 L.h <sup>-1</sup>	From 200°C to 500°C with 50°C stepwise increase at 10°C.min <sup>-1</sup> and 60 min step
11			2°C.min <sup>-1</sup> ascending/descending temperature ramp from 200°C to 500°C
12	NO oxidation	1000 ppm NO, (8%) O <sub>2</sub> , (4%) H <sub>2</sub> O, Q <sub>tot</sub> = 10 L.h <sup>-1</sup>	From 200°C to 500°C with 50°C stepwise increase at 5°C.min <sup>-1</sup> and 30 min step
13			2°C.min <sup>-1</sup> ascending/descending temperature ramp from 200°C to 500°C
14,19	STD SCR	1000 ppm NH <sub>3</sub> , 1000 ppm NO, (8%) O <sub>2</sub> , 0- (4%) H <sub>2</sub> O Q <sub>tot</sub> = 10 L.h <sup>-1</sup>	2°C.min <sup>-1</sup> ascending/descending temperature ramp from 200°C to 500°C
15		1000 ppm NH <sub>3</sub> , 1000 ppm NO, (8%) O <sub>2</sub> , (4%) H <sub>2</sub> O Q <sub>tot</sub> = 10 L.h <sup>-1</sup>	From 200°C to 500°C with 50°C stepwise increase at 10°C.min <sup>-1</sup> and 30 min step
22		0/1000 ppm NH <sub>3</sub> , 1000 ppm NO, (8%) O <sub>2</sub> , (4%) H <sub>2</sub> O, Q <sub>tot</sub> = 10 L.h <sup>-1</sup>	Validation test: Isothermal (200°C)



Volume	Tubing A to B	Total U-shaped Reactor B to C	Tubing C to D	Gas cell D to E	Tubing E to F
(ml)	100	5	90	260	100

Figure. VI-8. Experimental tests bench Process Flow Diagram with corresponding average volumes

### VI-3.2. Surface description : H-SAPO-34 & Cu-SAPO-34-IE

The followed approach for developing the kinetic model relied on semi-global reactions between bulk gas and adsorbed surface species both linked by the interfacial limit. These interactions were assumed to behave as an Eley-Rideal mechanism, commonly introduced during mechanistic investigations for such type of heterogeneous catalytic reduction process [201,202]. As developed during the Introduction section, Cu-SAPO-34 typically displays of two types of active sites: the Brønsted acid sites and the Lewis acid. Accordingly to the characterization results obtained during the previous studies about parent H-SAPO-34 support and Cu-SAPO-34-IE catalyst, different active site configurations, were considered as following:

H-SAPO-34 zeolite support is mainly constituted of weak (weakly bound species) and strong (typically bridged  $-\text{Si-OH-Al}-$ ) Brønsted and Lewis acid sites. In that respect, weak and strong sites inherent to the support were respectively denoted as S1 and S2, representing the main adsorption and desorption active sites of ammonia and water molecules. A strength difference further enlightened by  $\text{NH}_3$ -TPD experiments, which the obtained asymmetric desorption profiles in temperature can give first hint about both strength sites (Figure IV-7). In the current model, these sites represent the pure storage capacity of the zeolite support. As described by Wang et al. [205], their relations with redox active centers will take place through the dynamic of molecule adsorption and desorption from one site to another, thus constituting the exchange synergy capacity between sites. Through the deconvolution of the characterized

desorption profiles obtained at 150°C previously carried out, the model was hereby initialized with the obtained sites densities, corresponding to a total of 0.560 mmol.g<sup>-1</sup>. Ammonia and water molecules are assumed in this model to be adsorbed following a 1:1 ratio on the Brønsted acid sites.

Table VI-5. Representation of surface-active sites configurations defined in the multi-site kinetic model of Cu-SAPO-34-IE and H-SAPO-34 support

		Denomination	Species example	Relative position	
Catalyst Cu-SAPO-34-IE	Zeolite support H-SAPO-34	Weak <sup>1</sup> Brønsted acid sites	T-OH (T = Si, Al or P)	External (support) (S1)	
		Strong <sup>1</sup> Brønsted acid sites	T-OH-T (ex : Si-OH-Al)	Internal (support) (S2)	
	Strong Lewis acid sites: Exchanged copper cations		ZCu <sup>2+</sup> , ZCu <sup>+</sup>	Internal (6MR / 8MR) (S3)	
	Nano/Micro copper oxide surface cluster		ZCuO <sub>x</sub> (x≤1)	External (support surface) (S4)	

<sup>1</sup> from the point of view of NH<sub>3</sub> adsorption strength through investigated temperature [341–344]

Concerning Cu-SAPO-34-IE catalyst, made of the previously described H-SAPO-34 support, the precise Cu sites nature distribution through the catalyst was not studied in this work, requiring more thorough investigations. But the characterization of the most representative active species on this catalyst led the surface model description to be constructed with two types of active sites: one as redox active sites copper cations within the lattice in exchanged positions (S3), providing both adsorption sites for NH<sub>3</sub> and H<sub>2</sub>O and redox sites. And a second one, characterized as homogeneously distributed on the surface in nano-surface copper oxides clusters form (S4). Regarding the preparation method, these copper sites are in addition to the Brønsted acid sites S1 and S2 brought by the zeolite support, displaying close characteristics to H-SAPO-34 sites [230]. The exchanged active copper sites were previously characterized through temperature during our previous in-situ study experiments and are assumed here to be mainly depicted by copper cations located in the six-membered rings (S3) since the catalyst was under-exchanged as the calculated ratio informs Table VI-6 [244]. The ICP OES results reported in Table VI-6 below were used as first estimation of the copper sites densities within catalyst for parameter initialization. The exchanged

sites as  $\text{Cu}^{2+}$  within 6MR rings are characterized as the main active sites for  $\text{NH}_3$  SCR. Its interaction with ammonia was previously monitored during in-situ studies and further characterized through temperature Figure IV-7 A and Figure V-20. According with cations interaction with  $\text{NH}_3$  until elevated temperature, S3 is considered as strong active copper species in the model. In the other hand, the nano-sized surface cluster sites, are considered as low to medium temperature active sites, since their interactions with ammonia better occur between 200-350°C as it was previously suggested during  $\text{NH}_3$  TPD experiments and further characterized by in-situ techniques Chapter V.

Table VI-6. Zeolite support (H-SAPO-34) and catalyst (Cu-SAPO-34-IE) chemical composition

	Cu (wt%) <sup>a</sup>	Si (%wt) <sup>a</sup>	Al (%wt) <sup>a</sup>	P (%wt) <sup>a</sup>	Si/Al (molar ratio)	SSA ( $\text{m}^2\cdot\text{g}^{-1}$ ) <sup>b</sup>	Micro- porous volume ( $\text{cm}^3\cdot\text{g}^{-1}$ ) <sup>b</sup>	Total amount adsorbed $\text{NH}_3$ ( $\text{mmol g}^{-1}$ catalyst) (150°C) <sup>c</sup>	Exchanged level (%)
<b>Cu- SAPO 34-IE</b>	1.5	2.7	21	20	0.13	577	0.20	0.576	49
<b>H- SAPO- 34</b>	0	2.5	17	16	0.14	573	0.20	0.560	0

<sup>a</sup> Determined by ICP measurements

<sup>b</sup> Specific surface area (SSA) and total microporous volume determined by nitrogen adsorption/desorption experiments

<sup>c</sup> Measured through  $\text{NH}_3$  TPD experiments

### VI-3.3. Reactions and rate expressions

The standard SCR mechanism proposed in this study, take into consideration some of the key points inherent to the  $\text{NH}_3$ - SCR mechanism development problematic with Cu-CHA catalyst, as developed by Beale et al. through their published review [412]. The transcription of these different conclusions, from a modelling operation point of view, could express that the SCR detailed mechanism will strongly differ following the nature of the employed active sites, justifying the importance relevance of their definition and status through the model assumptions. Thus, following the active sites description,  $\text{NH}_3$  will be stored in different configurations and consequently, the copper active sites status and nature (hydroxylated  $\text{Cu}^{2+}\text{-OH}$ , naked  $\text{Cu}^{2+}$ , monomer, dimeric), will also be determinant for the mechanistic pathway construction. A speciation which finally define reactive adsorbed molecules and obtained products in the chemical equations. Furthermore, the detailed synergetic effect between the Brønsted and redox sites are not fully determined yet and required further investigations for a complete determination of the SCR cycle process. Additionally, the precise NO and  $\text{H}_2\text{O}$  implications within the SCR process still represent points of debates as surveyed by Beale et al. [412].

Concerning the adsorption and desorption process, only  $\text{NH}_3$  and  $\text{H}_2\text{O}$  were considered to competitively interact with the active sites in the current model, through the high affinity of the basic

ammonia molecule with the acid zeolite support and the spontaneous adsorption of water [235,464]. In that respect, the NH<sub>3</sub> and H<sub>2</sub>O adsorption on S1,2,3 and 4 was assumed as a non-activated process ( $E_{ads}^{S_{NH_3}} = 0 \text{ kJ.mol}^{-1}$ ) [234,457].

Typically for the desorption processes and reactions, the Arrhenius equation was employed to capture the temperature dependence of reactional rate constant  $k_j$ , defined as following:

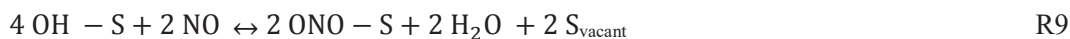
$$k_j = k_{0,j} \cdot \exp\left(\frac{-E_{a,j}}{RT_s}\right) \quad (24)$$

With  $k_{0,j}$  the pre-exponential factor of  $j^{\text{th}}$  reaction (which the dimensions depend on reaction rate expression),  $E_a$  the activation energy of  $j^{\text{th}}$  reaction ( $\text{kJ.mol}^{-1}$ ),  $R$  the gas constant ( $\text{J.K}^{-1}.\text{mol}^{-1}$ ) and  $T_s$  the catalyst temperature (K).

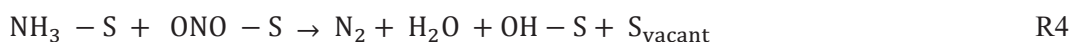
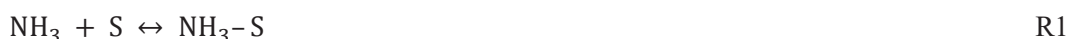
Thus, the direct NH<sub>3</sub> and H<sub>2</sub>O adsorption competition was implemented through the model, which the impact on SCR performances will be further detailed in next Section VI-4.4. Indeed, the consideration of important amount of water within the reaction mechanistic path is crucial for the catalyst behaviour representation, as it was further investigated by various studies on several zeolite-based catalyst [411,457]. Considerations of water impact on SCR performances are of primary importance for real exhaust conditions simulations knowing that H<sub>2</sub>O is hardly avoidable in the exhaust line. As experimentally investigated in previous Chapter V, the excess of water vapour in the exhaust line impact the SCR performances principally at low temperature, typically from 200°C to 350°C, where its adsorption onto the catalyst favour the conversions of NO<sub>x</sub> molecules. The detailed mechanism interaction of redox sites with water molecule is still under investigation [223,296], but several studies led to the conclusion of a hydroxylation step of copper sites as  $Z\text{Cu}(\text{OH})^+$  species, which further interact with NH<sub>3</sub> for a complex formation with monomeric copper species such as  $[\text{Cu}(\text{OH})(\text{NH}_3)_x]^+$  or dimeric Cu [157,465]. Next, this formation could react with NO type species as nitrites for finally produce both N<sub>2</sub> and H<sub>2</sub>O [216]. Thus, by considering H<sub>2</sub>O adsorption and desorption within the catalyst on the different proposed active sites (S1 to S4), the hydroxyl formation is proposed as the following reactions sequence below, where for model simplification, the oxygen adsorption (Eq. 25) and disproportionation (Eq. 26) on active sites were not detailed but better summarize by R3 :



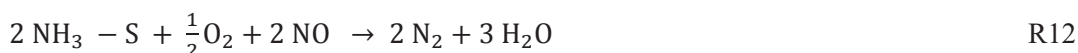
These hydroxyl group formations were described in the model following the dehydration step proposed by Komatsu et al. for NO reduction on Cu<sup>2+</sup>exchanged zeolites [209]. Thus, OH groups can react with interfacial NO molecules in order to form adsorbed nitrite species on redox sites. During the current SCR performances investigations in oxidative condition (8%vol O<sub>2</sub>), nitrite species were considered as key intermediates for standard SCR reactions on Cu-CHA catalyst. This assumption is in line with several recent studies which have demonstrated the nitrite route importance through time-resolved DRIFT experiments and corresponding kinetics experiments [207,211,402,423]. Following this, nitrite species can be thus retrieved in some proposed mechanistic path and model on Cu-CHA catalysts [216,230,338]. In that respect, adsorbed nitrite moieties were considered as the resultant interaction of NO with the surface, where the N atom is assumed to be in an (III) oxidation state. The following reaction R9, represents this reversible interaction in the proposed model:



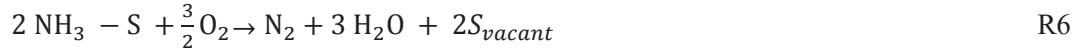
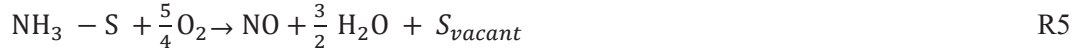
Therefore, the standard SCR reaction on redox sites, in presence of water, was described as the reaction between adsorbed ammonia and S-ONO species R4 consequently to the NH<sub>3</sub> adsorption R1:



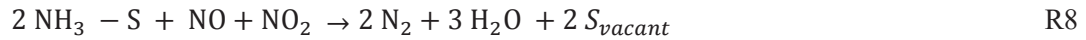
In dry condition, such behaviour is compromised but STD SCR reactions still occurs, a different operating condition considered in the kinetic model through the general reaction R12. Indeed, copper sites were assumed to readily disproportionate oxygen and react through a STD SCR stoichiometry with adsorbed NH<sub>3</sub> and interfacial NO, generally represented as R12:



Moreover, parallel oxidation reactions were represented in our mechanistic path, where a competition of ammonia oxidation rather in N<sub>2</sub> or in NO can occur during SCR conditions [355]. Such reactions take place at relatively elevated temperature and can further depend on the different active site configurations presence [174]. In order to represent these oxidation phenomena, which greatly impact the overall SCR process, the following reactions of NH<sub>3</sub> and NO oxidation were implemented, from R5 to R7 and R11 as gas phase oxidation reaction of NH<sub>3</sub> in NO was particularly characterized in gas phase reactor in SCR and NH<sub>3</sub> oxidation conditions (Figure V-2 and V-10). In order to not further complicate the model system, only the main gaseous ammonia oxidation in NO was taken into account, regarding the corresponding elevated production of NO:



Regarding the low ammonia coverage on the active sites at high temperature, following their temperature activated desorption, and the important NO<sub>x</sub> abatement which still occurs at such temperature, it is important to take into consideration the potential NO<sub>2</sub> production and interaction with the catalyst. Indeed, conditioned by the thermodynamic limits of gaseous reaction R7 and the nitrite decomposition in temperature R9 and R10, the observed NO<sub>2</sub> production will consequently impact the STD SCR behaviour at high temperature [216]. Therefore, the produced NO<sub>2</sub> could readily react with adsorbed ammonia and NO for Fast SCR reaction R8:



Depending on the NO/NO<sub>x</sub> ratio, R8 could proceed faster than the standard reaction R4 and impact the catalyst performance from relatively low to high temperature [198,210,424]. Correspondingly to NO<sub>2</sub> concentrations, N<sub>2</sub>O pollutant can be further produced through nitrate complex formation with ammonia and its following decomposition [221,466]. However, regarding the investigated set of experiments in this study, NO<sub>2</sub> was not fed in the system for the Standard SCR study purpose and the observed N<sub>2</sub>O concentrations during all our experiments remain extremely low, under the confidence interval limit of our apparatus. Such low production of N<sub>2</sub>O is an interesting feature of small-pore zeolite catalysts as Cu-CHA, previously described and compared to other catalysts in literature [467,468]. Thus, N<sub>2</sub>O formation was not implemented in the current model for complexity interest.

All reactions rates and corresponding reactions are displayed in Table VI-7, with the corresponding estimated parameters in Table VI-9 and 10.

During this study, the NH<sub>3</sub> and H<sub>2</sub>O adsorption and desorption parameters were firstly estimated, where the obtained parameters relative to the support alone (S1 and S2) were implemented as constants

values during adsorption and desorption process calibration for the parameter estimation of S3 and S4. This process allowing a first robust estimation of the kinetic parameters dedicated to adsorption and desorption process. Then, the overall data set of experiments was used for parallel parameters estimation of Cu-SAPO-34-IE and for verifying, under constraint, the estimated parameters relative to adsorption and desorption processes. Table VI-8 represent the number of parameters and observers for each steps of estimation process. The displayed parameters Table VI-9 and 10 are the final one, used for the different simulation displayed throughout the study concerning Cu-SAPO-34-IE catalyst. Note that the estimated parameters relative to gas phase reactions were displayed with corresponding experiments in Annexes materials Figure VI-2 and 3.



Table VI-7: Reaction networks and rate expressions of proposed reactional network

R	Reactions	Reactions on S1, S2, S3, S4	Reactions rate expressions (mol.m <sup>-3</sup> .s <sup>-1</sup> ) <sup>i</sup> th site = 1,2,3,4
1	NH <sub>3</sub> adsorption/desorption	$\text{NH}_3 + S_{\text{vacant}} \xrightleftharpoons[\text{I}_{2,\text{des}}]{\text{I}_{1,\text{ads}}} \text{NH}_3 - S$	$\text{I}_{1,\text{ads}} = k_{r1,\text{ads}} C_{\text{NH}_3} \theta_{\text{vacant}}^{S_i}$ $\text{I}_{2,\text{des}} = k_{r2,\text{des}} \theta_{\text{NH}_3}^{S_i}$
2	H <sub>2</sub> O adsorption/desorption	$\text{H}_2\text{O} + S_{\text{vacant}} \xrightleftharpoons[\text{I}_{4,\text{des}}]{\text{I}_{3,\text{ads}}} \text{H}_2\text{O} - S$	$\text{I}_{3,\text{ads}} = k_{r3,\text{ads}} C_{\text{H}_2\text{O}} \theta_{S \text{ vacant}}$ $\text{I}_{4,\text{des}} = k_{r4,\text{des}} \theta_{\text{H}_2\text{O}}^{S_i}$
<b>R</b>	<b>Reactions</b>	<b>Reactions on S3 and S4</b>	<b>Reactions rate expressions (mol.m<sup>-3</sup>.s<sup>-1</sup>)<sup>i</sup>th site = 3,4</b>
3	-OH- formation/decomposition	$\text{H}_2\text{O} - S + \text{O}_2 + S \xrightleftharpoons[\text{I}_6]{\text{I}_5} 2 \text{OH} - S$	$\text{I}_5 = k_{r5} \theta_{\text{H}_2\text{O}}^{S_i} \theta_{S \text{ vacant}} C_{\text{O}_2}^{0.5}$ $\text{I}_6 = k_{r6} \theta_{\text{OH}}^2$
4	Wet STD SCR	$\text{NH}_3 - S + \text{ONO} - S \xrightarrow{\text{I}_7} \text{N}_2 + \text{H}_2\text{O} + \text{OH} - S + S_{\text{vacant}}$	$\text{I}_7 = k_{r7} \theta_{\text{NH}_3}^{S_i} \theta_{\text{ONO}}^{S_i}$
5	NH <sub>3</sub> oxidation in NO	$\text{NH}_3 - S + \frac{5}{4} \text{O}_2 \xrightarrow{\text{I}_8} \text{NO} + \frac{3}{2} \text{H}_2\text{O} + S_{\text{vacant}}$	$\text{I}_8 = k_{r8} \theta_{\text{NH}_3}^{S_i} C_{\text{O}_2}^{0.5}$
6	NH <sub>3</sub> oxidation in N <sub>2</sub>	$2 \text{NH}_3 - S + \frac{3}{2} \text{O}_2 \xrightarrow{\text{I}_9} \text{N}_2 + 3 \text{H}_2\text{O} + 2 S_{\text{vacant}}$	$\text{I}_9 = k_{r9} \theta_{\text{NH}_3}^{S_i} C_{\text{O}_2}^{0.5}$
7	Gas phase NO oxidation in NO <sub>2</sub>	$\text{NO} + \frac{1}{2} \text{O}_2 \xrightleftharpoons[\text{I}_{10}]{\text{I}_{10}} \text{NO}_2$	$\text{I}_{10} = k_{r10} (C_{\text{NO}} C_{\text{O}_2}^{0.5} - \frac{C_{\text{NO}_2}}{K_{\text{eq}}})$
8	FAST SCR	$2 \text{NH}_3 - S + \text{NO} + \text{NO}_2 \xrightarrow{\text{I}_{11}} 2 \text{N}_2 + 3 \text{H}_2\text{O} + 2 S_{\text{vacant}}$	$\text{I}_{11} = k_{r11} \theta_{\text{NH}_3}^{S_i} C_{\text{NO}} C_{\text{NO}_2}$
9	NO surface interaction	$4 \text{OH} - S + 2 \text{NO} \xrightleftharpoons[\text{I}_{13}]{\text{I}_{12}} 2 \text{ONO} - S + 2 \text{H}_2\text{O} + 2 S_{\text{vacant}}$	$\text{I}_{12} = k_{r12} \theta_{\text{OH}}^{S_i} C_{\text{NO}}$ $\text{I}_{13} = k_{r13} \theta_{\text{ONO}}^{S_i} C_{\text{H}_2\text{O}} \theta_{S \text{ vacant}}$
10	-ONO- decomposition	$2 \text{ONO} - S + \text{H}_2\text{O} + \frac{1}{2} \text{O}_2 \xrightleftharpoons[\text{I}_{15}]{\text{I}_{14}} 2 \text{OH} - S + 2 \text{NO}_2$	$\text{I}_{14} = k_{r14} \theta_{\text{ONO}}^{S_i} C_{\text{H}_2\text{O}} C_{\text{O}_2}^{0.5}$ $\text{I}_{15} = k_{r15} \theta_{\text{OH}}^{S_i} C_{\text{NO}_2}$
11	Gas phase NH <sub>3</sub> oxidation in NO	$\text{NH}_3 + \frac{5}{4} \text{O}_2 \xrightarrow{\text{I}_{16}} \text{NO} + \frac{3}{2} \text{H}_2\text{O}$	$\text{I}_{16} = k_{r16} C_{\text{NH}_3} C_{\text{O}_2}^{0.25}$
12	Dry STD SCR	$2 \text{NH}_3 - S + \frac{1}{2} \text{O}_2 + 2 \text{NO} \xrightarrow{\text{I}_{17}} 2 \text{N}_2 + 3 \text{H}_2\text{O} + 2 S_{\text{vacant}}$	$\text{I}_{17} = k_{r17} \theta_{\text{NH}_3}^{S_i} C_{\text{NO}} C_{\text{O}_2}^{0.5}$

Table VI-8. Data points relative to experiments employed during parameters estimation processes

Strategy	Number of		Estimated Parameters
	Observers	Parameters	
Step 1: Brønsted acid sites S1, S2 parametrization from H-SAPO-34	130	15	$k_{ads}$ , $k_{0,des}$ , $Ea_{des}$ of R1 and R2 on S1 and S2 $k_{tot}$ , $\alpha_{S2}$ , $\Omega_S^{TOT}$ Brønsted
Step 2: Copper lewis acid site S3, S4 parametrization from Cu-SAPO-34-IE	280	24	$k_{ads}$ , $k_{0,des}$ , $Ea_{des}$ of R1 and R2 on S3 and S4 $k_{0,r5}$ , $Ea_{r5}$ , $k_{0,r6}$ , $Ea_{r6}$ of R5 on S3 and S4 $\alpha_{S1}$ , $\alpha_{S2}$ , $\Omega_{S3}^{TOT}$ , $\Omega_{S4}^{TOT}$ $k_{tot}$
Step 3: Overall data set for parallel parametrization	15000	65	$k_{ads}$ , $k_{0,des}$ , $Ea_{des}$ of R1 and R2 on S3 and S4 $k_{0,j}$ and $Ea_j$ from R3 to R12 on S3 and S4 $\alpha_{S1}$ , $\alpha_{S2}$ , $\Omega_{S3}^{TOT}$ , $\Omega_{S4}^{TOT}$ $k_{tot}$

Table VI-9 : Estimated kinetic parameters with 95% confidence intervals obtained through overall data set

R	Reaction rate (mol.m <sup>-3</sup> .s <sup>-1</sup> )	Pre-exponential factor $k_0^a$				Activation energy $Ea$ (J.mol <sup>-1</sup> )			
		S3	+/-	S4	+/-	S3	+/-	S4	+/-
3	r <sub>5</sub>	1.36.10 <sup>8</sup>	1.28.10 <sup>1</sup>	7.10.10 <sup>6</sup>	3.19.10 <sup>1</sup>	6.54.10 <sup>4</sup>	5.33.10 <sup>-1</sup>	5.08.10 <sup>4</sup>	1.25.10 <sup>1</sup>
	r <sub>6</sub>	1.35.10 <sup>6</sup>	1.54.10 <sup>1</sup>	1.44.10 <sup>6</sup>	8.52.10 <sup>1</sup>	2.75.10 <sup>4</sup>	8.31	3.82.10 <sup>4</sup>	1.49.10 <sup>1</sup>
4	r <sub>7</sub>	6.60.10 <sup>6</sup>	1.04.10 <sup>1</sup>	1.18.10 <sup>11</sup>	2.35.10 <sup>1</sup>	4.47.10 <sup>4</sup>	1.29	6.61.10 <sup>4</sup>	1.45.10 <sup>1</sup>
5	r <sub>8</sub>	6.35.10 <sup>7</sup>	1.89.10 <sup>1</sup>	2.71.10 <sup>7</sup>	1.38.10 <sup>1</sup>	1.04.10 <sup>5</sup>	2.41	8.79.10 <sup>4</sup>	1.54
6	r <sub>9</sub>	2.76.10 <sup>8</sup>	2.58.10 <sup>5</sup>	8.84.10 <sup>7</sup>	9.65.10 <sup>3</sup>	1.58.10 <sup>5</sup>	2.02.10 <sup>2</sup>	1.39.10 <sup>5</sup>	7.58.10 <sup>1</sup>
8	r <sub>11</sub>	2.65.10 <sup>13</sup>	1.40.10 <sup>1</sup>	5.85.10 <sup>13</sup>	1.41.10 <sup>1</sup>	8.61.10 <sup>4</sup>	6.31.10 <sup>-1</sup>	6.93.10 <sup>4</sup>	1.16
9	r <sub>12</sub>	9.11.10 <sup>7</sup>	1.01.10 <sup>1</sup>	1.39.10 <sup>8</sup>	3.27.10 <sup>1</sup>	3.30.10 <sup>4</sup>	7.28	4.31.10 <sup>4</sup>	2.36.10 <sup>1</sup>
	r <sub>13</sub>	1.06.10 <sup>6</sup>	1.01.10 <sup>1</sup>	6.90.10 <sup>6</sup>	2.79.10 <sup>1</sup>	3.16.10 <sup>4</sup>	7.56	4.40.10 <sup>4</sup>	1.22.10 <sup>1</sup>
10	r <sub>14</sub>	4.76.10 <sup>7</sup>	9.57	8.42.10 <sup>9</sup>	2.85.10 <sup>1</sup>	6.82.10 <sup>4</sup>	1.03	6.80.10 <sup>4</sup>	8.84
	r <sub>15</sub>	3.48.10 <sup>9</sup>	1.03.10 <sup>1</sup>	2.28.10 <sup>10</sup>	2.36.10 <sup>1</sup>	4.62.10 <sup>4</sup>	3.00	6.86.10 <sup>4</sup>	8.27
12	r <sub>17</sub>	7.21.10 <sup>4</sup>	6.32	1.16.10 <sup>6</sup>	2.37.10 <sup>1</sup>	2.57.10 <sup>4</sup>	7.62.10 <sup>-1</sup>	5.51.10 <sup>4</sup>	5.55

<sup>a</sup> dimensions depending on reaction constant expression Table VI-7

## VI-4. Results and discussions

### VI-4.1. NH<sub>3</sub> and H<sub>2</sub>O adsorption-desorption: R1, R2 and R3

NH<sub>3</sub> TPD experiments were conducted to apprehend the different NH<sub>3</sub> and H<sub>2</sub>O adsorption-desorption dynamics, tests displayed Figure VI-9 (A,B and C). The resulting estimated parameters issued from the model for both support and catalyst are displayed Table 9 and 10, as all the reaction network is implied in each performed experiment. The raw zeolite support was primarily investigated, at 150°C in presence of 4% water and 8% O<sub>2</sub> with a feed of 1000 ppm NH<sub>3</sub>. The complete profiles accounting for adsorption and desorption steps are displayed Figure VI-9 (A) with corresponding NH<sub>3</sub> concentration ( $C_{NH_3,g}^{outlet}$ ) simulation. As observed, the adsorption step occurs within the first minutes, where  $t_0$  corresponds to the switch through the reactor. After the active sites have been filled to their equilibrium capacity, until steady state, the NH<sub>3</sub> inlet was cut off for pure He. After signal stabilization under inert gas at constant temperature (150°C), the temperature ramp was initiated, and the desorption process began. Thus, regarding the H-SAPO-34 NH<sub>3</sub> TPD profile displayed Figure VI-9 (A), the parameters representing the adsorption-desorption process were fitted accordingly. The simulated profiles respect well both the adsorption and desorption phenomena through the whole temperature program. The desorption peak is accordingly represented by both S1 and S2 sites, where the dynamic coverage evolution in time inform about the complete sites desorption of NH<sub>3</sub>, reaching  $\theta_{NH_3}^{S2} = 0$  at around 430°C with the strongest Brønsted acid site. The tuned activation energies for both sites:  $Ea_{des}^{S1} = 72 \text{ kJ.mol}^{-1}$  and  $Ea_{des}^{S2} = 90 \text{ kJ.mol}^{-1}$  concord with similar estimation obtained in the literature on Cu-CHA catalysts [232,457]. However, regarding the different definition of active sites following the mentioned studies, the estimated parameters for lumped sites have to be compared with great care with parameters dedicated to discriminated sites, due to their different definition. Moreover, the total Brønsted acid site density ( $\Omega_S^{Brønsted}$ ) of the zeolite support was depicted as the sum of S1 ( $\Omega_{S1}$ ) and S2 ( $\Omega_{S2}$ ) relative site densities, related as  $\Omega_{S1} = \alpha^{S1} \Omega_S^{Brønsted}$  and  $\Omega_{S2} = (1 - \alpha^{S2}) \Omega_S^{Brønsted}$  with  $\alpha^S$  the presence ratio ( $0 \leq \alpha^S \leq 1$ ). In order to take into account the influence of future copper active sites incorporation on the Brønsted acid sites density, where exchanged cations substitute its closest bridged Brønsted acid sites (strong sites) after copper incorporation and can form weaker acid sites [285,370], the detailed density of the exchanged redox sites was depicted as  $\Omega_{S3} = (1 - \alpha^{S1} - \alpha^{S2}) \cdot \Omega_{S3}$ , while the fourth site density was directly estimated as  $\Omega_{S4}$ . Thus, the Brønsted acid sites fractions from the zeolite support constrain the estimation of exchanged sites fraction. In that respect, more  $\alpha^{S1}$  and  $\alpha^{S2}$  are estimated close to the support values, more the total active site proportion is similar to the zeolite support site fraction. Finally, the overall set of parameters representing the adsorption-desorption dynamics of S1 and S2 from the raw support was fixed as referenced value for the catalyst Cu-SAPO-34-IE and excluded from the estimation process, excepted the corresponding site coefficient  $\alpha^{S1}$  and  $\alpha^{S2}$ . In that respect, the estimation of S1 and S2 parameters from the parent support of the catalyst allow to not further burden the model simulation of Cu-SAPO-34-IE.

Table VI-10 : Estimated thermodynamic parameters related to NH<sub>3</sub> and H<sub>2</sub>O adsorption/desorption with 95% confidence intervals obtained through NH<sub>3</sub> TPD tests

	Site definition	Reaction	$k_{ads}^{Si}$ (s <sup>-1</sup> )	$k_{0,des}^{Si}$ (mol.m <sup>-3</sup> .s <sup>-1</sup> )	$Ea_{des}^{Si}$ (J.mol <sup>-1</sup> )	Site proportions	
Catalyst Cu-SAPO-34-IE	Zeolite support H-SAPO-34	S1 (Low temperature Brønsted acid sites)	R1	8.60.10 <sup>1</sup> +/- 12	1.2.10 <sup>7</sup> +/- 62	72.10 <sup>3</sup> +/- 3	$(\Omega_{S1}/\Omega_{S2})^{support} = 0.30$
		R2	6.99.10 <sup>2</sup> +/- 18	5.80.10 <sup>3</sup> +/- 9.10 <sup>2</sup>	39.10 <sup>3</sup> +/- 80	$(\Omega_{S1}/\Omega_{S2})^{cata} = 0.72$	
	S2 (High temperature Brønsted acid sites)	R1	1.83.10 <sup>2</sup> +/- 1	6.9.10 <sup>7</sup> +/- 15	90.10 <sup>3</sup> +/- 1	$\Omega_{S1} + \Omega_{S2} = \Omega_{S}^{Brønsted}$	
		R2	6.74.10 <sup>-2</sup> +/- 8	5.25.10 <sup>3</sup> +/- 8.10 <sup>2</sup>	55.10 <sup>3</sup> +/- 76		
S3 (exchanged cations copper)		R1	2.42.10 <sup>2</sup> +/- 3	1.10 <sup>7</sup> +/- 1.10 <sup>4</sup>	109.10 <sup>3</sup> +/- 37		
		R2	3.6.10 <sup>-1</sup> +/- 5.3	3.43.10 <sup>4</sup> +/- 21	48.10 <sup>3</sup> +/- 5		
	S4 (surface nano-sized copper cluster)	R1	6.84.10 <sup>2</sup> +/- 4	8.2.10 <sup>6</sup> +/- 9	57.10 <sup>3</sup> +/- 1		
		R2	2.3.10 <sup>-1</sup> +/- 36	9.6.10 <sup>4</sup> +/- 79	35.10 <sup>3</sup> +/- 15	$(\Omega_{S3}/\Omega_{S4})^{cata} = 0.14$	

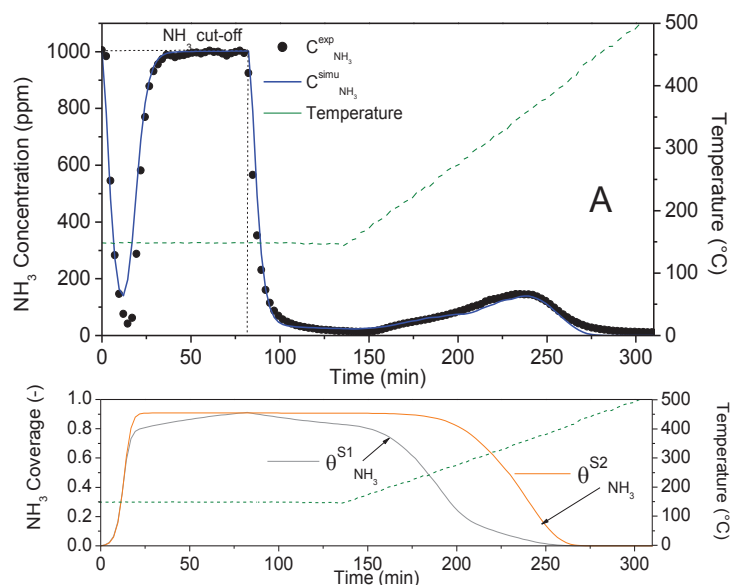
Next, the catalyst made of all the four depicted active sites was investigated in dry and wet  $\text{NH}_3$  TPD conditions, Figure VI-9 (B and C), where the parallel fit of both experiments with and without  $\text{H}_2\text{O}$  participates to the molecules adsorption and desorption description. Here the water impact can be observed, Figure VI-9 (B and C) at low temperature within  $150^\circ\text{C}$ - $250^\circ\text{C}$  with  $\text{NH}_3$  concentration profiles, where the lack of water implies a slight  $\text{NH}_3$  desorption uptake, due to the absence of adsorption competition at low temperature [457]. This difference is even more visible regarding the respective coverage ratios, where all sites reach maximum coverage capability ( $\theta_{\text{NH}_3}^{\text{S}}$ ) within first minutes of adsorption, which is not the case in presence of water due to the other adsorbed intermediaries. The adsorption competition between  $\text{H}_2\text{O}$  and  $\text{NH}_3$  can be clearly observed on the strongest redox sites, regarding the  $\theta_{\text{NH}_3}^{\text{S3}}$  increase during the adsorption step. Such low temperature interaction between  $\text{H}_2\text{O}$  and the main active redox species will be important for initiating the promoting effect of water in SCR conditions.

Moreover, as displayed by the simulated coverage evolutions on Figure VI-9 (B and C) after the  $\text{NH}_3$  cut off, the S4 profiles well represent the weak sites behaviour of surface species in temperature, desorbing the weakest bound  $\text{NH}_3$  readily after the cut off, under He flush. The rest of stored ammonia will desorb at low temperature between  $200^\circ\text{C}$  and  $360^\circ\text{C}$ , as observed during previous studies on similar catalysts [171,287,370]. The Brønsted acid sites desorption dynamics are maintained from the support behaviour where the strong one (S2) desorbs 50% of the stored  $\text{NH}_3$  around  $360^\circ\text{C}$ , a centred peak temperature in accordance with the sites desorption from bridged Brønsted and strongest Lewis acid sites as exchanged copper species [173,359,370,469]. However, at such intermediate temperature ( $360^\circ\text{C}$ ), exchanged copper cations are characterized to also desorb ammonia [370,372], only the strongest cations (S3) are better enabled to desorb at elevated temperature ( $400^\circ\text{C}$  –  $500^\circ\text{C}$ ) with the strongest Brønsted acid sites [154,276]. Similar observation can be made regarding Figure VI-9 (B and C), by following the S3 and S2 coverage evolution in time through the temperature ramp. However, the intermediate temperature desorption feature from weaker copper cation species is not represented here by the model through S3, this duality in the desorption behaviour greatly depends on the active cations species presence within the catalyst and cannot be captured with only one nature of exchanged sites following the Langmuir model approach. Additionally, it is important to notice that considered alone, the estimated parameters obtained through  $\text{NH}_3$  TPD measurements are not sufficient enough for adequately representing the adsorption and desorption process during SCR conditions. The set of adsorption-desorption parameters can be firstly approximated with TPD results, but the overall set have to be constraint by the chemical reactions for better fidelity. Indeed, when considering both chemical reactions and the adsorption/desorption of the species during the parameter estimation process, the relative kinetic parameters can be more accurately approximated through the temperature, considering the high temperature redox activities and making adequately correspond the different desorption activation energies of reactive species.

In that respect, the estimated parameters Table VI-10 are consistent with the depicted active sites, where the strength of exchanged cations S3 are characterized by an important activation energy

$Ea_{r2}^{S3} = 109 \text{ kJ.mol}^{-1}$ , of similar magnitude order with estimated parameters in literature on Cu-zeolite catalysts [232,235,457,470,471]. However, compared with previously cited studies defining lumped active sites by their nature, the corresponding estimated activation energy relative to  $\text{NH}_3$  desorption are systematically higher than the one obtained by our current model on S3. By discretizing the sites following their nature, the estimated activation energy do not represent the global participation of several sites and better represents the characteristic site activation energy, a phenomenon also observed by the  $\text{NH}_3$  storage model of Gong et al. [232], by adding one more active site in their model. Comparing both active sites S3 and S4, the capacity of exchanged cations to be active at high temperature is thus clearly demonstrated by the estimated parameters. In the other hand, the surface nano-sized copper cluster display a lower  $Ea_{r2}^{S4} = 57 \text{ kJ.mol}^{-1}$  and an important adsorption constant, which could be a consequence of their surface location displaying their ease to interact with flowing  $\text{NH}_3$  molecules from the interface. It will be noted that accordingly with the support functionalization process, the proportion of strong Brønsted acid sites decreased for weaker S1 sites proportion following the implementation of exchanged sites S3, as displayed by the different site ratios Table VI-10.

Finally,  $\text{H}_2\text{O}$  desorption activation energies from Brønsted acid sites are in accordance with the one estimated for similar zeolite support SAPO-34 respecting the strength order defined in the model:  $Ea_{r4}^{S1} < Ea_{r4}^{S2}$  and  $Ea_{r4}^{S4} < Ea_{r4}^{S3}$  and representing the water affinity with the surface at low temperature [472,473]. The water impact will be better considered regarding its implication within the kinetic mechanism, where the adsorption of  $\text{H}_2\text{O}$  will further form hydroxyl species on redox sites, important intermediaries for the low temperature SCR activity as it will be described in next section. Regarding the reactional mechanism and the excess of water within the reactive mixture, the  $\text{H}_2\text{O}$  adsorption constants from R2 reaction on each sites were strongly sensitive to variations which resulted in important confidence interval on the parameters.



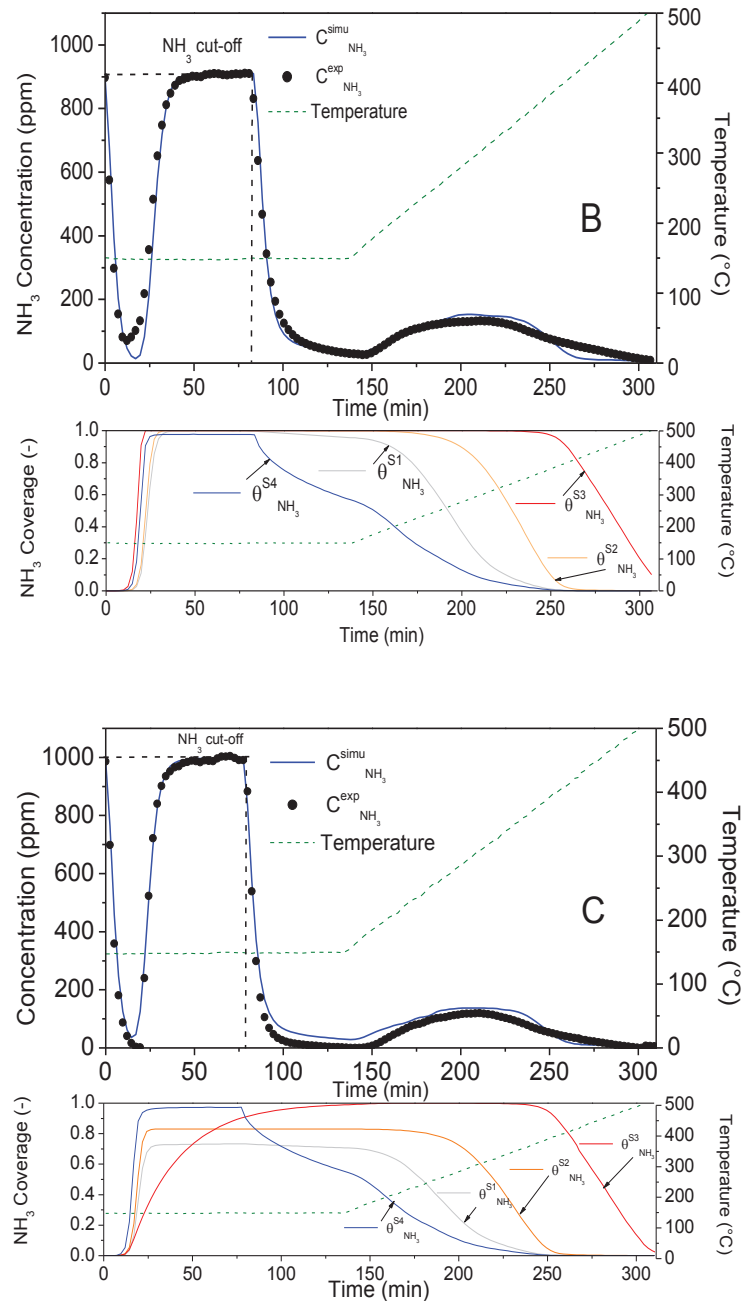


Figure VI-9. Ammonia adsorption and TPD experiments with the corresponding simulated profiles and coverage evolution in time (A,B,C) respectively H-SAPO-34, Cu-SAPO-34 (0% H<sub>2</sub>O) and Cu-SAPO-34 (4% H<sub>2</sub>O). Inlet gas composition: *adsorption of 1000 ppm NH<sub>3</sub>; 80000 ppm (8%) O<sub>2</sub>; 0-40000 ppm (4%) H<sub>2</sub>O and He as a balance at 150°C with a total Flow of 2.4 L/h*

VI-4.2. Cu-SAPO-34-IE NH<sub>3</sub> oxidation reactions: R5 and R6

Regarding the potential important impact of NH<sub>3</sub> oxidation on Cu-CHA SCR performances [468,474], and the key role of fast SCR reactions through the temperature window in NH<sub>3</sub>-SCR processes [152,424,475], the oxidation of NH<sub>3</sub> and NO was monitored and simulated according to the proposed model and the calibrated SCR parameters Table VI-9. Different transient conditions were carried out in

order to observe the influence of different inputs on the Cu-SAPO-34-IE catalyst behaviour in temperature. Therefore on one hand, transient experiments were made with a feed of 1000 ppm NH<sub>3</sub> with 40000 ppm (4%) H<sub>2</sub>O and 80000 ppm (8%) O<sub>2</sub> in He gas balance, following the incremental temperature increase between 200°C and 500°C of 50°C with a 10°C.min<sup>-1</sup> ramp, displayed Figure VI-10.

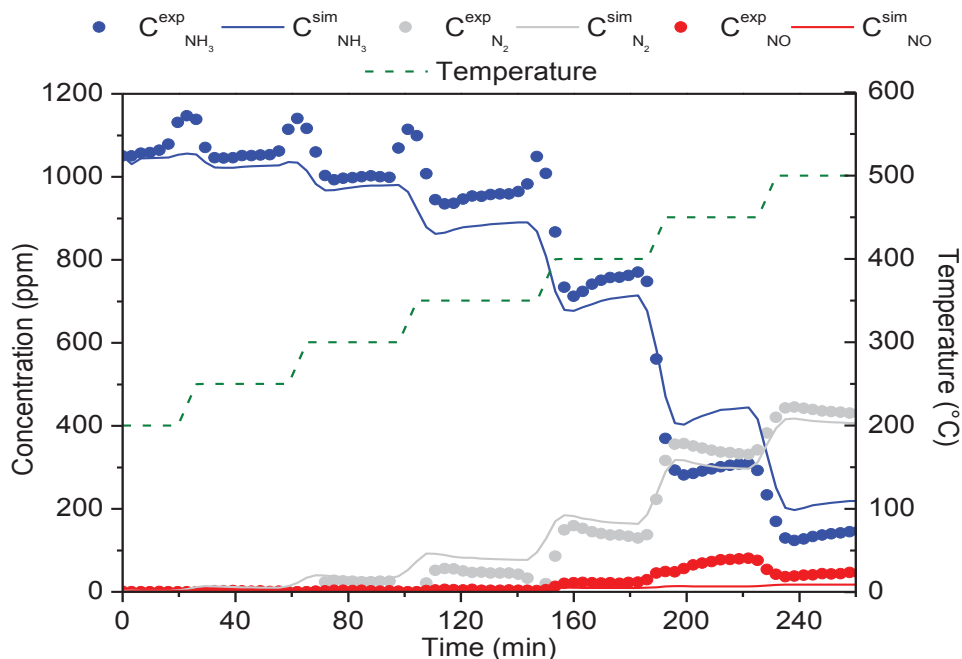


Figure VI-10. NH<sub>3</sub> oxidation experiments in transient conditions with steep (10°C.min<sup>-1</sup>) temperature input modification ramp. Inlet gas composition: adsorption of 1000 ppm NH<sub>3</sub> 80000 ppm (8%) O<sub>2</sub>, 40000 ppm (4%) H<sub>2</sub>O and He as a balance between 200°C and 500°C with a total Flow of 10 L.h<sup>-1</sup>

On the other hand, with similar inlet conditions, the temperature have been increased from 200°C to 500°C with a 2°C.min<sup>-1</sup> ramp Figure VI-11. As observed during the experimental runs, ammonia can be oxidized either in NO or in N<sub>2</sub>, through reaction R5 and R6. This oxidation step of NH<sub>3</sub> in NO is covered by some studies in the literature [183,355] and represent an important unselective reaction of NH<sub>3</sub> regarding the obtained NO concentration as depicted in Figure VI-10 and 11. No N<sub>2</sub>O were detected during the experimental NH<sub>3</sub> oxidation experiments and only N<sub>2</sub> and NO were the main reactions products.

Firstly, concerning NH<sub>3</sub> oxidation transient experiment Figure VI-10, it is interesting to notice that the 10°C.min<sup>-1</sup> ramp make the catalyst desorb large amount of weakly stored NH<sub>3</sub> between 200°C and 400°C, a feature usually observed for Cu-CHA during similar transient experiments [432,470]. Nevertheless, this phenomenon should not be mistaken for unique desorption from weak Brønsted sites. Indeed, this sudden temperature elevation from one step to another making NH<sub>3</sub> desorb, avoid its oxidation at low temperature on corresponding active redox sites. Which for each constated steep desorption, the N<sub>2</sub> concentration consequently drop until that NH<sub>3</sub> re-adsorbs on free active sites at the step temperature as it can be seen at t = 100min and 150 min. Here, the model does not achieve to completely represent this behaviour, where only small increase of NH<sub>3</sub> concentration is depicted at each beginning of ramp



temperature until 350°C. Following the current mechanistic path, this phenomenon is not sufficiently represented by the surface sites for such low temperature. The dual behaviour could be better represented by adding weaker redox sites, but in order to not further weighing down the model parameterization. However, both low and high temperature NH<sub>3</sub> oxidation in N<sub>2</sub> and NO are well depicted through the temperature evolution, regarding the low N<sub>2</sub> production between 200°C and 300°C and its increase in temperature. It is important to note that the detected NO<sub>2</sub> concentration was below the apparatus confidence limit during both experiment and was considered as null through the whole temperature range. A feature represented by the model with a simulated concentration of NO<sub>2</sub> equal to zero.

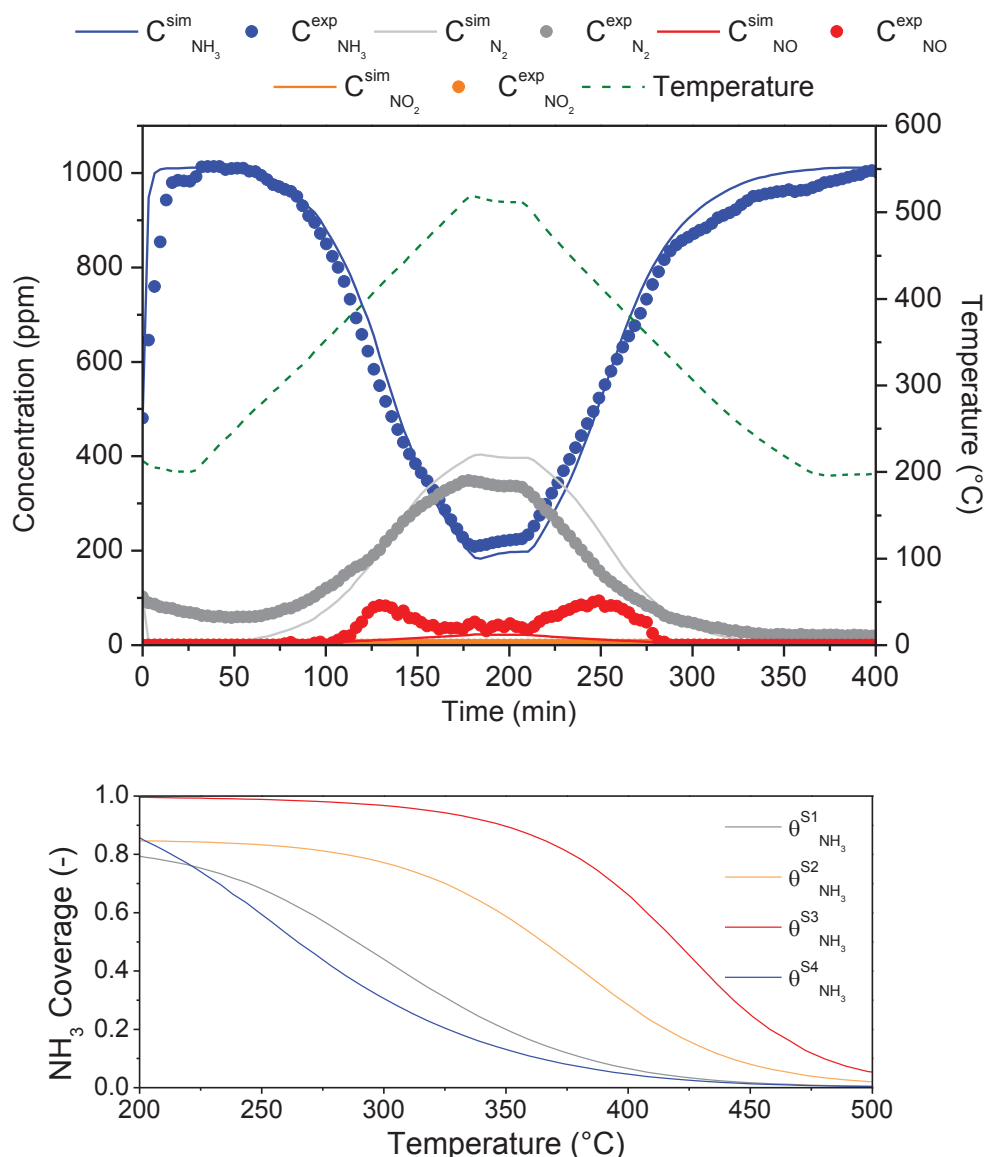


Figure VI-11. NH<sub>3</sub> oxidation experiments in transient conditions with slow (2°C.min<sup>-1</sup>) temperature input modification ramp with corresponding sites NH<sub>3</sub> coverages between 200°C-500°C decreasing ramp. Inlet gas composition: adsorption of 1000 ppm NH<sub>3</sub>, 80000 ppm (8%) O<sub>2</sub>, 40000 ppm (4%) H<sub>2</sub>O and He as a balance between 200°C and 500°C with a total Flow of 10 L.h<sup>-1</sup>

The second transient experiments employing slower temperature ramp, can further heighten the profile concentration differences between the simulation and the experiment as it is displayed Figure VI-11. Indeed, if the model well captures the NH<sub>3</sub> oxidation behaviour from  $t_0$  to the end of the temperature program, a slight difference remains visible through the N<sub>2</sub> production profiles at the highest temperature. The main gap concerns the NO concentration simulated profile, where the produced NO at high temperature seems readily consumed through SCR reactions accordingly with R4, R12 and the corresponding low SCR activation energies on S3 and S4 Table VI-9. Indeed at high temperature, both SCR reactions and NH<sub>3</sub> oxidation participate to the N<sub>2</sub> formation, while at lower temperature between 200°C and 300°C a slower reaction regime is visible. This difference in NH<sub>3</sub> oxidation behavior was previously observed during Gao et al. study [158] and also took into consideration in some NH<sub>3</sub>-SCR models employing Cu-CHA [216,233]. Indeed, NH<sub>3</sub> oxidation was previously characterized to be promoted by small copper surface cluster on Cu-CHA catalyst [173,174,183] and this activity was also represented in the model regarding the resulting estimated activation energies of NH<sub>3</sub> oxidation by S4 lower than S3 sites ( $E_{a_{r8}}^{S4} = 88 \text{ kJ.mol}^{-1} < E_{a_{r8}}^{S3} = 104 \text{ kJ.mol}^{-1}$  and  $E_{a_{r9}}^{S4} = 139 \text{ kJ.mol}^{-1} < E_{a_{r9}}^{S3} = 158 \text{ kJ.mol}^{-1}$ ), allowing a higher NH<sub>3</sub> oxidation capacity on S4 than S3. Accordingly, NH<sub>3</sub> coverage on S4 Figure VI-11 quickly drop between 200°C and 350°C. On the other hand, S3 sites seem to participate to the oxidation process at high temperature mainly (400-500°C). Moreover, the parallel NO production represented through the model by R5 on exchanged S3 and surface nano clusters S4 is in accordance with the copper oxide surface clusters oxidation role characterized in literature [476]. Finally, at elevated temperature, gas phase NH<sub>3</sub> oxidation also occurs and contributes to the NH<sub>3</sub> abatement as observed during dedicated experiments displayed in Supplementary Information Annexes Figure VI-3. This contribution was implemented in the model through the reaction R11 and its impact on oxidation evolution better underlined by the close activation energy ( $E_{a_{r11}} = 112 \text{ kJ.mol}^{-1}$ ) with R5 and R6 estimated parameters.

#### VI-4.3. NO oxidation reactions: R7, R9-11

NO oxidation experiments were used for reporting the oxidation step in NO<sub>2</sub> in presence of the catalyst for better representation during standard SCR conditions. Concerning the gas phase reaction R7, Gibbs function ( $\Delta G = \Delta H - T\Delta S$ ) was employed in order to estimate the equilibrium constant related with the partial pressure:  $K_{eq}^P = \exp\left(\frac{-\Delta G^\circ}{RT}\right)$ . The latter was expressed accordingly with the reaction rate equation  $r_8$  as :  $K_{eq}^P = K_{eq}^C \cdot \left(\frac{RT}{P}\right)^{\Delta n}$  with  $\Delta n = -0.5$  and  $R = 8.2057 \text{ m}^3.\text{atm.mol}^{-1}.\text{K}^{-1}$ . The different coefficient correlation for estimating the temperature dependent Gibbs function can be found elsewhere [438]. The resulting calibrated activation energy, after parallel parametrization,  $E_{a_{r10}} = 41 \text{ kJ.mol}^{-1}$  is therefore in accordance with energies reported in literature on similar exchanged copper zeolite catalyst [225,236,470].

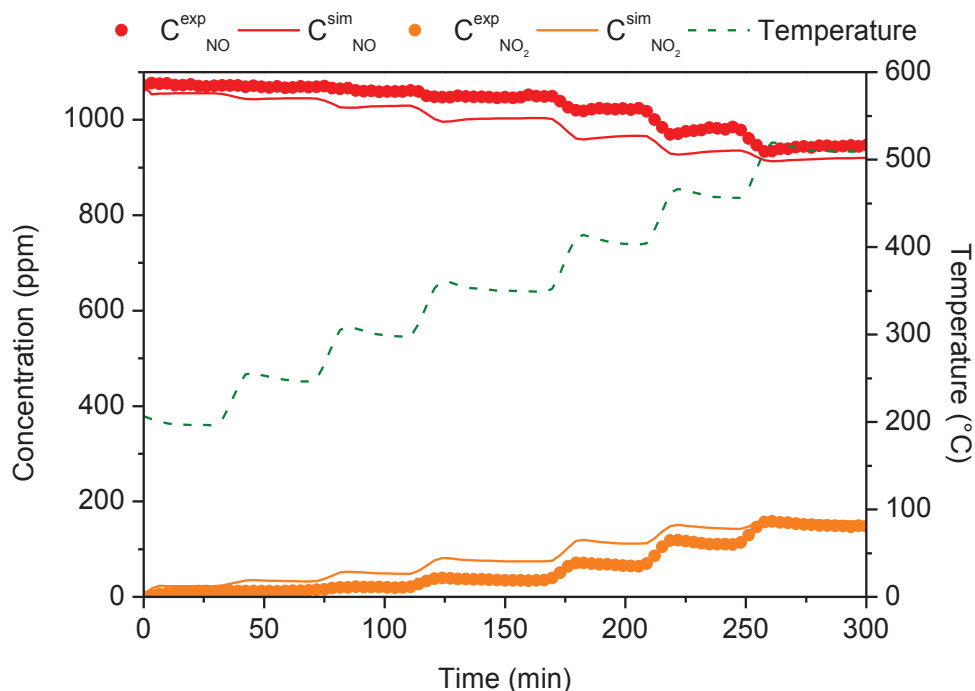


Figure VI-12. NO oxidation reaction with simulated profiles evolution with steep ( $10^{\circ}\text{C}\cdot\text{min}^{-1}$ ) temperature input modification ramp. Inlet gas composition: 1000 ppm NO, 80000 ppm (8%)  $\text{O}_2$ ; 40000 ppm (4%)  $\text{H}_2\text{O}$  and He as a balance between  $200^{\circ}\text{C}$  and  $500^{\circ}\text{C}$  with a total Flow of  $10\text{ L}\cdot\text{h}^{-1}$

At the same time, experiments in presence of Cu-SAPO-34-IE with a feed of 1000 ppm NO, 40000 ppm (4%)  $\text{H}_2\text{O}$  and 80000 ppm (8%)  $\text{O}_2$  was simultaneously employed during the overall parameter estimation. As shown Figure VI-12, the steep temperature increases carried out between  $200^{\circ}\text{C}$  and  $500^{\circ}\text{C}$  each  $50^{\circ}\text{C}$  ( $10^{\circ}\text{C}\cdot\text{min}^{-1}$  ramp) firstly informs about the lack of oxidation reaction at low temperature until  $350^{\circ}\text{C}$ . At higher temperature, the slight conversion of NO in  $\text{NO}_2$  (Conversion 18% at  $500^{\circ}\text{C}$ ), accurately described by the corresponding simulated profiles, indicates a full selectivity to  $\text{NO}_2$  on the whole temperature range. These measurements were of first interest for considering the NO interaction with the active surface sites and for taking into account possible fast reaction occurring at high temperature [210,424]. In this model,  $\text{NO}_2$  do not represent a key intermediate in standard conditions, a S-ONO nitrite specie was introduced instead, as the key function is supported by different literature characterizations [207,354,406,477] and also employed in some model construction [216,230]. Reactions 9 and 10 display the relation possibilities between NO and  $\text{NO}_2$  through the surface. For model complexity purposes, the NO interaction with the active sites was not further detailed through additional detailed steps, as it was developed through the model study of Fahami et al. [478], dedicated to NO oxidation with Cu-CHA catalysts. Therefore, the current model assumed to depict the nitrite formation on copper cations as a key step for STD SCR in wet conditions.

On the other hand, by employing a constant input temperature modification as displayed Figure VI-13, the NO oxidation reaction can be observed in a different regime. Compared with the oxidation experiment in gaseous phase (in Supplementary Material Annexes Figure VI-2.), the presence of Cu-SAPO-34-IE slightly increase the conversion of NO by 10% at the end of the temperature ramp. The observed slightly enhanced NO oxidation in presence of the catalyst is in accordance with the definition of exchanged active sites made in the model, knowing that the formation of copper moieties as  $[\text{Cu}^{\text{II}}-\text{O}-\text{Cu}^{\text{II}}]^{2+}$  from isolated cations could promote NO oxidation [382,478].

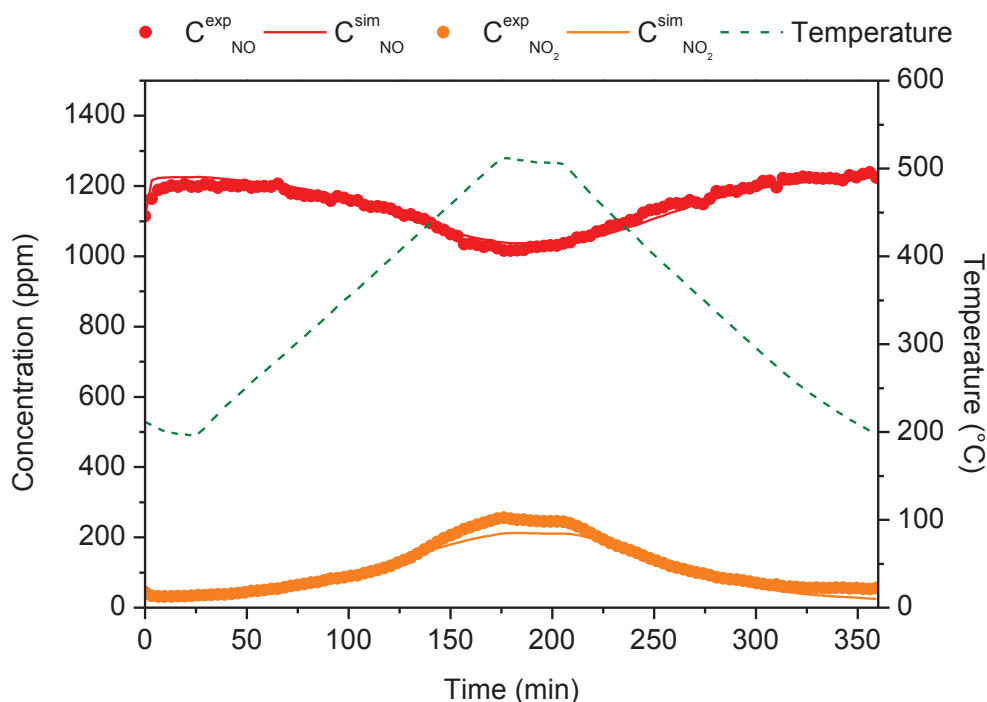


Figure VI-13. NO oxidation reaction with simulated profiles evolution with slow ( $2^{\circ}\text{C}\cdot\text{min}^{-1}$ ) temperature input modification ramp. Inlet gas composition: 1000 ppm NO, 80000 ppm (8%)  $\text{O}_2$ ; 40000 ppm (4%)  $\text{H}_2\text{O}$  and He as a balance between  $200^{\circ}\text{C}$  and  $500^{\circ}\text{C}$  with a total Flow of  $10 \text{ L}\cdot\text{h}^{-1}$

#### VI-4.4. Standard SCR behavior and parallel reactions: R4, R12

After the overview of adsorption/desorption processes and side oxidations reactions through the model, two separate experiments, both employed during the parameter estimation, were conducted for Cu-SAPO-34-IE SCR simulation performances. On one hand, an experiment deprived of water was primarily conducted under slow temperature ramp of  $2^{\circ}\text{C}\cdot\text{min}^{-1}$  in order to observe the catalyst performance without promotional effect and the corresponding adequation of the resulting simulation in dry conditions. The inlet gas feed was composed by 1000 ppm of  $\text{NH}_3$  and NO and 80000 ppm (8%)  $\text{O}_2$  with He as gas balance, from  $200^{\circ}\text{C}$  to  $500^{\circ}\text{C}$ . On the other hand, steep ( $10^{\circ}\text{C}\cdot\text{min}^{-1}$ ) and slow ( $2^{\circ}\text{C}\cdot\text{min}^{-1}$ ) temperature increase were applied in STD SCR conditions in presence of 40000 ppm (4%)  $\text{H}_2\text{O}$  with similar testing conditions for comparing the catalyst performances in NOx abatement and the relative intermediaries impact on  $\text{NH}_3$  and NO conversions.

Firstly Figure VI-14, the resulting measurements realized without water displays two distinct reaction regimes, one occurring at low temperature between 200°C and 350°C and one another at higher temperature from 350°C to 500°C. These steps are also represented with the model, where at low temperature, the SCR process between NO and NH<sub>3</sub> mainly depends on the NH<sub>3</sub> adsorption and desorption dynamic on redox sites.

Indeed at low temperature, without an excess of water, the direct formation of hydroxyl intermediaries is more difficult and only possible after water production from reactions (R1,5,6,8,9,12) themselves. Important intermediaries at low temperature for the nitrites formation R4. Therefore, Figure VI-14 informs as expected, about the lack of adsorbed H<sub>2</sub>O, representing the minor impact of produced water on dry SCR process here. According to the concerned estimated activation energies, the main active sites are principally defined as the copper cations S3 ( $E_{a_{r17}}^{S3} = 27 \text{ kJ.mol}^{-1}$ ) in the model, where the nano surface sites will less participate to the low temperature SCR reaction rate ( $E_{a_{r17}}^{S4} = 55 \text{ kJ.mol}^{-1}$ ). The respective NH<sub>3</sub> coverage evolutions, visible Figure VI-15, are in agreement with the observed sites activities, where the standard SCR operation is particularly visible on S3. Indeed, compared with ammonia coverage evolutions during NH<sub>3</sub> oxidation reactions Figure VI-11, if  $\theta_{\text{NH}_3}^{S4}$  displays a similar profiles in SCR conditions,  $\theta_{\text{NH}_3}^{S3}$  drop in accordance with its SCR activity compared with NH<sub>3</sub> oxidation conditions. Moreover at low temperature, N<sub>2</sub>O is susceptible to be produced from ammonium nitrate decomposition [221,466], however, no N<sub>2</sub>O concentrations were detected in the outlet for both SCR experiments. The concentrations were situated under our interval tolerance and were therefore removed from Figure VI-14 for clarity interest.

After 350°C and until the 500°C step, parallel oxidation strongly impacts the catalyst performance behavior. Indeed, if the SCR reaction regime is still activated with the temperature elevation, the ammonia oxidation in NO (R5) strongly contributes to the higher consumption of NH<sub>3</sub> after 350°C, in combination with R6. Therefore, NO concentration increases until the 500°C plateau. This characteristic is mainly due to the S4 activity, impacting the N<sub>2</sub> selectively by its higher NH<sub>3</sub> oxidation capability at elevated temperature. Simultaneously to ammonia oxidation, deNOx process is still performed, with a maximum reached conversion of 80%, as demonstrated in insert Figure VI-14. N<sub>2</sub> concentration appropriately reaches its maximum value at the end of the temperature ramp, thanks to not only the direct oxidation of NH<sub>3</sub> in N<sub>2</sub> but also the NO production and its potential reduction through SCR operation. As displayed Figure VI-14, at elevated temperature, the NO conversion starts to decrease, demonstrating a diminution of SCR performances as observed between 450°C and 500°C. This performance diminution is typical of Cu-CHA catalysts [98,170,479], and different causes can be responsible of this phenomenon, as important ammonia oxidation either in gas phase or with adsorbed NH<sub>3</sub>, less adsorbed reactive species, increasing contribution of different redox sites less effective or copper cations sites activity diminution. An increasing concentration that the proposed model also captures at the end of temperature ramp and until the NO concentration stabilization at the 500°C step. The slight detected NO<sub>2</sub> concentration in insert of Figure VI-

14, is also simulated by the model at high temperature. Regarding the activation energy corresponding to Fast SCR reaction on the exchanged sites:  $E_{a_{r11}}^{S3} = 86 \text{ kJ}\cdot\text{mol}^{-1}$ , the observed high temperature activity with Cu-SAPO-34-IE could be consequently impacted by its implication. Indeed, the  $\text{NO}_2$  implication at low and high temperature within the standard SCR mechanistic path is still under investigations, where its implication at low temperature was better characterized through the formation of key nitrites intermediates species [480]. Moreover, as the nitrate route is preferentially observed during Fast experiments, in conditions out of the scope of the current study, the global reaction R8 was implemented in the mechanistic path for taking into consideration the  $\text{NO}_2$  impact during transient measurements.

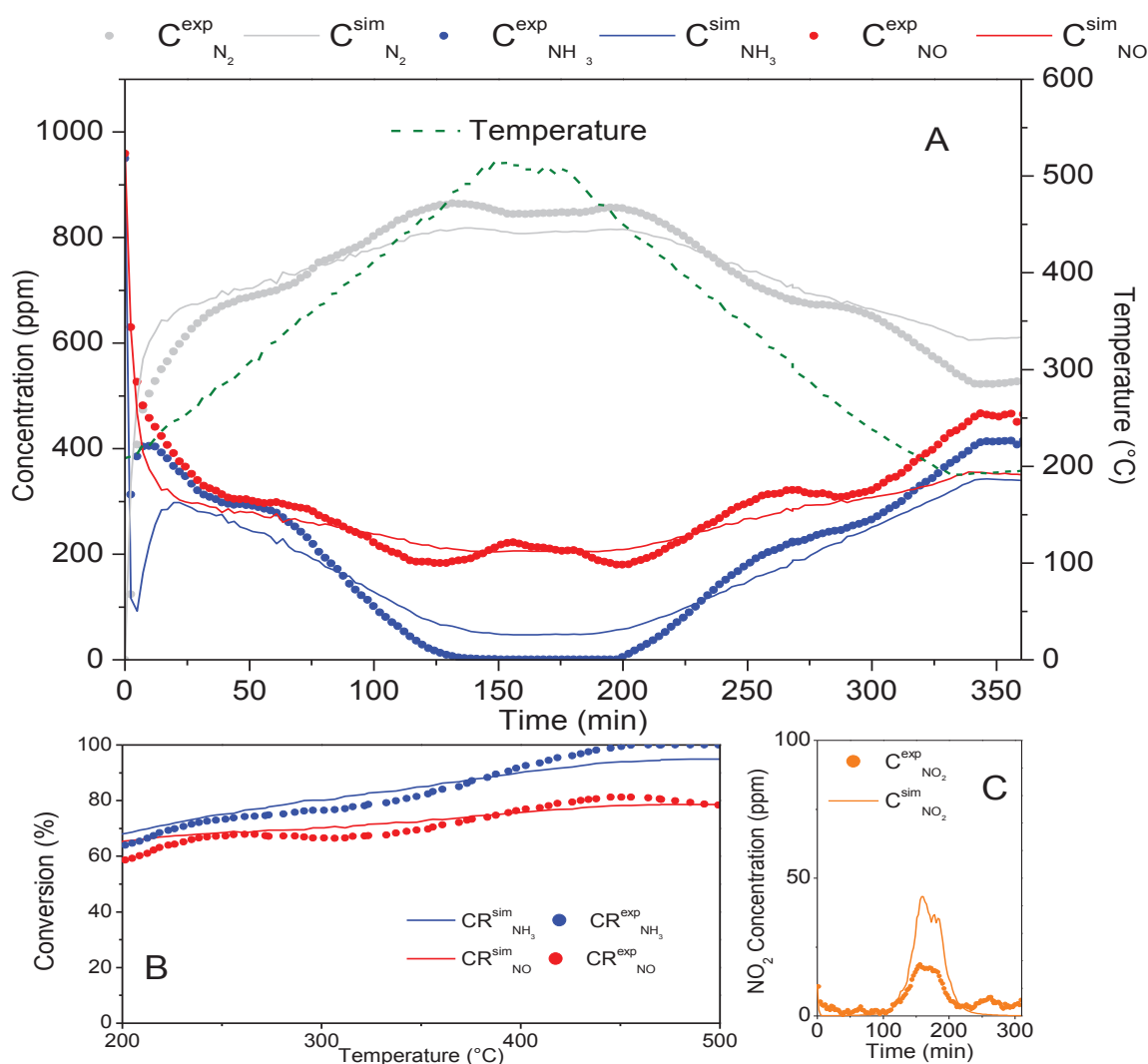


Figure VI-14. Experimental and simulated Standard SCR performances of Cu-SAPO-34-IE catalyst without water (A) accompanied by corresponding  $\text{NH}_3$  and  $\text{NO}$  conversion (B) and  $\text{NO}_2$  experimental and simulated concentrations in insert (C). Inlet gas composition:  $1000 \text{ ppm NH}_3$  and  $\text{NO}$ ;  $80000 \text{ ppm (8\% O}_2\text{)}$ ;  $0\% \text{ H}_2\text{O}$  and He as a balance between  $200^\circ\text{C}$  and  $500^\circ\text{C}$  (ascending and descending ramp) with a total Flow of  $10 \text{ L}\cdot\text{h}^{-1}$

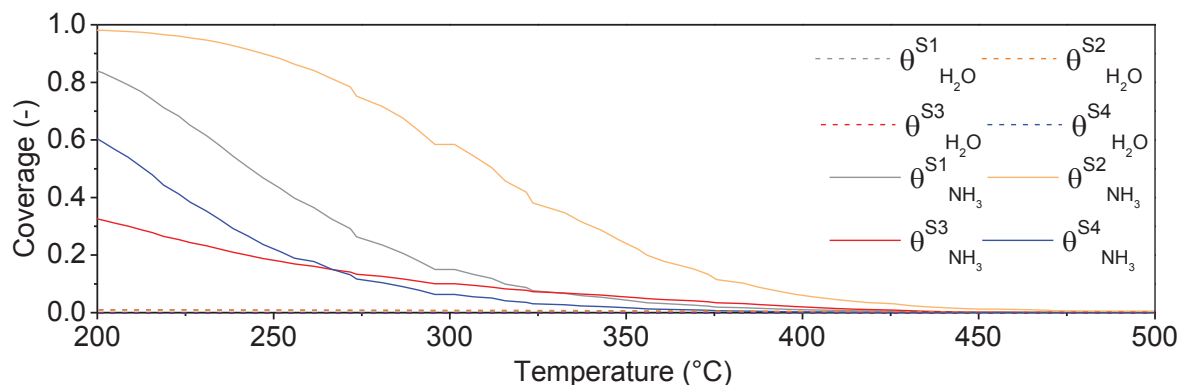


Figure VI-15. Corresponding coverage  $\text{NH}_3$  and  $\text{H}_2\text{O}$  evolution of S1,S2,S3 and S4 during Standard SCR in dry conditions through decreasing ramp temperature (200-500°C)

Additionally, experiments with 40000 ppm (4%)  $\text{H}_2\text{O}$  was also employed during the overall estimation of set of parameters. In that respect, STD SCR experiment was executed with steep temperature variations in similar gaseous conditions, displayed Figure VI-16. If the model adequately describes the different  $\text{NH}_3$ ,  $\text{NO}$ ,  $\text{NO}_2$  and  $\text{N}_2$  concentrations evolutions through the time at each temperature steps, the steep temperature increases can give further information on the catalyst behavior and so, on the model responses. As observed Figure VI-16, for each starting temperature ramp, a symmetrical drop of  $\text{NO}$  concentration and increase of  $\text{N}_2$  both passing through a minimum and maximum value, are experimentally constated and further followed by the model. This feature is a direct consequence of the so called  $\text{NH}_3$  inhibition effect [276,415]. The phenomenon is clearly visible Figure IV-16, a feature which is not exacerbated by employing low temperature ramp input as Figure VI-19. Indeed, during the rapid heating step, stored ammonia molecules on active redox sites desorb and give additional free positions for different active species formation. This rapid desorption helps the competition of adsorption in favor of  $\text{H}_2\text{O}$ , further allowing the rapid formation of hydroxyl and nitrite species on redox sites and their reactions. Indeed, as displayed on Figure VI-18,  $\text{OH}$  species are consequently formed with the decreased of  $\text{NH}_3$  coverage Figure IV-17, in accordance with the water adsorption competition. Clearly illustrated comparing  $\theta_{\text{H}_2\text{O}}^{\text{S1}}$ ,  $\theta_{\text{H}_2\text{O}}^{\text{S2}}$  evolutions with  $\theta_{\text{NH}_3}^{\text{S1}}$  and  $\theta_{\text{NH}_3}^{\text{S2}}$  at low temperature, from 200°C to 350°C, for the strongest bridged  $\text{OH}$ . Thus, the low activation energies concerning the formation of  $\text{OH}$  (R3),  $\text{ONO}$  species (R9) and its reaction with adsorbed  $\text{NH}_3$  (R4) accordingly explain the steep  $\text{N}_2$  production and  $\text{NO}$  consumption simulated concentrations. This inhibition effect further demonstrates that an optimized surface coverage from  $\text{NH}_3$  is required for a maximized  $\text{NO}$  conversion in  $\text{N}_2$  [481].

As represented by the  $\text{NH}_3$  coverage evolution Figure VI-17, the inhibition effect from ammonia adsorbed species can also be spotted regarding the corresponding coverage drop on S3 and S4 redox sites at the different temperature ramp beginning. In a same manner,  $\text{NH}_3$  consequently desorbs from S1 and S2, indicating that both copper and Brønsted acid sites, relatively to their strength capacity, contribute to the sharp desorption of  $\text{NH}_3$ . In that respect, steep transient experiments inform about the adsorption and

desorption responses of the modeled active sites and their sensitivities to temperature modification, a verified characteristic in the current model relative to the followed Langmuir theory approach.

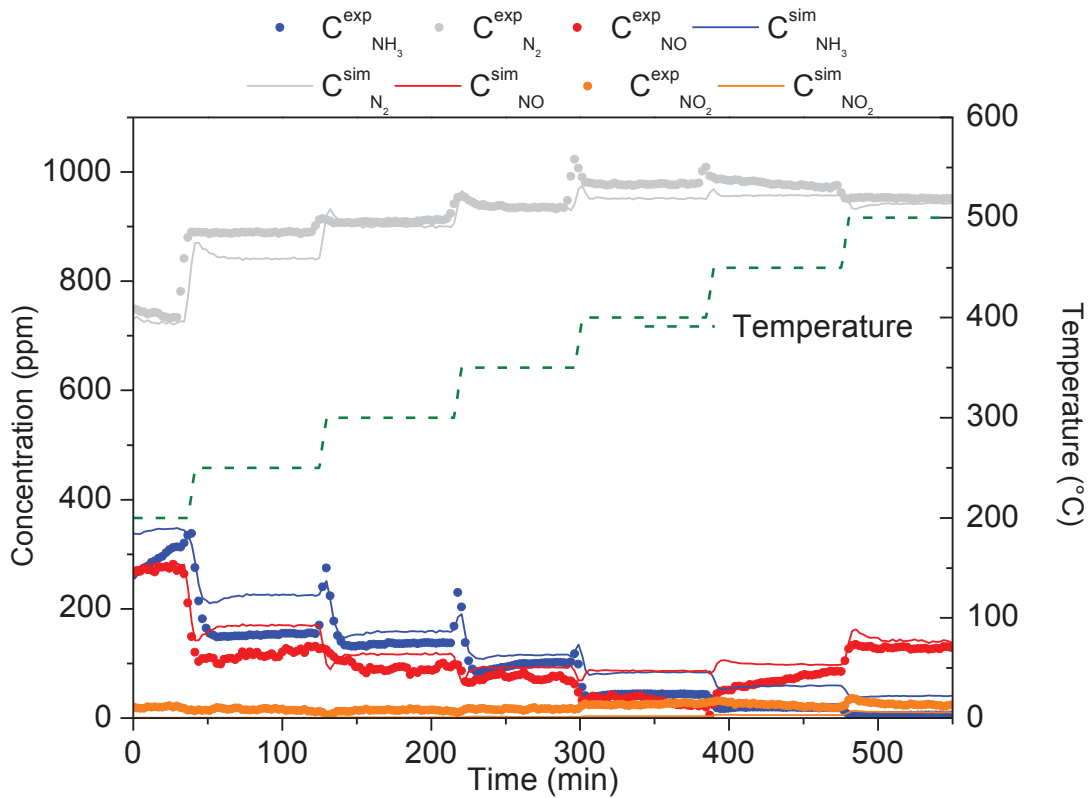


Figure VI-16. Experimental and simulated Standard SCR performances of Cu-SAPO-34-IE catalyst with water with steep temperature increases. Inlet gas composition:  $1000 \text{ ppm NH}_3$  and NO;  $80000 \text{ ppm (8\% O}_2$ ;  $40000 \text{ ppm (4\% H}_2\text{O}$  and He as a balance between  $200^\circ\text{C}$  and  $500^\circ\text{C}$  ( $10^\circ\text{C}\cdot\text{min}^{-1}$ ) with a total Flow of  $10 \text{ L}\cdot\text{h}^{-1}$



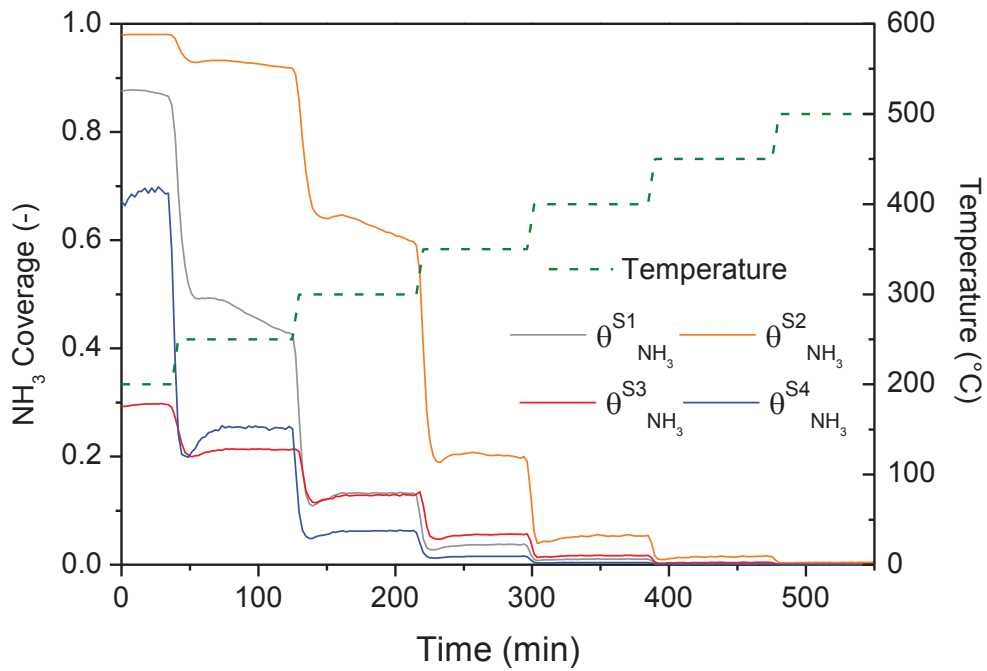


Figure VI-17. Simulated  $\text{NH}_3$  coverage evolution in time during step temperature modification. Inlet gas composition:  $1000 \text{ ppm NH}_3$  and  $\text{NO}$ ;  $80000 \text{ ppm (8\% O}_2\text{)}$ ;  $40000 \text{ ppm (4\% H}_2\text{O)}$  and  $\text{He}$  as a balance between  $200^\circ\text{C}$  and  $500^\circ\text{C}$  ( $1 \text{ }^\circ\text{C}\cdot\text{min}^{-1}$ ) with a total Flow of  $10 \text{ L}\cdot\text{h}^{-1}$

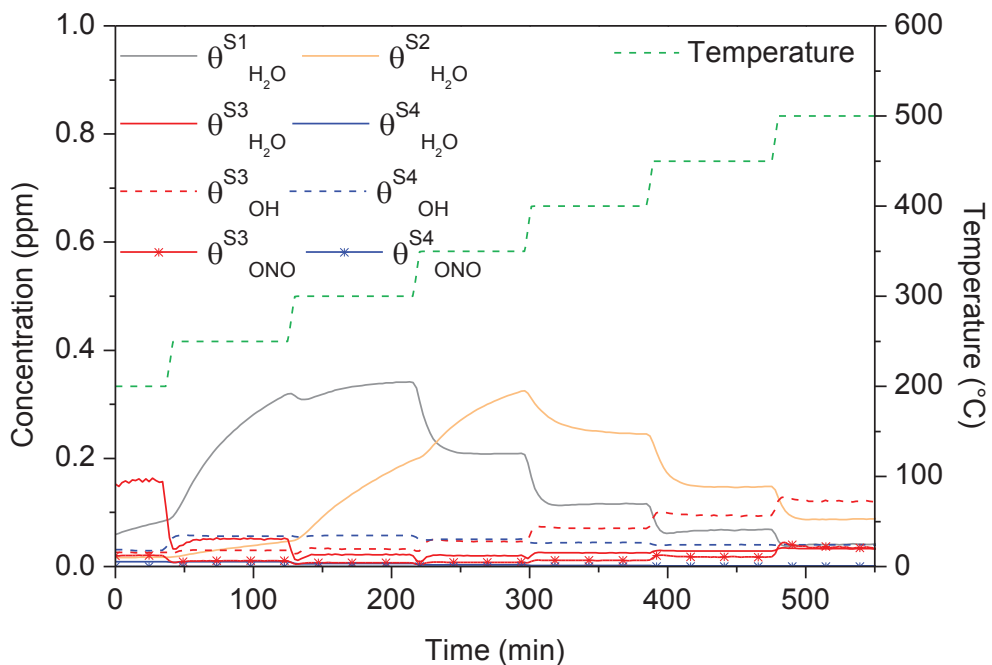


Figure VI-18. Simulated  $\text{NH}_3$  coverage evolution in time during step temperature modification. Inlet gas composition:  $1000 \text{ ppm NH}_3$  and  $\text{NO}$ ;  $80000 \text{ ppm (8\% O}_2\text{)}$ ;  $40000 \text{ ppm (4\% H}_2\text{O)}$  and  $\text{He}$  as a balance between  $200^\circ\text{C}$  and  $500^\circ\text{C}$  ( $10^\circ\text{C}\cdot\text{min}^{-1}$ ) with a total Flow of  $10 \text{ L}\cdot\text{h}^{-1}$

In addition, slow temperature ramp was employed under analogous STD SCR conditions Figure VI-19. As observed at low temperature within 200°C and 300°C between Figure VI-14 (B) and 19 (B), the overall SCR process is promoted, increasing the NH<sub>3</sub> and NO conversions about 10% where NH<sub>3</sub> and NO conversions reach more than 70% at the starting ramp temperature point 200°C. The responsible mechanism of this performance enhancement was assumed in this study to firstly proceed with H<sub>2</sub>O competing with NH<sub>3</sub> for adsorption on redox sites S3 and S4. Adsorbed H<sub>2</sub>O promptly produce hydroxyl groups on copper sites which promote the nitrite formation thanks to NO interaction with the catalyst surface. Thus, it is through the nitrite reaction with adsorbed NH<sub>3</sub> that the standard SCR in wet condition takes place in the current mechanistic path. The relative R1, R3, R4 and R9 implemented in the model are in line with previous mechanistic studies implying water in SCR process and further employed in various model construction [216,230]. Following this mechanism, the different adsorption/desorption and intermediaries reactions have to take place in sufficient proportion at low temperature for representing the measured evolution of NO, NH<sub>3</sub> and N<sub>2</sub> concentrations. Therefore, at low temperature, H<sub>2</sub>O adsorb on Brønsted and Lewis acid sites and further form OH species on the redox sites, which the estimated activation energy of OH formation displayed Table VI-9 are  $E_{r5}^{S3} = 65 \text{ kJ.mol}^{-1}$  and  $E_{r5}^{S4} = 51 \text{ kJ.mol}^{-1}$ . Note that similar H<sub>2</sub>O desorption activation energies were estimated on strong active copper species as had demonstrated Olsson et al. during previous model construction studies dedicated to water and ammonia impacts on zeolite catalyst [457]. In accordance with the current mechanistic pathway, regarding the estimated kinetic parameter for OH formation, the model achieves to describe the low temperature key intermediaries impact on SCR performances and to represent the ZCuOH site configuration on a large temperature range. Consequently, nitrite species are formed at low temperature through R9 on redox sites S3 and S4, where exchanged cations play the most important role as regarding the relative activation energies between both sites. Indeed, nitrite reacting species are principally involved on exchanged sites during the reduction process in standard conditions [221,338] and represent here a key linking reactive specie for standard SCR with H<sub>2</sub>O. Moreover, in line with different in-situ characterization studies [156,207], the low stability of nitrites in temperature can be represented here with the estimated low activation energies for backward reaction R9 displayed Table VI-9 for both sites. In that respect, as captured by the model, nitrite adsorbed on S3 will greatly depends on the dynamic of previously described reactions. Additionally, following the proposed reactional network and the corresponding estimated parameters for standard SCR R4:  $E_{r7}^{S3} = 45 \text{ kJ.mol}^{-1}$  and  $E_{r7}^{S4} = 66 \text{ kJ.mol}^{-1}$ , this is between 200°C and 350°C that the nitrites finally impact the most the SCR process, with S3 adequately representing the main active species. From this high SCR activity engaging ONO intermediates, it consequently results a low coverage on both redox sites as displayed Figure VI-21.

Concerning high temperature behaviour, the impact of ammonia oxidation is particularly observed where the NO conversion stops to increase around 450°C. The phenomenon is also simulated as regarding the NO conversions evolution between 450°C and 500°C, Figure VI-19. However, the model slightly over-predicts the NH<sub>3</sub> consumption and so the corresponding NO conversion during the temperature ramp,

which could be partially explained by the ammonia oxidation in NO and further conversion in  $N_2$  as depicted during  $NH_3$  oxidation experiments Figure VI-11. However, as depicted by the resulting conversions evolution and their corresponding prediction, the catalyst efficiency is adequately represented, through the whole temperature window, where the exchanged cations redox sites occupy the central role. Finally, as depicted in insert of Figure VI-19, the overall measured  $NO_2$  concentration remains low, informing about its near complete consumption. Nonetheless, this  $NO_2$  profile is not depicted by the model through the temperature window except once reaching the  $500^\circ C$  step according with the thermodynamic  $NO_2$  production limit. A difference which could be partially due to the overestimation of nitrite formation (backward R10) during the temperature ramp.

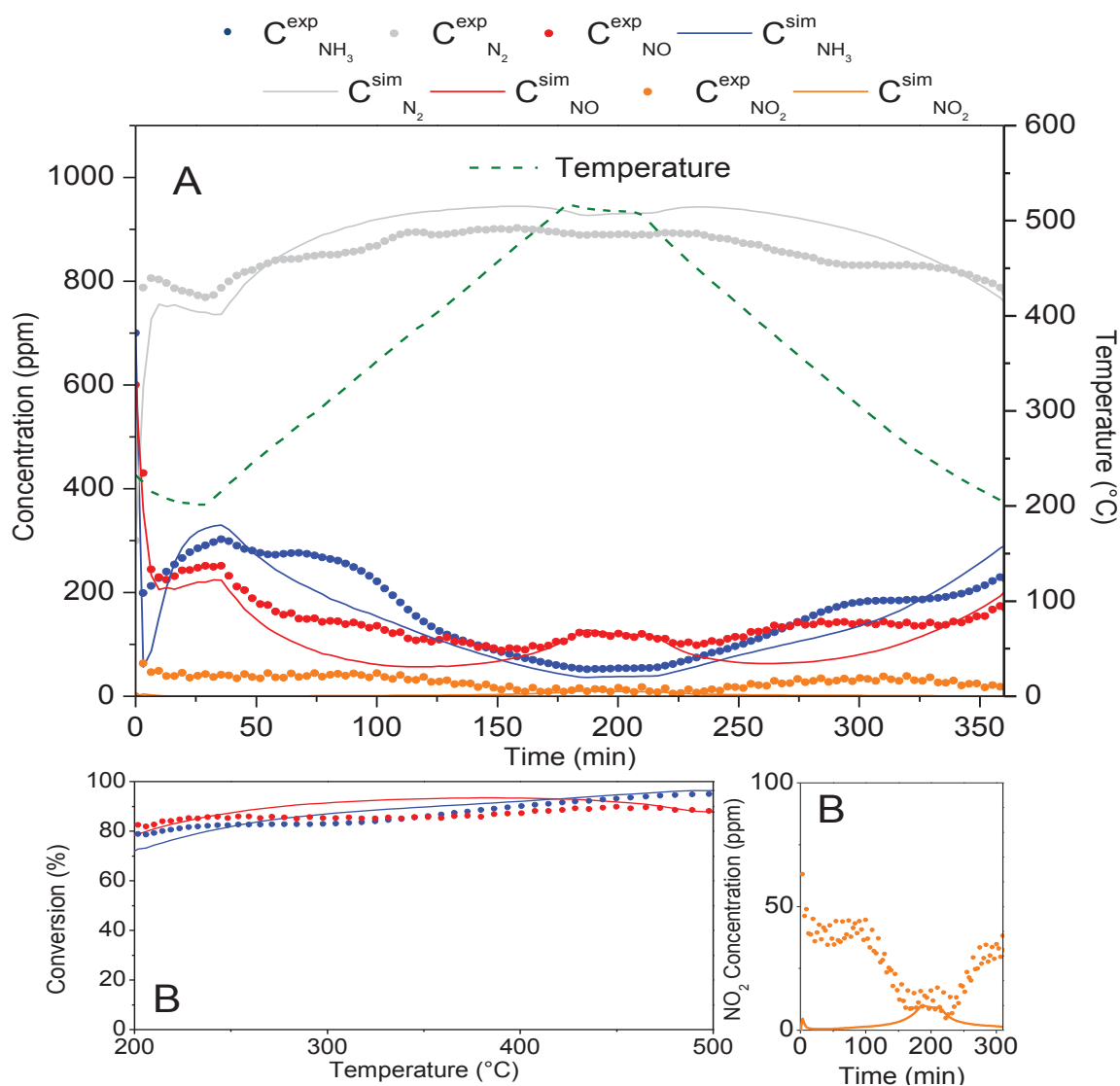


Figure VI-19. Experimental and simulated Standard SCR performances of Cu-SAPO-34-IE catalyst with water (A) accompanied by corresponding  $NH_3$  and NO conversion (B) and  $NO_2$  experimental and simulated concentrations in insert during slow temperature ramp (C). Inlet gas composition: 1000 ppm  $NH_3$  and NO; 80000 ppm (8%)  $O_2$ ; 40000 ppm (4%)  $H_2O$  and He as a balance between  $200^\circ C$  and  $500^\circ C$  ( $2^\circ C \cdot min^{-1}$ ) with a total Flow of  $10 L \cdot h^{-1}$

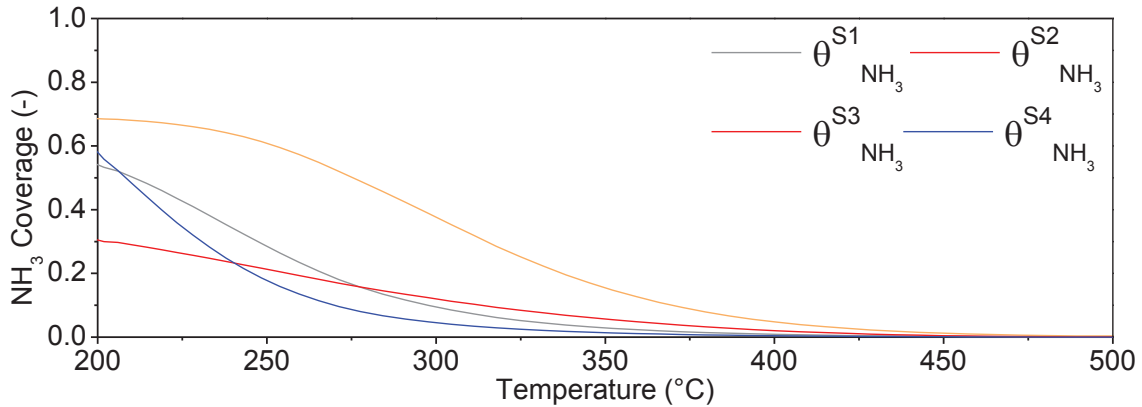


Figure VI-20. Corresponding NH<sub>3</sub> coverage evolution of S1, S2, S3 and S4 during Standard SCR in wet conditions through decreasing ramp temperature (200-500°C)

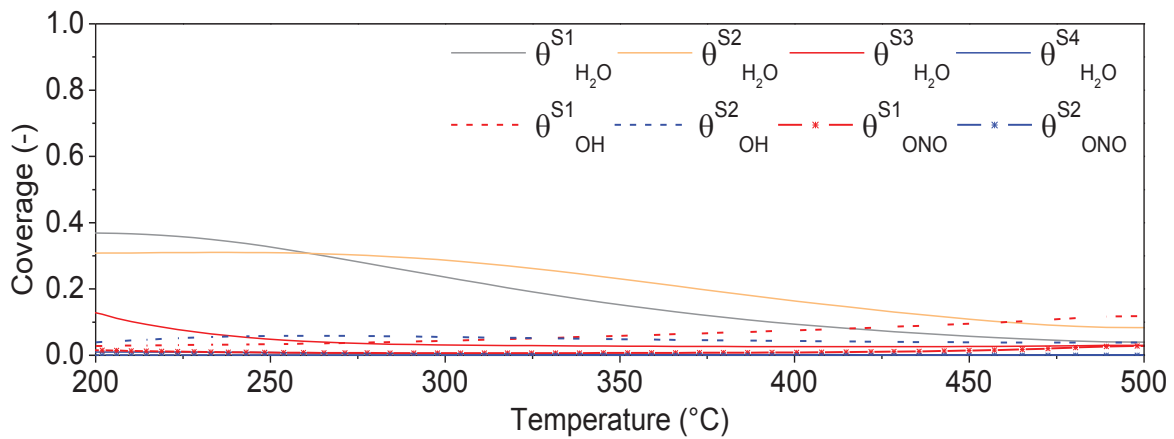


Figure VI-21. Corresponding H<sub>2</sub>O, OH and ONO intermediaries coverage evolution of S1,S2,S3 and S4 during Standard SCR in wet conditions through decreasing ramp temperature (200-500°C)

#### VI-4.5. Model validation and prediction results

Employing the currently developed model, one additional experiment was conducted, not involved in the parameter estimation process and realized under different operating conditions in order to verify the model behavior. In that respect, standard SCR conditions with a constant feeding of 1000 ppm NO, 40000 ppm (4%) H<sub>2</sub>O and 80000 ppm (8%) O<sub>2</sub> and a graduate increase of NH<sub>3</sub> concentration each 30 min with 100 ppm, were simulated in isothermal mode at 200°C. This experiment simulation, Figure VI-22, was conducted in order to exhibit the impact of low temperature on NO and NH<sub>3</sub> conversions and the corresponding intermediary formations. Within the first minutes, without any feed of NH<sub>3</sub>, the direct oxidation of NO in NO<sub>2</sub> is experimentally observed and consequently simulated in a less extent. An expected observation regarding the NO<sub>2</sub> evolution previously depicted Figure VI-19. This oxidation occurs in low proportion and as previously described through spectroscopic techniques and further assumed in different model construction [216,417], the NO<sub>2</sub> production can be directly related to ONO-S decomposition at low temperature (R10), a nitrite specie dependent of the water impact following the

current model construction. Starting from low temperature and 0 ppm of  $\text{NH}_3$ , the catalyst surface is deprived of adsorbed reductive molecule, when the  $\text{NH}_3$  feed increase in low proportion,  $\text{NH}_3$  is adsorbed and readily consumed better following a 1:1 equimolar ratio according to standard SCR reaction R4 thanks to the lack of  $\text{NH}_3$  inhibition possibilities. However, starting from 600 ppm  $\text{NH}_3$  in the feed, ammonia begins to be in excess regarding the DeNOx capability of Cu-SAPO-34-IE at 200°C as displayed by its presence in the outlet, a feature captured by the model. Indeed, it is better observed with the respective  $\theta_{\text{NH}_3}^{\text{S}3}$  and  $\theta_{\text{NH}_3}^{\text{S}4}$  evolution Figure VI-23, where ammonia coverage on the exchanged redox site starts to strongly increase once 600 ppm of  $\text{NH}_3$  is injected. Ammonia remains in adsorbed state in higher proportion and less consumed by SCR process. The same phenomenon is depicted on S4 but at lower  $\text{NH}_3$  concentration according with its lower NOx abatement performance. Simultaneously to the  $\text{NH}_3$  adsorption increase, the competition of adsorption with  $\text{H}_2\text{O}$  can be clearly observed Figure VI-24, according with the low temperature isothermal experience. In this condition,  $\text{H}_2\text{O}$  adsorption is enhanced at low  $\text{NH}_3$  concentration, but more  $\text{NH}_3$  injection increases, less  $\text{H}_2\text{O}$  manage to adsorb on Brønsted and also redox acid sites. Consequently, the hydroxyl and the nitrite coverage decrease. These dynamics are in accordance jointly with the water promoting and  $\text{NH}_3$  inhibition effects where for optimal  $\text{NH}_3$  coverages, the intermediaries performed the NOx abatement by the complete  $\text{NH}_3$  consumption. On the other hand, NO,  $\text{NO}_2$  and  $\text{N}_2$  concentrations are adequately simulated by the model with the  $\text{NH}_3$  stepwise increases, where the asymptotic  $\text{N}_2$  concentration evolution at elevated  $\text{NH}_3$  concentration, demonstrates the limit of the SCR process at 200°C from Cu-SAPO-34-IE.

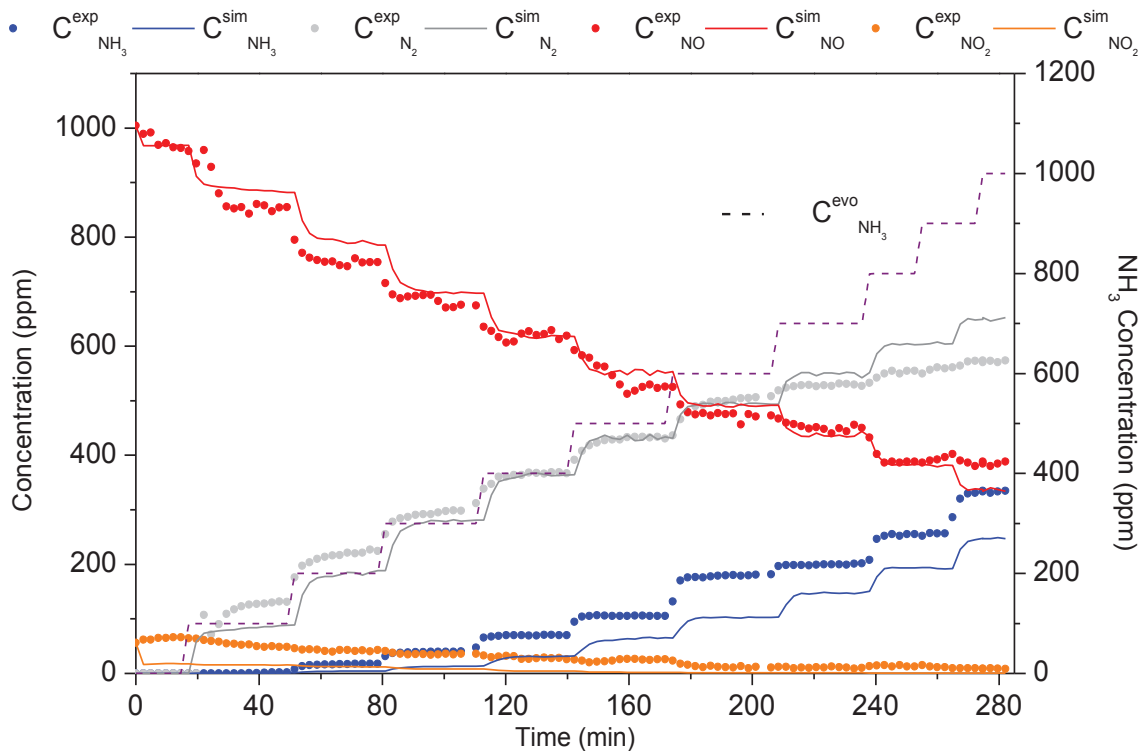


Figure VI-22. Experimental and simulated Standard SCR performances of Cu-SAPO-34-IE catalyst in transient conditions with water in isothermal mode (200° C) with stepwise increase feed  $\text{NH}_3$  (100 ppm). Inlet: 0-1000 ppm  $\text{NH}_3$  and 1000ppm NO; 80000 ppm (8%)  $\text{O}_2$ ; 40000 ppm (4%)  $\text{H}_2\text{O}$  and He as a balance with a total Flow of 10  $\text{L}\cdot\text{h}^{-1}$

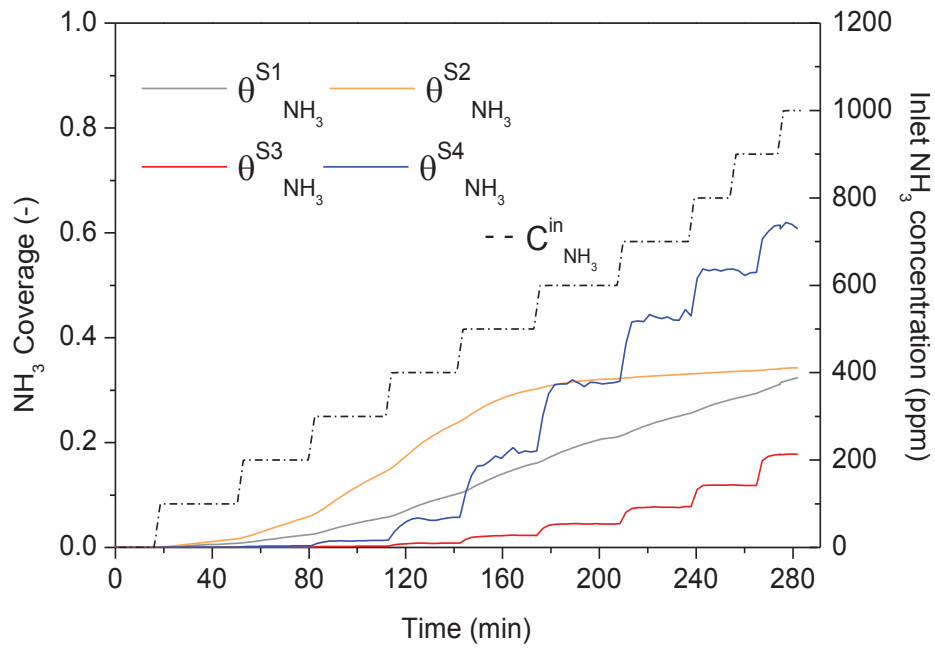


Figure VI-23. Simulated  $\text{NH}_3$  coverage evolution in time during step  $\text{NH}_3$  injection. Inlet gas composition: 0-1000 ppm  $\text{NH}_3$  and  $\text{NO}$ ; 80000 ppm (8%)  $\text{O}_2$ ; 40000 ppm (4%)  $\text{H}_2\text{O}$  and  $\text{He}$  as a balance at  $200^\circ\text{C}$  with a total Flow of  $10 \text{ L.h}^{-1}$

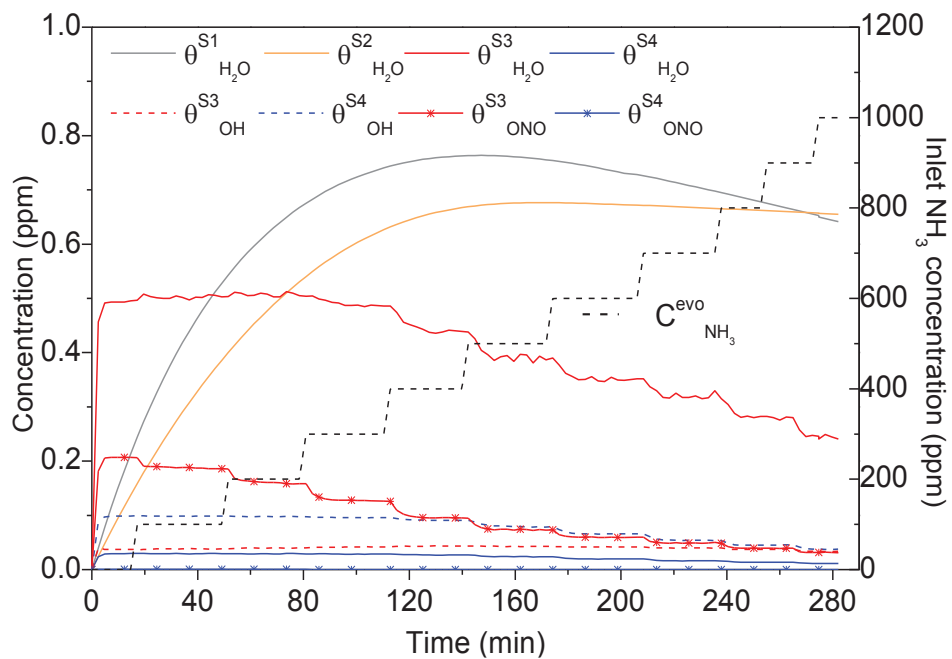


Figure VI-24. Simulated  $\text{H}_2\text{O}$ ,  $\text{OH}$  and  $\text{ONO}$  coverage evolution in time during step  $\text{NH}_3$  injection. Inlet gas composition: 0-1000 ppm  $\text{NH}_3$  and  $\text{NO}$ ; 80000 ppm (8%)  $\text{O}_2$ ; 40000 ppm (4%)  $\text{H}_2\text{O}$  and  $\text{He}$  as a balance at  $200^\circ\text{C}$  with a total Flow of  $10 \text{ L.h}^{-1}$

### VI-5. Characteristic times, parameters correlations and uncertainties intervals: Cu-SAPO-34-IE in STD SCR conditions

Once the model construction done and validated for the reference catalyst Cu-SAPO-34-IE, the model was employed for the obtention of further information concerning the STD SCR process, described through the mechanism proposed above. Therefore, the model allows to depict the different characteristic times relative to the main reaction STD SCR, employed as an example here (corresponding to Figure VI-19), to put these characteristic times into perspective with the estimated diffusional resistance for hypothesis appreciation and finally investigate the corresponding process limiting step. Moreover, the different parameter correlation coherences were pointed out for the same STD SCR reaction example, and the estimated parameter confidence intervals developed for Cu-SAPO-34-IE.

#### VI-5.1. Characteristic time and limiting steps

The total time of our heterogeneous catalytic process can be defined by this relation:

$$t_{tot} = \tau + \tau_{film} + \tau_{intragranular} + \tau_{ads} + \tau_{des} + \tau_{reaction} \quad (29)$$

Indeed, according with the model construction, different transport processes take place for the reactants, from the bulk gas to the active sites, which the required time to be performed are relevant to the system capabilities. Typically regarding the FPB reactor and applied mechanism, 5 types of characteristic times are depicted: 1) the mean residence time ( $\tau$ ), 2) the external mass transfer ( $\tau_{film}$ ) involving species diffusion from bulk gas to catalyst surface, 3) the internal mass transfer ( $\tau_{intragranular}$ ), for the species diffusion within the microporous catalyst, 4) the required time of adsorption and desorption of species from active sites ( $\tau_{ads}$  and  $\tau_{des}$ ) and 5) the chemical reactions involving all the depicted reactions ( $\tau_{reaction}$ ) Table VI-7. The fourth and fifth points are thus represented by 17 characteristic times which the expressions are displayed in Annexes materials Table VI-2. Where, depending on the reaction expression, a variable modification is done in order to obtain a reaction constant in temporal dimensions. In that respect, according to the definition in previous section (VI-2.3) we define:

$$\tau = \frac{Q_{tot}}{\varepsilon V_{bed}} \quad (30)$$

$$\tau_{film} = \frac{R_p}{3k_{fluid}} \quad (31)$$

$$\tau_{intragranular} = \frac{R_p^2}{15 D_c} \text{ with } \tau_{transf} = \tau_{film} + \tau_{intragranular} \quad (32)$$

$\tau_{reaction}$ ,  $\tau_{ads}$  and  $\tau_{des}$ , depending on the reaction expression Annexes Table VI-2.

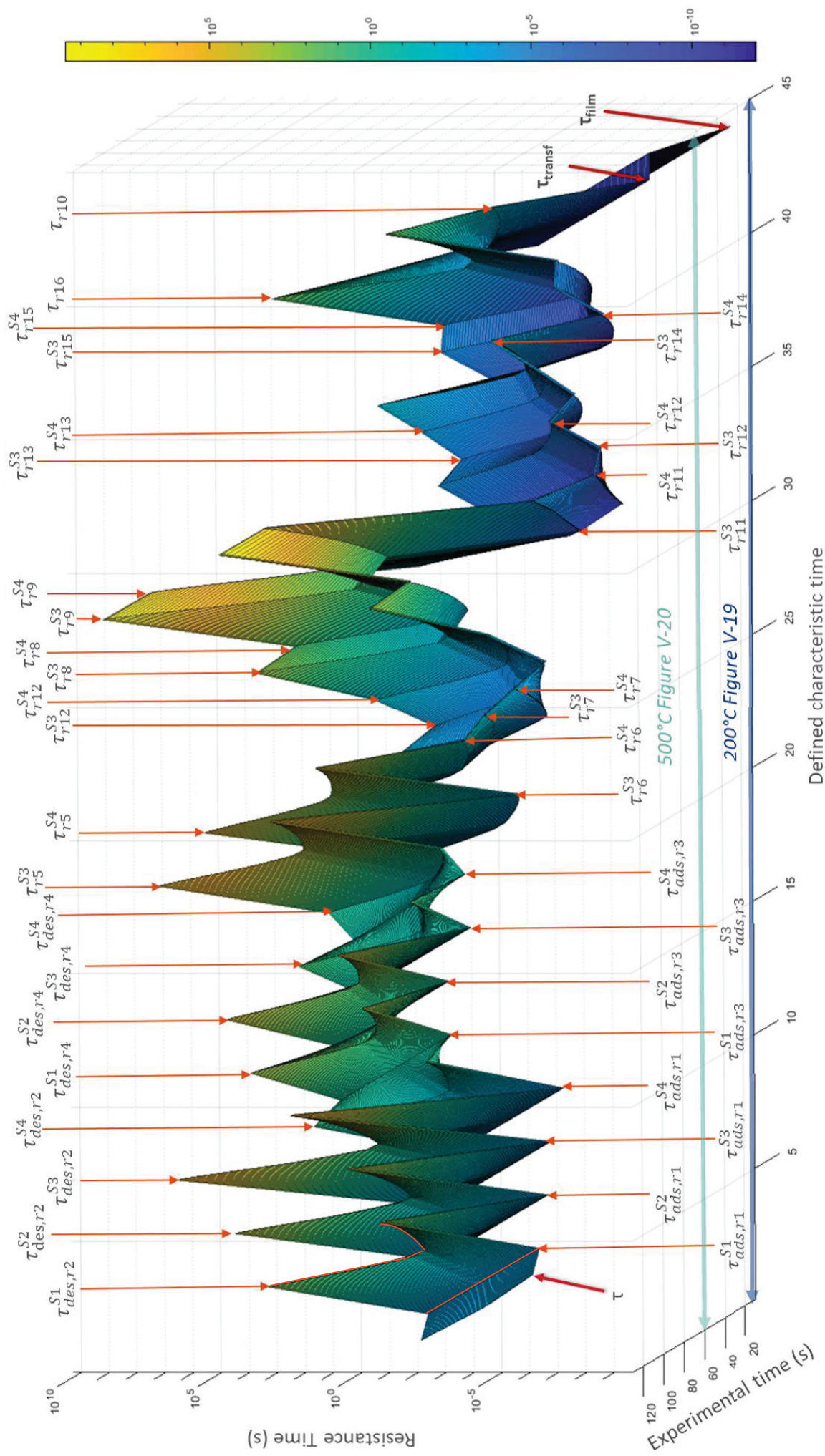


Figure VI-25. Characteristic time Map through the experimental time during STD SCR in wet condition, corresponding to Figure V-19 catalytic test



The characteristic times evolutions (44 in total) can be followed through the time during a catalytic test to identify the limiting process by comparison. In that respect, the characteristic times were plotted through the experimental time in log axis for more convenience in Figure VI-25 relatively to a typical STD SCR performance test, investigated earlier Figure VI-19. The representation of these different characteristic times is function of the experimental temperature passing by two minima at 200°C and one maximum of 500°C with 2°C.min<sup>-1</sup> ramp between, corresponding to 1 cycle test. A temperature evolution through the time represented here on the Figure VI-25 where the peaks correspond to the low temperature steps at 200°C at the beginning and the end of the experiment, and the valley to the 500°C plateau according with the slow temperature ramp applied (2°C.min<sup>-1</sup>).

Firstly, concerning the estimated mass transfer resistance  $\tau_{\text{transf}}$ , it is clearly depicted on the 2D Figure VI-26, profile of the 3D map corresponding to 200°C, that the  $\tau_{\text{transf}}$  resistance time is far lower than the ones relative to all the other characteristic times:  $\tau$ ,  $\tau_{\text{ads}}$ ,  $\tau_{\text{des}}$  and  $\tau_{\text{reaction}}$ . These characteristic times are respectively situated between 10<sup>-2</sup> and 10<sup>6</sup> s as observed on the 3D map Figure VI-25. Indeed, the chemical kinetic regime (when  $\tau_{\text{reaction}} > (\tau_{\text{ads}} \text{ or } \tau_{\text{des}})$ ) and thermodynamic regime (when  $(\tau_{\text{ads}} \text{ or } \tau_{\text{des}}) > \tau_{\text{reaction}}$ ) can take place on the whole temperature window during the STD SCR process regarding the low time required to impact the reactions by diffusional resistance at the surface ( $(\tau_{\text{ads}} \text{ or } \tau_{\text{des}}) > 0.9 \tau_{\text{transf}}$  and  $\tau_{\text{reaction}} > 0.9 \tau_{\text{transf}}$ ). In these conditions, the proportion of intragranular resistance (>99%) can be compared to the one relative to external diffusion (<1%) at a medium temperature (673K) where for a calculated  $\tau_{\text{film}} = 10^{-9}$  s according to Eq. 15. a  $\tau_{\text{intragranular}} = 10^{-6}$  s can be obtain by difference (Eq. 14). These characteristic times were reported on both Figure VI-25 and 26 on the right side by deep blue peaks. Thus, the impact of external and internal diffusion resistances were adequately ruled out accordingly with the previously described hypothesis. Moreover, a diffusional coefficient  $D_c$  can be estimated from Eq. 14 to 7.10<sup>-7</sup> m<sup>2</sup>.s<sup>-1</sup> at 673K, characteristic to zeolite displaying microporosity, better confined between 0.5 – 0.6 nm in pore size distribution, as with MFI (ZSM-5 for instance) zeolite support. An observation in accordance with the tendency followed by the measured mean pore size obtained through N<sub>2</sub> sorption experiment on Cu-SAPO-34-IE, which the support functionalization by copper incorporation slightly increased the pore size from 0.45 nm to 0.47 nm, different from the theoretical characteristic 0.39 nm (See pore size width profile differences Annexes III-2 and IV-2).

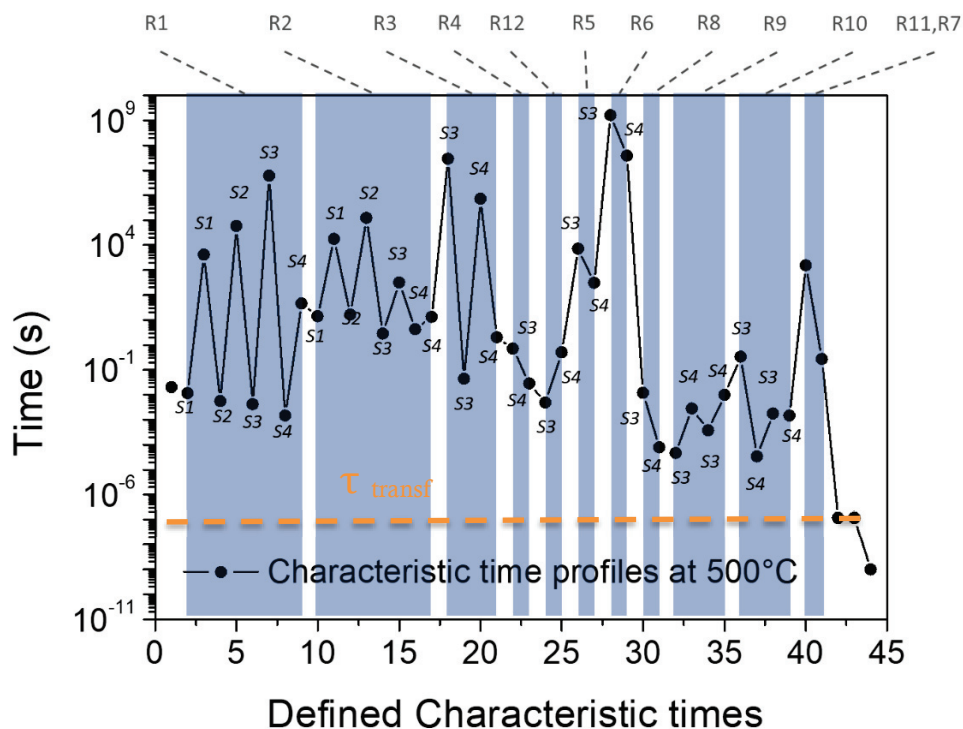


Figure VI-26. Characteristic time Map profile in 2D :  $\log \text{Time} = f(\text{Defined characteristic time})$ :  
200°C

On the other hand, the behavior of  $\text{NH}_3$  adsorption and desorption processes represented on the left side of the map Figure VI-25, are clearly observable, where the constant on each sites  $\tau_{ads,r1}^{Si}$  (with  $i=1,2,3$  and 4) are much lower than the desorption steps  $\tau_{des,r2}^{Si}$  (with  $i=1,2,3$  and 4). At low temperature, the different peaks relative to Brønsted S1,2 and redox site S3 display elevated characteristic times, representing their decisive role within the mechanism. Moreover, the time values follow the different sites strength defined in the model, where the strong exchanged cations S3 displays the highest characteristic time at low temperature. However, the characteristic time representing the desorption process on surface copper clusters S4 do not seems to be a limiting step for the network, displaying much lower value than the other sites. Thus, the desorption process from cluster surface site is less impacting, in accordance with its definition where the exchanged cations endorse the principal role of  $\text{NO}_x$  reduction.

In a similar observation, the water adsorption is much faster than its desorption step, displaying lower desorption times than  $\text{NH}_3$  desorption processes. Concerning the redox sites, the adsorption and desorption characteristic times are closer. In that respect, the  $\text{H}_2\text{O}$  desorption steps from S3 and S4 are not the limiting steps here. And the adsorption competition between  $\text{NH}_3$  and  $\text{H}_2\text{O}$  can be observed in favor of ammonia, as previously demonstrated during coverage evolution observations. A strong interaction of  $\text{NH}_3$  with the surface which in addition, was observed through the so called  $\text{NH}_3$  inhibition effect. The limiting process induced by ammonia with the active sites investigated through the model is in accordance with the quick-scanning EXAFS studies performed by Marberger et al [336], enlightening the low temperature interaction between copper cations and adsorbed  $\text{NH}_3$  as a potential rate-limiting step.

At low temperature, it is also observed the competition between adsorbed  $\text{NH}_3$  and hydroxyl formation through R3, where the formation of the key intermediaries OH will play a role as important as the  $\text{NH}_3$  desorption step of ammonia. Moreover, according with the implemented reactional network, ONO intermediaries formation has to present fast reaction rates regarding the  $\text{NH}_3$  adsorption and hydroxyl formation step for performing the water promotional effect. Indeed, in accordance with the mechanism and the low stability of these species in temperature, the characteristic times respect the following formation order:  $\tau_{r5}^{S3,S4} > \tau_{r12}^{S3,S4}$  thus displaying short time for the formation and decomposition of nitrites species as studied above. Though the 3D map observation, the intermediaries impact and their position within the mechanism can be readily observed, constituting an interesting tool for model engineering.

According with these key formations, the characteristic time corresponding to STD SCR reaction between adsorbed  $\text{NH}_3$  and nitrite species display low characteristic times on both sites S3 and S4, where the lower time noticed on S4 is directly proportional to the important site density  $\Omega_{S4}$ . In that respect, relatively to the  $\Omega_{S3}/\Omega_{S4}$  ratio displayed Table VI-10 and the time definition of  $\tau_{r7}^{S4}$  Annexe Table VI-2, the characteristic time is therefore lower than  $\tau_{r7}^{S3}$ . However, despite the more elevated density of surface site, the selectivity of S4 toward STD reactions is too low for participating in equivalent proportion with S3, a feature represented by the model. Concerning dry SCR reactions, compared with  $\tau_{r7}^{S3,S4}$ , the characteristic times display similar times, in line with the competition between both mechanism at low temperature.

Finally, the parasitic oxidation step of  $\text{NH}_3$  in NO and  $\text{N}_2$  clearly demonstrate elevated characteristic times, particularly with  $\tau_{r9}^{S3}$ , representing the difficulty to oxidize  $\text{NH}_3$  readily at 200°C on exchanged cations. A capacity enhanced on S4 but without main impact on SCR reactions regarding the gap between  $\tau_{r7}^{S3,S4}$ ,  $\tau_{r12}^{S3,S4}$  and  $\tau_{r9}^{S3,S4}$ .

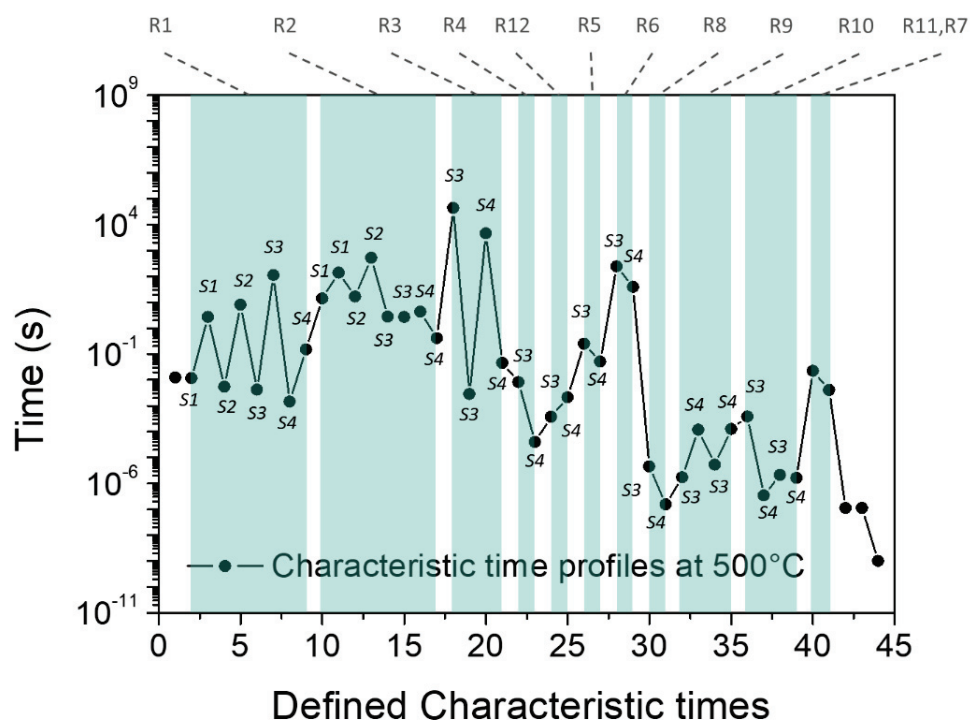


Figure VI-27. Characteristic time Map profile in 2D : log Time = f(Defined characteristic time): 500°C

The transition through the ramp temperature can be better appreciated with the 3D Map Figure VI-25, where the peaks and valleys change with the thermodynamics. In that respect, as reported on Figure VI-27, profile at the 500°C step, the limiting processes evolve, where the adsorption and desorption limitation of  $\text{NH}_3$  is too low regarding the  $\text{NH}_3$  catalyst storage capacity and its near complete desorption at elevated temperature. If the characteristic times relative to ammonia adsorption remain the same due to the assumed non activated process, the desorption better compete with  $\text{H}_2\text{O}$  adsorption/desorption dynamic as regarding their close time ranges. Accordingly at elevated temperature, the OH formation through R3 represent the reaction which takes most of the time, displaying the hydroxyl formation difficulties at such temperature. Here the process will be mainly limited by the  $\text{NH}_3$  adsorption capabilities on redox sites and the oxidation of ammonia in  $\text{N}_2$  through R6. Finally, in respect to the temperature increase, the fastest reactions as the ONO formation and decomposition displayed by R8 and R9 for instance, or the Fast SCR reaction, will start to compete with the diffusional limitation at the most elevated temperature. Therefore, the important impact of  $\text{NO}_2$  within the process is depicted here at high temperature and enlighten the necessity to consider FAST reaction in STD SCR operating conditions.

#### VI-5.2. Correlation between estimated parameters

After the parameter estimation process, their relative correlation can be investigated in order to better apprehend the model variations and put in perspective the relation between the reactions. Correlated coefficient do not imply a causality relation but represents the linear relationship between their variations. The calculated correlation coefficients obtained through the C square matrix Eq. 33 [482] varie between 0 and 1, where 0 represent the lack of variation dependency between both parameters and 1 the linear relation

between the parameter variation. The different correlation coefficients were reported Figure VI-28, gathered by reaction.

$$C_{ab} = \frac{\{(J'J^{-1})\}_{ab}}{\sqrt{\{(J'J^{-1})\}_{aa}\{(J'J^{-1})\}_{bb}}} \quad (33)$$

With  $C_{ab}$  the correlation coefficient (-) between a and b parameters and  $J'$  the transposed Jacobian matrix obtained after the *lsqnonlin* subroutine application.

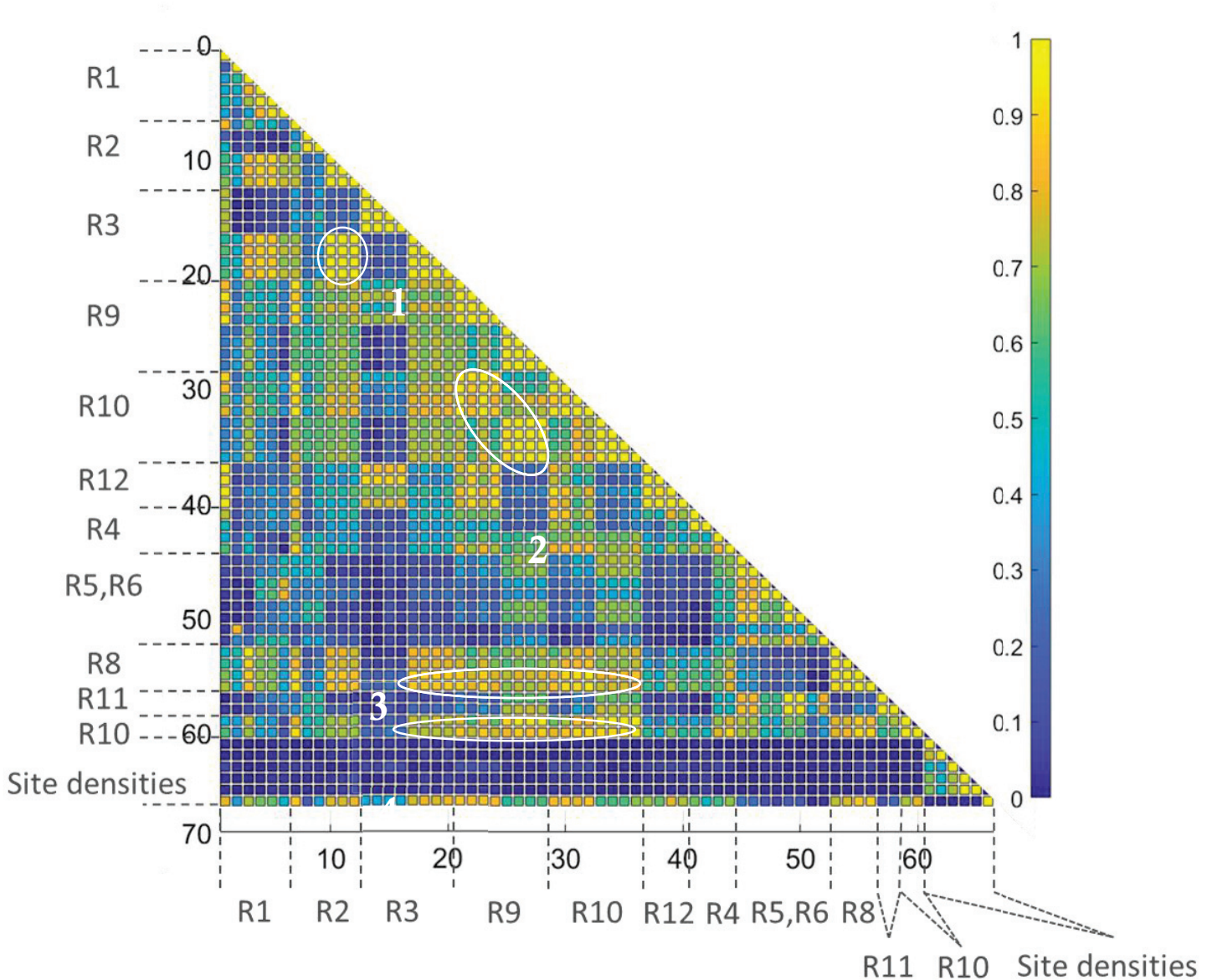


Figure VI-28. Correlation diagram between the 67 estimated parameters with Cu-SAPO-34-IE

First, according with the Arrhenius law employed for each reaction constant estimation, a strong correlation is induced between the pre-exponential factor and the activation energy of each  $i^{\text{th}}$  reactions. Indeed, the built-in correlation between these parameters cannot be avoided without employing a subjective centered temperature, as the mean temperature for instance, modifying the pre-exponential for

becoming the reaction constant at the chosen reference temperature ( $k_{ref}$ ). Without doing so, the natural correlation between these parameters, are clearly observed Figure VI-28 on the diagonal.

Despite this, regarding the Figure VI-28, strong correlations ( $\sim 1$ ) between different reactions are less remarked. Indeed, one can be observed in 1<sup>st</sup> circle between R3 and R2<sub>ads</sub> on S4 site precisely. If the direct relation between variation of adsorbed water molecules and the formation of OH species is obvious regarding the reactional network, it is interesting to observe on the other hand, that a similar correlation is not observed for S3 sites. Indeed, as S4 sites are less selective for the STD SCR process than S3, the reduction of potential ONO species is less performed. In that respect, the necessity to form such ONO nitrites is less important, decreasing the reaction rate of ONO formation. It was rendered through the model with a lower estimated activation energy  $Ea_{r12}^{S4} < Ea_{r12}^{S3}$  (Table VI-9). With OH on S4 and slow turn over by backward reaction or ONO formation, the variation of adsorption and desorption of H<sub>2</sub>O on S4 dictate the variation of OH on the site.

Moreover, regarding the relation between R9 and R10, where nitrites can decompose in NO<sub>2</sub> and NO<sub>2</sub> can interact with the surface forming ONO species, the variation of  $\theta_{ONO}^S$  will greatly impact R10 variations, as the presence of NO<sub>2</sub> in the gas phase. This relation is visible in Figure VI-28 within the 2<sup>nd</sup> circle, where on each sites S3 and S4, the one influence the other.

In accordance with this observation, the presence of NO<sub>2</sub> in the gas phase, which the variations are imposed by the system himself, without introduction of NO<sub>2</sub> regarding the applied STD conditions, is thus well correlated with the R10 and R9 variations depicted in 3<sup>rd</sup> circle. Finally, as expected and displayed in the 4<sup>th</sup> circle, the consumption of NO<sub>2</sub> induced by FAST reaction will consequently impact the variation of these reactions, and more intensely on S4 according with the coefficients.

Furthermore, the parameters relative to the site densities seem low correlated with the other parameter variations. Here the variation of the site densities do not strongly influence the variation of the different reactions, indeed, the model represent the catalytic regime in these conditions where number of active sites is not a limiting parameters.

### VI-5.3. Parameters uncertainties

Finally, the computed precision of the estimated parameters was obtained assuming that errors corresponding to two successive measures were independent and centered, following a normal distribution. Thus, the confidence interval for each parameter was established as [482]:

$$\hat{p} - s_{N-K} \sqrt{\frac{Diag(J'J)^{-1}}{N-K} \sum (y_i - \hat{y}_i)^2} < \hat{p} < \hat{p} + s_{N-K} \sqrt{\frac{Diag(J'J)^{-1}}{N-K} \sum (y_i - \hat{y}_i)^2} \quad (34)$$

With  $\hat{p}$  the estimated parameter, J the Jacobian matrix returned by *lsqnonlin* subroutine,  $s_{N-K}$  corresponding to a chosen student variable (corresponding to 95% of probability interval confidence)

of 1.7 according with the concerned degree of freedom, N the observation number and K the parameter number.

It is important to note, that the use of experiments with different temperature input modifications for the catalyst performance investigation and its modeling, allow to increase the estimated parameter accuracies by the consideration of large number of different operating conditions. Indeed, with an important N, the number of observations, significantly higher to the number of parameters, decrease the overall standard error. Regarding the number of parameters implied within the model, it's important to consider this point for the determination of accurate parameters. With steep temperature variations tests, steady state is consequently reached during each plateau at constant temperature, therefore the constant observations (concentrations) would be mistaken as data points for the determination of N which represents variable conditions. Therefore, N is in fact significantly lower than the number of data points. With a false higher degree of freedom ( $\nu = N - K$ ), the standard error would be underestimated. In that respect, the tests performed with slow temperature variations better allow to consider all the data points and to obtain higher degree of freedom for a similar operation.

On Figure VI-29 are depicted the relative parameters uncertainties in percentages in log y-axis of the estimated kinetic parameters of Cu-SAPO-34-IE displayed Table VI-9 and 10. Below the dotted dark blue line, it is represented the uncertainties estimated with less than 10% of error below second dotted line, uncertainties inferior to 1% of the estimated parameters.

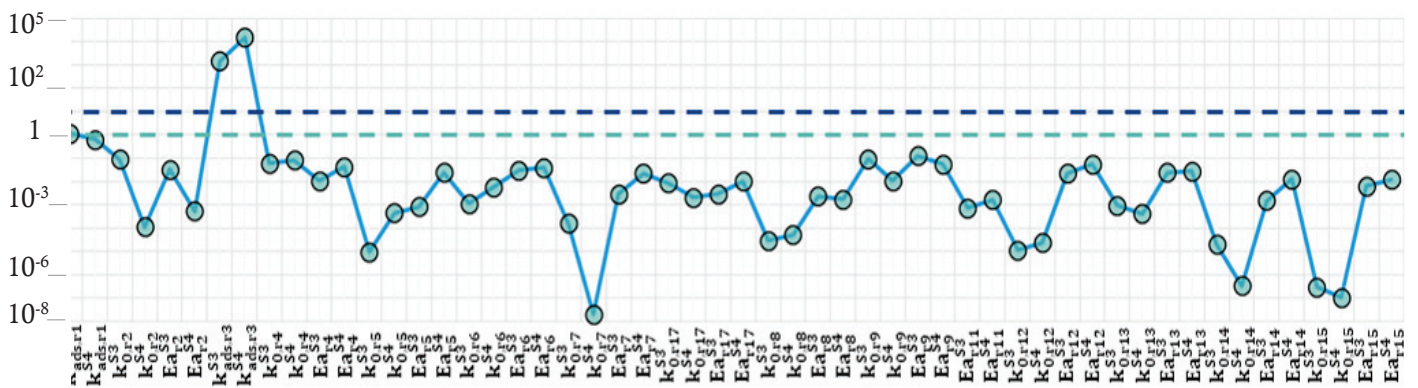


Figure VI-29. Log (% parameters uncertainties) = f (Defined kinetic parameters)

As observed on the Figure VI-29, almost all estimated parameters were estimated with less than 1% of standard error, displaying the parameters robustness estimated for the deployed model. However, strong uncertainties are observed on the adsorption coefficient of water on S3 and S4. The low reaction coefficient in  $10^{-2}$  magnitude order are sensitive to the variations, which is translated here.

Finally, the apparent parameters estimated in Chapter V for global reactions:  $Ea^{app}_{STD\ SCR} = 56$   $\text{kJ.mol}^{-1}$ ,  $Ea^{app}_{NH3\ oxi} = 71$   $\text{kJ.mol}^{-1}$  and  $Ea^{app}_{NO\ oxi} = 29$   $\text{kJ.mol}^{-1}$ , employed as initial value in the model and demonstrated in close range with literature, can be compared with the one estimated through the model.

Indeed, in the proposed reactional network, the STD SCR reaction was divided in two categories in order to take into account the catalysts performances without the formation of OH intermediaries. Despite this differentiation, the estimated  $Ea_{r7}^{S3}$ ,  $Ea_{r7}^{S4}$  and  $Ea_{r17}^{S3}$ ,  $Ea_{r17}^{S4}$  remain close to the approached one in first instance, as observed in Table VI-9, where both dry and wet reactions display comparable activation energy. In that respect, it informs also about the coherence of the estimated parameters for the intermediaries reactions, where non-coherent parameters would not allow similar STD SCR activation energies between experiences and model. However, the ammonia oxidation, differentiated in two reactions, with an oxidation whether in NO or N<sub>2</sub> in the model network, bring more precision on the kinetic parameter determination. Indeed, with experimental measurement, it is difficult to differentiate both reaction as NO can be readily consumed through SCR process by NH<sub>3</sub> to form N<sub>2</sub>. This differentiation is better performed with a model and further informs that the measured apparent activation energy seems to represent the oxidation in NO than in N<sub>2</sub> on surface nano clusters, where  $Ea_{r8}^{S4} < Ea_{r9}^{S4}$ , near to the measured value  $Ea_{app}^{NH_3\text{ oxi}}$ . Finally, the oxidation of NO was estimated with higher activation energy ( $Ea_{r10}^{S3,S4}$ ,  $Ea_{r14}^{S3,S4}$ ), closer with the cited literature in Table V-2, where the oxidation of NO and the NO<sub>2</sub> formation are intimately linked as observed through the correlation investigations above and thus impact the estimated apparent Ea. Taking into consideration some of these relations with the proposed mechanism, the estimation is more accurate than the assumption of a first order reaction made in first instance.

#### VI-6. Conclusion: Part 1: Multi-site kinetic model development

A kinetic model for NH<sub>3</sub> STD SCR was developed throughout this study in order to represent the catalytic behavior of a well characterized Cu-CHA catalyst: Cu-SAPO-34-IE. The reference catalyst, which the structural, chemical and physical properties were previously characterized, presented a SAPO-34 zeolite support composed of Brønsted and Lewis acid sites with incorporated exchanged copper cations and redox sites in nano-sized cluster form on the top surface catalyst. In that respect, the reference catalyst and its parent support were proposed to be defined in the model by two kinds of Brønsted acid sites, accounting for the weak (S1) and strong (S2) support interaction with NH<sub>3</sub> and water molecules. Concerning the redox active sites, the catalytic phase was depicted by the role of highly SCR active exchanged cations (S3) and surface cluster sites (S4) for NH<sub>3</sub> oxidation impact mainly, without ruling out their involvement in NOx abatement process.

Thus, by the study of NH<sub>3</sub> TPD experiments on both the raw support and catalyst and in presence or not of water in the fluid feed, the multi-site kinetic model well represented the adsorption step, the low and the high temperature desorption profile. Regarding the measured desorption profiles differences between raw support and catalyst, the model represents this difference by the desorption of weakly stored NH<sub>3</sub> on S4 and S1 which the relative proportion to S2 increased compared to the H-SAPO-34 support thanks to the presence of exchanged sites. The model informs also about the strong interaction of S3 with NH<sub>3</sub>, an important characteristic for the heterogeneous SCR process on the whole temperature window.



The  $\text{NH}_3$  and  $\text{H}_2\text{O}$  adsorption competition on the different sites was also taken into account with the multi-site model for a more accurate representation of STD SCR process at low temperature.

Indeed, regarding the promoting impact of water on the studied Cu-SAPO-34-IE, the mechanistic path proposed in the model represent the key formation and decomposition of hydroxyl OH-S and nitrites ONO-S intermediaries on redox sites, further characterized in literature through in-situ spectroscopic studies. In the model, it was therefore important to represent the NO interaction with the catalyst surface but also its oxidation in  $\text{NO}_2$  in gas phase in order to capture the high temperature  $\text{NO}_2$  involvement in SCR process. Moreover, side unselective oxidations of ammonia were considered in the mechanistic path, with both the possibilities to form NO or  $\text{N}_2$ . This feature was mainly represented by the surface nano-sized clusters sites regarding the corresponding estimated parameters, as it was suggested in literature on similar ionically exchanged catalyst. Without any observed  $\text{N}_2\text{O}$  formation in the studied operating conditions, the main SCR active sites were represented in the model to be exchanged S3 cations.

By the investigation of the model response through different temperature input variations, different characteristic features of Cu-CHA catalyst were represented by the model. For instance, the stepwise increase of temperature in time has particularly displayed the model capacity to depict the  $\text{NH}_3$  inhibition effect on the catalyst performance at low temperature. In the other hand, the use of slow temperature ramp during heating and cooling steps allows to accurately estimate the different parameter with narrow confidence band intervals.

To summarize, the developed multi-site kinetic model was capable to describe the different catalytic behaviour across the entire temperature window from  $200^\circ\text{C}$  to  $500^\circ\text{C}$  and brought further information regarding the determination of the most limiting processes, represented by adsorption and desorption dynamic of reactive species at low temperature, or the different correlations between the reactions defined within the reactional network.

## PART 2: MODEL EXTENSION TO DIFFERENT CATALYSTS

### VI-7. Introduction

In this second study, the descriptive quality of previously developed kinetic model was strengthened for taking into account supplementary active sites configurations. Consequently to Chapter III and IV, the catalysts synthesized through One pot method: Cu-SAPO-34-HT and classic impregnation route: Cu-SAPO-34-IMP, were employed for the model evolution. The last catalyst was considered here to be represented by all the different active sites defined in the model, in accordance with the study performed in first part of Chapter III. Thus, the exact same experimental set up was employed, only the catalysts are different for this study, allowing the conservation of the previously presented reactor model. The model construction only differs from the catalyst surface representation, keeping the same proposed mechanistic path for comparison purposes. As during the reference catalyst simulations, the parameter estimations were performed in two consecutive parts, where the first one consisted in the estimation of kinetic parameters related to adsorption and desorption behaviour by NH<sub>3</sub>TPD simulations. Based on the estimated H-SAPO-34 support parameters, a first set of parameters were estimated for HT catalyst, in order to accurately initialize the NH<sub>3</sub> and H<sub>2</sub>O interactions with the catalyst surface during the parallel estimation process. According with the simulated results, the model was further improved for adjusting the simulated profiles in order to better correspond with characterized phenomenon and active sites diversity. Note that, as during the Part 1, all the different results and presented kinetic parameters are the final one here, obtained at the end of our estimation process. After the estimation of HT catalyst's kinetic parameters, the IMP catalyst was then employed for simulation purpose only, in order to verify if the direct gathering of the obtained kinetic parameters characteristic to IE and HT catalysts could readily represent Cu-SAPO-34-IMP behaviour during STD SCR operating conditions. Finally, the differences between estimated kinetic parameters of all three catalysts were compared and put in perspective regarding their active site configurations.

### VI-8. Kinetic model: Cu-SAPO-34-HT and -IMP Surface description

As the catalysts were synthesized on purpose, and further characterized, with close chemical compositions and similar CHA zeolite support with the reference catalyst -IE, Cu-SAPO-34-HT and -IMP Brønsted acid sites were defined, within the model representation, similar to Cu-SAPO-34-IE. However, their relative proportion will be modulated regarding the different redox active sites proportions and configurations, as during the reference catalyst simulations, with the  $\alpha_s$  presence ratio declined for the added active sites.

In that respect, besides weak (S1) and strong (S2) Brønsted acid sites constituting the CHA supports, Cu-SAPO-34-HT presents large surface copper clusters, representing the main redox active

species. These characterized micro-clusters (S5) was described in a first attempt as unique active site for the catalyst performances simulations. Note that the HT catalyst displays similar ratio of weak and strong Brønsted acid sites with the raw H-SAPO-34, as observed during previously dedicated NH<sub>3</sub> TPD studies Chapter IV.

The last catalyst Cu-SAPO-34-IMP, obtained through impregnation protocol and displaying several active sites configurations, was defined in the model to be represented by the three developed redox active sites: exchanged copper cations (S3), surface nano and micro copper clusters (S4 and S5), in addition of the two Brønsted acid sites S1 and S2. The Table VI-11 summarize the active sites definitions made for the studied catalysts in Part 2.

Table VI-11. Representation of surface-active sites configurations defined in the multi-site kinetic model of Cu-SAPO-34-HT and Cu-SAPO-34-IMP.

		Denomination	Species example	Relative position	
Impregnated catalyst Cu-SAPO-34-IMP	Hydrothermal catalyst Cu-SAPO-34-HT	Weak Brønsted acid sites	T-OH (T = Si, Al or P)	External (support) (S1)	
		Strong Brønsted acid sites	T-OH-T (ex : Si-OH-Al)	Internal (support) (S2)	
		Strong Lewis acid sites: Exchanged copper cations	ZCu <sup>2+</sup> , ZCu <sup>+</sup>	Internal (6MR / 8MR) (S3)	
		Micro copper oxide surface cluster	ZCuO <sub>x</sub> (x≤1)	External (support surface) (S5)	
		Nano copper oxide surface cluster	ZCuO <sub>x</sub> (x≤1)	External (support surface) (S4)	

## VI-9. Cu-SAPO-34-HT : One Pot Catalyst

### VI-9.1. NH<sub>3</sub> and H<sub>2</sub>O adsorption-desorption

In similar conditions of the reference catalyst study, the NH<sub>3</sub> TPD were conducted at 150°C and in presence of water in order to investigate the following points: 1) to verify the Brønsted acid sites kinetic parameters pertinence (S1, S2) estimated from H-SAPO-34 simulations for the simulation of Cu-SAPO-34-HT Brønsted sites; 2) to estimate a first set of kinetic parameters relevant to the incorporated third redox copper site and to further review them after the parallel estimation process and 3) to observe, the water adsorption competition on a different catalyst, principally presenting large surface copper sites.

In that respect, Figure VI-30 regroups the different support and catalysts desorption profiles in order to enlighten their differences through the temperature window and were compared to the simulated experiments Figure VI-31. Note that the corresponding deconvoluted desorption quantities obtained from NH<sub>3</sub> TPD experiments in previous Chapters are reminded in Table VI-13 for better convenience. The simulated profiles were acquired regarding the estimated parameters Table VI-12. Through the Figure VI-30, the different categories of active site proportions can be directly observed, where on one hand, H-SAPO-34 which displays only storage acid sites as Brønsted and Lewis acid sites, share a similar desorption profile with HT catalyst. Here the impact of large copper cluster on the Brønsted density can be observed by the different peak intensities at high temperature (350°C). On the other hand, IE and IMP catalyst demonstrates close profiles, with different amplitude too. In this case, the rough impregnation decreased the strong sites proportions for the implementation of weaker sites, similar to the ones displayed by Cu-SAPO-34-IE. The correlation between these profile shapes were implemented in the model. Indeed, as characterised during the One pot active sites configuration study, Chapter IV, the incorporation of large surface copper cluster decreases the total amount of Brønsted acid sites. In that respect, this impact on strong and weak Brønsted acid sites was represented as following:  $\Omega_{S5} = (1 - \alpha^{S1} - \alpha^{S2}) \cdot \Omega_{micro}^{S5}$ , where  $\Omega_{micro}^{S5}$  represents the total initial value of S5 density within the catalyst. Thus, starting from H-SAPO-34 site densities ( $\Omega_{Bronsted}^S$ ) as initial conditions, the redox site density in S5 will be estimated jointly with S1 and S2, adjusting the different proportions during the parallel estimation with TPD and kinetic tests performances.  $\Omega_{micro}^{S5}$  was initialized with the obtained ICP measurements Table IV-2.

Table VI-12: Estimated kinetic parameters relative to S5 with 95% confidence intervals obtained through overall data set

	Reaction rate (mol.m <sup>-3</sup> .s <sup>-1</sup> )	Pre-exponential factor (k <sub>0</sub> <sup>a</sup> )		Activation energy (E <sub>a</sub> J.mol <sup>-1</sup> )	
		S5	+/-	S5	+/-
1	r <sub>1</sub>	0	0	6.51.10 <sup>2</sup>	3.93
	r <sub>2</sub>	2.94.10 <sup>7</sup>	4.76.10 <sup>1</sup>	8.13.10 <sup>4</sup>	5.65
2	r <sub>3</sub>	0	0	9.52.10 <sup>-1</sup>	5.01
	r <sub>4</sub>	3.64.10 <sup>4</sup>	2.13.10 <sup>1</sup>	4.96.10 <sup>4</sup>	8.72
3	r <sub>5</sub>	1.38.10 <sup>5</sup>	1.56.10 <sup>1</sup>	4.16.10 <sup>4</sup>	1.09.10 <sup>1</sup>
	r <sub>6</sub>	5.87.10 <sup>6</sup>	5.48	5.41.10 <sup>4</sup>	1.44.10 <sup>1</sup>
4	r <sub>7</sub>	1.50.10 <sup>9</sup>	3.18.10 <sup>1</sup>	5.94.10 <sup>1</sup>	2.86.10 <sup>1</sup>
5	r <sub>8</sub>	1.14.10 <sup>8</sup>	3.49.10 <sup>1</sup>	1.05.10 <sup>5</sup>	1.69
6	r <sub>9</sub>	1.16.10 <sup>10</sup>	2.95.10 <sup>1</sup>	1.39.10 <sup>5</sup>	1.81
8	r <sub>11</sub>	5.65.10 <sup>13</sup>	2.71.10 <sup>1</sup>	6.92.10 <sup>4</sup>	1.42.10 <sup>1</sup>
9	r <sub>12</sub>	8.94.10 <sup>5</sup>	3.79.10 <sup>1</sup>	3.44.10 <sup>4</sup>	9.73
	r <sub>13</sub>	5.79.10 <sup>6</sup>	3.10.10 <sup>1</sup>	5.55.10 <sup>4</sup>	2.68.10 <sup>1</sup>
10	r <sub>14</sub>	6.67.10 <sup>4</sup>	3.32.10 <sup>1</sup>	6.42.10 <sup>4</sup>	1.97.10 <sup>1</sup>
	r <sub>15</sub>	6.42.10 <sup>4</sup>	1.97.10 <sup>1</sup>	1.00.10 <sup>5</sup>	5.66.10 <sup>1</sup>
12	r <sub>17</sub>	9.87.10 <sup>7</sup>	1.46.10 <sup>1</sup>	7.69.10 <sup>4</sup>	1.05
		Site densities proportion		Site density (mmol.g <sup>-1</sup> )	
		$\left(\frac{\Omega_{S1}}{\Omega_{S2}}\right)_{support} = 0.44$		$\Omega_{S5} = 200$	

<sup>a</sup>dimension depending on reaction constant expression

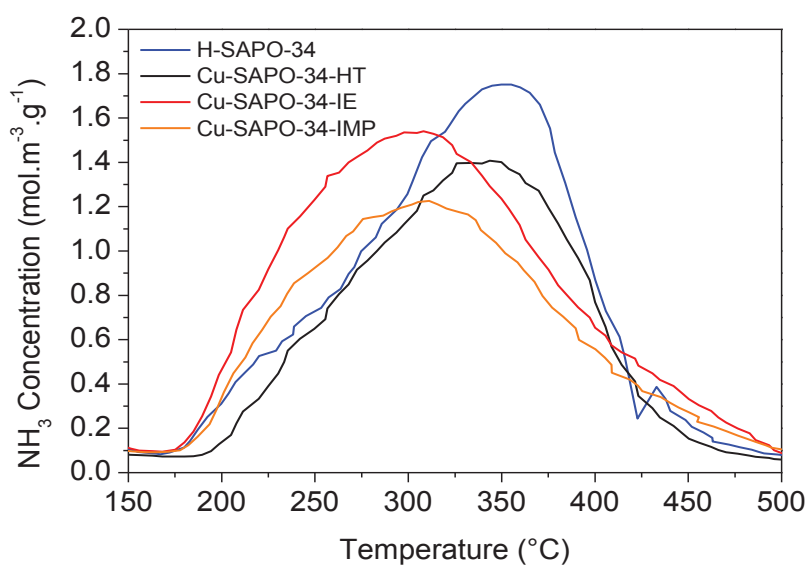


Figure VI-30. Stacked NH<sub>3</sub>-TPD profiles of H-SAPO-34 support, Cu-SAPO-34-IE, -HT and -IMP catalysts Inlet gas composition: *adsorption of 1000 ppm NH<sub>3</sub>; 80000 ppm (8%) O<sub>2</sub>; 40000 ppm (4%) H<sub>2</sub>O and He as a balance at 150°C with a total Flow of 40 mL/min*

Table VI-13. Corresponding deconvoluted desorbed quantities obtained through previous studies Chapter III, IV and V, relative to each centered peak Figure VI-30: Low, medium and high temperature peak (LT, MT, HT)

Peak category	H-SAPO-34			Cu-SAPO-34-HT			Cu-SAPO-34-IE			Cu-SAPO-34-IMP		
	LT	MT	HT	LT	MT	HT	LT	MT	HT	LT	MT	HT
Desorbed NH <sub>3</sub> (mmol g <sup>-1</sup> catalyst)	0.162	0.398	-	0.113	0.317	-	0.210	0.276	0.09	0.095	0.313	0.039
Total desorbed NH <sub>3</sub> (mmol g <sup>-1</sup> catalyst)	0.560			0.430			0.576			0.446		
Temperature (°C)	263	349	-	267	349	-	255	323	421	238	336	425

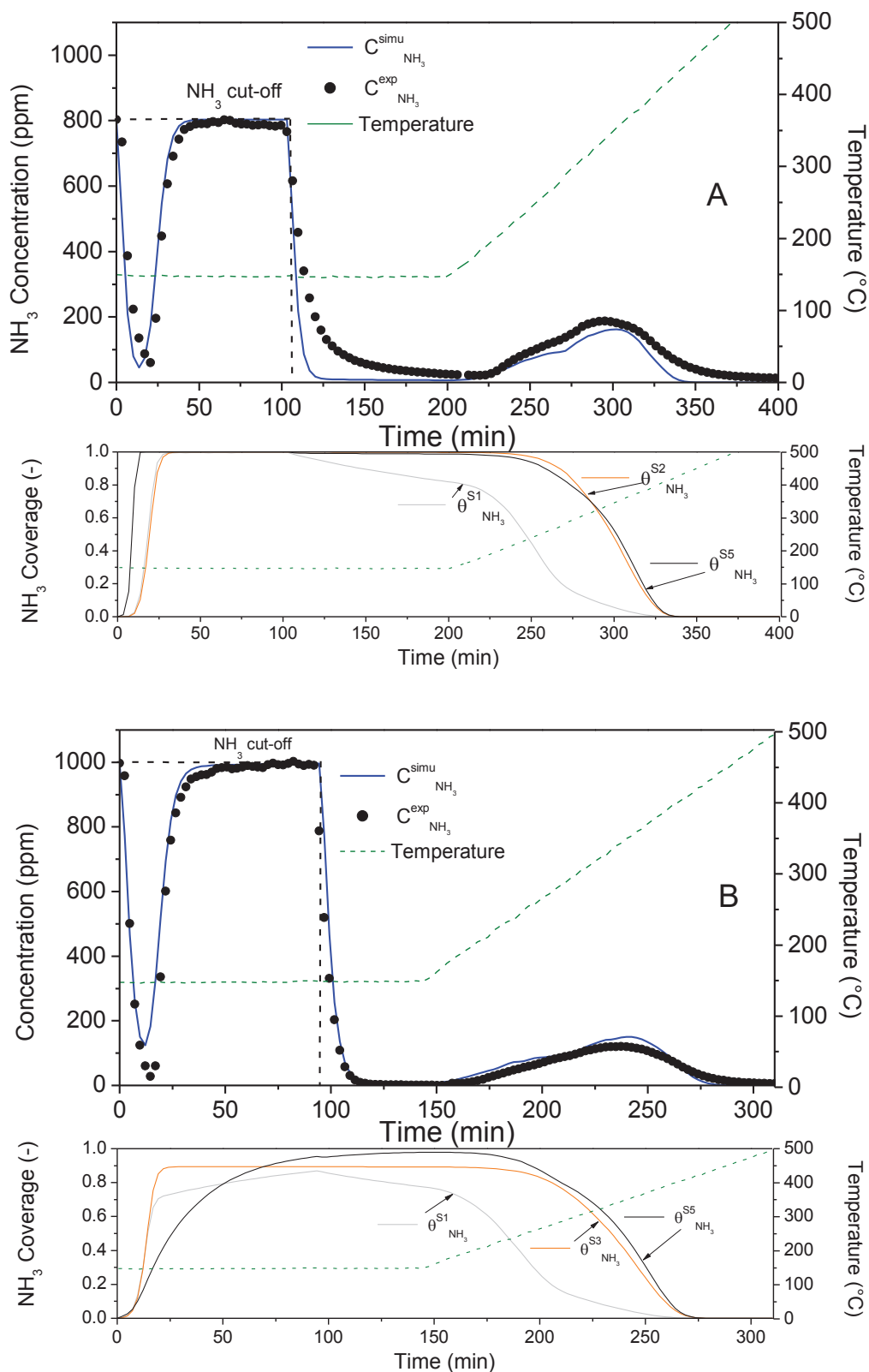


Figure VI-31. Ammonia adsorption and TPD experiments with the corresponding simulated profiles and coverage evolution in time of Cu-SAPO-34-HT without (A) and with (B) 4%  $\text{H}_2\text{O}$  respectively. Inlet gas composition: adsorption of 800 (A) and 1000 (B) ppm  $\text{NH}_3$ ; 80000 ppm (8%)  $\text{O}_2$ ; 0-40000 ppm (0-4%)  $\text{H}_2\text{O}$  and He as a balance at 150°C with a total Flow of 2.4 L/h

Thus, NH<sub>3</sub>TPD experiments were performed with and without water for the observation of water adsorption competition. Figure VI-31 displays the different profiles and the respective simulation for a 1000 ppm adsorption of NH<sub>3</sub> at 150°C and desorption until 500°C without and with 4% of injected water. As observed on the Figure VI-31 (A), the model well captures the adsorption step, which is translated by the steep increase of the different coverages. Without water, no competition occurs against NH<sub>3</sub> adsorption and according with the definition of the sum of coverages on *i*<sup>th</sup> site:  $1 = \sum_i^{Nk} \theta_i$ ,  $\theta_{NH_3}^S$  readily reached 1 within first minutes. Indeed, S1 sites which better adsorb NH<sub>3</sub> without water, consequently displays a larger desorption peak at low temperature, a feature also represented with the model by desorption peak profile comparison Figure VI-9 (B). It is also observed that the S5 redox sites desorb NH<sub>3</sub> in a same temperature window as the strong S2 sites. Indeed, the evolution  $\theta_{NH_3}^{S2}$  and  $\theta_{NH_3}^{S5}$  decreased in a similar way through the temperature, reaching a complete desorption at 400°C. This parallelism represents the close profile shape between the support and Cu-SAPO-34-HT, as displayed Figure VI-30 above, where similar peak at high temperature is observed. Therefore, the model informs about close strength capacity between strong Brønsted acid S2 and micro surface clusters S5. Moreover in the presence of water Figure VI-31 (B), the model well represents both the adsorption and the desorption processes on the whole investigated temperature window.

However without water Figure VI-31 (A), a divergence is noted between the experimental NH<sub>3</sub> concentration profile and the simulated one, right after the NH<sub>3</sub> cut off and during He flush. A divergence which is also visible on the simulated desorption profile during the temperature increase. Such difference between simulation and experience profile is observed only during this particular experiment Figure VI-31 (A), as the Table VI-14, reporting the differences between adsorbed and desorbed NH<sub>3</sub> quantities, depicts for better clarity. Note that the respective quantities for all experiments were depicted in Table II-1.

This deviation is an opportunity to better consider the experimental error obtained during TPD experiences. Indeed, in Table VI-14 are displayed the % differences between adsorbed ( $Q_{ads}$ ) and desorbed ( $Q_{des}+Q_{phys}$ ) estimated quantity through the experiments and model. These differences between total adsorbed and total desorbed quantities could represent the integrated area misled for desorbed NH<sub>3</sub>, knowing that the total desorbed quantity cannot be superior to the adsorbed one. Here this difference could typically correspond to the NH<sub>3</sub> hydrodynamic profile, consequence of the switching valves and pure He injection, where a 0% difference with the model corresponds to a negligible hydrodynamic impact after the inlet cut-off. A quantity difference representing less than 10% of the adsorbed amount with the model representation.

On the other hand, for the measured NH<sub>3</sub> quantities through experiments, it was observed that the differences between adsorbed and desorbed quantities were comprised between 4% and 15% typically. A difference mainly represented by the desorption of physisorbed molecule during He flush and the hydrodynamic behaviour of the flowing fluid after the cut off. These displayed percentages Table VI-14



were calculated relatively with the adsorption and desorption areas described in Experimental section Chapter II. In that respect, for the NH<sub>3</sub> TPD experiment in dry condition of -HT catalyst Figure VI-31 (A), a difference of 56% is particularly spotted between the total adsorbed and total desorbed experimental quantities. An experimental error visible through the slow decreased NH<sub>3</sub> concentration after the inlet cut-off. An important area which once integrated, participates to the total NH<sub>3</sub> desorbed quantity. A profile evolution better suspected to be an experimental error as the total adsorbed NH<sub>3</sub> quantity ( $Q_{ads} = 2.94 \cdot 10^{-5}$  mol) is close to the one desorbed during the temperature ramp ( $Q_{des} = 2.41 \cdot 10^{-5}$  mol), indicating that only a negligible quantity of physisorbed NH<sub>3</sub> would be detected and flushed with He prior to temperature ramp increase. A slight proportion which is not in accordance with the large profile tail Figure VI-31 (A) and representing half the quantity of adsorbed species. Therefore, this experimental deviation modifies the real desorption profile, assumed closer to the simulation as the model do not represents such experimental deviation.

Table VI-14. Absolute differences between adsorption and desorption for experimental and simulated quantities obtained through NH<sub>3</sub> TPD measurements

Support / Catalysts		Absolute difference between adsorbed and desorbed NH <sub>3</sub> quantities (%) <sup>a</sup>		Figure
		Experience	Model	
H-SAPO-34	WET	4	6	VI-9 (A)
Cu-SAPO-34-IE	DRY	12	4	VI-9 (B)
	WET	15	0	VI-9 (C)
Cu-SAPO-34-HT	DRY	56	8	VI-31 (A)
	WET	15	3	VI-31 (B)
Cu-SAPO-34-IMP	WET	7	5	VI-40

<sup>a</sup> the NH<sub>3</sub> amount were obtained considering a constant volumetric flow and a complete desorption at 500°C. Moreover, the displayed % are relative to the adsorbed quantity

#### VI-9.2. Cu-SAPO-34-HT NH<sub>3</sub> oxidation reactions

The ammonia oxidation process characterized with micro copper clusters, different in its temperature range of activity with nano copper sites investigated on Cu-SAPO-34-IE, are adequately represented by the simulated concentration profiles as observed Figure VI-32.

Indeed, S5 site activity display a strong NH<sub>3</sub> oxidation both in NO and NH<sub>3</sub>, at 400°C, which is 50°C higher than for the ionically exchanged catalyst. A noticeable difference regarding the catalyst DeNO<sub>x</sub> performances investigated in Chapter IV, where the delayed parasitic oxidation of ammonia allows a better consumption of NH<sub>3</sub> through NO reduction process. In that respect, S5 represents this behaviour at high temperature, with the parallel production of NO and NH<sub>3</sub>. However, as observed with Cu-SAPO-34-IE, a certain proportion of produced NO at high temperature do not react through SCR process and is retrieved in the outlet, a feature which the model did not depict well. In a same manner, regarding the estimated kinetic parameters,  $E_{a_{r8}}^{S5} = 105 \text{ kJ.mol}^{-1} < E_{a_{r9}}^{S5} = 139 \text{ kJ.mol}^{-1}$  Table VI-12, NO is more easily

produced than  $N_2$  with the increasing temperature and its reduction displays the well accordance between the simulation and experimental  $N_2$  concentrations. The observed gap between simulated and experimental NO concentration could therefore be due to an underestimated NO formation through gas phase for instance, where its gaseous production could also take place after the catalyst bed in the reactor volume at high temperature. Indeed, as the model was initialized with the gaseous kinetic parameters for R11 and R7 (Annexes VI-2, VI-3), the important amount of NO produced in gas phase was not performed in presence of catalyst, a kinetic regime readjusted through the estimation process passing from an initial  $E_{a16} = 71 \text{ kJ.mol}^{-1}$  to  $E_{a16} = 110 \text{ kJ.mol}^{-1}$  after parametrization. A similar assumption could take place with Cu-SAPO-34-IE experiments as the same operating conditions were employed.

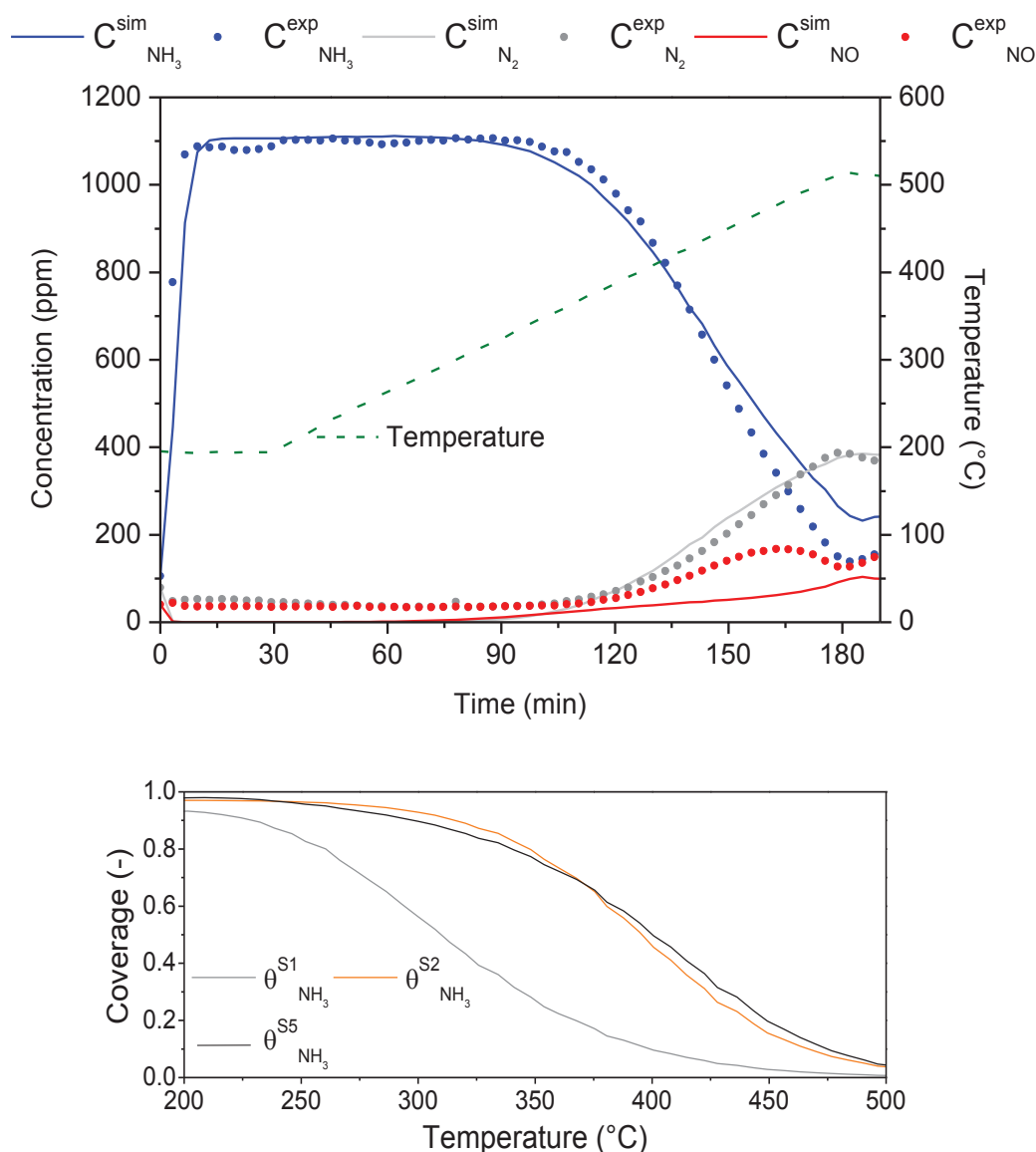


Figure VI-32.  $NH_3$  oxidation experiments in transient conditions with slow ( $2^\circ\text{C.min}^{-1}$ ) temperature input modification ramp with corresponding sites  $NH_3$  coverages between  $200^\circ\text{C}$ - $500^\circ\text{C}$  decreasing ramp. Inlet gas composition: adsorption of 1000 ppm  $NH_3$  80000 ppm (8%)  $O_2$ ; 40000 ppm (4%)  $H_2O$  and He as a balance between  $200^\circ\text{C}$  and  $500^\circ\text{C}$  with a total Flow of  $10 \text{ L.h}^{-1}$

Despite this difference, the estimated activation energies relative to R5 and R6 are in accordance with the literature on similar catalysts displaying copper surface cluster on the surface [153,154]. In accordance with the model, activation energies on S5 for  $\text{NH}_3$  oxidation are greater than the one determined with under-exchanged catalysts in literature, displaying higher proportion of nano surface sites suitable for low temperature oxidation:  $E_a = 85 \text{ kJ.mol}^{-1}$  [483],  $E_a = 72.7 \text{ kJ.mol}^{-1}$  [234],  $E_a = 93 \text{ kJ.mol}^{-1}$  [173].

As observed Figure VI-33, the low NO oxidation in  $\text{NO}_2$ , still completely selective, is in accordance with the redox sites defined for HT catalyst, where the implemented surface sites are less active for the NO oxidation. Indeed, as described previously, the copper moieties employing the Extra lattice oxygen (ELO) will be better favorable for NO oxidation. And compared with Cu-SAPO-34-IE displaying exchanged cations, more likely to interact with near ELO species, the NO oxidation is therefore less pronounced with the case of micro surface copper cluster. A low activity which is also represented through the model with the HT catalyst.

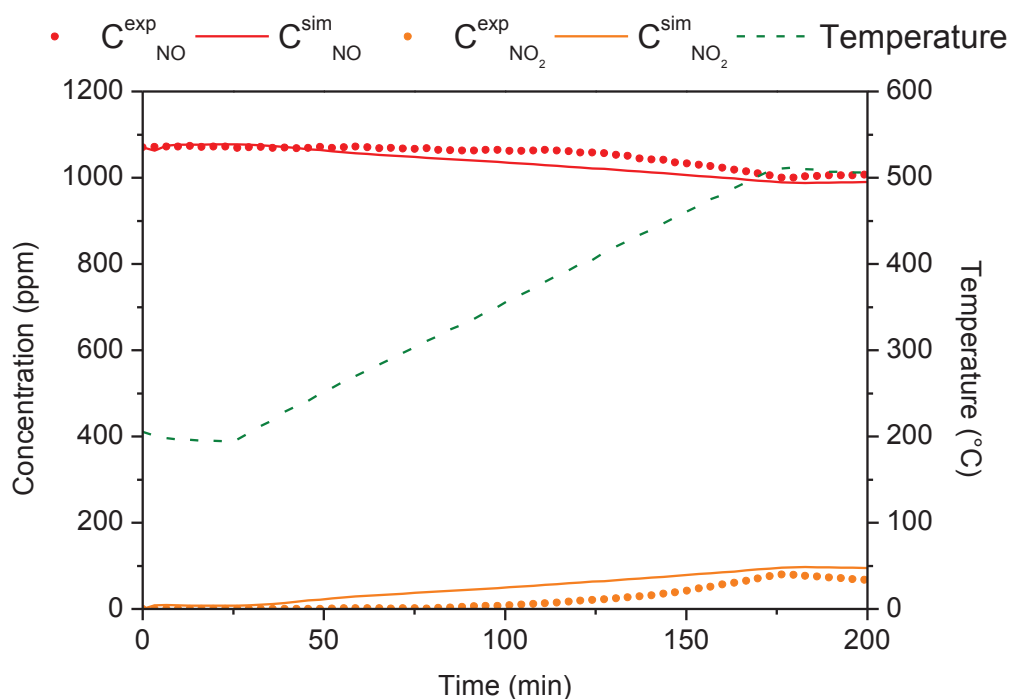


Figure VI-33. NO oxidation reaction with simulated profiles evolution with slow ( $2^\circ\text{C.min}^{-1}$ ) temperature input modification ramp. Inlet gas composition:  $1000 \text{ ppm NO}$ ,  $80000 \text{ ppm (8\%)} \text{ O}_2$ ;  $40000 \text{ ppm (4\%)} \text{ H}_2\text{O}$  and  $\text{He}$  as a balance between  $200^\circ\text{C}$  and  $500^\circ\text{C}$  with a total Flow of  $10 \text{ L.h}^{-1}$

### VI-9.3. Standard SCR behavior and parallel reactions

After the parallel reaction investigations on surface micro clusters S5, STD SCR experiments were performed with and without water in order to observe the  $\text{H}_2\text{O}$  promoting effect and the consequent generation of key intermediaries. A first experience was performed in wet conditions with Cu-SAPO-34-HT as observed Figure VI-35, extracted from Figure VI-34. Note that the  $\text{N}_2$  concentration for both STD

SCR experiences are not displayed due to experimental issues. Employing slow temperature ramps between 200°C and 500°C, the STD SCR performances can be monitored on similar temperature window than the reference catalyst Cu-SAPO-34-IE. Therefore, the first model deviation can be observed, where the S5 redox site alone seems not sufficient for the catalyst behavior description at elevated temperature in STD conditions. Indeed, two main issues are observed here, on one hand, the different kinetic regimes between 200°C and 300°C and then between 300°C and 400°C depicted by the experimental concentration evolutions are not clearly captured at low temperature. Indeed, this is the second regime taking place at 300°C which is better represented by the model here. And on the other hand, the elevated NO consumption until 400°C by SCR process is only partially represented. However once reached 400°C, the model displays the important oxidation step until 500°C. If the NH<sub>3</sub> concentration is accordingly depicted, regarding the conversion evolutions, until high temperature, the NO abatement is not completely represented through S5 activity.

In that respect, and according with the estimated parameters, the model informs about the active sites behavior themselves during the STD SCR process. Indeed, in accordance with the characterizations conducted in Chapter IV on Cu-SAPO-34-HT, the proposed mechanism occurring on this catalyst enlighten the migration of copper cations Cu (I) in exchanged positions to some extent. A characteristic which was suspected to enhance the overall catalytic performance of Cu-SAPO-34-HT. Actually, the proposed surface definition with S5 as only redox active sites is not sufficient enough for the complete description of the catalyst STD SCR performances. Following the model description, the catalyst displays of different redox sites at elevated temperature, less selective to NH<sub>3</sub> oxidation and better performing the SCR process. As proposed through the CO DRIFT in-situ characterisations in Chapter IV, ZCu<sup>+</sup> cations could migrate from the catalyst surface to the support lattice, better enhancing the SCR performances, which would be in accordance with the model responses.

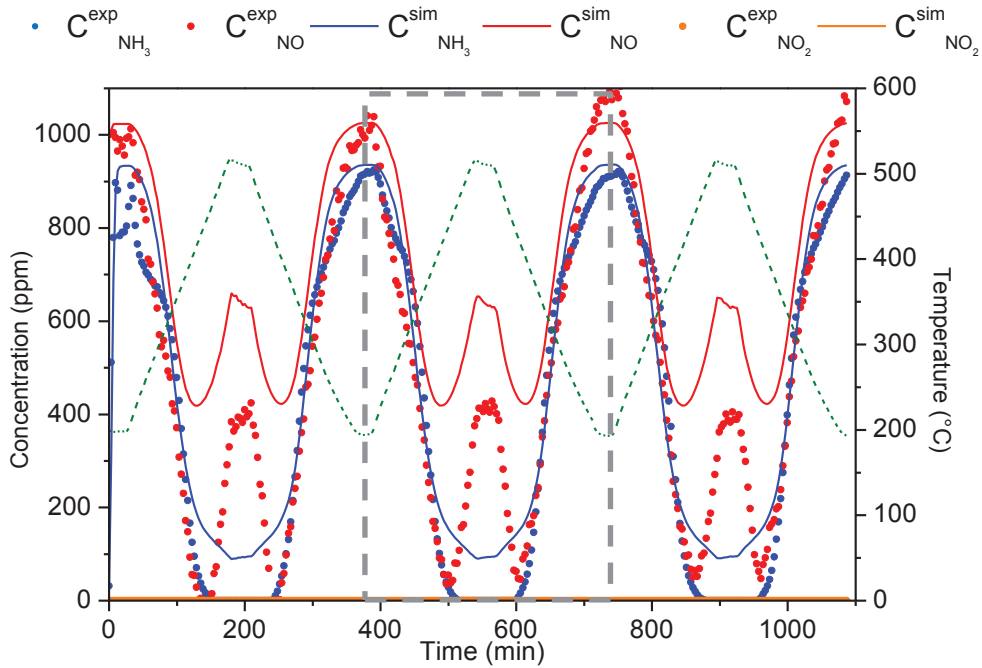
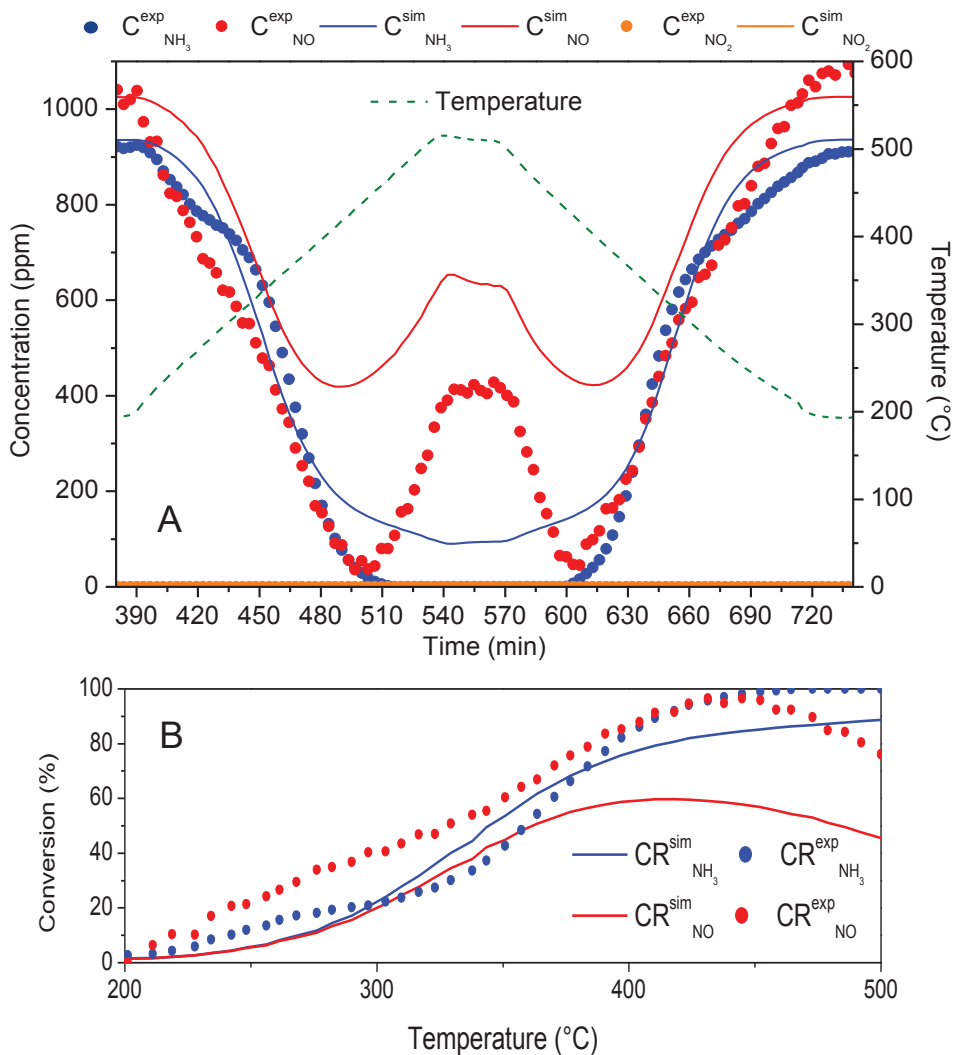


Figure VI-34. Experimental and simulated Standard SCR performances of Cu-SAPO-34-HT catalyst with water through the 3-temperature cycles test. Inlet gas composition: 950 ppm  $NH_3$  and 1000 ppm  $NO$ ; 80000 ppm (8%)  $O_2$ ; 40000 ppm (4%)  $H_2O$  and He as a balance between 200°C and 500°C ( $2^\circ C \cdot min^{-1}$ ) with a total Flow of  $10 L \cdot h^{-1}$



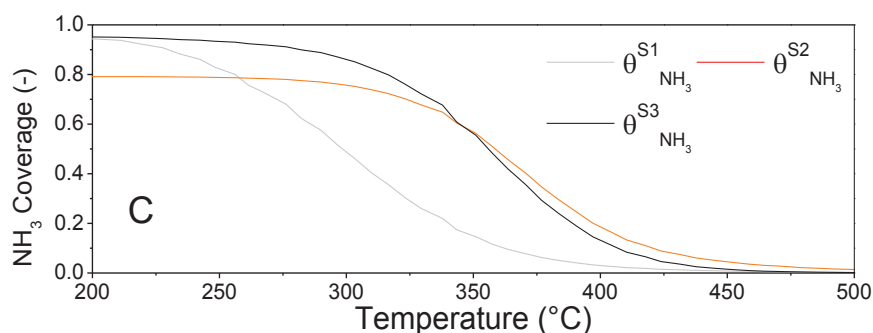


Figure VI-35. Experimental and simulated Standard SCR performances of Cu-SAPO-34-HT catalyst with water (corresponding 2<sup>nd</sup> cycle Figure VI-34) (A). This cycle is accompanied by corresponding NH<sub>3</sub> and NO conversions (B) and simulated NH<sub>3</sub> coverage ratios through decreasing ramp temperature (200-500°C) (C). Inlet gas composition: 950 ppm NH<sub>3</sub> and 1000 ppm NO; 80000 ppm (8%) O<sub>2</sub>; 40000 ppm (4%) H<sub>2</sub>O and He as a balance between 200°C and 500°C (2°C.min<sup>-1</sup>) with a total Flow of 10 L.h<sup>-1</sup>

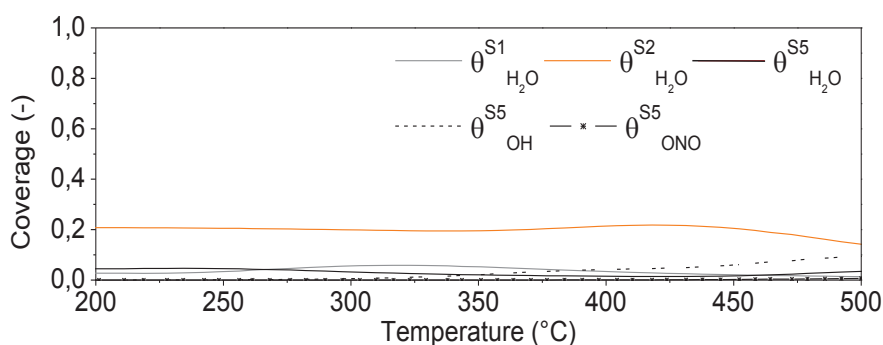


Figure VI-36. Corresponding H<sub>2</sub>O, OH and ONO intermediaries coverage evolution of S1, S2 and S5 during Standard SCR in wet conditions through decreasing ramp temperature (200-500°C)

Regarding the  $\theta_{\text{NH}_3}^{\text{S5}}$  evolution Figure VI-35 (C), ammonia almost completely reacts from S5 at 425°C, a corresponding temperature where the NH<sub>3</sub> oxidation in NO become preponderant. The model deviation is thus not a storage capacity issue from S5 sites, the coverage evolution adequately corresponding with the experimental NO consumption evolution jointly with the NH<sub>3</sub>TPD profiles in presence of water Figure VI-31 (B). An observed difference of NO abatement at high temperature which could be better represented by the role of different nature redox sites as exchanged cations in significant proportion.

Finally, STD SCR performances were investigated without water in order to better understand its impact on simulated NO consumption. In these conditions, the -HT catalyst initially deprived of strong exchanged cations ZCu<sup>2+</sup> is not active at 200°C, this is during the temperature increase that the SCR process occurs. Indeed, the implemented S5 sites are active enough to represent the NO conversion on the entire investigated temperature window regarding the simulated profiles. As the only differences was the

presence of 4% of water, it can be observed that H<sub>2</sub>O will play an important role for the catalyst performance, which further information can be withdrawn regarding the implemented model and its corresponding catalyst representation.

First, assuming that Cu<sup>+</sup> species migrate in 6MR and 8MR positions as demonstrated earlier, the catalytic performances would be enhanced at high temperature, which is not the case here. In fact, as the in-situ CO-DRIFT experiments were conducted in dry conditions for qualitative description purposes, the cation migration was detected in a certain extent only. Regarding the copper migration capability from the surface to exchanged positions in hydrothermal conditions specifically [183,184,340], the proportion of migrated cations during the performed wet STD SCR experiments would be more important than during dry conditions. Thus, without water, the cations migrate in some extent only, which is clearly not sufficient to display competitive DeNO<sub>x</sub> performances with the micro surface copper cluster initially present. Indeed, the dry conditions better reflect the characteristic low activity of the surface sites, a feature adequately simulated by the model in accordance with the implemented site definition. In that respect, with an accurate representation of S5, the differences between experimental and simulated profiles Figure VI-35 (A) could directly represent the activity of the migrated sites within the catalyst. By differences investigation, the model gives further insights about the mechanism occurring within the catalyst. Water also interact with S5 sites and performs the NO reduction through R4 regarding the lower estimated activation energy:  $E_{a_{r17}}^{S5} = 60 \text{ kJ.mol}^{-1}$  compared with  $E_{a_{r17}}^{S5} = 77 \text{ kJ.mol}^{-1}$  and the low OH an ONO coverage at low temperature on S5 (See Figure VI-35 (C)). However, considered alone, these sites are not the only one displaying the promoting effect observed between 200°C and 300°C during the first reaction regime. Indeed, the difference can better be visible through the respective NO conversions Figure VI-35 (B) and VI-38 (B), where  $CR_{NO, wet}^{exp} = 40\%$  at 300°C while  $CR_{NO, dry}^{exp}$  barely reaches 20% at the same low temperature. Despite this, the model depicts the NO conversion in a same manner with or without water.

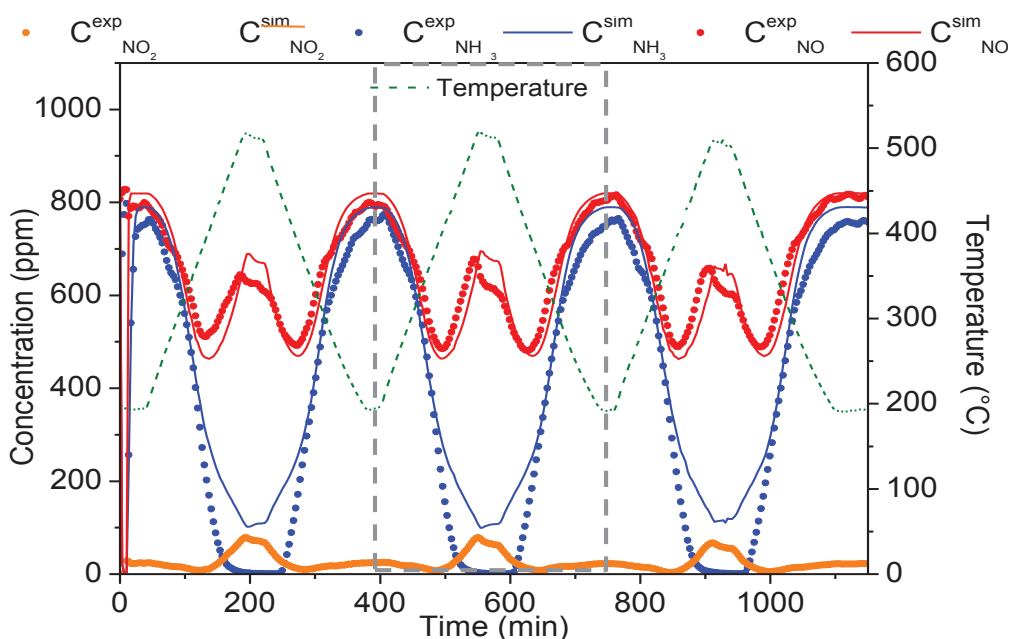


Figure VI-37. Experimental and simulated Standard SCR performances of Cu-SAPO-34-HT catalyst with water through the 3-temperature cycles test. Inlet gas composition: 800 ppm NH<sub>3</sub> and NO; 80000 ppm (8%) O<sub>2</sub>; 40000 ppm (4%) H<sub>2</sub>O and He as a balance between 200°C and 500°C

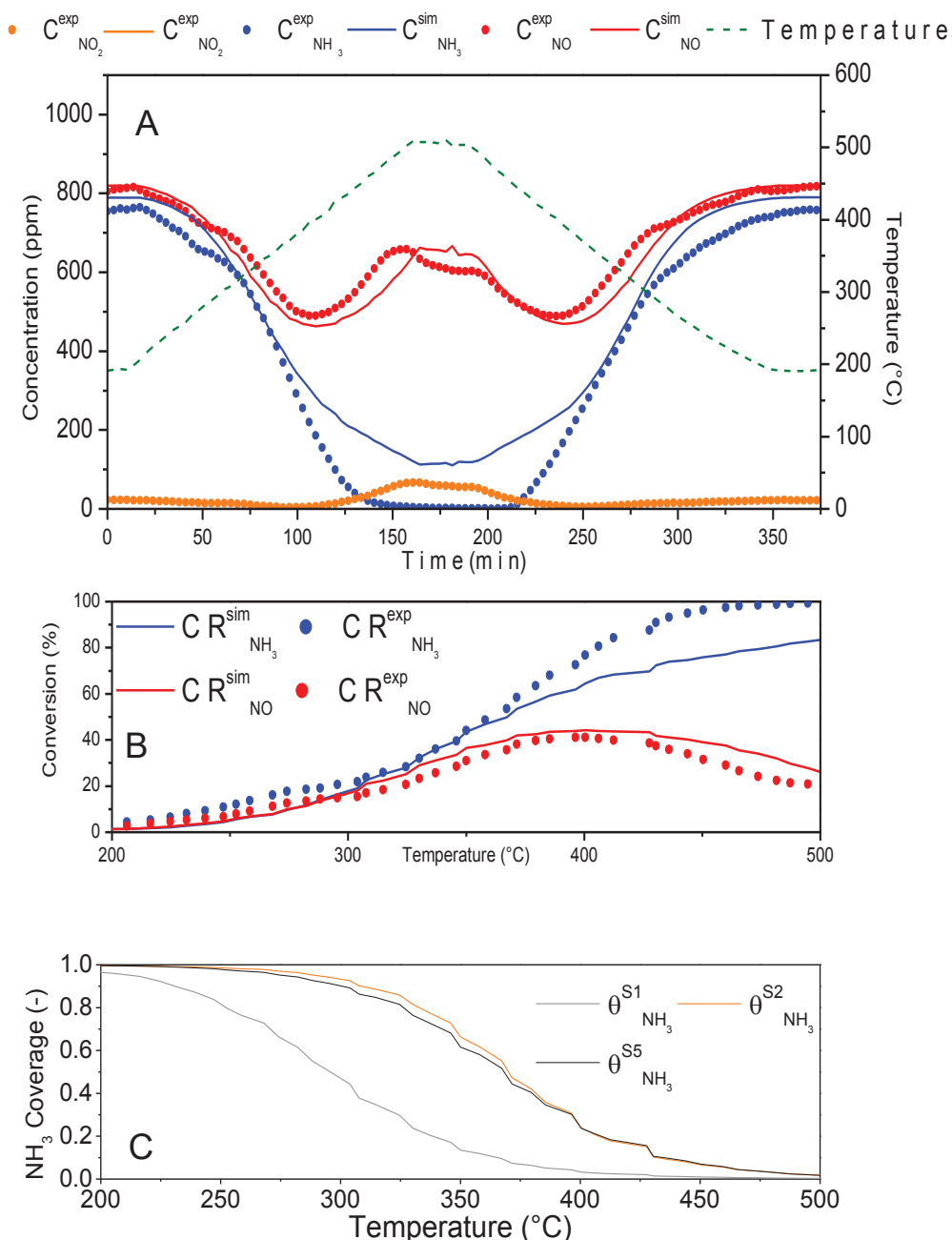


Figure VI-38. Experimental and simulated Standard SCR performances of Cu-SAPO-34-HT catalyst without water (corresponding 2<sup>nd</sup> cycle Figure VI-34) (A). This cycle is accompanied by corresponding  $NH_3$  and  $NO$  conversions (B) and simulated  $NH_3$  coverage ratios through decreasing ramp temperature (200-500°C) (C). Inlet gas composition: 800 ppm  $NH_3$  and  $NO$ ; 80000 ppm (8%)  $O_2$ ; 40000 ppm (4%)  $H_2O$  and He as a balance between 200°C and 500°C ( $2^\circ C \cdot min^{-1}$ ) with a total Flow of  $10 L \cdot h^{-1}$



S5 adequately represents the dry conversion, while in presence of water, the conversion is accentuated by migrated cations, which the promoting effect with water was demonstrated previously. In that respect the wet stream will allow two important features for the Cu-SAPO-34-HT performances: 1) the first one consists in the migration accentuation of exchanged copper species which the activity is particularly observed at high temperature and 2) the promoting effect of water on exchanged copper sites displaying better NO conversions at low temperature. Only the NO<sub>2</sub> formation seem underestimated where less than 100 ppm were detected in the outlet. A production which was not captured in dry conditions with Cu-SAPO-34-HT.

#### **VI-10. Cu-SAPO-34-IMP: Impregnated Catalyst**

Due to their different active sites configurations and consequent surface site definitions implemented, the proposed model accurately described, through an optimized reactions network, the STD SCR catalytic performances of Cu-SAPO-34-IE and Cu-SAPO-34-HT, and several others conditions as NH<sub>3</sub> and NO oxidation processes. Indeed, the model captures this speciation, displaying different behavior for each sites and thus different set of kinetic parameters. Each catalytic activity is thus defined following its site definition, where the main active sites condition the NO<sub>x</sub> abatement performance. In that respect, characterized exchanged copper cations S3 and surface micro clusters S5 hold the main role for NH<sub>3</sub> SCR, respectively in the case of IE and HT catalysts. The estimated set of kinetic parameters constitute a picture of the investigated catalysts and are consequently specific to the employed assumption and operating conditions. Employing these parameters for a different catalyst further imply a superposition of the previously obtained pictures, assuming an equal sites expression.

The hypothesis was therefore tested, assuming the Cu-SAPO-34-IMP surface definition made of S1, S2 (from H-SAPO-34 support), S3, S4 (from Cu-SAPO-34-IE) and S5 sites (from Cu-SAPO-34-HT), which the previously acquired kinetic parameters were gathered from precedent catalysts and directly incorporated in the model for simulation purposes. As expected, a straight additivity of these parameters, cannot represent the catalyst performances in similar operating conditions. In that respect, the whole set of parameters was re-adjusted through a last estimation process, starting with the gathered parameters (Table IV- 9,10 and 12) as initial values, processing the parallel parametrization with: NH<sub>3</sub> TPD experiments, STD SCR conditions and NH<sub>3</sub> oxidation. Note that the estimated parameters presented in Annexes material Table VI-3 concerning Cu-SAPO-34-IMP were estimated through one step with 109 free parameters for 540 data points. Regarding the elevated number of parameters, the parametrization until subroutine convergence to one minimal residual through least square regression method was too time consuming and necessitated to be stopped at regular interval for manual adjustments. In that respect, the results presented here for Cu-SAPO-34-IMP catalyst were acquired for the lower reached residual.

For clarity purposes and in order to investigate in which direction the parameters were adjusted, the different activation energies obtained for IMP catalyst and their corresponding variations from initial values are expressed in percentages variation, from R1 to R12 in Figure VI-39. This Figure represents the % variation of the estimated activation energy compared to the initial value corresponding to previously investigated catalysts. The calculated percentages are thus relative to their initial values. This is by investigating the largest shifts that the model tendency to promote the exchanged cations activity can be clearly evidenced.

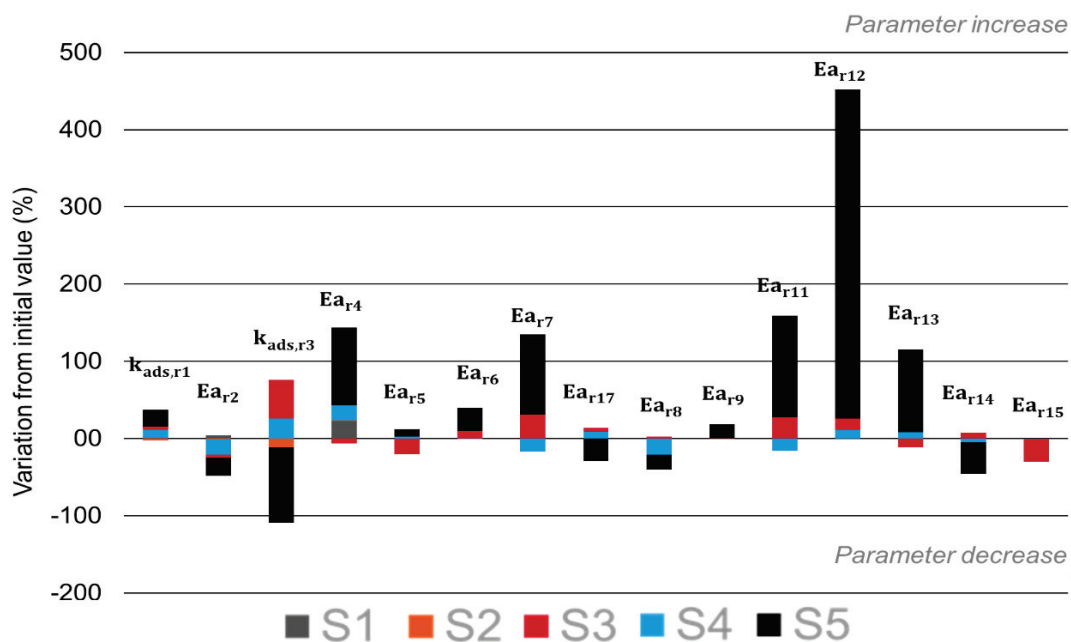


Figure VI-39. Percentage variation of estimated parameter for Cu-SAPO-34-IMP from initial H-SAPO-34, Cu-SAPO-34-IE and -HT kinetic parameters Table VI-9 and 12.

Thus, the model representation of the -IMP catalyst displaying both weak (S1) and strong (S2) Brønsted acid sites and 3 redox sites, which the roles were modified consequently to the re-estimation process of all the parameters, displays noticeable different behavior. First, regarding the NH<sub>3</sub> TPD test Figure VI-40, the model well captures both the adsorption and desorption steps, thanks to the NH<sub>3</sub> adsorption and desorption capacities modification of S4 and S5 and their corresponding sites densities. Densities which will be further investigated for all catalysts in the next section Figure VI-43. Through the observation of their NH<sub>3</sub> coverage ratios Figure VI-40, S4 and S5 were better depicted as weak redox sites, where NH<sub>3</sub> starts to desorb from the ammonia cut-off during the He flush for S5 and almost completely for S4, displaying even weaker adsorption capacities. Indeed, the model tend to better represent the experiment through the expression of 3 main sites, the Brønsted acid sites (S1, S2) and a strong redox sites S3. Moreover, as it will be further developed through Figure VI-43, the different sites densities were estimated with lower amount of S2 than S1 ( $\Omega_{S1}/\Omega_{S2} = 0.69$ ), compared with the raw support for instance ( $\Omega_{S1}/\Omega_{S2} = 0.30$ ). A decrease which is in accordance with the TPD profiles shape as depicted in Figure VI-30 above.

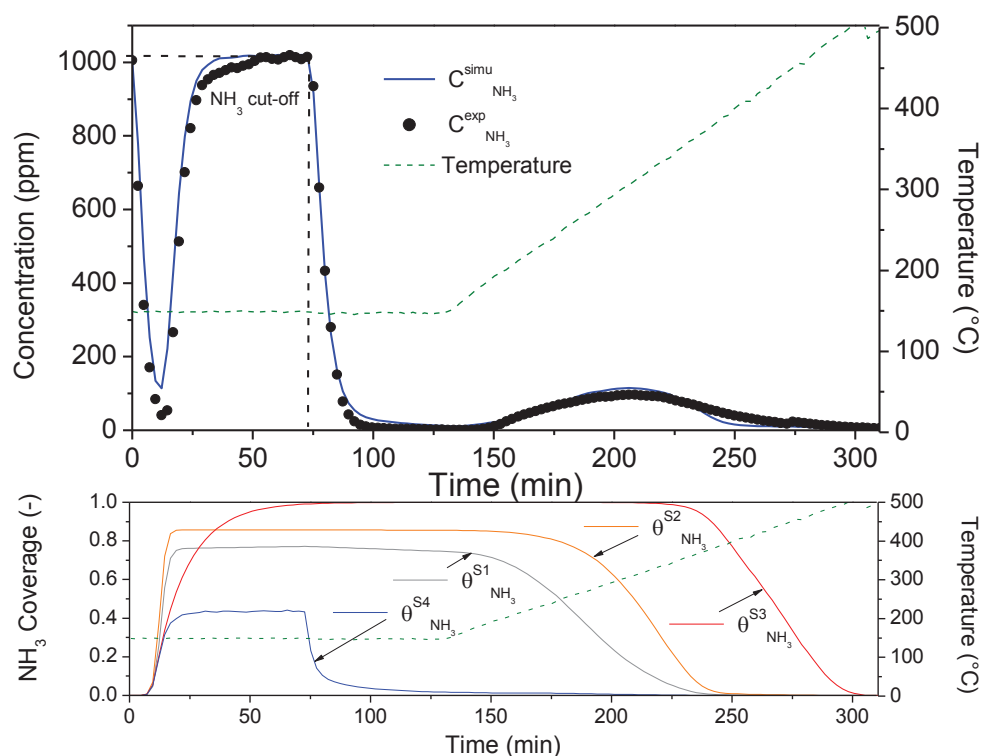


Figure VI-40. Ammonia adsorption and TPD experiments with the corresponding simulated profiles and coverage evolution in time respectively Cu-SAPO-34-IMP. Inlet gas composition: *adsorption of 1000 ppm NH<sub>3</sub>; 80000 ppm (8%) O<sub>2</sub>; 40000 ppm (4%) H<sub>2</sub>O and He as a balance at 150°C with a total Flow of 2.4 L/h*

However, as displayed by the NH<sub>3</sub> oxidation experiment Figure VI-41, the model overestimates the oxidation R6 of ammonia in N<sub>2</sub> readily after 250°C. Indeed, the oxidation step was previously characterized as particularly impacting the STD SCR performance at low temperature of Cu-SAPO-34-IMP, a characteristic which the model tends to represent through the oxidation of adsorbed NH<sub>3</sub> in NO on surface site S4 ( $Ea_{r8}^{S4} < Ea_{r8}^{S5} < Ea_{r8}^{S3}$ ) better than a direct reduction in N<sub>2</sub> ( $Ea_{r8}^{S4} < Ea_{r9}^{S4}$ ). A NO production which is consequently reduced in N<sub>2</sub> on S3 sites as observed through the overestimated N<sub>2</sub> concentrations.

Indeed, the main parameter variations come from the micro cluster S5, Figure VI-39, where the more important activation energy variations concerned the OH and ONO intermediaries formation on S5 ( $Ea_{r7}$  and  $Ea_{r12}$ ), the STD SCR ( $Ea_{r7}$ ) and Fast SCR ( $Ea_{r11}$ ) reactions. By the consequent Ea increases on S5, the model preferentially tends to promote the S3 and S4 expression through the SCR process, in accordance with the initially observed selectivity of exchanged cations and nano-sized sites compared to micro-clusters. Interestingly, the parametrization process tends also to maintain in some extent the S3 and S4 behavior on Cu-SAPO-34-IMP, regarding the lower parameter variations.

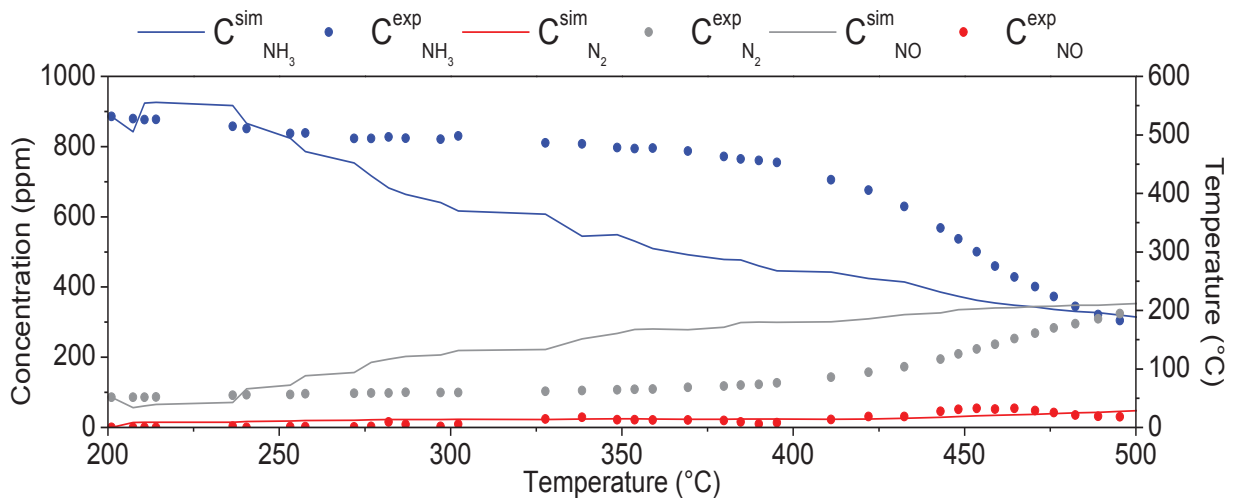


Figure VI-41.  $\text{NH}_3$  oxidation experiments in transient conditions with slow ( $2^\circ\text{C}\cdot\text{min}^{-1}$ ) temperature input modification ramp between  $200^\circ\text{C}$ - $500^\circ\text{C}$  decreasing ramp. Inlet gas composition: adsorption of  $1000 \text{ ppm NH}_3$ ,  $80000 \text{ ppm (8\%)} \text{ O}_2$ ;  $40000 \text{ ppm (4\%)} \text{ H}_2\text{O}$  and He as a balance between  $200^\circ\text{C}$  and  $500^\circ\text{C}$  with a total Flow of  $10 \text{ L}\cdot\text{h}^{-1}$

Finally, STD SCR test performance was simulated Figure VI-42. In accordance with above simulation, the model manages to depict the important oxidation process of  $\text{NH}_3$  in  $\text{N}_2$ , modeled by a strong NO formation. However, as the reaction R5 is overestimated, it requires to consume the produced NO through reduction (R4) on S3 and S4 mainly, which is depicted through their low coverages at  $200^\circ\text{C}$  Figure VI-42. Due to this low temperature compensation, the NO consumption through  $\text{NH}_3$  SCR cannot be increased with the temperature as  $\text{NH}_3$  is readily oxidized. Even if the global profile evolution is maintained for NO,  $\text{NH}_3$  and  $\text{N}_2$  concentrations until  $500^\circ\text{C}$ , the stable reaction regime occurring between  $250^\circ\text{C}$  and  $325^\circ\text{C}$  is only slightly represented by the model. Finally, the  $\text{NO}_2$  concentration was adequately represented by the model regarding the barely detected  $\text{NO}_2$  during the experience.

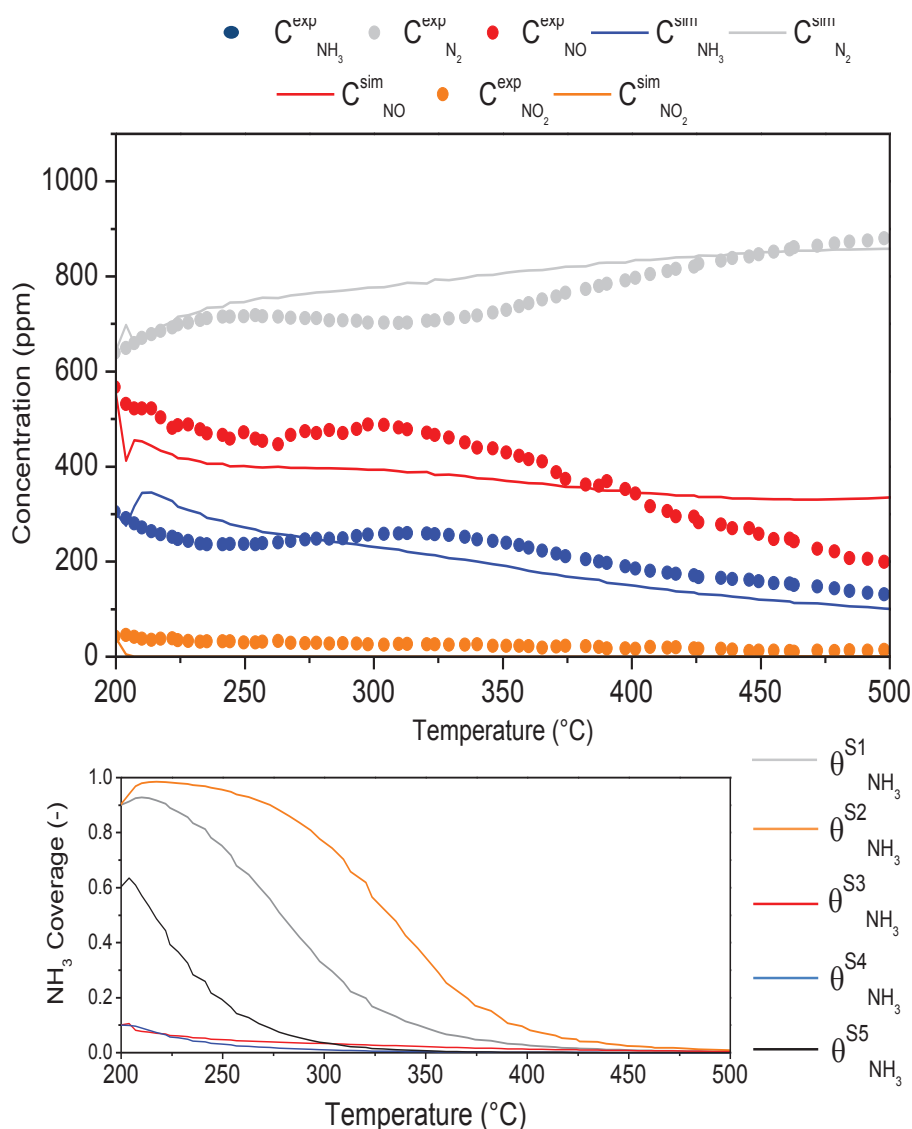


Figure VI-42. Experimental and simulated Standard SCR performances of Cu-SAPO-34-IMP catalyst with water accompanied by corresponding simulated  $NH_3$  coverage ratios during slow temperature ramp increase (200°C-500°C). Inlet gas composition: 1000 ppm  $NH_3$  and NO; 80000 ppm (8%)  $O_2$ ; 40000 ppm (4%)  $H_2O$  and He as a balance between 200°C and 500°C ( $2^\circ C \cdot min^{-1}$ ) with a total Flow of  $10 L \cdot h^{-1}$

In order to conclude on the model representation of the last catalyst, it was interesting to investigate in which direction the model tend to evolve certain kinetic parameters compared to others, indicating the principal active centers and the less important ones. It was observed that the performance representation from previously estimated parameters belonging to defined sites, is not directly possible on a different catalyst, which the active sites, even sharing similar configurations, have intrinsically different kinetic parameters. However, the shifts between estimated parameters will depend on the site activities and performances in the process, where the variations were more important for less selective micro copper clusters (S5) than for exchanged cations (S3) and nano surface clusters (S4). Therefore, the modified kinetic parameters define new active sites, slightly different by nature, from the ones characterized for Cu-SAPO-34-IE, compared to the one of Cu-SAPO-34-HT.

## VI-11. Catalysts differences observed through the model

### VI-11.1. Simulated sites densities comparison: Cu-SAPO-3-IE, -HT and -IMP

In order to resume the storage capacities differences between the parent support and the 3 investigated catalysts displaying different active sites configurations, their respective estimated sites densities were compared Figure VI-43.

As previously described, the thermodynamic parameters relevant to the H-SAPO-34 support were estimated in a first step, where the total site densities of Brønsted acid sites and their respective proportion through the support allowed to accurately represent the performed NH<sub>3</sub> TPD experiment on the support. The obtained Brønsted acid site density ( $\Omega_{\text{Brønsted}}$ ) was then assumed to be the maximal possible capacity for the following catalysts, which the redox sites densities finally modulate. Indeed, as observed on the Figure VI-43, compared to the support alone, the respective densities of S1 and S2 decreased with the incorporation of redox sites. More particularly, the incorporation of exchanged cations, as for Cu-SAPO-34-IE and -IMP, accordingly decreased the density of strong Brønsted acid sites and consequently formed weak Brønsted acid sites [285,370]. The decreased strong Brønsted acid sites is also visible for the one pot catalyst, also displaying a similar weak site (S1) density with the support, a profile tendency clearly evidenced between both support and -HT catalyst Figure VI-30, which the close desorbed quantity at low temperature enlighten. Concerning Cu-SAPO-34-IMP, different active site configurations are therefore present, which the exchanged sites and surface clusters strongly decrease the S2 density. Accordingly, the redox sites densities are representative of these Brønsted sites variations between catalysts, where Cu-SAPO-34-IE displays an important density of surface sites nano clusters (S4) compared to S3, and Cu-SAPO-34-HT a unique density of micro cluster (S5) as defined in the model.

Moreover, the estimated redox site density for -IE catalyst is coherent with the one measured through ICP. Indeed, one of the model assumptions was to consider that only one molecule can be adsorbed at a time on each site, which is typically the case for the adsorption on Brønsted acid sites in NH<sub>4</sub><sup>+</sup> form on hydroxyl, but different for redox sites (prior to any solvation process). It was characterized in previous studies [157,465] that until 4 NH<sub>3</sub> molecules can be adsorbed on a same copper sites, for the most active species ( $Z_2 [\text{Cu}^{\text{II}}(\text{NH}_3)_4]$ ). In that respect, the total density of redox sites for Cu-SAPO-34-IE were estimated to be four times higher ( $\Omega_{\text{S3}} + \Omega_{\text{S4}} = 400 \text{ mol.m}^{-3}$ ) than the one obtained through ICP measurements ( $\Omega^{\text{ICP}} = 100 \text{ mol.m}^{-3}$ ). Assuming that both S3 and S4 display the same capacity. Due to the consideration of one adsorption site per adsorbed molecule, the direct comparison between Brønsted and redox site densities is not representative and was therefore not made here. However concerning Cu-SAPO-34-HT, a lower ratio of two was calculated between  $\Omega_{\text{S5}}$  and  $\Omega^{\text{ICP}}$  copper site density, representing the weaker adsorption capacity on these sites.

These densities comparison between samples allow to display the model coherence with the characterized active site configurations, knowing that these thermodynamic parameters were obtained

under the constraint of different operating conditions, without which different set of parameters could be suitable for the NH<sub>3</sub> TPD profile simulations.

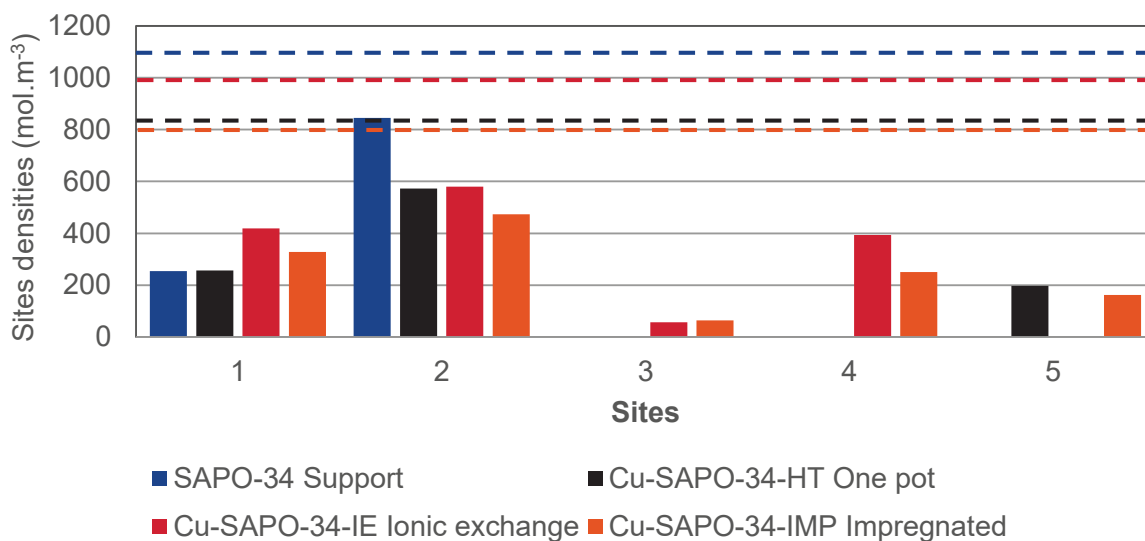


Figure VI-43. Bar chart representing the estimated site densities for redox and Brønsted acid sites defined in the model for H-SAPO-34 support, Cu-SAPO-34-IE, HT and IMP catalysts. The dotted line representing the total Brønsted acid sites densities of each samples.

#### VI-11.2. Estimated kinetic parameters comparison: Ionically exchanged and One pot Catalysts

The two first radar charts displayed Figure VI-44 and 45 represent the kinetic parameters relative to the adsorption reaction of NH<sub>3</sub> and H<sub>2</sub>O and the corresponding activation energies of desorption reaction respectively, on each site. Thanks to the logarithm scale on the first figure, the non-activated adsorption steps of NH<sub>3</sub> and H<sub>2</sub>O can be compared, where the ammonia adsorption display far more elevated reaction constants. An adsorption competition observed through the different coverage evolution and characteristic times. These elevated adsorption constants therefore depict the important affinity of NH<sub>3</sub> molecules with the solid surface. On the other hand, between sites themselves, if the water adsorption is displayed faster on redox sites than on Brønsted acid sites, the adsorption constant of water and ammonia on the different copper sites remain similar. It will be through the investigation of their respective activation energies that the sites strength can be monitored.

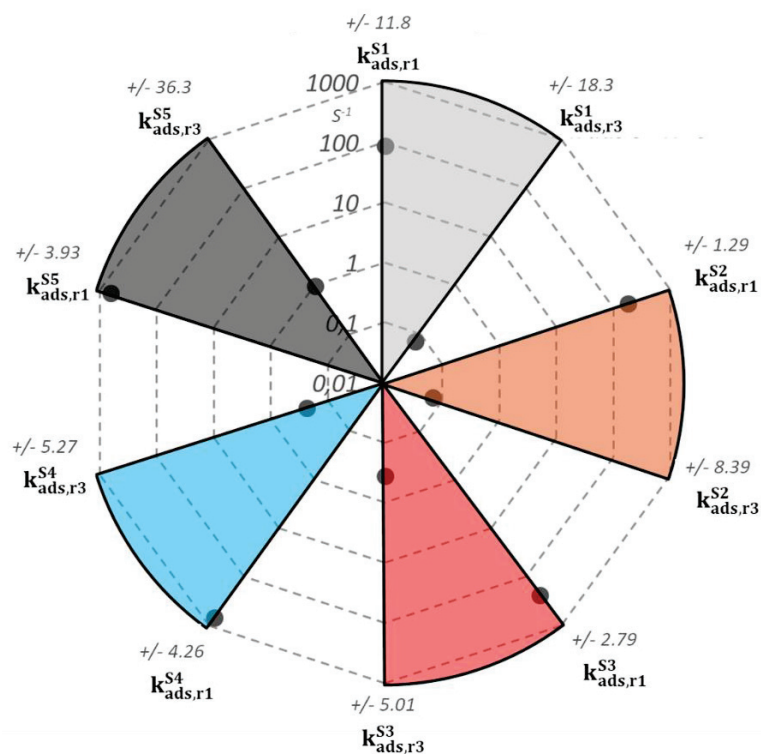


Figure VI-44. Radar chart representing the  $\text{NH}_3$  ( $r_1$ ) and  $\text{H}_2\text{O}$  ( $r_3$ ) non-activated adsorption constants for S1, S2, S3, S4 and S5 sites

In that respect the second Figure VI-45 displays the corresponding activation energies of desorption reaction from R1 and R2 on each site. Firstly, the model represents the following  $E_a$  order concerning the desorption reaction of  $\text{NH}_3$  :  $E_{a_{r_2}^{S4}} < E_{a_{r_2}^{S5}} < E_{a_{r_2}^{S3}}$ , demonstrating the different strength capacities of the different copper configurations. Note that the model also informs about a similar sites strength between strong Brønsted acid sites S2 and micro surface cluster S5 as the respective activation energies are similar ( $E_{a_{r_2}^{S5}} = 81 \text{ kJ.mol}^{-1}$  and  $E_{a_{r_2}^{S2}} = 89 \text{ kJ.mol}^{-1}$ ). An observation in accordance with the desorption profiles similarities between Cu-SAPO-34-HT and H-SAPO-34, where the micro cluster directly replaced a consequent proportion of strong Brønsted acid sites. Finally concerning  $\text{H}_2\text{O}$  desorption activation energy, the model adequately depicts the S2 Brønsted sites as the most stable position for adsorbed  $\text{H}_2\text{O}$ .



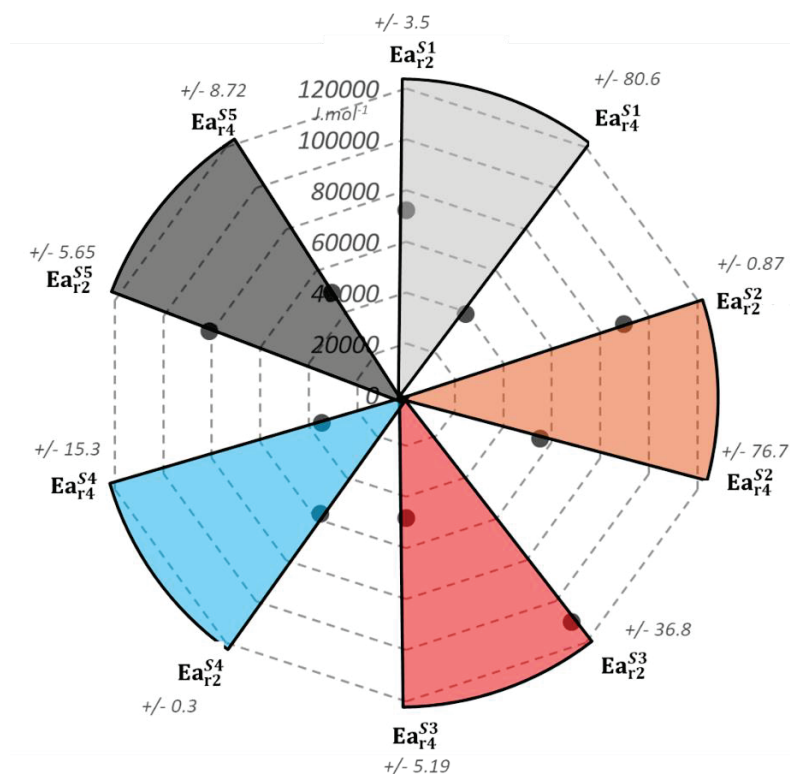


Figure VI-45. Radar chart representing the  $\text{NH}_3$  ( $r_2$ ) and  $\text{H}_2\text{O}$  ( $r_4$ ) desorption activation energies for S1, S2, S3, S4 and S5 sites

On the other hand, the respective activation energies of STD SCR, dry SCR,  $\text{NH}_3$  oxidation in NO and FAST SCR for each redox site are displayed on Figure VI-46. Thanks to this representation, the different kinetic parameters can be promptly compared following the copper sites configuration. For instance, activation energies relative to STD SCR reactions (R4 and R12) are adequately estimated lower on exchanged cation S3 than on S4 and S5 regarding the site activities. Similarly, the energy required to perform  $\text{NH}_3$  oxidation in NO is the lowest on S4, following the order:  $Ea_{r8}^{S4} < Ea_{r8}^{S3}$  and  $Ea_{r8}^{S4} < Ea_{r8}^{S5}$  in accordance with the oxidation capacity of copper sites. Nano cluster (S4) oxidizing  $\text{NH}_3$  at lower temperature than micro surface clusters (S5) a previously investigated characteristic. However, if S3 and S5 display similar capacities to perform Fast SCR reaction in temperature, S4 will require less energies to perform the reaction, a difference with exchanged cations which is less expected for nano-surface sites.

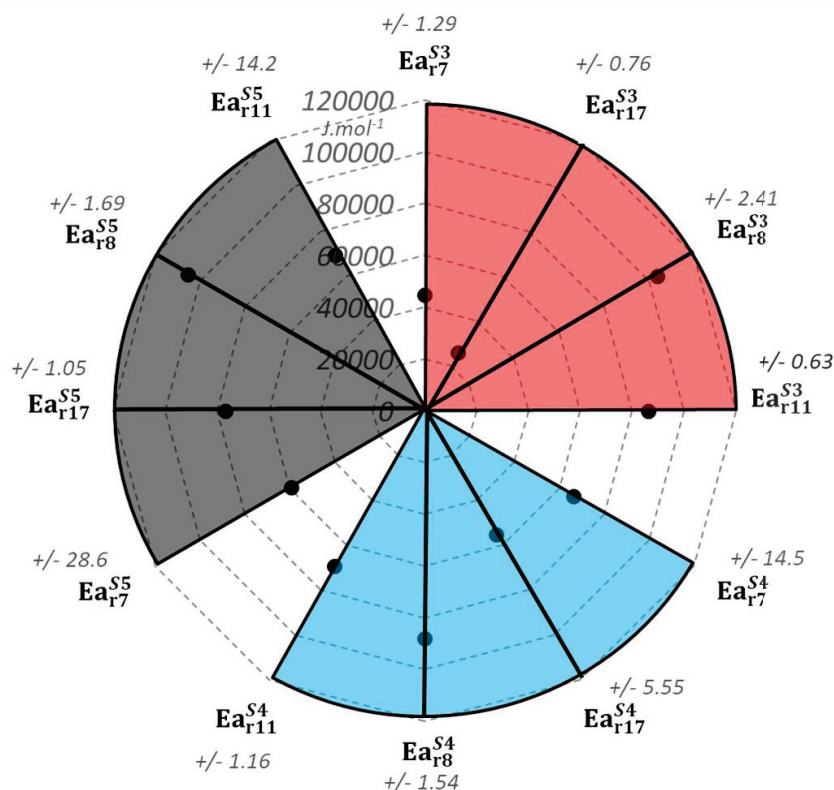


Figure VI-46. Radar chart representing the respective activation energies of wet STD SCR ( $r_7$ ), dry STD SCR ( $r_{17}$ ),  $\text{NH}_3$  oxidation in NO ( $r_8$ ) and FAST SCR ( $r_{11}$ ) for S3, S4 and S5 redox sites.

Finally, the last Figure VI-46 represents the  $E_a$  estimated for the reactions concerning the intermediary species, gathered by reactions, for each sites, with OH formation and decomposition (R3), ONO formation through NO interaction with the surface (R9) and through the  $\text{NO}_2$  decomposition (R10). Thus for R3, the surface sites S4 and S5 are observed to required less energies to form hydroxyl species than the exchanged one S3, which could be linked to the ease of  $\text{H}_2\text{O}$  interaction, therefore in excess in the flowing mixture, with surface site better than for active sites within the lattice.

Concerning R9, the low activation energies of ONO formation on each site, where the lowest value is estimated for S3, indicate the ease of nitrite formation on the redox site. On the other hand, their consequent low stabilities are displayed through the similarities between  $E_{a_{r12}}$  and  $E_{a_{r13}}$  values. Nitrites species which the model depicts as more easily formed on exchanged cations and micro surface cluster than the nano sized ones. A coherent  $E_a$  estimation, where the NO interaction with the exchanged sites and micro clusters were particularly monitored at low temperature during in-situ NO DRIFT measurements (See Chapter IV Figure IV-10), where NO easily interact with S5 during NO adsorption process on Cu-SAPO-34-HT. Therefore, the estimated  $E_{a_{r13}}^{S3} < E_{a_{r13}}^{S5}$  typically represent the better stability of surface nitrites species on copper micro clusters than on S3, in accordance with the observed NO desorption behavior from 35°C to 100°C and 500°C during dedicated DRIFT investigations (Se Figure IV-11).

Finally, the model inform also that the redox sites display similar activation energies for the formation of NO<sub>2</sub> from nitrites decomposition, but their capacities to interact with gaseous NO<sub>2</sub> to form ONO key intermediaries are spotted different. Indeed, the following order  $Ea_{r15}^{S3} < Ea_{r15}^{S4} < Ea_{r15}^{S5}$  depicts that NO<sub>2</sub> molecules seem more easily converted in nitrites species on exchanged cations than on surface sites S4 and S5, an important characteristic of these sites for elevated temperature performances and enlighten the importance of considering the NO<sub>2</sub> impact within the SCR process in STD conditions.

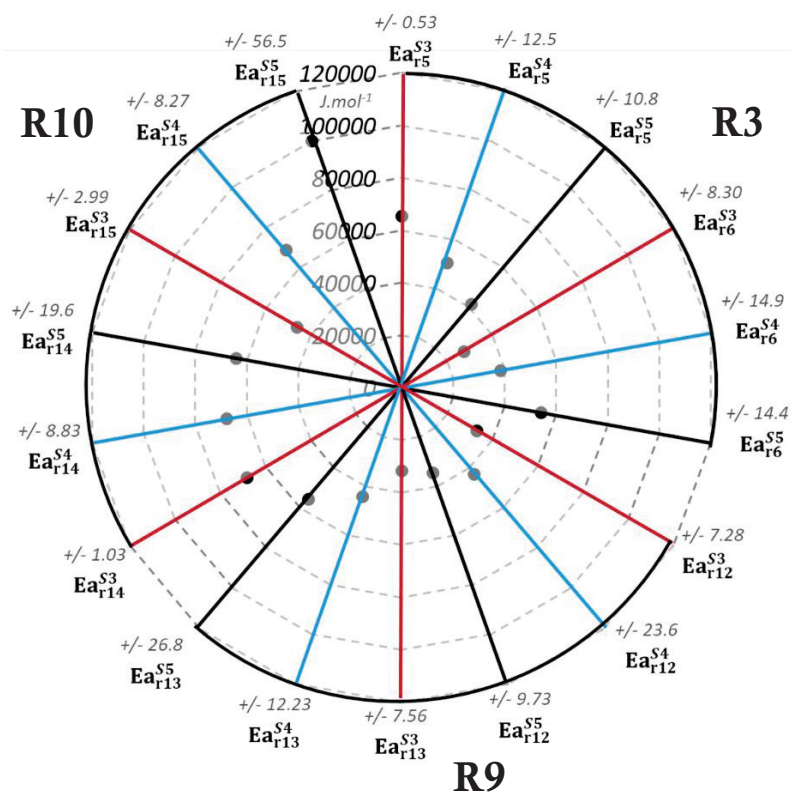


Figure VI-47. Radar chart representing the respective activation energies of intermediaries formation and decomposition (R3, R9, R10) on S3, S4 and S5 redox sites

### **VI-12. Conclusion: Part 2: Model Extension to different catalysts**

The kinetic model was consequently modified to take into consideration different active sites configurations, previously characterized during Chapter III and IV. Firstly, the surface site definition was adjusted to Cu-SAPO-34-HT, representing one main active site configuration for the NH<sub>3</sub>SCR process in addition to the Brønsted acid sites. Through the parallel estimation of several operating conditions, the set of estimated kinetic parameters allowed an accurate representation of the catalyst performance on the overall investigated temperature range. However, the model deviation from the experimental test in STD SCR condition and more precisely in presence of water, revealed the participation at elevated temperature of the migrated cations in exchanged positions, previously characterised. An active site proportion which was not initially implemented within the model and which the participation was correlated by model deviation. Moreover, the simulated behaviour was in accordance with the impact of water on the catalyst, evidencing the increasing proportion of migrated copper cations thanks to a better species mobility.

Once all the kinetic parameters gathered, it was assumed in a first attempt that the impregnated catalyst Cu-SAPO-34-IMP could be represented by the three different redox sites with exchanged cations (S3), nano-sized (S4) and micro-sized copper clusters (S5) as characterized during previous Chapter III. Nevertheless, if a direct simulation is not sufficiently accurate for representing the performance behavior of such a catalyst, the complete reparametrization brought further information. Indeed, the model deviated from a 3 redox site configuration to a re-adjusted two sites system mainly, in addition to Brønsted acid sites, in accordance with the selectivity of exchanged sites characterized within Cu-SAPO-34-IMP. Despite an overestimation of the NH<sub>3</sub> oxidation reaction, the model describes this operation through surface site, which is also compatible with the surface sites impact on STD SCR depicted earlier.

Finally, the estimated kinetic parameters were compared between the different site configurations from the point of view of their respective role within the SCR process. In that respect, the model coherence was investigated through the active site density description for each catalyst and the activation energies of the main reactions respectively corresponding to the active sites. The different activation energies were corroborated with the characterized behavior of the catalysts performed during previous Chapters. Respecting the experimental behavior on Cu-SAPO-34-IE and -HT catalysts, the model gave further insights concerning the impact of water and nitrites in the system and their indispensable consideration through the SCR mechanism.

# CONCLUSIONS & PERSPECTIVES

Within the most stringent challenges that the worldwide population have to stem this 21<sup>st</sup> century, the atmospheric depollution represents one's of the most colossal problematic due to its global hazard, as well on Human health as on global warming [484]. And among the pollutant emission sources, more precisely concerning the anthropogenic one's, the most important share, the mobile (light and heavy duty vehicles, ship, cargo...) and stationary sources (plant, manufacturer...) have to be urgently regulated for a near zero emission objective. This topic directly inscribed within the 2020 European "climate & energy package" [485], lead the pollutant emission regulations evolution, deploying more stringent standard as the years goes by [486]. For such requirements, different innovation technologies have been developed which one of them, the ammonia Selective Catalytic Reduction (NH<sub>3</sub>-SCR), is currently worldwide employed for its recognized nitrogen oxides (NO<sub>x</sub>) abatement efficiency, ones of the main greenhouse gas protagonists, within the exhaust line of the mobile and stationary sources employing lean burn conditions.

The technology lies on the ammonia generation made through urea hydrolysis in catalyst upper stream and its application as reductant for NO<sub>x</sub> conversion in heterogeneous catalysis on metal active sites. Among the developed catalysts for NH<sub>3</sub> SCR technology, recent metal-exchanged micropores zeolites as CHA (Chabazite) material supporting transition metal (iron (Fe) and/or copper (Cu)) further gain in interests regarding their high hydrothermal stability and SCR performances. However, different challenges still occur, from its synthesis to its catalytic behavior understandings, for its total control [333]. Thus, in order to participate to this development, the scope of the present work typically follows the R&D process of a new technologies generation, from the product synthesis to its application and kinetic modeling. Indeed, physico-chemical robust and accurate predictive models become valuable for reducing time and cost development of new catalysts but also to control NO<sub>x</sub> emission for embedded SCR sensor for instance.

## **Experimental study**

Prior to the model establishment for the behavior description of different catalysts, specific points are required. The first one was to determine a catalyst reference, which the model will be based on. For that purpose, the zeolitic support was primarily synthesized, by verifying through several characterization techniques as ICP, TGA, XRD, N<sub>2</sub>-adsorption/desorption, MAS NMR, H<sub>2</sub>-TPR and Ex-situ DRIFTS, that the SAPO-34 crystalline phase was obtained, deprived of major structural defects preventing the structure instability, an important specific surface area typical of CHA zeolite and a defined building unit configuration typically composed of tetrahedral Si(OAl)<sub>4</sub> and P(OAl)<sub>4</sub>. This investigation was performed by comparison with a commercially available H-SAPO-34 support, which the characterization revealed the initial presence of Si-island within the structure and important concentration of impurities as iron, undesirable attributes for mechanism study purposes and catalyst hydrothermal stability. A first approach of support functionalization was conducted with a conventional impregnation protocol on both support,

revealing the method reproducibility for incorporating several configurations of redox active sites as monomeric cations and surface clusters of different dimensions. An uncontrolled mix of active sites which the impregnation protocol promotes the formation of Si-islands through the support as it was characterized before and after the method on the pre-made catalyst. In that respect, the different active site configurations were also observed through the catalyst performances, where at low temperature (200-350°C) a strong oxidation of NH<sub>3</sub> in N<sub>2</sub> and NO was related to the participation of packed cations and surface clusters sites.

After a first acquisition of kinetic data relative to catalyst displaying various active sites, the active site configuration impacts on the catalyst behavior were further investigated through the comparison of an ionically exchanged and one pot catalysts. Such crucial information for the model construction in a multi-sites kinetic model approach. The first one displaying two main redox site configurations with cations inserted within the zeolite lattice near the 6MR and 8MR cages, and nano-sized surface sites principally. The second one, synthesized in a single step allowing to deprive the catalyst of exchanged cations, was characterized to be composed of redox sites situated at the top surface in a micro-size form. The main common point between these catalysts was their similar support composition displaying weak and strong Brønsted acid sites as the H-SAPO-34 was synthesized for comparable purposes. The synthesis methods were verified to not damage the structure by Si-island formation compared to impregnation protocol. In addition to previously cited characterization techniques, TEM, NH<sub>3</sub>TPD combined with in-situ DIRFTS experiments with several probe molecules as NH<sub>3</sub>, CO and NO allowed the deep active site configurations investigation relatively with their respective impact in NH<sub>3</sub> SCR process. Therefore, even with a consequent NH<sub>3</sub> oxidation above 350°C, the low temperature activity displayed by the ionically exchanged catalyst (>60%) and maintained through the temperature window (200°C-500°C) through the exchanged cations expression was representative of state of the art Cu-CHA catalyst for NH<sub>3</sub> SCR application. Comparatively, the progressive mechanism of NO<sub>x</sub> abatement in temperature occurring on the one pot catalyst was identified through different processes, where the desorbed NH<sub>3</sub> monitored by in-situ DRIFT analysis and NH<sub>3</sub> TPD reached the activated micro copper surface sites. With a slight copper cations migration near the 8MR lattice positions in temperature (observed with CO-DRIFT), the STD SCR activity was promoted, while the parasitic NH<sub>3</sub> oxidation was hindered due to the low proportion of these monomer sites. In that respect, this particular active site configuration was responsible of an important conversion of NO<sub>x</sub> at elevated temperature, higher than the one displayed by the reference catalyst within the 350-450°C temperature range.

Finally, the second main required information for the model construction was the determination of a representative reactional mechanism of the catalysts. For that purpose, a kinetic study was performed with the reference catalyst, which the experimentally measured kinetic parameters, comparable to literature studies, were employed as initial values in the kinetic model. The impact of water, inlet compositions, gas phase reactions, NH<sub>3</sub> inhibition effect as well as catalyst stability were investigated in order to propose an optimized reactional network taking into account the previously observed phenomenon. In addition, the

NO<sub>2</sub> and nitrite intermediary impacts were monitored during sequenced in-situ DRIFT STD SCR measurements. By the step adsorption of NH<sub>3</sub> on catalyst surface sites and consequent injection of NO in presence of oxygen, the depletion of stored ammonia on both, Brønsted and redox, type of sites demonstrated the NH<sub>3</sub> migration during the process and this until high temperature (500°C). At low temperature it was also observed adsorbed nitrites and nitrates species, proper to the key subsidiary step of NH<sub>3</sub> SCR process.

### **Kinetic model**

Once the active sites configurations of the different catalysts characterized and related to the respective catalytic behavior, and the set of reactional network defined, the kinetic model construction then begun. In that respect, the hydrodynamic behavior of the catalytic bench was therefore investigated prior to the kinetic parameter estimation in order to not impaired the kinetic simulations with hydrodynamic features. It was verified that the gas cell chamber of FTIR analyzer represents an important true dispersive volume, making the hydrodynamic of the overall bench evolving as 1 CSTR. After the definition of the required assumption for the model establishment, the kinetic model was defined by the support and catalysts surface definition, where the reference catalyst was assumed to be represented by exchanged cations (S3) and nano-surface sites (S4) in addition to the weak and strong Brønsted acid sites (S1, S2) brought by the support. The kinetic model was also defined following the proposed mechanistic reactional network, displaying a total of 12 reactions, where the adsorption competition between NH<sub>3</sub> and H<sub>2</sub>O, the low temperature water promoting effect on STD SCR reactions, the NO and NO<sub>2</sub> interaction with the catalyst surface forming the nitrite pathway, the FAST SCR and the gas phase impacts were represented. Prior to the chemical reactions, the kinetic parameters relative to Brønsted acid sites were firstly estimated thanks to the raw support, and injected as locked and reference values for the child catalyst ionically exchanged. A two steps process allowing a more robust parametrization concerning the adsorption and desorption dynamic regime of reactive species on distinct active sites. The overall catalyst behavior was finally further validated through an isothermal experiment at low temperature for further observation of the catalyst behavior within the temperature range.

Following the construction and validation of the model accuracy, further information was obtained thanks to the model representation of the reference catalyst. Employed as a reference reaction, the STD SCR was observed through the different relevant characteristic times, with the one respective to the reactions setup and the one to the mass transfer resistance occurring within the defined system. In that respect, the adsorption and desorption process as well as the OH intermediaries formation and decomposition were observed as potential rate limiting steps during the STD SCR process for the investigated operation conditions. The external and internal mass transfer limitations ruled out as first assumptions were also verified here by the several magnitude order gap between the fastest reaction and the characteristic time related to the mass transfer. It was only once reached the highest temperature that

the limitation could competes with some part of the reactional system as the nitrite formation and decomposition, less impacting the simulation consistency knowing the low stability of the species. The different parameter correlations during a typical STD SCR test as well as the final parameter uncertainties were investigated, emphasizing the model consistency and the reaction correlation between subsidiaries reactional steps as with the H<sub>2</sub>O adsorption and the consequent OH formation on the redox site the less active.

Then, the second part of the study consisted in the model extension for the impregnated and one pot catalysts. After the redefinition of the surface sites, the kinetic parameters of the one pot catalyst represented by S1,S2 and S3 with the latter as unique redox site, were estimated in similar conditions as the one applied for the reference catalyst. The model accurately described the NH<sub>3</sub> TPD profiles, NH<sub>3</sub> and NO oxidation behavior and STD SCR process in dry conditions. In presence of water, the model deviation from the experimental NH<sub>3</sub> and NO profiles represented the impact of migrated cations within the lattice as previously characterized during in-situ DRIFTS experiments. It was suspected that the water enhanced the copper site migration compared with the dry CO DRIFT experiment, better promoting the high temperature STD SCR performance of the catalyst. Once the kinetic parameters for the 5 sites gathered from H-SAPO-34 support, Cu-SAPO-34-IE and -HT catalyst, the parameters were used as initial values during the reparametrization step of Cu-SAPO-34-IMP, assumed to be composed of the 5 defined sites. If their direct utilization for simulation purpose was not valid, the parameter evolutions inform about the importance of exchanged sites for the catalytic behavior of this catalyst while micro-surface sites were completely redefined as the parameter were strongly different from the initial values. The surface sites were described by the model as weak sites of adsorption for NH<sub>3</sub> while the parameters relative to the exchanged one were mainly conserved. The strong oxidation at low temperature was therefore overestimated regarding the impact of the surface sites modified by the model, an oxidation step which interferes with the NO<sub>x</sub> reduction at elevated temperature regarding the NH<sub>3</sub> depletion on active sites.

Consequently, the estimated parameters relative to the different sites densities and to main reactions were compared following the sites definition for verifying the model coherence with the experimental investigations conducted on the active sites, respecting the important NH<sub>3</sub> SCR activity from exchanged cations, from the intermediary formation of OH and ONO species on S3 to the NH<sub>3</sub> oxidation promotion performed by surface sites as S4 and in a lesser extent S5. The respective sites strengths were also studied regarding the estimated kinetic parameters and compared between them, indicating the important storage role of each species and the needs to dissociate Brønsted acid site from redox copper active species for the catalyst behavior investigation.



## Perspectives

As a model is only one possible and biased representation of the reality, delimited by defined hypothesis, it is important to employ the simulation as a strong and complementary tool to the development of a new catalyst. Indeed, as the complex  $\text{NH}_3$ -SCR mechanism still presents numerous uncertainties, the deployment of kinetic models can be conducted with a certain liberty, explicating the number of various models retrieve in literature. However, the development of enhanced time resolved as XANES or DRIFT techniques and the decreasing constraint for DFT calculations tends to give definitive explanation of the different step occurring in the system, giving better direction for an accurate, consistent and robust catalytic model representation. From a diffusional point of view, which represent another delicate topic intrinsic to microporous structure, additional information and breakthrough are still required for a full implementation in a model representation. Where the behavior of the mobile species within a structure itself in motion, dependent of applied temperature and pressure represent an equally important dimension to implement as detail reactional mechanism.

Therefore, aside from the compromise between computational time and complexity, it would be greatly interesting to define the surface sites as a functional distribution, where statistical estimations, developed under specific assumptions, could allow the study of different active sites fraction through the whole sample and the spatial discretization of their distribution. In addition, the energy balance could also be plugged in for better accuracy following the operating conditions. With the definition of a more detailed reactional system and the behavior investigation of other type of active sites as with iron and other potential future promoters. In that way, starting from their respective parameters, as conducted with the impregnated catalyst, bi-metallic catalyst (as Cu/Fe CHA for instance) activities would be dissected. Moreover, the model could be enhanced with the consideration of  $\text{NO}_2$  as an initial reactant for operating conditions with a  $\text{NO}_2/\text{NO}_x$  ratio, and representing both mechanism of nitrates and  $\text{N}_2\text{O}$  formation.

# REFERENCES

- [1] M. Brundtland, Gro Harlem; Khalid, Our common future, 1987.
- [2] G. Alain, L'Épuisement Des Métaux Et Minéraux : Faut-Il S'Inquiéter ?, 2017. <https://www.ademe.fr/sites/default/files/assets/documents/epuisement-metaux-mineraux-fiche-technique.pdf>.
- [3] Organisation de coopération et de développement Économiques, Le principe Pollueur Payeur: Analyses et recommandations de l'OCDE, Paris, 1992.
- [4] D.H. Meadows, The Limits to growth; a report for the Club of Rome's project on the predicament of mankind, New York : Universe Books, [1972], New York, NY, 1972. <https://search.library.wisc.edu/catalog/999473210902121>.
- [5] Y. Mathieu, Un point sur les ressources en hydrocarbures, Panor. 2010. (2009).
- [6] ADEME, Un air sain chez soi, 2015.
- [7] L.M.V. Nedellec, Hierarchisation sanitaire des paramètres mesurés dans les bâtiments, PAR L'OBSERVATOIRE LA Qual. L'AIR Inter. (2002) 1–98.
- [8] M. Derbez, C. Mandin, J.-P. Lucas, O. Ramalho, J. Ribéron, S. Kirchner, Base de référence sur la qualité de l'air intérieur et le confort des bâtiments performants en énergie – Présentation du protocole OQAI-BPE, (2015) 56. [http://www.oqai.fr/userdata/documents/426\\_OQAI\\_BPE\\_Presentation\\_protocoleV4.pdf](http://www.oqai.fr/userdata/documents/426_OQAI_BPE_Presentation_protocoleV4.pdf).
- [9] B. D., Norback E., Björnsson C., Janson J., Widstrom G., Asthmatic symptoms and volatile organic compounds, formaldehyde, and carbon dioxide in dwellings, *Occup. Environ. Med.* 52 (1995) 388–395. <http://ovidsp.ovid.com/ovidweb.cgi?T=JS&PAGE=reference&D=emed3&NEWS=N&AN=1995181268>.
- [10] B.G. Wieslander G, Norbäck D, Björnsson E, Janson C, Asthma and the indoor environment: the significance of emission of formaldehyde and volatile organic compounds from newly painted indoor surfaces., *Int Arch Occup Env. Heal.* 69 (1997) 115.
- [11] J.B.J. Fourier, Remarques générales sur les températures du globe terrestre et des espaces planétaires, *Ann. Chim. Phys.* 27 (1824) 570–604.
- [12] J.B.J. Fourier, Œuvres de Fourier, Gauthier-V, Paris, 1890.
- [13] A.Cornu, Sur la limite ultra -violette du spectre solaire, *C.R. Acad. Sci. Paris.* (1879) 1101.
- [14] H. W.N., On the absorption spectrum of ozone, *J. Chem. Soc.* (1881) 57.
- [15] C. Joel Tarr; McShane, The Centrality of the Horse to the Nineteenth-Century American City, in: Mak. *Urban Am.*, Raymond Mo, SR Publishers, New York, NY, 1997: p. 105 130.
- [16] H. Ritchie, M. Roser, Urbanization, Our World Data. (2019). doi:and references within.
- [17] R.E. Train, Statements on proposed federal actions affecting the environment, *Fed. Regist.* 36 (1971) 7724.
- [18] Regional Office for Europe, Air quality guidelines for Europe. Copenhagen, WHO Regional Office for Europe, 1987 (WHO Regional Publications, European Series, No. 23)., WHO region, Copenhagen, 1987.
- [19] M. SCOTTO, La bataille des normes de pollution automobile va commencer à Luxembourg, *Le Monde.* (1985). [https://www.lemonde.fr/archives/article/1985/06/27/la-bataille-des-normes-de-pollution-automobile-va-commencer-a-luxembourg\\_2753868\\_1819218.html](https://www.lemonde.fr/archives/article/1985/06/27/la-bataille-des-normes-de-pollution-automobile-va-commencer-a-luxembourg_2753868_1819218.html).
- [20] U.S.E.P. Agency, Acide deposition Control, 1990. <https://www.epa.gov/airmarkets/title-iv-clean-air-act-acid-deposition-control>.
- [21] CITEPA, Dates marquantes dans l'histoire de la pollution atmosphérique, (2016). <https://www.citepa.org/fr/air-et-climat/histoire-de-la-pollution-de-l-air>.
- [22] V.D. Cyrille Bernagaud, Jean François Burkhart, Calcul des émissions de polluants des véhicules automobiles en tunnel, BRON, 2012. [http://www.cetu.developpement-durable.gouv.fr/IMG/pdf/CETU\\_DocInfo\\_Calcul\\_des\\_Emissions\\_2012.pdf](http://www.cetu.developpement-durable.gouv.fr/IMG/pdf/CETU_DocInfo_Calcul_des_Emissions_2012.pdf).

- [23] United Nations, Addendum Article 6: AGREEMENT CONCERNING THE ESTABLISHING OF GLOBAL TECHNICAL REGULATIONS FOR WHEELED VEHICLES, EQUIPMENT AND PARTS WHICH CAN BE FITTED AND/OR BE USED ON WHEELED VEHICLES, Geneva, 2007. <http://www.unece.org/fileadmin/DAM/trans/main/wp29/wp29wgs/wp29gen/wp29registry/ECE-TRANS-180a4e.pdf>.
- [24] E. PARLIAMENT, Type-approval of motor vehicles and engines with respect to emissions from heavy duty vehicles (Euro VI) and on access to vehicle repair and maintenance information, Off. J. Eur. Union. (2009).
- [25] W. Martin, M. Ray, A technical summary of Euro 6/VI vehicle emission standards, ICCT Brief. Pap. (2016) 1–17. [http://www.theicct.org/sites/default/files/publications/ICCT\\_Euro6-VI\\_briefing\\_jun2016.pdf](http://www.theicct.org/sites/default/files/publications/ICCT_Euro6-VI_briefing_jun2016.pdf).
- [26] M. Vojtisek-Lom, PORTABLE ON-BOARD MASS EMISSIONS MEASURING SYSTEM, US 6,308,130 B1, 2001.
- [27] H.C. Frey, A. Unal, N.M. Roupail, J.D. Colyar, On-road measurement of vehicle tailpipe emissions using a portable instrument, *J. Air Waste Manag. Assoc.* 53 (2003) 992–1002. doi:10.1080/10473289.2003.10466245.
- [28] S.C. Anenberg, J. Miller, R. Minjares, L. Du, D.K. Henze, F. Lacey, C.S. Malley, L. Emberson, V. Franco, Z. Klimont, C. Heyes, Impacts and mitigation of excess diesel-related NO<sub>x</sub> emissions in 11 major vehicle markets, *Nature*. 545 (2017) 467. <https://doi.org/10.1038/nature22086>.
- [29] R. Varella, B. Giechaskiel, L. Sousa, G. Duarte, Comparison of Portable Emissions Measurement Systems (PEMS) with Laboratory Grade Equipment, *Appl. Sci.* 8 (2018) 1633. doi:10.3390/app8091633.
- [30] S. OLSON, Accusé de tricherie Volkswagen est menacé de sanctions aux Etats-Unis, *Le Monde*2. (2015). [https://www.lemonde.fr/automobile/article/2015/09/20/accuse-de-tricherie-volkswagen-est-menace-de-sanctions-financieres-aux-etats-unis\\_4764397\\_1654940.html](https://www.lemonde.fr/automobile/article/2015/09/20/accuse-de-tricherie-volkswagen-est-menace-de-sanctions-financieres-aux-etats-unis_4764397_1654940.html).
- [31] European Commission, Antitrust: Commission sends Statement of Objections to BMW, Daimler and VW for restricting competition on emission cleaning technology, (2019). [http://europa.eu/rapid/press-release\\_IP-19-2008\\_en.htm](http://europa.eu/rapid/press-release_IP-19-2008_en.htm).
- [32] J.M. Ulises Hernandez, Methodological notes: Global vehicle sales database, Washington DC, 2015. <http://www.theicct.org/methodological-notes-global-vehicle-sales-database>.
- [33] U.L. Uwe Tietge, Nikiforos Zacharof, Peter Mock, Vicente Franco, John German, Anup Bandivadekar, Norbert Ligterink, FROM LABORATORY TO ROAD, 2015. [https://theicct.org/sites/default/files/publications/ICCT\\_LaboratoryToRoad\\_2015\\_Report\\_English.pdf](https://theicct.org/sites/default/files/publications/ICCT_LaboratoryToRoad_2015_Report_English.pdf).
- [34] ICCT, NO X emissions from heavy-duty and light-duty diesel vehicles in the EU: Comparison of real-world performance and current type-approval requirements, Report. (2016).
- [35] P. Bonnel, J. Kubelt, A. Provenza, Heavy-Duty Engines Conformity Testing Based on PEMS, 2011. doi:10.2788/56535.
- [36] A. Lawrence-Brown, Russia's Kamaz trucks support WFP operations in East and Central Africa, World Food Program. (2019). <https://www.wfp.org/news/russias-kamaz-trucks-support-wfp-operations-east-and-central-africa> (accessed August 11, 2019).
- [37] Fuels, TransportPolicy.Net. (n.d.). <https://www.transportpolicy.net/topic/fuels/> (accessed August 11, 2018).
- [38] Y. Cheng, C. Lambert, D.H. Kim, J.H. Kwak, S.J. Cho, C.H.F. Peden, The different impacts of SO<sub>2</sub> and SO<sub>3</sub> on Cu/zeolite SCR catalysts, *Catal. Today*. 151 (2010) 266–270. doi:10.1016/j.cattod.2010.01.013.
- [39] A. Williams, J. Burton, R.L. McCormick, T. Toops, A.A. Wereszczak, E.E. Fox, M.J. Lance, G. Cavataio, D. Dobson, J. Warner, R. Brezny, K. Nguyen, D.W. Brookshear, Impact of Fuel Metal Impurities on the Durability of a Light-Duty Diesel Aftertreatment System, *SAE Tech. Pap. Ser. 1* (2013). doi:10.4271/2013-01-0513.
- [40] D. Nicosia, I. Czekaj, O. Kröcher, Chemical deactivation of V<sub>2</sub>O<sub>5</sub>/WO<sub>3</sub>-TiO<sub>2</sub> SCR catalysts by additives and impurities from fuels, lubrication oils and urea solution: Part II. Characterization study of the effect of alkali and alkaline earth metals, *Appl. Catal. B Environ.* 77 (2008) 228–236. doi:<https://doi.org/10.1016/j.apcatb.2007.07.032>.

- [41] Secretary of State for Transport, Vehicle Emissions Testing Programme, :LOOLDPV/HD\*URXS, London, 2016. [https://assets.publishing.service.gov.uk/government/uploads/system/uploads/attachment\\_data/file/548148/vehicle-emissions-testing-programme-web.pdf](https://assets.publishing.service.gov.uk/government/uploads/system/uploads/attachment_data/file/548148/vehicle-emissions-testing-programme-web.pdf).
- [42] Bundesministerium für Verkehr und digitale Infrastruktur, Bericht der Untersuchungskommission „Volkswagen“, Berlin, 2016. [https://www.bmvi.de/SharedDocs/DE/Anlage/VerkehrUndMobilitaet/Strasse/bericht-untersuchungskommission-volkswagen.pdf?\\_\\_blob=publicationFile](https://www.bmvi.de/SharedDocs/DE/Anlage/VerkehrUndMobilitaet/Strasse/bericht-untersuchungskommission-volkswagen.pdf?__blob=publicationFile).
- [43] European Federation for Transport and Environment, Transport & Environment, Mind Gap 2015 - Closing Chasm between Test Real -World Car CO2 Emiss. (2015) 1–18. [http://www.transportenvironment.org/sites/te/files/publications/TE\\_Mind\\_the\\_Gap\\_2015\\_FINAL.pdf](http://www.transportenvironment.org/sites/te/files/publications/TE_Mind_the_Gap_2015_FINAL.pdf).
- [44] G. Jean-Claude, Les carburants et la combustion , Tech. l'ingénieur Mot. Therm. Aliment. Lubrif. base docum (2000). <https://www.techniques-ingenieur.fr/base-documentaire/mecanique-th7/moteur-thermique-alimentation-et-lubrification-42829210/les-carburants-et-la-combustion-bm2520/>.
- [45] D.B. Kittelson, Engines and nanoparticles: a review, *J. Aerosol Sci.* 29 (1998) 575–588. doi:[https://doi.org/10.1016/S0021-8502\(97\)10037-4](https://doi.org/10.1016/S0021-8502(97)10037-4).
- [46] United States Environmental Protection Agency, Nitrogen Oxides, Why and how they are controlled., *Tech. Bull.* (1999). <https://nepis.epa.gov/Exe/ZyNET.exe/000037B0.txt?ZyActionD=ZyDocument&Client=EPA&Index=1995Thru1999&Docs=&Query=&Time=&EndTime=&SearchMethod=1&TocRestrict=n&Toc=&TocEntry=&QField=&QFieldYear=&QFieldMonth=&QFieldDay=&UseQField=&IntQFieldOp=0&ExtQFieldOp=>.
- [47] S.M. CORREA, A Review of NO<sub>x</sub> Formation Under Gas-Turbine Combustion Conditions, *Combust. Sci. Technol.* 87 (1993) 329–362. doi:[10.1080/00102209208947221](https://doi.org/10.1080/00102209208947221).
- [48] C.P. Fenimore, Formation of nitric oxide in premixed hydrocarbon flames, , *Symp. Combust.* 13 (1971) 373–380. doi:[http://dx.doi.org/10.1016/S0082-0784\(71\)80040-1](http://dx.doi.org/10.1016/S0082-0784(71)80040-1).
- [49] S. Chapman, A Theory of Upper-Atmospheric Ozone, *Memories R. Meteorol. Soc.* 26 (1930) 103–125.
- [50] M. Camredon, B. Aumont, I – L'ozone troposphérique : production/consommation et régimes chimiques, *Pollut. Atmosphérique.* 193 (2007) 51–60.
- [51] C.C. C., Global patterns of terrestrial biological nitrogen (N-2) fixation in natural ecosystems, *Global Biogeochem. Cycles.* 13 (1999) 623–645.
- [52] M. BISSON, J. BUREAU, F. DEL GRATTA, J.P. LEFEVRE, A. LEVILAIN, OXYDES D'AZOTE NO<sub>x</sub>, 2011. <https://substances.ineris.fr/fr/substance/getDocument/2815>.
- [53] B.J. Finlayson-Pitts, J.N. Pitts, Atmospheric Chemistry of Tropospheric Ozone Formation: Scientific and Regulatory Implications, *Air Waste.* 43 (1993) 1091–1100. doi:[10.1080/1073161X.1993.10467187](https://doi.org/10.1080/1073161X.1993.10467187).
- [54] F.J. Dentener, P.J. Crutzen, Reaction of N<sub>2</sub>O<sub>5</sub> on tropospheric aerosols: Impact on the global distributions of NO<sub>x</sub>, O<sub>3</sub>, and OH, *J. Geophys. Res. Atmos.* 98 (1993) 7149–7163. doi:[10.1029/92JD02979](https://doi.org/10.1029/92JD02979).
- [55] CITEPA, Protoxyde d'azote - N<sub>2</sub>O, SECTEN. (2017). <https://www.citepa.org/fr/air-et-climat/polluants/effet-de-serre/protoxyde-d-azote-n2o> (accessed April 14, 2018).
- [56] G.J. Bartley, C.A. Sharp, Brief Investigation of SCR High Temperature N<sub>2</sub> O Production, *SAE Int. J. Engines.* 5 (2012) 683–687. <http://www.jstor.org/stable/26278392>.
- [57] K. Leistner, F. Brüsewitz, K. Wijayanti, A. Kumar, K. Kamasamudram, L. Olsson, Impact of copper loading on nh<sub>3</sub>-selective catalytic reduction, oxidation reactions and N<sub>2</sub>O formation over Cu/SAPO-34, *Energies.* 10 (2017). doi:[10.3390/en10040489](https://doi.org/10.3390/en10040489).
- [58] H. Sjövall, L. Olsson, E. Fridell, R.J. Blint, Selective catalytic reduction of NO<sub>x</sub> with NH<sub>3</sub> over Cu-ZSM-5—The effect of changing the gas composition, *Appl. Catal. B Environ.* 64 (2006) 180–188. doi:<https://doi.org/10.1016/j.apcatb.2005.12.003>.
- [59] S. Gil, J.M. Garcia-Vargas, L.F. Liotta, P. Vernoux, A. Giroir-Fendler, Single Brick Solution for Lean-Burn DeNO<sub>x</sub> and Soot Abatement, *Perovskites Relat. Mix. Oxides Concepts Appl.* (2015) 797–816.

doi:10.1002/9783527686605.ch35.

- [60] S. Gil, J.M. Garcia-Vargas, L.F. Liotta, P. Vernoux, A. Giroir-Fendler, Single Brick Solution for Lean-Burn DeNO<sub>x</sub> and Soot Abatement, in: V.I.P. and W.P. P. Granger, V. I. Parvulescu (Ed.), *Perovskites Relat. Mix. Oxides Concepts Appl.*, Wiley-VCH Verlag GmbH & Co. KGaA, Weinheim, Germany, 2016. doi:https://doi.org/10.1002/9783527686605.ch35.
- [61] M. Casarella, Urea Dosing Systems and Controls for Light Duty Diesel Applications, in: *SAE Light. Diesel Emiss. Symp.*, Ypsilanti, 2011.
- [62] T.A. Nijhuis, A.E.W. Beers, T. Vergunst, I. Hoek, F. Kapteijn, J.A. Moulijn, Preparation of monolithic catalysts, *Catal. Rev. - Sci. Eng.* 43 (2001) 345–380. doi:10.1081/CR-120001807.
- [63] A. Russell, W.S. Epling, Diesel Oxidation Catalysts, *Catal. Rev.* 53 (2011) 337–423. doi:10.1080/01614940.2011.596429.
- [64] A.M. Newton, Time Resolved Operando X-ray Techniques in Catalysis, a Case Study: CO Oxidation by O<sub>2</sub> over Pt Surfaces and Alumina Supported Pt Catalysts, *Catal.* 7 (2017). doi:10.3390/catal7020058.
- [65] M.J. Hazlett, M. Moses-Debusk, J.E. Parks, L.F. Allard, W.S. Epling, Kinetic and mechanistic study of bimetallic Pt-Pd/Al<sub>2</sub>O<sub>3</sub> catalysts for CO and C<sub>3</sub>H<sub>6</sub> oxidation, *Appl. Catal. B Environ.* 202 (2017) 404–417. doi:https://doi.org/10.1016/j.apcatb.2016.09.034.
- [66] S.J. Tauster, S.C. Fung, R.L. Garten, Strong metal-support interactions. Group 8 noble metals supported on titanium dioxide, *J. Am. Chem. Soc.* 100 (1978) 170–175. doi:10.1021/ja00469a029.
- [67] M.G. Sanchez, J.L. Gazquez, Oxygen vacancy model in strong metal-support interaction, *J. Catal.* 104 (1987) 120–135. doi:https://doi.org/10.1016/0021-9517(87)90342-3.
- [68] A. Williams, R. McCormick, J. Luecke, R. Brezny, A. Geisselmann, K. Voss, K. Hallstrom, M. Leustek, J. Parsons, H. Abi-Akar, Impact of Biodiesel Impurities on the Performance and Durability of DOC, DPF and SCR Technologies, *SAE Int. J. Fuels Lubr.* 4 (2011) 110–124. http://www.jstor.org/stable/26267419.
- [69] P. Anguita, J.M. García-Vargas, F. Gaillard, E. Iojoiu, S. Gil, A. Giroir-Fendler, Effect of Na, K, Ca and P-impurities on diesel oxidation catalysts (DOCs), *Chem. Eng. J.* 352 (2018) 333–342. doi:https://doi.org/10.1016/j.cej.2018.07.040.
- [70] P. Munnik, P.E. de Jongh, K.P. de Jong, Recent Developments in the Synthesis of Supported Catalysts, *Chem. Rev.* 115 (2015) 6687–6718. doi:10.1021/cr500486u.
- [71] M.A. Aramendía, V. Borau, C. Jiménez, J.M. Marinas, F. Rodero, M.E. Sempere, Hydrogenation of xylenes over supported Pt catalysts. Influence of different variables on their catalytic activity, *React. Kinet. Catal. Lett.* 46 (1992) 305–312. doi:10.1007/BF02070950.
- [72] A. Westermann, Élimination sélective d'un mélange d'hydrocarbures imbrûlés Diesel par adsorption sur des matériaux zéolithiques, Université de Lorraine, 2013. https://hal.univ-lorraine.fr/tel-01750621.
- [73] J.M. López, M. V Navarro, T. García, R. Murillo, A.M. Mastral, F.J. Varela-Gandía, D. Lozano-Castelló, A. Bueno-López, D. Cazorla-Amorós, Screening of different zeolites and silicoaluminophosphates for the retention of propene under cold start conditions, *Microporous Mesoporous Mater.* 130 (2010) 239–247. doi:https://doi.org/10.1016/j.micromeso.2009.11.016.
- [74] N.R. Burke, D.L. Trimm, R.F. Howe, The effect of silica:alumina ratio and hydrothermal ageing on the adsorption characteristics of BEA zeolites for cold start emission control, *Appl. Catal. B Environ.* 46 (2003) 97–104. doi:https://doi.org/10.1016/S0926-3373(03)00181-4.
- [75] National Research Council, *The Role of the Chemical Sciences in Finding Alternatives to Critical Resources: A Workshop Summary*, The National Academies Press, Washington, DC, 2012. doi:10.17226/13366.
- [76] R. Van Santen, Catalysis in Perspective : Historic Review, in: *Catal. from Princ. to Appl.*, 2012: pp. 3–19. doi:978-3-527-32349-4.
- [77] S. Verdier, E. Rohart, O. Larcher, V. Harle, M. Allain, Innovative Materials for Diesel Oxidation Catalysts, with High Durability and Early Light-Off, (2005). doi:10.4271/2005-01-0476.
- [78] P.C. Shukla, T. Gupta, N.K. Labhasetwar, R. Khobaragade, N.K. Gupta, A.K. Agarwal, Effectiveness of

- non-noble metal based diesel oxidation catalysts on particle number emissions from diesel and biodiesel exhaust, *Sci. Total Environ.* 574 (2017) 1512–1520. doi:<https://doi.org/10.1016/j.scitotenv.2016.08.155>.
- [79] D. Uner, M.K. Demirkol, B. Dernaika, A novel catalyst for diesel soot oxidation, *Appl. Catal. B Environ.* 61 (2005) 334–345. doi:<https://doi.org/10.1016/j.apcatb.2005.05.011>.
- [80] C.H. Kim, G. Qi, K. Dahlberg, W. Li, Strontium-Doped Perovskites Rival Platinum Catalysts for Treating NO<sub>x</sub> in Simulated Diesel Exhaust, *Science* (80-. ). 327 (2010) 1624 LP-1627. doi:10.1126/science.1184087.
- [81] W.A. Cutler, Overview of Ceramic Materials for Diesel Particulate Filter Applications, 28th Int. Conf. Adv. Ceram. Compos. A Ceram. Eng. Sci. Proc. (2004) 421–430. doi:[doi:10.1002/9780470291184.ch61](https://doi.org/10.1002/9780470291184.ch61).
- [82] A. Suresh, A. Yezerets, N. Currier, J. Clerc, Diesel Particulate Filter System – Effect of Critical Variables on the Regeneration Strategy Development and Optimization, *SAE Int. J. Fuels Lubr.* 1 (2009) 173–183. <http://www.jstor.org/stable/26272000>.
- [83] A.J.J. Warren, J.P. Allansson, R. Hawer, P.N. and Wilkins, Effects on after-treatment on particulate matter when using the Continuously Regenerating Trap (CRT), in: *Conference Semin. Diesel Engines - Part. Control*, London, 1998: pp. 45–55. <https://www.osti.gov/etdeweb/biblio/20042286>.
- [84] Z. Liu, Y. Ge, J. Tan, C. He, A.N. Shah, Y. Ding, L. Yu, W. Zhao, Impacts of continuously regenerating trap and particle oxidation catalyst on the NO<sub>2</sub> and particulate matter emissions emitted from diesel engine, *J. Environ. Sci.* 24 (2012) 624–631. doi:[https://doi.org/10.1016/S1001-0742\(11\)60810-3](https://doi.org/10.1016/S1001-0742(11)60810-3).
- [85] M. Colombo, G. Koltsakis, I. Koutoufaris, A Modeling Study of Soot and De-NO<sub>x</sub> Reaction Phenomena in SCRF Systems, in: *Highlighting Latest Powertrain, Veh. Infomobility Technol.*, SAE International, 2011. doi:<https://doi.org/10.4271/2011-37-0031>.
- [86] O. Salvat, P. Marez, G. Belot, Passenger Car Serial Application of a Particulate Filter System on a Common Rail Direct Injection Diesel Engine, in: *SAE 2000 World Congr.*, SAE International, 2000. doi:<https://doi.org/10.4271/2000-01-0473>.
- [87] J.H. Kwak, J.Z. Hu, D.H. Kim, J. Szanyi, C.H.F. Peden, Penta-coordinated Al<sup>3+</sup> ions as preferential nucleation sites for BaO on  $\gamma$ -Al<sub>2</sub>O<sub>3</sub>: An ultra-high-magnetic field 27Al MAS NMR study, *J. Catal.* 251 (2007) 189–194. doi:<https://doi.org/10.1016/j.jcat.2007.06.029>.
- [88] B.M. Weiss, K.B. Caldwell, E. Iglesia, NO<sub>x</sub> Interactions with Dispersed BaO: Adsorption Kinetics, Chemisorbed Species, and Effects of Oxidation Catalyst Sites, *J. Phys. Chem. C.* 115 (2011) 6561–6570. doi:10.1021/jp110604j.
- [89] H.-Y. Lin, C.-J. Wu, Y.-W. Chen, C.-H. Lee, NO<sub>x</sub> Storage and Reduction on Pt/Alumina Catalysts: Effects of Alkaline-Earth and Rare-Earth Metal Additives, *Ind. Eng. Chem. Res.* 45 (2006) 134–141. doi:10.1021/ie050574i.
- [90] Shangguan Wenfeng, *Catalytic Materials for Simultaneous NO<sub>x</sub>–Soot Removal*, in: *Simultaneous Catal. Remov. Diesel Soot NO<sub>x</sub>*, Springer Singapore, Singapore, 2019: pp. 35–45. doi:10.1007/978-981-10-7266-6.
- [91] J.R. Theis, J.A. Ura, R.W. McCabe, The Effects of Platinum and Rhodium on the Functional Properties of a Lean NO<sub>x</sub> Trap, in: *SAE World Congr. Exhib.*, SAE International, 2007. doi:<https://doi.org/10.4271/2007-01-1055>.
- [92] J.-S. Choi, W.P. Partridge, C.S. Daw, Sulfur impact on NO<sub>x</sub> storage, oxygen storage, and ammonia breakthrough during cyclic lean/rich operation of a commercial lean NO<sub>x</sub> trap, *Appl. Catal. B Environ.* 77 (2007) 145–156. doi:<https://doi.org/10.1016/j.apcatb.2007.07.025>.
- [93] Y. Jangjou, D. Wang, A. Kumar, J. Li, W.S. Epling, SO<sub>2</sub> Poisoning of the NH<sub>3</sub>-SCR Reaction over Cu- SAPO-34: Effect of Ammonium Sulfate versus Other S-Containing Species, *ACS Catal.* 6 (2016) 6612–6622. doi:10.1021/acscatal.6b01656.
- [94] J.R. Theis, J. Ura, R. McCabe, The Effects of Sulfur Poisoning and Desulfation Temperature on the NO<sub>x</sub> Conversion of LNT+SCR Systems for Diesel Applications, (2010). doi:<https://doi.org/10.4271/2010-01-0300>.
- [95] J.R. Asik, G.M. Meyer, D. Dobson, Lean NO<sub>x</sub> Trap Desulfation Through Rapid Air Fuel Modulation, in:

- SAE 2000 World Congr., SAE International, 2000. doi:<https://doi.org/10.4271/2000-01-1200>.
- [96] T. Lake, J. Stokes, R. Osborne, R. Murphy, M. Keenan, 4 - The lean boost combustion system for improved fuel economy, in: H.B.T.-A.D.I.C.E.T. and D. Zhao (Ed.), Woodhead Publishing, 2010: pp. 91–104. doi:<https://doi.org/10.1533/9781845697327.91>.
- [97] M. Shelef, G.W. Graham, Why Rhodium in Automotive Three-Way Catalysts?, *Catal. Rev.* 36 (1994) 433–457. doi:10.1080/01614949408009468.
- [98] I. Nova, E. Tronconi, Urea-SCR Technology for deNO<sub>x</sub> After Treatment of Diesel Exhausts, 2014. doi:10.1007/978-1-4899-8071-7.
- [99] M. Eichelbaum, R.J. Farrauto, M.J. Castaldi, The impact of urea on the performance of metal exchanged zeolites for the selective catalytic reduction of NO<sub>x</sub>: Part I. Pyrolysis and hydrolysis of urea over zeolite catalysts, *Appl. Catal. B Environ.* 97 (2010) 90–97. doi:<https://doi.org/10.1016/j.apcatb.2010.03.027>.
- [100] A.M. Bernhard, D. Peitz, M. Elsener, A. Wokaun, O. Kröcher, Hydrolysis and thermolysis of urea and its decomposition byproducts biuret, cyanuric acid and melamine over anatase TiO<sub>2</sub>, *Appl. Catal. B Environ.* 115–116 (2012) 129–137. doi:<https://doi.org/10.1016/j.apcatb.2011.12.013>.
- [101] L. Wallin, Investigation of urea deposit formation in vehicles with Selective Catalytic Reduction system, CHALMERS UNIVERSITY OF TECHNOLOGY, 2014.
- [102] F. Birkhold, U. Meingast, P. Wassermann, O. Deutschmann, Modeling and simulation of the injection of urea-water-solution for automotive SCR DeNO<sub>x</sub>-systems, *Appl. Catal. B Environ.* 70 (2007) 119–127. doi:10.1016/j.apcatb.2005.12.035.
- [103] J. J., Vanadia-Based Catalysts for Mobile SCR, in: T.E. Nova I. (Ed.), Urea-SCR Technol. DeNO<sub>x</sub> After Treat. Diesel Exhausts. *Fundam. Appl. Catal.*, New York, NY, 2014. doi:[https://doi.org/10.1007/978-1-4899-8071-7\\_3](https://doi.org/10.1007/978-1-4899-8071-7_3).
- [104] G.A. Andão, Junpei,; Ando, Junpei; Tohata, Heiichiro; Isaacs., NO<sub>x</sub> Abatement for Stationary Sources in Japan, Cincinnati, USA, 1976. <https://nepis.epa.gov/Exe/ZyNET.exe/91004N24.TXT?ZyActionD=ZyDocument&Client=EPA&Index=1976+Thru+1980&Docs=&Query=&Time=&EndTime=&SearchMethod=1&TocRestrict=n&Toc=&TocEntry=&QField=&QFieldYear=&QFieldMonth=&QFieldDay=&IntQFieldOp=0&ExtQFieldOp=0&XmlQuery=>.
- [105] B. Scarnegie, W.R. Miller, B. Ballmert, W. Doelling, S. Fischer, Recent DPF/SCR Results Targeting US2007 and Euro 4/5 HD Emissions, in: SAE 2003 World Congr. Exhib., SAE International, 2003. doi:<https://doi.org/10.4271/2003-01-0774>.
- [106] N.N. Sazonova, L.T. Tsykoza, A. V Simakov, G.B. Barannik, Z.R. Ismagilov, Relationship between sulfur dioxide oxidation and selective catalytic NO reduction by ammonia on V<sub>2</sub>O<sub>5</sub>-TiO<sub>2</sub> catalysts doped with WO<sub>3</sub> and Nb<sub>2</sub>O<sub>5</sub>, *React. Kinet. Catal. Lett.* 52 (1994) 101–106. doi:10.1007/BF02129856.
- [107] T. Xu, X. Wu, Y. Gao, Q. Lin, J. Hu, D. Weng, Comparative study on sulfur poisoning of V<sub>2</sub>O<sub>5</sub>-Sb<sub>2</sub>O<sub>3</sub>/TiO<sub>2</sub> and V<sub>2</sub>O<sub>5</sub>-WO<sub>3</sub>/TiO<sub>2</sub> monolithic catalysts for low-temperature NH<sub>3</sub>-SCR, *Catal. Commun.* 93 (2017) 33–36. doi:<https://doi.org/10.1016/j.catcom.2017.01.021>.
- [108] M. Inomata, A. Miyamoto, Y. Murakami, Mechanism of the reaction of NO and NH<sub>3</sub> on vanadium oxide catalyst in the presence of oxygen under the dilute gas condition, *J. Catal.* 62 (1980) 140–148. doi:[https://doi.org/10.1016/0021-9517\(80\)90429-7](https://doi.org/10.1016/0021-9517(80)90429-7).
- [109] A. Miyamoto, K. Kobayashi, M. Inomata, Y. Murakami, Nitrogen-15 tracer investigation of the mechanism of the reaction of nitric oxide with ammonia on vanadium oxide catalysts, *J. Phys. Chem.* 86 (1982) 2945–2950. doi:10.1021/j100212a027.
- [110] A.P. Walker, P.G. Blakeman, T. Ilkenhans, B. Magnusson, A.C. McDonald, P. Kleijwegt, F. Stunnenberg, M. Sanchez, The Development and In-Field Demonstration of Highly Durable SCR Catalyst Systems, *SAE Trans.* 113 (2004) 548–558. <http://www.jstor.org/stable/44740782>.
- [111] J.P. Chen, M.A. Buzanowski, R.T. Yang, J.E. Cichanowicz, Deactivation of the Vanadia Catalyst in the Selective Catalytic Reduction Process, *J. Air Waste Manage. Assoc.* 40 (1990) 1403–1409. doi:10.1080/10473289.1990.10466793.

- [112] V. Nikolov, A. Anastasov, Pretreatment of a vanadia-titania catalyst for partial oxidation of o-xylene under industrial conditions, *Ind. Eng. Chem. Res.* 31 (1992) 80–88. doi:10.1021/ie00001a012.
- [113] R.Y. Saleh, I.E. Wachs, S.S. Chan, C.C. Chersich, The interaction of V<sub>2</sub>O<sub>5</sub> with TiO<sub>2</sub>(anatase): Catalyst evolution with calcination temperature and O-xylene oxidation, *J. Catal.* 98 (1986) 102–114. doi:https://doi.org/10.1016/0021-9517(86)90300-3.
- [114] Z.G. Liu, N.A. Ottinger, C.M. Cremeens, Vanadium and tungsten release from V-based selective catalytic reduction diesel aftertreatment, *Atmos. Environ.* 104 (2015) 154–161. doi:https://doi.org/10.1016/j.atmosenv.2014.12.063.
- [115] P.A. Jacobs, E.M. Flanigen, J.C. Jansen, H. van Bekkum, *Introduction to Zeolite Science and Practice*, Elsevier Science, 2001. https://books.google.fr/books?id=UsLE2XGd8noC.
- [116] J. Weitkamp, L. Puppe, *Catalysis and Zeolites: Fundamentals and Applications*, Springer Berlin Heidelberg, 2013. https://books.google.fr/books?id=SzsCAAAQBAJ.
- [117] C.S. Cundy, P.A. Cox, The Hydrothermal Synthesis of Zeolites: History and Development from the Earliest Days to the Present Time, *Chem. Rev.* 103 (2003) 663–702. doi:10.1021/cr020060i.
- [118] P.G. Blakeman, E.M. Burkholder, H.-Y.Y. Chen, J.E. Collier, J.M. Fedeyko, H. Jobson, R.R. Rajaram, The role of pore size on the thermal stability of zeolite supported Cu SCR catalysts, *Catal. Today.* 231 (2014) 56–63. doi:https://doi.org/10.1016/j.cattod.2013.10.047.
- [119] Z. Li, J. Li, S. Liu, X. Ren, J. Ma, W. Su, Y. Peng, Ultra hydrothermal stability of CeO<sub>2</sub>-WO<sub>3</sub>/TiO<sub>2</sub> for NH<sub>3</sub>-SCR of NO compared to traditional V<sub>2</sub>O<sub>5</sub>-WO<sub>3</sub>/TiO<sub>2</sub> catalyst, *Catal. Today.* 258 (2015) 11–16. doi:https://doi.org/10.1016/j.cattod.2015.07.002.
- [120] R.Q. Long, R.T. Yang, Reaction Mechanism of Selective Catalytic Reduction of NO with NH<sub>3</sub> over Fe-ZSM-5 Catalyst, *J. Catal.* 207 (2002) 224–231. doi:https://doi.org/10.1006/jcat.2002.3528.
- [121] R.Q. Long, R.T. Yang, Catalytic Performance of Fe-ZSM-5 Catalysts for Selective Catalytic Reduction of Nitric Oxide by Ammonia, *J. Catal.* 188 (1999) 332–339. doi:https://doi.org/10.1006/jcat.1999.2674.
- [122] J. Eng, C.H. Bartholomew, Kinetic and Mechanistic Study of NO<sub>x</sub> Reduction by NH<sub>3</sub> over H-Form Zeolites, *J. Catal.* 171 (1997) 27–44. doi:https://doi.org/10.1006/jcat.1997.1769.
- [123] J. Pérez-Ramírez, C.H. Christensen, K. Egeblad, C.H. Christensen, J.C. Groen, Hierarchical zeolites: Enhanced utilisation of microporous crystals in catalysis by advances in materials design, *Chem. Soc. Rev.* 37 (2008) 2530–2542. doi:10.1039/b809030k.
- [124] T. Fjermestad, S. Svelle, O. Swang, Mechanistic comparison of the dealumination in SSZ-13 and the desilication in SAPO-34, *J. Phys. Chem. C.* 117 (2013) 13442–13451. doi:10.1021/jp4028468.
- [125] D.W. Fickel, R.F. Lobo, Copper Coordination in Cu-SSZ-13 and Cu-SSZ-16 Investigated by Variable-Temperature XRD, *J. Phys. Chem. C.* 114 (2010) 1633–1640. doi:10.1021/jp9105025.
- [126] B.F. Sels, L.M. Kustov, *Zeolites and Zeolite-like Materials*, 2016. doi:10.1016/C2014-0-00257-2.
- [127] G. Liu, P. Tian, Y. Zhang, J. Li, L. Xu, S. Meng, Z. Liu, Synthesis of SAPO-34 templated by diethylamine: Crystallization process and Si distribution in the crystals, *Microporous Mesoporous Mater.* 114 (2008) 416–423. doi:10.1016/j.micromeso.2008.01.030.
- [128] J. Tan, Z. Liu, X. Bao, X. Liu, X. Han, C. He, R. Zhai, Crystallization and Si incorporation mechanisms of SAPO-34, *Microporous Mesoporous Mater.* 53 (2002) 97–108. doi:10.1016/S1387-1811(02)00329-3.
- [129] E.M. Flanigen, R.L. Patton, S.T. Wilson, Structural, Synthetic and Physicochemical Concepts in Aluminophosphate-Based Molecular Sieves, in: P.J. Grobet, W.J. Mortier, E.F. Vansant, G.B.T.-S. in S.S. and C. Schulz-Ekloff (Eds.), *Innov. Zeolite Mater. Sci.*, Elsevier, 1988: pp. 13–27. doi:https://doi.org/10.1016/S0167-2991(09)60578-4.
- [130] C.S. Blackwell, R.L. Patton, Solid-state NMR of silicoaluminophosphate molecular sieves and aluminophosphate materials, *J. Phys. Chem.* 92 (1988) 3965–3970. doi:10.1021/j100324a055.
- [131] G. Sastre, D.W. Lewis, C. Richard, A. Catlow, Modeling of silicon substitution in SAPO-5 and SAPO-34 molecular sieves, *J. Phys. Chem. B.* 101 (1997) 5249–5262. doi:10.1021/jp963736k.



- [132] W. Shen, X. Li, Y. Wei, P. Tian, F. Deng, X. Han, X. Bao, A study of the acidity of SAPO-34 by solid-state NMR spectroscopy, *Microporous Mesoporous Mater.* 158 (2012) 19–25. doi:10.1016/j.micromeso.2012.03.013.
- [133] M. Briend, M. Derewinski, A. Lamy, D. Barthomeuf, Comparison of SAPO-37 With Faujasites in Cracking Reactions, in: L. GUCZI, F. SOLYMOSI, P.B.T.-S. in S.S. and C. TÉTÉNYI (Eds.), *New Front. Catal. - Proc. 10th Int. Congr. Catal. Budapest, 19-24 July 1992*, Elsevier, 1993: pp. 409–420. doi:https://doi.org/10.1016/S0167-2991(08)64027-6.
- [134] A.F. Ojo, J. Dwyer, J. Dewing, P.J. O'Malley, A. Nabhan, Synthesis and properties of SAPO-5 molecular sieves. Silicon incorporation into the framework, *J. Chem. Soc. Faraday Trans.* 88 (1992) 105–112. doi:10.1039/FT9928800105.
- [135] D. Wang, Y. Jangjou, Y. Liu, M.K. Sharma, J. Luo, J. Li, K. Kamasamudram, W.S. Epling, A comparison of hydrothermal aging effects on NH<sub>3</sub>-SCR of NO<sub>x</sub> over Cu-SSZ-13 and Cu-SAPO-34 catalysts, *Appl. Catal. B Environ.* 165 (2015) 438–445. doi:https://doi.org/10.1016/j.apcatb.2014.10.020.
- [136] L. Ma, Y. Cheng, G. Cavataio, R.W. McCabe, L. Fu, J. Li, Characterization of commercial Cu-SSZ-13 and Cu-SAPO-34 catalysts with hydrothermal treatment for NH<sub>3</sub>-SCR of NO<sub>x</sub> in diesel exhaust, *Chem. Eng. J.* 225 (2013) 323–330. doi:https://doi.org/10.1016/j.cej.2013.03.078.
- [137] R. Vomscheid, M. Briend, M.J. Peltre, P.P. Man, D. Barthomeuf, The Role of the Template in Directing the Si Distribution in SAPO Zeolites, *J. Phys. Chem.* 98 (1994) 9614–9618. doi:10.1021/j100089a041.
- [138] J. Fraissard, L. Petrakis, *Acidity and Basicity of Solids*, Springer Netherlands, netherlands, 1994.
- [139] A. Zecchina, C. Lamberti, S. Bordiga, Surface acidity and basicity: General concepts, *Catal. Today.* 41 (1998) 169–177. doi:https://doi.org/10.1016/S0920-5861(98)00047-9.
- [140] A.A. Sokol, C.R.A. Catlow, J.M. Garcés, A. Kuperman, Transformation of hydroxyl nests in microporous aluminosilicates upon annealing, *J. Phys. Condens. Matter.* 16 (2004) S2781–S2794. doi:10.1088/0953-8984/16/27/013.
- [141] C. Baerlocher, D.H. Olson, W.M. Meier, *Atlas of Zeolite Framework Types (formerly: Atlas of Zeolite Structure Types)*, Elsevier Science, 2001. https://books.google.fr/books?id=c5\_JGBc7VZgC.
- [142] L.S. Dent, J. V. Smith, Crystal Structure of Chabazite, a Molecular Sieve, *Nature.* 181 (1958) 1794. https://doi.org/10.1038/1811794b0.
- [143] J. Kärger, Single-File Diffusion in Zeolites BT - Adsorption and Diffusion, in: H.G. Karge, J. Weitkamp (Eds.), *Springer Berlin Heidelberg, Berlin, Heidelberg*, 2008: pp. 329–366. doi:10.1007/3829\_2007\_018.
- [144] A. Corma, Inorganic Solid Acids and Their Use in Acid-Catalyzed Hydrocarbon Reactions, *Chem. Rev.* 95 (1995) 559–614. doi:10.1021/cr00035a006.
- [145] D.J. Fisher, ed., *Diffusion and Conduction in Zeolites*, 2014. doi:https://doi.org/10.4028/www.scientific.net/DDF.351.
- [146] T. Masuda, Diffusion mechanisms of zeolite catalysts, *Catal. Surveys from Asia.* 7 (2003) 133–144. doi:10.4324/9781315158167.
- [147] R.M.A. Roque-Malherbe, *Adsorption and Diffusion in Nanoporous Materials*, 2nd ed., 2007.
- [148] D.W. Breck, *Zeolite molecular sieves: structure, chemistry, and use*, New York, 1973.
- [149] A.F. Ismail, K. Khulbe, T. Matsuura, *Gas Separation Membranes*, 1st ed., Springer International Publishing, 2015. doi:10.1007/978-3-319-01095-3.
- [150] K. Kamasamudram, N. Currier, T. Szailer, A. Yezerets, Why Cu- and Fe-Zeolite SCR Catalysts Behave Differently At Low Temperatures, *SAE Int. J. Fuels Lubr.* 3 (2010) 664–672. doi:10.1097/RMR.0b013e31827c2d13.
- [151] F. Gao, Y. Wang, M. Kollár, N.M. Washton, J. Szanyi, C.H.F.F. Peden, A comparative kinetics study between Cu/SSZ-13 and Fe/SSZ-13 SCR catalysts, *Catal. Today.* 258 (2015) 347–358. doi:https://doi.org/10.1016/j.cattod.2015.01.025.
- [152] M. Colombo, I. Nova, E. Tronconi, A comparative study of the NH<sub>3</sub>-SCR reactions over a Cu-zeolite and a

- Fe-zeolite catalyst, *Catal. Today*. 151 (2010) 223–230. doi:10.1016/j.cattod.2010.01.010.
- [153] S.Y. Joshi, A. Kumar, J. Luo, K. Kamasamudram, N.W. Currier, A. Yezerets, New insights into the mechanism of NH<sub>3</sub>-SCR over Cu- and Fe-zeolite catalyst: Apparent negative activation energy at high temperature and catalyst unit design consequences, *Appl. Catal. B Environ.* 226 (2018) 565–574. doi:10.1016/J.APCATB.2017.12.076.
- [154] P.S. Metkar, M.P. Harold, V. Balakotaiah, Experimental and kinetic modeling study of NH<sub>3</sub>-SCR of NO<sub>x</sub> on Fe-ZSM-5, Cu-chabazite and combined Fe- and Cu-zeolite monolithic catalysts, *Chem. Eng. Sci.* 87 (2013) 51–66. doi:10.1016/j.ces.2012.09.008.
- [155] A. Sultana, M. Sasaki, K. Suzuki, H. Hamada, Tuning the NO<sub>x</sub> conversion of Cu-Fe/ZSM-5 catalyst in NH<sub>3</sub>-SCR, *Catal. Commun.* 41 (2013) 21–25. doi:https://doi.org/10.1016/j.catcom.2013.06.028.
- [156] D. Wang, L. Zhang, K. Kamasamudram, W.S. Epling, In Situ-DRIFTS Study of Selective Catalytic Reduction of NO<sub>x</sub> by NH<sub>3</sub> over Cu-Exchanged SAPO-34, *ACS Catal.* 3 (2013) 871–881. doi:10.1021/cs300843k.
- [157] C. Paolucci, A.A. Parekh, I. Khurana, J.R. Di Iorio, H. Li, J.D. Albarracin Caballero, A.J. Shih, T. Anggara, W.N. Delgass, J.T. Miller, F.H. Ribeiro, R. Gounder, W.F. Schneider, Catalysis in a Cage: Condition-Dependent Speciation and Dynamics of Exchanged Cu Cations in SSZ-13 Zeolites, *J. Am. Chem. Soc.* 138 (2016) 6028–6048. doi:10.1021/jacs.6b02651.
- [158] F. Gao, E.D. Walter, M. Kollar, Y. Wang, J. Szanyi, C.H.F.F. Peden, Understanding ammonia selective catalytic reduction kinetics over Cu/SSZ-13 from motion of the Cu ions, *J. Catal.* 319 (2014) 1–14. doi:https://doi.org/10.1016/j.jcat.2014.08.010.
- [159] U. Deka, I. Lezcano-Gonzalez, S.J. Warrender, A. Lorena Picone, P.A. Wright, B.M. Weckhuysen, A.M. Beale, Changing active sites in Cu-CHA catalysts: deNO<sub>x</sub> selectivity as a function of the preparation method, *Microporous Mesoporous Mater.* 166 (2013) 144–152. doi:https://doi.org/10.1016/j.micromeso.2012.04.056.
- [160] Z. Qu, Y. Li, S. Huang, P. Chen, X. Ma, Clarification of copper species over Cu-SAPO-34 catalyst by DRIFTS and DFT study of CO adsorption, *Sci. China Chem.* 60 (2017) 912–919. doi:10.1007/s11426-016-9063-2.
- [161] J.H. Kwak, D. Tran, J. Szanyi, C.H.F. Peden, J.H. Lee, The Effect of Copper Loading on the Selective Catalytic Reduction of Nitric Oxide by Ammonia Over Cu-SSZ-13, *Catal. Letters*. 142 (2012) 295–301. doi:10.1007/s10562-012-0771-y.
- [162] S. Shwan, M. Skoglundh, L.F. Lundegaard, R.R. Tiruvalam, T.V.W. Janssens, A. Carlsson, P.N.R. Vennestrøm, Solid-State Ion-Exchange of Copper into Zeolites Facilitated by Ammonia at Low Temperature, *ACS Catal.* 5 (2015) 16–19. doi:10.1021/cs5015139.
- [163] I. Lezcano-Gonzalez, U. Deka, B. Arstad, A. Van Yperen-De Deyne, K. Hemelsoet, M. Waroquier, V. Van Speybroeck, B.M. Weckhuysen, A.M. Beale, Determining the storage, availability and reactivity of NH<sub>3</sub> within Cu-Chabazite-based Ammonia Selective Catalytic Reduction systems, *Phys. Chem. Chem. Phys.* 16 (2014) 1639–1650. doi:10.1039/c3cp54132k.
- [164] F. Giordanino, E. Borfecchia, K.A. Lomachenko, A. Lazzarini, G. Agostini, E. Gallo, A. V Soldatov, P. Beato, S. Bordiga, C. Lamberti, Interaction of NH<sub>3</sub> with Cu-SSZ-13 Catalyst: A Complementary FTIR, XANES, and XES Study, *J. Phys. Chem. Lett.* 5 (2014) 1552–1559. doi:10.1021/jz500241m.
- [165] S. Fan, J. Xue, T. Yu, D. Fan, T. Hao, M. Shen, W. Li, The effect of synthesis methods on Cu species and active sites over Cu/SAPO-34 for NH<sub>3</sub>-SCR reaction, *Catal. Sci. Technol.* 3 (2013) 2357–2364. doi:10.1039/c3cy00267e.
- [166] E.L. Uzunova, H. Mikosch, J. Hafner, Theoretical study of transition metal cation exchanged zeolites: Interaction with NO, *J. Mol. Struct. THEOCHEM.* 912 (2009) 88–94. doi:10.1016/j.theochem.2009.01.029.
- [167] C.W. Andersen, M. Bremholm, P.N.R. Vennestrøm, A.B. Blichfeld, L.F. Lundegaard, B.B. Iversen, Location of Cu<sup>2+</sup> in CHA zeolite investigated by X-ray diffraction using the Rietveld/maximum entropy method, *IUCrJ.* 1 (2014) 382–386. doi:10.1107/S2052252514020181.
- [168] J. Woo, K. Leistner, D. Bernin, H. Ahari, M. Shost, M. Zammit, L. Olsson, Effect of various structure directing agents (SDAs) on low-temperature deactivation of Cu/SAPO-34 during NH<sub>3</sub>-SCR reaction, *Catal.*

- Sci. Technol. 8 (2018) 3090–3106. doi:10.1039/c8cy00147b.
- [169] P. Chen, V. Rizzotto, A. Khetan, K. Xie, R. Moos, H. Pitsch, D. Ye, U. Simon, Mechanistic Understanding of Cu-CHA Catalyst as Sensor for Direct NH<sub>3</sub>-SCR Monitoring: The Role of Cu Mobility, *ACS Appl. Mater. Interfaces*. 11 (2019) 8097–8105. doi:10.1021/acsami.8b22104.
- [170] C. Niu, X. Shi, F. Liu, K. Liu, L. Xie, Y. You, H. He, High hydrothermal stability of Cu-SAPO-34 catalysts for the NH<sub>3</sub>-SCR of NO<sub>x</sub>, *Chem. Eng. J.* 294 (2016) 254–263. doi:10.1016/j.cej.2016.02.086.
- [171] F. Gao, E.D. Walter, N.M. Washton, J. Szanyi, C.H.F. Peden, Synthesis and evaluation of Cu/SAPO-34 catalysts for NH<sub>3</sub>-SCR 2: Solid-state ion exchange and one-pot synthesis, *Appl. Catal. B Environ.* 162 (2015) 501–514. doi:10.1016/j.apcatb.2014.07.029.
- [172] M. Iwasaki, K. Yamazaki, H. Shinjoh, NO<sub>x</sub> reduction performance of fresh and aged Fe-zeolites prepared by CVD: Effects of zeolite structure and Si/Al<sub>2</sub> ratio, *Appl. Catal. B Environ.* 102 (2011) 302–309. doi:https://doi.org/10.1016/j.apcatb.2010.12.016.
- [173] D. Wang, L. Zhang, J. Li, K. Kamasamudram, W.S. Epling, NH<sub>3</sub>-SCR over Cu/SAPO-34 - Zeolite acidity and Cu structure changes as a function of Cu loading, *Catal. Today*. 231 (2014) 64–74. doi:10.1016/j.cattod.2013.11.040.
- [174] T. Yu, J.J. Wang, Y. Huang, M. Shen, W. Li, J.J. Wang, NH<sub>3</sub> Oxidation Mechanism over Cu/SAPO-34 Catalysts Prepared by Different Methods, *ChemCatChem*. 6 (2014) 2074–2083. doi:10.1002/cctc.201402048.
- [175] P.N. Panahi, A. Niaei, D. Salari, S.M. Mousavi, G. Delahay, Ultrasound-assistant preparation of Cu-SAPO-34 nanocatalyst for selective catalytic reduction of NO by NH<sub>3</sub>, *J. Environ. Sci. (China)*. 35 (2015) 135–143. doi:10.1016/j.jes.2015.01.032.
- [176] T. Yu, D. Fan, T. Hao, J. Wang, M. Shen, W. Li, The effect of various templates on the NH<sub>3</sub>-SCR activities over Cu/SAPO-34 catalysts, *Chem. Eng. J.* 243 (2014) 159–168. doi:10.1016/j.cej.2014.01.008.
- [177] B. Chen, R. Xu, R. Zhang, N. Liu, Economical way to synthesize SSZ-13 with abundant ion-exchanged Cu<sup>+</sup> for an extraordinary performance in selective catalytic reduction (SCR) of NO<sub>x</sub> by ammonia, *Environ. Sci. Technol.* 48 (2014) 13909–13916. doi:10.1021/es503707c.
- [178] Q. Sun, Z. Xie, J. Yu, The state-of-the-art synthetic strategies for SAPO-34 zeolite catalysts in methanol-to-olefin conversion, *Natl. Sci. Rev.* 5 (2018) 542–558. doi:10.1093/nsr/nwx103.
- [179] C. Peng, Z. Liu, A. Horimoto, C. Anand, H. Yamada, K. Ohara, S. Sukenaga, M. Ando, H. Shibata, T. Takewaki, R.R. Mukti, T. Okubo, T. Wakihara, Preparation of nanosized SSZ-13 zeolite with enhanced hydrothermal stability by a two-stage synthetic method, *Microporous Mesoporous Mater.* 255 (2018) 192–199. doi:10.1016/j.micromeso.2017.07.042.
- [180] W. Su, Z. Li, Y. Peng, J. Li, Correlation of the changes in the framework and active Cu sites for typical Cu/CHA zeolites (SSZ-13 and SAPO-34) during hydrothermal aging, *Phys. Chem. Chem. Phys.* 17 (2015) 29142–29149. doi:10.1039/c5cp05128b.
- [181] A. Buchholz, W. Wang, M. Xu, A. Arnold, M. Hunger, Thermal stability and dehydroxylation of Brønsted acid sites in silicoaluminophosphates H-SAPO-11, H-SAPO-18, H-SAPO-31, and H-SAPO-34 investigated by multi-nuclear solid-state NMR spectroscopy, *Microporous Mesoporous Mater.* 56 (2002) 267–278. doi:https://doi.org/10.1016/S1387-1811(02)00491-2.
- [182] J. Wang, D. Fan, T. Yu, J. Wang, T. Hao, X. Hu, M. Shen, W. Li, Improvement of low-temperature hydrothermal stability of Cu/SAPO-34 catalysts by Cu<sup>2+</sup> species, *J. Catal.* 322 (2015) 84–90. doi:https://doi.org/10.1016/j.jcat.2014.11.010.
- [183] X. Liu, X. Wu, D. Weng, Z. Si, R. Ran, Evolution of copper species on Cu/SAPO-34 SCR catalysts upon hydrothermal aging, *Catal. Today*. 281 (2017) 596–604. doi:10.1016/j.cattod.2016.05.021.
- [184] P.N.R. Vennestrøm, A. Katerinopoulou, R.R. Tiruvalam, A. Kustov, P.G. Moses, P. Concepcion, A. Corma, Migration of Cu ions in SAPO-34 and its impact on selective catalytic reduction of NO<sub>x</sub> with NH<sub>3</sub>, *ACS Catal.* 3 (2013) 2158–2161. doi:10.1021/cs400499p.
- [185] D.M. Argyle, H.C. Bartholomew, Heterogeneous Catalyst Deactivation and Regeneration: A Review, *Catal.* 5 (2015). doi:10.3390/catal5010145.

- [186] M. Agarwal, G. Chauhan, S.P. Chaurasia, K. Singh, Study of catalytic behavior of KOH as homogeneous and heterogeneous catalyst for biodiesel production, *J. Taiwan Inst. Chem. Eng.* 43 (2012) 89–94. doi:https://doi.org/10.1016/j.jtice.2011.06.003.
- [187] G. Arzamendi, I. Campo, E. Arguñarena, M. Sánchez, M. Montes, L.M. Gandía, Synthesis of biodiesel with heterogeneous NaOH/alumina catalysts: Comparison with homogeneous NaOH, *Chem. Eng. J.* 134 (2007) 123–130. doi:https://doi.org/10.1016/j.cej.2007.03.049.
- [188] C. Wang, C. Wang, J. Wang, J. Wang, M. Shen, W. Li, Effects of Na<sup>+</sup> on Cu/SAPO-34 for ammonia selective catalytic reduction, *J. Environ. Sci.* 70 (2018) 20–28. doi:https://doi.org/10.1016/j.jes.2017.11.002.
- [189] J. Ma, Z. Si, D. Weng, X. Wu, Y. Ma, Potassium poisoning on Cu-SAPO-34 catalyst for selective catalytic reduction of NO<sub>x</sub> with ammonia, *Chem. Eng. J.* 267 (2015) 191–200. doi:https://doi.org/10.1016/j.cej.2014.11.020.
- [190] L. Olsson, K. Wijayanti, K. Leistner, A. Kumar, S.Y. Joshi, K. Kamasamudram, N.W. Currier, A. Yezerets, A kinetic model for sulfur poisoning and regeneration of Cu/SSZ-13 used for NH<sub>3</sub>-SCR, *Appl. Catal. B Environ.* 183 (2016) 394–406. doi:10.1016/j.apcatb.2015.11.001.
- [191] X. Liu, X. Wu, D. Weng, Z. Si, Durability of Cu/SAPO-34 catalyst for NO<sub>x</sub> reduction by ammonia: Potassium and sulfur poisoning, *Catal. Commun.* 59 (2015) 35–39. doi:https://doi.org/10.1016/j.catcom.2014.09.033.
- [192] K. Xie, K. Leistner, K. Wijayanti, A. Kumar, K. Kamasamudram, L. Olsson, Influence of phosphorus on Cu-SSZ-13 for selective catalytic reduction of NO<sub>x</sub> by ammonia, *Catal. Today.* 297 (2017) 46–52. doi:https://doi.org/10.1016/j.cattod.2017.07.016.
- [193] H.E. Van Der Bij, B.M. Weckhuysen, Phosphorus promotion and poisoning in zeolite-based materials: synthesis, characterisation and catalysis, *Chem. Soc. Rev.* 44 (2015) 7406–7428. doi:10.1039/c5cs00109a.
- [194] I. Lezcano-Gonzalez, U. Deka, H.E. van der Bij, P. Paalanen, B. Arstad, B.M. Weckhuysen, A.M. Beale, Chemical deactivation of Cu-SSZ-13 ammonia selective catalytic reduction (NH<sub>3</sub>-SCR) systems, *Appl. Catal. B Environ.* 154–155 (2014) 339–349. doi:https://doi.org/10.1016/j.apcatb.2014.02.037.
- [195] K. Xie, K. Leistner, K. Wijayanti, A. Kumar, K. Kamasamudram, L. Olsson, Influence of phosphorus on Cu-SSZ-13 for selective catalytic reduction of NO<sub>x</sub> by ammonia, *Catal. Today.* 297 (2017) 46–52. doi:10.1016/j.cattod.2017.07.016.
- [196] M. Schwidder, S. Heikens, A. De Toni, S. Geisler, M. Berndt, A. Brückner, W. Grünert, The role of NO<sub>2</sub> in the selective catalytic reduction of nitrogen oxides over Fe-ZSM-5 catalysts: Active sites for the conversion of NO and of NO/NO<sub>2</sub> mixtures, *J. Catal.* 259 (2008) 96–103. doi:10.1016/j.jcat.2008.07.014.
- [197] A. Grossale, I. Nova, E. Tronconi, Role of Nitrate Species in the “NO<sub>2</sub>-SCR” Mechanism over a Commercial Fe-zeolite Catalyst for SCR Mobile Applications, *Catal. Letters.* 130 (2009) 525–531. doi:10.1007/s10562-009-9942-x.
- [198] E. Tronconi, I. Nova, C. Ciardelli, D. Chatterjee, M. Weibel, Redox features in the catalytic mechanism of the “standard” and “fast” NH<sub>3</sub>-SCR of NO<sub>x</sub> over a V-based catalyst investigated by dynamic methods, *J. Catal.* 245 (2007) 1–10. doi:https://doi.org/10.1016/j.jcat.2006.09.012.
- [199] Y. Cui, F. Gao, Cu Loading Dependence of Fast NH<sub>3</sub>-SCR on Cu/SSZ-13, *Emiss. Control Sci. Technol.* 5 (2019) 124–132. doi:10.1007/s40825-019-00117-2.
- [200] A. Grossale, I. Nova, E. Tronconi, Ammonia blocking of the “Fast SCR” reactivity over a commercial Fe-zeolite catalyst for Diesel exhaust aftertreatment, *J. Catal.* 265 (2009) 141–147. doi:https://doi.org/10.1016/j.jcat.2009.04.014.
- [201] P. Forzatti, L. Lietti, E. Tronconi, Nitrogen Oxides Removal—Industrial, *Encycl. Catal.* (2010). doi:10.1002/0471227617.eoc155.pub2.
- [202] E. Tronconi, L. Lietti, P. Forzatti, S. Malloggi, Experimental and theoretical investigation of the dynamics of the SCR - DeNO<sub>x</sub> reaction, *Chem. Eng. Sci.* 51 (1996) 2965–2970. doi:https://doi.org/10.1016/0009-2509(96)00182-0.
- [203] W. Su, H. Chang, Y. Peng, C. Zhang, J. Li, Reaction pathway investigation on the selective catalytic

- reduction of NO with NH<sub>3</sub> over Cu/SSZ-13 at low temperatures, *Environ. Sci. Technol.* 49 (2015). doi:10.1021/es503430w.
- [204] D. Klukowski, P. Balle, B. Geiger, S. Wagloehner, S. Kureti, B. Kimmerle, A. Baiker, J.D. Grunwaldt, On the mechanism of the SCR reaction on Fe/HBEA zeolite, *Appl. Catal. B Environ.* 93 (2009) 185–193. doi:10.1016/j.apcatb.2009.09.028.
- [205] D. Wang, L. Zhang, K. Kamasamudram, W.S. Epling, In Situ-DRIFTS Study of Selective Catalytic Reduction of NO<sub>x</sub> by NH<sub>3</sub> over Cu-Exchanged SAPO-34, *ACS Catal.* 3 (2013) 871–881. doi:10.1021/cs300843k.
- [206] H. Sjövall, E. Fridell, R.J. Blint, L. Olsson, Identification of adsorbed species on Cu-ZSM-5 under NH<sub>3</sub> SCR conditions, *Top. Catal.* 42 (2007) 113–117. doi:10.1007/s11244-007-0162-6.
- [207] C. Tyrsted, E. Borfecchia, G. Berlier, K.A. Lomachenko, C. Lamberti, S. Bordiga, P.N.R. Vennestrøm, T.V.W. Janssens, H. Falsig, P. Beato, A. Puig-Molina, Nitrate-nitrite equilibrium in the reaction of NO with a Cu-CHA catalyst for NH<sub>3</sub>-SCR, *Catal. Sci. Technol.* 6 (2016) 8314–8324. doi:10.1039/c6cy01820c.
- [208] J. Wang, H. Zhao, G. Haller, Y. Li, Recent advances in the selective catalytic reduction of NO<sub>x</sub> with NH<sub>3</sub> on Cu-Chabazite catalysts, *Appl. Catal. B Environ.* 202 (2017) 346–354. doi:10.1016/j.apcatb.2016.09.024.
- [209] T. Komatsu, M. Nunokawa, I.S. Moon, T. Takahara, S. Namba, T. Yashima, Kinetic Studies of Reduction of Nitric Oxide with Ammonia on Cu<sup>2+</sup>-Exchanged Zeolites, *J. Catal.* 148 (1994) 427–437. doi:https://doi.org/10.1006/jcat.1994.1229.
- [210] A. Grossale, I. Nova, E. Tronconi, D. Chatterjee, M. Weibel, The chemistry of the NO/NO<sub>2</sub>–NH<sub>3</sub> “fast” SCR reaction over Fe-ZSM5 investigated by transient reaction analysis, *J. Catal.* 256 (2008) 312–322. doi:https://doi.org/10.1016/j.jcat.2008.03.027.
- [211] H.-Y. Chen, Q. Sun, B. Wen, Y.-H. Yeom, E. Weitz, W.M.H. Sachtler, Reduction over zeolite-based catalysts of nitrogen oxides in emissions containing excess oxygen: Unraveling the reaction mechanism, *Catal. Today.* 96 (2004) 1–10. doi:https://doi.org/10.1016/j.cattod.2004.05.002.
- [212] L. Ma, Y. Cheng, G. Cavataio, R.W. McCabe, L. Fu, J. Li, In situ DRIFTS and temperature-programmed technology study on NH<sub>3</sub>-SCR of NO<sub>x</sub> over Cu-SSZ-13 and Cu-SAPO-34 catalysts, *Appl. Catal. B Environ.* 156–157 (2014) 428–437. doi:https://doi.org/10.1016/j.apcatb.2014.03.048.
- [213] A. Corma, A. Palomares, F. Márquez, Determining the nature of the active sites of Cu-Beta zeolites for the selective catalytic reduction (SCR) of NO<sub>x</sub> by using a coupled reaction-XAES/XPS study, *J. Catal.* 170 (1997) 132–139. doi:10.1006/jcat.1997.1739.
- [214] S.T. Korhonen, D.W. Fickel, R.F. Lobo, B.M. Weckhuysen, A.M. Beale, Isolated Cu<sup>2+</sup> ions: active sites for selective catalytic reduction of NO, *Chem. Commun.* 47 (2011) 800–802. doi:10.1039/C0CC04218H.
- [215] A.J. O’Malley, I. Hitchcock, M. Sarwar, I.P. Silverwood, S. Hindocha, C.R.A. Catlow, A.P.E. York, P.J. Collier, Ammonia mobility in chabazite: Insight into the diffusion component of the NH<sub>3</sub>-SCR process, *Phys. Chem. Chem. Phys.* 18 (2016) 17159–17168. doi:10.1039/c6cp01160h.
- [216] M. Bendrich, A. Scheuer, R.E. Hayes, M. Votsmeier, Unified mechanistic model for Standard SCR, Fast SCR, and NO<sub>2</sub>SCR over a copper chabazite catalyst, *Appl. Catal. B Environ.* 222 (2018) 76–87. doi:10.1016/j.apcatb.2017.09.069.
- [217] E. Tronconi, I. Nova, The Role of NO<sub>2</sub> in the NH<sub>3</sub>–SCR Catalytic Chemistry BT - Urea-SCR Technology for deNO<sub>x</sub> After Treatment of Diesel Exhausts, in: I. Nova, E. Tronconi (Eds.), Springer New York, New York, NY, 2014: pp. 247–270. doi:10.1007/978-1-4899-8071-7\_9.
- [218] P. Chen, A. Khetan, M. Jabłońska, J. Simböck, M. Muhler, R. Palkovits, H. Pitsch, U. Simon, Local dynamics of copper active sites in zeolite catalysts for selective catalytic reduction of NO<sub>x</sub> with NH<sub>3</sub>, *Appl. Catal. B Environ.* 237 (2018) 263–272. doi:10.1016/j.apcatb.2018.05.091.
- [219] C. Paolucci, A.A. Verma, S.A. Bates, V.F. Kispersky, J.T. Miller, R. Gounder, W.N. Delgass, F.H. Ribeiro, W.F. Schneider, Isolation of the copper redox steps in the standard selective catalytic reduction on Cu-SSZ-13, *Angew. Chemie - Int. Ed.* 53 (2014) 11828–11833. doi:10.1002/anie.201407030.
- [220] H. Falsig, P.N.R. Vennestrøm, P.G. Moses, T.V.W. Janssens, Activation of Oxygen and NO in NH<sub>3</sub>-SCR

- over Cu-CHA Catalysts Evaluated by Density Functional Theory, *Top. Catal.* 59 (2016) 861–865. doi:10.1007/s11244-016-0560-8.
- [221] T. Yu, T. Hao, D. Fan, J. Wang, M. Shen, W. Li, Recent NH<sub>3</sub>-SCR Mechanism Research over Cu/SAPO-34 Catalyst, *J. Phys. Chem. C* 118 (2014) 6565–6575. doi:10.1021/jp4114199.
- [222] T. Yu, J. Wang, M. Shen, J. Wang, W. Li, The influence of CO<sub>2</sub> and H<sub>2</sub>O on selective catalytic reduction of NO by NH<sub>3</sub> over Cu/SAPO-34 catalyst, *Chem. Eng. J.* 264 (2015) 845–855. doi:10.1016/j.cej.2014.12.017.
- [223] B. Kerkeni, D. Berthout, D. Berthomieu, D.E. Doronkin, M. Casapu, J.D. Grunwaldt, C. Chizallet, Copper Coordination to Water and Ammonia in CuII-Exchanged SSZ-13: Atomistic Insights from DFT Calculations and in Situ XAS Experiments, *J. Phys. Chem. C* 122 (2018) 16741–16755. doi:10.1021/acs.jpcc.8b03572.
- [224] U. De-La-Torre, B. Pereda-Ayo, M.A. Gutiérrez-Ortiz, J.A. González-Marcos, J.R. González-Velasco, Steady-state NH<sub>3</sub>-SCR global model and kinetic parameter estimation for NO<sub>x</sub> removal in diesel engine exhaust aftertreatment with Cu/chabazite, *Catal. Today* 296 (2017) 95–104. doi:10.1016/j.cattod.2017.04.011.
- [225] Supriyanto, K. Wijayanti, A. Kumar, S. Joshi, K. Kamasamudram, N.W. Currier, A. Yezerets, L. Olsson, Global kinetic modeling of hydrothermal aging of NH<sub>3</sub>-SCR over Cu-zeolites, *Appl. Catal. B Environ.* 163 (2015) 382–392. doi:10.1016/j.apcatb.2014.07.059.
- [226] P.S. Metkar, V. Balakotaiah, M.P. Harold, Experimental and kinetic modeling study of NO oxidation: Comparison of Fe and Cu-zeolite catalysts, *Catal. Today* 184 (2012) 115–128. doi:10.1016/j.cattod.2011.11.032.
- [227] M. Moreno-González, R. Millán, P. Concepción, T. Blasco, M. Boronat, Spectroscopic Evidence and Density Functional Theory (DFT) Analysis of Low-Temperature Oxidation of Cu<sup>+</sup> to Cu<sup>2+</sup> + NO<sub>x</sub> in Cu-CHA Catalysts: Implications for the SCR-NO<sub>x</sub> Reaction Mechanism, *ACS Catal.* 9 (2019) 2725–2738. doi:10.1021/acscatal.8b04717.
- [228] P. Concepción, M. Boronat, R. Millán, M. Moliner, A. Corma, Identification of Distinct Copper Species in Cu-CHA Samples Using NO as Probe Molecule. A Combined IR Spectroscopic and DFT Study, *Top. Catal.* 60 (2017) 1653–1663. doi:10.1007/s11244-017-0844-7.
- [229] H. Sjövall, R.J. Blint, L. Olsson, Detailed kinetic modeling of NH<sub>3</sub> SCR over Cu-ZSM-5, *Appl. Catal. B Environ.* 92 (2009) 138–153. doi:10.1016/j.apcatb.2009.07.020.
- [230] M. Colombo, I. Nova, E. Tronconi, Detailed kinetic modeling of the NH<sub>3</sub>-NO/NO<sub>2</sub> SCR reactions over a commercial Cu-zeolite catalyst for Diesel exhausts after treatment, *Catal. Today* 197 (2012) 243–255. doi:10.1016/j.cattod.2012.09.002.
- [231] Kinetics of Reactions on Surfaces, *Concepts Mod. Catal. Kinet.* (2003) 267–299. doi:10.1002/3527602658.ch7.
- [232] J. Gong, K. Narayanaswamy, C.J. Rutland, Heterogeneous Ammonia Storage Model for NH<sub>3</sub>-SCR Modeling, *Ind. Eng. Chem. Res.* 55 (2016) 5874–5884. doi:10.1021/acs.iecr.6b01097.
- [233] R. Daya, C. Desai, B. Vernham, Development and Validation of a Two-Site Kinetic Model for NH<sub>3</sub>-SCR over Cu-SSZ-13. Part 1. Detailed Global Kinetics Development Based on Mechanistic Considerations, *Emiss. Control Sci. Technol.* 4 (2018) 143–171. doi:10.1007/s40825-018-0095-5.
- [234] L. Olsson, K. Wijayanti, K. Leistner, A. Kumar, S.Y. Joshi, K. Kamasamudram, N.W. Currier, A. Yezerets, A multi-site kinetic model for NH<sub>3</sub>-SCR over Cu / SSZ-13, *Appl. Catal. B Environ.* 175 (2015) 212–224. doi:10.1016/j.apcatb.2015.02.037.
- [235] N. Wilken, K. Kamasamudram, N.W. Currier, J. Li, A. Yezerets, L. Olsson, Heat of adsorption for NH<sub>3</sub>, NO<sub>2</sub> and NO on Cu-Beta zeolite using microcalorimeter for NH<sub>3</sub>SCR applications, *Catal. Today* 151 (2010) 237–243. <http://dx.doi.org/10.1016/j.cattod.2010.02.002>.
- [236] X. Auvray, W. Partridge, J.-S. Choi, J. Pihl, F. Coehlo, A. Yezerets, K. Kamasamudram, N. Currier, L. Olsson, Kinetic modeling of NH<sub>3</sub>-SCR over a supported Cu zeolite catalyst using axial species distribution measurements, *Appl. Catal. B Environ.* 163 (2015) 393–403. doi:<https://doi.org/10.1016/j.apcatb.2014.08.003>.

- [237] E.E.I. A. Giroir-Fendler, S. Gil, Reactive filter for motor vehicle, PCT/FR2015/052925, 2015.
- [238] M. Schiavoni, S. Campisi, A. Gervasini, Effect of Cu deposition method on silico aluminophosphate catalysts in NH<sub>3</sub>-SCR and NH<sub>3</sub>-SCO reactions, *Appl. Catal. A Gen.* 543 (2017) 162–172. doi:10.1016/j.apcata.2017.06.034.
- [239] L. Xie, F. Liu, L. Ren, X. Shi, F.S. Xiao, H. He, Excellent performance of one-pot synthesized Cu-SSZ-13 catalyst for the selective catalytic reduction of NO<sub>x</sub> with NH<sub>3</sub>, *Environ. Sci. Technol.* 48 (2014) 566–572. doi:10.1021/es4032002.
- [240] R.B. Borade, A. Clearfield, A comparative study of acidic properties of SAPO-5, -11, -34 and -37 molecular sieves, 88 (1994).
- [241] M. Xu, J.J.J. Wang, T. Yu, J.J.J. Wang, M. Shen, New insight into Cu/SAPO-34 preparation procedure: Impact of NH<sub>4</sub>-SAPO-34 on the structure and Cu distribution in Cu-SAPO-34 NH<sub>3</sub>-SCR catalysts, *Appl. Catal. B Environ.* 220 (2018) 161–170. doi:10.1016/j.apcatb.2017.08.031.
- [242] F. Gao, E.D. Walter, N.M. Washton, J. Szanyi, C.H.F. Peden, Synthesis and Evaluation of Cu-SAPO-34 Catalysts for NH<sub>3</sub>-SCR I: Aqueous Solution Ion Exchange, *Acs Catal.* 3 (2013) 2083–2093.
- [243] L. Wang, W. Li, G. Qi, D. Weng, Location and nature of Cu species in Cu/SAPO-34 for selective catalytic reduction of NO with NH<sub>3</sub>, *J. Catal.* 289 (2012) 21–29. doi:10.1016/j.jcat.2012.01.012.
- [244] P. Chen, J. Simböck, S. Schönebaum, D. Rauch, T. Simons, R. Palkovits, R. Moos, U. Simon, Monitoring NH<sub>3</sub> storage and conversion in Cu-ZSM-5 and Cu-SAPO-34 catalysts for NH<sub>3</sub>-SCR by simultaneous impedance and DRIFT spectroscopy, *Sensors Actuators, B Chem.* 236 (2016) 1075–1082. doi:10.1016/j.snb.2016.05.164.
- [245] F. Caruso, S. Mantellato, M. Palacios, R.J. Flatt, ICP-OES method for the characterization of cement pore solutions and their modification by polycarboxylate-based superplasticizers, *Cem. Concr. Res.* 91 (2017) 52–60. doi:https://doi.org/10.1016/j.cemconres.2016.10.007.
- [246] J. Rouquerol, P. Llewellyn, F. Rouquerol, Is the bet equation applicable to microporous adsorbents?, in: P.L. Llewellyn, F. Rodriguez-Reinoso, J. Rouquerol, N.B.T.-S. in S.S. and C. Seaton (Eds.), *Charact. Porous Solids VII*, Elsevier, 2007: pp. 49–56. doi:https://doi.org/10.1016/S0167-2991(07)80008-5.
- [247] B.C. Lippens, *Studies on Pore Systems in Catalysts*, 323 (1965) 319–323.
- [248] T.D. SMITH, R. BELL, Relation Between the Brunauer–Emmett–Teller and Harkins–Jura Isotherms, *Nature.* 162 (1948) 109–110. doi:10.1038/162109b0.
- [249] H.K. Livingston, The cross-sectional areas of molecules adsorbed on solid surfaces, *J. Colloid Sci.* 4 (1949) 447–458. doi:https://doi.org/10.1016/0095-8522(49)90043-4.
- [250] S.U.R. and R.T. Yang, Corrected Horvath-Kawazoe Equations for Pore-Size Distribution, *AIChE J.* 46 (2000) 734–750.
- [251] L.S. Cheng, Y. Ralph T, Improved Horvath—Kawazoe equations including spherical pore models for calculating micropore size distribution, *Chem. Eng. Sci.* 49 (1994) 2599–2609. doi:https://doi.org/10.1016/0009-2509(94)E0054-T.
- [252] K. Ramesh, K.S. Reddy, I. Rashmi, A.K. Biswas, K.R. Islam, Horvath-Kawazoe Model Based Evaluation of Pore Volume of Nanoporous Clinoptilolite, *Commun. Soil Sci. Plant Anal.* 47 (2016) 1622–1629. doi:10.1080/00103624.2016.1206118.
- [253] A.F. Venero, J.N. Chiou, Characterization of Zeolites by Gas Adsorption at Low Pressures, *MRS Proc.* 111 (1987) 235. doi:DOI: 10.1557/PROC-111-235.
- [254] École des mines D’Albi-Carmaux, La microporosité, (2016). [https://nte.mines-albi.fr/STP/co/uc\\_Microporosite.html#footnotesN231](https://nte.mines-albi.fr/STP/co/uc_Microporosite.html#footnotesN231) (accessed March 14, 2017).
- [255] IRCELyon, Diffractomètre Versatile Panalytical X’Pert Pro MPD, (n.d.). [http://www.ircelyon.univ-lyon1.fr/plateforme/\(syrcel\\_identifieur\)/RX/\(syrcel\\_vue\)/equipment](http://www.ircelyon.univ-lyon1.fr/plateforme/(syrcel_identifieur)/RX/(syrcel_vue)/equipment) (accessed May 1, 2017).
- [256] F. Gao, E.D. Walter, N.M. Washton, J. Szanyi, C.H.F. Peden, Synthesis and evaluation of Cu-SAPO-34 catalysts for ammonia selective catalytic reduction. 1. Aqueous solution ion exchange, *ACS Catal.* 3 (2013) 2083–2093. doi:10.1021/cs4004672.

- [257] IRCELYon, Microscopie électronique à transmission, (n.d.). [http://www.ircelyon.univ-lyon1.fr/plateforme/\(syrceel\\_identifier\)/MICROSCOPIE/\(syrceel\\_view\)/theory](http://www.ircelyon.univ-lyon1.fr/plateforme/(syrceel_identifier)/MICROSCOPIE/(syrceel_view)/theory) (accessed May 1, 2017).
- [258] J. Vedrine, Catalyst Characterization: Physical Techniques for Solid Materials, in: Pleum Press, New York, NY, 1994.
- [259] Z.L. Wang, Transmission Electron Microscopy of Shape-Controlled Nanocrystals and Their Assemblies, *J. Phys. Chem. B.* 104 (2000) 1153–1175. doi:10.1021/jp993593c.
- [260] B. Diehl, Chapter 1 - Principles in NMR Spectroscopy, in: U. Holzgrabe, I. Wawer, B.B.T.-N.M.R.S. in P.A. Diehl (Eds.), Elsevier, Amsterdam, 2008: pp. 1–41. doi:https://doi.org/10.1016/B978-0-444-53173-5.00001-9.
- [261] A.E. McDermott, T. Polenova, Solid State NMR Studies of Biopolymers (p.83), Wiley, 2010. <https://books.google.fr/books?id=atsaceAxLEwC>.
- [262] Linde, Nuclear Magnetic Resonance, (n.d.). [http://hiq.linde-gas.com/en/analytical\\_methods/nuclear\\_magnetic\\_resonance.html](http://hiq.linde-gas.com/en/analytical_methods/nuclear_magnetic_resonance.html) (accessed April 5, 2018).
- [263] J. Szanyi, J.H. Kwak, H. Zhu, C.H.F. Peden, Characterization of Cu-SSZ-13 NH<sub>3</sub> SCR catalysts: an in situ FTIR study, *Phys. Chem. Chem. Phys.* 15 (2013) 2368–2380. doi:10.1039/C2CP43467A.
- [264] J. Sirita, S. Phanichphant, F.C. Meunier, Quantitative Analysis of Adsorbate Concentrations by Diffuse Reflectance FT-IR, *Anal. Chem.* 79 (2007) 3912–3918. doi:10.1021/ac0702802.
- [265] F.C. Meunier, Pitfalls and benefits of: In situ and operando diffuse reflectance FT-IR spectroscopy (DRIFTS) applied to catalytic reactions, *React. Chem. Eng.* 1 (2016) 134–141. doi:10.1039/c5re00018a.
- [266] F.C. Meunier, A. Goguet, S. Shekhtman, D. Rooney, H. Daly, A modified commercial DRIFTS cell for kinetically relevant operando studies of heterogeneous catalytic reactions, *Appl. Catal. A Gen.* 340 (2008) 196–202. doi:10.1016/j.apcata.2008.02.034.
- [267] J.J. Venter, M.A. Vannice, Applicability of “DRIFTS” for the characterization of carbon-supported metal catalysts and carbon surfaces, *Carbon N. Y.* 26 (1988) 889–902. doi:10.1016/0008-6223(88)90112-1.
- [268] IFP, Oil & Gas Science and Technology, 59. (2004).
- [269] Matsui, W., T. Suzuki, Y. Ohta, Y. Daisho, H. Suzuki, H. Ishii, A Study on the Improvement of NO<sub>x</sub> Reduction Efficiency for a Urea-SCR System: Technical paper, 2011. doi:20115720, October.
- [270] M. Colombo, I. Nova, E. Tronconi, A comparative study of the NH<sub>3</sub>-SCR reactions over a Cu-zeolite and a Fe-zeolite catalyst, *Catal. Today.* 151 (2010) 223–230. doi:10.1016/j.cattod.2010.01.010.
- [271] U. Deka, I. Lezcano-Gonzalez, S.J. Warrender, A. Lorena Picone, P.A. Wright, B.M. Weckhuysen, A.M. Beale, Changing active sites in Cu-CHA catalysts: DeNO<sub>x</sub>selectivity as a function of the preparation method, *Microporous Mesoporous Mater.* 166 (2013) 144–152. doi:10.1016/j.micromeso.2012.04.056.
- [272] F. Gao, E.D. Walter, E.M. Karp, J. Luo, R.G. Tonkyn, J.H. Kwak, J. Szanyi, C.H.F.F. Peden, Structure–activity relationships in NH<sub>3</sub>-SCR over Cu-SSZ-13 as probed by reaction kinetics and EPR studies, *J. Catal.* 300 (2013) 20–29. doi:10.1016/j.jcat.2012.12.020.
- [273] Y. Xin, X. Wang, Q. Li, X. Ma, Y. Qi, L. Zheng, J.A. Anderson, Z. Zhang, The Potential of Cu-SAPO-44 in the Selective Catalytic Reduction of NO<sub>x</sub> with NH<sub>3</sub>, *ChemCatChem.* 8 (2016) 3740–3745. doi:10.1002/cctc.201601159.
- [274] L. Zhang, J. Bates, D. Chen, H.Y. Nie, Y. Huang, Investigations of formation of molecular sieve SAPO-34, *J. Phys. Chem. C.* 115 (2011) 22309–22319. doi:10.1021/jp208560t.
- [275] A. Shishkin, P.-A. Carlsson, H. Härelind, M. Skoglundh, Effect of Preparation Procedure on the Catalytic Properties of Fe-ZSM-5 as SCR Catalyst, *Top. Catal.* 56 (2013) 567–575. doi:10.1007/s11244-013-0016-3.
- [276] J. Wang, T. Yu, X. Wang, G. Qi, J. Xue, M. Shen, W. Li, The influence of silicon on the catalytic properties of Cu/SAPO-34 for NO<sub>x</sub>reduction by ammonia-SCR, *Appl. Catal. B Environ.* 127 (2012) 137–147. doi:10.1016/j.apcatb.2012.08.016.
- [277] B.I. Palella, M. Cadoni, A. Frache, H.O. Pastore, R. Pirone, G. Russo, S. Coluccia, L. Marchese, On the hydrothermal stability of CuAPSO-34 microporous catalysts for N<sub>2</sub>O decomposition: a comparison with



- CuZSM-5, *J. Catal.* 217 (2003) 100–106. doi:[https://doi.org/10.1016/S0021-9517\(03\)00033-2](https://doi.org/10.1016/S0021-9517(03)00033-2).
- [278] Q. Ye, L. Wang, R.T. Yang, Activity, propene poisoning resistance and hydrothermal stability of copper exchanged chabazite-like zeolite catalysts for SCR of NO with ammonia in comparison to Cu/ZSM-5, *Appl. Catal. A Gen.* 427–428 (2012) 24–34. doi:<https://doi.org/10.1016/j.apcata.2012.03.026>.
- [279] A. Material, SAPO-34 ACS Material, (n.d.). <https://www.acsmaterial.com/sapo-1364.html> (accessed January 30, 2019).
- [280] XFNANO, SAPO-34 XFNANO, (n.d.). <https://en.xfnano.com/Product/pro316.aspx> (accessed January 30, 2019).
- [281] NOVARIALS, SAPO-34 NOVARIALS, (n.d.). <https://www.novarials-store.com/products/sapo-34> (accessed January 30, 2019).
- [282] Ø.B. Vistad, D.E. Akporiaye, F. Taulelle, K.P. Lillerud, In situ NMR of SAPO-34 crystallization, *Chem. Mater.* 15 (2003) 1639–1649. doi:10.1021/cm021317w.
- [283] P. Emrani, S. Fatemi, S. Ashraf Talesh, Effect of synthesis parameters on phase purity, crystallinity and particle size of SAPO-34, *Iran. J. Chem. Chem. Eng.* 30 (2011) 29–36.
- [284] L. Xu, A. Du, Y. Wei, Y. Wang, Z. Yu, Y. He, X. Zhang, Z. Liu, Synthesis of SAPO-34 with only Si(4Al) species: Effect of Si contents on Si incorporation mechanism and Si coordination environment of SAPO-34, *Microporous Mesoporous Mater.* 115 (2008) 332–337. doi:10.1016/j.micromeso.2008.02.001.
- [285] C. Petitto, G. Delahay, Selective catalytic reduction of NO<sub>x</sub> by NH<sub>3</sub> on Cu-SAPO-34 catalysts : Influence of silicium content on the activity of calcined and hydrotreated samples, *Chem. Eng. J.* 264 (2015) 404–410. doi:10.1016/j.cej.2014.11.111.
- [286] J.J. Wang, Y. Huang, T. Yu, S. Zhu, M. Shen, W. Li, J.J. Wang, The migration of Cu species over Cu-SAPO-34 and its effect on NH<sub>3</sub>oxidation at high temperature, *Catal. Sci. Technol.* 4 (2014) 3004–3012. doi:10.1039/c4cy00451e.
- [287] M. Xu, J. Wang, T. Yu, J. Wang, M. Shen, New insight into Cu/SAPO-34 preparation procedure: Impact of NH<sub>4</sub>-SAPO-34 on the structure and Cu distribution in Cu-SAPO-34 NH<sub>3</sub>-SCR catalysts, *Appl. Catal. B Environ.* 220 (2018) 161–170. doi:<https://doi.org/10.1016/j.apcatb.2017.08.031>.
- [288] F. Popa, Elaboration et étude de poudres magnétiques douces (Ni-Fe, Ni-Fe-X, Ni-Fe-X-Y) à l'état nanocristallin par broyage mécanique de haute énergie, Université Joseph-Fourier, 2008. doi:tel-00258428f.
- [289] Y. Wan, W. Zhao, Y. Tang, L. Li, H. Wang, Y. Cui, J. Gu, Y. Li, J. Shi, Ni-Mn bi-metal oxide catalysts for the low temperature SCR removal of NO with NH<sub>3</sub>, *Appl. Catal. B Environ.* 148–149 (2014) 114–122. doi:<https://doi.org/10.1016/j.apcatb.2013.10.049>.
- [290] J. Zhu, F. Gao, L. Dong, W. Yu, L. Qi, Z. Wang, L. Dong, Y. Chen, Studies on surface structure of MxOy/MoO<sub>3</sub>/CeO<sub>2</sub> system (M=Ni, Cu, Fe) and its influence on SCR of NO by NH<sub>3</sub>, *Appl. Catal. B Environ.* 95 (2010) 144–152. doi:<https://doi.org/10.1016/j.apcatb.2009.12.021>.
- [291] D. Fang, F. He, X. Liu, K. Qi, J. Xie, F. Li, C. Yu, Low temperature NH<sub>3</sub>-SCR of NO over an unexpected Mn-based catalyst: Promotional effect of Mg doping, *Appl. Surf. Sci.* 427 (2018) 45–55. doi:<https://doi.org/10.1016/j.apsusc.2017.08.088>.
- [292] M.-L. Tarot, M. Barreau, D. Duprez, V. Lauga, E.E. Iojoiu, X. Courtois, F. Can, Influence of the Sodium Impregnation Solvent on the Deactivation of Cu/Fe-Exchanged Zeolites Dedicated to the SCR of NO<sub>x</sub> with NH<sub>3</sub>, *Catal.* 8 (2018). doi:10.3390/catal8010003.
- [293] T. Yu, J. Wang, M. Shen, W. Li, NH<sub>3</sub>-SCR over Cu/SAPO-34 catalysts with various acid contents and low Cu loading, *Catal. Sci. Technol.* 3 (2013) 3234–3241. doi:10.1039/C3CY00453H.
- [294] B. Zibrowius, E. Löffler, M. Hunger, Multinuclear MAS n.m.r. and i.r. spectroscopic study of silicon incorporation into SAPO-5, SAPO-31, and SAPO-34 molecular sieves, *Zeolites.* 12 (1992) 167–174. doi:10.1016/0144-2449(92)90079-5.
- [295] C. Lin, Y. Cao, X. Feng, Q. Lin, H. Xu, Y. Chen, Effect of Si islands on low-temperature hydrothermal stability of Cu/SAPO-34 catalyst for NH<sub>3</sub>-SCR, *J. Taiwan Inst. Chem. Eng.* 81 (2017) 288–294. doi:10.1016/j.jtice.2017.09.050.

- [296] C.S.- Selective, C. Reduction, Recent Progress in Atomic-Level Understanding of Cu/SSZ-13 Selective Catalytic Reduction Catalysts, *Catalysts*. 8 (2018) 140. doi:10.3390/catal8040140.
- [297] F. Gao, J. Hun, K. Janos, C.H.F. Peden, Current Understanding of Cu-Exchanged Chabazite Molecular Sieves for Use as Commercial Diesel Engine DeNO<sub>x</sub> Catalysts, (2013) 1441–1459. doi:10.1007/s11244-013-0145-8.
- [298] A. Godiksen, F.N. Stappen, P.N.R. Vennestrøm, F. Giordanino, S.B. Rasmussen, L.F. Lundegaard, S. Mossin, Coordination Environment of Copper Sites in Cu-CHA Zeolite Investigated by Electron Paramagnetic Resonance, *J. Phys. Chem. C*. 118 (2014) 23126–23138. doi:10.1021/jp5065616.
- [299] A. Godiksen, F.N. Stappen, P. Nicolai, R. Vennestrøm, S. Rasmussen, L.F. Lundegaard, S. Mossin, Coordination Environment of Copper in Cu-CHA Zeolite Investigated by EPR, (2014). doi:10.1021/jp5065616.
- [300] L. Zhang, A.J. Herna, Thermal Detemplantation of Na-SAPO-34 : Effect on Sr<sup>2+</sup> Ion Exchange and CO<sub>2</sub> Adsorption, (2010) 14755–14762.
- [301] P. 1974 International Center for Diffraction Data, Swarthmore, Joint Committee for Powder Diffraction Standards, Powder Diffraction File no. 05-0661,JCPDS, (n.d.).
- [302] M. Charghand, M. Haghighi, S. Saedy, S. Aghamohammadi, Efficient hydrothermal synthesis of nanostructured SAPO-34 using ultrasound energy: Physicochemical characterization and catalytic performance toward methanol conversion to light olefins, *Adv. Powder Technol.* 25 (2014) 1728–1736. doi:10.1016/j.apt.2014.06.022.
- [303] G. HORVATH, K. KAWAZOE, Method for the calculation of effective pore size distribution in molecular sieve carbon, *J. Chem. Eng. Japan*. 16 (1983) 470–475. doi:10.1252/jcej.16.470.
- [304] T.S. K. S. W. SING, D. H. EVERETT , R. A. W. HAUL, L. MOSCOU , R. A. PIEROTTI, J. ROUQUEROL, Reporting physisorption data for, *Pure Appl. Chem.*, 57 (1985) 603–619.
- [305] J. Fraissard, ed., *Physical Adsorption: Experiment, Theory and Applications*, Springer Netherlands, 1997.
- [306] T.T.H. Dang, H.-L.L. Zubowa, U. Bentrup, M. Richter, A. Martin, Microwave-assisted synthesis and characterization of Cu-containing AlPO<sub>4</sub>-5 and SAPO-5, *Microporous Mesoporous Mater.* 123 (2009) 209–220. doi:https://doi.org/10.1016/j.micromeso.2009.04.003.
- [307] L. Liping, C. Xiaojing, L. Junfen, W. Jianguo, Synthesis of sa-po-34/zsm-5 composite and its catalytic performance in the conversion of methanol to hydrocarbons, *J. Braz. Chem. Soc.* 26 (2015) 290–296. doi:10.5935/0103-5053.20140279.
- [308] C. Ram, S. Sivamani, T. Micha Premkumar, V. Hariram, The NH<sub>3</sub>-SCR over Cu/SAPO-34 catalysts with various acid contents at low Cu loading Tie, *ARPN J. Eng. Appl. Sci.* 12 (2017) 6397–6406. doi:10.1039/b000000x.
- [309] C. Baerlocher, L.B. McCusker, Database of Zeolite Structure, (n.d.). <http://www.iza-structure.org/databases/> (accessed April 7, 2017).
- [310] Y. Watanabe, A. Koiwai, H. Takeuchi, S.A. Hyodo, S. Noda, Multinuclear NMR studies on the thermal stability of SAPO-34, *J. Catal.* 143 (1993) 430–436. doi:10.1006/jcat.1993.1287.
- [311] G.A.V. Martins, G. Berlier, S. Coluccia, H.O. Pastore, G.B. Superti, G. Gatti, L. Marchese, Revisiting the nature of the acidity in chabazite-related silicoaluminophosphates: Combined FTIR and<sup>29</sup>Si MAS NMR study, *J. Phys. Chem. C*. 111 (2007) 330–339. doi:10.1021/jp063921q.
- [312] Ø.B. Vistad, D.E. Akporiaye, F. Taulelle, K.P. Lillerud, Morpholine, an in Situ <sup>13</sup>C NMR pH Meter for Hydrothermal Crystallogenesi of SAPO-34, *Chem. Mater.* 15 (2003) 1650–1654. doi:10.1021/cm021318o.
- [313] Y. Watanabe, A. Koiwai, H. Takeuchi, S.A. Hyodo, S. Noda, Multinuclear NMR Studies on the Thermal Stability of SAPO-34, *J. Catal.* 143 (1993) 430–436. doi:https://doi.org/10.1006/jcat.1993.1287.
- [314] H.-L. Zubowa, E. Alsdorf, R. Fricke, F. Neissendorfer, J. Richter-Mendau, E. Schreier, D. Zeigan, B. Zibrowius, Synthesis and properties of the silicoaluminophosphate molecular sieve SAPO-31, *J. Chem. Soc. Faraday Trans.* 86 (1990) 2307–2312. doi:10.1039/FT9908602307.
- [315] J. Xue, X. Wang, G. Qi, J. Wang, M. Shen, W. Li, Characterization of copper species over Cu/SAPO-34 in

- selective catalytic reduction of NO<sub>x</sub> with ammonia: Relationships between active Cu sites and de-NO<sub>x</sub> performance at low temperature, *J. Catal.* 297 (2013) 56–64. doi:10.1016/j.jcat.2012.09.020.
- [316] M. Richter, M.J.G. Fait, R. Eckelt, M. Schneider, J. Radnik, D. Heidemann, R. Fricke, Gas-phase carbonylation of methanol to dimethyl carbonate on chloride-free Cu-precipitated zeolite Y at normal pressure, *J. Catal.* 245 (2007) 11–24. doi:10.1016/j.jcat.2006.09.009.
- [317] R.G. Herman, J.H. Lunsford, H. Beyer, P.A. Jacobs, J.B. Uytterhoeven, Redox behavior of transition metal ions in zeolites. I. Reversibility of the hydrogen reduction of copper Y zeolites, *J. Phys. Chem.* 79 (1975) 2388–2394. doi:10.1021/j100589a009.
- [318] D. Berthomieu, G. Delahay, Recent Advances in CuI/IIY: Experiments and Modeling, *Catal. Rev.* 48 (2006) 269–313. doi:10.1080/01614940600796349.
- [319] J. Hun Kwak, H. Zhu, J.H. Lee, C.H.F. Peden, J. Szanyi, Two different cationic positions in Cu-SSZ-13, *Chem. Commun.* 48 (2012) 4758–4760. doi:10.1039/C2CC31184D.
- [320] F. Gao, E.D. Walter, E.M. Karp, J. Luo, R.G. Tonkyn, J.H. Kwak, J. Szanyi, C.H.F.F. Peden, Structure–activity relationships in NH<sub>3</sub>-SCR over Cu-SSZ-13 as probed by reaction kinetics and EPR studies, *J. Catal.* 300 (2013) 20–29. doi:10.1016/j.jcat.2012.12.020.
- [321] R. Zhang, Y. Li, T. Zhen, Ammonia selective catalytic reduction of NO over Fe/Cu-SSZ-13, *RSC Adv.* 4 (2014) 52130–52139. doi:10.1039/C4RA09290B.
- [322] C. Yin, P. Cheng, X. Li, R.T. Yang, Selective catalytic reduction of nitric oxide with ammonia over high-activity Fe/SSZ-13 and Fe/one-pot-synthesized Cu-SSZ-13 catalysts, *Catal. Sci. Technol.* 6 (2016) 7561–7568. doi:10.1039/C6CY01027J.
- [323] A. Wang, Y. Wang, E.D. Walter, R.K. Kukkadapu, Y. Guo, G. Lu, R.S. Weber, Y. Wang, C.H.F. Peden, F. Gao, Catalytic N<sub>2</sub>O decomposition and reduction by NH<sub>3</sub> over Fe/Beta and Fe/SSZ-13 catalysts, *J. Catal.* 358 (2018) 199–210. doi:https://doi.org/10.1016/j.jcat.2017.12.011.
- [324] P.N. Panahi, G. Delahay, Comparative Study of the Support Role on the Activity of Copper Species for Nitric Oxide Reduction, *Russ. J. Appl. Chem.* 90 (2017) 1627–1633. doi:10.1134/S1070427217010111.
- [325] P.E. Fanning, M.A. Vannice, A DRIFTS Study of Cu–ZSM-5 Prior to and during Its Use for N<sub>2</sub>O Decomposition, *J. Catal.* 207 (2002) 166–182. doi:https://doi.org/10.1006/jcat.2002.3518.
- [326] B. Onida, Z. Gabelica, J. Lourenço, E. Garrone, Spectroscopic Characterization of Hydroxyl Groups in SAPO-40. 1. Study of the Template-Free Samples and Their Interaction with Ammonia, *J. Phys. Chem.* 100 (1996) 11072–11079. doi:10.1021/jp9600874.
- [327] F. Gao, Y. Zheng, R.K. Kukkadapu, Y. Wang, E.D. Walter, B. Schwenzer, J. Szanyi, C.H.F. Peden, Iron Loading Effects in Fe/SSZ-13 NH<sub>3</sub>-SCR Catalysts: Nature of the Fe Ions and Structure-Function Relationships, *ACS Catal.* 6 (2016) 2939–2954. doi:10.1021/acscatal.6b00647.
- [328] S. Andonova, S. Tamm, C. Montreuil, C. Lambert, L. Olsson, The effect of iron loading and hydrothermal aging on one-pot synthesized Fe/SAPO-34 for ammonia SCR, *Appl. Catal. B Environ.* 180 (2016) 775–787. doi:10.1016/j.apcatb.2015.07.007.
- [329] F. Gao, M. Kollár, R.K. Kukkadapu, N.M. Washton, Y. Wang, J. Szanyi, C.H.F. Peden, Fe/SSZ-13 as an NH<sub>3</sub>-SCR catalyst: A reaction kinetics and FTIR/Mössbauer spectroscopic study, *Appl. Catal. B Environ.* 164 (2015) 407–419. doi:10.1016/j.apcatb.2014.09.031.
- [330] W. Duo, K. Dam-Johansen, K. Østergaard, Ammonia and Oxygen, *Can. J. Chem. Eng.* 70 (1992).
- [331] D.W. Fickel, E. D’Addio, J.A. Lauterbach, R.F. Lobo, The ammonia selective catalytic reduction activity of copper-exchanged small-pore zeolites, *Appl. Catal. B Environ.* 102 (2011) 441–448. doi:10.1016/j.apcatb.2010.12.022.
- [332] F. Gao, Y. Wang, M. Kollár, N.M. Washton, J. Szanyi, C.H.F. Peden, A comparative kinetics study between Cu/SSZ-13 and Fe/SSZ-13 SCR catalysts, *Catal. Today.* 258 (2015). doi:10.1016/j.cattod.2015.01.025.
- [333] A.M. Beale, F. Gao, I. Lezcano-Gonzalez, C.H.F. Peden, J. Szanyi, Recent advances in automotive catalysis for NO<sub>x</sub> emission control by small-pore microporous materials, *Chem. Soc. Rev.* 44 (2015) 7371–7405. doi:10.1039/c5cs00108k.

- [334] A.A. Verma, S.A. Bates, T. Anggara, C. Paolucci, A.A. Parekh, K. Kamasamudram, A. Yezerets, J.T. Miller, W.N. Delgass, W.F. Schneider, F.H. Ribeiro, NO oxidation: A probe reaction on Cu-SSZ-13, *J. Catal.* 312 (2014) 179–190. doi:<https://doi.org/10.1016/j.jcat.2014.01.017>.
- [335] U. Deka, A. Juhin, E.A. Eilertsen, H. Emerich, M.A. Green, S.T. Korhonen, B.M. Weckhuysen, A.M. Beale, Confirmation of Isolated Cu<sup>2+</sup> Ions in SSZ-13 Zeolite as Active Sites in NH<sub>3</sub>-Selective Catalytic Reduction, *J. Phys. Chem. C.* 116 (2012) 4809–4818. doi:[10.1021/jp212450d](https://doi.org/10.1021/jp212450d).
- [336] A. Marberger, A.W. Petrov, P. Steiger, M. Elsener, O. Kröcher, M. Nachtegaal, D. Ferri, Time-resolved copper speciation during selective catalytic reduction of NO on Cu-SSZ-13, *Nat. Catal.* 1 (2018) 221–227. doi:[10.1038/s41929-018-0032-6](https://doi.org/10.1038/s41929-018-0032-6).
- [337] G. Yang, J. Ran, X. Du, X. Wang, Y. Chen, L. Zhang, Different copper species as active sites for NH<sub>3</sub>-SCR reaction over Cu-SAPO-34 catalyst and reaction pathways: A periodic DFT study, *Microporous Mesoporous Mater.* 266 (2018) 223–231. doi:[10.1016/j.micromeso.2018.01.034](https://doi.org/10.1016/j.micromeso.2018.01.034).
- [338] J.H. Kwak, J.H. Lee, S.D. Burton, A.S. Lipton, C.H.F. Peden, J. Szanyi, A common intermediate for N<sub>2</sub> formation in enzymes and zeolites: Side-On Cu-nitrosyl complexes, *Angew. Chemie - Int. Ed.* 52 (2013) 9985–9989. doi:[10.1002/anie.201303498](https://doi.org/10.1002/anie.201303498).
- [339] J. Rudolph, C.R. Jacob, Computational insights into the mechanism of the selective catalytic reduction of NO<sub>x</sub>: Fe- versus Cu-doped zeolite catalysts, (2019) 1–22.
- [340] L. Wang, J.R. Gaudet, W. Li, D. Weng, Migration of Cu species in Cu/SAPO-34 during hydrothermal aging, *J. Catal.* 306 (2013) 68–77. doi:[10.1016/j.jcat.2013.06.010](https://doi.org/10.1016/j.jcat.2013.06.010).
- [341] N. Katada, K. Suzuki, T. Noda, G. Sastre, M. Niwa, Correlation between brønsted acid strength and local structure in zeolites, *J. Phys. Chem. C.* 113 (2009) 19208–19217. doi:[10.1021/jp903788n](https://doi.org/10.1021/jp903788n).
- [342] S. Bhatia, J. Beltramini, D.D. Do, Temperature programmed analysis and its applications in catalytic systems, *Catal. Today.* 7 (1990) 309–438. doi:[10.1016/0920-5861\(90\)87001-j](https://doi.org/10.1016/0920-5861(90)87001-j).
- [343] M. Devadas, Selective Catalytic Reduction (SCR) of Nitrogen Oxides with Ammonia over Fe-ZSM5, PhD Thesis. (2006) 161.
- [344] C. Costa, I. Dzikh, J.M. Lopes, F. Lemos, F.R. Ribeiro, Activity–acidity relationship in zeolite ZSM-5. Application of Brønsted-type equations, *J. Mol. Catal. A Chem.* 154 (2000) 193–201. doi:[10.1016/S1381-1169\(99\)00374-X](https://doi.org/10.1016/S1381-1169(99)00374-X).
- [345] T. Álvaro-Muñoz, C. Márquez-Álvarez, E. Sastre, Use of different templates on SAPO-34 synthesis: Effect on the acidity and catalytic activity in the MTO reaction, *Catal. Today.* 179 (2012) 27–34. doi:<https://doi.org/10.1016/j.cattod.2011.07.038>.
- [346] T. Ishihara, M. Kagawa, F. Hadama, Y. Takita, Copper ion-exchanged SAPO-34 as a thermostable catalyst for selective reduction of NO with C<sub>3</sub>H<sub>6</sub>, *J. Catal.* 169 (1997) 93–102. doi:[10.1006/jcat.1997.1681](https://doi.org/10.1006/jcat.1997.1681).
- [347] A.M. Prakash, S. Unnikrishnan, Synthesis of SAPO-34: High silicon incorporation in the presence of morpholine as template, *J. Chem. Soc. Faraday Trans.* 90 (1994) 2291–2296. doi:[10.1039/FT9949002291](https://doi.org/10.1039/FT9949002291).
- [348] D. Su, X. Xie, S. Dou, G. Wang, CuO single crystal with exposed {001} facets-A highly efficient material for gas sensing and Li-ion battery applications, *Sci. Rep.* 4 (2014) 1–9. doi:[10.1038/srep05753](https://doi.org/10.1038/srep05753).
- [349] S. Kakuta, T. Abe, Structural Characterization of Cu<sub>2</sub>O After the Evolution of H<sub>2</sub> under Visible Light Irradiation, *Electrochem. Solid-State Lett.* 12 (2009) P1. doi:[10.1149/1.3054330](https://doi.org/10.1149/1.3054330).
- [350] Y.R. Du, S. Zhao, L.F. Shen, Nuclear magnetic resonance studies of micelles, *Annu. Reports NMR Spectrosc.* 48 (2002) 145–194. doi:[10.1016/S0066-4103\(02\)48006-4](https://doi.org/10.1016/S0066-4103(02)48006-4).
- [351] M. Briend, R. Vomscheid, M.J. Peltre, P.P. Man, D. Barthomeuf, Influence of the Choice of the Template on the Short- and Long-Term Stability of SAPO-34 Zeolite, *J. Phys. Chem.* 99 (1995) 8270–8276. doi:[10.1021/j100020a060](https://doi.org/10.1021/j100020a060).
- [352] J.H. Kwak, D. Tran, S.D. Burton, J. Szanyi, J.H. Lee, C.H.F. Peden, Effects of hydrothermal aging on NH<sub>3</sub>-SCR reaction over Cu/zeolites, *J. Catal.* 287 (2012) 203–209. doi:[10.1016/j.jcat.2011.12.025](https://doi.org/10.1016/j.jcat.2011.12.025).
- [353] G.V.A.A. Martins, G. Berlier, C. Bisio, S. Coluccia, H.O. Pastore, L. Marchese, Quantification of brønsted acid sites in microporous catalysts by a combined FTIR and NH<sub>3</sub>-TPD study, *J. Phys. Chem. C.* 112 (2008)

- 7193–7200. doi:10.1021/jp710613q.
- [354] T. Yu, T. Hao, D. Fan, J. Wang, M. Shen, W. Li, Recent NH<sub>3</sub> - SCR Mechanism Research over Cu / SAPO-34 Catalyst, (2014).
- [355] F. Piubello, B. Yasser Jangjou, B. Isabella Nova, B.S. William Epling, Study of NO Formation During NH<sub>3</sub> Oxidation Reaction Over a Cu-SAPO-34 SCR catalyst, *Catal. Letters*. 146 (2016) 1552–1561. doi:10.1007/s10562-016-1783-9.
- [356] K. Hadjiivanov, D. Klissurski, G. Ramis, G. Busca, Fourier transform IR study of NO<sub>x</sub> adsorption on a CuZSM-5 DeNO<sub>x</sub> catalyst, *Appl. Catal. B Environ.* 7 (1996) 251–267. doi:https://doi.org/10.1016/0926-3373(95)00034-8.
- [357] J. Szanyi, M.T. Paffett, The Adsorption of NO and Reaction of NO with O<sub>2</sub> on H-, NaH-, CuH-, and Cu-ZSM-5: An in Situ FTIR Investigation, *J. Catal.* 164 (1996) 232–245. doi:https://doi.org/10.1006/jcat.1996.0378.
- [358] C. Negri, P.S. Hammershoi, T.V.W. Janssens, P. Beato, G. Berlier, S. Bordiga, Investigating the Low Temperature Formation of CuII-(N,O) Species on Cu-CHA Zeolites for the Selective Catalytic Reduction of NO<sub>x</sub>, *Chem. - A Eur. J.* 24 (2018) 12044–12053. doi:10.1002/chem.201802769.
- [359] L. Shi, T. Yu, X.Q. Wang, J. Wang, M.Q. Shen, Properties and roles of adsorbed NH<sub>3</sub> and NO<sub>x</sub> over Cu/SAPO-34 zeolite catalyst in NH<sub>3</sub>-SCR process, *Wuli Huaxue Xuebao/ Acta Phys. - Chim. Sin.* 29 (2013) 1550–1557. doi:10.3866/PKU.WHXB201304283.
- [360] K.I. HADJIIVANOV, Identification of Neutral and Charged N<sub>x</sub>O<sub>y</sub> Surface Species by IR Spectroscopy, *Catal. Rev.* 42 (2000) 71–144. doi:10.1081/CR-100100260.
- [361] K.I. Hadjiivanov, Identification of neutral and charged N<sub>x</sub>O<sub>y</sub> surface species by IR spectroscopy, *Catal. Rev. - Sci. Eng.* 42 (2000) 71–144. doi:10.1081/CR-100100260.
- [362] S. Velu, K. Suzuki, M. Vijayaraj, S. Barman, C.S. Gopinath, In situ XPS investigations of Cu<sub>1-x</sub>Ni<sub>x</sub>ZnAl-mixed metal oxide catalysts used in the oxidative steam reforming of bio-ethanol, *Appl. Catal. B Environ.* 55 (2005) 287–299. doi:https://doi.org/10.1016/j.apcatb.2004.09.007.
- [363] J. Wang, Z. Liu, G. Feng, L. Chang, W. Bao, In situ synthesis of CuSAPO-34/cordierite and its selective catalytic reduction of nitrogen oxides in vehicle exhaust: The effect of HF, *Fuel*. 109 (2013) 101–109. doi:https://doi.org/10.1016/j.fuel.2012.09.046.
- [364] W. Gruenert, N.W. Hayes, R.W. Joyner, E.S. Shpiro, M.R.H. Siddiqui, G.N. Baeva, Structure, Chemistry, and Activity of Cu-ZSM-5 Catalysts for the Selective Reduction of NO<sub>x</sub> in the Presence of Oxygen, *J. Phys. Chem.* 98 (1994) 10832–10846. doi:10.1021/j100093a026.
- [365] Z. Chen, C. Fan, L. Pang, S. Ming, P. Liu, D. Zhu, J. Wang, X. Cai, H. Chen, Y. Lai, T. Li, Direct synthesis of submicron Cu-SAPO-34 as highly efficient and robust catalyst for selective catalytic reduction of NO by NH<sub>3</sub>, *Appl. Surf. Sci.* 448 (2018) 671–680. doi:10.1016/j.apsusc.2018.04.076.
- [366] L. Huang, X. Wang, S. Yao, B. Jiang, X. Chen, X. Wang, Cu-Mn bimetal ion-exchanged SAPO-34 as an active SCR catalyst for removal of NO<sub>x</sub> from diesel engine exhausts, *Catal. Commun.* 81 (2016) 54–57. doi:10.1016/j.catcom.2016.03.010.
- [367] P. Gaudin, P. Fioux, S. Dorge, H. Nouali, M. Vierling, E. Fiani, M. Molière, J.-F. Brillhac, J. Patarin, Formation and role of Cu<sup>+</sup> species on highly dispersed CuO/SBA-15 mesoporous materials for SO<sub>x</sub> removal: An XPS study, *Fuel Process. Technol.* 153 (2016) 129–136. doi:https://doi.org/10.1016/j.fuproc.2016.07.015.
- [368] Y. Li, J. Deng, W. Song, J. Liu, Z. Zhao, M. Gao, Y. Wei, L. Zhao, Nature of Cu species in Cu-SAPO-18 catalyst for NH<sub>3</sub>-SCR: Combination of experiments and DFT calculations, *J. Phys. Chem. C*. 120 (2016) 14669–14680. doi:10.1021/acs.jpcc.6b03464.
- [369] J. Luo, F. Gao, K. Kamasamudram, N. Currier, C.H.F. Peden, A. Yezerets, New insights into Cu/SSZ-13 SCR catalyst acidity. Part I: Nature of acidic sites probed by NH<sub>3</sub> titration, *J. Catal.* 348 (2017) 291–299. doi:10.1016/j.jcat.2017.02.025.
- [370] K. Leistner, K. Xie, A. Kumar, K. Kamasamudram, L. Olsson, Ammonia Desorption Peaks Can Be Assigned to Different Copper Sites in Cu/SSZ-13, *Catal. Letters*. 147 (2017) 1882–1890.

doi:10.1007/s10562-017-2083-8.

- [371] X. Dong, J. Wang, H. Zhao, Y. Li, The promotion effect of CeO<sub>x</sub> on Cu-SAPO-34 catalyst for selective catalytic reduction of NO<sub>x</sub> with ammonia, *Catal. Today*. 258 (2015) 28–34. doi:10.1016/j.cattod.2015.04.015.
- [372] L. Wang, W. Li, S.J. Schmiegel, D. Weng, Role of Brønsted acidity in NH<sub>3</sub> selective catalytic reduction reaction on Cu/SAPO-34 catalysts, *J. Catal.* 324 (2015) 98–106. doi:10.1016/j.jcat.2015.01.011.
- [373] Y. Duan, J. Wang, T. Yu, M. Shen, J. Wang, The role and activity of various adsorbed ammonia species on Cu/SAPO-34 catalyst during passive-SCR process, *RSC Adv.* 5 (2015) 14103–14113. doi:10.1039/c4ra13984d.
- [374] K. Hadjiivanov, H. Knözinger, FTIR study of CO and NO adsorption and coadsorption on a Cu/SiO<sub>2</sub> catalyst: Probing the oxidation state of copper, *Phys. Chem. Chem. Phys.* 3 (2001) 1132–1137. doi:10.1039/B009649K.
- [375] C. Lamberti, A. Zecchina, E. Groppo, S. Bordiga, Probing the surfaces of heterogeneous catalysts by in situ IR spectroscopy, *Chem. Soc. Rev.* 39 (2010) 4951–5001. doi:10.1039/C0CS00117A.
- [376] K.I. Hadjiivanov, M.M. Kantcheva, D.G. Klissurski, IR study of CO adsorption on Cu-ZSM-5 and CuO/SiO<sub>2</sub> catalysts:  $\sigma$  and  $\pi$  components of the Cu<sup>+</sup>—CO bond, *J. Chem. Soc. Faraday Trans.* 92 (1996) 4595–4600. doi:10.1039/FT9969204595.
- [377] G. Spoto, S. Bordiga, D. Scarano, A. Zecchina, C. Inorganica, C. Fisica, Well defined Cu ~ (NO), Cu ~ (NO)<sub>2</sub> and CuI (NO)X (X = O- and / or NO<sub>2</sub>) complexes in Cu ~ -ZSM5 prepared by interaction of H-ZSM5 with gaseous CuCl, *Inorg. Chim. Acta*, 13 (1992) 39–44.
- [378] E.L. Uzunova, H. Mikosch, J. Hafner, Adsorption of NO on Cu-SAPO-34 and Co-SAPO-34: A Periodic DFT Study, *J. Phys. Chem. C*. 112 (2008) 2632–2639. doi:10.1021/jp0774903.
- [379] F. Giordanino, P.N.R. Vennestrøm, L.F. Lundegaard, F.N. Stappen, S. Mossin, P. Beato, S. Bordiga, C. Lamberti, Characterization of Cu-exchanged SSZ-13: A comparative FTIR, UV-Vis, and EPR study with Cu-ZSM-5 and Cu- $\beta$  with similar Si/Al and Cu/Al ratios, *Dalt. Trans.* 42 (2013) 12741–12761. doi:10.1039/c3dt50732g.
- [380] K.H. Stern, High Temperature Properties and Decomposition of Inorganic Salts Part 3, Nitrates and Nitrites, *J. Phys. Chem. Ref. Data* 1. 1 (1972) 747–772. doi:https://doi-org.docelec.univ-lyon1.fr/10.1063/1.3253104.
- [381] G. Centi, S. Perathoner, Nature of active species in copper-based catalysts and their chemistry of transformation of nitrogen oxides, *Appl. Catal. A Gen.* 132 (1995) 179–259. doi:https://doi.org/10.1016/0926-860X(95)00154-9.
- [382] H.Y. Chen, Z. Wei, M. Kollar, F. Gao, Y. Wang, J. Szanyi, C.H.F. Peden, NO oxidation on zeolite supported Cu catalysts: Formation and reactivity of surface nitrates, *Catal. Today*. 267 (2016) 17–27. doi:10.1016/j.cattod.2015.11.039.
- [383] G.J. Millar, A. Canning, G. Rose, B. Wood, L. Trewartha, I.D.R. Mackinnon, Identification of Copper Species Present in Cu-ZSM-5 Catalysts for NO<sub>x</sub>Reduction, *J. Catal.* 183 (1999) 169–181. doi:https://doi.org/10.1006/jcat.1999.2391.
- [384] G. Moretti, C. Dossi, A. Fusi, S. Recchia, R. Psaro, A comparison between Cu-ZSM-5, Cu-S-1 and Cu-mesoporous-silica-alumina as catalysts for NO decomposition, *Appl. Catal. B Environ.* 20 (1999) 67–73. doi:https://doi.org/10.1016/S0926-3373(98)00096-4.
- [385] Jean-François Lepage, *Catalyse de contact, conception préparation et mise en oeuvre des catalyseurs industriels*, 1978.
- [386] J. Wiley, K. Hepburn, O. Levenspiel, *Chemical Reaction Engineering - third edition*, 1999. doi:10.1016/0009-2509(64)85017-X.
- [387] D.E. Mears, Tests for Transport Limitations in Experimental Catalytic Reactors, *Ind. Eng. Chem. Process Des. Dev.* 10 (1971) 541–547. doi:10.1021/i260040a020.
- [388] L.A. Burwell, M.J. Boudart, Effects of Transport Limitations on Rates of Solid-Catalyzed Reactions, in: J. C G Problem, Hill (Ed.), *An Introd. to Chem. Eng. Kinet. React. Des.*, 1977: p. 192.

- [389] X. Hu, M. Yang, D. Fan, G. Qi, J. Wang, J. Wang, T. Yu, W. Li, M. Shen, The role of pore diffusion in determining NH<sub>3</sub>SCR active sites over Cu/SAPO-34 catalysts, *J. Catal.* 341 (2016) 55–61. doi:10.1016/j.jcat.2016.05.022.
- [390] E.M. Davis, R.J. Davis, *Fundamentals of Chemical Reaction Engineering*, 2003. doi:10.1021/ed043pA758.1.
- [391] R. Aris, On shape factors for irregular particles—I: The steady state problem. *Diffusion and reaction, Chem. Eng. Sci.* 6 (1957) 262–268. doi:https://doi.org/10.1016/0009-2509(57)85028-3.
- [392] J. Wei, Nonlinear Phenomena in Zeolite Diffusion and Reaction, *Ind. Eng. Chem. Res.* 33 (1994) 2467–2472. doi:10.1021/ie00034a031.
- [393] H. Yucel, D.M. Ruthven, Diffusion of CO<sub>2</sub> in 4A and 5A zeolite crystals, *J. Colloid Interface Sci.* 74 (1980) 186–195. doi:https://doi.org/10.1016/0021-9797(80)90182-4.
- [394] D.M. Ruthven, Diffusion in type A zeolites: New insights from old data, *Microporous Mesoporous Mater.* 162 (2012) 69–79. doi:https://doi.org/10.1016/j.micromeso.2011.12.025.
- [395] S. Bhatia, *Zeolite Catalysts: Principles and Applications*, 1989.
- [396] A. Schuler, M. Votsmeier, P. Kiwic, J. Gieshoff, W. Hauptmann, A. Drochner, H. Vogel, NH<sub>3</sub>-SCR on Fe zeolite catalysts – From model setup to NH<sub>3</sub> dosing, *Chem. Eng. J.* 154 (2009) 333–340. doi:https://doi.org/10.1016/j.cej.2009.02.037.
- [397] S. Brandenberger, O. Kröcher, A. Tissler, R. Althoff, The determination of the activities of different iron species in Fe-ZSM-5 for SCR of NO by NH<sub>3</sub>, *Appl. Catal. B Environ.* 95 (2010) 348–357. doi:10.1016/j.apcatb.2010.01.013.
- [398] W. Ostwald, *Lehrbuch der allgemeinen Chemie*, W. Engelmann, 1886. https://www.wfp.org/news/russias-kamaz-trucks-support-wfp-operations-east-and-central-africa.
- [399] J. Marangozis, Comparison and analysis of intrinsic kinetics and effectiveness factors for the catalytic reduction of nitrogen oxide (NO) with ammonia in the presence of oxygen, *Ind. Eng. Chem. Res.* 31 (1992) 987–994. doi:10.1021/ie00004a001.
- [400] G. Busca, L. Lietti, G. Ramis, F. Berti, Chemical and mechanistic aspects of the selective catalytic reduction of NO<sub>x</sub> by ammonia over oxide catalysts: A review, *Appl. Catal. B Environ.* 18 (1998) 1–36. doi:https://doi.org/10.1016/S0926-3373(98)00040-X.
- [401] T.J. Mason, J.P. Lorimer, A method for the determination of the activation energy for a reaction from a single kinetic run, *Comput. Chem.* 7 (1983) 159–163. doi:https://doi.org/10.1016/0097-8485(83)85008-6.
- [402] L. Ma, Y. Cheng, G. Cavataio, R.W. McCabe, L. Fu, J. Li, In situ DRIFTS and temperature-programmed technology study on NH<sub>3</sub>-SCR of NO<sub>x</sub> over Cu-SSZ-13 and Cu-SAPO-34 catalysts, *Appl. Catal. B Environ.* 156–157 (2014) 428–437. doi:10.1016/j.apcatb.2014.03.048.
- [403] A.P. Altshuller, Thermodynamic considerations in the interactions of nitrogen oxides and oxy-acids in the atmosphere, *J. Air Pollut. Control Assoc.* 6 (1956) 97–100. doi:10.1080/00966665.1956.10467740.
- [404] W. S. Epling, L. Campbell, A. Yezerets, N. Currier, J. Parks II, Overview of the Fundamental Reactions and Degradation Mechanisms of NO<sub>x</sub> Storage/Reduction Catalysts, *Catal. Rev. Eng. - CATAL REV-SCI ENG.* 46 (2007) 163–245. doi:10.1081/CR-200031932.
- [405] I. Nova, C. Ciardelli, E. Tronconi, D. Chatterjee, M. Weibel, NH<sub>3</sub>-NO/NO<sub>2</sub>SCR for diesel exhausts after treatment: Mechanism and modelling of a catalytic converter, *Top. Catal.* 42–43 (2007) 43–46. doi:10.1007/s11244-007-0148-4.
- [406] M.P. Ruggeri, T. Selli, M. Colombo, I. Nova, E. Tronconi, Identification of nitrites/HONO as primary products of NO oxidation over Fe-ZSM-5 and their role in the Standard SCR mechanism: A chemical trapping study, *J. Catal.* 311 (2014) 266–270. doi:https://doi.org/10.1016/j.jcat.2013.11.028.
- [407] G. Madia, M. Koebel, M. Elsener, A. Wokaun, Side Reactions in the Selective Catalytic Reduction of NO<sub>x</sub> with Various NO<sub>2</sub> Fractions, *Ind. Eng. Chem. Res.* 41 (2002) 4008–4015. doi:10.1021/ie020054c.
- [408] D.J. Cole, C.F. Cullis, D.J. Hucknall, Studies of heterogeneous oxidation catalysts. Part 1.—The vanadium(V) oxide + titanium(IV) oxide system, *J. Chem. Soc. Faraday Trans. 1 Phys. Chem. Condens.*

- Phases. 72 (1976) 2185–2196. doi:10.1039/F19767202185.
- [409] Q. Sun, Z.-X. Gao, H.-Y. Chen, W.M.H. Sachtler, Reduction of NO<sub>x</sub> with Ammonia over Fe/MFI: Reaction Mechanism Based on Isotopic Labeling, *J. Catal.* 201 (2001) 89–99. doi:https://doi.org/10.1006/jcat.2001.3228.
- [410] G. Liu, W. Zhang, P. He, S. Guan, B. Yuan, R. Li, Y. Sun, D. Shen, H<sub>2</sub>O and/or SO<sub>2</sub> Tolerance of Cu-Mn/SAPO-34 Catalyst for NO Reduction with NH<sub>3</sub> at Low Temperature, *Catalysts*. 9 (2019) 289. doi:10.3390/catal9030289.
- [411] M. Gaulke, V. Guschin, S. Knapp, S. Pappert, W. Eckl, A unified kinetic model for adsorption and desorption – Applied to water on zeolite, *Microporous Mesoporous Mater.* 233 (2016) 39–43. doi:10.1016/j.micromeso.2016.06.034.
- [412] A.M. Beale, F. Gao, I. Lezcano-Gonzalez, C.H.F. Peden, J. Szanyi, Recent advances in automotive catalysis for NO<sub>x</sub> emission control by small-pore microporous materials, *Chem. Soc. Rev.* 44 (2015) 7371–7405. doi:10.1039/C5CS00108K.
- [413] I. Nova, L. Lietti, E. Tronconi, P. Forzatti, Transient response method applied to the kinetic analysis of the DeNO<sub>x</sub>–SCR reaction, *Chem. Eng. Sci.* 56 (2001) 1229–1237. doi:https://doi.org/10.1016/S0009-2509(00)00344-4.
- [414] R. Oord, J.E. Schmidt, B.M. Weckhuysen, Methane-to-methanol conversion over zeolite Cu-SSZ-13, and its comparison with the selective catalytic reduction of NO<sub>x</sub> with NH<sub>3</sub>, *Catal. Sci. Technol.* 8 (2018) 1028–1038. doi:10.1039/C7CY02461D.
- [415] I. Nova, M. Colombo, E. Tronconi, P. Milano, V. Schmeisser, M. Weibel, The NH<sub>3</sub> Inhibition Effect in the Standard SCR Reaction over a Commercial Fe-zeolite Catalyst for Diesel Exhaust Aftertreatment : An Experimental and Modeling Study, 4 (2018). doi:10.4271/2011-01-1319.
- [416] B.B. Sobalik Z, Jisa K, Jirglova H, Simultaneous FTIR/UV-Vis study of reactions over metallo-zeolites: Approach to quantitative in situ studies, *Catal. Today.* 126 (2007) 73–80.
- [417] T.V.W.W. Janssens, H. Falsig, L.F. Lundegaard, P.N.R.R. Vennestrøm, S.B. Rasmussen, P.G. Moses, F. Giordanino, E. Borfecchia, K.A. Lomachenko, C. Lamberti, S. Bordiga, A. Godiksen, S. Mossin, P. Beato, A consistent reaction scheme for the selective catalytic reduction of nitrogen oxides with ammonia, *ACS Catal.* 5 (2015) 2832–2845. doi:10.1021/cs501673g.
- [418] D. Chatterjee, K. Rusch, Urea-SCR Technology for deNO<sub>x</sub> After Treatment of Diesel Exhausts, (2014). doi:10.1007/978-1-4899-8071-7.
- [419] R.Q. Long, R.T. Yang, Selective catalytic oxidation (SCO) of ammonia to nitrogen over Fe-exchanged zeolites, *J. Catal.* 201 (2001) 145–152. doi:10.1006/jcat.2001.3234.
- [420] F. Gao, N.M. Washton, Y. Wang, M. Kollár, J. Szanyi, C.H.F. Peden, Effects of Si/Al ratio on Cu/SSZ-13 NH<sub>3</sub>-SCR catalysts: Implications for the active Cu species and the roles of Brønsted acidity, *J. Catal.* 331 (2015) 25–38. doi:https://doi.org/10.1016/j.jcat.2015.08.004.
- [421] S.Y. Joshi, A. Kumar, K. Kamasamudram, N.W. Currier, Diagnostic of Zeolite-based SCR catalyst deactivation modes using NO oxidation as a probe reaction, 1 (2012) 47201.
- [422] S.A. Skarlis, D. Berthout, A. Nicolle, C. Dujardin, P. Granger, Multisite Modeling of NH<sub>3</sub> Adsorption and Desorption over Fe-ZSM5, (2012).
- [423] M. Li, Y. Yeom, E. Weitz, W.M.H. Sachtler, Possible reasons for the superior performance of zeolite-based catalysts in the reduction of nitrogen oxides, *J. Catal.* 235 (2005) 201–208. doi:https://doi.org/10.1016/j.jcat.2005.06.022.
- [424] M. Iwasaki, H. Shinjoh, A comparative study of “standard”, “fast” and “NO<sub>2</sub>” SCR reactions over Fe/zeolite catalyst, *Appl. Catal. A Gen.* 390 (2010) 71–77. doi:https://doi.org/10.1016/j.apcata.2010.09.034.
- [425] F. Gao, M. Kollar, K. RK, W. NM, W. YL, J. Szanyi, P. CHF, M. Kollár, R.K. Kukkadapu, N.M. Washton, Y. Wang, J. Szanyi, C.H.F. Peden, M. Kollar, K. RK, W. NM, W. YL, J. Szanyi, P. CHF, M. Kollár, R.K. Kukkadapu, N.M. Washton, Y. Wang, J. Szanyi, C.H.F. Peden, M. Kollar, K. RK, W. NM, W. YL, J. Szanyi, P. CHF, Fe/SSZ-13 as an NH<sub>3</sub>-SCR catalyst: A reaction kinetics and FTIR/Mössbauer spectroscopic study, *Appl. Catal. B Environ.* 164 (2015) 407–419. doi:10.1016/j.apcatb.2014.09.031.



- [426] F. Gao, M. Kollar, K. RK, W. NM, W. YL, J. Szanyi, P. CHF, Fe/SSZ-13 as an NH<sub>3</sub>-SCR catalyst: A reaction kinetics and FTIR/Mossbauer spectroscopic study, *Appl. Catal. B Environ.* 164 (2015) 407–419. doi:10.1016/j.apcatb.2014.09.031.
- [427] Y. Cheng, J. Hoard, C. Lambert, J.H. Kwak, C.H.F. Peden, NMR studies of Cu/zeolite SCR catalysts hydrothermally aged with urea, *Catal. Today.* 136 (2008) 34–39. doi:10.1016/j.cattod.2008.01.019.
- [428] S.J. Schmieg, S.H. Oh, C.H. Kim, D.B. Brown, J.H. Lee, C.H.F. Peden, D.H. Kim, Thermal durability of Cu-CHA NH<sub>3</sub>-SCR catalysts for diesel NO<sub>x</sub> reduction, *Catal. Today.* 184 (2012) 252–261. doi:10.1016/j.cattod.2011.10.034.
- [429] T.L.P. Dantas, F.M.T. Luna, I.J. Silva Jr, A.E.B. Torres, D.C.S. de Azevedo, A.E. Rodrigues, R.F.P.M. Moreira, Modeling of the fixed - bed adsorption of carbon dioxide and a carbon dioxide - nitrogen mixture on zeolite 13X, *Brazilian J. Chem. Eng.* 28 (2011) 533–544. doi:doi.org/10.1590/S0104.
- [430] J.A.C. Silva, A.E. Rodrigues, Fixed-Bed Adsorption of n-Pentane/Isopentane Mixtures in Pellets of 5A Zeolite, *Ind. Eng. Chem. Res.* 36 (1997) 3769–3777. doi:10.1021/ie9701581.
- [431] F. Benyahia, K.E. O'Neill, Enhanced Voidage Correlations for Packed Beds of Various Particle Shapes and Sizes, *Part. Sci. Technol.* 23 (2005) 169–177. doi:10.1080/02726350590922242.
- [432] H. Sjövall, R.J. Blint, A. Gopinath, L. Olsson, A Kinetic Model for the Selective Catalytic Reduction of NO<sub>x</sub> with NH<sub>3</sub> over an Fe-zeolite Catalyst, *Ind. Eng. Chem. Res.* 49 (2010) 39–52. doi:10.1021/ie9003464.
- [433] C. Hahn, S. Füger, M. Endisch, A. Pacher, S. Kureti, Kinetic Modelling of the Adsorption and Desorption of NH<sub>3</sub> on Fe/BEA Zeolite, *Zeitschrift Für Phys. Chemie.* 229 (2015) 739–757. doi:10.1515/zpch-2014-0607.
- [434] J. Ammann, B. Michel, P.W. Ruch, Characterization of transport limitations in SAPO-34 adsorbent coatings for adsorption heat pumps, *Int. J. Heat Mass Transf.* 129 (2019) 18–27. doi:https://doi.org/10.1016/j.ijheatmasstransfer.2018.09.053.
- [435] J. Villermaux, Génie de la réaction chimique: conception et fonctionnement des réacteurs, Tec & Doc, 1993. <https://books.google.fr/books?id=e7GmAAAACAAJ>.
- [436] M.F. Edwards, J.F. Richardson, Gas dispersion in packed beds, *Chem. Eng. Sci.* 23 (1968) 109–123. doi:https://doi.org/10.1016/0009-2509(68)87056-3.
- [437] H. Petersen, The properties of helium: density, specific heats, viscosity, and thermal conductivity [sic] at pressures from 1 to 100 bar and from room temperatur, 6 Jellerups Boghandel. (1970) 1–42.
- [438] B.E. Poling, J.M. Prausnitz, J.P. O'Connell, The Properties of Gases and Liquids ISBN 0-07-0, 2001. doi:10.1036/0070116822.
- [439] P. Trambouze, J.-P. Euzen, Les réacteurs chimiques de la conception à la mise en œuvre, Technip, 2002.
- [440] D.M. Ruthven, Principles of adsorption & adsorption processes, *AIChE J.* 31 (1985) 523–524. doi:10.1002/aic.690310335.
- [441] R. Krishna, J.A. Wesselingh, The Maxwell-Stefan approach to mass transfer, *Chem. Eng. Sci.* 52 (1997) 861–911. doi:https://doi.org/10.1016/S0009-2509(96)00458-7.
- [442] R. Krishna, A unified approach to the modelling of intraparticle diffusion in adsorption processes, *Gas Sep. Purif.* 7 (1993) 91–104. doi:https://doi.org/10.1016/0950-4214(93)85006-H.
- [443] R. Krishna, Multicomponent surface diffusion of adsorbed species: a description based on the generalized Maxwell—Stefan equations, *Chem. Eng. Sci.* 45 (1990) 1779–1791. doi:https://doi.org/10.1016/0009-2509(90)87055-W.
- [444] F. Kapteijn, J.A. Moulijn, R. Krishna, The generalized Maxwell—Stefan model for diffusion in zeolites:: sorbate molecules with different saturation loadings, *Chem. Eng. Sci.* 55 (2000) 2923–2930. doi:https://doi.org/10.1016/S0009-2509(99)00564-3.
- [445] S. Song, F. Gao, Y. Zhang, X. Li, M. Zhou, B. Wang, R. Zhou, Preparation of SSZ-13 membranes with enhanced fluxes using asymmetric alumina supports for N<sub>2</sub>/CH<sub>4</sub> and CO<sub>2</sub>/CH<sub>4</sub> separations, *Sep. Purif. Technol.* 209 (2019) 946–954. doi:https://doi.org/10.1016/j.seppur.2018.09.016.

- [446] R. Krishna, A Maxwell-Stefan-Glueckauf description of transient mixture uptake in microporous adsorbents, *Sep. Purif. Technol.* 191 (2018) 392–399. doi:<https://doi.org/10.1016/j.seppur.2017.09.057>.
- [447] E. Glueckauf, J.I. Coates, 241. Theory of chromatography. Part IV. The influence of incomplete equilibrium on the front boundary of chromatograms and on the effectiveness of separation, *J. Chem. Soc.* (1947) 1315–1321. doi:10.1039/JR9470001315.
- [448] D.H. Kim, Linear Driving Force Formulas for Unsteady-State Diffusion and Reaction in Slab, Cylinder and Sphere Catalyst, *AIChE J.* 55 (2009) 1–6. doi:10.1002/aic.11702.
- [449] S. Sircar, J.R. Hufton, Why does the linear driving force model for adsorption kinetics work?, *Adsorption*. 6 (2000) 137–147. doi:10.1023/A:1008965317983.
- [450] M.H. Chahbani, D. Tondeur, Mass transfer kinetics in pressure swing adsorption, *Sep. Purif. Technol.* 20 (2000) 185–196. doi:[https://doi.org/10.1016/S1383-5866\(00\)00108-8](https://doi.org/10.1016/S1383-5866(00)00108-8).
- [451] A. Rita, M. Prates, S. Prof, F. Gomes, R. Ist, D.B. Ifpen, NH<sub>3</sub> adsorption / desorption modeling in a fixed bed reactor, (2014).
- [452] D. Schweich, *Génie de la réaction chimique*, n.d.
- [453] D. Kunii, O. Levenspiel, Fluidization Engineering, in: D. Kunii, O.B.T.-F.E. (Second E. Levenspiel (Eds.)), 2nd ed., Butterworth-Heinemann, Boston, 1991: p. 491. doi:<https://doi.org/10.1016/B978-0-08-050664-7.50017-2>.
- [454] P.S. Metkar, V. Balakotaiah, M.P. Harold, Experimental study of mass transfer limitations in Fe- and Cu-zeolite-based NH<sub>3</sub>-SCR monolithic catalysts, *Chem. Eng. Sci.* 66 (2011) 5192–5203. doi:10.1016/j.ces.2011.07.014.
- [455] S. Kolitcheff, E. Jolimaitre, A. Hugon, J. Verstraete, M. Rivallan, P. Carrette, F. Couenne, M. Tayakout-fayolle, Catalysis Science & Technology Tortuosity and mass transfer limitations in industrial hydrotreating catalysts : effect of particle shape and size distribution †, (2018). doi:10.1039/c8cy00831k.
- [456] A. Pant, S.J. Schmieg, Kinetic Model of NO<sub>x</sub> SCR Using Urea on Commercial Cu À Zeolite Catalyst, (2011) 5490–5498.
- [457] H. Sjövall, R.J. Blint, L. Olsson, Detailed Kinetic Modeling of NH<sub>3</sub> and H<sub>2</sub>O Adsorption, and NH<sub>3</sub> Oxidation over Cu-ZSM-5, *J. Phys. Chem. C.* 113 (2009) 1393–1405. doi:10.1021/jp802449s.
- [458] R. Krishna, Diffusion in porous crystalline materials, *Chem. Soc. Rev.* 41 (2012) 3099–3118. doi:10.1039/c2cs15284c.
- [459] X. Auvray, W. Partridge, J. Choi, J. Pihl, F. Coehlo, A. Yezerets, K. Kamasamudram, N. Currier, L. Olsson, Applied Catalysis B : Environmental Kinetic modeling of NH<sub>3</sub>-SCR over a supported Cu zeolite catalyst using axial species distribution measurements, "Applied Catal. B, Environ. 163 (2015) 393–403. doi:10.1016/j.apcatb.2014.08.003.
- [460] Mathworks, Help topic : ode15i, (n.d.). <https://fr.mathworks.com/help/matlab/ref/ode15i.html> (accessed July 10, 2019).
- [461] Mathworks, Help topic : lsqnonlin, (n.d.). <https://fr.mathworks.com/help/optim/ug/lsgnonlin.html> (accessed July 10, 2019).
- [462] R.J. Gorte, What do we know about the acidity of solid acids ? \*, 62 (1999) 1–13.
- [463] A. Buchholz, W. Wang, M. Xu, A. Arnold, M. Hunger, Sequential Steps of Ammoniation of the Microporous Silicoaluminophosphates H-SAPO-34 and H-SAPO-37 Investigated by In Situ CF MAS NMR Spectroscopy, *J. Phys. Chem. B.* 108 (2004) 3107–3113. doi:10.1021/jp030249d.
- [464] L. Lietti, I. Nova, P. Forzatti, Selective catalytic reduction ( SCR ) of NO by NH<sub>3</sub> over TiO<sub>2</sub>-supported V<sub>2</sub>O<sub>5</sub> – WO<sub>3</sub> and V<sub>2</sub>O<sub>5</sub> – MoO<sub>3</sub> catalysts, 12 (2000) 111–122.
- [465] W.B. Williamson, D.R. Flentge, J.H. Lunsford, Ammonia oxidation over Cu(II)NaY zeolites, *J. Catal.* 37 (1975) 258–266. doi:[https://doi.org/10.1016/0021-9517\(75\)90160-8](https://doi.org/10.1016/0021-9517(75)90160-8).
- [466] G. Delahay, S. Kieger, B. Neveu, B. Coq, Origine de N<sub>2</sub>O en réduction de NO par NH<sub>3</sub> sur Cu-zéolithes, *Comptes Rendus l'Académie Des Sci. - Ser. IIC - Chem.* 1 (1998) 229–235.

doi:[https://doi.org/10.1016/S1387-1609\(98\)80039-X](https://doi.org/10.1016/S1387-1609(98)80039-X).

- [467] J.H. Kwak, R.G. Tonkyn, D.H. Kim, J. Szanyi, C.H.F. Peden, Excellent activity and selectivity of Cu-SSZ-13 in the selective catalytic reduction of NO<sub>x</sub> with NH<sub>3</sub>, *J. Catal.* 275 (2010) 187–190. doi:<https://doi.org/10.1016/j.jcat.2010.07.031>.
- [468] J.H. Kwak, D. Tran, S.D. Burton, J. Szanyi, J.H. Lee, C.H.F. Peden, Effects of hydrothermal aging on NH<sub>3</sub>-SCR reaction over Cu/zeolites, *J. Catal.* 287 (2012) 203–209. doi:<https://doi.org/10.1016/j.jcat.2011.12.025>.
- [469] L. Chen, T.V.W. Janssens, M. Skoglundh, H. Grönbeck, Interpretation of NH<sub>3</sub>-TPD Profiles from Cu-CHA Using First-Principles Calculations, *Top. Catal.* 62 (2019) 93–99. doi:10.1007/s11244-018-1095-y.
- [470] L. Olsson, H. Sjövall, R.J. Blint, A kinetic model for ammonia selective catalytic reduction over Cu-ZSM-5, *Appl. Catal. B Environ.* 81 (2008) 203–217. doi:10.1016/j.apcatb.2007.12.011.
- [471] M. Valdez Lancinha Pereira, A. Nicolle, D. Berthout, Hydrothermal aging effects on Cu-zeolite NH<sub>3</sub>-SCR catalyst, *Catal. Today.* 258 (2015) 424–431. doi:10.1016/j.cattod.2015.03.027.
- [472] M. Fischer, Water adsorption in SAPO-34: Elucidating the role of local heterogeneities and defects using dispersion-corrected DFT calculations, *Phys. Chem. Chem. Phys.* 17 (2015) 25260–25271. doi:10.1039/c5cp04189a.
- [473] Y. Luo, H.H. Funke, J.L. Falconer, R.D. Noble, Adsorption of CO<sub>2</sub>, CH<sub>4</sub>, C<sub>3</sub>H<sub>8</sub>, and H<sub>2</sub>O in SSZ-13, SAPO-34, and T-Type Zeolites, *Ind. Eng. Chem. Res.* 55 (2016) 9749–9757. doi:10.1021/acs.iecr.6b02034.
- [474] S. Suárez, S.M. Jung, P. Avila, P. Grange, J. Blanco, Influence of NH<sub>3</sub> and NO oxidation on the SCR reaction mechanism on copper/nickel and vanadium oxide catalysts supported on alumina and titania, *Catal. Today.* 75 (2002) 331–338. doi:[https://doi.org/10.1016/S0920-5861\(02\)00055-X](https://doi.org/10.1016/S0920-5861(02)00055-X).
- [475] I. Nova, C. Ciardelli, E. Tronconi, D. Chatterjee, B. Bandl-Konrad, NH<sub>3</sub>-NO/NO<sub>2</sub> chemistry over V-based catalysts and its role in the mechanism of the Fast SCR reaction, *Catal. Today.* 114 (2006) 3–12. doi:<https://doi.org/10.1016/j.cattod.2006.02.012>.
- [476] J. Wang, Y. Huang, T. Yu, S. Zhu, M. Shen, W. Li, J. Wang, The migration of Cu species over Cu-SAPO-34 and its effect on NH<sub>3</sub> oxidation at high temperature, *Catal. Sci. Technol.* 4 (2014) 3004–3012. doi:10.1039/C4CY00451E.
- [477] M.P. Ruggeri, T. Selleri, I. Nova, E. Tronconi, J.A. Pihl, T.J. Toops, W.P. Partridge, New Mechanistic Insights in the NH<sub>3</sub>-SCR Reactions at Low Temperature, *Top. Catal.* 59 (2016) 907–912. doi:10.1007/s11244-016-0567-1.
- [478] A.R. Fahami, I. Nova, E. Tronconi, A kinetic modeling study of NO oxidation over a commercial Cu-CHA SCR catalyst for diesel exhaust aftertreatment, *Catal. Today.* 297 (2017) 10–16. doi:10.1016/j.cattod.2017.05.098.
- [479] J. Cheng, S. Han, Q. Ye, S. Cheng, T. Kang, H. Dai, Effects of hydrothermal aging at high and low temperatures on the selective catalytic reduction of NO<sub>x</sub> with NH<sub>3</sub> over Cu/SAPO-34, *Res. Chem. Intermed.* 45 (2019) 2023–2044. doi:10.1007/s11164-018-03712-0.
- [480] M. Colombo, I. Nova, E. Tronconi, NO<sub>2</sub> adsorption on Fe- and Cu-zeolite catalysts: The effect of the catalyst red-ox state, *Appl. Catal. B Environ.* 111–112 (2012) 433–444. doi:10.1016/j.apcatb.2011.10.031.
- [481] I. Nova, M. Colombo, E. Tronconi, Kinetic Modeling of Dynamic Aspects of the Standard NH<sub>3</sub>-SCR Reaction Over V<sub>2</sub>O<sub>5</sub>-WO<sub>3</sub>/TiO<sub>2</sub> and Fe-Zeolite Commercial Catalysts for the Aftertreatment of Diesel Engines Exhausts, *Oil Gas Sci. Technol. – Rev. d'IFP Energies Nouv.* 66 (2011) 681–691. doi:10.2516/ogst/2011132.
- [482] A. Rasmuson, B. Andersson, L. Olsson, R. Andersson, *Mathematical Modeling in Chemical Engineering*, Cambridge University Press, Cambridge, 2014. doi:DOI: 10.1017/CBO9781107279124.
- [483] Y. Jangjou, M. Ali, Q. Chang, D. Wang, J. Li, A. Kumar, W.S. Epling, Effect of SO<sub>2</sub> on NH<sub>3</sub> oxidation over a Cu-SAPO-34 SCR catalyst, *Catal. Sci. Technol.* 6 (2016) 2679–2685. doi:10.1039/C5CY02212F.
- [484] W.R.O. for Europe, *Evolution of WHO air quality guidelines: past, present and future*, Copenhagen, 2017.
- [485] L.P. P. Capros, N. Tasios, A. DeVita, L. Mantzos, Technical report accompanying the analysis of options to

move beyond 20 % GHG emission reduction in the EU by 2020 : Member State results, (2012).

- [486] E. Borfecchia, P. Beato, S. Svelle, U. Olsbye, C. Lamberti, S. Bordiga, Cu-CHA-a model system for applied selective redox catalysis, *Chem. Soc. Rev.* 47 (2018) 8097–8133. doi:10.1039/c8cs00373d.

## Annexes II

### Annexes II-1. Materials and Methods : DRIFT

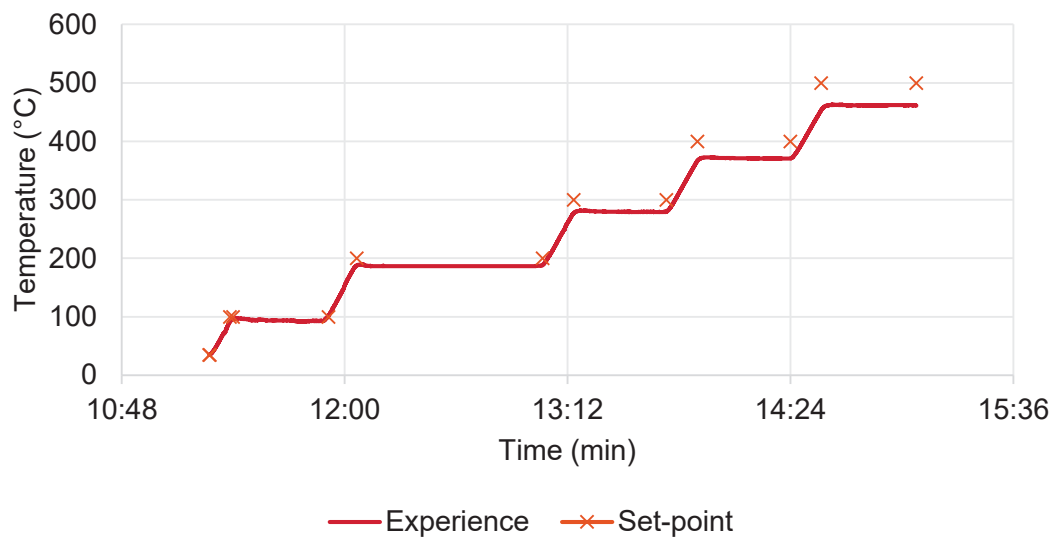


Figure II-1. Deviation between set-point temperature and catalyst bed in DRIFT Cell ( $10^{\circ}\text{C}\cdot\text{min}^{-1}$  ramp each and 30 min isothermal step (60 min for  $200^{\circ}\text{C}$ )).

## Annexes III

### Annexes III-1. H-SAPO-34 and H-SAPO-34-COM Textural properties

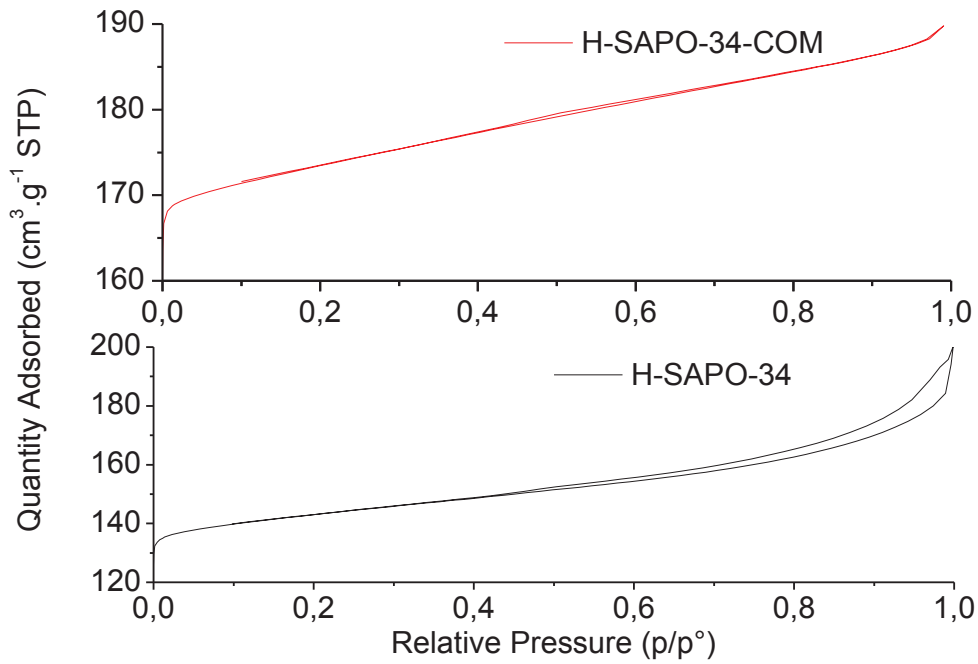


Figure III-1 . Nitrogen adsorption-desorption isotherm of laboratory made and commercial support SAPO-34

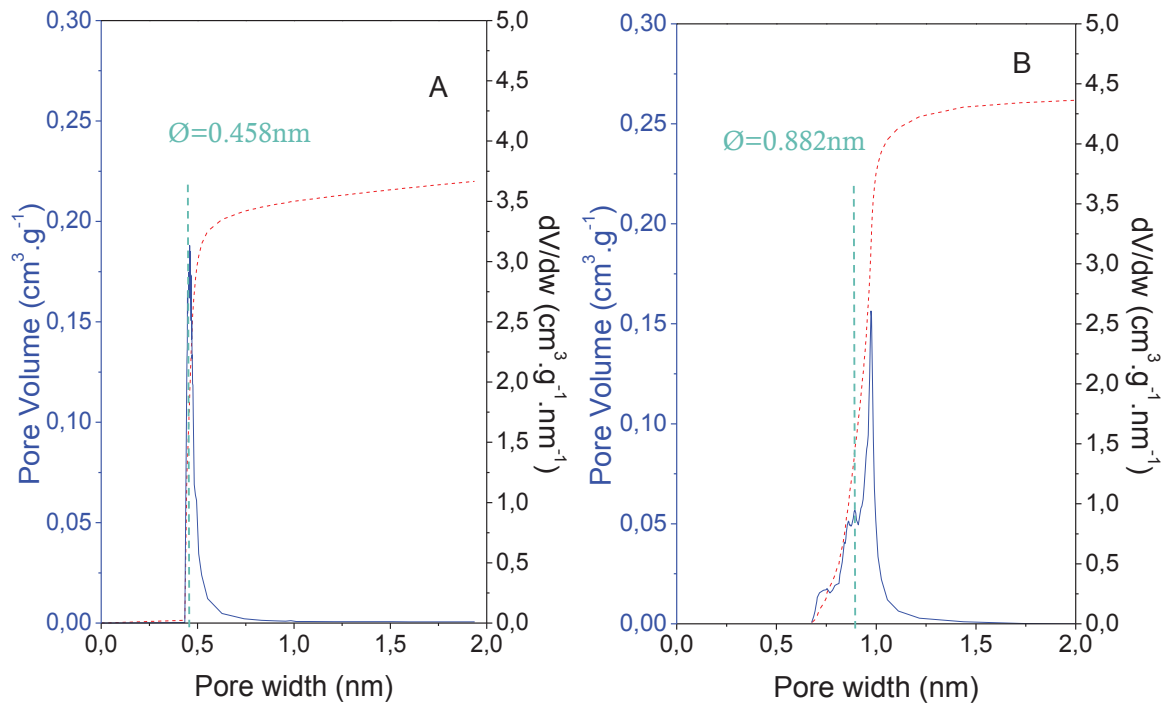


Figure III-2. Pore size distribution according with HK model of H-SAPO-34 (A) and H-SAPO-34-COM (B) supports

## Annexes IV

*Annexes IV-1: Textural properties of prepared support and catalysts*

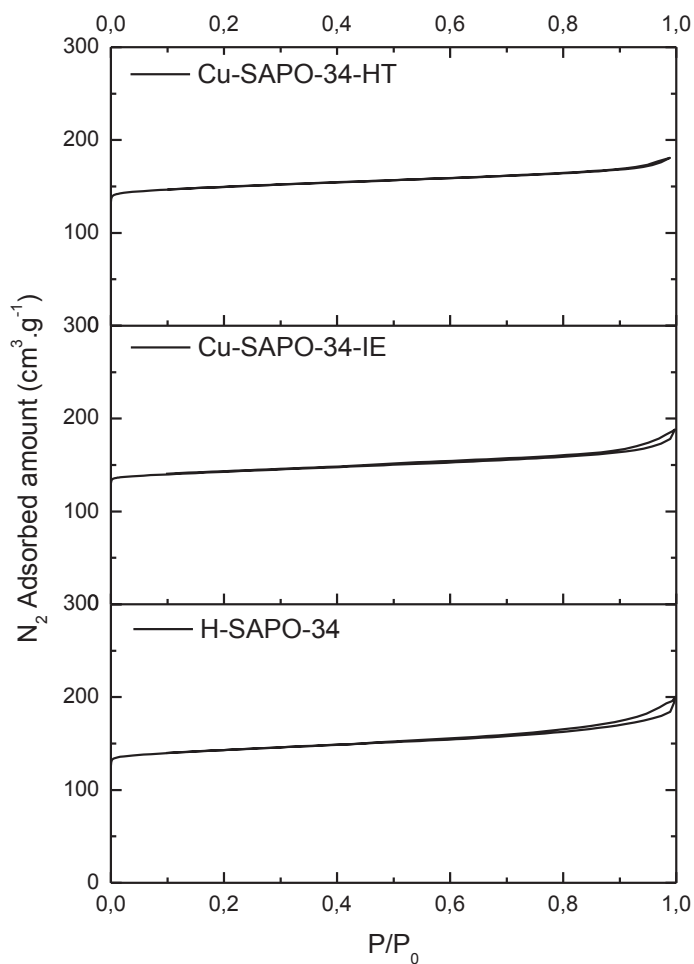


Figure IV-1. N<sub>2</sub> adsorption/desorption isotherm of H-SAPO-34 support, Cu-SAPO-34-IE and -HT catalysts for comparison

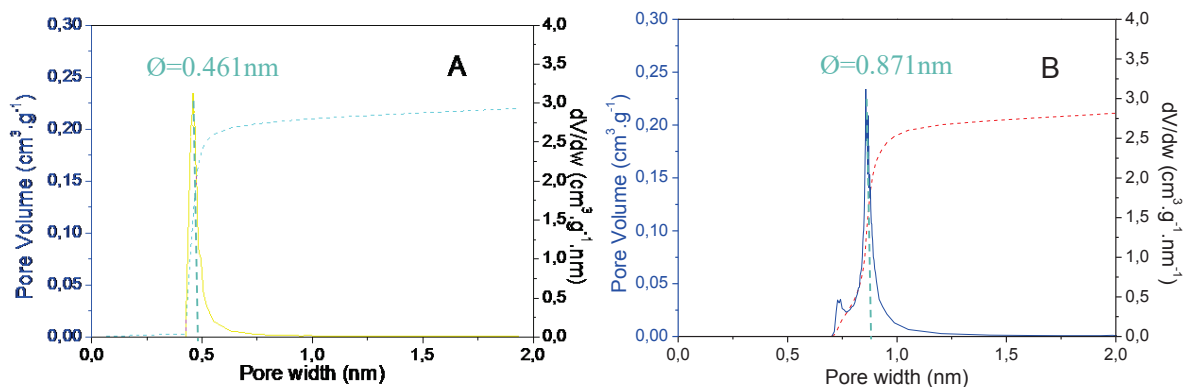


Figure IV-2. Pore size distribution according with HK model of Cu-SAPO-34-IE (A) and Cu-SAPO-34-HT (B)

## Annexes V

### Annexes V-1: Catalyst stability verification

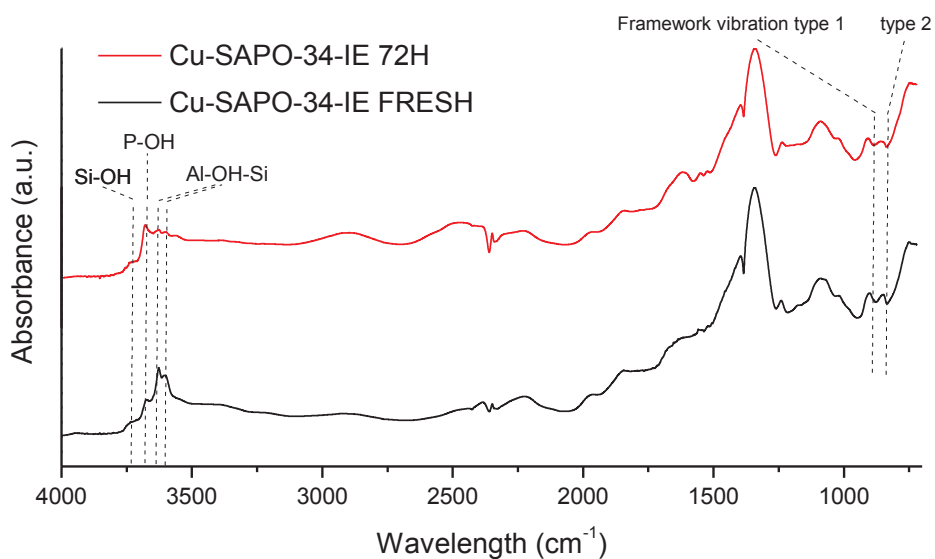


Figure V-1. Ex-situ Drift comparison between fresh and used (72h STD SCR) reference Cu-SAPO-34-IE



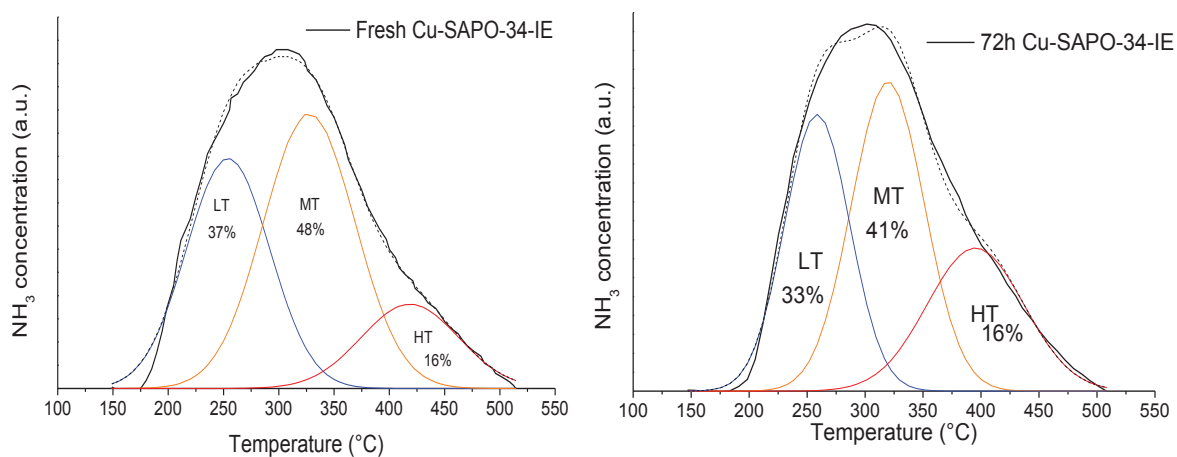


Figure V-2.  $\text{NH}_3$  TPD desorption profiles of Fresh and used during 72h of STD SCR conditions Cu-SAPO-34-IE. The profiles were recorded during a  $2^\circ\text{C}\cdot\text{min}^{-1}$  temperature ramp from  $200^\circ\text{C}$  to  $500^\circ\text{C}$  after adsorption at  $150^\circ\text{C}$  of 1000 ppm  $\text{NH}_3$

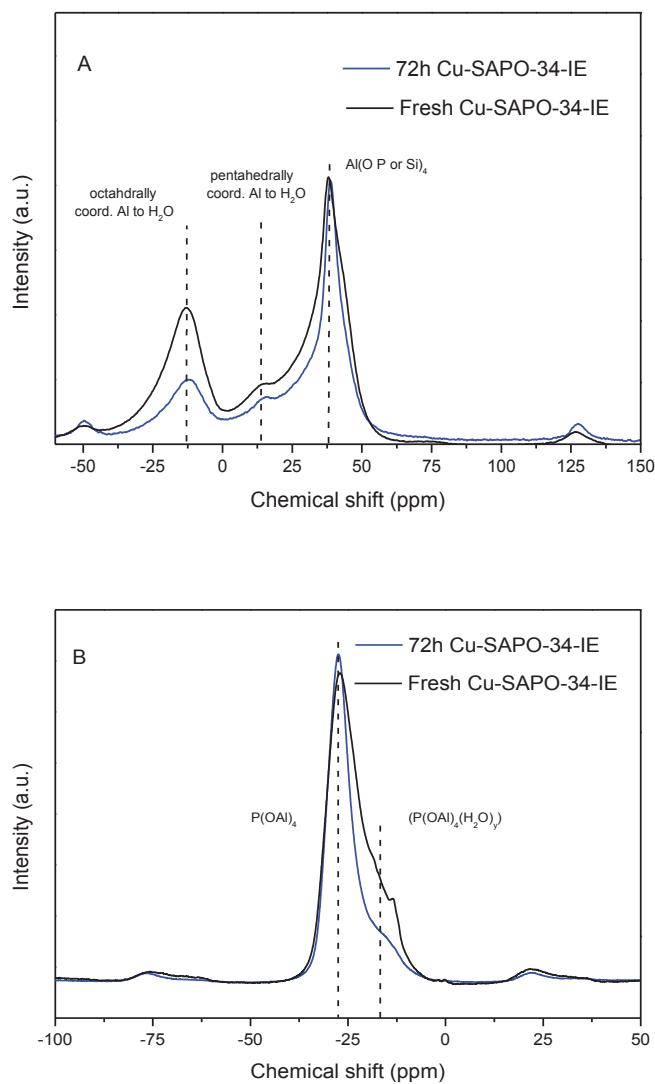


Figure V-3. Solid state MAS NMR spectra of  $^{27}\text{Al}$  (A) and  $^{31}\text{P}$  (B) of fresh and used 72h under STD SCR operating conditions Cu-SAPO-34-IE

Annexes V-2. Sequenced In-situ Drift Analysis

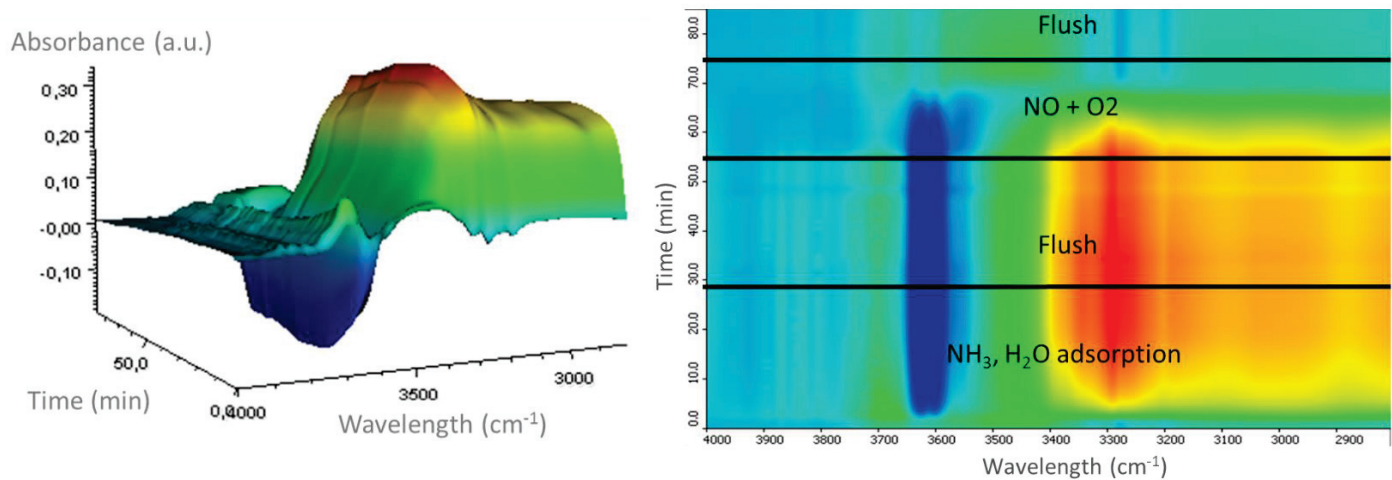


Figure V-4. Time resolved In-situ DRIFT analysis at 300°C in Bronsted acid sites range

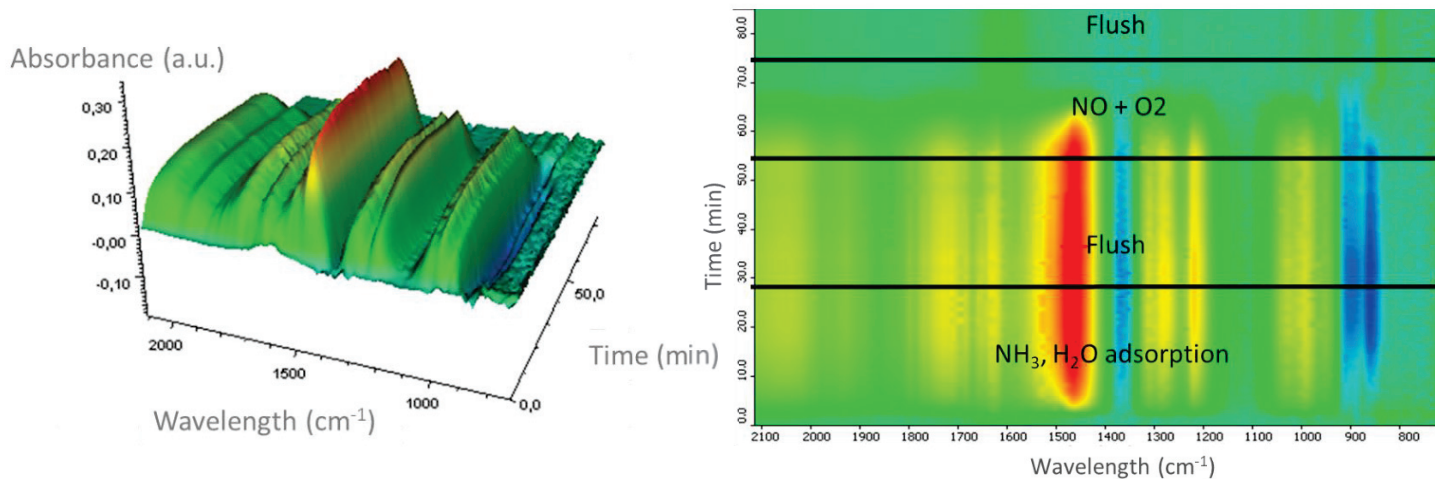


Figure V-5. Time resolved In-situ DRIFT analysis at 300°C in Lewis acid sites range

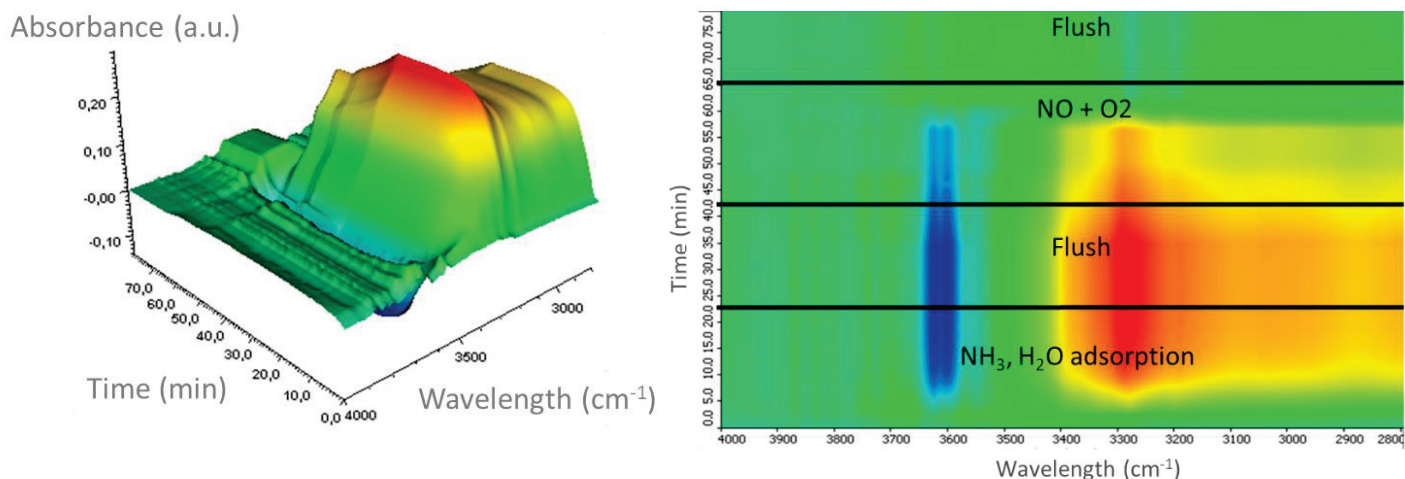


Figure V-6. Time resolved In-situ DRIFT analysis at 400°C in Bronsted acid sites range

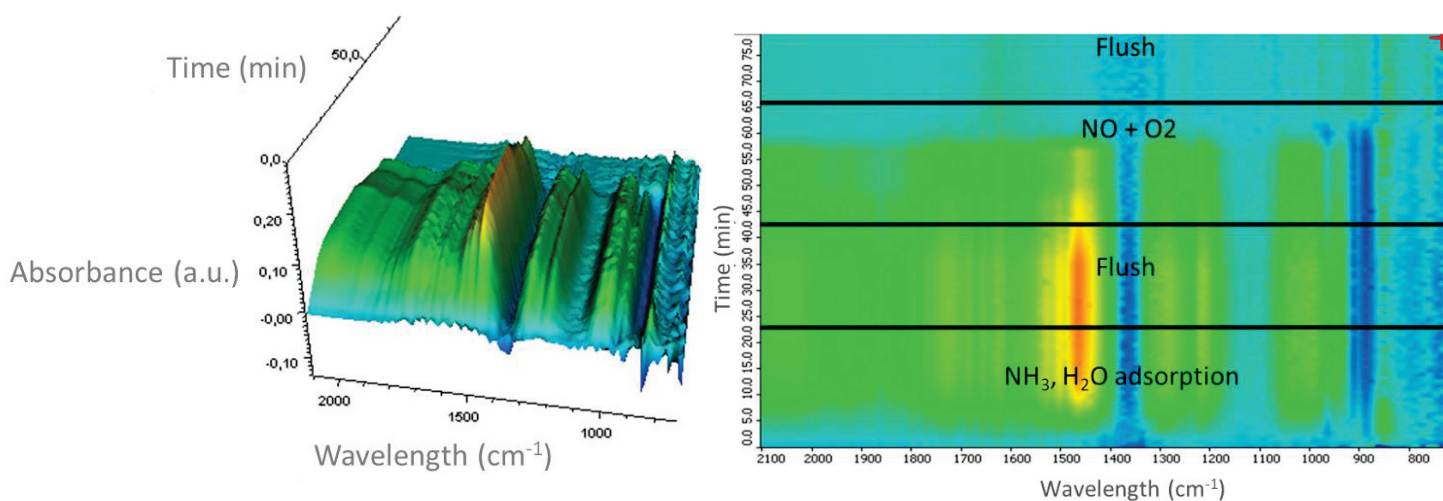


Figure V-7. Time resolved In-situ DRIFT analysis at 400°C in Lewis acid sites range

## Annexes VI

### Annexes VI. STD SCR relative enthalpies

In typical conditions of standard SCR reaction (constant pressure 1atm), with He as dilutive gas and  $Q_{tot} = 160 \text{ ml} \cdot \text{min}^{-1}$ , a  $50^\circ\text{C}$  variation applied by the furnace would imply a thermal power generation of 80 mW through the fluid ( $\dot{Q} = \rho C_p \Delta T$ ), according with He density<sup>620K</sup> =  $0.078 \text{ kg} \cdot \text{m}^{-3}$  and He  $C_p = 3160 \text{ J} \cdot \text{K}^{-1} \cdot \text{kg}^{-1}$  [438]. On the other hand, the consumption of 500 ppm of  $\text{NO}_x$  according to the calculated STD SCR enthalpy of reaction below, would produces four times less energy than the one brought by the fluid. Different enthalpies of reaction are reported in Table VI-1-A, according with the literature [98].

Supplementary Materials

Moreover, regarding the typical low heat of NH<sub>3</sub> desorption from the surface ( $\Delta h_{des\ NH_3} = -120\ \text{kJ.mol}^{-1}$ ) [418], the corresponding thermal power can still be neglected regarding the one brought by the fluid. Finally, regarding the small dimensions of the cylindrical FPB (3 mm x 6 mm) compared to the larger furnace isothermal zone (10 cm x 20 cm), the temperature applied by the controlled furnace from 150°C to 500°C and further measured in the FPB, was assumed as the one on the catalyst surface. Therefore, the amount of heat stored by the FPB is assumed as negligible during the model construction.

Table VI-1. Specific Heats and enthalpies of reaction in gaseous media for global NH<sub>3</sub> SCR.

Exchanged through the reaction		Ref
NO Cp <sup>620K</sup> (J.K <sup>-1</sup> .kg <sup>-1</sup> ) <sup>a</sup>	1050	[438]
NH <sub>3</sub> Cp <sup>620K</sup> (J.K <sup>-1</sup> .kg <sup>-1</sup> ) <sup>a</sup>	3058	
O <sub>2</sub> Cp <sup>620K</sup> (J.K <sup>-1</sup> .kg <sup>-1</sup> ) <sup>a</sup>	1009	
H <sub>2</sub> O Cp <sup>620K</sup> (J.K <sup>-1</sup> .kg <sup>-1</sup> ) <sup>a</sup>	2034	
N <sub>2</sub> Cp <sup>620K</sup> (J.K <sup>-1</sup> .kg <sup>-1</sup> ) <sup>a</sup>	1082	
STD SCR $\Delta H_r^\circ(T=620K)$ (kJ.mol <sup>-1</sup> ) <sup>b</sup>	-325	[98]
FAST SCR $\Delta H_r^\circ(T=298K)$ (kJ.mol <sup>-1</sup> )	-378	
NO <sub>2</sub> SCR $\Delta H_r^\circ(T=298K)$ (kJ.mol <sup>-1</sup> )	-341	
NO oxidation $\Delta H_r^\circ(T=298K)$ (kJ.mol <sup>-1</sup> )	-57	
NH <sub>3</sub> oxidation $\Delta H_r^\circ(T=298K)$ (kJ.mol <sup>-1</sup> )	-312	

<sup>a</sup>Estimated through following correlation:  $Cp=1000(\alpha+\beta T+\gamma T^2+\delta T^3)/M_i$  with T the temperature (K) and  $\alpha, \beta, \gamma$  and  $\delta$  coefficient provided in [438] Tables and  $M_i$  the species molar mass (g.mol<sup>-1</sup>).

<sup>b</sup>Corresponding Enthalpy of reaction:  $\Delta H_r^\circ(T=620K) = \sum_i^n \mu_i \Delta H_{f,i}^o(298) + \int_{298}^{620} Cp_i^o dT$  with  $\mu_i$  the stoichiometric coefficients and  $\Delta H_{f,i}^o$  the formation enthalpy of specie i.

## Annexes VI. NO oxidation in gas phase

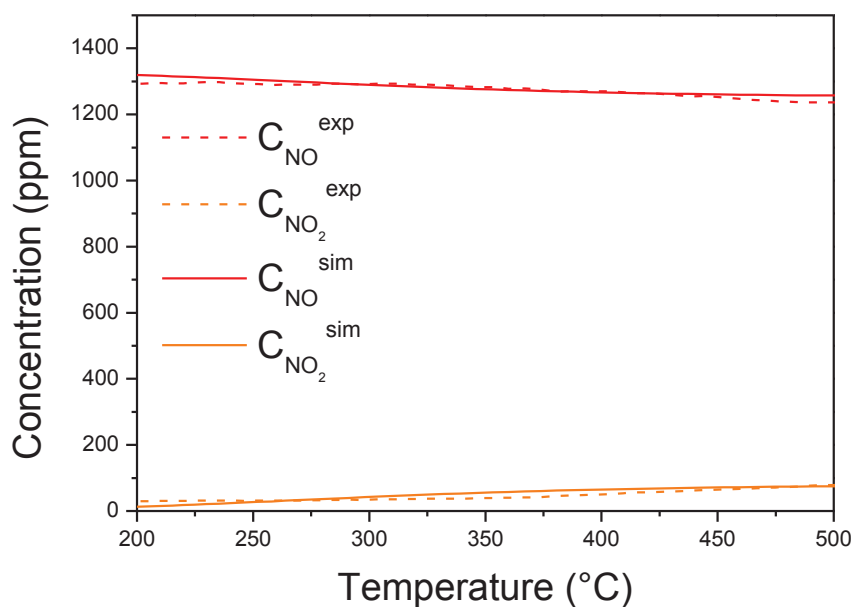


Figure. VI-2. NO oxidation reaction with simulated profiles evolution (A) in gas phase only, through decreasing ramp temperature (200-500°C). Inlet gas composition: *adsorption of 1000 ppm NO, 8% O<sub>2</sub>; 4% H<sub>2</sub>O and He as a balance between 200°C and 500°C with a total Flow of 10 L.h<sup>-1</sup>*

According to Fig. S1, the complete selectivity of NO oxidation reaction in NO<sub>2</sub> represent a low conversion rate (10%) in gas phase environment and was therefore taken into consideration for model construction. The simulated profiles were conducted regarding R7 reaction as defined during the kinetic model, with a determined  $E_{a_{r10}} = 55 \text{ kJ.mol}^{-1}$  and  $A_{r10} = 7.11.10^0 \text{ (m}^3.\text{mol}^{-1})^{0.5}.\text{s}^{-1}$ .

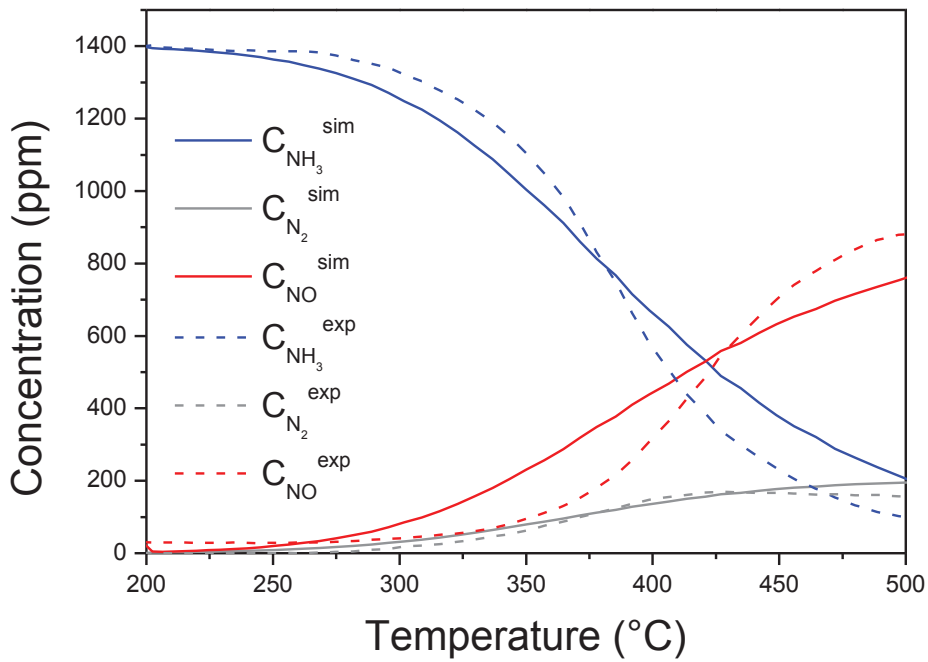
Annexes VI.  $\text{NH}_3$  oxidation in gas phase

Figure VI-3.  $\text{NH}_3$  oxidation reaction with simulated profiles evolution in gas phase only, through decreasing ramp temperature (200-500°C). Inlet gas composition: *adsorption of 1400 ppm  $\text{NH}_3$ , 8%  $\text{O}_2$ ; 4%  $\text{H}_2\text{O}$  and He as a balance between 200°C and 500°C with a total Flow of 10  $\text{L}\cdot\text{h}^{-1}$*

In a same objective as for NO oxidation role in SCR mechanism, the strong oxidation of  $\text{NH}_3$  in NO in phase gas was plug within the model reaction network for its potential impact on SCR reactions. The simulated profiles were performed thanks to the R11 reaction defined in the model with characteristic activation energy  $E_{a_{r17}} = 79 \text{ kJ}\cdot\text{mol}^{-1}$  with  $A_{r17} = 4.7 \cdot 10^7 (\text{m}^3 \cdot \text{mol}^{-1})^{0.5} \cdot \text{s}^{-1}$  and employed as initial parameter.

## Annexes VI. Characteristic time expressions

Table VI-2. Characteristic times expressions and corresponding variable modifications employed for investigations Figure VI-25

R	Characteristic time: i <sup>th</sup> site = 1,2,3,4	
1	$\tau_{ads,r1}^{Si} = \frac{1}{k_{ads,r1}^{Si}}$	$\tau_{des,r2}^{Si} = \frac{\Omega_{Si} \cdot \theta_{NH_3}^{Si}}{r_{2,des}^{Si}}$
2	$\tau_{ads,r3}^{Si} = \frac{1}{k_{ads,r3}^{Si}}$	$\tau_{des,r4}^{Si} = \frac{\Omega_{Si} \cdot \theta_{H_2O}^{Si}}{r_{4,des}^{Si}}$
R	Characteristic time: i <sup>th</sup> site = 3,4	
3	$\tau_{r5}^{Si} = \frac{C_{O_2}^{0.5} \cdot \theta_{Vacant}^{Si} \cdot \theta_{H_2O}^{Si} \cdot \Omega_{Si}^{0.5}}{r_5^{Si}}$	$\tau_{r6}^{Si} = \frac{\theta_{OH}^{Si^2} \cdot \Omega_{Si}^{0.5}}{r_6^{Si}}$
4	$\tau_{r7}^{Si} = \frac{\theta_{ONO}^{Si} \cdot \theta_{NH_3}^{Si} \cdot \Omega_{Si}}{r_7^{Si}}$	
5	$\tau_{r8}^{Si} = \frac{C_{O_2}^{0.5} \cdot \theta_{NH_3}^{Si} \cdot \Omega_{Si}^{0.5}}{r_8^{Si}}$	
6	$\tau_{r9}^{Si} = \frac{C_{O_2}^{0.5} \cdot \theta_{NH_3}^{Si} \cdot \Omega_{Si}^{0.5}}{r_9^{Si}}$	
7	$\tau_{r10}^{Si} = \frac{C_{NO,g}}{r_{10}}$	
8	$\tau_{r11}^{Si} = \frac{C_{NO_2} \cdot C_{NO_2} \cdot \theta_{NH_3}^{Si}}{r_{11}^{Si} \cdot \Omega_{Si}}$	
9	$\tau_{r12}^{Si} = \frac{1}{k_{r12}^{Si}}$	$\tau_{r13}^{Si} = \frac{1}{k_{r13}^{Si}}$
10	$\tau_{r14}^{Si} = \frac{C_{O_2}^{0.5} \cdot \theta_{ONO}^{Si} \cdot \theta_{H_2O}^{Si}}{r_{14}^{Si} \cdot \Omega_{Si}^{0.5}}$	$\tau_{r15}^{Si} = \frac{1}{k_{r15}^{Si}}$
11	$\tau_{r16}^{Si} = \frac{C_{NH_3,g}}{r_{16}}$	
12	$\tau_{r17}^{Si} = \frac{C_{O_2}^{0.5} \cdot \theta_{NH_3}^{Si} \cdot C_{NO}}{r_{17}^{Si} \cdot \Omega_{Si}^{0.5}}$	

## Annexes VI. Estimated Parameters corresponding to Cu-SAPO-34-IMP

Table VI-3. Set of Parameters estimated for Cu-SAPO-34-HT

Reaction	Reaction rate (mol.m <sup>-3</sup> .s <sup>-1</sup> )	Pre-exponential factor (k <sub>0</sub> )				
		S5	S3	S4	S1	S2
1	r <sub>1</sub>	0	0	0	0	0
	r <sub>2</sub>	3.44E+07	1.08E+07	1.06E+07	1.30E+07	6.88E+07
2	r <sub>3</sub>	0.00E+00	0.00E+00	0.00E+00	0.00E+00	0.00E+00
	r <sub>4</sub>	1.50E+05	1.50E+05	3.27E+04	5.29E+03	5.25E+03
3	r <sub>5</sub>	2.91E+08	1.50E+08	7.46E+06	-	-
	r <sub>6</sub>	5.86E+06	1.17E+06	1.46E+06	-	-
4	r <sub>7</sub>	4.55E+08	6.70E+06	1.32E+11	-	-
5	r <sub>8</sub>	1.13E+08	5.27E+07	2.51E+07	-	-
6	r <sub>9</sub>	1.12E+11	2.77E+08	8.86E+07	-	-
8	r <sub>11</sub>	1.63E+10	2.57E+13	6.39E+13	-	-
9	r <sub>12</sub>	1.18E+10	1.04E+08	1.39E+08	-	-
	r <sub>13</sub>	1.93E+08	8.25E+05	6.89E+06	-	-
10	r <sub>14</sub>	6.74E+10	4.58E+07	8.41E+09	-	-
	r <sub>15</sub>	3.79E+04	7.32E+04	6.47E+04	-	-
12	r <sub>17</sub>	1.58E+07	7.48E+04	1.17E+06	-	-
Reaction	Reaction rate (mol.m <sup>-3</sup> .s <sup>-1</sup> )	Activation energie Ea (J.mol <sup>-1</sup> )				
		S5	S3	S4	S1	S2
1	r <sub>1</sub>	7.92E+02	2.53E+02	7.52E+02	8.68E+01	1.78E+02
	r <sub>2</sub>	6.21E+04	1.06E+05	4.63E+04	7.55E+04	8.82E+04
2	r <sub>3</sub>	1.86E-02	5.38E-01	2.94E-01	7.00E-02	6.00E-02
	r <sub>4</sub>	9.95E+04	4.50E+04	4.50E+04	4.83E+04	5.56E+04
3	r <sub>5</sub>	4.54E+04	5.23E+04	5.22E+04	-	-
	r <sub>6</sub>	7.04E+04	3.02E+04	3.81E+04	-	-
4	r <sub>7</sub>	1.21E+05	5.85E+04	5.49E+04	-	-
5	r <sub>8</sub>	8.52E+04	1.06E+05	6.94E+04	-	-
6	r <sub>9</sub>	1.64E+05	1.58E+05	1.39E+05	-	-
8	r <sub>11</sub>	1.60E+05	1.10E+05	5.79E+04	-	-
9	r <sub>12</sub>	1.81E+05	3.78E+04	4.80E+04	-	-
	r <sub>13</sub>	1.15E+05	2.80E+04	4.75E+04	-	-
10	r <sub>14</sub>	3.79E+04	7.32E+04	6.47E+04	-	-
	r <sub>15</sub>	9.96E+04	3.31E+04	6.80E+04	-	-
12	r <sub>17</sub>	5.44E+04	2.69E+04	6.02E+04	-	-